



*The action of antimicrobial peptides on supported lipid bilayers investigated by biophysical methods*

**Stefania Piantavigna**

A thesis submitted to the Faculty of Science  
Monash University, in fulfilment of the  
requirements for the degree of  
**DOCTOR OF PHILOSOPHY**

School of Chemistry  
Monash University  
Clayton, Australia

May 2014

## **Copyright Notices**

### **Notice 1**

Under the Copyright Act 1968, this thesis must be used only under the normal conditions of scholarly fair dealing. In particular no results or conclusions should be extracted from it, nor should it be copied or closely paraphrased in whole or in part without the written consent of the author. Proper written acknowledgement should be made for any assistance obtained from this thesis.

**TABLE OF CONTENT**

**THE ACTION OF ANTIMICROBIAL PEPTIDES ON SUPPORTED LIPID BILAYERS INVESTIGATED BY BIOPHYSICAL METHODS ..... II**

**ABSTRACT..... II**

**ACKNOWLEDGEMENTS..... VI**

**ABBREVIATION LIST ..... VIII**

**ANTIMICROBIAL PEPTIDES: A GENERIC OVERVIEW ..... 2**

1 CLASSIFICATION..... 5

2 MECHANISM OF PEPTIDE ACTION ..... 8

    2.1 *Membrane disruption*..... 8

    2.2 *Intracellular targets*..... 12

3 METHOD OF INVESTIGATIONS..... 13

    3.1 *Studies with model membranes* ..... 13

4 BACTERIAL DEFENCE MECHANISM..... 16

5 APPLICATIONS OF AMPS ..... 16

6 CONCLUSIONS ..... 18

7 BIBLIOGRAPHY..... 20

**THE CELL MEMBRANE: NATURAL AND ARTIFICIAL..... 26**

1 INTRODUCTION ..... 26

    1.1 *Natural membranes: composition and organization*..... 27

        1.1.1 The membrane architecture..... 27

        1.1.2 The membrane components ..... 28

        1.1.3 Lipid composition in cell membranes ..... 28

        1.1.4 Cholesterol..... 30

    1.2 *The polymorphism of the membrane determines its physical and chemical properties*..... 32

        1.2.1 Phases..... 32

        1.2.2 The membrane curvature ..... 34

    1.3 *Artificial membranes*..... 36

        1.3.1 Liposomes ..... 37

        1.3.2 Supported lipid bilayers (SLBs)..... 39

## Table of content

2	TECHNIQUES.....	42
2.1	<i>Membrane properties studied using a Quartz crystal microbalance with dissipation monitoring (QCM-D).....</i>	42
2.1.1	<i>Osmotic pressure .....</i>	47
3	PAPER 1: .....	48
3.1	<i>Structure and homogeneity of pseudo-physiological phospholipid bilayers and their deposition characteristics on carboxylic acid terminated self-assembled monolayers. ....</i>	48
4	PAPER 2: .....	59
4.1	<i>QCM-D fingerprinting of membrane-active peptides.....</i>	59
5	SCANNING ELECTROCHEMICAL MICROSCOPY (SECM) .....	72
6	BIBLIOGRAPHY .....	75
<b>THE ACTION ON SLBS BY TWO LYTIC <math>\alpha</math>-HELICAL AMPS: MELITTIN AND MAGAININ 2.....</b>		<b>82</b>
1	INTRODUCTION.....	82
1.1	<i>Magainins .....</i>	82
1.2	<i>Melittin.....</i>	83
1.3	<i>Sequence of <math>\alpha</math>-helical AMPs .....</i>	83
1.3.1	<i>Hydrophobicity in magainin and melittin.....</i>	84
1.4	<i>Peptide conformation in lipid bilayers .....</i>	84
1.4.1	<i>Conformation in membrane of magainin and melittin .....</i>	85
1.5	<i>Mechanisms of <math>\alpha</math>-helical AMP action .....</i>	88
1.5.1	<i>The toroidal pore formation hypothesis for magainin .....</i>	89
1.5.2	<i>Structural variations: the disordered toroidal pore .....</i>	94
1.5.3	<i>Melittin: from barrel stave to toroidal pore .....</i>	95
1.6	<i>The role of the membrane in pore formation .....</i>	96
1.7	<i>The role of cholesterol.....</i>	98
1.8	<i>Aims 99</i>	
2	MATERIAL AND METHODS.....	101
2.1	<i>Peptides .....</i>	101
2.2	<i>Buffer preparation.....</i>	101
2.3	<i>Liposome preparation .....</i>	101
2.4	<i>Modification of QCM-D sensor chips.....</i>	102
2.5	<i>QCM-D experiments .....</i>	102

## Table of content

3	RESULTS .....	104
	3.1.1 Melittin and magainin 2 on DMPC artificial membranes .....	104
	3.1.2 Melittin.....	104
	3.1.3 Magainin 2.....	106
	3.1.4 A comparison between melittin and magainin 2: the $\Delta f$ - $\Delta D$ plots 107	
	3.2 <i>Melittin and magainin 2 on DMPC/DMPG (4:1) SLBs</i> .....	111
	3.2.1 Melittin.....	111
	3.2.2 Magainin 2.....	113
	3.2.3 A comparison between melittin and magainin 2: the $\Delta f$ - $\Delta D$ plots 114	
	3.3 <i>Melittin and magainin 2 on DMPC/DMPG (2:1) SLBs</i> .....	116
	3.3.1 Melittin.....	116
	3.3.2 Magainin 2.....	118
	3.3.3 Comparing the lytic action of melittin and magainin 2: the $\Delta f$ - $\Delta D$ plots 119	
	3.4 <i>Melittin and magainin 2 on DMPC/cholesterol SLBs</i> .....	121
	3.4.1 Melittin.....	121
	3.4.2 Magainin 2.....	123
	3.4.3 A comparison between melittin and magainin 2: the $\Delta f$ - $\Delta D$ plots 124	
4	DISCUSSION .....	128
	4.1 <i>Transition from toroidal pore to disruptive mechanism</i> .....	128
	4.1.1 Melittin: from the “pore-state” to a carpet mechanism .....	128
	4.1.2 The influence of the lipid phase on the peptide action.....	130
	4.1.3 The lipid affinity and mode of action function of the peptide structure 131	
	4.1.4 The influence of DMPG in a DMPC membrane .....	132
	4.2 <i>The influence of cholesterol on peptide action</i> .....	134
5	CONCLUSIONS .....	135
6	BIBLIOGRAPHY.....	137
	<b>PROLINE-RICH AMPS</b> .....	<b>144</b>
1	INTRODUCTION .....	144
	1.1 <i>Proline-rich peptides</i> .....	144

## Table of content

1.1.1	Examples of Pr-rich antimicrobial peptides.....	145
1.1.2	Apidaecin peptides.....	146
1.2	<i>The importance of proline.....</i>	147
1.3	<i>Intracellular activity.....</i>	149
1.3.1	Internalization.....	151
1.4	<i>Applications for Pr-rich AMPs.....</i>	152
1.5	<i>General outcomes for the Pr-AMPs investigated here.....</i>	153
2	PAPER 3:.....	154
2.1	<i>Cell Penetrating Apidaecin Peptide Interactions with Biomimetic Phospholipid Membranes.....</i>	154
3	PAPER 4:.....	165
3.1	<i>Api88 Is a Novel Antibacterial Designer Peptide To Treat Systemic Infections with Multidrug-Resistant Gram-Negative Pathogens.....</i>	165
4	PAPER 5:.....	179
4.1	<i>Oncocin (VDKPPYLPRPRPPRRIYNR-NH2): A Novel Antibacterial Peptide Optimized against Gram-Negative Human Pathogens.....</i>	179
5	BIBLIOGRAPHY:.....	190
<b>ARGININE-RICH PEPTIDES: THE TAT PEPTIDE, A CPP AND AMP.....</b>		<b>194</b>
1	INTRODUCTION.....	194
1.1.1	Cell penetrating peptides (CPPs).....	194
1.1.2	CPP Classification.....	195
1.1.3	Mechanism of CPPs uptake.....	198
1.1.4	Properties of the amino acid arginine.....	201
1.1.5	Applications: examples of CPPs as AMPs:.....	203
1.1.6	Papers included in this chapter.....	203
2	BIBLIOGRAPHY.....	205
3	PAPER 6:.....	209
3.1	<i>A mechanistic investigation of cell-penetrating Tat peptides with supported lipid membranes.....</i>	209
4	PAPER 7:.....	219
4.1	<i>Membrane perforation and passive translocation of Tat peptides.....</i>	219
<b>RUTHENOCENOYL MOIETY INCORPORATED IN SHORT TRYPTOPHAN AND ARGININE RICH PEPTIDES.....</b>		<b>238</b>
1	INTRODUCTION.....	238

## Table of content

1.1	<i>The benefits and disadvantages of synAMPs</i> .....	239
1.2	<i>The influence of Tryptophan</i> .....	240
1.2.1	Location in the membrane .....	240
1.2.2	Examples of Trp-Arg containing AMPs .....	242
1.2.3	Organometallic compounds as antibacterial agents .....	245
1.2.4	Ruthenocene .....	246
1.3	<i>Aims</i> .....	247
2	MATERIAL AND METHODS .....	248
2.1	<i>Peptides</i> .....	248
2.2	<i>Buffer preparation</i> .....	248
2.3	<i>Liposome preparation</i> .....	248
2.4	<i>Modification of QCM-D sensor chips</i> .....	249
2.5	<i>QCM-D experiments</i> .....	249
3	RESULTS .....	251
3.1	<i>In DMPC membranes</i> .....	251
3.1.1	(RW) <sub>3</sub> .....	251
3.1.2	RcCO-W(RW) <sub>2</sub> .....	252
3.1.3	Evaluation of $\Delta f$ - $\Delta D$ plots for DMPC .....	254
3.2	<i>The second addition of material at DMPC/DMPG (4:1)</i> .....	257
3.2.1	(RW) <sub>3</sub> .....	257
3.2.2	RcCO-W(RW) <sub>2</sub> .....	259
3.3	<i>The peptide interaction with DMPC/cholesterol</i> .....	260
3.3.1	(RW) <sub>3</sub> .....	260
3.3.2	RcCO-W(RW) <sub>2</sub> .....	262
3.3.3	$\Delta f$ - $\Delta D$ in DMPC/cholesterol .....	263
4	DISCUSSION .....	266
4.1	<i>The influence of Trp on the interaction with DMPC membranes</i> .....	266
4.2	<i>Secondary adsorption highlights the equilibrium, between two processes</i> ..	268
4.3	<i>The presence of a metallocene: the secondary addition in zwitterionic and negatively charged SLBs</i> .....	269
4.4	<i>Attempts to form pores in SLBs containing cholesterol</i> .....	269
5	CONCLUSIONS .....	271
6	BIBLIOGRAPHY .....	272

<b>DUAL BEHAVIOUR OF THE SELF-AGGREGATING AMP, UPERIN 3.5, ON SLBS .....</b>	<b>276</b>
1 INTRODUCTION.....	276
1.1 <i>Uperin 3.5</i> .....	276
1.2 <i>HDPs as amyloidogenic peptides</i> .....	277
1.3 <i>Amyloid structure</i> .....	279
1.3.1 The process of amyloid formation.....	279
1.4 <i>The role of the membrane in fibrillogenesis</i> .....	281
1.4.1 Permeabilisation of the membrane by the protofibrils .....	283
1.4.2 Factors that influence membrane activity .....	283
1.5 <i>Aims</i> 284	
2 MATERIALS AND METHODS.....	286
2.1 <i>Buffer preparation</i> .....	286
2.2 <i>Liposome preparation</i> .....	286
2.3 <i>Modification of QCM-D sensor chips</i> .....	287
2.4 <i>QCM-D experiments</i> .....	287
3 RESULTS.....	289
3.1 <i>Control of aggregation</i> .....	289
3.1.1 DMPC versus DMPC/ DMPG (4:1) SLBs .....	289
3.1.2 The role of cholesterol in DMPC membrane .....	294
4 DISCUSSION.....	298
4.1 <i>DMPC membranes</i> .....	298
4.1.1 The disruption mechanism .....	298
4.1.2 The “leaky slit model” .....	300
4.2 <i>DMPC/DMPG (4:1) artificial membranes</i> .....	301
4.3 <i>DMPC/Cholesterol</i> .....	302
5 CONCLUSIONS.....	303
6 APPENDIX:.....	305
6.1 <i>The action of U3.5 retro on DMPC artificial membranes</i> .....	305
7 BIBLIOGRAPHY .....	307
<b>CONCLUSIONS .....</b>	<b>312</b>
<b>APPENDICES.....</b>	<b>314</b>



## *Abstract*

The emergence of bacteria that have developed resistance towards “traditional” antibiotics is becoming a serious global health threat. Consequently, alternative approaches are needed to find new drugs that can act directly as antibiotics or to assist traditional drugs to improve efficacy. The emergence of antimicrobial peptides (AMPs) as a possible new class offers promise. AMPs represent a large and varied group of “natural antibiotics” present in virtually every organism. However, in order to develop new drugs derived from AMPs knowledge of the bioactivity of these is needed, such as concentration ranges and specific bacterial targets. Of great practical importance is to have a comprehensive understanding of the mechanism of action of AMPs, so that the risk of cross-reactivity and development of new bacterial resistance is minimised.

All AMPs interact with the cell membrane, which is a complex and dynamic system, mostly containing phospholipids and proteins. Phospholipids are not simple “bricks” of the membrane, but they themselves are involved in various cellular processes. Therefore, biomimetic membranes, e.g. supported lipid bilayers (SLBs), represent a valid approach for investigating the interactions between lipids and AMPs. Creation of a supported membrane reduces the complexity of those studies to just one variable. Many variables influence the formation of SLBs and a protocol regarding the formation of SLBs assembled on gold-coated sensors is described in **Paper 1**. The membrane deposition and the peptide-membrane interactions were investigated using a Quartz Crystal Microbalance with Dissipation monitoring (QCM-D) (**Paper 2**). Thus, the action of various peptides were investigated with zwitterionic membranes, which contained negatively charged lipid (bacterial membranes), or cholesterol (mammalian membranes).

The action of the two most widely studied AMPs, melittin and magainin 2, on SLBs, has been examined using QCM-D in **Chapter 3**. These peptides formed “toroidal pores”, which lead to membrane disruption. However, the action of these peptides has been found to be both concentration and composition dependent.

Many AMPs are enriched in a particular amino acid residue. The influence of several of these peptide residues has been investigated using QCM-D in **Chapters 4, 5 and 6**. The action of proline-rich peptides apidaecins HbI and HbII, the variant Api88 and oncocin peptides on SLBs, are illustrated in **Papers 3, 4 and 5**, respectively. These peptides were found to insert into the membrane without any evidence of disruption.

The influence of lipid composition on the activity of the arginine-rich peptide Tat has also been investigated with QCM together with scanning electrochemical microscopy (SECM) (**Chapter 5**). The cell-penetrating Tat peptide was shown to act as a lytic AMP in the presence of negatively charged membranes (**Papers 6 and 7**).

The addition of tryptophan residues in the sequence of a short arginine-rich peptide, (RW)<sub>3</sub>, caused a dramatic switch from cell penetrating to lytic activity, while the inclusion of ruthenocene in the peptide RcCO-W(RW)<sub>2</sub> did not affect the peptide activity (**Chapter 6**).

Finally, in **Chapter 7**, Uperin 3.5, an amyloid-like AMP, demonstrated that the amyloid fibrils are not necessary for the membrane-disruption. However, the action of Uperin 3.5 towards zwitterionic membranes is switched to insertion if cholesterol is present in the membrane.

Thus, QCM has been demonstrated to be an invaluable technique for characterising, in real time, the action of various peptides on SLBs of bacterial mimetic composition and mammalian. However, the combination of QCM with other techniques e.g. SECM, is always encouraged to reinforce this data and to gain a wide perspective of activity.

# Monash University

## Declaration for thesis based or partially based on conjointly published or unpublished work

### General Declaration

In accordance with Monash University Doctorate Regulation 17 Doctor of Philosophy and Research Master's regulations the following declarations are made:

I hereby declare that this thesis contains no material which has been accepted for the award of any other degree or diploma at any university or equivalent institution and that, to the best of my knowledge and belief, this thesis contains no material previously published or written by another person, except where due reference is made in the text of the thesis.

This thesis includes 7 original papers published in peer-reviewed journals and 1 unpublished publications; in addition, one published paper is included in the appendices and two unpublished publication. The core theme of the thesis is "The action of antimicrobial peptides on supported lipid bilayers investigated by biophysical methods". The ideas, development and writing up of all the papers in the thesis were the principal responsibility of me, the candidate, working within the School of Chemistry under the supervision of Lisa L. Martin and Adam Mechler.

The inclusion of co-authors reflects the fact that the work came from active collaboration between researchers and acknowledges input into team-based research. A portion of QCM-D experiments in Paper 1 was performed by Steven Heaton and Slavica Praporski and in paper 2 by Slavica Praporski and George Mc Cubbin. DLS experiment in paper 1 were performed by Steven Heaton and Slavica Praporski. SECM experiments in paper 7 were performed with the assistance of Muhammad Abdelhamid and so the analysis of the SECM data. The antimicrobial testing, dye leakage, fluorescence microscopy, hemolytic activity in papers 3, 4 and 5 were performed by Ralf Hoffmann's group

In all the papers, my contribution to the work involved the following: performing QCM experiments, some SECM experiments (paper 7), data analysis and interpretation of these experiments. Preparation of figures for manuscripts, contribution in writing and revise them

<b>Thesis chapter</b>	<b>Publication title</b>	<b>Publication status*</b>	<b>Nature and extent of candidate's contribution</b>
2	<i>Structure and homogeneity of pseudo-physiological phospholipid bilayers and their deposition characteristics on carboxylic acid terminated self-assembled monolayers</i>	<i>published</i>	20%
2	<i>QCM-D fingerprinting of membrane-active peptides</i>	<i>published</i>	20%
4	<i>Cell Penetrating Apidaecin Peptide Interactions with Biomimetic Phospholipid Membranes</i>	<i>published</i>	40%
4	<i>Api88 Is a Novel Antibacterial Designer Peptide To Treat Systemic Infections with Multidrug-Resistant Gram-Negative Pathogens</i>	<i>published</i>	10%
4	<i>Oncocin (VDKPPYLPRPRPPRRRIYNR-NH<sub>2</sub>): A Novel Antibacterial Peptide Optimized against Gram-Negative Human Pathogens</i>	<i>published</i>	30%
5	<i>A mechanistic investigation of cell-penetrating Tat peptides with supported lipid membranes</i>	<i>published</i>	40%
5	<i>Membrane perforation and passive translocation of Tat peptides</i>	<i>in preparation</i>	35%

[ \* For example, 'published' / 'in press' / 'accepted' / 'returned for revision' ]

I have renumbered sections of submitted or published papers in order to generate a consistent presentation within the thesis.

**Signed:** .....

**Date:** .....

## *Acknowledgements*

I have to thank all the people I meet during this long journey because they made me realize how important is the communication, the exchange of thoughts, ideas, which helped me to open to new perspectives, to see and understand sides of research under a new way to look at.

Firstly, I would like to thank my supervisors Assoc. Prof. Lisa Martin and Dr Adam Mechler for all their support and guidance throughout this “never ending” PhD. You had faith in me without really knowing my abilities and you are always being supportive since the first day I started my PhD, unaware of my pregnancy. Most important, I have learnt from you that research is teamwork and the organization is fundamental in science as in the normal life. Thanks to you, I learnt a lot during this journey and what I learnt I could also apply in other aspects of my life. Your enthusiasm, passion and hunger for new discoveries have always been very “contagious”. It has been a privilege having you as my mentors.

This thesis is the result of various collaborations around the “globe”; therefore, I would like to thank Prof. Ralf Hoffmann and his group. The peptides (and assistance) that he provided have been an important part of my project. Moreover, he will be my first employer after the submission of my PhD thesis.

I would like also to thank the other collaborators: Leone Spiccia, Anthony O’ Mullane, Chuan Zhao, Xiaohu Qu, Bim Graham, Bauke Albada and Annika Gross for providing peptides to work on and for their assistance.

An important thank for the enormous assistance, help, advises, friendship etc to Muhammad Abdelhamid. I have to say that this thesis could not be written without his big help. Thanks to Jinzhen Lu, Nguyen Vo for helping me during my writing. Of course, a big thank to the other members of the group past and present; in particular to Slavica Praporski, Rhiannon Jones, Sumay Ng and Marleen de Vej.

## *Acknowledgements*

The last but very important thank to Lakmali for looking after my daughters like a second mum since when they were few months old. To my family: mamma and papa' for supporting and helping in looking after my daughters and house when visiting us. This thesis is also for you. Thanks to my daughters, which they are my “real PhD” for the rest of my life. Thanks to my husband, Matthew that always supported me during these years, just hoping that one day I will be finally a “Doctor”.

## *Abbreviation List*

$\alpha$	Alpha
Å	Angstrom
A $\beta$	Amyloid Beta
AFM	Atomic Force Microscopy
AMP	Antimicrobial Peptide
Arg	Arginine
$\beta$	Beta
CD	Circular Dichroism
Chol	Cholesterol
CL	Cardiolipin
CPP	Cell Penetrating Peptide
$D$	Dissipation energy
$\Delta D$	Dissipation change
$\Delta f$	Frequency change
$\Delta m$	Mass change
$D_T$	Diffusion coefficient,
DMPC	1,2-dimyristoyl- <i>sn</i> -glycero-3-phosphocholine

## *Abbreviation List*

<b>DMPG</b>	1,2-dimyristoyl- <i>sn</i> -glycero-3-phospho- <i>rac</i> -(1-glycerol) (sodium salt)
<b>DNA</b>	Deoxyribonucleic acid
<b>DPC</b>	Dodecylphosphocholine
<b><i>E. coli</i></b>	<i>Escherichia coli</i>
<b>e.g.</b>	For instance
<b>Etc.</b>	Etcetera
<b>HDP</b>	Host Defence Peptide
<b>HIV-1</b>	Human Immunodeficiency Virus type 1
<b>HSV</b>	Herpes Simplex Virus
<b>Hz</b>	Hertz
<b>i.e.</b>	That is
<b>IAPP</b>	Islet Amyloid Polypeptide
<b>IM</b>	Inner Membrane
<b>L<sub>α</sub> or L<sub>d</sub></b>	Liquid-disordered or Liquid crystalline
<b>L<sub>o</sub></b>	Liquid-ordered
<b>L<sub>o</sub>'</b>	Gel phase with not tilted lipid chains
<b>LPC</b>	Lysophosphatidylcholines
<b>LPS</b>	Anionic lipopolysaccharides
<b>LUV</b>	Large Unilamellar Vesicles
<b>MAP</b>	Amphipathic Model Peptide

## *Abbreviation List*

<b>MHA</b>	6-mercaptohexanoic acid
<b>MIC</b>	Minimum Inhibitory Concentration
<b>Min</b>	Minutes
<b>MPA</b>	Mercaptopropionic acid
<b>NMR</b>	Nuclear Magnetic Resonance
<b>OCD</b>	Oriented Circular Dichroism
<b>OM</b>	Outer Membrane
<b>P<math>\beta</math>'</b>	Ripple phase
<b>P/L</b>	Peptide to Lipid molar ratio
<b>PA</b>	Phosphatidic Acid
<b>PDB</b>	Protein Data Bank
<b>PBS</b>	Phosphate Buffered Saline
<b>PC</b>	Phosphatidylcholine
<b>PE</b>	Phosphatidylethanolamine
<b>PG</b>	Phosphatidylglycerol
<b>PP-II</b>	Helix poly-L-proline type II helical conformation
<b>Pr-AMP</b>	Proline rich AMP
<b>PS</b>	Phosphatidylserine
<b>PTD</b>	Protein transduction domain
<b>Rc</b>	Ruthenocene

## *Abbreviation List*

<b>RcCO</b>	Ruthenocenoyl
<b>S</b>	Order parameter
<b>SAM</b>	Self-Assembled Monolayer
<b>SAXS</b>	Small-Angle X-ray Scattering
<b>SDS</b>	Anionic Sodium Dodecyl Sulfate
<b>SECM</b>	Scanning Electrochemical Microscopy
<b>siRNA</b>	Small interfering RNA
<b>SLBs</b>	Supported Lipid Membranes
<b>SM</b>	Sphingomyelin
<b>S<sub>o</sub> or L<sub>β</sub></b>	Gel phase with tilted lipid chains
<b>SPR</b>	Surface Plasmon Resonance
<b>SUV</b>	Small Unilamellar Vesicle
<b>SynAMPs</b>	Synthetic Antimicrobial Peptides
<b>TAR</b>	Trans-Activation Responsive
<b>TEM</b>	Transmission Electron Microscopy
<b>TFA</b>	Trifluoroacetic acid
<b>TFE</b>	2,2,2-trifluoroethanol
<b>T<sub>m</sub></b>	Main transition Temperature
<b>T<sub>p</sub></b>	Pre-transition Temperature
<b>Trp</b>	Tryptophan

## *Abbreviation List*

<b>U3.5</b>	Uperin 3.5
<b>UME</b>	Ultramicroelectrode



# *Antimicrobial peptides: a generic overview*

*“The World Health Organisation's (WHO) first worldwide report into antimicrobial resistance has found the problem is no longer just a serious prediction for the future, but is happening now”*

*As reported by Sophie Scott, [www.abc.net.au/news](http://www.abc.net.au/news), on the 1<sup>st</sup> May 2014*

Antimicrobial peptides (AMPs) constitute the main effector molecules of the innate immunity of plants, invertebrate and vertebrate organisms<sup>1</sup>. They represent a successful strategy against various infections caused by microbes, such as bacteria, fungi and viruses since they have been present from the primordial stage of the evolution. These peptides are very effective because, unlike antibodies, they can be active towards a wide spectrum of pathogens. Indeed, a single peptide can exert its action on two or more pathogens. Antimicrobial peptides are able to respond in a matter of hours to a pathogenic infection before the adaptive immune system can be sufficiently mobilised. Furthermore, they avoid the problem of triggering an autoimmunity response by being segregated in compartments inside the cell and by targeting microbes that are not part of the host organism. Another benefit from AMPs is that their actions control the proliferation of the natural flora, present in different niches of animals such as the skin, intestine, and the mouth, keeping a steady state of growth and balanced inflammatory response<sup>2</sup>.

Furthermore, some AMPs behave as immune modulators through a range of activities, as shown in Fig. 1: they increase the production and the release of chemokines by immune and epithelial cells, they exert pro and anti-apoptotic effects on various kinds of immune cells and they act as immunological adjuvants in promoting specific immunity<sup>1,3,4</sup>. Therefore, these various activities suggest that a distinction can be made between the term

‘antimicrobial peptide’ and ‘host defence peptide’. The latter should be used when referring to anti-infective action that augments or modulates the host immune response to pathogens, while ‘AMP’ should be used when direct antimicrobial activity is being examined<sup>3,4</sup>. However, direct antimicrobial activity does not only refer to the lysis of cellular membranes, but, as some studies in vitro showed, it also includes the interference of membrane associated-biosynthesis, the macromolecular synthesis in the cytosol and other metabolic functions<sup>3,5,6</sup>.

Some AMPs have been shown to attract chemotactically phagocytes, mediate the “non-opsonic” phagocytosis (when microbes are recognised by directly interacting with phagocytic receptors)<sup>7,8</sup>, and repress or induce the dissolution of biofilms<sup>3</sup>.

Since the majority of AMPs require high concentrations for an effective activity, they are stored in the vertebrates at high concentration in phagocyte granules, in the crypts of the intestine and near degranulating phagocytes to enhance their antimicrobial action<sup>3,9</sup>.

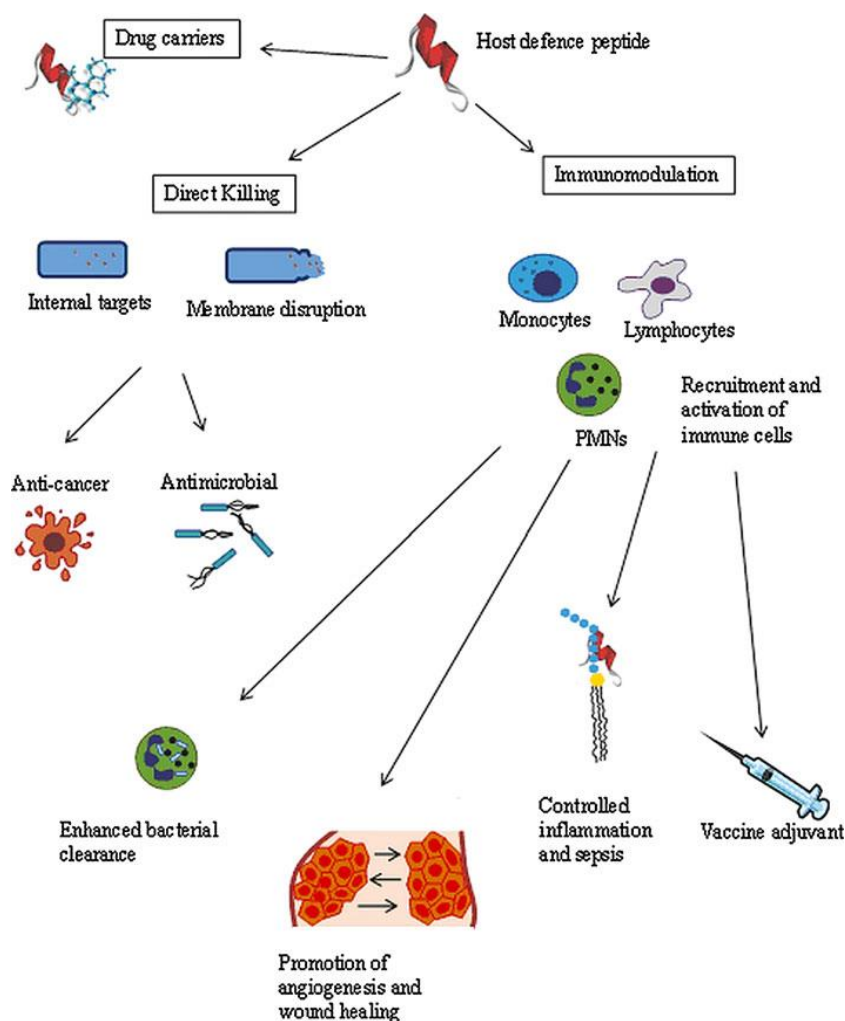


**Fig. 1:** The different possible roles covered by host-defense peptides in the immune system of vertebrates<sup>6</sup>.

Antimicrobial peptides constitute a very large group with a high diversity in their amino acid sequences. Indeed, 2399 antimicrobial peptides and proteins have been catalogued in the “*Antimicrobial peptide database*” so far<sup>10</sup>. These are mainly from prokaryotic and eukaryotic organisms. Most of these peptides are short (10-50 amino acids) and many have a net positive charge, between +2 and +9<sup>4</sup>. The primary structure of these peptides often contains amphipathic properties when they adopt a  $\alpha$ -helical conformation. In this conformation, hydrophobic and charged residues are structurally organized into domains which are spatially separate when the peptide contacts the membrane<sup>4,11,12</sup>.

AMPs are gene-encoded biomolecules. After their synthesis, they undergo post-translational modification, which includes proteolytic processing, carboxy-terminal amidation (e.g. melittin, indolicidin)<sup>13,14</sup>, glycosylation (e.g. drosocin)<sup>15</sup>

halogenation<sup>11</sup>, and conversion from L to D isoform of their residues (e.g. the amphibian peptides bombina)<sup>13</sup>. The final result of these amino acid modifications to the peptide structure increases biological activity<sup>2</sup>. Moreover, some peptides are the result of cyclization processes (e.g.  $\theta$ -defensin), whereas others derive from proteolysis of proteins, such as lactoferrocin from lactoferrin<sup>11</sup>. Another characteristic that distinguishes these peptides is that they are gene-regulated, e.g. drosomycin, an antifungal peptide in *Drosophila*<sup>16</sup>, with the presence of different pathways that are activated depending on the nature of the hazard<sup>11</sup>. There is such a high diversity amongst the amino acid sequences of these AMPs that similarity can be found only within a defined group of peptides that usually originate from closely related species. For peptides derived from the same species, a conservation of amino acid residues can be found in the pre-proregion of their precursor molecules. Single mutations in the amino acid sequences can change the activity of the peptide dramatically, so this diversity can be seen as a consequence of the adaption to the microbial environment<sup>4,11</sup>.

## 1 Classification

AMPs are usually grouped into five subclasses based on the primary sequence and structure<sup>5</sup>:

1. *Anionic AMPs*: are small molecules that are present in surfactant extracts, in the bronchoalveolar lavage fluid, and in the airway epithelial cells of mammals<sup>17</sup>. These peptides are synthesised in mM concentrations and are active against both Gram-negative and Gram-positive bacteria. In order to be functional they require zinc as a cofactor<sup>5</sup>. An example is dermcidin peptide, which is secreted from human sweat glands<sup>18</sup>.
2. *Linear, mostly helical cationic AMPs*: contain less than 40 amino acid residues and never contain cysteine. The primary structure of

some of these peptides presents a hinge or “kink” in the middle, ie. melittin<sup>12</sup>. In solution, many of these peptides have a random structure, whereas in the presence of liposomes, trifluoroethanol, sodium dodecyl sulphate (SDS) micelles or lipid A, all or part of the amino acid sequence forms an  $\alpha$ -helix<sup>19</sup>. Typical examples are: cecropins<sup>2</sup>, melittin<sup>14</sup> from insects, magainin (Fig. 2), bombinin, buforin II from amphibians<sup>2</sup> and LL-37 from humans (Fig. 2)<sup>20</sup>. Moreover, a direct correlation between the extent of the  $\alpha$ -helix with the efficacy of antimicrobial activity towards both Gram-negative and Gram positive bacteria has been observed<sup>21</sup>.

3. *Cationic AMPs enriched in certain amino acids*: this class includes peptides that are rich in proline (e.g. abaecin from honeybee<sup>2,22</sup>); glycine-rich peptides such as hymenoptaecin from honeybees<sup>2</sup>; tryptophan-rich peptides such as indolicidin from cattle (Fig.2)<sup>23</sup>; and histidine-rich polypeptides like histatins, which are secreted by parotid and submandibular salivary glands in humans<sup>24</sup>. There are also peptides which have amino acid sequence rich in two residues: proline and arginine-rich peptides (e.g. apidaecins from honeybee<sup>25</sup>, drosocin from *Drosophila melanogaster*<sup>15,22</sup>, and PR-39 from pigs<sup>22</sup>); proline and phenylalanine-rich peptides (e.g. prophenin from pigs<sup>24</sup>); and peptides enriched in glycine and proline, such as coleopteracin and holotricin from beetles<sup>2</sup>. These peptides lack in cysteine residues and are linear, albeit some can form extended coils.
4. *Anionic and cationic AMPs having cysteine in their sequence forming disulphide bonds and stable  $\beta$ -sheet*: this category contains peptides with one disulfide bond, which is often located in the C-terminal part of peptide sequence (loop peptides)<sup>2</sup>. Examples are brevinins-1 and 2 from a Japanese and European *Rana* species<sup>26</sup>, bactenicin from bovine neutrophils<sup>27</sup>; peptides with two disulfide bonds such as protegrin from pigs (Fig. 2)<sup>2</sup>; peptides with three or

more disulfide bonds such defensins peptides isolated from vertebrates and insects (Fig. 2)<sup>2,28</sup>.

5. *Anionic and cationic AMPs that are fragments of larger proteins:* although their role in innate immunity is still not clear yet, examples include lactoferricin (Fig. 2) from lactoferrin and AMPs created by the proteolytic digestion of lysozyme<sup>29</sup>.

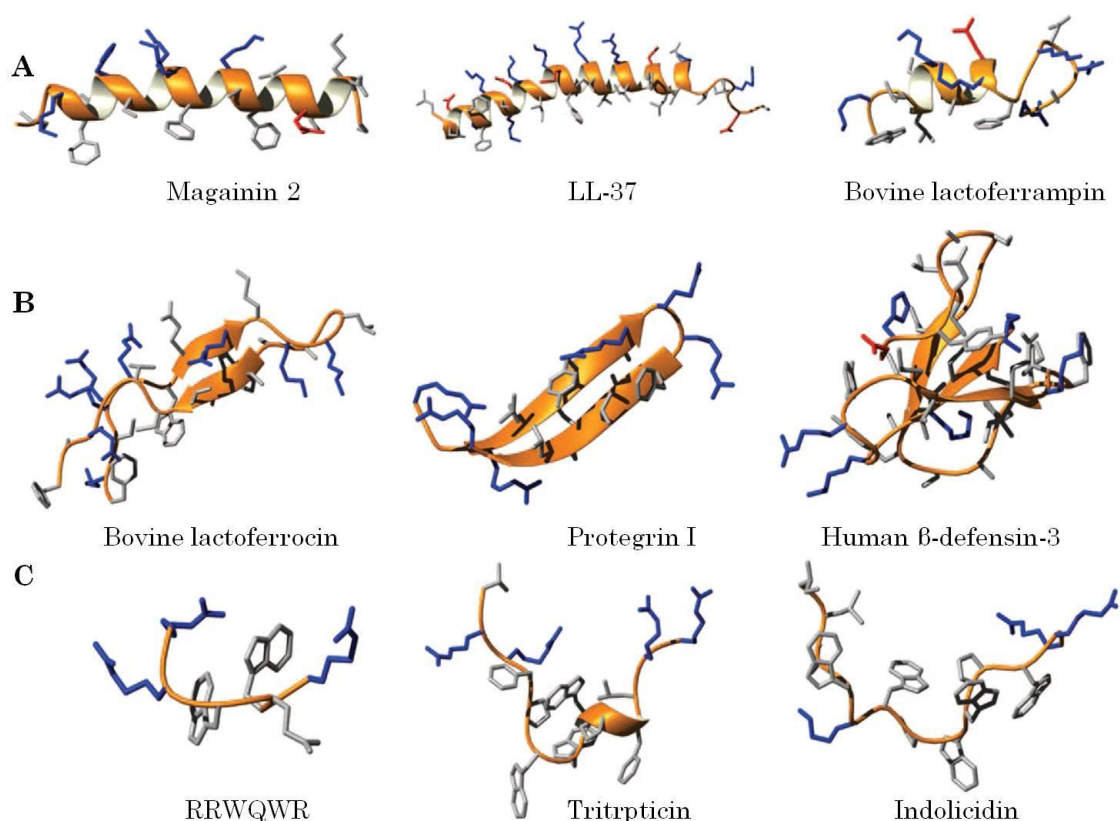


**Fig. 2:** Examples of AMP secondary structures. (A) a-Helical peptides, (B)  $\beta$ -sheet peptides and (C) extended peptides. All of these structures were solved by solution NMR spectroscopy in the presence of detergent micelles, except for the  $\beta$ -sheet peptides, which were studied in aqueous solution. Positively charged side chains are coloured in blue, negatively charged side chains in red and remaining side chains in grey. PDB IDs: magainin 2, 2MAG; LL-37, 2K60; bovine lactoferricin, 1LFC; protegrin 1, 1PG1; human b-defensin-3, 1KJ5; tritrpticin, 1D6X; indolicidin, 1G89<sup>30</sup>.

Despite this classification being based on the structure, there is not a strong correlation between the secondary structure and the mode of action. In fact, peptides that have different conformations in solution, can act in a similar way as they come in contact with a membrane<sup>31 3</sup>.

## **2 Mechanism of peptide action**

### **2.1 Membrane disruption**

Many of the AMPs act towards pathogens by altering the membrane permeability, which results in lysis of the cell membrane. These peptides firstly attach to the bacterial membrane surface in order to exert this type of antimicrobial action. This usually happens through electrostatic interactions since most of the AMPs are cationic and the microbial surfaces are negatively charged<sup>12,32,33</sup>. In fact, in the case of Gram-negative bacteria, AMPs interact initially with the lipopolysaccharides (LPS)-rich external leaflet of the outer membrane, which is negatively charged. This interaction has been described by Hancock as a “self-promoted uptake”<sup>34</sup>. According to this model, peptides access the outer and inner membrane by displacing LPS-associated divalent cations ( $Mg^{2+}$  and  $Ca^{2+}$ ) and disrupting the non-covalent bridging interactions between LPS molecules. In the case of Gram-positive bacteria, which have a thick layer of peptidoglycan instead, peptides interact with the negatively charged polysaccharides teichoic and teichuronic acids and with the amino acid carboxyl groups presented in the multilayered peptidoglycan. Once these peptides reach the plasma membrane, they interact with the negatively charged polar head of phospholipids<sup>12,35</sup>.

The peptide-binding and selectivity to the membrane is enhanced by AMPs' structural characteristics<sup>3,9,35-37</sup>:

1. the presence of basic amino acid residues such as arginine or lysine and aromatic residues, mainly tryptophan;
2. the prevalence of positive charges, usually between +2 to +9, which result in strong electrostatic interactions with the negatively charged lipids in bacterial membranes;
3. the presence of hydrophobic residues, which influence the partition of water-soluble AMPs into the membrane. However, it seems that a high content of hydrophobic residues in the peptide sequence

correlates to an increase in haemolytic activity and a reduction in antimicrobial activity of AMPs;

4. the peptide conformations adopted when in contact with the membrane, which are mainly  $\alpha$ -helical, antiparallel  $\beta$ -sheet and relaxed coils. The adoption of a helical conformation determines the segregation of polar and non polar residues in two opposite peptide domains, which affect the peptide activity;
5. the level of amphipathicity (i.e. the relative proportion and distribution of hydrophobic and hydrophilic residues or domains within a peptide), which is essential for the AMPs mechanism of action. Indeed, for amphipathic peptides the positively charged polar face will establish the initial electrostatic interactions with the lipid membrane, and then the non-polar side of the peptide will insert into the hydrocarbon chain of the membrane core through hydrophobic and van der Waals interactions<sup>38</sup>.

On the other hand, bacteria have some characteristics of their membranes, which also contribute to a favourable binding<sup>3,35</sup>:

1. the high content of anionic phospholipids (up to 20% mol) of the membrane, which gives a negative net charge at physiological pH;
2. the absence of sterols such as cholesterol, which affect the fluidity, the thickness and the dipole potential of the plasma membrane<sup>39</sup>;
3. a very negative transmembrane potential (-120 mV) across most of the bacterial membranes, which operates as a driving force for peptide binding and insertion;
4. the asymmetry in the membrane composition, which influence the membrane curvature and, consequently, the peptide activity<sup>40</sup>.

At the beginning of the interaction with the membrane bilayer, peptides typically orientate themselves parallel to the membrane plane. At this stage, the ratio between peptides and lipids (P/L)<sup>3,5,36,41</sup> is low because of the low peptide concentration. Here peptides bind and insert themselves into the lipid head-groups, but they are functionally inactive. However, during this phase

peptides can cause an increase in the membrane tension, which results in membrane-thinning. This event is directly proportional to the peptide concentration<sup>36,41,42</sup>. As this concentration increases, the ratio P/L increases as well reaching a threshold value in which the peptide molecules can change their orientation from parallel into perpendicular to the membrane, producing a transmembrane insertion, usually resulting in pore formation (see Fig. 3).

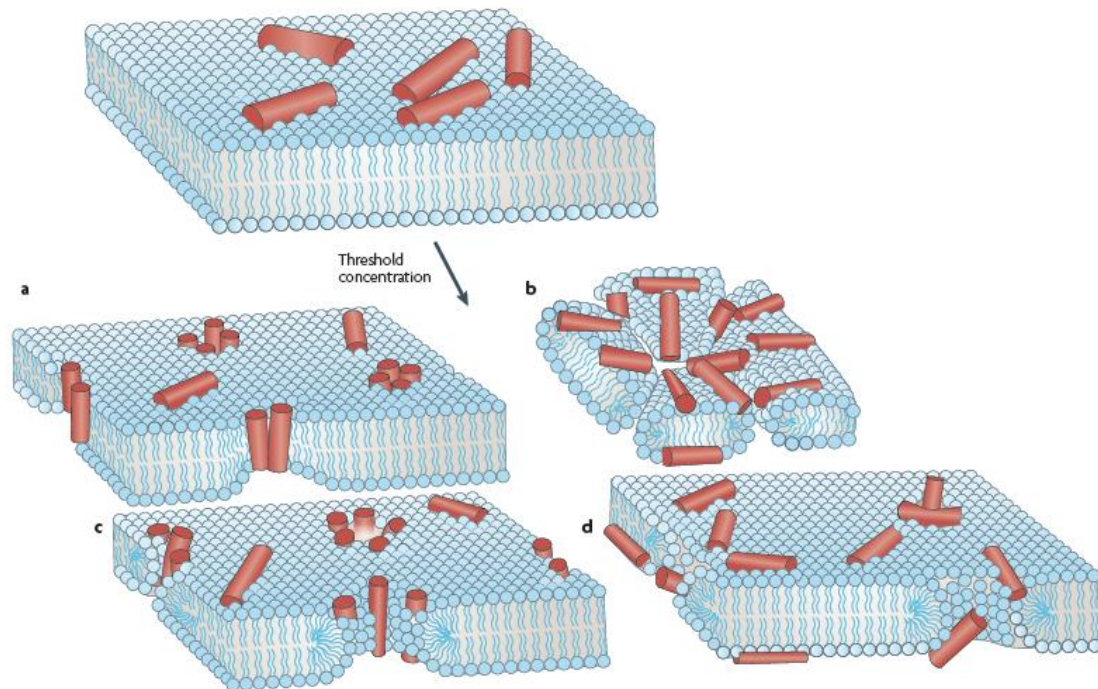


**Fig. 3:** Suggested lytic antimicrobial mechanisms targeting the plasma membrane: after a critical peptide:lipid ratio has been reached. Disruption occurs through various processes: (a) barrel-stave pore; (b) carpet mechanism; (c) toroidal pore, and (d) disordered toroidal pore where the peptides assume a less-rigid conformation and orientation in the bilayer, and the pore lumen is aligned by the lipid polar heads<sup>9</sup>.

Therefore, membrane permeabilization can occur mainly through the formation of stable pores: the ‘barrel-stave model’ and the ‘toroidal-pore model’; or by membrane micellization in a detergent-manner (carpet model):

1. in the “barrel-stave model” (Fig. 3a), the peptide helices insert perpendicular to the membrane and group together forming a barrel with a central lumen, where the hydrophobic peptide region is aligned with the lipid core region of the bilayer<sup>5,36</sup>. This structure

is not very common among antimicrobial peptides since it needs to satisfy some criteria (peptide needs to be hydrophobic, peptide sequences must have 22 residues at least, requires self-association of peptide molecules when bound to the membrane)<sup>33</sup>. The typical example of barrel-stave is the trans-membrane pore induced by the insertion of alamethicin in the lipids as a bundle, where 3-11 parallel helices of the peptide represent the staves of the barrel, which has a diameter of ~1.8 nm (inner) and ~4.0 nm (outer). This structure was derived from analysis of synchrotron-based X-ray scattering<sup>43,44</sup>, oriented circular dichroism (OCD) and neutron scattering<sup>45</sup>;

2. in the “toroidal pore or wormhole model”<sup>46</sup> (Fig. 3c), the peptide monomers insert in a transmembrane manner such that the polar face of the peptide is always associated with the lipid head-group<sup>36,39</sup>. The pore is formed by an intercalation between peptide and lipid head groups resulting in a continuous bending of the membrane from the top leaflet to the bottom leaflet through a toroidal hole<sup>47</sup>. This mechanism of pore formation is thought to be the most adopted by various peptides, such as magainin and melittin<sup>39,45</sup>. Indeed, neutron scattering experiments indicate that water filled cavities are present (“wormholes”) in aligned membranes for magainin concentrations higher than 3.3 mol%<sup>46</sup>. A further increase in the peptide concentration results in the collapse of the bilayer probably into micelles<sup>48</sup>. A variation of the toroidal pore is the disordered toroidal pore<sup>49</sup>, as shown in Fig. 3d, which will be described in Chapter 3;
3. finally, the “carpet-model”<sup>35</sup> consists of peptides adsorbing and spanning the bilayer surface. Peptides lie parallel to the membrane and interact electrostatically with the anionic lipid head-groups, covering the surface of the membrane in a carpet-like manner (Fig. 3b). Once the critical threshold concentration of peptides has been reached, peptides might form toroidal transient holes in the

membrane, which results in more peptide molecules accessing the membrane. This causes the breakdown of the membrane into micelles after disruption of the membrane curvature<sup>5,39,50</sup>. This mode of action is adopted usually by peptides that are too short to span the membrane bilayer. The “carpet-model” has been proposed as a mechanism following the toroidal pore mechanism when peptide concentrations are high<sup>30,51</sup>. This mechanism has been proposed firstly in a study conducted with Dermaseptin, a 34-residue peptide isolated from the skin of *Phyllomedusa* frogs<sup>52</sup>. Another peptide shown to disrupt the membrane in a carpet-manner is melittin when interacting with negatively charged membranes<sup>53</sup>. Interestingly, Bechinger<sup>39</sup> distinguished the action of disintegrating the membrane “carpeted” by peptide molecules, with consequent formation of lipid-peptide micelles, as a “detergent-like effect”.

These different modes of acting on the membrane are not independent or exclusive, but it has been suggested that exists a continuous gradation among them<sup>35,54</sup>. Furthermore, in some cases the same AMP can interact with a membrane in several different ways (e.g. magainin<sup>30</sup> or melittin<sup>51</sup>). As a consequence, various factors influence the activity of AMP such as the lipid-peptide ratio<sup>36</sup>, the composition of the lipids (charge and size of their polar head groups)<sup>53</sup>, hydrophobic interactions with the core of the membrane<sup>35</sup>, the curvature of the membrane<sup>40</sup> and the salt concentration<sup>11,55</sup>. For example, the peptide action of AMPs such as cecropin<sup>56</sup> and magainin<sup>53,57</sup> is reduced or modified when cholesterol is present.

## 2.2 Intracellular targets

Some AMPs are able to suppress bacteria through the inhibition of essential intracellular pathways. These peptides do not permeabilise the cell membrane, but once translocated into the cytosol, they can target biosynthetic or other intracellular targets. For example, they can restrain the bacterial cell-wall synthesis, e.g. mersacidin, an l-antibiotic from Gram-positive bacteria that

interferes with the synthesis of peptidoglycan. Other intracellular targets include the binding to proteins such as DnaK, as in the case of pyrrolicin, drosocin and apidaecin, which bind specifically to a 70-kDa heat-shock protein<sup>58</sup>; or at the bacterial chaperone protein by drosocin and pyrrolicin, which impede the protein folding pathway<sup>59</sup>. Moreover, some peptides can have more than one target. Indolicidin and PR-39 are both examples of peptides that are able to inhibit the cell division and the synthesis of nucleic acids and proteins. These activities depend on their intracellular concentration<sup>5</sup>.

### 3 Method of investigations

Understanding the interactions that AMPs establish with their targets is important because information of this kind can help in the development of new strategies for the treatment of infections caused by pathogens. However, every technique used for this purpose gives “a piece of the entire picture” of the peptide action, thus, integration of data from various techniques is important to achieve a good understanding of the mechanism. For example, microscopy techniques, such as scanning and transmission electron microscopy have been used in illustrating the damage done by AMPs such as SMAP29 on bacterial cells<sup>60</sup>. The influence of the peptide secondary structure has been investigated with confocal laser-scanning microscopy showed the importance of proline in enabling the entry into the cell by creating a hinge in the secondary structure of the buforin II peptide, whereas magainin 2, with no proline, binds to the cell membrane without penetrating<sup>5,21</sup>.

#### 3.1 Studies with model membranes

While the use of various microscopy methods is useful in visualizing *in vivo* the general target sites of the AMPs, the employment of model membranes can give detailed information about the mechanism of action adopted by AMPs. Model membranes can be used in investigating the influence of specific lipids, the peptide orientation, and changes in thickness and integrity of the

membrane as a consequence of the interaction with peptides. Examples of biophysical methods that employ artificial membranes are listed below:

1. *fluorescent dyes* have been employed to detect the ability of some peptides to permeabilise the membrane by using liposomes containing dyes, such as dextran, calcein etc<sup>61,62</sup>. The influence of the temperature, peptide/lipid ratio and membrane composition on the release of fluorescent labelled probes has been investigated<sup>63</sup>. For example, this approach was used to show that melittin formed pores of 2.5-3.0 nm in POPC vesicles at a peptide/lipid ratio of 50<sup>61</sup> and the size of these pores was correlate to the lipid/peptide ratio<sup>64</sup>;
2. *the planar lipid bilayer method* for the screening of possible voltage-gate channels created by peptides inserted into the membrane. Using this approach Herce et al<sup>65</sup> showed the formation of transient pores by Arg-9 peptides;
3. *Circular dichroism (CD)* is used to determine the orientation and the secondary structure of a peptide bound to a lipid bilayer (in a controlled humidity environment)<sup>5,66,67</sup>. This method highlights the influence of the surrounding environments in inducing conformational changes in the peptide structure, which are essential for the interaction with the membrane. Indolicidin peptide is an example: from a disordered conformation in liquid and organic solutions, it assumes an ordered conformation in the presence of SDS micelles and lipid bilayers<sup>68</sup>. Oriented circular dichroism (OCD)<sup>47</sup>, a variant of CD, discriminates the parallel or perpendicular orientations of magainin and melittin bound to membranes<sup>45</sup>;
4. *Solid-state NMR spectroscopy* gives information about the secondary structure, the orientation and penetration of peptides in the liquid-crystalline state of a lipid bilayer<sup>39</sup>. For example, solid-state NMR spectroscopy was used in determining the random coil structure of Tat (48-60) in anionic lipid bilayers<sup>69</sup>;

5. *Neutron diffraction* can detect the formation of pores in a membrane. Neutron in-plane scattering showed that alamethicin and magainin induced pores in a membrane<sup>5</sup>. However, the pore created by these peptides differ in size, as the neutron off-plane scattering technique was able to detect with accuracy;
6. the employment of *X-ray diffraction* highlights a correlation between the concentration of host defence peptide and the thinning of the membrane<sup>47</sup>. For example, the translocation of the Tat peptide through pore formation in the membrane has been investigated with the use of synchrotron-based X-ray scattering<sup>70</sup>;
7. *Surface plasmon resonance (SPR)* is an optical method that is used to assess the interaction between peptides and supported artificial membranes. Examples include the investigations with magainin and melittin, which showed differences in membrane affinity for magainin and different interactions of melittin as a function of the membrane composition<sup>53</sup>;
8. *Quartz crystal microbalance (QCM)* is an acoustic method, which has been employed for determining the peptide affinity to various membranes in term of mass, such as melittin<sup>71</sup>. This technique will be described in detail in Chapter 2.

The advantages of investigating *in vitro* are to focus on determinate aspects and to be able to control environmental parameters. However, this approach is not able to show any possible cooperation between the peptide of interest with other factors *in vivo*. Moreover, there is the risk to simplify systems that are complex in reality. For example, the cell membrane is not only a uniform and passive physical barrier, but it is also involved in metabolic and defensive processes.

## 4 Bacterial defence mechanism

Resistance towards AMPs is unlikely because these peptides have multiple hydrophobic and/or polyanionic targets, in which only one of these is the membrane. Also because often the mode of action *in vivo* is a cooperation amongst various peptides<sup>72</sup>.

However, there are some reports of bacterial resistance towards AMPs; their insertion and also change in membrane permeability<sup>5</sup>. Bacterial strategies include degradation of peptides by proteolytic enzymes present in the cell; for example LL-37 is cleaved and inactivate by a *S. aureus* metalloproteinase named aureolysin<sup>5</sup>. An intriguing strategy by *S. aureus* includes the reduction of the negative surface charges in the membrane by increasing basic amino acid residues. Also, a component of the LPS named Lipid A was modified in the *Salmonella* species to decrease the interaction with cationic AMPs. In addition, hydrophobic interactions were increased between the acyl tails of Lipid A so the fluidity of the outer membrane was rendered unfavourable to attachment by peptides. Another way to hinder peptide attachment is the presence of a polysaccharide capsule that encapsulates the cell, as in the case of *K. Pneumonia*. Another mechanism is the efflux of AMPs through porin-mediated pumps for example. This efflux is a strategy adopted by many bacteria to avoid intracellular accumulation of AMPs, thus avoiding the reaching of lethal concentrations after which AMPs exert their antibacterial action<sup>11,35</sup>.

## 5 Applications of AMPs

Antimicrobial peptides constitute a very effective defence mechanism against pathogenic microbes. For their characteristics described above, they have many possible applications. They can be used as a template in the synthesis of new antibiotics, increasing the potency of traditional antibiotics by assisting the passage of antibiotics through the bacterial membrane. Impeding microbial colonization of the surfaces of medical devices made of synthetic

polymeric materials, and also inserting their genes into plant and animal genomes to enhance benefits against infections<sup>11</sup>. Furthermore, since AMPs have a wide antimicrobial spectrum of activity, suggestions have been made for use as “chemical condoms” to restrict the spread of sexually transmitted diseases such as human immunodeficiency virus HIV, *Chlamydia*, and Herpes simplex virus (HSV)<sup>11,73</sup>.

However, there is a major impediment in the application of AMPs as systemic drugs. Most AMPs are strongly antagonized by mono and divalent cations present in the serum as well as polyanionic polymers<sup>3</sup>, they are required to be administered at high dosage, close to being toxic, to be effective in the model animals<sup>11</sup> and there is the risk of apoptosis and mast-cell degranulation<sup>74</sup>. Moreover, some peptides, such as LL-37, showed the ability to translocate freely into the cells carrying also other molecules with them. For all these reasons, clinical trials of AMPs pertain to topical applications predominately, which are clinically safer<sup>4</sup>. Another disadvantage in the use of natural host defense peptides is high susceptibility to the action of proteases, and the high cost in synthesising them in large quantities<sup>4</sup>.

Currently a new approach is to design novel AMPs in silico as a way to optimize the activity. New peptides are designed by modifying the sequences of known AMPs or applying various computer-assisted strategies like molecular dynamics simulations<sup>75</sup>, virtual screening studies in predicting the activity and molecular descriptors that provide information about the whole-molecule properties. The main focus of these approaches is to produce cost effective sequences, which are small without post-translational modifications. These molecules have to be highly active, with a broad-spectrum activity without any toxicity implied, good pharmacokinetics and a desired selectivity profile. Moreover, the artificial peptides should be effective without the need of other peptides<sup>3</sup>.

## 6 Conclusions

AMPs constitute a promising platform from which new effective pharmaceutical components can be designed to be employed against pathogens. For this reason, it is essential to understand in detail how these host defence molecules interact with the membrane and how they exert their activity. However, the way these peptides act is influenced by their secondary structure, their size, the presence of charges, the amphipathicity and the hydrophobicity. In addition, the single modifications in the primary sequence affect the activity and specificity. Moreover, all these parameters are very closely related and therefore altering one of them means introducing changes in the others<sup>12</sup>. Other factors playing an important role are the physiological conditions *in vivo*: the actual concentration of the peptide at the site of infection, possible synergies with other substances present like lysozyme, the presence of inhibiting substances (e.g. salt concentration and serum proteins) and the properties of bacteria during their reproduction *in vivo*<sup>5</sup>. Taking into consideration all these factors simultaneously is practically impossible in studies conducted *in vitro*. Instead, others crucial variables can be examined in artificial systems, like the role of the microbial and plasma membrane surface composition in determining the mechanisms adopted by host defence peptides. Alternatively, consideration should be given to the influence exerted by the salt concentration present in the liquid environment, the concentration of the AMPs and other external variables.

In this thesis the action of several important classes of AMPs are described in terms of the interaction with a supported lipid bilayer (SLB). Each chapter has a focus on a specific example of an AMP class such as, melittin and magainin 2 (Chapter 3) two of the most widely studied  $\alpha$ -helical peptides. A clear outcome, from this investigation is finding that the mode action of these two AMPs, was that they form pores which could led to a membrane disruption mechanism. However, the action of these peptides has been found to be dependent on both the concentration and the membrane composition. The consecutive Chapters in this thesis include AMPs enriched in a specific amino

acid residues: proline-rich peptides (Chapter 4), arginine-rich peptides (Chapter 5), arginine and tryptophan-rich peptides (Chapter 6). A similar approach to investigate the membrane action of magainin 2 and melittin was also employed for these classes of peptides. However, these amino acid enriched peptides differed in the action among each class. The last chapter (Chapter 7) investigates the action of uperin 3.5, an AMP that self-aggregates. The investigation of the membrane action of all these classes of AMPs (Chapters 3-7) has used a quartz crystal microbalance with dissipation monitoring (QCM-D) modified to include a biomimetic membrane layer. Furthermore, QCM-D has been used as a complementary technique with scanning electrochemical microscopy (SECM) in order to characterise the action of the cell-penetrating peptide Tat (Chapter 5). The theoretical and experimental principles of the QCM-D and SECM are described in Chapter 2. Chapter 2 also describes the preparation and characterisation of SLBs of bacterial and mammalian mimetic composition that have been employed for this study.

## 7 Bibliography

- 1 Boman, H. G. Antibacterial peptides: basic facts and emerging concepts. *J. Intern. Med.* **254**, 197-215, (2003).
- 2 Boman, H. G. Peptide antibiotics and their role in innate immunity. *Annu. Rev. Immunol.* **13**, 61-92, (1995).
- 3 Fjell, C. D. *et al.* Designing antimicrobial peptides: form follows function. *Nat. Rev. Drug Discov.* **11**, 37-51, (2012).
- 4 Hancock, R. E. W. & Sahl, H. G. Antimicrobial and host-defense peptides as new anti-infective therapeutic strategies. *Nat. Biotechnol.* **24**, 1551-1557, (2006).
- 5 Brogden, K. A. Antimicrobial peptides: pore formers or metabolic inhibitors in bacteria? *Nat. Rev. Microbiol.* **3**, 238-250, (2005).
- 6 Yeung, A. T. Y. Multifunctional cationic host defence peptides and their clinical applications. *Cell. Mol. Life Sci.* **68**, 2161-2176, (2011).
- 7 Chung, Y. S. A. Recognition of pathogenic microbes by the Drosophila phagocytic pattern recognition receptor eater. *J. Biol. Chem.* **286**, 26524-26532, (2011).
- 8 Shiratsuchi, A. *et al.* Independent Recognition of Staphylococcus aureus by Two Receptors for Phagocytosis in Drosophila. *J. Biol. Chem.* **287**, 21663-21672, (2012).
- 9 Melo, M. N. *et al.* Antimicrobial peptides: Linking partition, activity and high membrane-bound concentrations. *Nat. Rev. Microbiol.* **7**, 245-250, (2009).
- 10 Wang, G. *et al.* APD2: The updated antimicrobial peptide database and its application in peptide design. *Nucleic Acids Res.* **37**, D933-D937, (2009).
- 11 Zasloff, M. Antimicrobial peptides of multicellular organisms. *Nature* **415**, 389-395, (2002).
- 12 Tossi, A. *et al.* Amphipathic,  $\alpha$ -helical antimicrobial peptides. *Pept. Sci.* **55**, 4-30, (2000).
- 13 Bulet, P. *et al.* Anti-microbial peptides: From invertebrates to vertebrates. *Immunol. Rev.* **198**, 169-184, (2004).
- 14 Raghuraman, H. & Chattopadhyay, A. Melittin: A membrane-active peptide with diverse functions. *Biosci. Rep.* **27**, 189-223, (2007).
- 15 Bulet, P. *et al.* Enlarged scale chemical synthesis and range of activity of drosocin, an O-glycosylated antibacterial peptide of Drosophila. *Eur. J. Biochem.* **238**, 64-69, (1996).
- 16 Imler, J. L. & Hoffmann, J. A. Toll receptors in innate immunity. *Trends Cell Bio.* **11**, 304-311, (2001).

- 17 Brogden, K. A. *et al.* Isolation of an ovine pulmonary surfactant-associated anionic peptide bactericidal for *Pasteurella haemolytica*. *Proc. Natl. Acad. Sci.* **93**, 412-416, (1996).
- 18 Schitteck, B. *et al.* Dermcidin: a novel human antibiotic peptide secreted by sweat glands. *Nat. Immunol.* **2**, 1133-1137, (2001).
- 19 Gennaro, R. & Zanetti, M. Structural features and biological activities of the cathelicidin-derived antimicrobial peptides. *Pept. Sci.* **55**, 31-49, (2000).
- 20 Oren, Z. *et al.* Structure and organization of the human antimicrobial peptide LL-37 in phospholipid membranes: Relevance to the molecular basis for its non-cell-selective activity. *Biochem. J.* **341**, 501-513, (1999).
- 21 Park, C. B. *et al.* Structure-activity analysis of buforin II, a histone H2A-derived antimicrobial peptide: The proline hinge is responsible for the cell-penetrating ability of buforin II. *Proc. Natl. Acad. Sci.* **97**, 8245-8250, (2000).
- 22 Otvos, L. The short proline-rich antibacterial peptide family. *Cell. Mol. Life Sci.* **59**, 1138-1150, (2002).
- 23 Rozek, A. *et al.* Structure of the bovine antimicrobial peptide indolicidin bound to dodecylphosphocholine and sodium dodecyl sulfate micelles. *Biochemistry* **39**, 15765-15774, (2000).
- 24 Sitaram, N. Antimicrobial peptides with unusual amino acid compositions and unusual structures. *Curr. Med. Chem.* **13**, 679-696, (2006).
- 25 Casteels, P. *et al.* Apidaecins: antibacterial peptides from honeybees. *EMBO J.* **8**, 2387-2391, (1989).
- 26 Morikawa, N. *et al.* Brevinin-1 and -2, unique antimicrobial peptides from the skin of the frog, *Rana brevipoda porsa*. *Biochem. Biophys. Res. Commun.* **189**, 184-190, (1992).
- 27 Romeo, D. *et al.* Structure and bactericidal activity of an antibiotic dodecapeptide purified from bovine neutrophils. *J. Biol. Chem.* **263**, 9573-9575, (1988).
- 28 Bulet, P. *et al.* Antimicrobial peptides in insects; structure and function. *Dev. Comp. Immunol.* **23**, 329-344, (1999).
- 29 Chan, D. I. *et al.* Tryptophan- and arginine-rich antimicrobial peptides: Structures and mechanisms of action. *BBA- Biomembr.* **1758**, 1184-1202, (2006).
- 30 Nguyen, L. T. *et al.* The expanding scope of antimicrobial peptide structures and their modes of action. *Trends Biotechnol.* **29**, 464-472, (2011).
- 31 Huang, H. W. *et al.* Molecular mechanism of peptide-induced pores in membranes. *Phys. Rev. Lett.* **92**, 198304-198301, (2004).

- 32 Shai, Y. Mechanism of the binding, insertion and destabilization of phospholipid bilayer membranes by  $\alpha$ -helical antimicrobial and cell non-selective membrane-lytic peptides. *BBA- Biomembr.* **1462**, 55-70, (1999).
- 33 Shai, Y. Mode of action of membrane active antimicrobial peptides. *Biopolymers - Peptide Science Section* **66**, 236-248, (2002).
- 34 Hancock, R. E. W. Peptide antibiotics. *Lancet* **349**, 418-422, (1997).
- 35 Teixeira, V. *et al.* Role of lipids in the interaction of antimicrobial peptides with membranes. *Prog. Lipid Res.* **51**, 149-177, (2012).
- 36 Yeaman, M. R. & Yount, N. Y. Mechanisms of antimicrobial peptide action and resistance. *Pharmacol. Rev.* **55**, 27-55, (2003).
- 37 Kinnunen, P. K. J. Amyloid formation on lipid membrane surfaces. *Open Biol.* **2**, 163-175, (2009).
- 38 Hancock, R. E. W. & Chapple, D. S. Peptide antibiotics. *Antimicrob. Agents Chemother.* **43**, 1317-1323, (1999).
- 39 Bechinger, B. The structure, dynamics and orientation of antimicrobial peptides in membranes by multidimensional solid-state NMR spectroscopy. *BBA- Biomembr.* **1462**, 157-183, (1999).
- 40 Matsuzaki, K. *et al.* Relationship of membrane curvature to the formation of pores by magainin 2. *Biochemistry* **37**, 11856-11863, (1998).
- 41 Huang, H. W. Action of antimicrobial peptides: Two-state model. *Biochemistry* **39**, 8347-8352, (2000).
- 42 Chen, F. Y. *et al.* Evidence for membrane thinning effect as the mechanism for peptide-induced pore formation. *Biophys. J.* **84**, 3751-3758, (2003).
- 43 Spaar, A. *et al.* Conformation of Peptides in Lipid Membranes Studied by X-Ray Grazing Incidence Scattering. *Biophys. J.* **87**, 396-407, (2004).
- 44 He, K. *et al.* Antimicrobial Peptide Pores in Membranes Detected by Neutron In-Plane Scattering. *Biochemistry* **34**, 15614-15618, (1995).
- 45 Yang, L. *et al.* Barrel-stave model or toroidal model? A case study on melittin pores. *Biophys. J.* **81**, 1475-1485, (2001).
- 46 Ludtke, S. J. Membrane pores induced by magainin. *Biochemistry* **35**, 13723-13728, (1996).
- 47 Huang, H. W. Molecular mechanism of antimicrobial peptides: The origin of cooperativity. *BBA- Biomembr.* **1758**, 1292-1302, (2006).
- 48 Bechinger, B. Peptide structural analysis by solid-state NMR spectroscopy. *Biopolymers* **51**, 174-190, (1999).
- 49 Sengupta, D. *et al.* Toroidal pores formed by antimicrobial peptides show significant disorder. *BBA- Biomembr.* **1778**, 2308-2317, (2008).
- 50 Oren, Z. & Shai, Y. Mode of action of linear amphipathic  $\alpha$ -helical antimicrobial peptides. *Biopolymers* **47**, 451-463, (1998).

- 51 Lee, M. T. *et al.* Process of inducing pores in membranes by melittin. *Proc. Natl. Acad. Sci. U. S. A.* **110**, 14243-14248, (2013).
- 52 Pouny, Y. Interaction of antimicrobial dermaseptin and its fluorescently labeled analogues with phospholipid membranes. *Biochemistry* **31**, 12416-12423, (1992).
- 53 Papo, N. & Shai, Y. Exploring peptide membrane interaction using surface plasmon resonance: Differentiation between pore formation versus membrane disruption by lytic peptides. *Biochemistry* **42**, 458-466, (2003).
- 54 Dathe, M. & Wieprecht, T. Structural features of helical antimicrobial peptides: their potential to modulate activity on model membranes and biological cells. *BBA- Biomembr.* **1462**, 71-87, (1999).
- 55 Wieprecht, T. Influence of the angle subtended by the positively charged helix face on the membrane activity of amphipathic, antibacterial peptides. *Biochemistry* **36**, 12869-12880, (1997).
- 56 Silvestro, L. *et al.* The concentration-dependent membrane activity of cecropin A. *Biochemistry* **36**, 11452-11460, (1997).
- 57 Matsuzaki, K. Control of cell selectivity of antimicrobial peptides. *BBA- Biomembr.* **1788**, 1687-1692, (2009).
- 58 Otvos, L. *et al.* Interaction between heat shock proteins and antimicrobial peptides. *Biochemistry* **39**, 14150-14159, (2000).
- 59 Kragol, G. *et al.* The antibacterial peptide pyrrolicorin inhibits the ATPase actions of DnaK and prevents chaperone-assisted protein folding. *Biochemistry* **40**, 3016-3026, (2001).
- 60 Kalfa, V. C. *et al.* Congeners of SMAP29 kill ovine pathogens and induce ultrastructural damage in bacterial cells. *Antimicrob. Agents Chemother.* **45**, 3256-3261, (2001).
- 61 Ladokhin, A. S. *et al.* Sizing membrane pores in lipid vesicles by leakage of co-encapsulated markers: pore formation by melittin. *Biophys. J.* **72**, 1762-1766, (1997).
- 62 Long Zhu, W. L. & Shin, S. Y. Effects of dimerization of the cell-penetrating peptide Tat analog on antimicrobial activity and mechanism of bactericidal action. *J. Pept. Sci.* **15**, 345-352, (2009).
- 63 Matsuzaki, K. *et al.* Kinetics of Pore Formation by an Antimicrobial Peptide, Magainin 2, in Phospholipid Bilayers. *Biochemistry* **34**, 12553-12559, (1995).
- 64 Matsuzaki, K. *et al.* Pore formation and translocation of melittin. *Biophys. J.* **73**, 831-838, (1997).
- 65 Herce, H. D. *et al.* Arginine-rich peptides destabilize the plasma membrane, consistent with a pore formation translocation mechanism of cell-penetrating peptides. *Biophys. J.* **97**, 1917-1925, (2009).

- 66 Wu, Y. *et al.* Method of oriented circular dichroism. *Biophys. J.* **57**, 797-806, (1990).
- 67 Lee, M. T. *et al.* Energetics of Pore Formation Induced by Membrane Active Peptides. *Biochemistry* **43**, 3590-3599, (2004).
- 68 Ladokhin, A. S. *et al.* Bilayer interactions of indolicidin, a small antimicrobial peptide rich in tryptophan, proline, and basic amino acids. *Biophys. J.* **72**, 794-805, (1997).
- 69 Su, Y. *et al.* Membrane-bound dynamic structure of an arginine-rich cell-penetrating peptide, the protein transduction domain of HIV tat, from solid-state NMR. *Biochemistry* **49**, 6009-6020, (2010).
- 70 Mishra, A. *et al.* HIV TAT forms pores in membranes by inducing saddle-splay curvature: Potential role of bidentate hydrogen bonding. *Angew. Chem. Int. Ed.* **47**, 2986-2989, (2008).
- 71 Lu, N. *et al.* Molecular response and cooperative behavior during the interactions of melittin with a membrane: Dissipative quartz crystal microbalance experiments and simulations. *J. Phys. Chem. B* **116**, 9432-9438, (2012).
- 72 Cassone, M. & Otvos Jr, L. Synergy among antibacterial peptides and between peptides and small-molecule antibiotics. *Expert Rev. Anti-Infect. Ther.* **8**, 703-716, (2010).
- 73 Yasin, B. *et al.* Evaluation of the Inactivation of Infectious Herpes Simplex Virus by Host-Defense Peptides. *EJCMID* **19**, 187-194, (2000).
- 74 Bowdish, D. M. E. *et al.* A re-evaluation of the role of host defence peptides in mammalian immunity. *Curr. Protein Pept. Sci.* **6**, 35-51, (2005).
- 75 Mátyus, E. *et al.* Computer simulation of antimicrobial peptides. *Curr. Med. Chem.* **14**, 2789-2798, (2007).



# *The cell membrane: natural and artificial*

## **1 Introduction**

All AMPs come in contact with cell membranes, which can be the primary target or “an obstacle” to overcome to reach the final intracellular target. Thus an understanding of the membrane during the interaction of biomolecules, such as AMPs, has important consequences on the integrity and functionality of the membrane and, consequently on the entire cell.

The membrane is involved in many aspects of the cell existence, through delimiting and protecting the cytoplasm from the extracellular environment. Indeed the plasma membrane is also the location for almost half of cells reactions to occur. The membrane takes also part in signal transduction, energy transduction, solute transport, DNA replication, cell duplication, protein targeting and trafficking, cell-cell-recognition and secretion<sup>1,2</sup>.

The first model of biological membranes, the “fluid-mosaic” model proposed by Singer and Nicholson<sup>3</sup> (Fig. 4), depicts the membrane as a complex and dynamic mosaic composed of lipid molecules, which form a two-dimensional liquid, and proteins inserted into this fluid. Because of this fluidity, all the membrane molecules are free to move in the lateral direction of the membrane and contribute to physiological processes<sup>3,4</sup>.

The plasma membranes is more like a semi-crystalline array in which a liquid-crystalline environment coexists<sup>5</sup>. Furthermore, the plasma membrane is characterised by some localized ordering of the lipid distribution since some lipids can organise in patches, named “domains”, which are characterised by a different composition and physical state from the rest of the bilayer<sup>4</sup>. These domains, which can contain proteins, are associated with the regulation of

numerous cellular processes such as cellular polarity, protein trafficking<sup>6</sup> and endocytic pathways<sup>7</sup>.

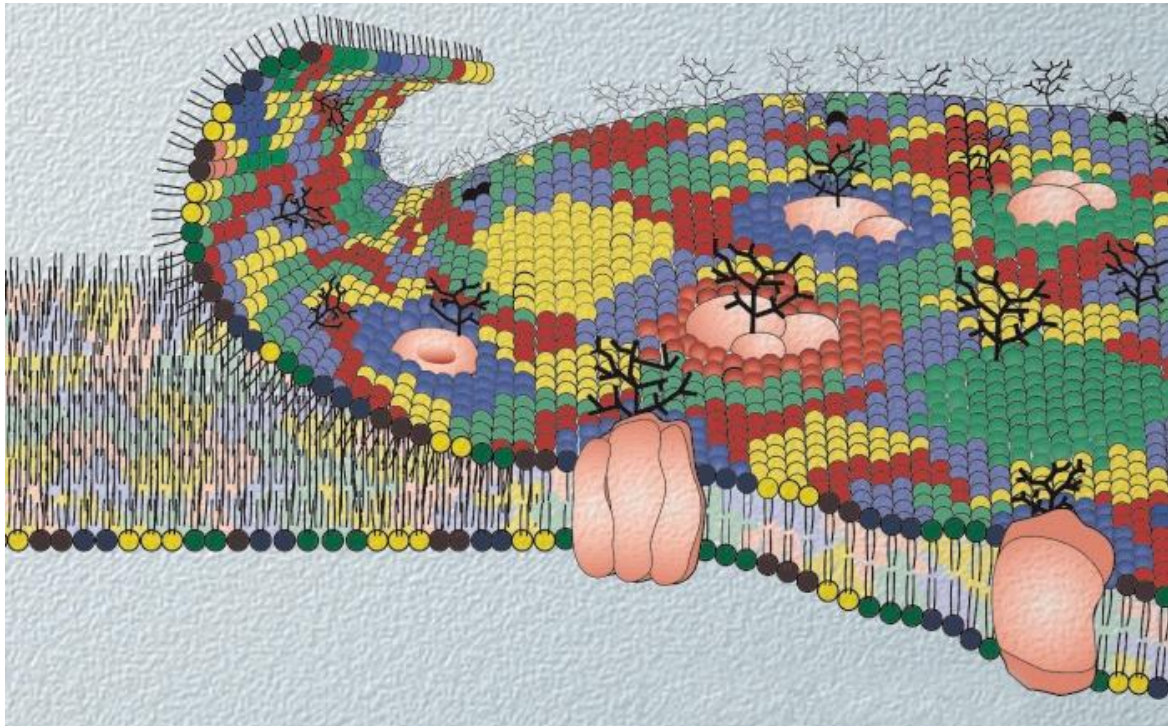


**Fig. 4:** The fluid mosaic membrane of Singer and Nicolson. Different lipids are represented by different colours; the globular structures are proteins and the black branches rising from the bilayer are glycolipids or carbohydrates<sup>4</sup>.

## 1.1 Natural membranes: composition and organization

### 1.1.1 The membrane architecture

The plasma membrane consists of a lipid bilayer (Fig. 4) held together by hydrophobic forces. These hydrophobic forces derive from the amphipathic nature of the lipid molecules. Each lipid molecule has a hydrophilic and a hydrophobic portion. The head group is hydrophilic, capable of interacting with water molecules and with each other, whereas the hydrophobic acyl chains self-associate in order to minimise any contact with the aqueous environment. This amphipathic property of the lipids enables the spontaneous formation of membranes, where the lipid acyl chains associate together in the interior of the bilayer and the polar heads are in contact with the aqueous environment on either side<sup>3,4,8</sup>.

**1.1.2 The membrane components**

A biological lipid bilayer is characterised by variable thickness, between 4 and 8 nm<sup>3,8</sup>. This variation is mainly due to the enormous assortment of lipids that contribute to the cell membrane; differentiated in acyl chain length and size of the polar headgroup<sup>2,4</sup>. Indeed, the nature of the lipid influences the membrane dynamics, including permeability and stiffness of the membrane<sup>9</sup>. Moreover, the membrane also constitutes a platform for some proteins, which can insert into the bilayer (integral proteins) or attach at the lipid surface (peripheral membrane proteins)<sup>4,8</sup>. Proteins and lipids cooperate synergistically since the lipids regulate the distribution of a protein into the membrane and consequently their functions. Also, proteins are involved in the transport and distribution of the lipid molecules throughout the membrane<sup>2,10</sup>. Other components of the plasma membrane are sterols, such as cholesterol and ergosterol, which are responsible for regulation of the eukaryotic membrane fluidity<sup>2,11</sup> and carbohydrates.

**1.1.3 Lipid composition in cell membranes**

The major structural components of the lipid bilayer in cell membranes are the phospholipids (see Fig. 5 for some examples), which consist of lipids containing hydrophobic hydrocarbon chains commonly 16 to 18 carbon atoms long. They can be divided into two major classes: glycerophospholipids and sphingolipids<sup>2</sup>.

Glycerophospholipids differ by the head group, i.e. phosphatidylcholine (PC), phosphatidylethanolamine (PE), phosphatidylserine (PS), phosphatidylinositol (PI), phosphatidic acid (PA), phosphatidylglycerol (PG) and cardiolipin (CL, which is effectively a dimer of PG)<sup>2,12</sup>. The hydrophobic portion consists of diacylglycerol, which contains saturated and/or *cis*-unsaturated fatty acyl chains of 16-18 carbons<sup>2</sup>.

Sphingolipids are the other lipid components, which are present solely in eukaryotic membranes, as showed by the graph in Fig. 5. They have a ceramide instead of a diacylglycerol linkage and examples are sphingomyelin (SM) and glycosphingolipids (GSLs). Sphingolipids have saturated or *trans*-unsaturated

acyl chains so they pack more tightly and are able to form longer, taller structures when compared to PC molecules with the same acyl chain length<sup>2</sup>. These lipids are fluidised by sterols, the other major component of eukaryotic membranes. Cholesterol is the most abundant sterol present in mammalian membranes whereas ergosterol is in yeast<sup>2</sup>.

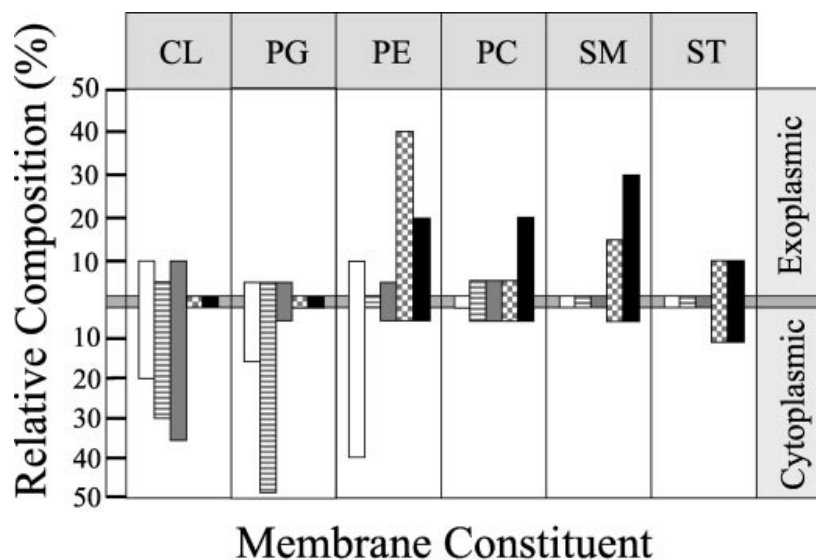


**Fig. 5:** Comparative architecture of microbial and human cytoplasmic membranes. Cytoplasmic membranes of bacterial (*E. coli*, *S. aureus*, or *B. subtilis*) and fungal (*C. albicans*) pathogens are compared with that of the human erythrocyte in relative composition and distribution between inner and outer membrane leaflets. Membrane constituents ranging from anionic (left) to zwitterionic or neutral (right) are CL, PG, PE, PC, SM, and sterols (cholesterol or ergosterol), ST. Legend of the bar content: open, *E. coli*; horizontal hatching, *S. aureus*; shaded, *B. subtilis*; checkered, *C. albicans*, solid, human erythrocyte<sup>12</sup>.

Eukaryotic membranes are particularly rich in zwitterionic lipids such as PC, which might represent more than 50% of the total phospholipids. Moreover, most of the phosphatidylcholine has one *cis*-unsaturated acyl chain, which renders them fluid at room temperature. This phospholipid, together with SM, is concentrated at the outer leaflet of the membrane<sup>12-14</sup>. Thus, due to this preferential location of PC, the eukaryotic cell membranes are considered neutral. The other major phospholipids of the plasma membrane are PS, which cover ca. 20 mol% of the total lipids<sup>15</sup> and are more concentrated within the cytosolic leaflet, together with PE. In some diseases PS is exposed on the outer monolayer of the membrane e.g. cancer, apoptotic and neural cells<sup>15,16</sup>.

Phospholipids present at lower concentrations are: PI and PA in the cytosolic leaflet of eukaryotic membranes and GSLs in the outer leaflet of the bilayer<sup>14</sup>.

The major lipid structure of prokaryotic membranes is the same as for the eukaryotic membrane; however, overall are negatively charged. This is due to the high content in PG, CL and PS, which carry a net negative charge in the membrane<sup>12,16</sup>. Bacterial membranes also include zwitterionic lipids such as PE, which in general are more abundant in the membranes of Gram-negative than Gram-positive bacteria<sup>17</sup>.

### 1.1.4 Cholesterol

Cholesterol is an essential membrane component of animal cells. Indeed, the concentration of this sterol is usually in the range between 20-30 mol%<sup>11</sup>. Only a few microbes contain cholesterol in their membrane<sup>18</sup>.

Cholesterol is not only a precursor for the synthesis of hormones and vitamins but also plays a central role in the membrane by regulating the function of the membrane proteins and is also involved in several membrane trafficking and trans-membrane signalling processes<sup>19</sup>.

The distribution of cholesterol in mammalian membranes is not homogeneous since it appears to associate preferentially with sphingolipids forming small, dynamic lipid domains, called rafts, which function as platforms for specific protein interaction for a range of cellular processes<sup>6,19</sup>.

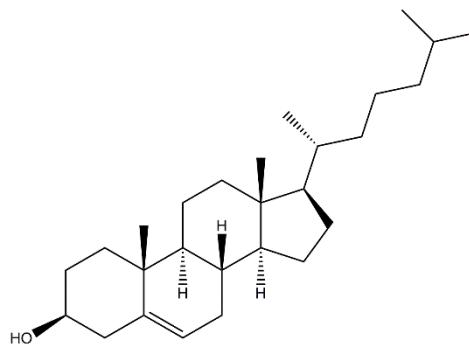


**Fig. 6:** Molecule of cholesterol.

Moreover, cholesterol has another important role: it increases the mechanical strength of the membrane, reduces passive permeability towards water and other small molecules and regulates membrane fluidity<sup>11,19,20</sup>. This

ability is determined by its structure (Fig. 6) consisting of a ring system, a short hydrocarbon chain attached to the steroid ring at position 17 and a small 3 $\beta$ -hydroxyl group, which confers an amphipathic nature to the entire cholesterol molecule<sup>11,21</sup>. Thus, the structure of cholesterol confers special biophysical properties for the membrane due to increased ordering (cohesion and packing) of neighbouring lipids. The rigid ring structure enables cholesterol to be positioned, preferentially, in close proximity to the saturated hydrocarbon chains of neighbouring lipids, as these are more inflexible and elongated compared with those of unsaturated lipids. This increase in the lateral ordering of lipids decreases the fluidity of the membrane and so it reduces permeability to polar molecules. The membrane permeability is also decreased by another effect of cholesterol, the condensing effect, defined as the decrease surface area occupied by phospholipid molecules in mixed lipid bilayers containing cholesterol<sup>6,11,22</sup>. Together, the ordering and condensing effect make the hydrocarbon chains of the phospholipid molecules orientate perpendicularly to the plane of the membrane, increasing the thickness of the membrane<sup>11,20,22</sup>. The effect of cholesterol on a layer of phospholipids does depend on several factors (as indicated on the left side in Fig. 7), i.e. cholesterol concentration, temperature, and the structure of phospholipids<sup>11</sup>. For example, cholesterol has been shown to increase the thickness of a C16:0/C18:1 phosphatidylcholine bilayer (from 35 Å to 40 Å) but not if the lipid is sphingomyelin<sup>10</sup>. In addition, the presence of double bonds in the hydrocarbon chains of lipids weakens the order and condensing effect of the cholesterol since the presence of non-saturation in the acyl chains does not encourage a close association of the rigid ring structure of the cholesterol parallel to the lipid hydrocarbon tails<sup>6,11,21</sup>.

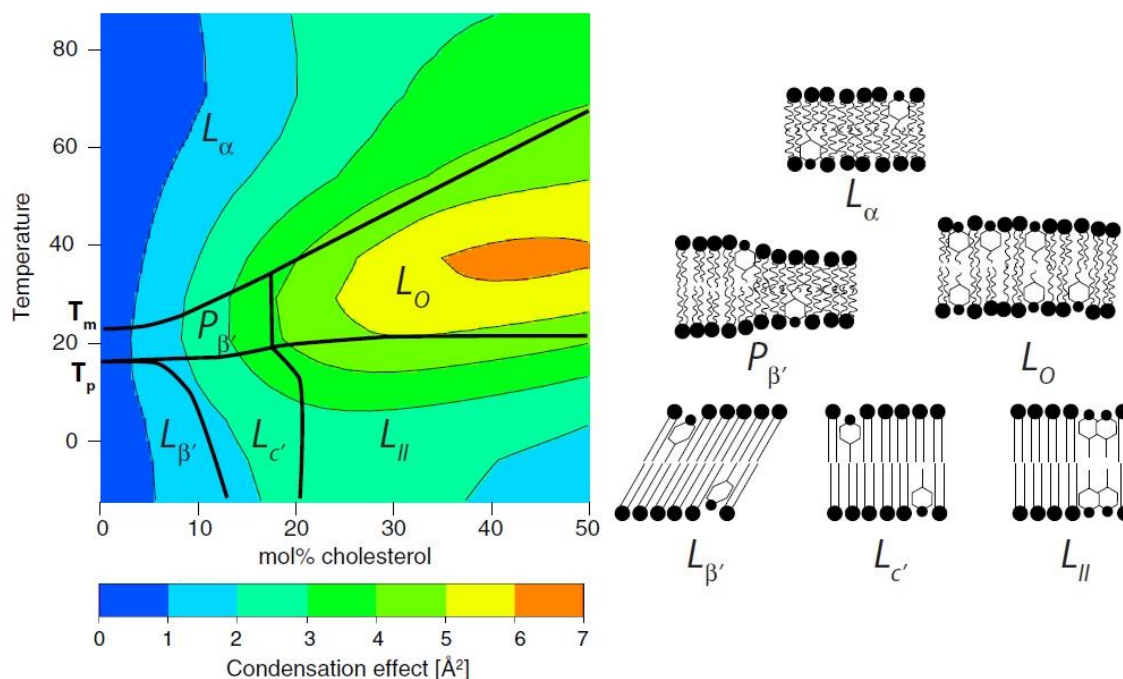


**Fig. 7:** The effect of cholesterol on a DMPC bilayer. (*Left*) The computed-phase diagram as a function of temperature (in degrees celsius) and cholesterol concentration. The black lines give the phase boundaries. On the bottom, the legend regarding the condensation effect goes from blue, which indicates very little condensation, to orange, which indicates a large condensation effect. (*Right*) A schematic representation of the various phases.  $L_{\alpha}$ , lipids in the liquid phase;  $P_{\beta'}$ , ripple phase;  $L_{\alpha}$ , liquid-ordered phase;  $L_{\beta'}$ , gel phase with tilted lipid chains;  $L_{c'}$ , gel phase with lipid chains not tilted;  $L_{II}$ , gel phase, similar to  $L_{c'}$ , containing small cholesterol clusters<sup>20</sup>.

## 1.2 The polymorphism of the membrane determines its physical and chemical properties

### 1.2.1 Phases

Membranes at the physiological temperature are mainly fluid, although not always homogeneously. This is determined mainly by the combination of structurally different lipids which differentiate in the spatial arrangement and mobility of the lipids and that provide the coexistence of fluid and solid phases within the same membrane<sup>2</sup>. Every phase has a characteristic behaviour generated from the interaction between lipid molecules is defined by two parameters: the order parameter of a segment of acyl chain,  $S$ ; and, the translational (positional) order in the bilayer plane diffusion coefficient,  $D_T$ <sup>2</sup>. Variation in these two parameters results in three main phases, which have been well characterised. (1) The liquid-crystalline or liquid-disordered ( $L_{\alpha}$  or  $L_d$ ),

which is the “normal” fluid phase in biological membranes and is characterised by having the acyl chains in a disordered conformation (low S) and a high lateral mobility of the lipids (fast  $D_T$ ). (2) The non-physiological ordered gel (solid) phase ( $S_o$  or  $L_\beta$ ), which is characterised by a high S and a slow  $D_T$ . (3) The liquid-ordered ( $L_o$ ) phase that occurs at most physiological temperatures. Here the lipids are ordered (high S as in  $S_o$ ) but retain their free rotational and lateral diffusion (fast  $D_T$  as in  $L_d$ )<sup>2,14</sup>. Hence, the lipid distribution among these phases depends on the lipid structure: lipid with long, saturated acyl chains, for instance SM, can be found in solid-like phases; whereas lipids with unsaturated hydrocarbon chains are in a liquid-phase. However, these phases are dynamic, in which their composition remains constant for a certain time, usually longer than the time required for a biomolecule (peptide, protein or virus) to bind or bud from the plasma membrane<sup>2</sup>.

Hydrated lipid bilayers can undergo phase transitions as a function of temperature<sup>6</sup>. The temperature required for a transition from solid-like to a liquid-like phase is named the main transition temperature ( $T_m$ ) and is characteristic for each lipid type, (for example DMPC and DMPG have a  $T_m$  of 24 °C in pure water)<sup>6,8</sup>. More precisely,  $T_m$  characterises the transition from  $P_\beta'$  to  $L_\alpha$ <sup>8</sup>, where  $P_\beta'$  is the ripple-gel phase.  $P_\beta'$  is a microphase characterized by the coexistence of both, (i) domains in which the bilayer is thick and the lipids are ordered and (ii) domains in which the bilayer is thin and lipids are disordered<sup>20</sup>. The temperature at which the transition from the solid phase  $L_\beta$  to  $P_\beta'$  occurs is called the pre-transition ( $T_p$ ) and for DMPC is ~14 °C in pure water<sup>8,20,23</sup>.

In nature, the membrane is characterised by lateral heterogeneity from the coexistence of liquid domains, which are immiscible with other liquid domains<sup>6</sup>. For example, in a mixture of phosphatidylcholine plus cholesterol the  $L_\alpha$  and the  $L_o$  phases can coexist. Cholesterol at sufficient molar fractions (~20 mol%) can convert  $L_d$  or  $S_o$  phases to liquid-ordered ( $L_o$ ) phases. This is possible because the characteristic structure of cholesterol enforces some conformational ordering upon the aliphatic chain lying closest to the cholesterol, without imposing a corresponding drastic reduction of the positional mobility of the lipid

layer overall<sup>6,8,21</sup>. In this phase, the thickness of the bilayer is an intermediate between the solid-phase and the liquid-disordered phase<sup>8,20</sup>.

The transitions between various phases for a DMPC bilayer on addition of cholesterol has been the object of simulation studies<sup>20,23</sup> illustrated in Fig. 7. These simulations confirmed most of the experimental data<sup>22,24,25</sup>, such that phase transitions of saturated phospholipids e.g. DMPC are a function of the molar concentration of cholesterol and the temperature. Indeed, a transition from ripple ( $P_{\beta}'$ ) phase to liquid-ordered ( $L_0$ ) phases occurs at  $\sim 20$  mol% cholesterol, at a temperature above  $T_p$ <sup>6</sup>. Interestingly, these simulations revealed a major condensing effect by cholesterol in the  $L_0$  phase, at a cholesterol concentration above 35 mol%.

In addition, the phase transition of the lipid is not influenced only by the presence of cholesterol in the membrane, but also from the interaction with AMPs. An example is arenicin-1, which showed to influence the transition from gel-phase to liquid-phase of monolayers composed of anionic phospholipids<sup>26</sup>. However, this effect is not unidirectional since it has been shown that also changes in the phase of the lipids can influence the orientation of the peptide in the membrane hence its action. For instance, alamethicin changes orientation within the membrane from trans-membrane, responsible of pore formation, to parallel to the membrane plane when the lipid changes from fluid to gel phase<sup>27</sup>. Furthermore, the lytic action of aurein 1.2 peptide towards DMPC membranes was further enhanced by the lipid transition from fluid to gel phase<sup>28</sup>.

### **1.2.2 The membrane curvature**

The polymorphism of the membrane is also a key factor in determining the spontaneous curvature of the membrane. Indeed, biological membranes are not linear platforms but have local intrinsic curvatures. These curvature are the result of a combination between: (a), the asymmetrical composition; (b), the lateral distribution of the lipids; (c), the forces applied to the membrane; (d), the presence of integral and peripheral membrane proteins, (e), the insertion of amphipathic helices of proteins and peptides, and (f), the changes in the cytoskeleton<sup>5,9,14</sup>. Fundamentally, the structure of the lipids has a relevant

influence in determining the curvature of the membrane<sup>8</sup>: the relative size of the head groups with respect to the size of the acyl tails determines the shape of a lipid molecule<sup>10</sup>. A “cylindrical” lipid such as PC and PS (see Fig. 8) confers zero intrinsic curvature resulting in a flat monolayer or bilayer; lipids with small head-groups, like PE, are defined as “cone-shaped” and confer an intrinsic negative curvature to the monolayer. In contrast, the shape of lipids having large head groups in respect to the hydrophobic part such as lysophosphatidylcholines (LPC) are named inverted cones<sup>8,10</sup>.

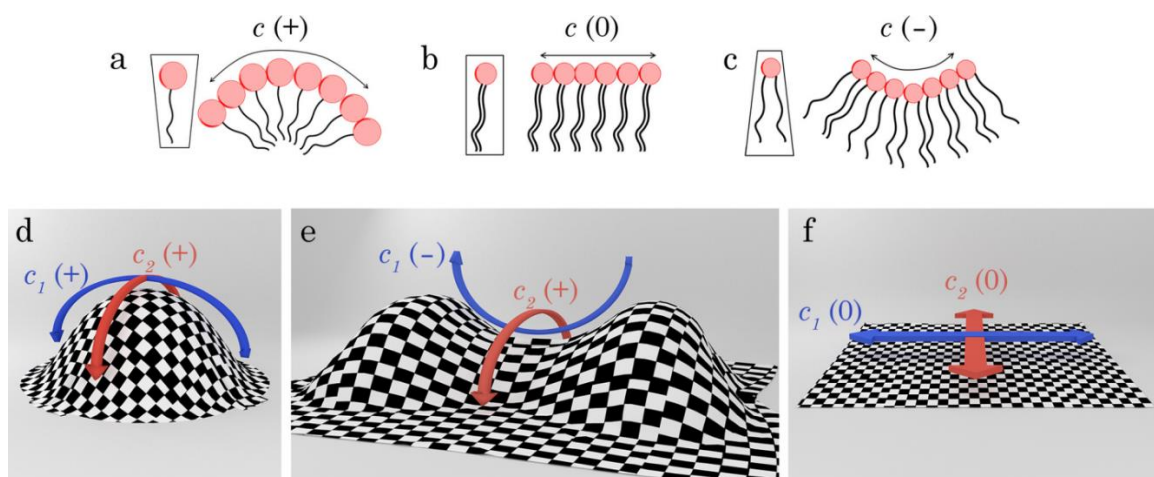


**Fig. 8:** Illustration of the three possible curvature values “ $c$ ” (a, b, and c) and the arising molecular shapes of phospholipids monolayer bending as a result of the combination of two main curvature values (i.e.  $c_1$  and  $c_2$ ). (d) inverted cone (e.g. lysophosphatidylcholines (LPC)), which forms monolayers having high positive curvatures, i.e. micelles, (e) cone-shaped (e.g. PE), which originates from monolayers having negative intrinsic curvature, i.e. inverted micelles, and (f) cylindrical shape (e.g. PC), which forms planar monolayers (zero intrinsic curvature)<sup>8,10</sup>.

The lipid molecules forming a monolayer determine the intrinsic curvature, therefore the sum of the curvatures of the two monolayers determine the spontaneous curvature of a bilayer. For example, if the two monolayers are identical in composition their spontaneous curvatures cancel<sup>29</sup>.

Overall, two main curvatures ( $c_1$  and  $c_2$ ) for each point of the membrane are used in determining the curvature along the two perpendicular principal directions of the membrane (see Fig. 8). These curvatures can be positive or negative and thus define the shape of the membrane in that point<sup>30</sup>. Examples of membranes with a positive curvature are vesicles that are budding, whereas membranes with negative curvature are observed during cell cleavage while

duplicating, or membrane that fuse with another membrane<sup>8,10,30</sup>. The combination of these two principal curvatures is used to describe the main shapes of the membrane: plane, cylinder, sphere or saddle<sup>30</sup>. In the plane geometry, both  $c_1$  and  $c_2$  are zero. A sphere has both positive curvature ( $c_1=c_2$ ), whereas a saddle-like shape has one positive and one negative curvature ( $-c_1=c_2$ )<sup>30,31</sup>. Saddle-like curvature are topologically necessary for the formation of membrane pores, membrane invaginations (such as those in endocytosis) and membrane protrusions (such as those in macropinocytosis)<sup>31,32</sup>.

The curvature of the membrane can influence the interactions of biomolecules such as AMPs (i.e. magainin)<sup>33</sup> and CPPs (i.e. Tat peptide)<sup>29</sup>. However, this influence is not unidirectional since the membrane can change its spontaneous curvature when it comes into contact with some proteins, for example, BAR-domain containing proteins or COPI & II complexes<sup>28</sup> or when in contact with AMPs, such as melittin<sup>31</sup>.

### 1.3 Artificial membranes

Since the plasma membrane is a very complex and dynamic mixture of lipids and proteins, many of its properties are difficult to characterize *in vivo*, such as the lipid phase transition, the influence of cholesterol and the membrane curvatures. Consequently, artificial membranes, which are a simplified representation of the membrane core, the phospholipid bilayer, represent a good alternative for experimental investigations. For instance, visualization of the coexisting phases or domains can be observed by fluorescence microscopy on biomimetic membranes but not in the biomembranes of living cells<sup>2,19</sup>. Furthermore, the possible interactions with biomolecules such as proteins and peptides can be investigated in a controlled environment, which can be manipulated (temperature, membrane composition, etc) to detect variations in these interactions.

However, for the same reason, given the simplicity of the model membranes, it should be always kept in mind that there is not always a direct

correlation between the natural and artificial membranes. That is, the results obtained with artificial membranes cannot always be directly transposed or does not reflect, in a direct manner, what happens with natural membranes<sup>34</sup>. Thus, systems with model membranes often are complementary since they can contribute to the interpretation of experimental observations and the development of mechanistic models, or be the prelude for new scenarios that can be tested in more complex biological settings at a later time.

The main focus of the work here presented and discussed is the characterization of the action of AMPs towards artificial membranes using a quartz crystal microbalance (QCM) technique. QCM uses a gold coated sensor, which can be used in subsequent methods, such as, scanning electrochemical microscopy (SECM). A working condition in both of these techniques is that the sample (in this case an artificial membrane) is immobilized on the sensor surface. Therefore, the membrane used for these studies must to be a stable bilayer “spread” on across the sensor surface. Liposomes were deposited enabling a lipid bilayer to form on the support following liposome rupture.

### **1.3.1 Liposomes**

Artificial membranes are numerous, as shown in Fig. 9, and are typically designed for a specific application. Lipid vesicles or liposomes are commonly used for spectroscopic assays, such as dye-leakage<sup>35</sup>, CD<sup>36</sup>, confocal microscopy<sup>37</sup>, and synchrotron X-ray scattering (SAXS)<sup>31,32,37</sup>. A complete review of liposomes and their preparation methods has been written by Samad et al.<sup>38</sup>. Briefly, liposomes can be categorized according to lamellarity (multi- or unilamellar) and size, typically as small vesicles of 20-100 nm (SUV), large vesicles of approximately 100 nm to 1  $\mu\text{m}$  (LUV) and giant vesicles with a diameter above 1  $\mu\text{m}$  (GUV)<sup>36</sup>. Usually, LUVs are used in spectroscopy measurements, while SUVs are the preferential vesicles used for the formation of supported lipid bilayers (SLBs)<sup>39</sup>.

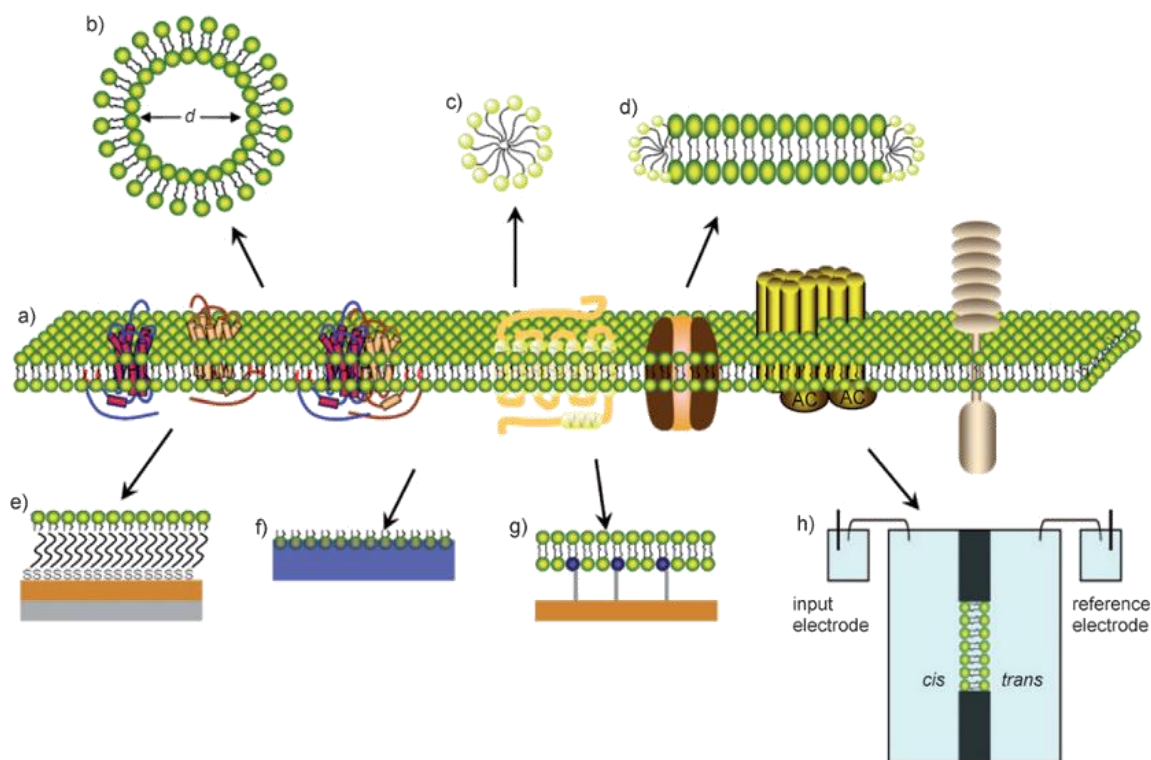


**Fig. 9:** Examples of artificial membranes as models of: a) natural cell membrane; b) vesicle or liposome; c) micelle; d) bicelle; e) supported lipid monolayer; f) self-assembled lipid monolayer at the air–water interface; g) tethered supported lipid bilayer; h) planar lipid bilayer<sup>33</sup>.

In this work, liposomes were used to create SLBs in order to investigate possible interactions with peptides of various origins. These liposomes were prepared from stock solutions of DMPC, DMPG (see Fig. 10) and cholesterol, prepared by dissolution in chloroform (small amount of methanol was required for DMPG). The concentration for each lipid was 5 mM. Mixtures of DMPC and DMPG corresponding to a volume ratio of 4:1 and 2:1 were used to mimic bacterial membranes since DMPG is present at high concentrations in many bacterial membranes<sup>12</sup>. Indeed, DMPG is important because not only because it confers a negative charge to the membrane surface, but also because it is involved in DNA synthesis and cell growth and it influences the insertion and translocation of proteins across prokaryotic membranes. In the same way, DMPC is present in high concentrations in eukaryotic cell membranes, gram-negative bacteria and in many gram-positive bacteria<sup>1</sup>. In order to closely resemble an eukaryotic membrane, cholesterol was added (30 mol%) to DMPC forming thus a mixture with a volume ratio of 3:7.

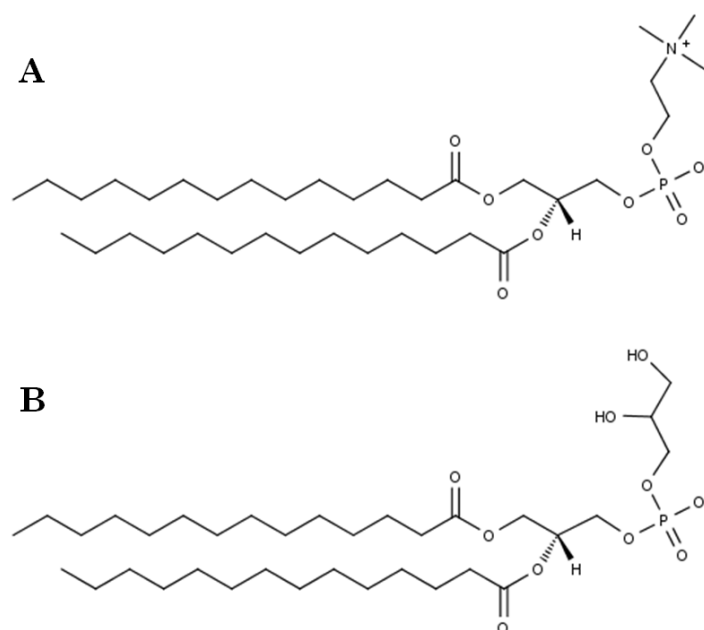


**Fig. 10:** The phospholipids used in this study. (A) 1,2-dimyristoyl-*sn*-glycero-3-phosphocholine (DMPC), which is zwitterionic; and (B) 1,2-dimyristoyl-*sn*-glycero-3-phosphoglycerol (DMPG), which is negatively charged at physiological pH.

The choice of the lipids DMPC, DMPG (Fig. 10) and cholesterol has the advantage that the formation of the membrane with these lipids is achieved more easily. Although the natural membrane is mainly composed of unsaturated phospholipids with longer acyl chains, the use of these lipids with saturated acyl chains (Fig. 10) allows for easier control of deposition in the QCM instrument. Moreover, the same membrane composition has been used in many *in vitro* investigations with various peptides<sup>40-44</sup>.

### 1.3.2 Supported lipid bilayers (SLBs)

SLBs consist of planar lipid bilayers, mostly phospholipids formed by the deposition of unilamellar vesicles on a solid surface that does not influence the membrane properties<sup>35,45</sup>. The use of liposomes is preferred over the Langmuir-Blodgett trough because it is a simple method, only basic laboratory equipment is needed and it is used by many researchers and in commercial applications<sup>46-48</sup>.

SLBs can be applied across a diversity of fields of biology and biotechnology<sup>41</sup>. For example, in determining the influence of lipids on aggregation of peptides or proteins<sup>35,49</sup>, investigating the action of peptides such

AMPs<sup>50-52</sup> or CPPs<sup>32,37</sup> on membranes, as well as the effect of nanoparticles on artificial membranes<sup>53</sup>.

The use of SLBs presents a few advantages: it is cost-effective, it does not require long and difficult protocols; moreover, the surface of the sensor can be regenerated after each use. SLBs have also the advantage of being stable allowing experiments that last 24 hours or more. Furthermore, the employment of SLBs allows detection and comparison, in real time, of various mechanisms adopted by the AMPs when in contact with the membrane. An aspect that the liposomes employed for dye-leakage assays are not able to provide<sup>35</sup>. Nevertheless, the formation of SLBs is not straight forward and requires some time, unlike the generation of liposomes, which is easier and quicker to achieve. Moreover, the assumption to have a homogeneous bilayer is not straightforward since it is influenced by many factors such as the nature of the lipid, the size of the liposome used for their formation, the surface, the osmotic pressure<sup>54-56</sup>. However, the variation in SLBs formation using liposomes was investigated by QCM, AFM and DLS (see paper 1 in this chapter), and the expected values found to be a frequency change ( $\Delta f$ ) – 15 Hz for in and a dissipation change ( $\Delta D$ ) less than  $4 \times 10^{-6}$  for a bilayer.

However, the mechanism of liposome deposition and fusion needed to create these SLBs is still the object of several studies, albeit there has been important progress in our understanding of this process during the past few years<sup>57,58</sup>. In particular to analyse these processes, several different techniques have been used, often in combination, such as SPR, for quantify the mass deposited<sup>59</sup>; quartz crystal microbalance (QCM), mainly for mechanistic information<sup>60</sup>; and AFM for revealing differences in the morphology of lipid deposition<sup>61</sup>.

### 1.3.2.1 Self-assembled monolayers (SAMs)

Different kinds of surfaces are employed for the deposition of liposomes, mostly depending of the experimental instrumentation. For instance, the surfaces used in AFM consist of flat gold, mica or silica; gold as a surface is used

also in SPR<sup>35,62</sup> and QCM<sup>37</sup>, whereas glass is used for X-ray and neutron scattering studies<sup>63,64</sup>.

Among these surfaces, gold is used extensively for analytical techniques such as SPR, QCM and ellipsometry, because it represents a good surface for the formation of self-assembled monolayers (SAMs). Several reasons justify this choice: thin films of gold are easily obtained by physical vapour deposition, electrodeposition, or sputtering. Moreover, gold is easy to handle, manipulate and clean since it does not oxidise at temperatures below its melting point; it does not react with most of the chemicals and with atmospheric oxygen<sup>55</sup>. Furthermore, gold has a high affinity for thiols, which spontaneously form alkanethiol SAMs on it and are stable for long periods<sup>65,66</sup>. Another reason for using thiols is the formation of well-defined monolayers in just few minutes from the initial contact with the surface, upon which there is a slow reorganization over a period of several hours<sup>67</sup>. The formation of self-assembled monolayers (SAMs) on a surface has some advantages: e.g. they contribute to the rupture of liposomes forming SLBs. Also, the existence of a SAM underneath a supported membrane enhances the resistance of the membrane to high mechanical stress, such as those due to flushing of solutions at high speed over the membrane layer.

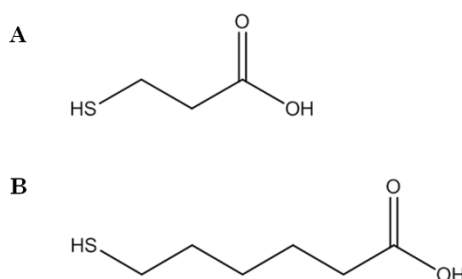


**Fig. 11:** Molecular structures of thiol-substituted carboxylic acid compounds used in this study as SAM: (A) 3-mercapto-propionic acid (MPA), (B) 6-mercaptohexanoic acid (MHA). The presence of the carboxylic acid is responsible for the formation of a hydrophilic layer, which assists in the vesicle deposition, rupture and consequently formation of a lipid bilayer.

SAMs are used to build molecular layers because they can form well-ordered and packed layers thus generally lacking in defects<sup>55</sup>. Naturally, this order is a function of the smoothness of the surface and of the molecule length<sup>57</sup>.

However, the formation of a uniform monolayer on the surface sensor cannot be verified by QCM. For this reason, SAMs of 6-mercaptohexanoic acid (MHA) (Fig. 11) were used for investigating the interactions of Tat peptides with SLBs (see Chapter 5) by scanning electrochemical microscopy (SECM): a length of six carbons instead of three (3-mercapto-propionic acid (MPA)) (Fig. 11) was shown to create a more ordered, compact insulating monolayer. Otherwise, SAMs of MPA were employed in order to aid the rupture of liposomes on gold sensor surfaces, as shown in Fig. 12.

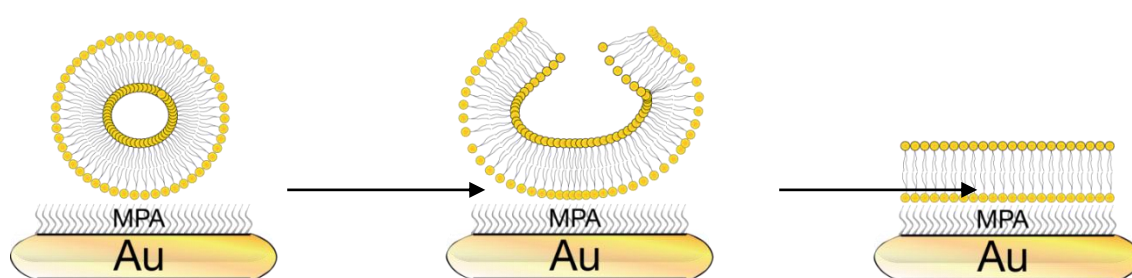


Fig. 12: Graphic representation of the process of membrane deposition by vesicles rupture.

## 2 Techniques

### 2.1 Membrane properties studied using a Quartz crystal microbalance with dissipation monitoring (QCM-D)

The formation of artificial membranes on solid support (SLBs) can be investigated using several analytical instruments. Quartz crystal microbalance with dissipation monitoring (QCM-D) is among these. QCM-D is a label-free surface sensitive technique that measures changes in mass/ thickness and viscoelastic properties of thin films deposited on a sensor surface by measuring the change in frequency of a quartz crystal resonator.

QCM-D is an acoustic sensor, which is a combination of a molecular recognition detector and a transducer. Thus, as an acoustic sensor, it can provide a broad range of information in real time of events happening *in situ* such as the adsorption/ desorption of mass, and changes in density and

viscoelasticity<sup>50,68,69</sup>. For this reason, QCM now has been applied in various research fields. A recent review of the application of QCM can be found by Speight and Cooper<sup>70</sup>. Briefly, QCM has been applied in characterizing the deposition and formation of SLBs<sup>55,56,58,71</sup>, and in characterizing the interactions between SLBs and AMPs<sup>42,50,72,73</sup> or proteins<sup>74,75</sup>.

The working principle of QCM is based on the piezoelectric properties of a quartz crystal. Piezoelectricity is the coupling between a material's mechanical and electrical behaviours<sup>58</sup>. This means that when a piezoelectric material is subject to an electrical field, it mechanically deforms, and vice versa. Thus, when an oscillating electrical field is applied to a QCM sensor, which has gold electrodes plated on both sides (see Fig. 3), an internal mechanical stress is created. This stress results in a mechanical shear (tangential) wave which propagates through the crystal in a direction orthogonal to the crystal surface. This direction is achieved by cutting the crystal in a specific orientation: indeed the QCM crystals are AT-cut (i.e. a disk cut from a quartz mineral at a 35.25° orientation to its optical axis)<sup>69,76</sup>.



**Fig. 13:** A picture of the two sides of the QCM-D sensor: (a) under surface and (b) working surface.

Resonance will occur when the frequency of the applied potential corresponds to the resonant frequencies of the quartz crystal sensor ( $n = 1, 3, 5, \dots$ ) and is disrupted by adding or removing mass from the sensor surface. The relationship between the change in mass ( $\Delta m$ ) and the change in the oscillation of the  $n^{\text{th}}$  harmonic in frequencies ( $\Delta f_n$ ) is described by the Sauerbrey equation (1):

$$\frac{\Delta f_n}{n} = -\frac{2f_o^2}{A\sqrt{\rho_q\mu_q}}\Delta m \quad (1)$$

where  $f_o$  is the fundamental resonant frequency,  $A$  is the piezoelectric crystal active area (between the electrodes),  $\rho_q$  is the density of the quartz (2.648 g/cm<sup>3</sup>) and  $\mu_q$  is the shear modulus of the quartz (2.947x10<sup>11</sup> g · cm<sup>-1</sup> · s<sup>-2</sup>)<sup>50,77</sup>. Therefore, the change in frequency is inversely related to the change in mass attached to the sensor:

$$\Delta m = -C \frac{\Delta f_n}{n} \quad (2)$$

where  $C$  is the mass sensitivity constant and corresponds to 17.7 ng cm<sup>-2</sup> Hz<sup>-1</sup> for a sensor with fundamental frequency of 5 MHz that oscillates at its fundamental mode ( $n= 1$ ). This linear relationship is valid for rigid and thin films evenly distributed on the sensor surface. However, viscoelastic films do not couple well to the oscillation of the crystal, thus the Sauerbrey equation must be adjusted taking in consideration the viscosity and the density of the film. Kanazawa and Gordon<sup>78</sup> modified the Sauerbrey equation (1) for crystals immersed in solutions:

$$\Delta f = f_o^{3/2} \sqrt{\frac{\rho_l\eta_l}{\pi\mu_q\rho_q}} \quad (3)$$

where  $\rho_l$  and  $\eta_l$  are the density and the viscosity of the film, respectively. Thus, the change in the resonant frequencies is a function of the liquid density and viscosity. Furthermore, the distance covered by this acoustic wave before it decays is defined as penetration depth ( $\delta$ ), which is a function of the viscosity and density of the liquid:

$$\delta = \sqrt{\frac{\eta_l}{\pi f \rho_l}} \quad (4)$$

Thus, each harmonic of a sensor crystal can be correlated with changes in various depths of a film deposited on the crystal: the higher the frequency, the shorter is the distance covered by the shear wave.

In order to obtain information about changes in the structural properties of the film adsorbed, Rodhal et al.<sup>79</sup> developed the QCM-D instrument to include measurement of changes in the dissipation energy ( $D$ ), which is defined as the ratio of the energy dissipated during one oscillation cycle after removing the AC voltage and the total energy stored in the sensor<sup>58</sup>:

$$D = \frac{1}{2\pi} \times \frac{E_{dissipated}}{E_{stored}} \quad (5)$$

Indeed, when the drive potential applied is switched off, the voltage over the crystal decays as an exponentially damped sinusoidal<sup>73</sup>:

$$A(t) = A_0 e^{t/\tau} \sin(2\pi f t + \varphi) \quad (6)$$

where  $\tau$  is the decay time constant,  $f$  the frequency and  $\varphi$  is the phase angle. The decay time constant is related to the  $D$  by the relation<sup>73</sup>:

$$D = \frac{1}{\pi f \tau} \quad (7)$$

Changes in  $D$  are obtained simultaneously with the changes in frequency by switching off the voltage once every second. Thus, if a viscoelastic film is deposited on this crystal but is not fully coupled to the oscillation of the crystal, it will dampen the crystal's oscillation. This causes an increase in the energy lost and thus in  $D$ .

A typical QCM-D experiment is illustrated in Fig. 14. Briefly, initially (phase **i**), the QCM sensor is oscillating in a pure aqueous environment, which is exchanged with a high-salt PBS solution (100mM NaCl). Then (**ii**), a liposome containing solution is introduced, which causes a decrease in the frequency and an increase in dissipation. Once the frequency reaches a value corresponding to

the formation of a complete bilayer, the flow is interrupted. In (iii), the introduction of a low-salt PBS (0.03 mM NaCl) washes any unburst or embedded liposomes. In (iv), high-salt PBS is flushed until a stable baseline is established and in step (v) the peptide solution is introduced. After the flow of peptide solution is terminated, in phase (vi), the overall system is left to equilibrate for at least 30 min. In the final phase (vii), high-salt buffer is flushed into the chamber. Importantly for both parameters,  $f$  and  $D$ , values are recorded for the third, fifth, seventh and ninth harmonics to give an analysis of the depth of an interaction. The experiments discussed in this work were done in triplicate, at a working temperature of 19.1°C and at pH 6.9, unless otherwise stated. The temperature of 19.1°C was chosen for experimental reasons. At this temperature to the formation of air bubbles in solution is minimised, which can compromise the QCM experiment.

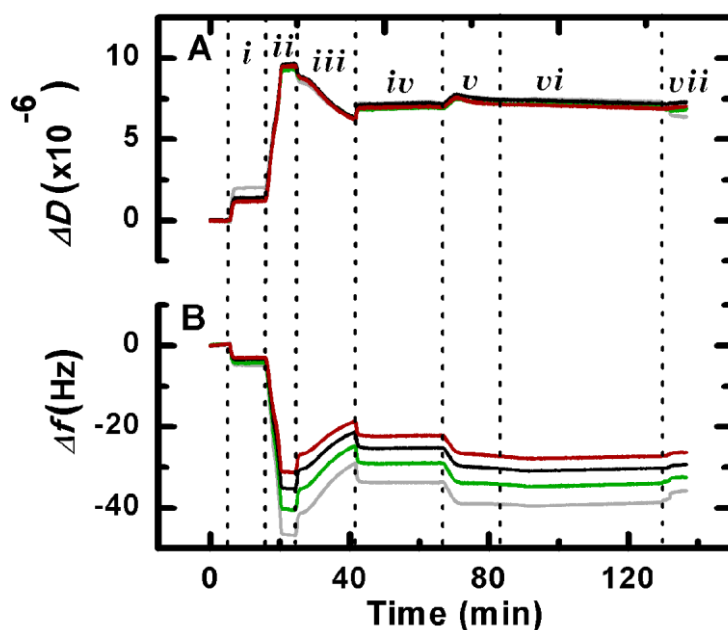


**Fig. 14:** A typical example of a QCM-D experiment from work in this thesis. The upper trace illustrates  $\Delta D$ - $t$  (A) and  $\Delta f$ - $t$  (B) plots, respectively. See text for further explanation. Grey, green, black and red traces correspond to the 3<sup>rd</sup>, 5<sup>th</sup>, 7<sup>th</sup>, and 9<sup>th</sup> harmonics respectively. The normal mass sensitivity in water is  $\sim 1.8 \text{ ng/cm}^2$  and the normal dissipation in water is  $\sim 1 \times 10^{-6}$ .

### **2.1.1 Osmotic pressure**

The introduction of the PBS buffer containing a salt concentration lower in salt (NaCl 0.03 mM) (see Fig. 14, *iii*) was used in the protocol for membrane deposition in QCM after the publication of paper 1.

The lipid bilayer is a semi-permeable membrane as small molecules and water molecules can pass through although very slowly<sup>80</sup>. Thus, the creation of an osmotic stress to assist with the rupture and fusion of liposomes on solid support has been already employed in early investigations, which demonstrated that hyposmotic solutions caused the vesicles to burst and fuse<sup>81-83</sup>. For this reason, this thesis employs the use of low-salt buffer in order to aid the rupture of vesicles that were still attached on the sensor surface before the PBS high-salt (100 mM NaCl) solution was re-introduced. Thus, the lipid vesicles containing a high salt concentration (100 mM) are impacted by the low salt concentration in the bulk solution (0.03 mM). This osmotic pressure difference causes the vesicles to swell and rupture, leaving a lipid bilayer.

However, the use of osmotic stress to assist with the vesicle deposition has also been investigated by other researchers using the QCM-D method and they reported that a better deposition of the bilayer occurred when the vesicles were exposed to buffers with higher salt concentrations<sup>60,71,84</sup>.

### **3 Paper 1:**

**3.1 Structure and homogeneity of pseudo-physiological phospholipid bilayers and their deposition characteristics on carboxylic acid terminated self-assembled monolayers.**

Monash University

**Declaration for paper 1****Declaration by candidate**

In the case of Chapter 1, the nature and extent of my contribution to the work was the following:

<b>Nature of contribution</b>	<b>Extent of contribution (%)</b>
QCM experiments	20%

The following co-authors contributed to the work. If co-authors are students at Monash University, the extent of their contribution in percentage terms must be stated:

<b>Name</b>	<b>Nature of contribution</b>	<b>Extent of contribution (%) for student co-authors only</b>
<b>Adam Mechler</b>	Key ideas, AFM interpretation, manuscript preparation	
<b>Slavica Praporski</b>	Design and performance of QCM-D and DLS experiments, data analysis and Voigt modelling, manuscript review	20%
<b>Steven M. Heaton</b>	DLS and QCM-D experiments	5%
<b>Kristopher N.Hall</b>	AFM imaging	10%
<b>Marie-Isabel Aguilar</b>	Key ideas, manuscript review	
<b>Lisandra L. Martin</b>	Key ideas, manuscript review	

## Chapter 2

The undersigned hereby certify that the above declaration correctly reflects the nature and extent of the candidate's and co-authors' contributions to this work\*.

<b>Candidate's Signature</b>		<b>Date</b> 23/05/14
<b>Main Supervisor's Signature</b>		<b>Date</b> 23/05/14

\*Note: Where the responsible author is not the candidate's main supervisor, the main supervisor should consult with the responsible author to agree on the respective contributions of the authors.



## Structure and homogeneity of pseudo-physiological phospholipid bilayers and their deposition characteristics on carboxylic acid terminated self-assembled monolayers

Adam Mechler<sup>a,\*</sup>, Slavica Praporski<sup>a</sup>, Stefania Piantavigna<sup>a</sup>, Steven M. Heaton<sup>a</sup>, Kristopher N. Hall<sup>b</sup>, Marie-Isabel Aguilar<sup>b</sup>, Lisandra L. Martin<sup>a,\*</sup>

<sup>a</sup> School of Chemistry, Monash University, Clayton, Victoria 3800, Australia

<sup>b</sup> Department of Biochemistry and Molecular Biology, Monash University, Clayton, Victoria 3800, Australia

### ARTICLE INFO

#### Article history:

Received 19 August 2008

Accepted 21 October 2008

Available online 9 November 2008

#### Keywords:

Lipid

Membrane

Liposome

AFM

Surface topography

Biomimetic material

### ABSTRACT

Supported phospholipid bilayers are frequently used to establish a pseudo-physiological environment required for the study of protein function or the design of enzyme-based biosensors and biocatalytic reactors. These membranes are deposited from bilayer vesicles (liposomes) that rupture and fuse into a planar membrane upon adhesion to a surface. However, the morphology and homogeneity of the resulting layer is affected by the characteristics of the precursor liposome suspension and the substrate. Here we show that two distinct liposome populations contribute to membrane formation – equilibrium liposomes and small unilamellar vesicles. Liposome deposition onto carboxylic acid terminated self-assembled monolayers resulted in planar mono- and multilayer, vesicular and composite membranes, as a function of liposome size and composition. Quartz crystal microbalance data provided estimates for layer thicknesses and shear moduli and were used for classification of the final structure. Finally, atomic force microscopy data illustrated the inherently inhomogeneous and dynamic nature of these membranes.

© 2008 Elsevier Ltd. All rights reserved.

### 1. Introduction

Biomimetic membranes are artificial mixtures of phospholipids that imitate the composition of a cell membrane and are used to study biological membrane processes [1,2]. Biological activity and gating of ion channels [3], membrane disruption by antimicrobial peptides [4], electrochemistry of biological charge transfer [5] can all be studied in a controlled environment this way, while biosensor, biocatalytic reactor and artificial cell designs also rely extensively on biomimetic membranes. Analytical tools such as surface plasmon resonance [6] or quartz crystal microbalance (QCM) [7] use biomimetic membranes to establish a pseudo-physiological environment for the study of protein function. It is therefore crucial to create biomimetic membranes in a reproducible way with well defined and controlled properties.

The aim of our study was to characterize the process of liposome deposition, where surface adhesion (and deformation [8–10]),

rupture, collapse and concomitant fusion of phospholipid bilayer vesicles (liposomes) results in the formation of a biomimetic membrane [11]. Liposome deposition is believed to create homogeneous, single bilayer membranes [2] or stable vesicular layers [12–14], depending on the substrate material [12,13,15] and liposome size [15–17]. However, a clear differentiation between vesicular and planar layers is not always possible [16]. The deposition process does not always stop at a single bilayer [18] and often the nanometer scale morphology of the deposited material undergoes a slow post-deposition rearrangement in which liposomes burst after reaching a critical surface concentration [14] or slowly fuse into a bilayer while retaining a small population of unopened liposomes [17,19]. Nanometer scale domain separation of lipid mixtures may influence the homogeneity of membranes [20–22]. These “lipid raft” nanodomains are preferred regions for protein incorporation in cellular membranes [20,23] and represent the coexistence of stable gel- and fluid phase mixtures at a given temperature [24]. Thus, there is significant variation in the morphology and structure of liposome-deposited biomimetic membranes.

Liposomes readily form upon sonication and/or vortexing of a lipid suspension in buffer solution. The assembly of lipid

\* Corresponding authors. Fax: +61 3 9905 4597.

E-mail addresses: [adam.mechler@sci.monash.edu.au](mailto:adam.mechler@sci.monash.edu.au) (A. Mechler), [lisa.martin@sci.monash.edu.au](mailto:lisa.martin@sci.monash.edu.au) (L.L. Martin).

molecules into such bilayer vesicles can be explained by two contrasting models. The molecular self-assembly model [25] assumes that liposomes form spontaneously, under thermodynamic control; the globular shape and the size distribution represent an equilibrium. The continuum model [26] treats liposomes as metastable distortions of a planar membrane, where a high potential energy barrier prevents the liposomes from returning to the planar form. The models contrast in the prediction of expected liposome size, shape and stability criteria. The continuum model permits arbitrary diameters that are conserved until the liposome bursts. A local energy minimum might be achieved through geometric variations; thus a variety of liposome shapes, e.g. globular, donut and dumbbell are predicted [8,27]. In the molecular model, the free energy minimum is reached at a certain diameter, determined by both enthalpic and entropic factors, accordingly, an equilibrium size distribution evolves. The two models converge by defining the smallest liposome attainable, called the Small Unilamellar Vesicle (SUV) [28] which is often cited as the optimal precursor of membrane deposition [12,13,29]. The existence of the SUV is explained either with 'molecular packing constraints', comprising of critical distance and angle of neighbouring molecules that can still support a bilayer [25], or as an empirical "persistence length", a factor relating the critical liposome radius to the bending rigidity of the membrane [30]. The two models can be reconciled further by recognising that in the continuum model the energy gap between a planar and a vesicular membrane is not necessarily large, thus entropic factors can contribute and a thermodynamic equilibrium size distribution is possible [30,31]. Therefore, different liposome sizes might evolve as a function of accessible entropy-increasing mechanisms, such as widening or polydisperse size distribution, variations in geometrical shape, or surface waves – undulations – on larger vesicles. Spontaneous "ripening", changing size distribution, has been reported experimentally for some lipids [31,33], suggesting that individual phospholipid molecules can be exchanged between liposomes. The process can be accelerated, but not altered, by using sonication [31] or freeze-thaw cycles [30,32]. As equilibrium is often reached at larger sizes, the SUV might not be the only population in a lipid suspension, nor the dominant one. In the majority of cases, however, it is unclear how is the equilibrium influenced by external factors such as salt concentration or lipid composition, and how do these factors affect membrane deposition.

As part of a broader study targeting the interaction of selected biomolecules with biomimetic membrane surfaces: membrane-peptide interactions [1,4,34], biomimetic membrane systems [3,35], membrane mediated biological redox processes [5,36] and high resolution AFM bioimaging [37,38], here we present the study of membrane formation from liposome precursors.

## 2. Materials and methods

### 2.1. Buffers

Sodium chloride (Ultra,  $\geq 99.5\%$  (AT)), potassium phosphate monobasic (ACS reagent,  $\geq 99\%$ ), potassium phosphate dibasic (ACS reagent,  $\geq 99\%$ ), and tris-hydroxymethyl-aminomethane (TRIS) base were all purchased from Sigma-Aldrich (Castle Hill, NSW, Australia). Ultrapure water with a resistivity of 18.2 M $\Omega$  was used (Sartorius).

### 2.2. Liposome preparation

1,2-Dimyristoyl-*sn*-Glycerol-3-Phosphocholine (DMPC) and 1,2-Dimyristoyl-*sn*-Glycerol-3-Phospho-*rac*-91-glycerol (sodium salt) (DMPG) were purchased from Avanti Polar Lipids (Alabaster, AL, USA). Chloroform (ACS Reagent,  $\geq 99.8\%$ ) and methanol (HPLC Grade,  $\geq 99.9\%$ , Riedel-de Haen, Chromosolv) were purchased from Sigma-Aldrich (Castle Hill, NSW, Australia).

Dry lipid was dissolved in chloroform (DMPC) or a chloroform/methanol mixture  $\sim 75:25$  v/v (DMPG) to create individual stock solutions. These stock solutions were then aliquoted out into test tubes in the desired ratios: DMPC, DMPG/DMPC (4:1 v/v). The solvent was then evaporated under a gentle stream of N<sub>2</sub> and vacuum desiccated overnight. Lipids were resuspended in 20 mM PBS (100 mM NaCl

at pH 6.9) or 10 mM TRIS (pH 7.4) with slow maceration, vortexed and briefly sonicated before use.

While several sources recommend it, we did not extrude the liposomes. In case of extrusion, it was found that the liposome size depends on the applied pressure rather than the pore size or the flow rate [39]. As liposomes were found to evolve towards equilibrium size, distributions created via extrusion might not remain stable.

### 2.3. Chip cleaning and surface modification

Ethanol absolute (GR for analysis ACS), acetone (Technical Grade), propan-2-ol (Extra pure) and hydrogen peroxide (30%, GR for analysis ISO) were purchased from Merck (Kilsyth, Victoria, Australia). Ammonia solution (28%, Analytical Univar Reagent) was purchased from Ajax Finechem (Seven Hills, NSW, Australia). 3-Mercaptopropionic acid (MPA) (HPLC Grade,  $\geq 99.9\%$ ) was purchased from Fluka, Bio-Chimica (Switzerland). Before assembling into the chamber, new or electrochemically cleaned QCM chips were rinsed with ethanol and dried under a gentle stream of N<sub>2</sub> gas, after which they were placed into a 1:1:3 mixture of ammonia (28%), hydrogen peroxide (30%) and water, at  $\sim 75$  °C for 15–20 min. After this, chips were thoroughly rinsed with ultrapure water and ethanol, then dried and immediately assembled into the QCM chamber ready to use. The gold surface of the chip was thiolized in situ or ex situ with MPA that provide a self-assembled monolayer (SAM) in approx. 20 min.

### 2.4. QCM experiments

QCM measurements were performed with the Q-SENSE E4 system (Q-SENSE, Sweden). The sensor crystals used were 5 MHz, AT-cut, polished quartz discs (chips) with electrodes evaporated on both sides (Q-SENSE). The resonance frequency and energy dissipation were measured simultaneously at four odd harmonics (5, 15, 25, 35 MHz). In the followings, the fundamental frequency of the crystal is called the 1st harmonic. The values reported throughout for  $\Delta F$  and  $\Delta D$  are measured at the 7th harmonic (35 MHz), unless otherwise stated. The working temperature was 19 °C. Raw data was analysed by QTools (Q-SENSE) and Origin 7.5 (OriginLab, USA) software.

Experiments were performed by slowly flushing 1 ml of the liposome solution through the QCM cell at 50  $\mu$ L/min flow. The flow was then stopped, and the cell left for equilibrating. The cell was rinsed with buffer at 30 mins from the start of the experiment (that is, the start of flushing in the liposome solution) with 300  $\mu$ L/min flow rate. Deposited mass density was calculated from the frequency change ( $\Delta F$ ), based on the Sauerbrey [7] equation and/or Voigt modeling [40].

### 2.5. DLS experiments

Liposome size measurements were performed by Dynamic Light Scattering (DLS) technique, using Brookhaven Instruments Corporation ZetaPlus™ (New York, USA) and Zetasizer Nano ZS instrument (Malvern Instruments Ltd, Malvern Worcestershire, UK) instruments. DLS measures the fluctuations in the intensity of scattered light due to the Brownian motion of the particles. Detectable particle size range is 0.6 nm–6  $\mu$ m. All experiments were performed at 25 °C. Measurements were repeated at least five times, with different stock solutions; outliers (dust particles, bubbles) were discarded based on the analysis of the correlation function. Numerical modeling of particle sizes to fit the autocorrelation function was done within the softwares provided with the instruments. Resulting scatter plots of intensity vs. size were Gaussian fitted to identify the peak and error of the population distributions.

Liposome solutions were sonicated in a bath-type sonicator for 30 s. The concentration of lipid solutions was varied between 0.0125 and 0.1 mM. NaCl concentration was varied between 0.01 and 1 M.

### 2.6. AFM experiments

AFM experiments were performed on a Multimode Nanoscope IV AFM (VEECO/Digital Instruments, USA). Images were taken in buffer solution in tapping mode with NSC36 B cantilevers (MikroMasch, Estonia). In all AFM experiments atomically flat mica surface was used, as the roughness of the QCM sensor chips ( $\sim 2$ –3 nm) does not allow for high resolution imaging. Importantly, the surface of hydrated mica consists mostly of silol and siloxyl groups, and thus it is a chemically similar surface to the carboxylic acid terminated MPA SAM. The operating temperature was approx. 25 °C. 30  $\mu$ L drops of lipid solution were deposited onto freshly cleaved mica sheets then incubated at 37 °C for a period of 30 min. The samples were then rinsed with buffer and imaged under liquid, or rinsed with water, dried under a stream of nitrogen and imaged in air.

## 3. Results and discussion

### 3.1. Size distribution of DMPC and DMPG:DMPC 4:1 liposomes

The experiments were designed to correlate liposome size distribution in thermodynamic equilibrium to the structure of

deposited biomimetic membranes in terms of homogeneity, thickness and liposome content. Liposomes rupture to form a planar bilayer when adhesion to the surface causes deformation beyond a critical point as described by Reimhult et al. [16]. Adhesion is a function of the surface energies of the liposome, the substrate and the buffer solution. Therefore, liposome composition and size are key parameters in determining whether a vesicular layer or a planar membrane is formed.

The effect of sonication time, lipid- and salt concentration on the size distribution of liposomes were investigated by Dynamic Light Scattering (DLS) for neat DMPC (PC) and DMPC:DMPG 4:1 (PCPG) mixture. Results are shown in Fig. 1. Size distributions were bimodal, with the radii of the two populations centered at  $\sim 50$  and  $\sim 300$  nm, respectively. A small percentage of large lipid aggregates was also observed. Sonication did not affect size distribution significantly although this method is often used to break down larger liposomes to generate SUVs. After only a short ( $\sim 30$  s) time, equilibrium was reached as the size of the two populations did not change upon prolonged sonication. Notably, we used a low energy sonic bath, whereas high energy ultrasonic guns were used by others, however, application of freeze-thaw cycles yielded similar results to ours [31]. While the liposome sizes did not change after 30 s of sonication time, the number of small vesicles decreased slightly (Fig. 1a) indicating that larger liposomes are thermodynamically favored. Spontaneous fusing of SUVs into larger liposomes has been reported previously [41] although it is unclear whether in that case aggressive sonication produced liposomes below the optimal SUV size.

Empirical evidence of a bimodal size distribution where SUVs coexist with larger vesicles has been described for phospholipids [42] and other surfactants [43]. The larger liposome population was attributed to multilamellar liposomes [42]. An alternative explanation, assuming thermodynamic control, is more feasible. In a mixture of various size liposomes, individual molecules are exchanged, such that the entire system achieves a lower free energy state. This can occur via shrinkage, where the entropy gain from the smaller size, larger numbers and higher mobility compensates for the increase in curvature energy. A lower free energy state can also occur at larger sizes, where entropy factors from geometric variability such as undulations, etc. balance the curvature energy, thus leading to an equilibrium for the size of individual liposomes (equilibrium unilamellar vesicle, EUV). Collisions between liposomes provide the opportunity for exchanging individual phospholipid molecules. In effect, curvature tensions of the liposomes determine the direction of transfer during molecule exchange between liposomes of different size. This process is analogous to the example of two soap bubbles connected through a pipe, where the pressure difference arising from Laplace's law will cause the smaller bubble to shrink and the larger one to grow further. In the case of liposomes, shrinking is limited by the membrane persistence length, determining the smallest liposome possible, the SUV. In the larger EUV population, the curvature tension decreases and thus the drive of molecule transfer diminishes. Accordingly, from most precursor liposome mixtures with a random (but reasonably large) size distribution, a bimodal distribution would develop, provided that the molecule transfer rate is sufficiently high. This scenario was also predicted based on theoretical considerations [33].

The radius of the equilibrium vesicles changes from  $\sim 200$  to  $\sim 350$  nm as a function of the lipid concentration over the range 12.5–100.0  $\mu\text{M}$  (Fig. 1b). Such concentration dependence is expected if mixing entropy, the energy cost of formation of molecular assemblies in liquid [44], determines the liposome size for this population. The SUV population was insensitive of lipid concentration further proving that SUV size is determined by geometric constraints. Importantly, the SUV radius of  $\sim 50$  nm is much larger

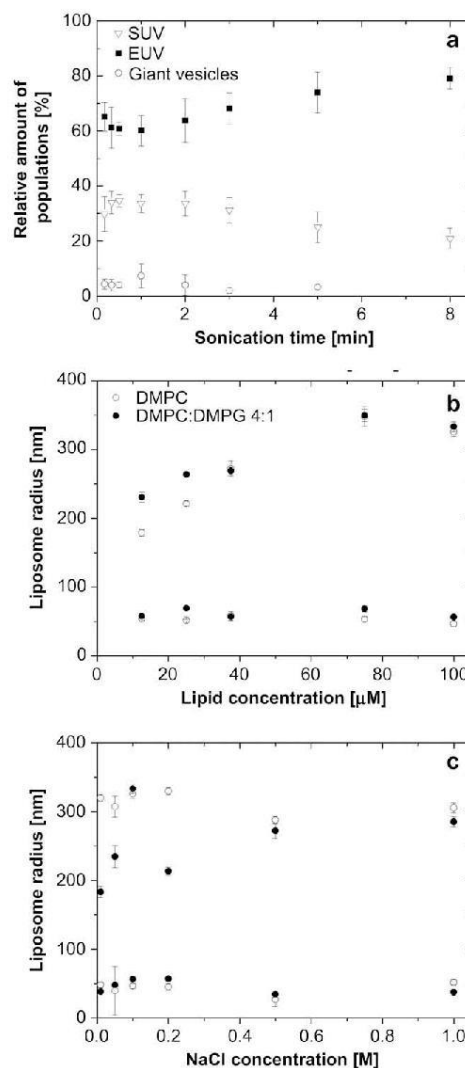


Fig. 1. Size distribution of DMPC and DMPC:DMPG 4:1 liposomes. (a) The changes of the relative amounts of the populations with prolonged sonication; (b) changes of liposome size as a function of lipid concentration; (c) change of liposome size as a function of buffer ionic strength. Note the bimodal distribution. The smaller population is interpreted as small unilamellar vesicles (SUV) while the larger, concentration-dependent population consists of entropy-stabilized equilibrium liposomes.

than the  $R \approx 10$  nm reported earlier [44], suggesting that membrane persistence length is longer under our conditions. The difference might be explained when considering that in [44] water was used as the solvent, which, for a zwitterionic lipid, permits dipole interaction between the headgroups. At higher ionic strength, such as in our study, charge shielding decreases head-group interaction in the membrane. Thus, the presence of 100 mM

NaCl in the buffer solution can explain the liposome size difference [31].

Addition of PG to the PC lipid does not have a significant effect on size. PC liposomes tend to be somewhat smaller at low concentrations than the PCPG mixture. This is likely caused by a thickening of the membrane due to electrostatic interactions between the positive charge “head” of the zwitterionic PC with the anionic phosphate of the PG lipid (Fig. 1b).

To test the effect of charge shielding, buffer ionic strength was varied using NaCl concentrations of 0.01–1.00 M (Fig. 1c). Both populations of neat PC were insensitive to ionic strength, suggesting that a very low salt concentration is enough to maintain the persistence length. In contrast, the PCPG mixture shows a prominent dependence on salt concentration: from a near linear increasing trend at low concentrations, through a sudden decrease at ~200 mM NaCl, it arrives at a “stable” size with a radius of ~300 nm. This trend is similar to that reported earlier for DOPG as a function of NaBr concentration [31]. The initial increase is explained by structural rearrangement as the charge shielding reduces the dominance of electrostatic PC:PG interaction. In summary, the equilibrium vesicle size in our case is determined by the lipid concentration and, depending on the lipid composition, the buffer ionic strength.

For the deposition of supported membranes, the total amount of material in a certain population is more relevant than the actual number of vesicles. The material content of a liposome is proportional to the surface area, and so is the light scattering cross section; thus, DLS data can reveal the material content using a Gaussian function to determine the populations. Accordingly, the EUV population represents a comparable (or slightly higher) mass to the SUVs, and thus expected to contribute equally to membrane formation. The actual mechanism of liposome rupture and membrane fusion is not known. However, the liposome stability criteria suggest that larger vesicles are expected to rupture easier. The adhesion and concomitant deformation of EUVs on the surface decreases the degree of freedom, thus stabilizing factors such as undulation entropy are lost. In stark contrast, SUVs are stiff, do not deform, interact with a much smaller surface area and exhibit much higher shear moduli (as deformation is prohibited by geometrical constraints). Thus, SUVs are less likely to adhere to the surface upon collision and less likely to rupture once adhered, consistent with a thresholded collective behaviour [17]. Adhesion is determining also in the continuum-mechanical liposome fusion model [45]. Taken together these data suggest that instantaneous adhesion and rupture is more likely when EUVs are used for membrane deposition.

Numerous literature reports assume SUVs to be the precursors for membrane formation [13,29,44]. Early studies found that SUVs

are dominant after sonication; however, ultracentrifugation was used to remove particles of the sonicator tip, and likely the larger liposomes as well [12,13,29]. More recent studies omit the centrifugation step and/or refer to the use of SUVs without actually measuring the vesicle size. Accordingly, in most cases, the likely precursor of deposition was a bimodal liposome distribution, with a significant EUV content.

### 3.2. Membrane deposition

We proceeded to create supported membranes onto MPA-modified gold surfaces using QCM to monitor the amount of lipid deposited. Micromolar lipid concentrations were used for slow deposition to observe the kinetics of the process. All experiments were performed “blind” by flushing 1 mL of the liposome solution through the measurement chamber at ~50  $\mu\text{L}/\text{min}$ , after which the flow was stopped and left to equilibrate, prior to flushing with buffer solution after 30 min. As a result, a significant variation in deposited mass was observed, thus the results could be used for data mining. In all cases, a steady mass (and dissipation) increase was observed that proceeded to an almost linear slope after only ~5 min. Upon flushing the cell with pure buffer, mass and dissipation decreased slightly due to the removal of non-fused liposomes. Notably, we did not see liposomes bursting open as reported previously [2,12] likely due to the low lipid concentration: liposomes adhere, rupture, flatten and fuse into bilayers continuously.

We applied a data mining approach to the analysis of the experimental results. In Fig. 2, dissipation change,  $\Delta D$ , is plotted against frequency change,  $\Delta F$  (modulus), at the end of deposition, for 170 independent experiments: 76 for PC and 94 for PCPG 4:1 (Fig. 2a and b, respectively). For the PC data, two trends can be distinguished: a near straight line with a slope of  $\sim 3.8 \times 10^{-6}/13$  (dash-dot line) and an asymptotic curve. In both deposition pathways, but especially along the straight line, there are clusters of data outcomes (circled), at regular intervals. The Kelvin–Voigt model of viscoelasticity suggests that dissipative energy loss increases linearly with the layer thickness. Thus, it is feasible to assume that these frequency-dissipation pairs represent complete bilayers that form on top of each other: a single bilayer at 13 Hz, with subsequent bilayer assembly at 26 and 39 Hz, respectively. In the literature, 25 Hz is frequently identified as the frequency change corresponding to a single bilayer [2,14,46]. As frequency change reflects mass density, different sensor geometries do not influence the result. Accordingly, our measurement of a  $\Delta F = 13$  Hz step could indicate the formation of a lipid monolayer, as suggested by Keller et al. [12]. However, this is unlikely as the gold surface has

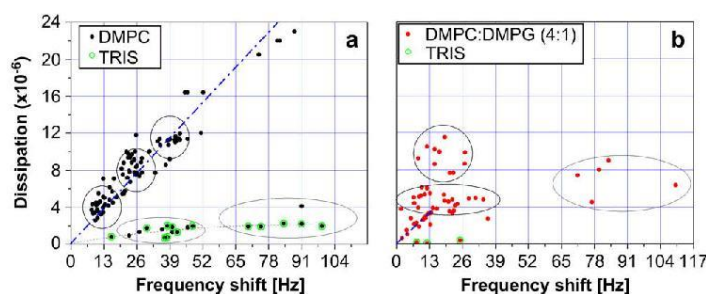


**Fig. 2.** Data mining of membrane deposition. Dissipation vs. frequency change (modulus of  $\Delta F$ ) plots used to establish deposition characteristics of DMPC (a) and DMPC:DMPG 4:1 mixture (b). The 5th harmonic of the sensor resonance is plotted. Tick and grid spacing is set to the frequency change representative of complete bilayers. Straight lines on (a) and (b) mark bilayer pathways. Concentrations of data points revealing different deposit structures are encircled.

been modified with hydrophilic carboxyl groups. Furthermore, the molecular footprint based on 13 Hz (for DMPC) is  $0.339 \times 10^{-9}$  mol/cm<sup>2</sup>, or  $\sim 0.49$  nm<sup>2</sup> per molecule. The headgroup area per lipid molecule in a bilayer is reported to fall into the range of 0.60–0.75 nm<sup>2</sup>, depending on lateral pressure [47]. In a tension-free bilayer, the headgroup area cannot be smaller than under external stress. Thus the 13 Hz value corresponds to a *single bilayer* rather than a monolayer. Voigt simulation of our data sets from the 13 Hz group indicates  $\sim 7$  nm layer thickness, also consistent with a single bilayer (Fig. 3b). AFM imaging of neat PC deposits in PBS buffer always show bilayer membranes: patches at low surface coverage, or featureless membrane surfaces – with occasional transient holes – at higher lipid concentrations. Quick drying, however, was found to stabilize intermediates, likely *via* changing the surface tension, and thus the membrane formation can be imaged. In Fig. 4 intact and partially collapsed DMPC liposomes, as well as multiple bilayer membrane stacks can be seen. Note the partial collapse of liposomes (arrows) which are similar to those obtained by Jass et al. [19].

The second trendline in Fig. 2a, which exhibits saturation in terms of dissipation, suggests that the overall viscosity of the layer does not differ much from that of water, so the layer is not homogeneous. Notably, these data points arise mostly from deposits in which the liposome solution was in TRIS buffer, whereas the linear trendline was formed in PBS. We have attributed these low dissipation data to layers of unopened liposomes and this will be discussed in more detail below.

Deposition of PCPG mixtures leads to a different pattern (Fig. 2b). A linear trend ending at the completion of the first bilayer ( $\Delta F = 13$  Hz,  $\Delta D = 3.8 \times 10^{-6}$ ) can be observed, beyond which the data points are scattered: once a complete bilayer is formed, any further liposomes remain intact (unopened) on top of the bilayer. Different groups of the scattered data (circled in Fig. 2b) reveal different size liposomes, or multiple layers of liposomes on top of the first bilayer. Notably, the few experiments performed in TRIS

buffer instead of PBS again resulted in negligible dissipation (Fig. 2b, open circles).

### 3.3. Voigt modeling of depositograms

To identify the deposits as bilayers or vesicle layers, we analysed the sensograms with the Qtools software, applying a simple Voigt model, which was shown to be applicable for viscoelastic thin films [40]. The results are depicted in Fig. 3. The first panel is a combination of representative data points selected from Fig. 2a and b. Panel B shows the modeled thickness versus the frequency change. Notably, there is a linear relationship for PC in PBS at 13, 26 and 39 Hz (squares), where the thicknesses were  $\sim 7$ , 13 and 20 nm. AFM measurements find the typical thickness of a hydrated single bilayer membrane between 4 and 6 nm, where a slight compression of the layer by the AFM probe cannot be excluded. Thus, our QCM data is in good agreement with the thickness expected for single, double and triple bilayers, respectively. There is also a good agreement for PCPG with thicknesses at 13 Hz, consistent with a single bilayer on the carboxylic acid-modified surface.

Layers characterized by either too much or too little thickness (Fig. 3b) compared to the bilayer pathway (dashed line) can also be explained by examining the distribution of viscosities and shear moduli from the simulation. Viscosity values are distributed at  $\sim 1.35$  mPa s (Fig. 3c), exhibiting considerable scatter, with a vague trend of increasing towards higher  $\Delta F$ . Increasing viscosity of thicker layers suggests that the amount of enclosed defects (such as holes or incorporated vesicles) decreases with increasing layer thickness. However, differences are more characteristic of lipid composition than the layer structure. A notable result is for PCPG/TRIS, exhibiting lower viscosity than water, suggesting that a non-viscous, primarily elastic deposit has formed.

The shear modulus is a better descriptor of membrane structure, being largely insensitive to membrane thickness for lipid bilayers (Fig. 3d). For non-bilayer deposits the results can be

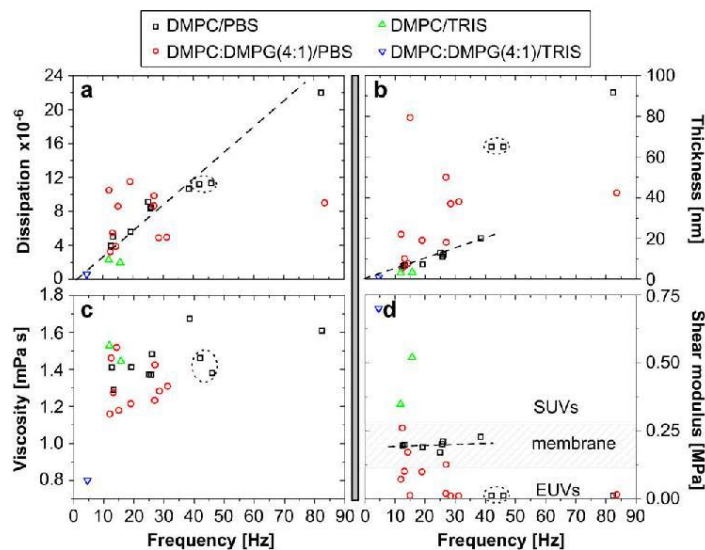


Fig. 3. Voigt modelling of deposit properties for selected data points from Fig. 2. (a) Data points combined from Fig. 2a and b; (b) thicknesses, (c) viscosities, (d) shear moduli of the deposits.

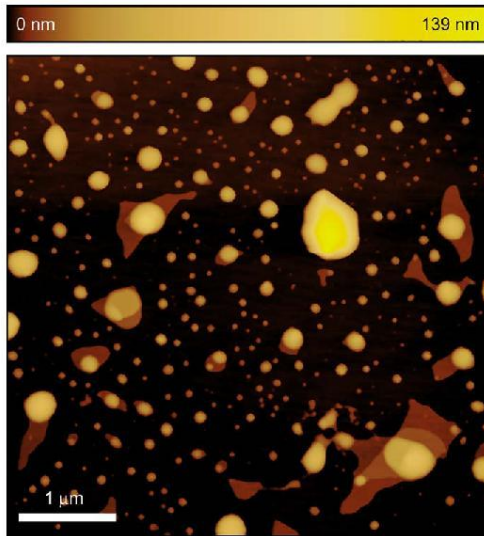


Fig. 4. DMPC membrane deposition. Imaged in ambient air immediately after drying the surface under a stream of nitrogen. Liposomes are seen adhered to the mica surface; few collapsed into bilayers. Partially collapsed liposomes are indicated with arrows.

divided into primarily elastic (above the line) and viscous layers (below the line). In both cases, shear moduli reflect different structural types, presumably due to the presence of intact liposomes. Where the shear modulus is low, the liposomes have the freedom to change shape, thus they are attributed to EUVs, however, the high shear moduli data suggest the presence of rigid SUVs either forming the whole layer or remaining entrapped in lamellar membranes.

As an example of determining the structure of a deposit, we analyze two select data points (dashed circle): (i) from the  $\Delta D$  vs  $\Delta F$  graph these fit well on the bilayer pathway; (ii) modelling reveals

larger thickness than expected for planar membranes; (iii) the viscosities do not differ much from the other data and (iv) the shear moduli are very low. From the moderate mass, large thickness and low shear modulus it can be concluded that in these examples the lipid bilayer has incorporated EUVs.

The dissipation difference between layers deposited in PBS and TRIS buffer is surprising as the pH difference is negligible. In TRIS, large mass with minimal dissipation implies the formation of a very rigid deposit. A layer of closely packed and slightly distorted vesicles might be seen as a honeycomb of water-filled containers: tight packing enhances rigidity as local curvatures are persistence length limited while the measured mass includes the enclosed water. The effect of TRIS buffer to stabilize liposomes was surprising, as the pH difference (pH 7.4 vs. pH 6.9 PBS) is not significant; we speculate that TRIS molecules attach to the liposome surface and prohibit rupture. Observation of vesicular layers of very low dissipation for PCPG in TRIS buffer supports this reasoning. Interestingly, in reports that describe intact liposomes TRIS buffer was also used [14,17].

It is unclear which are the governing factors that determine whether further deposition on top of a bilayer proceeds to planar or vesicular (or any) layers. Nevertheless, the stability of the liposomes and the physicochemical nature of the surface are likely to be contributing factors. Neat PC forms multiple bilayers. In the case of the PCPG mixtures, liposomes fuse into a bilayer on the MPA surface, but appear to remain intact on top of this bilayer. Apparently, the stronger “headgroup” interaction between PC and PG (as opposed to neat PC) is overcome only by the high charge of the carboxylic acid on the surface, whereas the surface energy of the fused bilayer is insufficient to induce vesicular rupture.

Fig. 5 shows an AFM image of the PCPG mixture immediately after deposition and the subsequent morphology changes of the membrane over time in PBS buffer (see animated version online). The membrane bilayer was fully formed, with some initial discontinuities (holes) where the mica substrate is visible. Intact liposomes can be also observed on the membrane surface. Importantly, these liposomes remain stable over the 86 min of observation, in a good agreement with the predictions of the QCM experiments and modelling.

### 3.4. Domain separation of PCPG layers

Domain separation was also observed in the PCPG bilayer (Fig. 5). The height difference between the two domains is

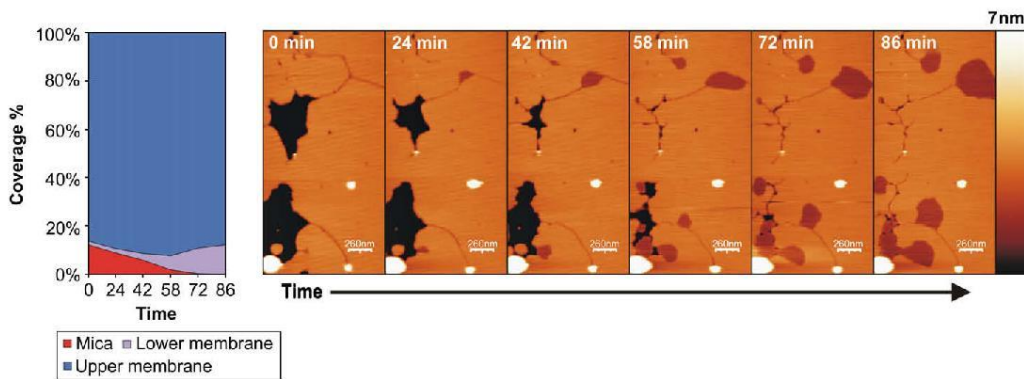
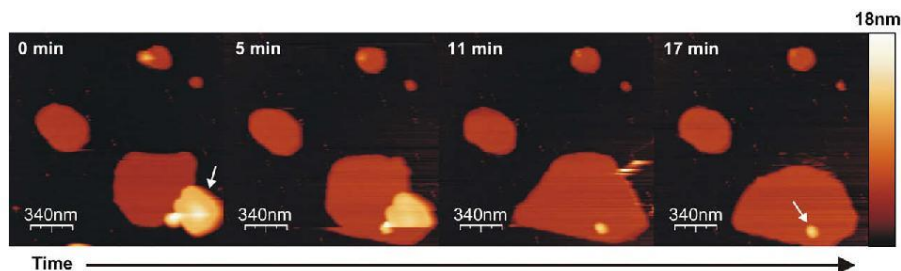


Fig. 5. AFM pictures of the morphological changes of a DMPC:DMPG 4:1 mixed membrane over time. Images taken under liquid. Initially the mica substrate is visible through holes in the membrane. Unopened liposomes (white round objects) are stable after 86 min. Diagram: the time evolution of the surface area occupied by the mica substrate, the lower and the taller phospholipid domains.



**Fig. 6.** Morphology changes of a DMPC/DMPG/cholesterol (16:4:5) deposit imaged over time. Images taken under liquid. This figure shows a variety of phases of deposition. On the leftmost picture, single and double bilayers (arrow) can be observed with intact liposomes sitting on top. Over time the multilayer merges to form a single bilayer. Importantly, there is still an intact liposome observable in the last frame (arrow).

approximately 1 nm, which, when compared to the overall height of 5.5–6 nm of the membrane indicates that the lower domain is not a monolayer. Domain separation has been attributed to thermodynamic phase transitions before [18,24]. However, we observed similar domain separation over the range of ~18 to 27 °C. In biological systems, and thus isolated membranes, domain formation may be caused by asymmetry, the localization of certain lipids to one side of the bilayer [23]. It is however highly unlikely in our case, since the spontaneous formation of an asymmetric membrane is entropically prohibited; in living systems the asymmetry is maintained by specialized enzymes [48]. Asymmetry was artificially induced *via* manipulation of surface charges by the introduction and removal of calcium [49]; in our case, however, no such treatment was implemented. Nanometer scale domains have also been reported for different acyl chain lengths [21], however, in our experiments only the headgroups differed. Enclosure of immiscible fluid and gel phase domains of different ratios of the constituent phospholipids was also described [24]. However, we observed that over time the exposed mica surface was “filled” by material from the lower membrane domain, suggesting that the domain separation is a spontaneous process that proceeds towards equilibrium. The phospholipid structure offers a simple explanation. In a mixture of a zwitterionic (DMPC) and an anionic (DMPG) phospholipid, the negative charge is at the same distance from the acyl chain end while the positive charge center of the PC lipid is situated about 0.5 nm higher. It is thus likely that the anionic PG will be slightly shifted towards the cationic portion of the PC leading to an increase in layer thickness with 0.5 + 0.5 nm in the two leaflets and an energy minimum compared to neat PC. The phase separation would thus reveal a separation of neat DMPC. This height difference agrees well with the domain height difference we observed. As for the change over time, similar dynamic domain separation was observed upon changes in lateral pressure implemented with a Langmuir–Blodgett trough [50]. As the expansion of the membrane is not restricted in our case, relaxation and accompanying change of lateral membrane pressure might cause domain separation: while the membrane proceeds towards equilibrium, forming an ideal DMPC:DMPG mixture ratio, the excess DMPC is expelled.

### 3.5. Effect of changing membrane stiffness on the deposition process

Addition of cholesterol is known to reduce membrane stiffness; thus, it is expected that liposomes rupture, and membrane stacks fuse faster in the presence of cholesterol. Fig. 6 shows the deposition of a DMPC:DMPG:cholesterol 16:4:5 mixture over time.

Immediately after deposition (same conditions as in Fig. 5) single bilayer patches and a secondary bilayer (on top) can be seen (Fig. 5, arrow). Notably, double bilayers have not been observed for PCPG lipid without cholesterol. Over time, the multilayer merged to form a single bilayer. The fusion of the upper bilayer occurred between two scan lines, that is, less than 1 s (third panel). This observation suggests a mechanism that involves a transient migration of individual phospholipid molecules from the upper to the lower bilayer, rather than the upper bilayer “sliding down” to the substrate and fusing from the side as previously suggested [19]. A few intact liposomes also remained on top of the bilayer patches over the 17 min of observation, similar to the PCPG case.

## 4. Conclusions

Liposome deposition of DMPC and DMPC:DMPG 4:1 biomimetic membranes onto carboxylic acid terminated self-assembled monolayers was studied using DLS, QCM and AFM. It was found that the precursor phospholipid vesicle solutions typically exhibit bimodal size distributions: SUVs and EUVs. It was established that the size of EUVs depends on lipid concentration and buffer ionic strength, but only weakly dependent on the lipid composition, for the two cases examined. It was found that the deposition of supported bilayers proceeds to multiple bilayers for DMPC and single bilayers with a high enclosed/adhered liposome content for DMPC:DMPG mixtures. Data mining established that the surface density of a single bilayer is ~1 nm<sup>2</sup>/molecule pair. Shear modulus, obtained from the Voigt model was used to distinguish between planar and vesicular layers. Dynamic post-deposition domain separation in a DMPC:DMPG mixture was revealed by AFM. These results demonstrate that, in most cases, liposome deposition results in a composite membrane of bilayer stacks, embedded vesicles and raft-like structures that evolve over time.

## Acknowledgements

Support from the ARC Discovery grant scheme is gratefully acknowledged and LLM and MIA also acknowledge funding from NHMRC. AM acknowledges award of a Monash Fellowship.

## Appendix

Figures with essential colour discrimination. Certain figures in this article, especially Figs. 4–6 are difficult to interpret in black and white. The full colour images can be found in the on-line version, at doi:10.1016/j.biomaterials.2008.10.016.

### Appendix A. Supplementary material

Supplementary material associated with this article can be found, in the online version, at doi:10.1016/j.biomaterials.2008.10.016.

### References

- [1] Lee TH, Aguilar MI. Trends in the development and application of functional biomembrane surfaces. *Biotechnol Annu Rev* 2006;12:85–136.
- [2] Richter RP, Berat R, Brisson AR. Formation of solid-supported lipid bilayers: an integrated view. *Langmuir* 2006;22:3497–505.
- [3] Thimm J, Mechler A, Lin H, Rhee S, Lal R. Calcium-dependent open/closed conformations and interfacial energy maps of reconstituted hemichannels. *J Biol Chem* 2005;280:10646–54.
- [4] Mozsolits H, Wirth H-J, Werkmeister J, Aguilar M-I. Analysis of antimicrobial peptide interactions with hybrid bilayer membrane systems using surface plasmon resonance. *Biochim Biophys Acta* 2001;1512:64–76.
- [5] Mechler A, Nawaratna G, Aguilar M-I, Martin LL. A study of protein electrochemistry on a supported membrane electrode. *Int J Peptide Res Ther* 2006;12:217–24.
- [6] Salamon Z, Macleod HA, Tollin G. Surface plasmon resonance spectroscopy as a tool for investigating the biochemical and biophysical properties of membrane protein systems 1. Theoretical principles. *Biochim Biophys Acta* 1997;1331:117–29.
- [7] Sauerbrey G. Verwendung von schwingquarzen zur wagung dunner schichten und zur mikrowagung. *Zeitschrift fur Physik* 1959;155:206–22.
- [8] Seifert U. Adhesion of vesicles in two dimensions. *Phys Rev A* 1991;43:6803–14.
- [9] Shanahan MER. Adhesion of a liquid-filled spherical membrane. *J Adhesion* 2003;79:881–91.
- [10] Liu K-K. Deformation behaviour of soft particles: a review. *J Phys D Appl Phys* 2006;39:R189–99.
- [11] Brian AA, McConnell HM. Allogeneic stimulation of cytotoxic t cells by supported planar membranes. *Proc Natl Acad Sci U S A* 1984;81:6159–63.
- [12] Keller CA, Kasemo B. Surface specific kinetics of lipid vesicle adsorption measured with a quartz crystal microbalance. *Biophys J* 1998;75:1397–402.
- [13] Richter R, Mukhopadhyay A, Brisson A. Pathways of lipid vesicle deposition on solid surfaces: a combined QCM-D and AFM study. *Biophys J* 2003;85:3035–47.
- [14] Keller CA, Glasmästar K, Zhdanov VP, Kasemo B. Formation of supported membranes from vesicles. *Phys Rev Lett* 2000;84:5443–6.
- [15] Reviakine I, Brisson A. Formation of supported phospholipid bilayers from unilamellar vesicles investigated by atomic force microscopy. *Langmuir* 2000;16:1806–15.
- [16] Reimhult E, Höök F, Kasemo B. Intact vesicle adsorption and supported membrane formation from vesicles in solution: influence of surface chemistry, vesicle size, temperature, and osmotic pressure. *Langmuir* 2003;19:1681–92.
- [17] Reimhult E, Höök F, Kasemo B. Vesicle adsorption on SiO<sub>2</sub> and TiO<sub>2</sub>: dependence on vesicle size. *J Chem Phys* 2002;117:7401–4.
- [18] Tokumasu F, Jin AJ, Dvorak JA. Lipid membrane phase behaviour elucidated in real time by controlled environment atomic force microscopy. *J Electron Microscop* 2002;51:1–9.
- [19] Jass J, Ijarnhage T, Pui G. From liposomes to supported, planar bilayer structures on hydrophilic and hydrophobic surfaces: an atomic force microscopy study. *Biophys J* 2000;79:3153–63.
- [20] Lawrence JC, Saslowky DE, Edwardson JM, Henderson RM. Real-time analysis of the effects of cholesterol on lipid raft behavior using atomic force microscopy. *Biophys J* 2003;84:1827–32.
- [21] Tokumasu F, Jin AJ, Feigenson GW, Dvorak JA. Nanoscopic lipid domain dynamics revealed by atomic force microscopy. *Biophys J* 2003;84:2609–18.
- [22] Schneider J, Barger W, Lee GU. Nanometer scale surface properties of supported lipid bilayers measured with hydrophobic and hydrophilic atomic force microscope probes. *Langmuir* 2003;19:1899–907.
- [23] Quinn PJ, Tessier C, Rainteau D, Koumanov KS, Wolf C. Structure and thermotropic phase behaviour of detergent-resistant membrane raft fractions isolated from human and ruminant erythrocytes. *Biochim Biophys Acta* 2005;1713:5–14.
- [24] Kraft ML, Weber PK, Longo ML, Hutcheon ID, Boxer SG. Phase separation of lipid membranes analyzed with high-resolution secondary ion mass spectrometry. *Science* 2006;313:1948–51.
- [25] Israelachvili JN, Mitchell DJ, Ninham BW. Theory of self-assembly of hydrocarbon amphiphiles into micelles and bilayers. *J Chem Soc Faraday Trans* 1976;2(72):1525–68.
- [26] Helfrich W. Elastic properties of lipid bilayers – theory and possible experiments. *Zeitschrift Für Naturforschung C* 1973;28:693–703.
- [27] Safran SA. Curvature elasticity of thin films. *Adv Phys* 1999;48:395–448.
- [28] Lentz BR, Litman BJ. Effect of head group on phospholipid mixing in small, unilamellar vesicles: mixtures of dimyristoylphosphatidylcholine and dimyristoylphosphatidylethanolamine. *Biochemistry* 1978;17:5537–43.
- [29] Salafsky J, Groves JT, Boxer SG. Architecture and function of membrane proteins in planar supported bilayers: a study with photosynthetic reaction centers. *Biochemistry* 1996;35:14773–81.
- [30] Claessens MMAE, van Oort BF, Leermakers FAM, Hoekstra FA, Cohen Stuart MAC. Bending rigidity of mixed phospholipid bilayers and the equilibrium radius of corresponding vesicles. *Phys Rev E* 2007;76:011903.
- [31] Claessens MMAE, van Oort BF, Leermakers FAM, Hoekstra FA, Cohen Stuart MA. Charged lipid vesicles: effects of salts on bending rigidity, stability, and size. *Biophys J* 2004;87:3882–93.
- [32] Jung HT, Coldren B, Zasadzinski JA, lampietro DJ, Kaler EW. The origins of stability of spontaneous vesicles. *Proc Natl Acad Sci U S A* 2001;98:1353–7.
- [33] Olsson U, Wennerstrom H. On the ripening of vesicle dispersions. *J Phys Chem B* 2002;106:5135–8.
- [34] Mechler A, Praporski S, Atmuri K, Boland M, Separovic F, Martin LL. Specific and selective peptide-membrane interactions revealed using quartz crystal microbalance. *Biophys J* 2007;93:3907–16.
- [35] Mechler A. Chapter 4: characterization and analysis of biomimetic membranes. In: Martin D, editor. *Nanobiotechnology of biomimetic membranes*. New York: Springer Science, ISBN 978-0-387-37738-4; 2007.
- [36] Fleming BD, Praporski S, Bond AM, Martin LL. Electrochemical quartz crystal microbalance study of azurin adsorption onto an alkanethiol self-assembled monolayer on gold. *Langmuir* 2008;24:323–7.
- [37] Mechler A, Kokavecz J, Heszler P, Lal R. Surface energy maps of nanostructures: atomic force microscopy and numerical simulation study. *Appl Phys Lett* 2003;82:3740–2.
- [38] Mechler A, Kopiczny J, Kokavecz J, Hoel A, Granqvist C-G, Heszler P. Anomalies in nanostructure size measurements by AFM. *Phys Rev B* 2005;72:125,407.
- [39] Frisken BJ, Asman C, Patty PJ. Studies of vesicle extrusion. *Langmuir* 2000;16:928–33.
- [40] Voinova MV, Rodahl M, Jonson M, Kasemo B. Viscoelastic acoustic response of layered polymer films at fluid-solid interfaces: continuum mechanics approach. *Physica Scripta* 1999;59:391–6.
- [41] Gaber BP, Sheridan JP. Kinetic and thermodynamic studies of the fusion of small unilamellar phospholipid vesicles. *Biochim Biophys Acta* 1982;685:87–93.
- [42] Kwok R, Evans E. Thermoelasticity of large lecithin bilayer vesicles. *Biophys J* 1981;35:637–52.
- [43] Radlinska EZ, Zemb TN, Dalbiez J-P, Ninham BW. Lamellar to vesicle transitions of highly charged bilayers. *Langmuir* 1993;9:2844–50.
- [44] Cornell BA, Middlehurst J, Separovic F. Small unilamellar phospholipid vesicles and the theory of membrane formation. *Faraday Discuss Chem Soc* 1986;81:163–78.
- [45] Lipowsky R, Seifert U. Adhesion of vesicles and membranes. *Mol Crystals* 1991;202:17–25.
- [46] Richter RP, Brisson AR. Following the formation of supported lipid bilayers on mica: a study combining AFM, QCM-D, and ellipsometry. *Biophys J* 2005;88:3422–33.
- [47] Marsh D. Lateral pressure in membranes. *Biochim Biophys Acta* 1996;1286:183–223.
- [48] Yeagle PL. *The dynamics of membrane lipids*. Boca Raton: CRC Press; 1992.
- [49] Rossetti FF, Textor M, Reviakine I. Asymmetric distribution of phosphatidylserine in supported phospholipid bilayers on titanium dioxide. *Langmuir* 2006;22:3467–73.
- [50] Takeda Y, Horito S. Atomic force microscopy studies of ganglioside GM1z in dioleoylphosphatidylcholine/dipalmitoylphosphatidylcholine mixed monolayers and hybrid bilayers. *Colloids Surf B* 2005;41:111–6.

## **4 Paper 2:**

### **4.1 QCM-D fingerprinting of membrane-active peptides.**

Monash University

**Declaration for paper 2****Declaration by candidate**

In the case of Chapter 2, the nature and extent of my contribution to the work was the following:

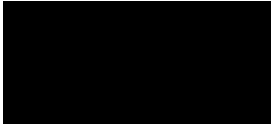
<b>Nature of contribution</b>	<b>Extent of contribution (%)</b>
QCM experiments, data analysis, manuscript review	20%

The following co-authors contributed to the work. If co-authors are students at Monash University, the extent of their contribution in percentage terms must be stated:

<b>Name</b>	<b>Nature of contribution</b>	<b>Extent of contribution (%) for student co-authors only</b>
<b>George A. McCubbin</b>	QCM-D experiments, data analysis, manuscript preparation and review	10%
<b>Slavica Praporski</b>	QCM-D experiments, data analysis, manuscript preparation and review	20%
<b>Daniel Knappe</b>	Manuscript review	
<b>Ralf Hoffmann</b>	Manuscript review	
<b>John H. Bowie</b>	Manuscript review	
<b>Frances Separovic</b>	Manuscript review	
<b>Lisandra L. Martin *</b>	Key ideas, manuscript review	

## Chapter 2

The undersigned hereby certify that the above declaration correctly reflects the nature and extent of the candidate's and co-authors' contributions to this work\*.

<b>Candidate's Signature</b>		<b>Date</b> 17/04/14
<b>Main Supervisor's Signature</b>		<b>Date</b> 17/04/14

\*Note: Where the responsible author is not the candidate's main supervisor, the main supervisor should consult with the responsible author to agree on the respective contributions of the authors.

## QCM-D fingerprinting of membrane-active peptides

George A. McCubbin · Slavica Praporski · Stefania Piantavigna · Daniel Knappe · Ralf Hoffmann · John H. Bowie · Frances Separovic · Lisandra L. Martin

Received: 11 October 2010 / Revised: 17 November 2010 / Accepted: 23 November 2010 / Published online: 16 December 2010  
© European Biophysical Societies' Association 2010

**Abstract** The increasing prevalence of antibiotic-resistant bacteria is becoming a public health crisis. Antimicrobial peptides (AMPs) are a promising solution, because bacterial resistance is less likely. Quartz crystal microbalance with dissipation monitoring (QCM-D) is a versatile and valuable technique for investigation of these peptides. This article looks at the different approaches to the interpretation of QCM-D data, showing how to extract the maximum information from the data. Five AMPs of diverse charge, length and activity are used as case studies: caerin 1.1 wild-type, two caerin 1.1 mutants (Gly15Gly19-caerin 1.1 and Ala15Ala19-caerin 1.1), aurein 1.2 and oncocin. The interaction between the AMP and a 1,2-dimyristoyl-*sn*-glycero-3-phosphocholine (DMPC) membrane is analysed *inter alia* using frequency–dissipation plots ( $\Delta f$ – $\Delta D$  plots) to ascertain the mechanism of action of the AMP. The  $\Delta f$ – $\Delta D$  plot can then be used to provide a

fingerprint for the AMP–membrane interaction. Building up a database of these fingerprints for all known AMPs will enable the relationship between AMP structure and membrane activity to be better understood, hopefully leading to the future development of antibiotics without bacterial resistance.

**Keywords** Antimicrobial peptide · Quartz crystal microbalance · Frequency–dissipation plot · Membrane pore · Membrane disruption

**Abbreviations**

AMP	Antimicrobial peptide
QCM-D	Quartz crystal microbalance with dissipation monitoring
DMPC	1,2-Dimyristoyl- <i>sn</i> -glycero-3-phosphocholine
MPA	3-Mercaptopropionic acid
DMPG	1,2-Dimyristoyl- <i>sn</i> -glycero-3-phospho- <i>rac</i> -(1-glycerol)
PBS	Phosphate buffered saline
AFM	Atomic force microscopy

Membrane-active peptides: 455th WE-Heraeus-Seminar and AMP 2010 Workshop.

G. A. McCubbin · S. Praporski · S. Piantavigna · L. L. Martin (✉)  
School of Chemistry, Monash University,  
Clayton, VIC 3800, Australia  
e-mail: [REDACTED]

D. Knappe · R. Hoffmann  
Institute of Bioanalytical Chemistry,  
Leipzig University, 04103 Leipzig, Germany

J. H. Bowie  
Department of Chemistry, The University of Adelaide,  
Adelaide, SA 5005, Australia

F. Separovic  
School of Chemistry, Bio21 Institute, University of Melbourne,  
Melbourne, VIC 3010, Australia

**Introduction**

There is an urgent need for novel antibacterial drugs. The Infectious Diseases Society of America estimates that 70% of bacterial infections acquired in hospitals are resistant to at least one antibiotic and, in 2002, there were 362,000 estimated cases of antibiotic-resistant infections in US hospitals (IDSA 2004). Despite the increasing need, the development of new antibiotics is dwindling. In 2006, only six antibiotics were in phase 2 or phase 3 clinical trials,

compared with 313 other drugs (Katz et al. 2006). Antimicrobial peptides (AMPs) are promising candidates for the next generation of antibiotics. Generally, they are selective, act rapidly and have broad-spectrum activity (Gordon et al. 2005; Shai 2002). Importantly, bacterial resistance to AMPs is considered “improbable” (Zaslouff 2002). The retention of their antimicrobial activity for millions of years demonstrates such improbability.

Most known AMPs are linear, short (<100 amino acids), cationic, composed of predominantly hydrophobic residues ( $\geq 50\%$ ) and unstructured in water, and form amphipathic  $\alpha$ -helical structures in a membrane environment (Powers and Hancock 2003). AMPs kill bacteria via a diverse range of mechanisms; for example, they can interact with the lipid membrane via a ‘pore’ or ‘carpet’ mechanism (Shai 1999). According to the ‘pore’ mechanism, the peptides span the bilayer perpendicular to the membrane surface and assemble to form a pore lined by peptides (called ‘barrel-stave’) or peptides and lipid (‘toroidal’). Conversely, in the ‘carpet’ mechanism, the peptides sit on the bilayer parallel to the surface with their hydrophobic face embedded into the hydrophobic core of the membrane. Once a threshold concentration is reached, the peptides disrupt the bilayer in a detergent-like manner. Both mechanisms kill the cell by allowing free diffusion of species into and out of the cell, either by permeabilising the bilayer or simply destroying it. AMPs can also act on intracellular targets, leaving the lipid membrane intact (Shai 2002). Often, AMPs will adopt more than one of these mechanisms, explaining why the development of bacterial resistance towards them is so difficult (Peschel and Sahl 2006).

Three fundamental questions are raised when investigating an AMP: Is it selective for bacteria? Does it have high activity towards bacteria? And, how does it interact with the membrane? A wide range of biophysical techniques have been employed to help answer these questions; for example, solid-state nuclear magnetic resonance (NMR) (Balla et al. 2004; Marcotte et al. 2003), fluorescence spectroscopy (Ambroggio et al. 2005), atomic force microscopy (Lam et al. 2006; Mechler et al. 2007) and surface plasmon resonance (Papo and Shai 2003). Quartz crystal microbalance with dissipation monitoring (QCM-D) has been the subject of a small number of studies investigating AMPs (Briand et al. 2010; Christ et al. 2007; Knappe et al. 2010; Mechler et al. 2007; Nielsen and Otzen 2010; Piantavigna et al. 2009; Sherman et al. 2009). QCM-D is an attractive technique because it examines the interaction between an AMP and a biological membrane in real time and in situ, and provides information about the mass and structural changes occurring to the membrane (Mechler et al. 2007). Therefore, using this single instrument, it is possible to answer all three questions posed above. This study will demonstrate different methods of

presenting the raw data obtained by QCM-D and how these plots can be interpreted to yield the maximum information about AMPs.

#### Principles of QCM-D

In a QCM instrument, an alternating-current (AC) voltage is applied across a gold-coated quartz chip to cause the chip to oscillate in shear mode at its fundamental resonance frequency and harmonics of the fundamental frequency. This frequency of oscillation is denoted by  $f_n$ , where  $n$  is the harmonic number. When mass is adsorbed to the gold surface, the resonance frequency *decreases* proportional to the added mass (Sauerbrey 1959). In addition, in a QCM-D instrument, the driving AC voltage is periodically removed (about once per second) to measure the energy loss of the chip into the surrounding environment. The dissipation factor ( $D$ ) is calculated from this energy loss according to the equation (Rodahl et al. 1995)

$$D = \frac{E_{\text{dissipated}}}{2\pi E_{\text{stored}}}, \quad (1)$$

where  $E_{\text{dissipated}}$  is the energy lost during a single oscillation after removing the driving voltage and  $E_{\text{stored}}$  is the initial energy of the chip. A high  $D$  means the chip loses its energy quickly and suggests there is something thick, soft or loose on the surface; conversely, a low  $D$  suggests the film on the surface is rigid and compact (Rodahl et al. 1997).

Thus, changes in  $f$  and  $D$  give information about mass and structure, respectively. In addition, the  $f$  and  $D$  values for the different harmonics can provide three-dimensional information (Mechler et al. 2007). The penetration depth of the harmonic wave is inversely proportional to the frequency of the wave (Rodahl and Kasemo 1996). Therefore, higher harmonics probe close to the surface of the quartz chip, while lower harmonics probe further away from the surface. The following case studies use the third, fifth, seventh and ninth harmonics. The fundamental frequency is not used as, sensing the furthest from the chip surface, it is very sensitive to flow changes within the cell and thus gives noisy and unreliable data.

When referring to the ‘mass’ detected by the QCM-D, it is important to remember that it includes both the dry mass of the materials on the chip and associated water that is coupled to the chip due to direct hydration of the materials, entrapment in cavities in the film or viscous drag (Höök and Kasemo 2001). This has two notable consequences: firstly, the mass determined by the QCM-D may be significantly larger than the dry mass [even as much as four times larger, depending on the system (Rickert et al. 1997)]; and, secondly, it will cause an inherent differential response in the harmonics for thick films, as the third

harmonic will probe both the film on the chip and the bulk solution that is coupled to the chip whereas the ninth harmonic will only probe the film.

In a typical experiment, a 1,2-dimyristoyl-*sn*-glycero-3-phosphocholine (DMPC) 'bilayer' is deposited on the gold surface modified with 3-mercaptopropionic acid (MPA), to mimic the cell membrane of eukaryotes. Other cell membranes can be mimicked by using different lipid compositions; for example, DMPC/1,2-dimyristoyl-*sn*-glycero-3-phospho-*rac*-(1-glycerol) (DMPG) mimics prokaryotic cell membranes (Mechler et al. 2007). Bilayer deposition is achieved by flowing a solution of the liposomes through the QCM-D cell. The liposomes adsorb and spontaneously rupture on the MPA surface, forming a lipid bilayer (Mechler et al. 2009). It is hypothesised that a decrease in resonance frequency of ca. 15 Hz at the seventh harmonic corresponds to one complete lipid bilayer (Mechler et al. 2009), so flow is stopped when this value is reached. After equilibration with phosphate buffered saline (PBS), the peptide solution is then introduced into the cell. The peptide is left to incubate with the lipid bilayer before being rinsed with PBS. In all experiments in this paper, the time window presented begins when the peptide was introduced into the cell and ends immediately before the PBS rinse (except for Fig. 6, where the PBS rinse is shown).

#### $\Delta f$ - $\Delta D$ plot interpretation

Once the QCM-D experiment has been completed, we commonly use three methods to present and interpret the data collected. Firstly,  $\Delta f$ - $t$  and  $\Delta D$ - $t$  plots are prepared, usually showing one concentration with all harmonics (e.g. Figs. 3a or 4a). The  $\Delta f$  and  $\Delta D$  parameters refer to the raw  $f$  and  $D$  data at a certain time, normalised by the values at the start of the experiment (i.e.  $\Delta f_{\text{at time}=t} = f_{\text{at time}=t} - f_{\text{at time}=0}$ ). Secondly, the raw data may be analysed in the commercial software package QTools (Q-Sense AB, Västra Frölunda, Sweden) to extract either the Sauerbrey mass of the film, or its thickness and viscoelasticity by using the Voigt viscoelastic model (Voinova et al. 1999). Finally, plots of  $\Delta f$  versus  $\Delta D$  may be prepared (hereinafter called ' $\Delta f$ - $\Delta D$  plots').

$\Delta f$ - $\Delta D$  plots are a unique way of presenting the effect of a peptide on a lipid bilayer, first introduced by Rodahl et al. (1997). They essentially show how the structure of the lipid bilayer changes per unit mass addition.  $\Delta f$ - $\Delta D$  plots consist of a number of discrete points. Each point represents the value of  $\Delta f$  and  $\Delta D$  at a particular point in time.  $\Delta f$  values are plotted in *reverse* on the  $x$ -axis ( $+$   $\rightarrow$   $-$ ) in order to reflect mass increase (i.e.  $-\Delta f \cong \Delta m$ ), and  $\Delta D$  values are plotted on the  $y$ -axis (Fig. 1). Thus the point ( $x$ ,  $y$ ) corresponds to ( $\Delta f_{\text{time}=t}$ ,  $\Delta D_{\text{time}=t}$ ). In  $\Delta f$ - $\Delta D$  plots, time is *not* an explicit parameter. However, time can be inferred. The

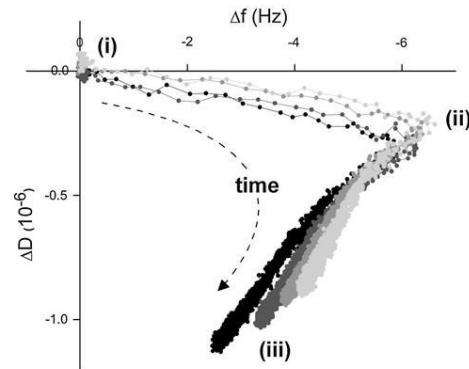


**Fig. 1** Example of a  $\Delta f$ - $\Delta D$  plot for the addition of a peptide solution to a lipid bilayer. The behaviour of the third, fifth, seventh and ninth harmonics are shown (darkest to lightest dots). Connecting lines are used as a visual aid only. All figures in this paper were prepared using OriginPro 8 (OriginLab Corp., Northampton, USA)

point (0,0) corresponds to time = 0 min, and time increases following the trace outward from the origin (Fig. 1).

$\Delta f$ - $\Delta D$  plots are useful for a number of reasons. Firstly, they quickly show the behaviour of the peptide. This will be explained below. Secondly, they highlight mechanistic processes. Generally, where there is a change in the direction of the trace this suggests a different process is occurring [e.g. (i)-(ii) and (ii)-(iii) in Fig. 1] (Rodahl et al. 1997). Thirdly, kinetic information can be extracted from the plots. Data points are acquired by the QCM-D every ca. 1 s, thus where the points are spread out the process is rapid [e.g. (i)-(ii) in Fig. 1], and where the points are closely spaced the process is slow [e.g. (ii)-(iii) in Fig. 1] (Rodahl et al. 1997). Finally, the trace can be used as a *fingerprint* for the interaction between that peptide with the membrane. This may enable relationships between peptides to be discovered. Peptides with similar  $\Delta f$ - $\Delta D$  traces have similar mechanisms of action, which may help us understand which amino acid residues are responsible for that mechanism and, hence, activity.

To interpret the behaviour of the peptide during each process, it is useful to draw an arrow beginning at the start of the process and pointing towards the end of that process (e.g. for the first process in Fig. 1, the arrow would be pointing south-east). Next, use Fig. 2 as a guide to ascertain what that arrow indicates. If the arrow is pointing south, the process is causing the bilayer to become more rigid; conversely, if the arrow is pointing north, the bilayer is becoming less rigid. If the arrow is pointing east, the process adds mass to the bilayer; conversely, if the arrow is pointing west, there is mass loss from the bilayer. For example, a south-east arrow suggests an increase in mass

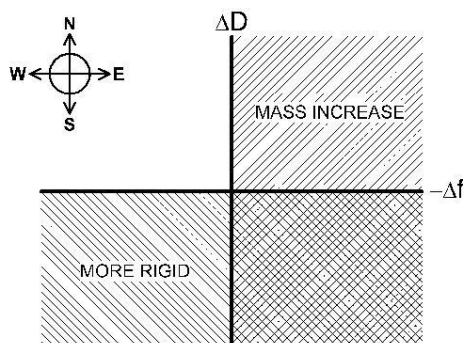


**Fig. 2** Interpretative guide for  $\Delta f$ - $\Delta D$  plots. North is up, and east is to the right. See text for explanation

with a corresponding increase in rigidity. This paper provides four case studies to assist in the understanding of this interpretation process.

#### Peptides under investigation

Five diverse AMPs will be used as case studies in this paper: caerin 1.1 wild-type, Gly15Gly19-caerin 1.1, Ala15Ala19-caerin 1.1, aurein 1.2 and oncocin. The amino acid sequences of these peptides are provided in Table 1.

Caerin 1.1 is a wide-spectrum antibiotic from the Australian green tree frog, *Litoria splendida*. It has higher activity against Gram-positive than Gram-negative bacteria (Wong et al. 1997) and also has antiviral and anticancer properties (VanCompernelle et al. 2005). The solution-state structure of caerin 1.1 shows that it forms two amphipathic  $\alpha$ -helices (between Leu2-Lys11 and Val17-His24) with a central flexible region containing two proline residues (at positions 15 and 19), which cause the C- and N-terminal helices to be angled at  $105^\circ$  with respect to each other, such that it resembles a boomerang (Pukala et al. 2004; Wong et al. 1997).

In Gly15Gly19-caerin 1.1 and Ala15Ala19-caerin 1.1, the two proline residues have been replaced with two glycines and two alanines, respectively. The substitution

increases the angle between the two  $\alpha$ -helices, making the peptides more linear, and decreases their flexibility (Pukala et al. 2004). This results in decreased antibiotic activity, with the glycine mutant having only intermediate activity and the alanine mutant being essentially inactive (Pukala et al. 2004). It is suggested that the kink in the structure of caerin 1.1 wild-type reorientates the two  $\alpha$ -helices such that there is a continuous hydrophobic and hydrophilic face; however, as a result of the substitutions, the kink is significantly reduced in the mutants, causing Lys11 to lie at the interface of the two faces in Gly15Gly19-caerin 1.1 and actually project into the hydrophobic face in Ala15Ala19-caerin 1.1 (Pukala et al. 2004).

Aurein 1.2 is a short AMP secreted by the southern bell frog, *Litoria raniformis*. It shows both antibiotic and anti-cancer activity (Rozek et al. 2000). The solution structure of aurein 1.2 shows it forms an  $\alpha$ -helix with well-defined hydrophilic and hydrophobic zones (Rozek et al. 2000). It was hypothesised by Rozek et al. (2000) that aurein 1.2 is unable to span the lipid bilayer because, with 13 amino acid residues, it is too short, and thus operates via the carpet mechanism. This was confirmed by QCM-D results published by our group (Mechler et al. 2007).

Finally, oncocin (peptide 10) is a novel AMP based on the native *Oncopeltus* antibacterial peptide isolated from *Oncopeltus fasciatus* (Knappe et al. 2010). Oncocin was optimised to have high activity against Gram-negative bacteria, low toxicity towards human cell lines and human red blood cells and a prolonged biological half-life. Unlike the other AMPs discussed in this article, oncocin exerts its antibacterial activity through a non-lytic, bacteriostatic mechanism. It was demonstrated by Knappe et al. (2010) that oncocin freely penetrates bacterial membranes, as evidenced by confocal fluorescence microscopy and QCM-D.

This research article will analyse the QCM-D data obtained for the interaction of these five AMPs with mammalian-like DMPC membranes, showing how  $\Delta f$ - $\Delta D$  plots aid in the interpretation of their mode of action. The first two case studies for caerin 1.1 wild-type and Gly15Gly19-caerin 1.1/Ala15Ala19-caerin 1.1 illustrate how  $\Delta f$ - $\Delta D$  plots may be used to determine the individual mechanistic processes that occur during the interaction

**Table 1** Sequence of AMPs investigated

Name	Sequence	Ref.
Caerin 1.1 wild-type	GLLSVLGSAKHVLPVVPVIAEHL-NH <sub>2</sub>	(Stone et al. 1992)
Gly15Gly19-caerin 1.1	GLLSVLGSAKHVLGHVVGVIAEHL-NH <sub>2</sub>	(Pukala et al. 2004)
Ala15Ala19-caerin 1.1	GLLSVLGSAKHVLAHVVAVIAEHL-NH <sub>2</sub>	(Pukala et al. 2004)
Aurein 1.2	GLFDIHKIAESF-NH <sub>2</sub>	(Rozek et al. 2000)
Oncocin (peptide 10)	VDKPPYLPVPRPPRIYNR-NH <sub>2</sub>	(Knappe et al. 2010)

between peptide with the membrane. The last two case studies for aurein 1.2 and oncocin show two different ways  $\Delta f$ - $\Delta D$  plots can be used to extract additional information, that is, by comparing them for different concentrations or by including the buffer rinse that is performed after peptide incubation.

### Case studies

#### Case study 1: caerin 1.1 wild-type

All experiments in this study were conducted as previously reported by Mechler et al. (2007). Figure 3a shows the simplest representation of QCM-D data. The top panel in Fig. 3a is a  $\Delta f$ - $t$  plot, which shows the changes in mass of the membrane after the introduction of the peptide solution. The bottom panel (Fig. 3a) is a  $\Delta D$ - $t$  plot, which shows changes in the structure of the membrane. It can be concluded from these plots that, upon interaction of caerin 1.1 wild-type with a DMPC membrane, there is an overall loss of mass from and a stiffening of the membrane, evidenced by a positive shift in the  $\Delta f$  values at the end of the experiment with respect to the start and a negative shift in the  $\Delta D$  values.

The  $\Delta f$ - $\Delta D$  plot is a complementary method of presenting the data (Fig. 3b). One advantage of the  $\Delta f$ - $\Delta D$  plot is that it highlights the mechanistic processes occurring during the experiment (Rodahl et al. 1997); for example, in Fig. 3b there are two distinct turning points in

the trace, which suggests that there are three mechanistic processes [labelled (i)–(iii) in Fig. 3b].

The first process can be represented by a north-east arrow [arrow (i) in Fig. 3b], which, according to Fig. 2, is interpreted as an increase in mass of the membrane with a corresponding loss of rigidity. In the experiment shown, this process was very rapid (taking 40 s). However, in some experiments it is not observed at all, suggesting that it is a real effect, albeit dependent on variables such as membrane structure, rather than an apparent effect caused by a difference in density or viscosity of the peptide solution being introduced in the QCM-D chamber (Kanazawa and Gordon 1985). This process corresponds to the addition of peptide to the membrane, until a critical concentration is reached.

During the second process, represented by a south-west arrow [arrow (ii) in Fig. 3b], mass is rapidly lost from the membrane and it becomes more rigid. This suggests that caerin 1.1 wild-type *disrupts* mammalian-like DMPC membranes. In Fig. 3b the traces of the four harmonics do not overlap, but rather they are spread out. The third and fifth harmonics, which probe further from the chip surface, show the greatest loss of mass, suggesting that more mass is lost from the top of the membrane (Mechler et al. 2007). Rapid disruption was observed at peptide concentrations of  $\geq 5$   $\mu\text{M}$ , with a slow gradual disruption at 2  $\mu\text{M}$ , showing the potency of this peptide towards DMPC membranes (data not shown). Its potency is also emphasised by the speed of membrane disruption, with both processes 1 and 2 taking less than 2 min.

**Fig. 3** Interaction of caerin 1.1 wild-type with DMPC membrane. **a** Change in  $\Delta f$  and  $\Delta D$  with time on introduction of a 20  $\mu\text{M}$  solution of the peptide into the QCM-D chamber. The response of the third, fifth, seventh and ninth harmonics are shown (darkest to lightest lines).  $\Delta f$ -time and  $\Delta D$ -time plots have been smoothed using the Adjacent-Averaging method, with 20 points of window. **b** Corresponding  $\Delta f$ - $\Delta D$  plot for the 20  $\mu\text{M}$  sample. To assist with interpretation, arrows representing each distinct mechanistic process are shown. The arrows labelled (i)–(iii) correspond to the first to third processes, respectively

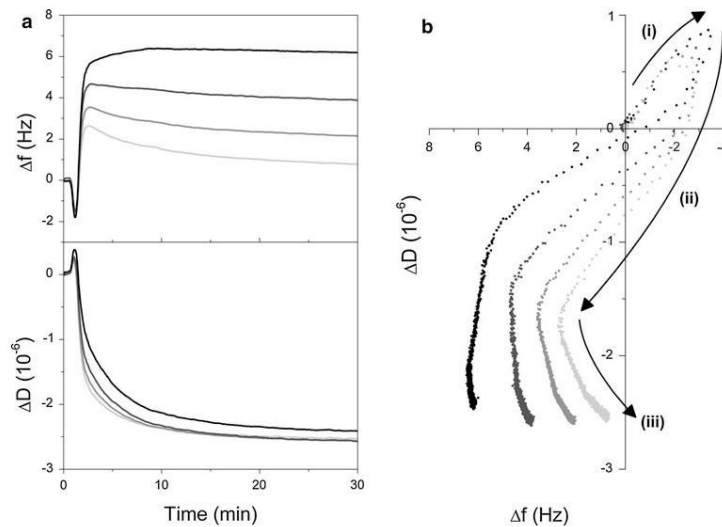
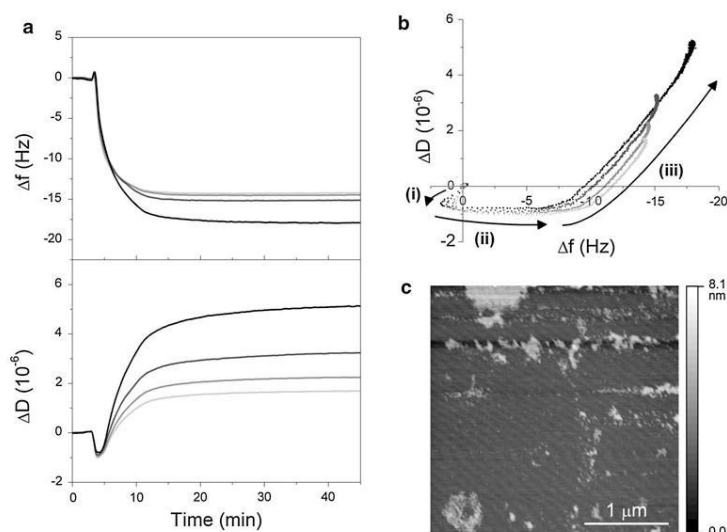


**Fig. 4** Interaction of caerin 1.1 mutants with DMPC membrane. **a** Change in  $\Delta f$  and  $\Delta D$  with time on introduction of a 20  $\mu\text{M}$  solution of Gly15Gly19-caerin 1.1 into the QCM-D chamber. The response of the third, fifth, seventh and ninth harmonics are shown (darkest to lightest lines).  $\Delta f$ -time and  $\Delta D$ -time plots have been smoothed using the Adjacent-Averaging method, with 20 points of window. **b** Corresponding  $\Delta f$ - $\Delta D$  plot for the 20  $\mu\text{M}$  sample. To assist with interpretation, arrows representing each distinct mechanistic process are shown. The arrows labelled (i)–(iii) correspond to the first to third processes, respectively. **c** AFM image of 0.5  $\mu\text{g}$  Ala15Ala19-caerin 1.1 incubated with a DMPC membrane in PBS. Image was processed using the free software Gwyddion 2.20



Finally, the third process [arrow (iii) in Fig. 3b] involves very slow mass gain on the higher harmonics with a continuing increase in rigidity of the membrane. This process is consistent with a rearrangement of the peptide and lipid remaining on the chip. During this process there is no overall change in mass of the film, evidenced by there being no change in the third harmonic, but mass gain in the chip surface-sensing higher harmonics. This suggests that weakly bound material is diffusing from the top of the film inwards, thus resulting in a more densely packed film with no overall change in mass.

In summary, caerin 1.1 wild-type disrupts DMPC membranes. The three distinct processes in this mechanism (addition, disruption and rearrangement), while not readily identifiable from the  $\Delta f$ - $t$  and  $\Delta D$ - $t$  plots, are clearly distinguished in the  $\Delta f$ - $\Delta D$  plot. By including all harmonics in the  $\Delta f$ - $\Delta D$  plot, it is possible to obtain information about the three-dimensional structure of the lipid membrane. This conclusion is consistent with solid-state NMR studies, which have shown that caerin 1.1 wild-type appears to “partially insert” before “cell lysis” in DMPC bilayers (Marcotte et al. 2003). However, we can now define this peptide as acting on DMPC by a disruption consistent with a *carpet mechanism*. This conclusion differs from our earlier QCM-D work that suggested that caerin 1.1 wild-type formed transmembrane pores (Mechler et al. 2007). One possible explanation for this discrepancy is the presence of trace amounts of trifluoroacetic acid in the original peptide sample, which were not present in the sample used in this study.

Case study 2: Gly15Gly19-caerin 1.1 and Ala15Ala19-caerin 1.1

Fig. 4a shows the  $\Delta f$ - $t$  and  $\Delta D$ - $t$  plots for Gly15Gly19-caerin 1.1. Remarkably, when comparing the plots in Figs. 3a and 4a, it is observed that the  $\Delta f$ - $t$  plot in Fig. 4a resembles the  $\Delta D$ - $t$  plot in Fig. 3a. Thus, substitution of the two proline residues in the wild-type with two glycines radically changes the behaviour of the peptide. The only similarity between the interaction of the wild-type and the mutant peptide with a DMPC membrane is that their  $\Delta f$ - $\Delta D$  plots both indicate a three-stage mechanism (Fig. 4b). The behaviour of Ala15Ala19-caerin 1.1 is very similar to that of Gly15Gly19-caerin 1.1, showing the same  $\Delta f$ - $\Delta D$  fingerprint with only slight differences in magnitude, hence the QCM-D data is not presented.

In interpreting the  $\Delta f$ - $\Delta D$  plot (Fig. 4b) it is useful to work in reverse, that is, first to understand the overall effect of the peptide on the membrane, and then to elucidate how this outcome is reached. Therefore, starting with the third process [arrow (iii) in Fig. 4b], we note there is an increase in both mass and energy dissipation. This process corresponds to *aggregation* of the peptide on the surface. Figure 4b illustrates this aggregation, as the mass and dissipation increase is greatest for the third harmonic, suggesting that there is a non-rigid structure extending high above the chip surface. Furthermore, this conclusion is supported by atomic force microscopy (AFM) images, which reveal that Ala15Ala19-caerin 1.1 forms large aggregates, some as large as 800 nm in width and 8 nm in

height, on DMPC bilayers (Fig. 4c). Clearly, the substitutions have changed the disruptive mechanism of the wild-type peptide to a non-disruptive mechanism on DMPC membranes. Accordingly, Gly15Gly19-caerin 1.1 is a better candidate for an antibiotic because it does not disrupt mammalian membranes, while having the same activity against certain bacteria as the wild-type, including *Bacillus cereus*, *Micrococcus luteus* and *Streptococcus uberis* (Pukala et al. 2004).

To ascertain whether the membrane was causing or promoting aggregation, Ala15Ala19-caerin 1.1 was added to an MPA-modified chip without lipid. A similar amount of peptide added to the surface, but it formed a very compact structure, as evidenced by a change in  $\Delta D$  of  $<0.5 \times 10^{-6}$  and no spreading of the harmonics (data not shown). Thus, while the membrane is not causing aggregation, it does facilitate the formation of larger and highly dissipating aggregates.

In the second process [arrow (ii) in Fig. 4b], mass rapidly increases with no change in energy dissipation. It is not uncommon for peptides to bind to bilayers with no change in dissipation; we have observed this for non-lytic AMPs, e.g. apidaecin 1a and 1b (Piantavigna et al. 2009) and oncocin (Knappe et al. 2010). The rationale behind this is that non-lytic AMPs must be able to freely traverse the membrane, which requires a low energy for membrane penetration and thus suggests that changes to the membrane during penetration must be minimised. Thus, during this second process, peptide is added to the membrane with little conformational change. Once saturation of the membrane is achieved, the third process commences.

The first process can be represented by a south-west arrow [arrow (i) in Fig. 4b], which suggests a loss of mass from the chip surface with a corresponding decrease in energy dissipation (Fig. 2). This process was observed at all peptide concentrations and in all experiments involving Gly15Gly19-caerin 1.1. A similar amount of mass is lost at all concentrations; however, the mass loss is slower for the lower concentrations (data not shown). Furthermore, this process was only observed on interaction with DMPC membranes and not DMPC/DMPG membranes (data not shown). This suggests that, similar to the first process for caerin 1.1 wild-type, this process cannot be attributed to the difference in density or viscosity of the peptide solution, otherwise it would be observed in all experiments regardless of lipid composition and at different magnitudes for the different peptide concentrations. Clearly, the introduction of the peptide solution causes an instantaneous structural change to the membrane. This structural change may expel water molecules associated to the lipid headgroups, offsetting any increase in mass due to peptide addition (Nilebäck et al. 2010). However, the actual mechanism through which this is achieved is, at the moment, unclear.

The  $\Delta f$ - $\Delta D$  plot again allows us to access mechanistic information not readily apparent from the individual  $\Delta f$ - $t$  and  $\Delta D$ - $t$  plots. For the addition of Gly15Gly19-caerin 1.1 and Ala15Ala19-caerin 1.1 to a DMPC membrane, three processes are observed. These are consistent with, firstly, addition of a small amount of peptide to the membrane in a manner that changes its structure, secondly, addition of peptide until membrane saturation and, thirdly, further addition of peptide to the surface of the membrane to form aggregates.

### Case study 3: aurein 1.2

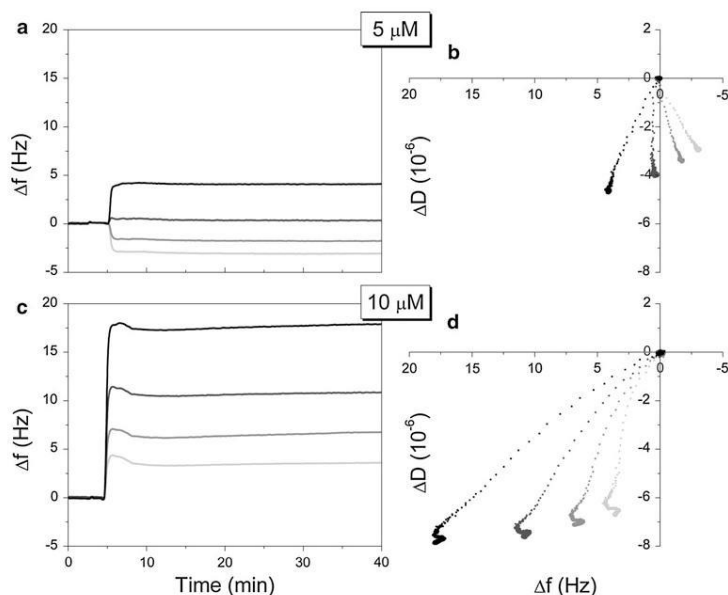
In the previous case studies, the response of the different harmonics was used to ascertain the mechanism of action of the peptides. An important additional source of information is the behaviour of the peptide over a range of concentrations. In general, the higher concentrations reveal the overall mode of action of the peptide (e.g. membrane disruption, pore formation), while the lower concentrations elucidate how this mode of action is achieved (e.g. the orientation of the peptide in the membrane, the effect of binding on the structure of the membrane) (Mechler et al. 2007). The aurein 1.2 case study provides an illustration of this strategy.  $\Delta f$ - $t$  plots of a low concentration of aurein 1.2 (5  $\mu$ M) and a higher concentration (10  $\mu$ M) are shown in Fig. 5a and c, respectively. The corresponding  $\Delta f$ - $\Delta D$  plots are shown in Fig. 5b and d.

Beginning with the high-concentration sample (Fig. 5c and d), it is observed that there is essentially one mechanistic process that can be represented by a south-west arrow, which indicates a rapid loss of mass with a decrease in energy dissipation (Fig. 2). Thus, aurein 1.2 causes an *instantaneous disruption* of the DMPC membrane. Similar to caerin 1.1 wild-type, the spreading of the harmonics suggests that more mass is lost from the surface of the membrane. However, because of the rate of this process, it is difficult to identify how this disruption proceeds. This is where the data from the lower peptide concentration becomes useful.

The low-concentration sample (Fig. 5a and b) causes a decrease in resonance frequency at the seventh and ninth harmonics, but an increase in frequency at the third and fifth harmonics; that is, the harmonics sensing closer to the chip surface (seventh and ninth) show a mass gain, but those sensing further away from the surface (third and fifth) show a mass loss. This could correspond to an addition of peptide to the membrane, followed by an instantaneous redistribution of mass from the top leaflet to the bottom leaflet. However, the third harmonic essentially represents what is happening to the overall mass of the membrane on the surface. A redistribution of mass would not cause a mass loss at the third harmonic, as mass is conserved.

**Fig. 5** Interaction of aurein 1.2 with DMPC membrane.

**a** Change in  $\Delta f$  with time on introduction of a 5  $\mu\text{M}$  solution of the peptide into the QCM-D chamber. The response of the third, fifth, seventh and ninth harmonics are shown (*darkest to lightest lines*). **b** Corresponding  $\Delta f$ - $\Delta D$  plot for the 5  $\mu\text{M}$  sample. **c**  $\Delta f$ -time plot for a 10  $\mu\text{M}$  sample. **d** Corresponding  $\Delta f$ - $\Delta D$  plot for the 10  $\mu\text{M}$  sample. All  $\Delta f$ -time plots have been smoothed using the Adjacent-Averaging method, with 20 points of window



An alternative explanation is that aurein 1.2 binds to the surface of membrane, decreasing the interaction between the membrane surface and the bulk solution (Mechler et al. 2007). Thus, the third and fifth harmonics indicate mass loss, because less solution and hence mass is coupled to the membrane, while the seventh and ninth harmonics indicate mass gain, because they only sense the membrane, which has increased in mass due to the addition of the peptide. This suggests that aurein 1.2 associates with the surface of the membrane. Therefore, when combined with the information extracted from Fig. 5c and d, it can be concluded that aurein 1.2 acts via a *carpet mechanism*.

By comparing the  $\Delta f$ - $\Delta D$  plots for different concentrations, additional information about the mechanism of action of the peptide can be obtained, which is not readily available in either; for example, for aurein 1.2, the high-concentration  $\Delta f$ - $\Delta D$  plot showed that it disrupted the membrane, and the low-concentration plot showed that it initially binds to the surface. Together, they thus establish that the peptide acts via a surface-based carpet mechanism.

#### Case study 4: oncocin

$\Delta f$ - $\Delta D$  plots can be used to show more than just the initial addition of peptide to a membrane. Additional experimental steps can also be included in the  $\Delta f$ - $\Delta D$  plot. In the oncocin case study, we have included the buffer rinse that

is performed after peptide addition and incubation (indicated by a star in Fig. 6).

Addition of oncocin to a DMPC membrane reveals a two-stage mechanism (Fig. 6b). The first process [arrow (i) in Fig. 6b] corresponds to a rapid insertion of the peptide into the membrane with no change in dissipation. All harmonics overlap, indicating that there is an even distribution of peptide throughout the membrane (Mechler et al. 2007). Secondly, after this initial interaction, there is a very small and gradual increase in energy dissipation with a small increase in mass [arrow (ii) in Fig. 6b]. This could correspond to either a further addition of peptide behaving in a different manner, and/or a rearrangement of the peptide added during process (i); for example, since it is known that oncocin freely penetrates bacterial membranes (Knapp et al. 2010), the peptide within the membrane may have diffused into the small pockets of trapped solution that exist between the bottom leaflet of the membrane and the quartz chip surface, increasing the energy dissipation.

The buffer rinse, indicated by a star in Fig. 6, removes ca. 50% of the peptide from the membrane. This suggests that insertion is an equilibrium process. Removing peptide from the bulk solution causes peptide within the membrane to diffuse into the solution to compensate. However, this is not completely reversible. In particular, the increase in dissipation observed during process (ii) does not change.

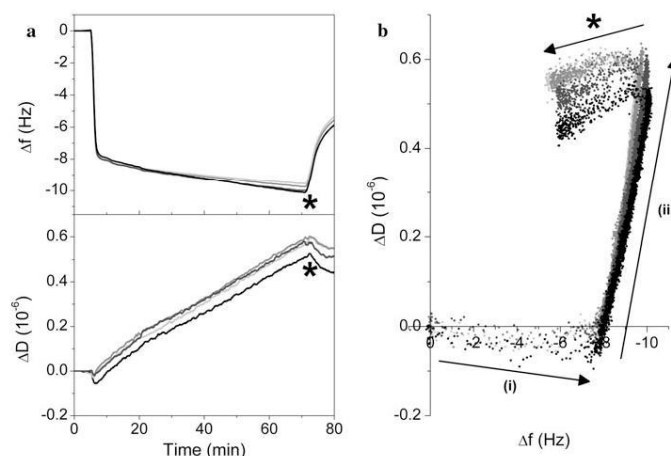


**Fig. 6** Interaction of oncocin with DMPC membrane. **a** Change in  $\Delta f$  and  $\Delta D$  with time on introduction of a 15  $\mu\text{M}$  solution of the peptide into the QCM-D chamber. At the time point indicated by a star, the chamber was flushed with buffer at 300  $\mu\text{l min}^{-1}$ . The response of the third, fifth, seventh and ninth harmonics are shown (darkest to lightest lines).  $\Delta f$ -time and  $\Delta D$ -time plots have been

smoothed using the Adjacent-Averaging method, with 20 points of window. **b** Corresponding  $\Delta f$ - $\Delta D$  plot for the 15  $\mu\text{M}$  sample. To assist with interpretation, arrows representing each distinct mechanistic process are shown. The arrows labelled (i) and (ii) correspond to the first and second processes, respectively, and the arrow marked with a star corresponds to the buffer rinse

This reinforces the interpretation that either the peptide has bound in a manner that irreversibly changed the membrane structure, or some peptide is trapped at the membrane–chip surface interface.

In conclusion, including the buffer rinse in  $\Delta f$ - $\Delta D$  plots provides additional information such as the reversibility of the peptide interaction, which may assist in understanding its mechanism. In this case study, the non-lytic mechanism of oncocin was established by two observations; firstly, the due-east arrow in the  $\Delta f$ - $\Delta D$  plot and, secondly, the loss of peptide during the buffer rinse.

### Conclusions

QCM-D can screen potential AMPs for activity towards a variety of membranes and hence determine their selectivity; for example, in case studies 1 and 2 it was concluded that caerin 1.1 wild-type disrupts mammalian membranes, while the mutants do not. Membrane choice is almost limitless, with even complex cell membranes being mimicked in QCM-D [e.g. the stratum corneum membrane of the epidermis (Lee et al. 2009)]. QCM-D can determine the relative potency of the AMP, by determining what concentration of peptide is required for membrane disruption or pore formation. Importantly, QCM-D can investigate the mechanism of action of the AMP. Both mass and structural changes to the membrane are detected with time resolution

of seconds; for example, the first mechanistic process in case study 2 was over in 15 s. Therefore, QCM-D is a versatile and valuable technique for investigation of AMPs.

The  $\Delta f$ - $\Delta D$  plot is a useful analytical tool to interpret QCM-D results. This paper has showcased how it can be used to elucidate potential mechanisms for five AMPs with diverse activity. By including all the harmonics in the  $\Delta f$ - $\Delta D$  plot it is possible to ascertain where the disruption is occurring (a differential response of the harmonics suggests mass loss is occurring at the surface, e.g. case studies 1 and 3), or whether there is aggregation on the membrane (a large energy dissipation at the third harmonic suggests the formation of aggregates, e.g. case study 2). By comparing the  $\Delta f$ - $\Delta D$  plots for different concentrations, a more complete understanding of the mechanism can be achieved (e.g. case study 3). Finally, including additional steps in the  $\Delta f$ - $\Delta D$  plot, such as the buffer rinse, gives information about the reversibility of the peptide interaction (e.g. case study 4). Other biophysical techniques can then be used to refine the model.

Furthermore, once the  $\Delta f$ - $\Delta D$  plot has been used to determine the mechanism of action, it then becomes a fingerprint for that peptide. AMPs with similar  $\Delta f$ - $\Delta D$  plots have similar mechanisms. Therefore, the  $\Delta f$ - $\Delta D$  plot allows classification of peptides based on their activity towards different membranes. This can lead to a greater understanding of AMPs and, as a result, the development of better antibiotics in the future.

## References

- Ambroggio EE, Separovic F, Bowie JH, Fidelio GD, Bagatolli LA (2005) Direct visualization of membrane leakage induced by the antibiotic peptides: maculatin, citropin, and aurein. *Biophys J* 89:1874–1881
- Balla MS, Bowie JH, Separovic F (2004) Solid-state NMR study of antimicrobial peptides from Australian frogs in phospholipid membranes. *Eur Biophys J* 33:109–116
- Briand E, Humblot V, Pradier C-M, Kasemo B, Svedhem S (2010) An OEGylated thiol monolayer for the tethering of liposomes and the study of liposome interactions. *Talanta* 81:1153–1161
- Christ K, Wiedemann I, Bakowsky U, Sahl HG, Bendas G (2007) The role of lipid II in membrane binding of and pore formation by nisin analyzed by two combined biosensor techniques. *Biochim Biophys Acta* 1768:694–704
- Gordon YJ, Romanowski EG, McDermott AM (2005) A review of antimicrobial peptides and their therapeutic potential as anti-infective drugs. *Curr Eye Res* 30:505–515
- Höök F, Kasemo B (2001) Variations in coupled water, viscoelastic properties, and film thickness of a Mefp-1 protein film during adsorption and cross-linking: a quartz crystal microbalance with dissipation monitoring, ellipsometry, and surface plasmon resonance study. *Anal Chem* 73:5796–5804
- IDSAs (2004) Bad bugs, no drugs: as antibiotic discovery stagnates, a public health crisis brews. <http://www.idsociety.org/>. Accessed 28 Sept 2010
- Kanazawa KK, Gordon JG (1985) frequency of a quartz microbalance in contact with liquid. *Anal Chem* 57:1770–1771
- Katz ML, Mueller LV, Polyakov M, Weinstock SF (2006) Where have all the antibiotic patents gone? *Nat Biotechnol* 24:1529–1531
- Knappe D, Piantavigna S, Hansen A, Mechler A, Binas A, Nolte O, Martin LL, Hoffmann R (2010) Oncocin (VDKPPYLPRPRPR-RIYNR-NH<sub>2</sub>): a novel antibacterial peptide optimized against gram-negative human pathogens. *J Med Chem* 53:5240–5247
- Lam KLH, Ishitsuka Y, Cheng Y, Chien K, Waring AJ, Lehrer RI, Lee KYC (2006) Mechanism of supported membrane disruption by antimicrobial peptide protegrin-1. *J Phys Chem B* 110:21282–21286
- Lee D, Ashcraft N, Verploegen E, Pashkovski E, Weitz DA (2009) Permeability of model stratum corneum lipid membrane measured using quartz crystal microbalance. *Langmuir* 25:5762–5766
- Marcotte I, Wegener KL, Lam Y-H, Chia BCS, de Planque MRR, Bowie JH, Auger M, Separovic F (2003) Interaction of antimicrobial peptides from Australian amphibians with lipid membranes. *Chem Phys Lipids* 122:107–120
- Mechler A, Praporski S, Atmuri K, Boland M, Separovic F, Martin LL (2007) Specific and selective peptide-membrane interactions revealed using quartz crystal microbalance. *Biophys J* 93:3907–3916
- Mechler A, Praporski S, Piantavigna S, Heaton SM, Hall KN, Aguilar M-I, Martin LL (2009) Structure and homogeneity of pseudo-physiological phospholipid bilayers and their deposition characteristics on carboxylic acid terminated self-assembled monolayers. *Biomaterials* 30:682–689
- Nielsen SB, Otzen DE (2010) Impact of the antimicrobial peptide Novicidin on membrane structure and integrity. *J Colloid Interface Sci* 345:248–256
- Nilebäck E, Westberg F, Deinum J, Svedhem S (2010) Viscoelastic sensing of conformational changes in plasminogen induced upon binding of low molecular weight compounds. *Anal Chem* 82:8374–8376
- Papo N, Shai Y (2003) Exploring peptide membrane interaction using surface plasmon resonance: differentiation between pore formation versus membrane disruption by lytic peptides. *Biochemistry* 42:458–466
- Peschel A, Sahl H-G (2006) The co-evolution of host cationic antimicrobial peptides and microbial resistance. *Nat Microbiol* 4:529–536
- Piantavigna S, Czihal P, Mechler A, Richter M, Hoffmann R, Martin LL (2009) Cell penetrating apidaecin peptide interactions with biomimetic phospholipid membranes. *Int J Pept Res Ther* 15:139–146
- Powers JPS, Hancock REW (2003) The relationship between peptide structure and antibacterial activity. *Peptides* 24:1681–1691
- Pukala TL, Brinkworth CS, Carver JA, Bowie JH (2004) Investigating the importance of the flexible hinge in caerin 1.1: solution structures and activity of two synthetically modified caerin peptides. *Biochemistry* 43:937–944
- Rickert J, Brecht A, Göpel W (1997) QCM operation in liquids: constant sensitivity during formation of extended protein multilayers by affinity. *Anal Chem* 69:1441–1448
- Rodahl M, Kasemo B (1996) On the measurement of thin liquid overlayers with the quartz-crystal microbalance. *Sens Actuators A Phys* 54:448–456
- Rodahl M, Höök F, Krozer A, Brzezinski P, Kasemo B (1995) Quartz crystal microbalance setup for frequency and Q-factor measurements in gaseous and liquid environments. *Rev Sci Instrum* 66:3924–3930
- Rodahl M, Höök F, Fredriksson C, Keller CA, Krozer A, Brzezinski P, Voinova M, Kasemo B (1997) Simultaneous frequency and dissipation factor QCM measurements of biomolecular adsorption and cell adhesion. *Faraday Discuss* 107:229–246
- Rozeck T, Wegener KL, Bowie JH, Olver IN, Carver JA, Wallace JC, Tyler MJ (2000) The antibiotic and anticancer active aurein peptides from the Australian bell frogs *Litoria aurea* and *Litoria raniformis*. *Eur J Biochem* 267:5330–5341
- Sauerbrey G (1959) The use of quartz oscillators for weighing thin layers and for microweighing. *Z Phys* 155:206–222
- Shai Y (1999) Mechanism of the binding, insertion and destabilization of phospholipid bilayer membranes by K-helical antimicrobial and cell non-selective membrane-lytic peptides. *Biochim Biophys Acta* 1462:55–70
- Shai Y (2002) Mode of action of membrane active antimicrobial peptides. *Biopolymers* 66:236–248
- Sherman PJ, Jackway RJ, Gehman JD, Praporski S, McCubbin GA, Mechler A, Martin LL, Separovic F, Bowie JH (2009) solution structure and membrane interactions of the antimicrobial peptide fallaxidin 4.1a: an NMR and QCM study. *Biochemistry* 48:11892–11901
- Stone DJM, Bowie JH, Tyler MJ, Wallace JC (1992) The structure of caerin 1.1, a novel antibiotic peptide from Australian tree frogs. *J Chem Soc, Chem Commun* (17):1224–1225
- VanCompernelle SE, Taylor RJ, Oswald-Richter K, Jiang J, Youree BE, Bowie JH, Tyler MJ, Conlon JM, Wade D, Aiken C, Dermody TS, KewalRamani VN, Rollins-Smith LA, Unutmaz D (2005) Antimicrobial peptides from amphibian skin potently inhibit human immunodeficiency virus infection and transfer of virus from dendritic cells to T cells. *J Virol* 79:11598–11606
- Voinova MV, Rodahl M, Jonson M, Kasemo B (1999) Viscoelastic acoustic response of layered polymer films at fluid-solid interfaces: continuum mechanics approach. *Phys Scr* 59:391–396
- Wong H, Bowie JH, Carver JA (1997) The solution structure and activity of caerin 1.1, an antimicrobial peptide from the Australian green tree frog, *Litoria splendida*. *Eur J Biochem* 247:545–557
- Zaslloff M (2002) Antimicrobial peptides of multicellular organisms. *Nature* 415:389–395

## 5 Scanning electrochemical microscopy (SECM)

Scanning electrochemical microscopy (SECM) is an electrochemical technique developed in 1989 by Bard et al in order to characterise and probe the electrochemical activity of liquid/solid and liquid/liquid interfaces<sup>85-87</sup>. In current work, it is used to detect any reaction intermediates at the working electrode surface. Fig. 15 shows the configuration and instrumentation used for the SECM experiments. Briefly, a typical SECM instrument consists of an ultramicroelectrode (UME, probe), a bipotentiostat and a 3D-positioner. The UME is the main tool for probing the reaction (or surface). It consists of a conductive disk of metal or carbon enclosed by an insulating sheath and it can be made of different sizes between 5-25  $\mu\text{m}$  in diameter. The UME is connected to a bipotentiostat (i.e. with two working electrode connections), which controls the applied potential versus a reference electrode across the UME and/or another substrate to measure the output current.

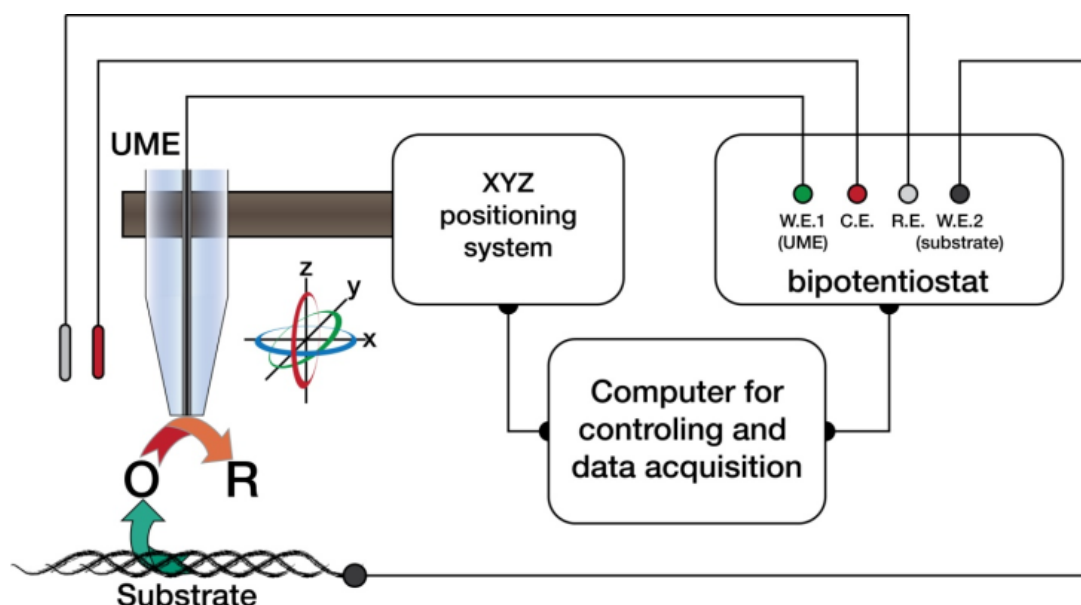


**Fig. 15:** Schematic illustration shows SECM instrument configuration used here.

The probe is held by a 3D-positioner in order to move the tip over the substrate's surface in x, y and z directions. The 3D-positioner mainly utilises a

step motor for rough positioning of the probe over the sample and a  $x, y, z$  piezo-motor for accurate and fine positioning of the probe's tip down to micron movements. Finally, a computer connects to the bipotentiostat and the 3D-positioner for controlling the parameters and data acquisition<sup>62,88</sup>.

The SECM tip is usually placed via a mediator solution to within 10 micron of the working/substrate electrode. The operating principle behind the SECM is based on measuring the current associated with the diffusion layer near the UME's tip<sup>89</sup>. When the UME is biased at a negative potential that is sufficient to reduce an oxidised species (e.g.  $\text{H}_2\text{O}_2$ ) in proximity to its surface (i.e. in the diffusion layer), a diffusion limited current is generated at the UME's tip and vice versa. This current is controlled by the diffusion of the oxidised species towards the tips surface and it is described by Equation 8 ;

$$i_d = 4nFCDa \tag{8}$$

where  $i_d$  is the diffusion limited current,  $n$  is the number of electrons,  $F$  is Faraday constant,  $C$  is the reactant concentration,  $D$  is the diffusion coefficient and  $a$  is the radius of the UME's tip.

SECM measurements can be executed in two main operation modes: the feedback mode and the generation/collection mode, which include the tip generation/substrate collection (TG/SC) and the substrate generation/tip collection (SG/TC)<sup>52</sup>. Feedback mode was used in all studies reported here. In this operation mode, the UME tip oxidises the reduced species (i.e. mediator), thus producing a steady-state current that is limited in the bulk solution by the hemispherical diffusion around the tip surface. As the tip approaches the substrate, the collected current may change in two different ways. If the substrate is conductive, the oxidised species formed at the tip are reduced by the conductive surface. This leads to an increase in the current collected at the tip, which is translated as a positive feedback. On the other hand, if the substrate is insulating, it cannot "regenerate" the oxidized species, and the hemispherical diffusion to the UME is hindered as the tip approaches the

substrate. Consequently, the collected current is decreased, which is interpreted as a negative feedback<sup>85,90</sup>.

SECM has been used in various fields of research, such as for corrosion phenomena<sup>91</sup>, in investigating the surface of SAMs<sup>92</sup>, in imaging biological samples such as DNA, cells<sup>93</sup>, enzymes liposomes<sup>94</sup> or the permeability of pores created by peptides in SLBs<sup>95</sup>. In this work, SECM has been applied to characterize the changes in permeability of SLBs due to the interactions with the Tat peptide as a membrane active peptide.



**Fig. 16:** Experimental set up for the investigation of the change in permeability of SLBs by Tat peptide (see Chapter 5). The QCM sensor is coated with lipid to represent substrate. The tip of the UME (the “B” labelled electrode) was biased at a potential sufficient to oxidise the mediator potassium ferrocyanide in PBS.

## 6 Bibliography

- 1 Dowhan, W. MOLECULAR BASIS FOR MEMBRANE PHOSPHOLIPID DIVERSITY: Why Are There So Many Lipids? *Annu. Rev. Biochem.* **66**, 199-232, (1997).
- 2 Van Meer, G. *et al.* Membrane lipids: Where they are and how they behave. *Nat. Rev. Mol. Cell Biol.* **9**, 112-124, (2008).
- 3 Singer, S. J. & Nicolson, G. L. The fluid mosaic model of the structure of cell membranes. *Science* **175**, 720-731, (1972).
- 4 Edidin, M. Lipids on the frontier: A century of cell-membrane bilayers. *Nat. Rev. Mol. Cell Biol.* **4**, 414-418, (2003).
- 5 Zimmerberg, J. & Gawrisch, K. The physical chemistry of biological membranes. *Nat. Chem. Biol.* **2**, 564-567, (2006).
- 6 Simons, K. & Vaz, W. L. C. MODEL SYSTEMS, LIPID RAFTS, AND CELL MEMBRANES<sup>1</sup>. *Annu. Rev. Bioph. Biom.* **33**, 269-295, (2004).
- 7 Conner, S. D. Regulated portals of entry into the cell. *Nature* **422**, 37-44, (2003).
- 8 Sanderson, J. M. Peptide lipid interactions: insights and perspectives. *Org. Biomol. Chem.* **3**, 201-212, (2005).
- 9 McMahon, H. T. & Gallop, J. L. Membrane curvature and mechanisms of dynamic cell membrane remodelling. *Nature* **438**, 590-596, (2005).
- 10 Sprong, H. *et al.* How proteins move lipids and lipids move proteins. *Nat. Rev. Mol. Cell Biol.* **2**, 504-513, (2001).
- 11 Róg, T. *et al.* Ordering effects of cholesterol and its analogues. *BBA-Biomembr.* **1788**, 97-121, (2009).
- 12 Yeaman, M. R. & Yount, N. Y. Mechanisms of antimicrobial peptide action and resistance. *Pharmacol. Rev.* **55**, 27-55, (2003).
- 13 Matsuzaki, K. Magainins as paradigm for the mode of action of pore forming polypeptides. *BBA- Rev. Biomembr.* **1376**, 391-400, (1998).
- 14 Devaux, P. F. & Morris, R. Transmembrane Asymmetry and Lateral Domains in Biological Membranes. *Traffic* **5**, 241-246, (2004).
- 15 Kinnunen, P. K. J. Amyloid formation on lipid membrane surfaces. *Open Biol.* **2**, 163-175, (2009).
- 16 Matsuzaki, K. Control of cell selectivity of antimicrobial peptides. *BBA-Biomembr.* **1788**, 1687-1692, (2009).
- 17 Epanand, R. M. & Epanand, R. F. Bacterial membrane lipids in the action of antimicrobial agents. *J. Pept. Sci.* **17**, 298-305, (2011).
- 18 LaRocca, T. J. *et al.* Proving Lipid Rafts Exist: Membrane Domains in the Prokaryote *Borrelia burgdorferi* Have the Same Properties as Eukaryotic Lipid Rafts. *PLoS Pathog.* **9**, e1003353, (2013).

- 19 Ikonen, E. Cellular cholesterol trafficking and compartmentalization. *Nat. Rev. Mol. Cell Biol.* **9**, 125-138, (2008).
- 20 de Meyer, F. & Smit, B. Effect of cholesterol on the structure of a phospholipid bilayer. *Proc. Natl. Acad. Sci.* **106**, 3654-3658, (2009).
- 21 Ohvo-Rekilä, H. *et al.* Cholesterol interactions with phospholipids in membranes. *Prog. Lipid Res.* **41**, 66-97, (2002).
- 22 Hung, W. C. *et al.* The condensing effect of cholesterol in lipid bilayers. *Biophys. J.* **92**, 3960-3967, (2007).
- 23 De Meyer, F. J. M. *et al.* Molecular simulation of the DMPC-cholesterol phase diagram. *J. Phys. Chem. B* **114**, 10451-10461, (2010).
- 24 Huang, J. & Feigenson, G. W. A microscopic interaction model of maximum solubility of cholesterol in lipid bilayers. *Biophys. J.* **76**, 2142-2157, (1999).
- 25 Needham, D. *et al.* Thermomechanical and transition properties of dimyristoylphosphatidylcholine/cholesterol bilayers. *Biochemistry* **27**, 4668-4673, (1988).
- 26 Travkova, O. G. *et al.* Influence of arenicin on phase transitions and ordering of lipids in 2d model membranes. *Langmuir* **29**, 12203-12211, (2013).
- 27 Yang, P. *et al.* Lipid fluid-gel phase transition induced alamethicin orientational change probed by sum frequency generation vibrational spectroscopy. *J. Phys. Chem. C* **117**, 17039-17049, (2013).
- 28 Fernandez, D. I. *et al.* Membrane defects enhance the interaction of antimicrobial peptides, aurein 1.2 versus caerin 1.1. *BBA- Biomembr.* **1828**, 1863-1872, (2013).
- 29 Parthasarathy, R. & Groves, J. T. Curvature and spatial organization in biological membranes. *Soft Matter* **3**, 24-33, (2007).
- 30 Zimmerberg, J. & Kozlov, M. M. How proteins produce cellular membrane curvature. *Nat. Rev. Mol. Cell Biol.* **7**, 9-19, (2006).
- 31 Schmidt, N. *et al.* Arginine-rich cell-penetrating peptides. *FEBS Lett.* **584**, 1806-1813, (2010).
- 32 Mishra, A. *et al.* HIV TAT forms pores in membranes by inducing saddle-splay curvature: Potential role of bidentate hydrogen bonding. *Angew. Chem. Int. Ed.* **47**, 2986-2989, (2008).
- 33 Matsuzaki, K. *et al.* Relationship of membrane curvature to the formation of pores by magainin 2. *Biochemistry* **37**, 11856-11863, (1998).
- 34 Hancock, J. F. Lipid rafts: contentious only from simplistic standpoints. *Nat. Rev. Mol. Cell Biol.* **7**, 456-462, (2006).
- 35 Butterfield, S. M. & Lashuel, H. A. Amyloidogenic protein-membrane interactions: Mechanistic insight from model systems. *Angew. Chem. Int. Ed.* **49**, 5628-5654, (2010).

- 36 Ladokhin, A. *et al.* CD Spectroscopy of Peptides and Proteins Bound to Large Unilamellar Vesicles. *J. Membr. Biol.* **236**, 247-253, (2010).
- 37 Mishra, A. *et al.* Translocation of HIV TAT peptide and analogues induced by multiplexed membrane and cytoskeletal interactions. *Proc. Natl. Acad. Sci.* **108**, 16883-16888, (2011).
- 38 Samad, A. Liposomal drug delivery systems: An update review. *Curr. Drug Delivery* **4**, 297-305, (2007).
- 39 Cho, N. J. *et al.* Quartz crystal microbalance with dissipation monitoring of supported lipid bilayers on various substrates. *Nat. Protoc.* **5**, 1096-1106, (2010).
- 40 Kamimori, H. *et al.* Evaluation of the Membrane-binding Properties of the Proximal Region of the Angiotensin II Receptor (AT1A) Carboxyl Terminus by Surface Plasmon Resonance. *Anal. Sci.* **21**, 171-174, (2005).
- 41 Ludtke, S. J. Membrane pores induced by magainin. *Biochemistry* **35**, 13723-13728, (1996).
- 42 Sherman, P. J. *et al.* Solution structure and membrane interactions of the antimicrobial peptide fallaxidin 4.1a: An NMR and QCM study. *Biochemistry* **48**, 11892-11901, (2009).
- 43 Hall, K. *et al.* Real-time measurement of membrane conformational states induced by antimicrobial peptides: Balance between recovery and lysis. *Scientific Reports* **4**, (2014).
- 44 Hall, K. *et al.* The role of electrostatic interactions in the membrane binding of melittin. *J. Mol. Recognit.* **24**, 108-118, (2011).
- 45 Brian, A. A. & McConnell, H. M. Allogeneic stimulation of cytotoxic T cells by supported planar membranes. *Proc. Natl. Acad. Sci.* **81**, 6159-6163, (1984).
- 46 Keller, C. A. & Kasemo, B. Surface specific kinetics of lipid vesicle adsorption measured with a quartz crystal microbalance. *Biophys. J.* **75**, 1397-1402, (1998).
- 47 Thimm, J. *et al.* Calcium-dependent open/closed conformations and interfacial energy maps of reconstituted hemichannels. *J. Biol. Chem.* **280**, 10646-10654, (2005).
- 48 Boxer, S. G. Molecular transport and organization in supported lipid membranes. *Curr. Opin. Chem. Biol.* **4**, 704-709, (2000).
- 49 Chi, E. Y. *et al.* Lipid membrane templates the ordering and induces the fibrillogenesis of Alzheimer's disease amyloid- $\beta$  peptide. *Proteins: Struct., Funct., Genet.* **72**, 1-24, (2008).
- 50 Wang, K. F. *et al.* Characterization of supported lipid bilayer disruption by chrysopsin-3 using QCM-D. *J. Phys. Chem. B* **115**, 15228-15235, (2011).
- 51 Papo, N. & Shai, Y. Exploring peptide membrane interaction using surface plasmon resonance: Differentiation between pore formation

- versus membrane disruption by lytic peptides. *Biochemistry* **42**, 458-466, (2003).
- 52 Lee, T. H. *et al.* Interaction of amphipathic peptides with an immobilised model membrane. *Lett. Pept. Sci.* **6**, 371-380, (1999).
- 53 Mecke, A. *et al.* Synthetic and natural polycationic polymer nanoparticles interact selectively with fluid-phase domains of DMPC lipid bilayers. *Langmuir* **21**, 8588-8590, (2005).
- 54 Reimhult, E. *et al.* Vesicle adsorption on SiO<sub>2</sub> and TiO<sub>2</sub>: Dependence on vesicle size. *J. Chem. Phys.* **117**, 7401-7404, (2002).
- 55 Reimhult, E. *et al.* Intact vesicle adsorption and supported biomembrane formation from vesicles in solution: Influence of surface chemistry, vesicle size, temperature, and osmotic pressure. *Langmuir* **19**, 1681-1691, (2003).
- 56 Richter, R. *et al.* Pathways of Lipid Vesicle Deposition on Solid Surfaces: A Combined QCM-D and AFM Study. *Biophys. J.* **85**, 3035-3047, (2003).
- 57 Reimhult, E. *et al.* Rupture pathway of phosphatidylcholine liposomes on silicon dioxide. *Int. J. Mol. Sci.* **10**, 1683-1696, (2009).
- 58 Richter, R. P. & Brisson, A. R. Following the formation of supported lipid bilayers on Mica: A study combining AFM, QCM-D, and ellipsometry. *Biophys. J.* **88**, 3422-3433, (2005).
- 59 Keller, C. A. *et al.* Formation of Supported Membranes from Vesicles. *Phys. Rev. Lett.* **84**, 5443-5446, (2000).
- 60 Zhu, T. *et al.* Effect of Osmotic Stress on Membrane Fusion on Solid Substrate. *Langmuir* **29**, 6377-6385, (2013).
- 61 Serro, A. P. *et al.* Formation of an intact liposome layer adsorbed on oxidized gold confirmed by three complementary techniques: QCM-D, AFM and confocal fluorescence microscopy. *Surf. Interface Anal.* **44**, 426-433, (2012).
- 62 Casero, E. AFM, SECM and QCM as useful analytical tools in the characterization of enzyme-based bioanalytical platforms. *Analyst* **135**, 1878-1903, (2010).
- 63 Huang, H. W. Molecular mechanism of antimicrobial peptides: The origin of cooperativity. *BBA- Biomembr.* **1758**, 1292-1302, (2006).
- 64 Li, C. *et al.* Biomimetic membranes of lipid-peptide model systems prepared on solid support. *J. Phys.- Condens. Mat* **16**, (2004).
- 65 Love, J. C. *et al.* Self-assembled monolayers of thiolates on metals as a form of nanotechnology. *Chem. Rev.* **105**, 1103-1169, (2005).
- 66 Wanunu, M. *et al.* Widely-Applicable Gold Substrate for the Study of Ultrathin Overlayers. *J. Am. Chem. Soc.* **126**, 5569-5576, (2004).

- 67 Gooding, J. J. & Ciampi, S. The molecular level modification of surfaces: From self-assembled monolayers to complex molecular assemblies. *Chem. Soc. Rev.* **40**, 2704-2718, (2011).
- 68 Cooper, M. A. & Singleton, V. T. A survey of the 2001 to 2005 quartz crystal microbalance biosensor literature: applications of acoustic physics to the analysis of biomolecular interactions. *J. Mol. Recognit.* **20**, 154-184, (2007).
- 69 Ferreira, G. N. M. *et al.* Acoustic wave biosensors: physical models and biological applications of quartz crystal microbalance. *Trends Biotechnol.* **27**, 689-697, (2009).
- 70 Speight, R. E. & Cooper, M. A. A Survey of the 2010 Quartz Crystal Microbalance Literature. *J. Mol. Recognit.* **25**, 451-473, (2012).
- 71 Reimhult, E. On the formation of supported phospholipid bilayers. *Doktorsavhandlingar vid Chalmers Tekniska Hogskola*, (2004).
- 72 Lu, N. *et al.* Molecular response and cooperative behavior during the interactions of melittin with a membrane: Dissipative quartz crystal microbalance experiments and simulations. *J. Phys. Chem. B* **116**, 9432-9438, (2012).
- 73 Briand, E. *et al.* Combined QCM-D and EIS study of supported lipid bilayer formation and interaction with pore-forming peptides. *Analyst* **135**, 343-350, (2010).
- 74 Fraser, S. J. *et al.* Surface immobilization of bio-functionalized cubosomes: Sensing of proteins by quartz crystal microbalance. *Langmuir* **28**, 620-627, (2012).
- 75 Praporski, S. *et al.* Organization of cytochrome P450 enzymes involved in sex steroid synthesis: Protein-protein interactions in lipid membranes. *J. Biol. Chem.* **284**, 33224-33232, (2009).
- 76 O'Sullivan, C. K. & Guilbault, G. G. Commercial quartz crystal microbalances - Theory and applications. *Biosens. Bioelectron.* **14**, 663-670, (1999).
- 77 Sauerbrey, G. Verwendung von Schwingquarzen zur Wägung dünner Schichten und zur Mikrowägung. *Zeitschrift für Physik* **155**, 206-222, (1959).
- 78 Kanazawa, K. K. & Gordon, J. G. Frequency of a quartz microbalance in contact with liquid. *Anal. Chem.* **57**, 1770-1771, (1985).
- 79 Rodahl, M. & Kasemo, B. On the measurement of thin liquid overlayers with the quartz-crystal microbalance. *Sens. Actuators, A* **54**, 448-456, (1996).
- 80 Fuertes, G. *et al.* A lipocentric view of peptide-induced pores. *Eur. Biophys. J.* **40**, 399-415, (2011).
- 81 Taupin, C. Osmotic pressure induced pores in phospholipid vesicles. *Biochemistry* **14**, 4771-4775, (1975).

- 82 Finkelstein, A. *et al.* Osmotic swelling of vesicles: its role in the fusion of vesicles with planar phospholipid bilayer membranes and its possible role in exocytosis. *Annu. Rev. Physiol.* **48**, 163-174, (1986).
- 83 Cohen, F. S. *et al.* Osmotic swelling of phospholipid vesicles causes them to fuse with a planar phospholipid bilayer membrane. *Science* **217**, 458-460, (1982).
- 84 Jackman, J. A. *et al.* Influence of osmotic pressure on adhesion of lipid vesicles to solid supports. *Langmuir* **29**, 11375-11384, (2013).
- 85 Bard, A. J. *et al.* Scanning electrochemical microscopy. Introduction and principles. *Anal. Chem.* **61**, 132-138, (1989).
- 86 Sun, P. & Mirkin, M. V. Kinetics of electron-transfer reactions at nanoelectrodes. *Anal. Chem.* **78**, 6526-6534, (2006).
- 87 Barker, A. L. *et al.* Scanning electrochemical microscopy: Beyond the solid/liquid interface. *Anal. Chim. Acta* **385**, 223-240, (1999).
- 88 Sun, P. *et al.* Scanning electrochemical microscopy in the 21st century. *PCCP* **9**, 802-823, (2007).
- 89 Engstrom, R. C. *et al.* Measurements within the diffusion layer using a microelectrode probe. *Anal. Chem.* **58**, 844-848, (1986).
- 90 O'Mullane, A. P. *et al.* Monitoring cuprous ion transport by scanning electrochemical microscopy during the course of copper electrodeposition. *J. Electrochem. Soc.* **155**, D538-D541, (2008).
- 91 Wittstock, G. *et al.* Scanning electrochemical microscopy for direct imaging of reaction rates. *Angew. Chem. Int. Ed.* **46**, 1584-1617, (2007).
- 92 Wittstock, G. *et al.* Patterned Self-Assembled Alkanethiolate Monolayers on Gold. Patterning and Imaging by Means of Scanning Electrochemical Microscopy. *Electroanalysis* **9**, 746-750, (1997).
- 93 Zhan, D. *et al.* The Kv channel blocker 4-aminopyridine enhances Ag<sup>+</sup> uptake: A scanning electrochemical microscopy study of single living cells. *Proc. Natl. Acad. Sci. U. S. A.* **105**, 12118-12122, (2008).
- 94 Zhan, W. & Bard, A. J. Scanning electrochemical microscopy. 56. Probing outside and inside single giant liposomes containing Ru(bpy)<sub>3</sub><sup>2+</sup>. *Anal. Chem.* **78**, 726-733, (2006).
- 95 Wilburn, J. P. *et al.* Imaging of voltage-gated alamethicin pores in a reconstituted bilayer lipid membrane via scanning electrochemical microscopy. *Analyst* **131**, 311-316, (2006).



# *The action on SLBs by two lytic $\alpha$ -helical AMPs: melittin and magainin 2*

## 1 Introduction

Melittin and magainin are two of the most intensely investigated AMPs in relation to peptide-lipid interactions, in order to understand their biological function<sup>1</sup>. Melittin and magainin are components of the linear  $\alpha$ -helical AMP group. This group of peptides have less than 40 residues, are cationic and adopt an  $\alpha$ -helical secondary structure in the presence of an anisotropic environment, such the cell membrane<sup>2-4</sup>. Peptides from this group originate from various organisms, which are evolutionary distant. Furthermore, these peptides can be found in different tissues, like the hemolymph of insects, gastric mucosa, intestinal epithelia and in the amphibian skin secretion<sup>3</sup>.

### 1.1 Magainins

Magainins are part of the big group of peptides from amphibians, which also includes dermaseptin, temporin, caerin, aurein and uperin peptides<sup>5</sup>. Magainins (derived from the Hebrew word "magain", which means "shield") are cationic 23-residues  $\alpha$ -helical peptides that have been isolated from the skin and intestine of the African clawed frog *Xenopus laevis*<sup>6,7</sup>. Other AMPs that have been isolated from this frog are the peptides named xenopus, which are 20-25 amino acid residues long, and 27-residues long peptides named CPFs<sup>3</sup>.

Magainin 1 (GIGKFLHSAGKFGKAFVGEIMKS), and magainin 2 (GIGKFLHSAKKFGKAFVGEIMNS) form the group of magainins<sup>7,8</sup>. These peptides are amphipathic and positively charged at neutral pH<sup>7</sup>. Magainins are lethal towards bacteria (both Gram-positive and Gram-negative), some fungi and protozoa microorganisms at a concentration range of 2-50  $\mu$ M<sup>7</sup>. However, at these concentrations magainins are not toxic towards mammalian cells since they showed haemolysis in 50% of human erythrocytes only at a concentration

above 1000  $\mu\text{M}$ <sup>9</sup>. Magainin 2 and its analogues do offer therapeutic benefits with some anticancer activity towards ovarian cancer cells<sup>10</sup>.

## 1.2 Melittin

Melittin is a haemolytic peptide and is the major component of the venom of the European honeybee *Apis mellifera*, contributing up to 50% of the poison's dry weight<sup>4,7,11</sup>. Melittin is a linear peptide composed of 26 amino acid residues (GIGAVLKVLTTGLPALISWIKRKRQQ-NH<sub>2</sub>). The first 20 residues are mainly hydrophobic, whereas the residues at the C-terminal region are hydrophilic<sup>12,13</sup>. Indeed, this peptide is cationic with 6 positive residues and four of these are located at the C-terminus<sup>14</sup>.

Melittin has antimicrobial, antifungal and anticancer action, being cytotoxic towards prokaryotic and eukaryotic cells, in a non specific manner<sup>12</sup>. Melittin does not only target the plasma membrane in a non-specific manner, but also acts specifically by inhibiting the activity of various ATPase pumps located in the membrane, such the sodium potassium pump (Na<sup>+</sup> K<sup>+</sup> -ATPase) and suppressing the viral gene expression of HIV-1<sup>12</sup>.

## 1.3 Sequence of $\alpha$ -helical AMPs

The sequences of amphipathic  $\alpha$ -helical AMPs are very variable. However, from the work of Tossi et al., which compared more than 150 peptides, these peptides can be fitted into distinct groups on the basis of homologies in the sequences<sup>3</sup>. Examples of these groups are: the cecropins (33 peptides), the melittins (4 peptides), the magainins (2 peptides), and the caerins (26 peptides)<sup>3</sup>.

Moreover, Tossi scrutinized the first 20 residues from the N-terminal domain of each sequence of  $\alpha$ -helical peptide and found some interesting features. Notably, most of these peptides have a glycine residue in position 1 (see melittin and magainin sequences). This was explained by the ability of glycine to act as a capping residue<sup>3,15</sup>, and by the resistance acquired so against the aminopeptidases<sup>3</sup>. Glycine is also often present in position 14 thus inducing

a kink in the middle of the sequence similar to proline<sup>16</sup>. A further common characteristic found in various peptides was the C-terminal amidation, which confers stability towards degradation by carboxypeptidases<sup>3</sup>.

Native  $\alpha$ -helical AMPs have variable hydrophobicity, and their total charge spans the range between 0 and +16. However, most have a positive charge between 4 to 6. In cases where the net positive charges are below 4, the potency of the peptide is strongly affected by the net charge, whereas above 6 positive charges, the peptide activity could be affected by the establishment of intra and intermolecular repulsions, which prevent the adoption of the helical conformation<sup>3,4</sup>.

### ***1.3.1 Hydrophobicity in magainin and melittin***

Magainins have their positive charges distributed along the whole peptide chain (+4 at physiological pH). Thus, they do not have defined hydrophobic and hydrophilic domains in their sequence. As a consequence, magainins interact preferential with negatively charged membranes and lack in haemolytic activity<sup>17</sup>.

In contrast, melittin has a net charge of + 6 at physiological pH with four cationic residues concentrated at the C-terminus. Thus, the melittin sequence is characterized by a very hydrophobic N-terminus and an extremely polar, charged C-terminus. These distinct domains within the melittin sequence promotes the interactions with both neutral membranes, through strong hydrophobic interactions, and also with negatively charged lipid bilayers, through predominantly ionic interactions<sup>4</sup>. Interestingly, only a few studies demonstrate the importance of the C-terminus when melittin interacts with both zwitterionic and anionic membranes<sup>18,19</sup>.

## **1.4 Peptide conformation in lipid bilayers**

The structure of the linear  $\alpha$ -helical AMPs in aqueous and non-aqueous solvent has been extensively characterized using CD or and NMR spectroscopies<sup>4,5,20</sup>. The  $\alpha$ -helix has a periodicity of three to four residues per turn, with the polar side chains aligned along one side and the hydrophobic

residues aligned along the opposite side of the helical core<sup>4</sup>. This structure is amphiphilic and thus optimal for interaction with amphipathic membranes and for the folding of monomeric  $\alpha$ -helices<sup>21,22</sup>.

Many factors play a determining role in stabilising these helical structures, such as the presence of stabilising residues (i.e. leucine, alanine, lysine), the scarcity of proline, and the C-terminal amidation, which provides an extra hydrogen bond to stabilise the secondary structure<sup>3,22</sup>. Furthermore, the formation of the helix is supported in the membrane by the establishment of hydrogen bonds, even for relatively short peptides. Establishment of these intramolecular hydrogen bonds facilitates peptide insertion into the membrane by decreasing the “energetic cost” required<sup>3,23</sup>.

In solution the AMPs are unstructured. However, in contact with biomembranes, these peptides rapidly adopt a helical structure, in a period of 10-5 sec<sup>23</sup>. Thus, upon adoption of the  $\alpha$ -helical conformation the peptide orients itself lying parallel to the membrane plane with the charged side facing outward, towards the lipid head groups, and the hydrophobic side embedded into the acyl tail core<sup>16</sup>. This disposition allows the peptide to be soluble in water and, at the same time, to be immersed into the membrane<sup>3</sup>.

### ***1.4.1 Conformation in membrane of magainin and melittin***

Investigations using CD, solid-state NMR, Raman and Fourier transform infrared techniques show that magainin is unstructured in aqueous solutions, at neutral pH, while an  $\alpha$ -helical conformation, as shown in Fig.17A, is adopted upon binding with the acidic phospholipid bilayer<sup>8,24,25</sup>. This  $\alpha$ -helix is amphipathic, as shown in Fig.17B, with almost equal hydrophilic and hydrophobic regions, which facilitates orientation of the peptide parallel to the membrane bilayer<sup>24</sup>.

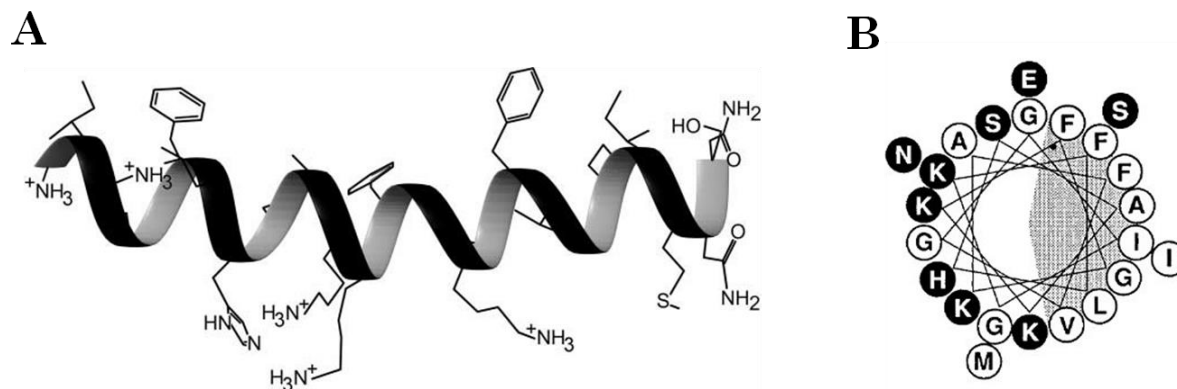


**Fig. 17:** On the left side (A), the structure of magainin 2 determined by 2D NMR study in micelles<sup>5</sup>. On the right side (B), the helical wheel representation of magainin 2 where the residues in the black circles are hydrophilic and the residues in the white circles are hydrophobic. The shade area in the wheel indicates the hydrophobic surface of the  $\alpha$ -helix<sup>8</sup>.

Melittin, like magainin, is unstructured in aqueous solution and when it is at low concentrations. As shown in Fig. 18, it adopts an  $\alpha$ -helical conformation in methanol, in contact with lipid micelles or at high peptide concentrations<sup>26,27</sup>. This  $\alpha$ -helix has a hinge in the middle due to the proline residue at position 14. The hinge divides the  $\alpha$ -helix into two amphipathic helical regions and is responsible for the insertion of the peptide into the bilayer in a pseudo-transmembrane manner<sup>12,14,28</sup>, which results in a more effective interaction with the membrane than magainin<sup>6</sup>. The presence of a kink in the middle of an AMP sequence is not particular to melittin, as other helical AMPs have similar features such as caerin1.1, which has a proline at position 15, and buforin II, which has a proline at position 11<sup>29</sup>. Moreover, it seems that these peptides are less cytotoxic than those that form a single  $\alpha$ -helical structure<sup>6</sup>.

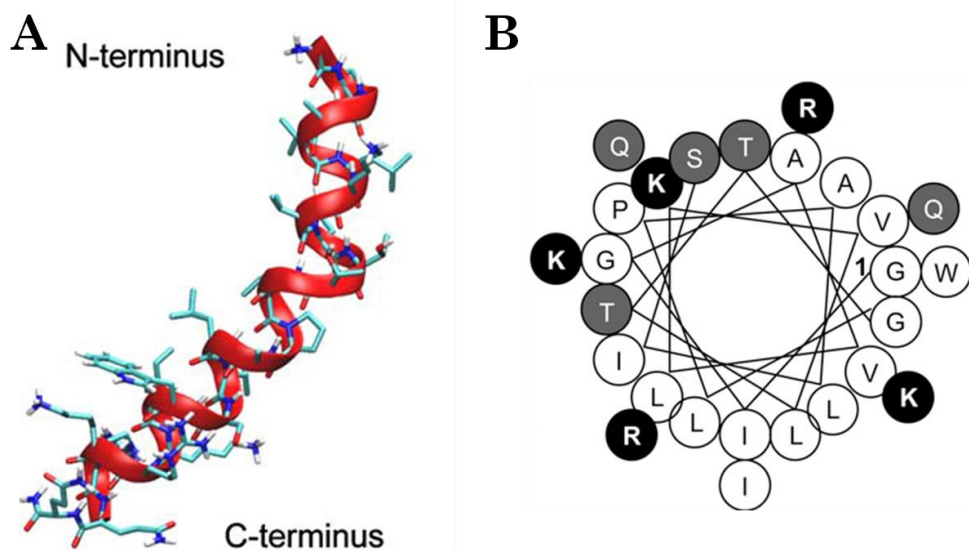


**Fig. 18:** On the left side (A), the single crystal structure of melittin<sup>30-32</sup>. On the right side (B), the helical wheel representation projection for melittin. The beginning of the helix is marked with 1. Cationic residues are in black, the hydrophobic residues are in white and the polar residues are grey<sup>3333</sup>.

#### 1.4.1.1 The aggregation of helical peptides

Some amphipatic AMPs aggregate and form fibrils, especially in contact with negatively charged lipids: examples are the amphibian peptides temporin B and L<sup>34,35</sup>, the dermaseptins S9 and PD-3-7<sup>34,36</sup>, magainin-2 and melittin<sup>35,37</sup>. Indeed, the accumulation of peptide monomers on the membrane is enhanced by electrostatic interactions with negatively charged lipids<sup>12,23,36</sup>. This leads to a local concentration of the peptide greater than the bulk concentration, by up to two orders of magnitude<sup>38</sup>. This clustering of the peptides monomers facilitates reaching a threshold concentration needed for formation of aggregates/fibrils<sup>23,36</sup>. In fact, Trp-substituted magainins have shown to aggregate at a P/L molar ratio above 0.02 with negatively charged membranes<sup>24</sup>, while melittin aggregated at P/L above 1:100 molar ratio in the presence of fluid phase membranes in solutions with low ionic strength<sup>11</sup>. The formation of aggregates seems to be a prerequisite for pore formation by these peptides, with the oligomerization phase being the rate-limiting step<sup>12,23,35,36,39</sup>. However, it has been pointed out that peptide aggregation occurs only after the

insertion of the peptide monomers into the membrane since the insertion of pre-existing aggregates is a process thermodynamically unfavourable<sup>23,40</sup>.

Magainin and melittin can aggregate also in aqueous solutions<sup>11,12</sup>. Magainin, which is monomeric up to high concentrations (10 mM) at neutral pH, aggregates at low pH or at high NaCl concentration (500 mM) and can form filaments with a diameter of 13 nm<sup>24</sup>. Melittin aggregates at high peptide concentration with neutral pH or at low pH and/or high salt concentration in the solution<sup>41</sup>. The melittin aggregates are tetramers that consist of four almost identical monomers in the conformation of a slightly bent  $\alpha$ -helix<sup>12,42</sup>.

## 1.5 Mechanisms of $\alpha$ -helical AMP action

The  $\alpha$ -helical AMPs are active against a wide range of pathogens, including Gram-positive and Gram-negative bacteria, viruses, fungi and protozoa<sup>3,5,43</sup>. The action of these peptides is mainly towards the cell membrane, without any membrane receptor mediation, since both the D and L diastereomers of the same peptide showed no differences in their actions<sup>8,44</sup>.

Initially, two mechanisms were suggested for the action of  $\alpha$ -helical peptides towards the plasma membrane: the barrel stave, and the carpet model<sup>2</sup>. However, a third lytic mechanism, initially called wormhole by Ludtke and toroidal pore by Matsuzaki, was suggested following experiments conducted by Matsuzaki and by Ludtke, who investigated independently the interactions of magainin with biomimetic membranes using dye leakage<sup>17,45,46</sup>, oriented CD (OCD)<sup>25,43</sup> and neutron scattering techniques<sup>14</sup>.

However, as previously mentioned in the first chapter, the toroidal pore could also be interpreted as a transient stage of the carpet mechanism, as illustrated by the Shai-Matsuzaki-Huang model (Fig. 19)<sup>1,8,47-49</sup>. In this model the membrane is initially covered as a carpet by a layer of electrostatically attracted monomers of peptide (**a**). As the peptides accumulate and are incorporated into the membrane, the outer leaflet of the bilayer expands relative to the inner leaflet, which results in a strain within the bilayer (indicated by the broad grey arrows in Fig. 19b). The bilayer adopts a positive

curvature, and at the same time, becomes thinner and weaker due to the spreading of lipids molecules by peptides (b). This tension is relieved by a phase transition in which peptides, along with associated lipids, breaks down in transient pores or “wormhole” lesions (c), which facilitate the translocation of lipids and AMPs to the inner leaflet (d). At this point, the membrane may break down into micelles consisting of membrane-peptides complexes (f) or it retains its integrity since the peptides reach intracellular targets (e).

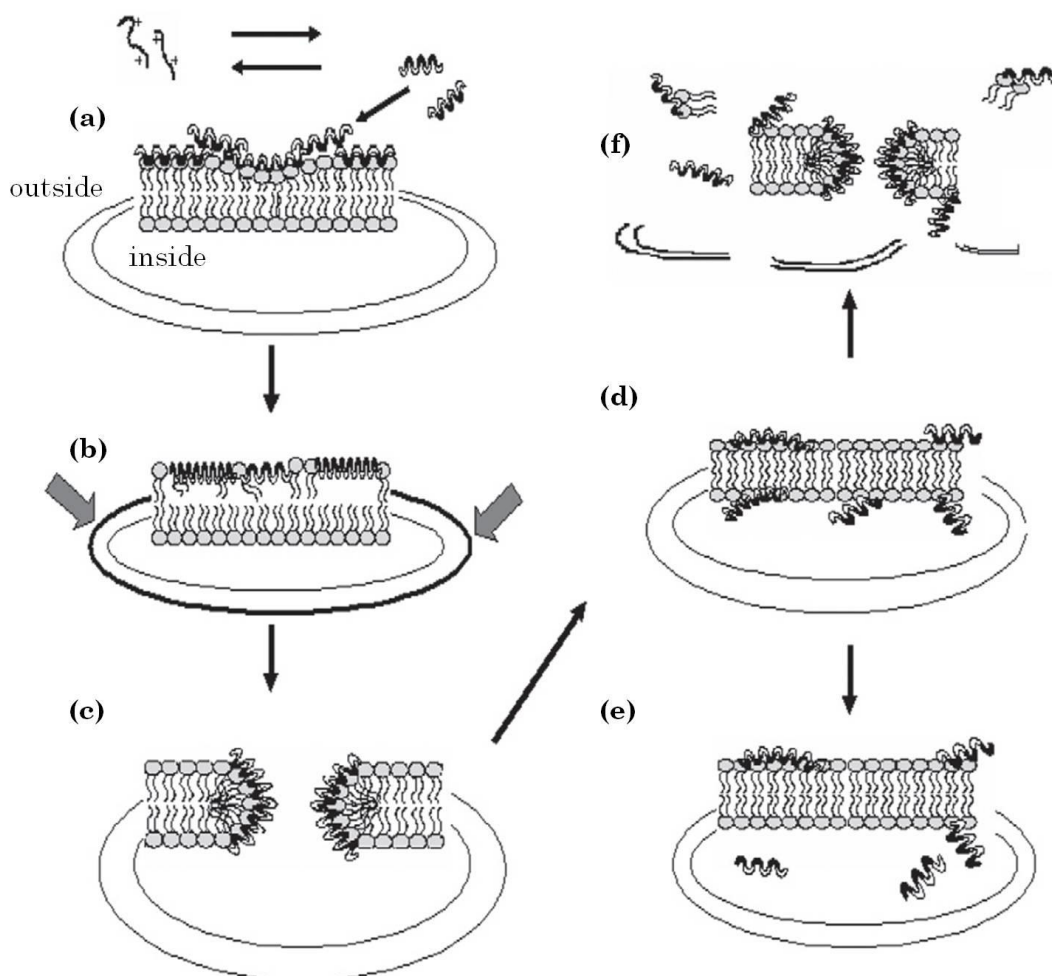


**Fig. 19:** The Shai-Matsuzaki-Huang model of the mechanism of action of a  $\alpha$ -helical peptide. Each step is described in the text<sup>49</sup>.

### 1.5.1 The toroidal pore formation hypothesis for magainin

Magainin has been extensively studied to define and characterize pore formation in the membrane<sup>17,25,40,43,45</sup>. Early studies explained the cytolytic action of magainins as a result of instituting unstable and discrete “ion channels” formed by oligomers of magainin. These channels were prevalently

cationic, selective and permeable to species of low molecular weight such sucrose (MW 342), 5(6)-carboxyfluorescein (MW 376) and calcein (MW 623)<sup>17,43</sup>. Later studies introduced the peptide to lipid molar ratio threshold ( $P/L^*$ ) concept in order to explain the entire process of channel formation<sup>43</sup>. If under this  $P/L^*$  value, most of the magainin peptide would be localized laying parallel to the membrane surface in an  $\alpha$ -helical conformation<sup>25,43</sup>. That is, only a few “ion channels” would originate occasionally, due to thermal fluctuations at the membrane, which permit casual and transient insertion of these peptides. This parallel orientation has been demonstrated by OCD spectroscopy<sup>25,43</sup> and solid-state NMR spectroscopy<sup>50</sup>. However, the binding of magainin peptides parallel to the membrane surface causes a lateral expansion of the membrane, which results in a thinning of the bilayer. Therefore, decrease of the bilayer thickness is proportional to the  $P/L$  value<sup>25</sup>. Once this  $P/L$  reaches a threshold  $P/L^*$ , which is highly peptide and lipid (phase and composition) dependent (e.g.  $\sim 1/30$  for DMPC/DMPG membranes<sup>43</sup>), the majority of peptide molecules change their orientation with respect to the membrane surface from parallel to orthogonal, inserting thus into the membrane. As a consequence, the number of “ionic channels” increases, which leads to rupture of the membrane<sup>43</sup>.

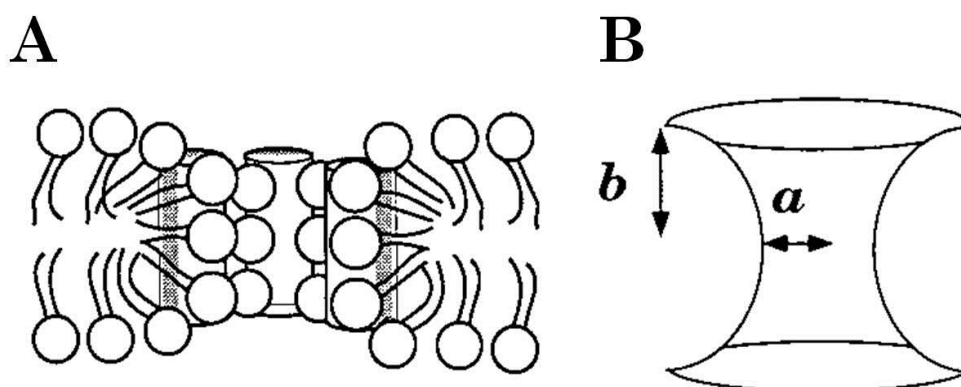


**Fig. 20:** One of the first representations of the model for the magainin-lipid supramolecular complex pore, named later a toroidal pore. **(A)** The helical peptide molecules (cylinders) are intercalated between the lipid head-groups (spheres). Shaded and open zones correspond to hydrophobic and hydrophilic regions, respectively. **(B)** The toroidal pore is characterized by two curvatures, which can be described by the radius of the narrowest part of the pore,  $a$ , and the lipid monolayer thickness,  $b$ <sup>17</sup>.

This hypothesis of “ion channel” formation in the membrane was the result of studies with OCD and neutron in-plane scattering, and was further confirmed by using fluorescent lipids: magainin 2 was able to accelerate the “flip-flop” of these lipids in the membrane<sup>45</sup>. From all these observations, these “ion channels” resembled a supermolecular peptide-lipid pore (Fig. 20), which consisted of 4-7 peptide helices intercalated with the polar head-group of the membrane-lipids. The pore-lining lipids comprise the outer and inner leaflets of the membrane a continuum where not only ions pass but also lipids through a lateral diffusion along the wall of the pore<sup>17,45</sup>. This super-molecular complex was named “toroidal pore” or wormhole by Ludtke et al.<sup>25</sup>. However, the formation of “toroidal pores” is a transient process observable mainly during the early stage of the peptide insertion into the membrane, where magainin peptides translocate into the inner monolayer of the bilayer<sup>17,24</sup>.

### 1.5.1.1 *The two-state model*

Outcomes from investigations with magainin, described above, gave a fundamental contribution in the formulation of the “two-state model” by Huang<sup>40</sup>. This model distinguishes the process of insertion and pore formation of  $\alpha$ -helical (and  $\beta$ -sheets) AMPs in two states: a surface adsorption state, abbreviated as “S”, and a multiple-pore state, abbreviated as “I”<sup>51,52</sup>. In the “S” state, most of the helical peptides are aligned parallel to the membrane surface since the P/L value is under the threshold value P/L\* required for pore formation. The “I” state is characterized by P/L being above the P/L\*. Thereby, the majority of the peptides change their orientation from parallel to orthogonal with respect to the membrane surface thus forming trans-membrane pores. This P/L\* threshold, as seen for magainin, is highly peptide and membrane composition dependent<sup>40,43,51</sup>.

The parallel orientation during the “S” state has been verified independently also by other studies that used solid-state NMR<sup>53</sup> or fluorescence spectroscopy<sup>45</sup>. Both these techniques demonstrated that peptides such as magainin, at low concentration, are parallel to the membrane surface, embedded between the head groups and the acyl chains of the lipids. This

embedding introduces a tension in the membrane, which cause area stretching and membrane thinning<sup>52</sup>, as shown by X-ray diffraction<sup>40,51</sup>. This tension increases with increase of the P/L until reaching a  $P/L^*$  where the peptides form trans-membrane pores in order to reduce the internal membrane tension<sup>51</sup>. These pores are variable in term of size and structure but in general, they are not over 2 nm in diameter<sup>40</sup> (e.g. magainin forms pore having a diameter of 1.8 nm)<sup>25</sup>. However, the formation of few transient pores can occur also at P/L lower, at the “S” state<sup>54,55</sup>.

The “two-state” model can be considered as the initial steps of the more generic Shai-Matsuzaki-Huang model. Indeed, the “S” state is represented in the steps (a) and (b) in Fig. 3, while the “T” state corresponds to the step (c) in Fig. 19. Furthermore, the “T” phase can be seen in the Fig. 19f as the prelude of membrane lysis, which can occur if at peptide concentrations above the threshold  $P/L^*$ <sup>52,56</sup>.

#### *1.5.1.2 Comparison from the two-state model*

The two-state model predicts that stable toroidal pores are created by peptides that change their orientation from parallel to orthogonal to the membrane surfaces. However, leakage studies using magainin 2 with GUVs done by Tamba et al.<sup>57</sup> showed that the presence of peptides induce the formation of transient trans-membrane pores, which consists only of lipids.

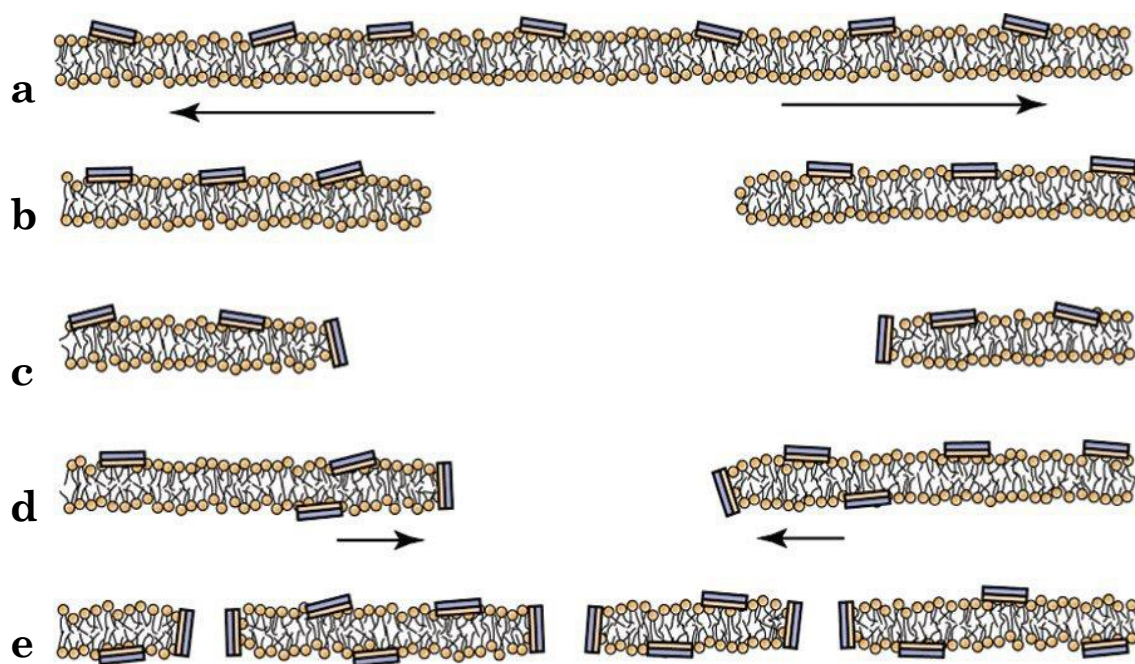


**Fig. 21:** Mechanism of magainin 2 induced pore formation in lipid membranes hypothesized by Tamba et al<sup>57</sup>. In step a, the arrows highlight the external tension induced in the outer monolayer by the peptide adsorption. While in step d, the arrows indicate the decreasing of the radius of the pore.

Indeed, as illustrated in Fig. 21, the adsorption of peptides in a parallel orientation at the membrane interface creates a membrane tension (step **a**). Consequently, the rise of this tension by the continual addition of peptide stretches the membrane until a pore forms in the membrane stochastically (step **b**). However, what differentiates this mechanism from the model described previously is that this pore is formed only by lipids (as illustrated in the step **b**). Moreover, the size of this dynamic pore keeps increasing over the time, reaching a radius of  $5 \pm 1 \mu\text{M}$ , until the tension of the external layer is the same as that of the internal monolayer (step **c**). Finally, the peptide monomers start then to translocate to the other side of the membrane through the rim of the pore (step **d**). Consequently with this peptide translocation, the area of internal monolayer of the membrane increases, which induces a decrease in the pore radius. Furthermore, the rearrangement of magainin peptides in the rim of this pore can cause a membrane rearrangement resulting in the formation of several smaller stable pores (step **e**)<sup>57</sup>.

### 1.5.2 Structural variations: the disordered toroidal pore

The toroidal pore formed by magainin and other peptides consists of 4-7 monomers, which are intercalated in an orthogonal manner between the lipid molecules, forming a rim with an internal diameter of *circa* 1.8 nm<sup>2</sup>, as shown in Fig. 22. However, molecular dynamics simulations, which have been done with magainin (MG-H2) and melittin interacting with neutral phospholipids, illustrated that these two peptides form pores that are structurally different from the classical toroidal organization<sup>39,58</sup>. These pores were renamed disordered toroidal pores (see Fig. 22)<sup>58</sup>. The name itself suggests that the pore structure has a low structural organization, is not perfectly cylindrical, with an internal diameter of *circa* 1.5 nm, and with an opening almost twice as large as the centre (0.5-1 nm wider). This pore is formed almost entirely by lipid molecules and only one or two peptides contribute to the pore. The remaining peptides lie nearly parallel to the membrane, at the rim of the pore stabilizing its curvature<sup>58</sup>.

While the concentration threshold, the initial electrostatic interactions and the thinning of the membrane are conditions contemplated in both the “classical” and disordered toroidal model, in the latter model a further condition is required: peptide aggregation. This aggregation could happen prior to or after the peptide binding at the membrane. On the other hand, the disordered toroidal model does not consider the helical conformation and the perpendicular orientation as requirements to have a trans-membrane pore<sup>39</sup>.

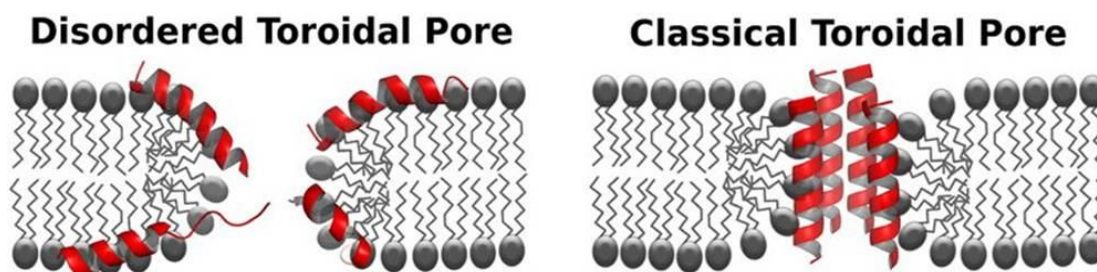


**Fig. 22:** A graphic comparison between the disordered and classical toroidal pore. In the disordered model, a well-defined peptide orientation is absent, while the classical model entails an orthogonal orientation<sup>39</sup>.

### 1.5.3 Melittin: from barrel stave to toroidal pore

Melittin demonstrates some variation in its interaction with a membrane; both micellisation or detergent-like mechanisms<sup>28,59,60</sup> and pore formation have been proposed<sup>2,14</sup>. This duality in the action of melittin is shown to be dependent on the nature of the lipids<sup>12,28,59</sup>. In the presence of zwitterionic lipids, such as POPC and DOPC, melittin permeabilises the membrane through pore formation. The addition of anionic lipids in the lipid bilayer seems to cause a change in the mechanism from pore formation to detergent-like<sup>28,59</sup>. However, this distinction between two mechanisms as a function of the lipid seems not to be valid anymore since Lee et al. proposed the pore formation as a phase transition, which can lead to membrane disruption if the P/L is above than the P/L\* value.

Melittin appears to form stable pores after a threshold P/L\* is reached, which lies in the micromolar range. Each pore, which consists of four to seven peptide monomers, has an inner diameter that varies between 1 and 6 nm<sup>14,61</sup>. The mechanism of pore formation by melittin was initially suggested to be a barrel-stave<sup>2,3,62</sup>. This was based on an increase in the permeability of anions in a planar lipid membrane when a trans-negative membrane potential was applied to melittin treated samples<sup>63</sup>. However, recent studies with OCD and neutron scattering<sup>14</sup> demonstrated that the pores formed by melittin had a similar size to the pores formed by magainin and that they crystallized in the same manner as magainin pores. Thus, the toroidal pore was also considered a likely model for the melittin peptide<sup>14</sup>.

The formation of melittin pores presumes the change of melittin orientation from parallel to orthogonal with respect to the plane of the membrane bilayer<sup>14,40,55</sup>. However, recent MD simulations on the interaction of melittin with membranes demonstrated that melittin pores consist predominantly of peptides that are in a pseudo-transmembrane orientation or in a bent conformation with both the N- and C-terminus of the melittin sequence anchored to the same leaflet of the bilayer, like a “U” shape<sup>12,14,28,64</sup>. The

adoption of this “U” conformation is responsible for the disordered toroidal structure<sup>39,64</sup>.

Furthermore, the change in orientation has been put in discussion also by van den Bogaart’s work<sup>65</sup>. From results of dye leakage, van den Bogaart suggested that melittin could either lie parallel or insert perpendicular on membranes constituted by zwitterionic phospholipids. Therefore, the transition from parallel to perpendicular orientation does not happen, but the parallel orientation of melittin on the membrane reduces available space for other melittin molecules to insert directly. Basically, this model predicts that two competing processes, inhibition or formation of pores, happen on the membrane at the same time<sup>65</sup>.

### 1.6 The role of the membrane in pore formation

The ability of amphipathic peptides to penetrate the membrane through pore formation and/or disrupt the membrane is mainly a function of the P/L ratio rather than the absolute peptide concentration at the membrane. The P/L\* for each peptide is dependent on several variables such the lipid type, the temperature, the salt in the solution and the level of hydration of the bilayer<sup>12,40,59,66</sup>. For instance, pores formed by magainin required a higher P/L when PS was included in the lipid mixture used to create a membrane<sup>17</sup>.

Therefore, the membrane composition has a fundamental role in assessing the peptide-membrane structure such pore formation and also pore size<sup>42</sup>. Indeed, the lipid composition regulates the local physicochemical properties of the membrane, such as surface charge, fluidity, and curvature strains<sup>17</sup>. The charges on the membrane surface are crucial for the initial adsorption of peptides molecules at the membrane and for determining the cell selectivity. For instance, some AMPs, e.g. cecropins, magainins and dermaseptins show a low affinity for zwitterionic phospholipids because of their low hydrophobicity<sup>2,17</sup>.

Specifically, for magainins the lipid composition of a membrane is an important modulating factor in the mode of action. In fact magainins have been

show to interact electrostatically and to permeabilise preferentially membranes containing negatively charged lipids, such as PG, PA and PS. Among these phospholipids, PG showed the highest susceptibility to magainin-induced pore formation<sup>17</sup>. This preference could be because magainin peptides, when embedded between the head-groups of the lipid, impose a positive curvature strain to bilayers containing PG lipids, which results in the formation of stable toroidal pores<sup>17</sup>.

Melittin has a good affinity towards neutral membranes<sup>4,67,68</sup>. Indeed, it forms toroidal pores by imposing a positive curvature strain to membranes containing zwitterionic phospholipids. However, in membranes composed of negatively charged lipids, the formation of pores by melittin does not always happen despite the affinity of melittin for anionic membranes being 100-fold greater than that of zwitterionic lipids<sup>18,38,67</sup>. This inability could be due to melittin imposing a negative curvature strain to bilayers containing acidic phospholipids. However, this imposition is not the same for all the acidic phospholipids. For example, melittin has a decreased probability to form toroidal pores with PA than with PG because of the imposition of a bigger negative curvature strain<sup>17</sup>.

The influence of the lipid composition in the membrane curvature, and therefore in the AMPs activity, has been already illustrated in Chapter 2. However, a correlation can be made with the P/L\* value needed for pore formation. Indeed, in the presence of lipid with small head-groups (negative curvature), such as PS and PE, more peptide is required to be absorbed per unit area to achieve the same degree of lateral expansion compared to a monolayer of lipids with larger-volume head groups, such as PG<sup>47</sup>. For instance, the concentrations of melittin or magainin needed for pore formation in lipid vesicles is higher with PE than with LPC<sup>51</sup>.

In addition, the lipid phase influences the membrane action of melittin and magainin. Membranes in gel-phase seem to be less susceptible to magainin than membranes in liquid-phase<sup>69</sup>, and for melittin high concentrations result in micelle formation for zwitterionic membranes in their gel-phase<sup>70</sup>.

The other influencing factor is the saturation of the acyl chains in the lipids. Indeed, the presence of double bonds in the acyl chains of the phospholipids seems to decrease the micellisation propensity of melittin<sup>71</sup>.

## **1.7 The role of cholesterol**

Melittin is considered to be a haemolytic peptide since its binding causes lesions at the erythrocyte membrane, thus inducing leakage of haemoglobin<sup>12</sup>. Conversely, magainins are considered non-toxic towards eukaryotic cells since the concentration required for haemolysis is extremely high, above 1000  $\mu\text{M}$ <sup>9</sup>. However, haemolysis is regulated by the presence of cholesterol in the plasma membrane. A partial depletion of cholesterol (~55 %) from rat erythrocyte plasma membrane increased the haemolytic activity of melittin<sup>12</sup>. However, in general, the presence of cholesterol causes a decrease in the lytic activity of most AMPs<sup>12,70,72</sup>. This reduction of the lytic activity could be because either cholesterol stabilizes the lipid bilayer in a liquid crystalline state, which means a tighter assembly of the acyl chains, or because cholesterol participates in direct interactions with peptides<sup>8,46</sup>.

Studies with model membranes have shown that cholesterol can decrease the association of melittin with model membranes due to its membrane-condensing effect, which preclude a deeper penetration of melittin into the bilayers<sup>12,13</sup>. Indeed a shallow insertion of melittin into the membrane was demonstrated by investigating the depth of penetration of the tryptophan residue of melittin binding to DOPC/cholesterol using the parallax method<sup>73</sup>. Moreover, melittin showed a specific interaction with cholesterol in the membrane by study of resonance energy transfer between the tryptophan residue in melittin and dehydroergosterol, an analogue of cholesterol. This demonstrated a preferential interaction of dehydroergosterol in membrane near the tryptophan residue of membrane-bound melittin<sup>12</sup>. Therefore, the results of this study showed that cholesterol reduces the binding of melittin to the membrane phospholipids<sup>73</sup>.

The lytic action of magainin is also inhibited by the presence of cholesterol in the membrane<sup>8</sup>. It has been suggested that this inhibitory effect could be due to the interactions between the glutamic acid at position 19 of magainin and the OH group of cholesterol. This binding could: (a) interfere with the reorientation of magainin from a parallel to a perpendicular orientation, necessary for pore formation, (b) reduce the penetration of the peptide into cholesterol-containing membranes<sup>74,75</sup>.

## **1.8 Aims**

Magainin and melittin are two of the most characterized AMPs; and their activity has been extensively studied using various biophysical methods. Examples are NMR spectroscopies<sup>44</sup>, cryo-TEM<sup>13</sup>, SPR<sup>28,67</sup>, fluorescence spectroscopy<sup>45</sup>, leakage experiments<sup>45,46,65,76</sup>, EIS<sup>66</sup>, OCD and neutron diffraction<sup>25,47</sup> etc. In addition, molecular simulation studies have been done with these two peptides<sup>39,58,64</sup>. Although these investigations generally agree about the formation of trans-membrane pores by both magainin and melittin peptides, they could not provide mechanistic details of the entire membrane interaction process. For this reason, QCM-D is a valuable device for detecting in real time structural changes to the membrane caused by the peptide action, having a maximum time resolution of *circa* 100 data points per second. Moreover, QCM-D is able to provide details on the interaction of AMPs with various SLBs using well-defined experimental conditions such as temperature, which influence the physical properties of the membrane.

QCM has been employed already to characterize the disruptive action of melittin on different lipid surfaces<sup>60,77-79</sup>, while the behaviour of magainin has not been reported yet. Even so, the experimental conditions and the approaches used presented some differences for melittin; for example the lipid used and the surface of the sensor, with variability in the resulting outcomes. In this case, the interactions between magainin 2 amide or melittin and supported biomimetic membranes were investigated with the purpose to identify possible concentration thresholds towards membranes and to benchmark and reveal

possible similarities among the lytic mechanisms, such as pore formation and detergent action between these two peptides.

## 2 Material and methods

### 2.1 Peptides

Melittin and magainin 2 were synthesised commercially with purity  $\geq 97\%$  (checked by HPLC and MS) by GL Biochem (Shanghai, China), using L-amino acids and standard solid-phase methods. Peptide stock solutions of 500  $\mu\text{M}$  were made by dissolving a certain amount of peptide in ultrapure water and then stored at  $-20\text{ }^\circ\text{C}$ . For the experiments, aliquots of these stock solution were diluted in phosphate-buffered saline (PBS) at the desired concentration.

### 2.2 Buffer preparation

Sodium chloride ( $\geq 99.5\%$ ), potassium phosphate monobasic (anhydrous,  $\geq 99.0\%$ ) and potassium phosphate dibasic (anhydrous,  $\geq 98\%$ ) were purchased from Sigma-Aldrich (Castle Hill, Australia). Ultrapure water was used with an initial resistivity of  $18.2\text{ M}\Omega\cdot\text{cm}$  (Sartorius AG, Göttingen, Germany). Phosphate buffered saline (PBS, pH  $6.9 \pm 0.1$ ) was prepared having 20 mM phosphate and either 100 mM (“high-salt”) or 30 mM (“low-salt”) sodium chloride in water.

### 2.3 Liposome preparation

1,2-Dimyristoyl-sn-glycero-3-phosphocholine (DMPC) and 1,2-dimyristoyl-sn-glycero-3-phospho-rac-(1-glycerol) (sodium salt) (DMPG) were purchased from Avanti Polar Lipids (Alabaster, USA). Cholesterol, chloroform ( $\geq 99.8\%$ ) and methanol ( $\geq 99.9\%$ ) were purchased from Sigma-Aldrich (Castle Hill, Australia). DMPC and cholesterol were dissolved in chloroform and DMPG was dissolved in chloroform/methanol (ca. 3:1) to create individual 5 mM stock solutions. These solutions were then aliquoted into test tubes to obtain the desired lipid composition (DMPC/cholesterol 7:3 v/v, and DMPC/DMPG 4:1 and 2:1 v/v). The solvent was evaporated under a stream of nitrogen and the test tubes were then dried under vacuum. To prepare the liposomes, the lipids were

resuspended in high-salt PBS (100 mM NaCl) to a lipid concentration of 0.5 mM and then incubated at 37 °C, vortexed and briefly sonicated (between 5 and 10 min) in a bath sonicator prior to use.

## **2.4 Modification of QCM-D sensor chips**

Absolute ethanol ( $\geq 99.7\%$ ), propan-2-ol ( $\geq 99.0\%$ ) and hydrogen peroxide (30%) were purchased from Merck (Kilsyth, Australia). Ammonium hydroxide solution (28%) was obtained from Ajax Finechem (Seven Hills, Australia). 3-Mercaptopropionic acid (MPA,  $\geq 99.0\%$ ) was purchased from Fluka, BioChimica (Buchs, Switzerland). The QCM-D sensor crystals used were polished, gold-coated, AT-cut quartz chips with a fundamental frequency of ca. 5 MHz (Q-Sense, Västra Frölunda, Sweden). Immediately before measurements the chips were cleaned in a solution of ammonium hydroxide: hydrogen peroxide: water (1:1:3 v/v) for 20–25 min at ca. 70 °C. The chips were then rinsed thoroughly with water. Surface modification with MPA was conducted by immersing a freshly cleaned chip into a 1 mM solution of MPA in propan-2-ol for at least 1 h. This creates a self-assembled monolayer of negative charge on the chip surface. Excess MPA was removed by rinsing with propan-2-ol. The chips were then dried under a stream of nitrogen and assembled into the QCM-D chambers ready for use.

## **2.5 QCM-D experiments**

QCM-D experiments were performed using the E4 system with flow cells (Q-Sense, Västra Frölunda, Sweden). The QCM-D instrument measures the relative changes to the resonance frequency ( $f$ ) and energy dissipation ( $D$ ) of the chip over the course of the experiment.  $\Delta f$  and  $\Delta D$  were measured simultaneously at the fundamental frequency and the 3rd, 5th, 7th and 9th harmonics. All plots presented in this study will use the 7th harmonic unless otherwise stated. Data for the fundamental frequency is not presented as it is inherently noisy and unreliable. The original data was processed in QTools (Q-Sense) before being exported for further analysis in OriginPro 8 (OriginLab

Corp., Northampton, USA). All experiments were conducted at a temperature of  $19.10 \pm 0.05$  °C and repeated at least three times. In a typical experiment, firstly, a lipid membrane was formed on the chip surface by the introduction of a liposome solution into the QCM-D chamber at a flow rate of 50–100  $\mu\text{L}/\text{min}$ . The liposomes adsorb onto the MPA-monolayer, deform, rupture and fuse together to form a lipid bilayer. Weakly attached liposomes were removed by washing with high-salt PBS (100 mM NaCl) at 300  $\mu\text{L}/\text{min}$  and any embedded liposomes were ruptured by washing with low-salt PBS (30 mM NaCl) at 300  $\mu\text{L}/\text{min}$ . This second washing step was introduced to ensure the formation of a homogeneous membrane and works by creating an osmotic pressure difference between the interior of the embedded liposomes (having a high salt concentration) and the low-salt exterior environment, which causes the liposomes to swell and then burst. Secondly, after a stable baseline was observed, 1 mL of peptide solution was introduced at 50  $\mu\text{L}/\text{min}$ . After the flow was stopped, the peptide was left to incubate with the lipid membrane for 30 min and then the chamber was rinsed with high-salt PBS.

## 3 Results

Melittin and magainin 2 amide peptides were purchased from GL Biochem (Shanghai) Ltd, China, and stored at  $-20^{\circ}\text{C}$ . Stock solutions of these peptides were made by dissolving a certain amount of peptide in ultrapure water and then stored at  $-20^{\circ}\text{C}$ .

QCM-D was used in examining these peptides over a range of four concentrations: 2, 5, 10 and 20  $\mu\text{M}$  for melittin, and 1, 5, 10 and 15  $\mu\text{M}$  for magainin 2 amide. The concentration 1  $\mu\text{M}$  was chosen for magainin because an aim was to see the effect on the membrane of peptides below the concentration threshold; and the experiments with melittin, which were done prior to investigating magainin, showed that 2  $\mu\text{M}$  was already above the concentration threshold. Moreover, from the choice of 1  $\mu\text{M}$  as the lowest concentration for magainin, a serial increase of 5  $\mu\text{M}$  was kept to define the range of four concentrations used in this study.

### *3.1.1 Melittin and magainin 2 on DMPC artificial membranes*

Initially, the interaction of melittin and magainin with DMPC membranes was determined. The data for melittin and magainin are shown in Fig.23 and 24, respectively. They illustrate the plots of  $\Delta f$  versus time and  $\Delta D$  versus time and are typical interactions with a DMPC membrane. Both the peptides showed an immediate decrease in both the frequency and dissipation, that is, that the addition of mass on the lipid membrane deposited on the sensor surface created a firmer layer.

### *3.1.2 Melittin*

At each of the four concentrations tested (2, 5, 10 and 20  $\mu\text{M}$ ), melittin bound initially at the membrane, with a frequency decrease of 11-14 Hz (see Fig.23). This binding was rapid since it was completed in  $\sim 5$  minutes for 5-20  $\mu\text{M}$ , as shown by the first vertical dashed line (Fig 23; *(i)*). Only the lowest (2  $\mu\text{M}$ ) concentration showed a slower binding rate due to the smaller amount of melittin available. After the flow ceased, a slow, yet constant, removal of material mass (0.5-1 Hz) was observed at concentrations of 5 and 20  $\mu\text{M}$ . The

10  $\mu\text{M}$  did not show apparent signs of membrane disruption while the peptide solution was running, but only at the equilibration phase (*ii*) a very small loss of mass was observed. In the final step (phase *iii*), buffer solution was flushed into the chamber to remove any weakly or non-specifically adsorbed material and to verify the strong attachment of the peptide to the membrane. Indeed, this buffer rinse removed some materials since the frequency increased in all four curves (phase *iii* in Fig. 23). However, more than half of the peptide remained attached to the membrane (about 9.5 Hz), with the exception of 20  $\mu\text{M}$  ( $\Delta f$  final  $\sim 3.6$  Hz). The mass removed in the phase *iii* through the buffer rinse could be due to peptide loosely bound or a combination of both peptide/lipids when membrane lysis occurs during phases *i* and/or *ii*. A clear discrimination is not possible in this experiment. However, in the case of peptide where only peptide insertion occurs, we assume that the mass lost effects only the bound peptide since as during the incubation time (phase *ii*) the frequency does not increase (loss in mass). This invariability in frequency is interpreted as the peptide binding to the membrane without destabilize it.

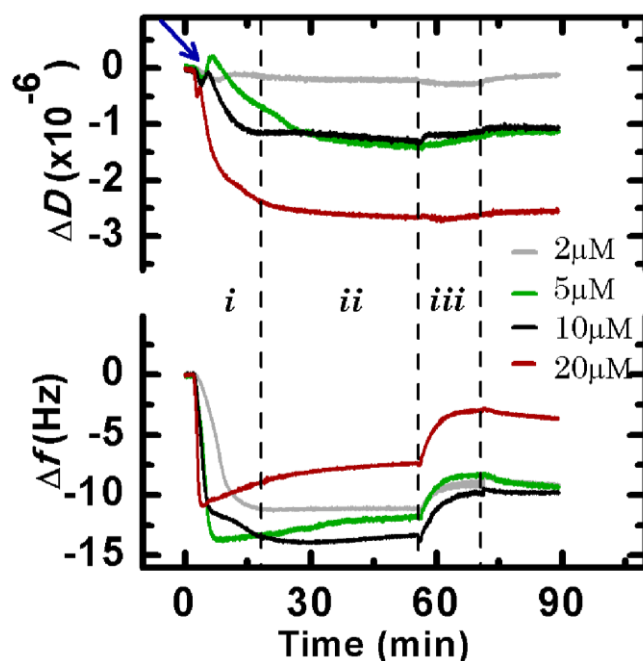


**Fig. 23:** Typical  $\Delta f$  and  $\Delta D$  versus time plots of melittin interacting with supported membranes of DMPC. The dashed lines mark the end of each phase. Phase *i* corresponds to the beginning of peptide action, whereas *ii* denotes the peptide incubation phase. The rinse with PBS solution corresponds to phase *iii*. The harmonic represented is the 7<sup>th</sup>.

The interaction of melittin with the DMPC membrane caused the dissipation to decrease rapidly for most of the concentrations, with the exception of 2  $\mu\text{M}$  (Fig. 23, upper graph). The largest decrease was detected for 20  $\mu\text{M}$  melittin ( $\Delta D$  final  $\sim 2.7 \times 10^{-6}$ ). This change in dissipation implies a structural rearrangement of the membrane with the peptide-membrane system becoming less viscoelastic. This reorganization of the membrane indicates the peptides have inserted into the membrane. Interestingly, the trace for the dissipation showed a particular feature, like a “rebound”: an initial small decrease of the dissipation that indicated an immediate interaction was followed by an increase (emphasized by a blue arrow in Fig. 23) within the first four minutes. Then, finally, the dominant decrease in  $\Delta D$  for 5-20  $\mu\text{M}$  melittin.

### **3.1.3 Magainin 2**

The interaction of magainin 2 with a DMPC membrane is shown in Fig. 24. This interaction was very fast and resulted in mass acquisition for each concentration tested (1, 5, 10 and 15  $\mu\text{M}$ ). This binding was not linearly correlated to the peptide concentration since the major decrease in frequency was observed in the 10  $\mu\text{M}$  trace ( $\sim 8$  Hz), whereas the frequency decrease was  $\sim 7$  Hz for 15  $\mu\text{M}$  and 5  $\mu\text{M}$  as well. The trace corresponding to 1  $\mu\text{M}$  showed instead a decrease of  $\sim 6$  Hz. Thus, the trend indicates similar behaviour with  $\Delta f$  6-8 Hz for 1-20  $\mu\text{M}$  magainin.

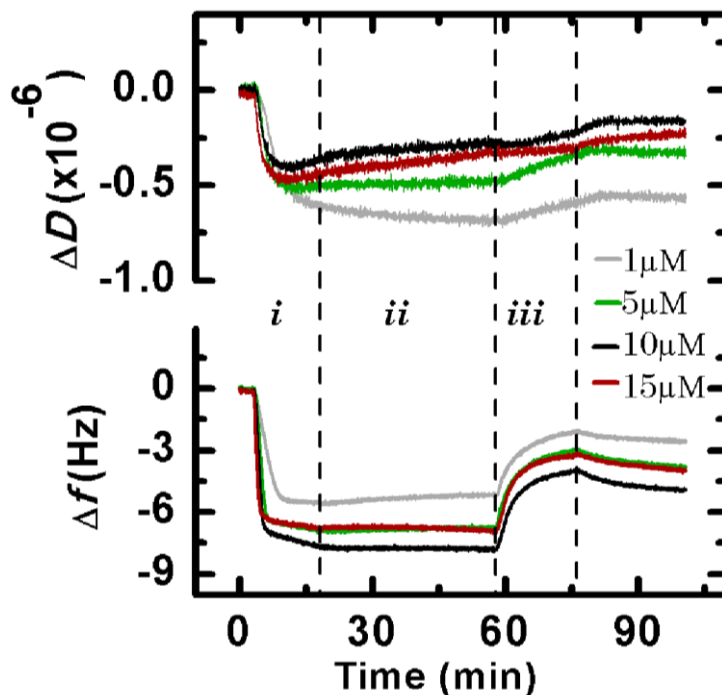


**Fig. 24:** Typical  $\Delta f$  and  $\Delta D$  versus time plots of magainin 2 interacting with supported membranes of DMPC. The 7<sup>th</sup> harmonic is represented. The various phases are described in Fig. 23.

During the equilibration phase (phase *ii*), a slight drift (less than 0.5 Hz) could be observed for 1  $\mu\text{M}$ . However, significant removal of some mass ( $\sim 3$  Hz) occurred during the final wash with PBS (phase *iii*). Thus, at the end of the wash the final  $\Delta f$  was 2.5, 4, 5, and 4 Hz for 1, 5, 10 and 15  $\mu\text{M}$ , respectively.

Magainin caused only a small decrease in the dissipation during its binding (phase *i*). This decrease of 0.3-0.7 ( $\times 10^{-6}$ ) was followed by a very slow (almost a drift) increase during the phases *ii* and/or *iii*. Therefore, the adsorption of magainin on the membrane seemed to have a little effect on the viscoelastic properties of the membrane.

### 3.1.4 A comparison between melittin and magainin 2: the $\Delta f$ - $\Delta D$ plots

The  $\Delta f$ - $t$  and  $\Delta D$ - $t$  data alone illustrate the effect that these peptides have on the DMPC membrane. However, a more detailed analysis of the interaction process could be obtained by plotting the  $\Delta D$  data versus the  $\Delta f$  data (“ $\Delta f$ - $\Delta D$  plots”)<sup>77</sup>, as shown in Fig. 25. Briefly, the visual correlation of these “ $\Delta f$ - $\Delta D$  plots” gives a qualitative and quantitative analysis of how the structure of the membrane-peptide system changes per unit mass addition<sup>78</sup>.

The harmonics 3<sup>rd</sup>, 5<sup>th</sup>, 7<sup>th</sup> and 9<sup>th</sup> harmonics were plotted in this manner for each concentration mainly for two reasons: to visualize any difference in the structural change along the cross-section of the lipid film since each harmonic probes a different depth, and to see if progressive increase in the peptide availability introduces further steps in the mechanistic process. In Fig. 25, the coordinates  $(0,0)$  correspond to the time 0 of Fig. 23 and 24, which is the start of the peptide injection into the QCM chambers. The buffer-rinsing step (phase *iii*, in Fig. 23 and 24) is not included, thus the last point in each trace corresponds to the end of the equilibrium phase.

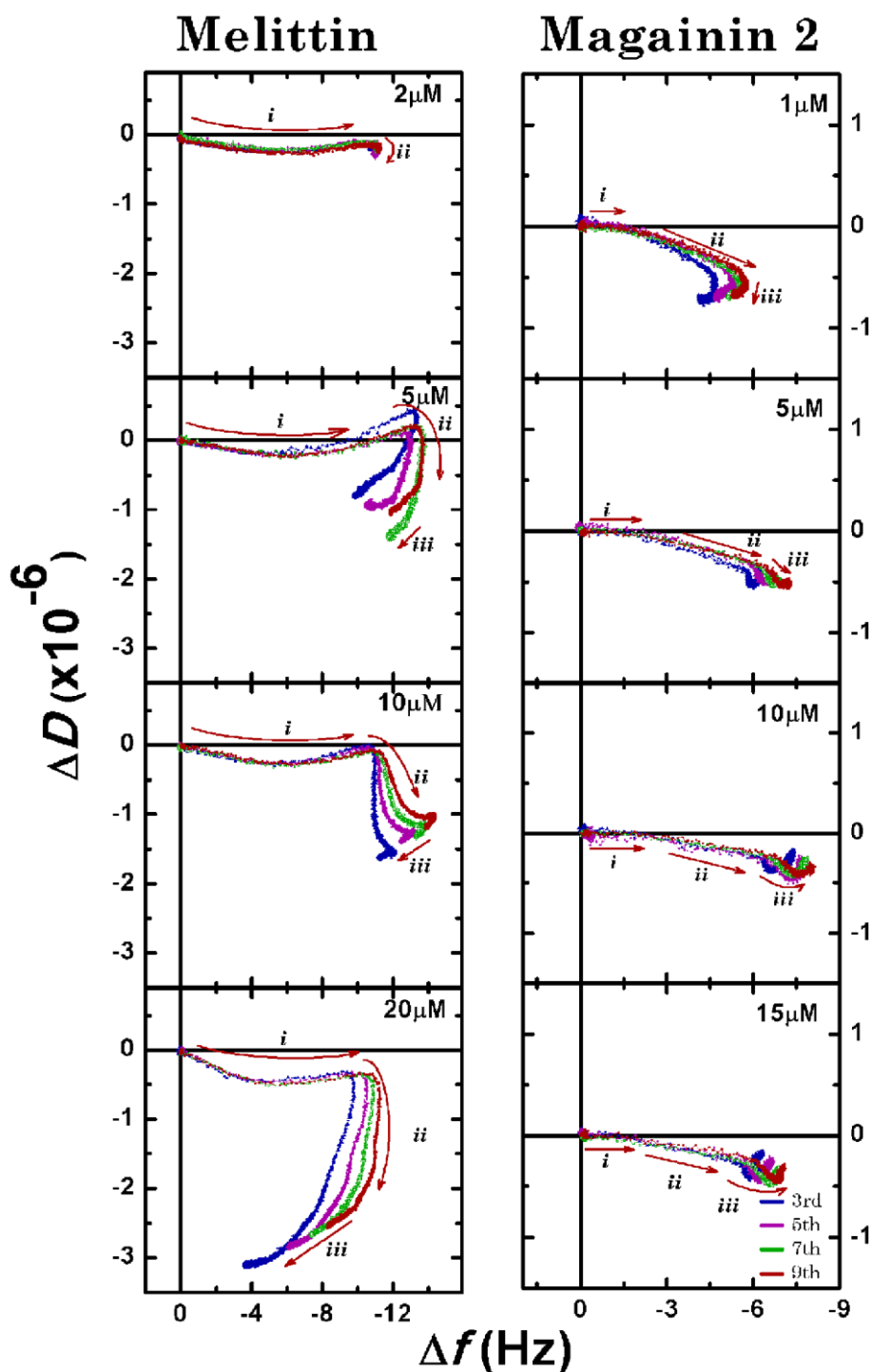


**Fig. 25:** Typical  $\Delta f$ - $\Delta D$  plots illustrating the interaction of melittin (left column) and magainin 2 (right column), at various concentrations, on a DMPC artificial membrane. The response of the 3rd, 5th, 7th, and 9th harmonic is presented.

#### 3.1.4.1 Melittin

From the  $\Delta f$ - $\Delta D$  plots of melittin interacting with DMPC (Fig. 25, left column) it is possible to describe the entire process in three consecutive steps,

consistent with pore formation. Moreover, the vertical alignment of the various panels allows an immediate visual comparison among the concentrations, providing clear identification of the concentration threshold for the mechanism.

The first step of this process is indicated by the arrow **i** and consists of the adsorption of melittin to the membrane. Evidence for melittin insertion into the membrane bilayer results from the analysis at the four harmonics examined (3<sup>rd</sup>, 5<sup>th</sup>, 7<sup>th</sup> and 9<sup>th</sup>) which overlap. In addition, during this first phase (**i**), the dissipation showed little change although a bending decrease (less than  $0.3 \times 10^{-6}$ ) was observed. However, the dissipation returned to  $\sim$ zero. A frequency value of 10 Hz marks a transition from the first (**i**) to the second phase (**ii**). Interestingly, the end of the first phase occurred approximately at the same frequency value in each concentration of melittin.

The second step (indicated by the arrow **ii**), which is more accentuated for the 5  $\mu$ M melittin, is characterized by a definitive decrease of the dissipation and with frequency values approximately unchanged or with a small increase.

Finally, the third and last phase for melittin, which is indicated by the arrow **iii**, occurred during the period of incubation for the 5, 10 and 20  $\mu$ M. This step is characterized by a small increase in frequency while the dissipation remains unchanged.

#### 3.1.4.2 Magainin 2

The  $\Delta f$ - $\Delta D$  plots of magainin 2 interacting with DMPC (Fig. 25, right column) show magainin 2 inserts into the membrane since all the four overtones overlap for each concentration. As observed for melittin, the entire process of binding can be divided in three phases although these differ. The initial adsorption of magainin, which is identified by a red arrow **i**, is characterized by a frequency decrease of *circa* 2 Hz with zero change in dissipation. The second phase (indicated by the arrow **ii**) has a steady decrease in both dissipation and frequency ( $\Delta f$  final 6-7 Hz for the concentrations studied, at the 9<sup>th</sup> harmonic). Interestingly, a slightly higher binding is observed at the 9<sup>th</sup> overtone than the 3<sup>rd</sup>, like what is observed with melittin.

The third phase (*iii*) for 5-15  $\mu\text{M}$  magainin 2 showed only a small decrease in frequency ( $\sim 1.5$  Hz), followed by an increase. Although the change in dissipation was small, the feature was characteristic of magainin and possibly reflected a dynamic organization of magainin in DMPC.

## 3.2 Melittin and magainin 2 on DMPC/DMPG (4:1) SLBs

Membranes composed of DMPC/DMPG (4:1) represent simplified biomimetic bacterial membranes and were used for the experiments with melittin and magainin 2. The action of melittin and magainin towards DMPC/DMPG (4:1) are shown in Fig. 26 and 27. These figures illustrate the plots  $\Delta f$  versus time and  $\Delta D$  versus time and are typical of the interaction with a DMPC/DMPG (4:1) membrane. Both figures show an initial decrease in the frequency and in dissipation as the peptides bind, similar to interactions for DMPC membranes. However, in the case of melittin, this initial binding was immediately followed by mass removal, which is an indication of disruptive action.

### 3.2.1 Melittin

All four concentrations of melittin (2-20  $\mu\text{M}$ ) showed a fast initial binding to the membrane, as seen in Fig. 26, which was immediately followed by a slower removal of mass of likely membrane and peptide composition. In the presence of the negative charged membrane, a concentration threshold for the membrane lysis could not be identified since all four concentrations were capable of disrupting the membrane. The  $\Delta f$  vs time data shows in the first 8 minutes from injection of the peptide solution, the frequency decreased by  $\sim 6$ , 11, 10 and 12 Hz, respectively, for the melittin concentrations of 2, 5, 10 and 20  $\mu\text{M}$ . Then, after approx. 5 minutes from the point of peptide introduction, melittin started to disrupt the membrane, as the traces in Fig. 26 show. This disruptive process starts during phase *i*, i.e. as the injection of sample is still in progress, and continues during phase *ii* (i.e. incubation). Further mass loss was observed in the last step of the experiment (phase *iii*) ( $\Delta f \sim 2$  Hz), as PBS was

flushed into the QCM cell. Only the data corresponding to 2  $\mu\text{M}$  melittin differed from the rest with a slower and late binding and a minor loss of mass with the PBS wash ( $\sim 1$  Hz).

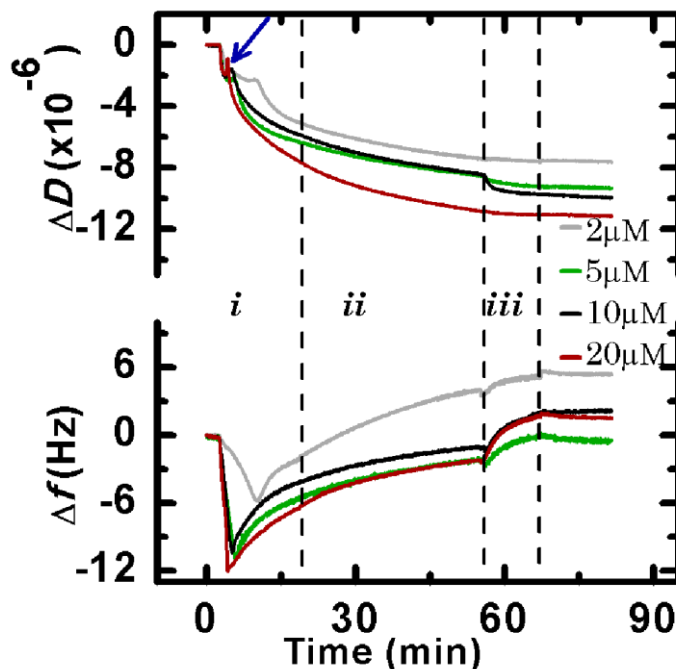


**Fig. 26:** Typical  $\Delta f$  and  $\Delta D$  versus time plots of melittin interacting with supported membranes of DMPC/DMPG (4:1). The dashed lines mark the end of each phase. Phase *i* corresponds to the beginning of peptide action, whereas *ii* denotes the peptide incubation phase. The rinse with PBS solution corresponds to phase *iii*. The 7<sup>th</sup> harmonic is represented.

Immediately, as melittin starts to adsorb at the membrane, the dissipation decreases overall in all four concentrations used here, reaching a plateau only after the final rinse with PBS. Interestingly, as observed with DMPC membranes, dissipation plots showed the “rebound” feature, after  $\sim 3$  minutes from the introduction of the melittin solution. A possible explanation could be that monomers of melittin start to self-assemble in membrane areas and start to insert into the membrane, although this happens at the same time as further melittin binding. Therefore, this initial insertion may destabilize the membrane, which is identified by the increase in dissipation followed by the main trend to a steady decrease in  $\Delta D$ .

### 3.2.2 Magainin 2

The binding of magainin 2 peptide at the DMPC/DMPG (4:1) membrane is similar to the DMPC, as illustrated in Fig. 27. During the incubation time (phase *ii*), the frequency vs time plots were generally featureless, although at 15  $\mu\text{M}$  a tiny increase was observed ( $\Delta f < 1\text{Hz}$ ), while at 1 and 5  $\mu\text{M}$ , frequency drifted towards more negative  $\Delta f$  values. These little changes of the frequency during the incubation time could be the result of rearrangement of an unstable under layer.

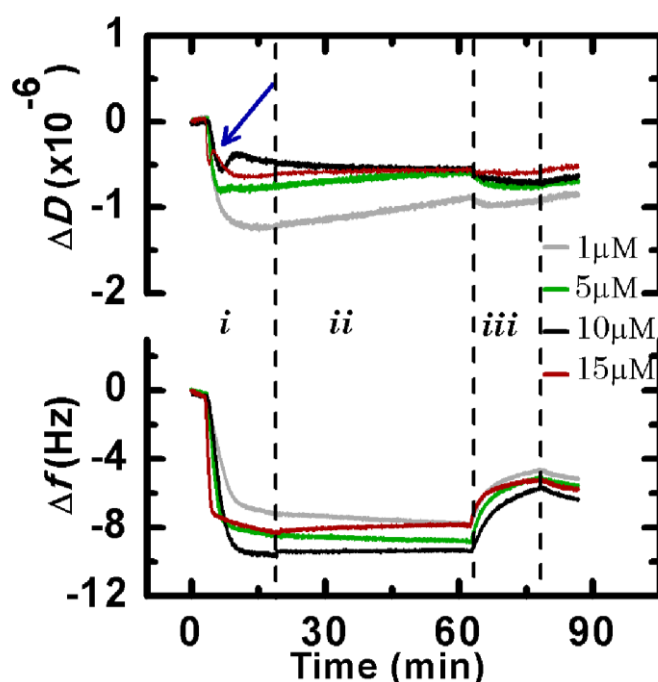


**Fig. 27:** Typical  $\Delta f$  and  $\Delta D$  versus time plots of magainin 2 interacting with supported membranes of DMPC/DMPG (4:1). The 7<sup>th</sup> harmonic is represented. The various phases are described in Fig. 26.

Thus, the resulting peptide uptake before the final wash (at ~60 minutes) was  $\Delta f_{final} \sim 8\text{ Hz}$  for 1 and 15  $\mu\text{M}$ , 9 Hz for 5  $\mu\text{M}$  and ~10 Hz for 10  $\mu\text{M}$ . However, at all the concentrations, with the PBS rinse (phase *iii*) 3-4 Hz of the peptide was washed from the membrane leaving ~5 Hz. This highlighted a stronger interaction of magainin 2 with the membrane compared to melittin.

The dissipation decreased for each concentration during the initial adsorption of magainin at the membrane. This decrease was small and unstable for 1 and 5  $\mu\text{M}$ , with a drifting increase in  $\Delta f$  vs time. Furthermore, the

dissipation curve for the concentrations of 10 and 15  $\mu\text{M}$  magainin showed the small “rebound” feature (indicated by a blue arrow), observed for melittin. Thus, magainin 2 appeared to share with melittin similar mechanistic stages of membrane association, although the variation in dissipation with magainin 2 was much smaller than with melittin.

### 3.2.3 A comparison between melittin and magainin 2: the $\Delta f$ - $\Delta D$ plots

The  $\Delta f$ - $\Delta D$  plots in Fig. 28 illustrate similarities in the interaction of melittin and magainin 2 with a membrane of DMPC/DMPG (4:1). The difference being that the melittin interaction ends with membrane disruption, while for magainin the last step, clearly visible at 15  $\mu\text{M}$ , appears to be the start of a disruptive action.

#### 3.2.3.1 Melittin

The entire interaction of melittin with a DMPC/DMPG (4:1) membrane could be divided in three steps: the first step (red arrow *i*) is almost vertical especially for the frequency probing the deeper layer (the 7<sup>th</sup> and 9<sup>th</sup> harmonic decreases to a max value of  $\sim 5$  Hz) as the dissipation decreased. The corresponding 3<sup>rd</sup> and 5<sup>th</sup> harmonics showed small  $\Delta f$  decrease but all showed  $\Delta D$  decreasing.

The second step (indicated by the arrow *ii*) started at 5-6 Hz approx for the 9<sup>th</sup> harmonic at 2  $\mu\text{M}$  melittin. This phase is characterized by a further insertion of melittin since the frequency keeps decreasing, with the maximum binding recorded at the 9<sup>th</sup> harmonic and with almost constant dissipation. This step was very fast since a change in the dissipation is very hard to detect from the  $\Delta D$ - $t$  plots in Fig. 28. Finally, this second phase ended with a slight increase in dissipation while the frequency was still decreasing. This was also observed on DMPC, i.e. a bow-like shape. In the final stage (arrow *iii*), the melittin action is the removal of mass, which is characterized by a large decrease in dissipation and a simultaneous increase in the frequency. This disruptive action was more obvious at the surface of the bilayers, since the 3<sup>rd</sup> and 5<sup>th</sup> harmonics traces showed a bigger increase in  $\Delta f$ .

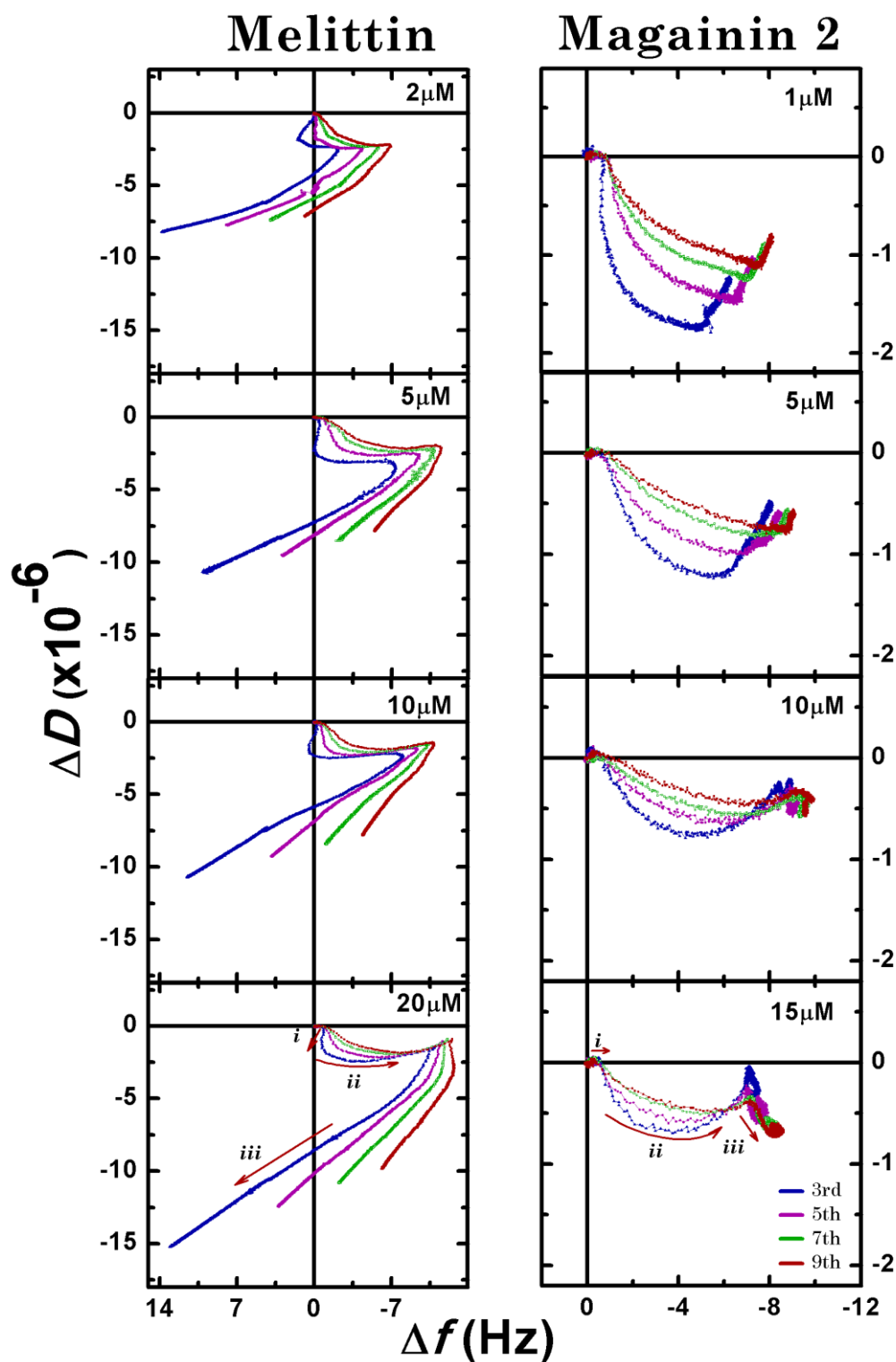


**Fig. 28:** Typical  $\Delta f$ - $\Delta D$  plots for the interaction of various concentrations of melittin (left column) and magainin 2 (right column) on a DMPC/DMPG (4:1) artificial membrane. The response of the 3rd, 5th, 7th, and 9th harmonic is presented. The wash with PBS is not included.

### 3.2.3.2 Magainin 2

The interaction of magainin with DMPC/DMPG (4:1) resembles the first two steps of the interaction of melittin with the same “bow-shaped” feature in the  $\Delta f$  vs  $\Delta D$ . However, at the highest concentration (15  $\mu\text{M}$ ), three steps can be distinguished (*i-iii*). The peptide action initiates with a very small binding ( $\Delta f \sim 1$  Hz) without any change in dissipation (arrow *i*). The second step consisted of a decrease in dissipation and in frequency for all the overtones (arrow *ii*). However, the dissipation decreases more at the lowest magainin concentration (1  $\mu\text{M}$ ) than at the highest concentration (15  $\mu\text{M}$ ). The frequency decreased, more for the 9<sup>th</sup> than for the 3<sup>rd</sup> harmonic, indicating a deep insertion into the membrane like with the DMPC membranes.

Finally, a third phase (arrow *iii*) could be identified for the 10 and 15  $\mu\text{M}$  concentrations. In this phase, the dissipation decreased while the frequency remained almost constant. This decrease could be explained as a transition from the pore state to an initial lysis of the membrane; however, the P/L ratio did not look sufficient for a consistent disruption of the membrane.

## 3.3 Melittin and magainin 2 on DMPC/DMPG (2:1) SLBs

In order to explore the influence of increased negative charges, a PC/PG ratio of 2:1 was used to determine the influence on the peptide action. The major consequence of this increase of negatively charged PG content in the membrane was a stronger lytic mechanism for magainin. Melittin, however was not affected significantly in its mode of action. The entire process will be described in the next section.

### 3.3.1 Melittin

As previous mentioned, melittin showed the identical mode of action already seen with SLBs of DMPC/DMPG (4:1), which resulted with membrane disruption. Indeed, the  $\Delta f$ - $t$  plots in Fig.29 show membrane disruption in all the four traces using DMPC/DMPG (2:1). An immediate binding preceded the disruption. Indeed, this peptide uptake happened in the first 9 minutes from

the time 0 (Fig. 29) and corresponded with a linear decrease of frequency to  $\Delta f_{final}$ : 6 Hz, 8 Hz, 10 Hz and 11 Hz from 2  $\mu\text{M}$  to 20  $\mu\text{M}$ , respectively. This fast binding was immediately followed by a slower increase in frequency, once again like was found in the case of DMPC/DMPG (4:1). This increase in  $\Delta f$  proceeded during the incubation time (phase *ii*), with the exception of 20  $\mu\text{M}$ .

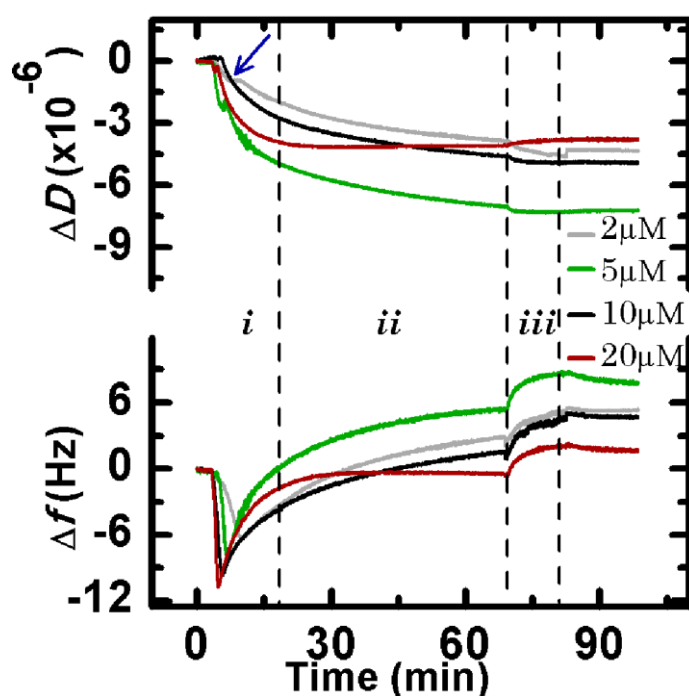


**Fig. 29:** Typical  $\Delta f$  and  $\Delta D$  versus time plots of melittin interacting with supported membranes of DMPC/DMPG (2:1). The dashed lines mark the end of each phase. Phase *i* corresponds to the beginning of peptide action, whereas *ii* denotes the peptide incubation phase. The rinse with PBS solution corresponds to phase *iii*. The 7<sup>th</sup> harmonic is represented here.

Meanwhile, the action of melittin on DMPC/DMPG (2:1) caused the dissipation to decrease. The  $\Delta D$ - $t$  plots showed the same trend observed with DMPC/DMPG (4:1) membranes (Fig. 26): the dissipation had a continuous decrease from the beginning (*i*) until the final rinse with the buffer (*iii*). Only the dissipation corresponding to 20  $\mu\text{M}$  plateaued during the incubation time, since the membrane disruption was completed already in this phase. However, the “rebound” feature occurred at various times with the (2:1) membrane: at around 4 minutes for 10  $\mu\text{M}$  and 20  $\mu\text{M}$ ; at 6 and 8 minutes in the case of 5  $\mu\text{M}$  and 2  $\mu\text{M}$  (blue arrow in Fig. 29). Clearly, a characteristic initial interaction with membranes of many compositions results with melittin.

### 3.3.2 Magainin 2

Interestingly, the action of magainin was found to be a function of the content of PG lipid in the membrane. Indeed, the graph  $\Delta f$ - $t$  in Fig. 20 shows that the high concentrations of magainin were able to disrupt the DMPC/DMPG (2:1) membrane. However, as observed with DMPC/DMPG (4:1) (cf Fig. 27), magainin action starts with membrane binding. This binding was  $\sim 2$  Hz for concentrations 5-15  $\mu\text{M}$ . Only for 1  $\mu\text{M}$ , the peptide uptake was 5.5 Hz. However, at higher concentrations, this binding was immediately followed by a removal of mass. Thus, a concentration threshold could be defined between 5  $\mu\text{M}$  and 10  $\mu\text{M}$ . After  $\sim 6$  min the removal of material ended and, as indicated by a blue arrow, a very slow and only minuscule binding ( $\sim 0.2$  Hz) occurred until the flow was ceased. No further change in frequency (mass) was observed during the equilibration phase (*ii*) (19 – 60 mins).

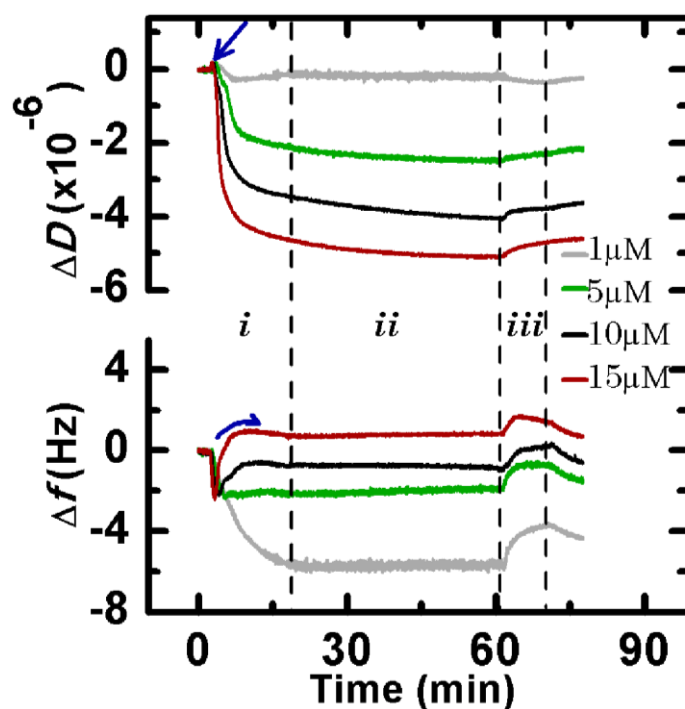


**Fig. 30:** Typical  $\Delta f$  and  $\Delta D$  versus time plots of magainin 2 interacting with supported membranes of DMPC/DMPG (2:1). The 7<sup>th</sup> harmonic is represented. The various phases are described in Fig. 29.

The initial interaction of magainin with DMPC/DMPG (2:1) membranes caused a minuscule increase in the dissipation, as indicated by the blue arrow in the  $\Delta D$ - $t$  plots of Fig.30. This is reminiscent of the “rebound” observed in some

of the earlier traces. A linear decrease followed immediately for 15  $\mu\text{M}$ , although data from lower concentrations showed indications of possibly two stages. The magnitude of the decrease in  $\Delta D$  was greater with DMPC/DMPG (2:1) than with DMPC/DMPG (4:1) (Fig. 28) and was maintained during the incubation phase (ii).

### 3.3.3 Comparing the lytic action of melittin and magainin 2: the $\Delta f$ - $\Delta D$ plots

#### 3.3.3.1 Melittin

Further details regarding the melittin mode of action could be detected from the  $\Delta f$ - $\Delta D$  plots displayed in Fig. 31. In the case of melittin (left column), the  $\Delta f$ - $\Delta D$  plots were almost identical with those of DMPC/DMPG (4:1) in Fig. 28. Thus, apparently melittin adopts the same mode of action with both the DMPC/DMPG (4:1) and (2:1) membranes, which consist of three steps. Briefly, in the first stage (i) the dissipation decreases during a small frequency variation, between 2 and -2 Hz. Then, in the second step (ii), the dissipation remained constant, with a decrease in the frequency. This second step corresponded to the initial binding ( $\Delta f$  negative) observed in Fig.29. The entire process finishes in the third step (iii) with disruption of the membrane evident, which corresponds to the frequency shifting towards positive values and the dissipation decreasing until the end of the process. The major loss of mass obtained with 5  $\mu\text{M}$  could be attributed to a slightly higher lipid deposition (32.5 Hz) characterizing that particular membrane and so these data, from 5-20  $\mu\text{M}$ , are similar.

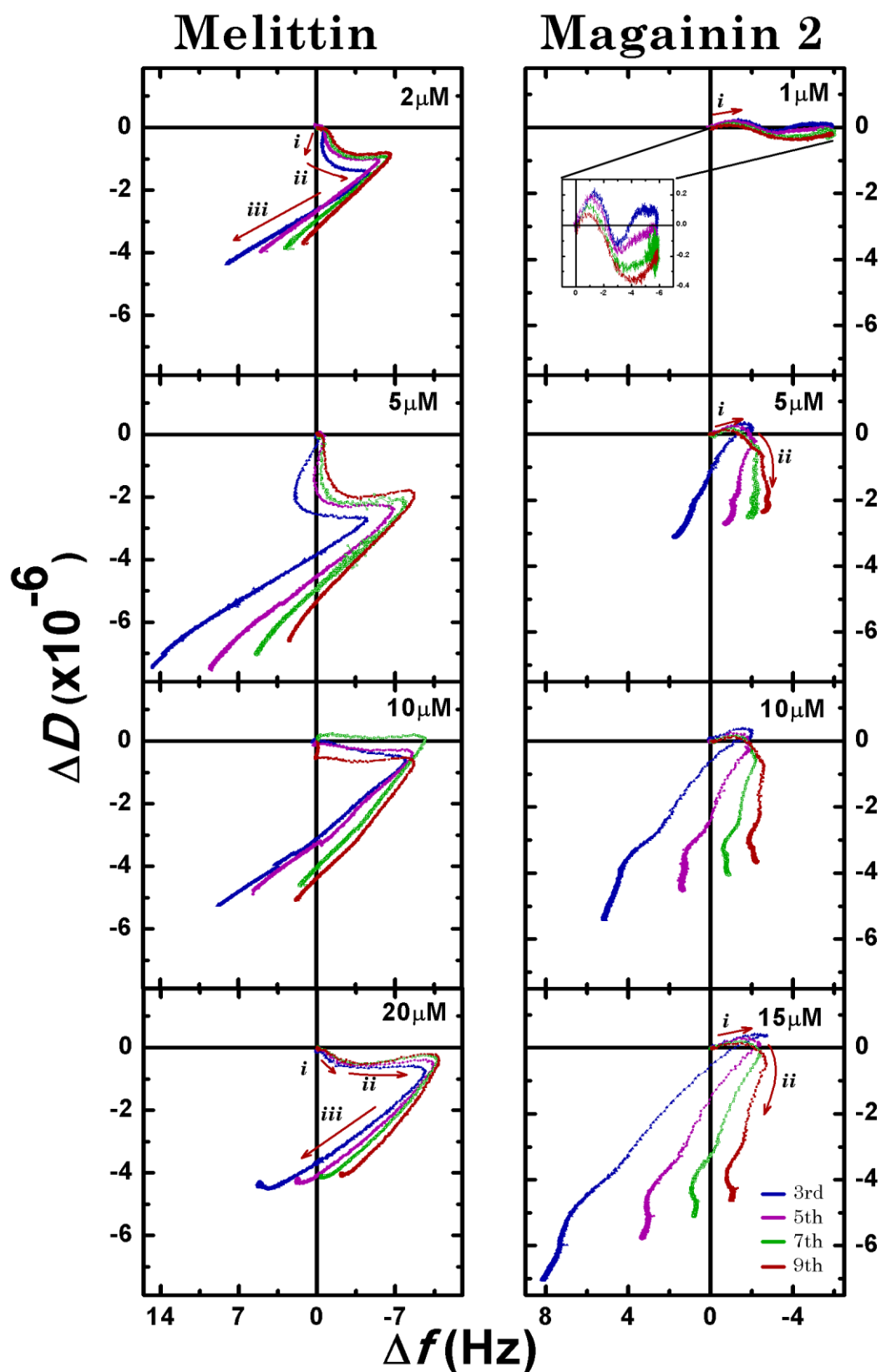


**Fig. 31:** Typical  $\Delta f$ - $\Delta D$  plots for the interaction of various concentrations of melittin (left column) and magainin 2 (right column) on a DMPC/DMPG (2:1) artificial membrane. The response of the 3rd, 5th, 7th, and 9th harmonic is presented. The wash with PBS is not included.

### 3.3.3.2 Magainin 2

The action of magainin, displayed on the right column in Fig. 31, is dramatically different from that observed on DMPC/DMPG (4:1) Fig. 28, and is characterized by a transition from trans-membrane insertion to a lytic effect for magainin 2. It is noticeable that the concentration threshold required for disrupting the membrane is between 1 and 5  $\mu\text{M}$ , which is lower than previously determined by looking only at the 7<sup>th</sup> harmonic curves illustrated in Fig. 29. Two mechanistic steps define the entire action of magainin on DMPC/DMPG (2:1): the first step (*i*) consists of the binding to the membrane, which is characterized by the decrease in frequency ( $-\Delta f \sim 2$  Hz for 5-15  $\mu\text{M}$ ) and with a very small change in dissipation, especially for the 3<sup>rd</sup> harmonic. The switch from insertion to disruption marked the beginning of the second step (*ii*), which starts as the frequency of -2 Hz is reached (5-15  $\mu\text{M}$  data only). This stage was distinguished by an increase in the frequency mainly localized at the surface. For example, at 15  $\mu\text{M}$  an increase of 8 Hz for the 3<sup>rd</sup> harmonic and  $\sim 4$  Hz for the 5<sup>th</sup> was seen. Interestingly, it looks like that this increase in the frequency (disruption) is a function of the magainin 2 concentration.

## 3.4 Melittin and magainin 2 on DMPC/cholesterol SLBs

Experiments were undertaken also with the addition of cholesterol in PC membranes. The aim was to see if the peptide action was influenced by the presence of cholesterol. The concentration of cholesterol used was 30 molar %, which is in the physiological range<sup>79</sup>.

In the presence of cholesterol, both peptides adsorbed on the membrane. However, some differences could be detected between the action of melittin and magainin 2 peptides with the membrane composed of DMPC only.

### 3.4.1 Melittin

Melittin showed only binding towards DMPC/cholesterol membrane, as the  $\Delta f$ - $t$  graph shows (Fig. 32). This is verified for all the concentrations examined, 2, 5 and 10  $\mu\text{M}$ . The  $\Delta f$ - $t$  plots show that the membrane is saturated

at the moment of stopping the flow, which is marked by the dash line indicating the end of the phase *i*. Only the trace corresponding to 2  $\mu\text{M}$  seems to reach a steady state, presumably due to depletion of the peptide concentration. However, melittin traces appear not to reach a saturation in the binding as a very small binding ( $\sim 1$  Hz) occurs during phase *ii*. This could be due to a reorganization of DMPC and cholesterol in the membrane due to the presence of melittin. This reorganization would permit more peptide molecules to bind, and would slow down the peptide binding compared to pure DMPC membranes. At the end of the period of incubation, the resulting melittin bound to the membrane corresponded to 12, 17 and 19 Hz for 2, 5 and 10  $\mu\text{M}$ , respectively. Although 20  $\mu\text{M}$  is not displayed on the graph above, it showed similar binding to the 10  $\mu\text{M}$  melittin.

During the final wash with PBS (phase *iii*), most of the peptide ( $\sim 75\%$ ) remained in the membrane. This, in addition to a greater magnitude of peptide binding with DMPC membranes containing cholesterol compared with DMPC only (Fig. 23), could indicate that the amphipathic nature of melittin is responsible for a strong binding to the cholesterol rich DMPC membrane.

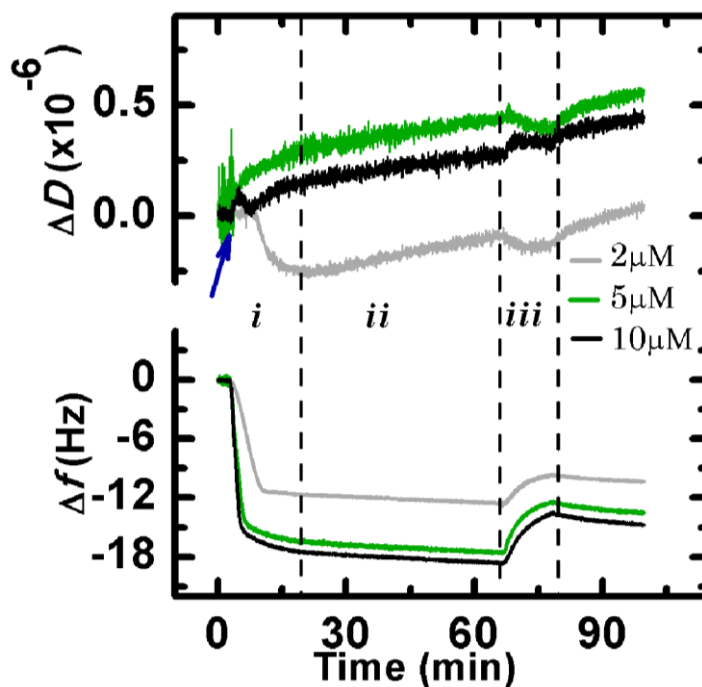


**Fig. 32:** Typical  $\Delta f$  and  $\Delta D$  versus time plots of melittin interacting with supported membranes of DMPC/chol (30 mol%). The dashed lines mark the end of each phase. Phase *i* corresponds to the beginning of peptide action, whereas *ii* denotes the peptide incubation phase. The rinse with PBS solution corresponds to phase *iii*. The 7<sup>th</sup> harmonic is represented.

The  $\Delta D$ - $t$  graph (Fig. 32) shows only small changes in the dissipation values for DMPC/chol, generally “drifting” towards positive values. However, negative  $\Delta D$  was observed for 2  $\mu\text{M}$  with a small decrease of  $0.25 \times 10^{-6}$  seen initially, while for the higher concentrations (5, 10  $\mu\text{M}$ ) this did not occur. This could be the consequence of the presence of cholesterol, which could reduce the area available for the peptide to accumulate and insert into the membrane or it could sequester melittin peptides. Indeed, for the concentration 10  $\mu\text{M}$ , a very minuscule “rebound” feature can be detected, as indicated by the blue arrow in Fig.32, which could mean the beginning of pore formation.

### 3.4.2 Magainin 2

Magainin showed less binding to the DMPC/chol membranes than melittin, as shown by the  $\Delta f$ - $t$  graph (cf Fig. 32 for melittin). Indeed, after an initial fast binding, the peptide adsorption stopped before the injection ceased (dash line in phase *i*). This addition resulted in a frequency decrease of 6 for 1  $\mu\text{M}$  and 7 Hz for 5 and 10  $\mu\text{M}$  magainin 2. The strong association of magainin 2

with the DMPC/chol membrane was indicated by the loss of material for the PBS wash (*iii*), only  $\sim 3\text{Hz}$  irrespective of the peptide concentration.

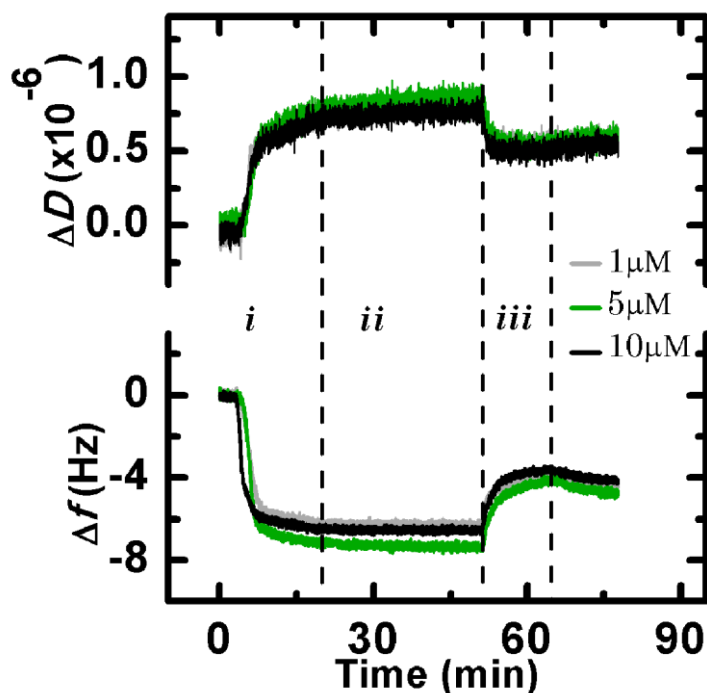


**Fig. 33:** Typical  $\Delta f$  and  $\Delta D$  versus time plots of magainin 2 interacting with supported membranes of DMPC/chol (30 mol%). The 7<sup>th</sup> harmonic is represented. The various phases are described in Fig. 32.

Magainin peptide uptake caused a small increase in dissipation (less than  $1 \times 10^{-6}$ ) for each concentration used, as shown in Fig. 33. Although small, this increase in  $\Delta D$  could mean that the magainin molecules were mainly located at the membrane interface. The small decrease of dissipation ( $0.5 \times 10^{-6}$ ) that occurs with the introduction of PBS, is correlated to desorption of some mass from the membrane.

### 3.4.3 A comparison between melittin and magainin 2: the $\Delta f$ - $\Delta D$ plots

#### 3.4.3.1 Melittin

The concentration dependent  $\Delta f$ - $\Delta D$  plots for both melittin and magainin 2 are shown in Fig. 34. For melittin interacting with a DMPC/chol membrane (left column), the  $\Delta f$ - $\Delta D$  action is similar, although the importance of the melittin concentration, or better the P/L ratio, shows similarities with the

interaction process of magainin with a membrane of DMPC (cf Fig. 25). As described for magainin on DMPC, an initial step (arrow *i*) can be identified, which is characterized by peptide uptake without significant changes to the dissipation. This phase terminated at negative frequency values between 13.5 Hz and 14 Hz for 5 and 10  $\mu\text{M}$ , and  $\Delta f_{final}$  at  $-9$  Hz for 2  $\mu\text{M}$ . Then, a second step (arrow *ii*), consisted of a decrease and then an increase in the dissipation while the frequency kept decreasing again, very similar to that of magainin interacting with DMPC membranes. In this final phase, no loss of material occurred although the dissipation showed a small decrease.

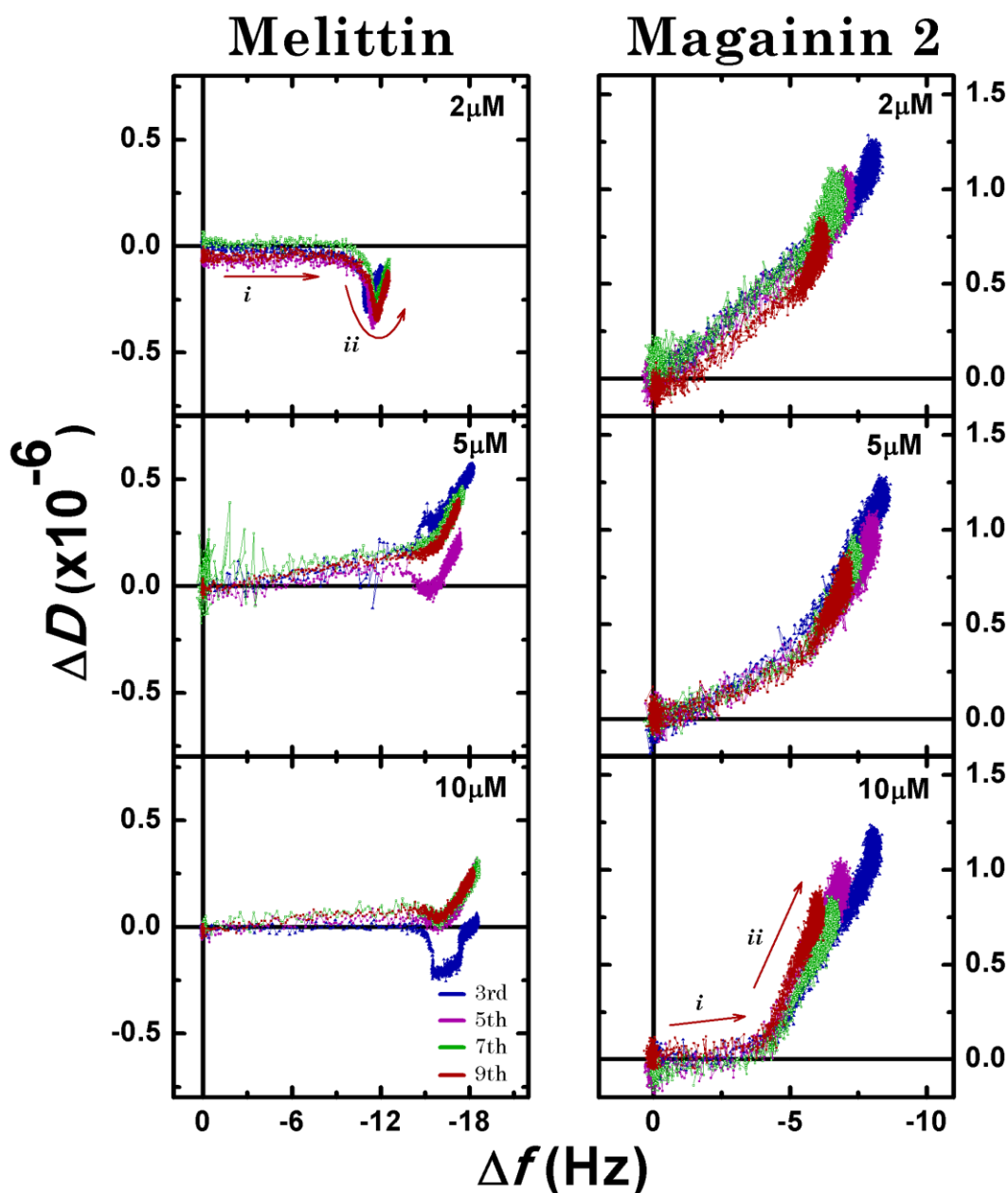


**Fig. 34:** Typical  $\Delta f$ - $\Delta D$  plots for the interaction of various concentrations of melittin (left column) and magainin 2 (right column) on a DMPC/chol 30 mol% SLB. The response of the 3rd, 5th, 7th, and 9th harmonics is presented. The wash with PBS is not included.

### 3.4.3.2 Magainin 2

In the case of magainin on DMPC/chol, the  $\Delta f$ - $\Delta D$  plots (Fig. 34, right column), underline a threshold of action between 5 and 10  $\mu\text{M}$ , which could not be detected from the  $\Delta f$ - $t$  in Fig. 33. In effect, for 10  $\mu\text{M}$ , an initial binding phase (arrow *i*) seemed to occur with no change in dissipation. The second phase (*ii*) followed and featured a sharp increase of the dissipation while the frequency keep decreasing. At the end of this second phase, the major binding and change

of the dissipation was similar for all three concentrations. The contrast with the lower (2, 5  $\mu\text{M}$ ) concentrations of magainin are that the first phase is not present and only the second phase is seen.

**Table 1:** Summary of the peptide action on the membranes examined.

	DMPC	DMPC/DMPG (4:1)	DMPC/DMPG (2:1)	DMPC/chol
<b>Melittin</b>	<b>i:</b> adsorption ( $\Delta f \downarrow$ , $\Delta D \leq -0.5$ ); <b>ii:</b> ( $\Delta f \sim 0$ , $\Delta D \downarrow$ ); <b>iii:</b> initiation lysis ( $\Delta f \uparrow$ , $\Delta D \sim 0$ )	<b>i:</b> adsorption ( $\Delta f \downarrow$ , $\Delta D \downarrow$ ); <b>ii:</b> ( $\Delta f \downarrow$ , $\Delta D \sim 0$ ); <b>iii:</b> lysis ( $\Delta f \uparrow$ , $\Delta D \uparrow$ )	<b>i:</b> adsorption ( $\Delta f \downarrow$ , $\Delta D \downarrow$ ); <b>ii:</b> ( $\Delta f \downarrow$ , $\Delta D \sim 0$ ); <b>iii:</b> lysis ( $\Delta f \uparrow$ , $\Delta D \uparrow$ )	<b>i:</b> adsorption ( $\Delta f \downarrow$ , $\Delta D = 0$ ); <b>ii:</b> ( $\Delta f \downarrow$ , $\Delta D \downarrow$ & $\uparrow$ )
<b>Magainin 2</b>	<b>i:</b> adsorption ( $\Delta f \downarrow$ , $\Delta D = 0$ ); <b>ii:</b> ( $\Delta f \downarrow$ , $\Delta D \downarrow$ ); <b>iii:</b> ( $\Delta f \downarrow \leq 2$ , $\Delta D \sim 0$ )	<b>i:</b> adsorption ( $\Delta f \downarrow$ , $\Delta D = 0$ ); <b>ii:</b> ( $\Delta f \downarrow$ , $\Delta D \downarrow$ & $\uparrow$ ); <b>iii:</b> ( $\Delta f \sim 0$ , $\Delta D \downarrow$ )	<b>i:</b> adsorption ( $\Delta f \downarrow$ , $\Delta D \leq 0.5$ ); <b>ii:</b> lysis ( $\Delta f \uparrow$ , $\Delta D \downarrow$ )	<b>i:</b> adsorption ( $\Delta f \downarrow$ , $\Delta D = 0$ ); <b>ii:</b> ( $\Delta f \downarrow$ , $\Delta D \uparrow$ )

## 4 Discussion

Many studies have been undertaken with the aim to define and characterize from a molecular point of view the membrane action of AMPs, especially for melittin and magainin 2, which have been extensively studied on artificial membranes using various techniques<sup>8,12,66</sup>. The general conclusion from all these studies is that these peptides, and AMPs in general, can act on the membrane in different ways. The predominance of a specific mechanism is determined by the cooperation between structural properties of the peptides, the composition of the membrane and other environmental factors, such as the temperature, the salt concentration and the pH<sup>4,50,80</sup>.

The influence of some of these variables, such the membrane composition and the peptide concentration, has been examined in this study using the QCM-D technique. Importantly, QCM proved to be a valuable technique in distinguishing the various mechanistic steps, hence defining the peptide mode of action.

### 4.1 Transition from toroidal pore to disruptive mechanism

#### 4.1.1 *Melittin: from the “pore-state” to a carpet mechanism*

The formation of pores in membrane can be identified in the step *ii* of “ $\Delta f$ - $\Delta D$  plots” of melittin interacting with DMPC (Fig. 25). This phase was characterized by a spread of the harmonics occurring in term of frequency change, with the 9th harmonic recording the higher binding. The dissipation, instead, was uniform for all four harmonics (3rd- 9th). Thus, according to the model suggested by Wang et al., the step *ii* could be the “fingerprint” of a toroidal pore, who suggested that the formation of a toroidal pore should be characterized by a negative and uneven change in frequency and by a negative change in dissipation as well<sup>81</sup>.

This process of pore formation seems to agree with the “two-state” model theorized by Huang<sup>51,52</sup>. This model could be characterized in the initial two

steps showed in Fig. 25. Step *i* (the initial binding) represents the initial interfacial adsorption of melittin since it is characterized by tight overlapping of all the overtones. This adsorption stage possibly creates a tension in the membrane that results in a thinning of it, which is identified by a homogeneous and small decrease in dissipation. Once a threshold value for the peptide concentration is reached, (see Fig. 25, end of step *i*), the majority of the melittin is inserted deeply into the membrane forming toroidal pores. The beginning of deeper insertion into the bilayer as a consequence of melittin orientation change (from parallel at the membrane surface), which leads to the “pore state”, could be identified as the “rebound” feature in the dissipation, which was also highlighted by a blue arrow in Fig. 23, followed by a decrease in dissipation (step *ii*).

An understanding the meaning in the change of the dissipation during the pore formation phase comes from simulation studies done by Santo et al<sup>64</sup>. These simulations showed that melittin, when interacting with the lipid molecules, cause a small thinning of the membrane, before melittin translocated across the membrane. This translocation caused a rearrangement of lipids between the leaflets, and a reorientation of the phosphate head-groups in order to create a toroidal pore<sup>64</sup>. Therefore, in the case of QCM experiments, this rearrangement of the lipids could be inferred by the changes in the dissipation occurring in phase *ii* (Fig. 25).

Furthermore, this gradual change in the dissipation ruled out the possibility of competition between these two orientations, as suggested by van den Bogart<sup>65</sup>, because the change in the dissipation, and thus the transition from adsorption to pore formation, could be seen as a progression from the lowest to the highest concentration (see Fig. 25).

Finally, the transition from a “pore-state” to a more destabilizing phase could be identified in the third step (*iii*) detected in Fig. 25 for the melittin concentration at 5, 10  $\mu\text{M}$  and definitely, for the peptide concentration of 20  $\mu\text{M}$ . In this phase, which started when the peptide solution was still being introduced, the final number of melittin peptides inserted into the membrane

was enough to cause the transition from pore formation to a disruptive mechanism, which was characterized by an increase in frequency and a small decrease in dissipation. The loss of some mass accompanying disruption happened at all the four overtones, suggesting thus a “detergent” action, which led to the formation of micelles of melittin-membrane. The membrane disruption observed by QCM confirmed what other studies had already demonstrated<sup>55,59,66</sup>.

The introduction of PBS buffer wash into the melittin-membrane system did not cause much material loss (see Fig. 23). This may indicate that melittin was strongly bound to the membrane establishing electrostatic and hydrophobic interaction with the lipids, as already predicted by previous studies<sup>38,67</sup>.

#### ***4.1.2 The influence of the lipid phase on the peptide action***

The ambient temperature, together with the level of hydration of the lipids, have a big influence on the interaction and orientation of the peptide and therefore on its ability to form pores<sup>14,59</sup>. At temperatures sufficiently high to create a fluid membrane, melittin is able to penetrate the lipid chain more extensively than at temperatures lower than the  $T_m$ , due to increased lipid motility<sup>67</sup>. Results obtained with other methods suggested that melittin is prevalently oriented parallel when adsorbed at a membrane of DMPC in the gel-phase<sup>14</sup>. However, the QCM results presented here showed pore formation of melittin in membranes of DMPC in the “ripple-phase” (see Chapter 2) at a temperature of  $19.1 \pm 0.1^\circ\text{C}$ . Despite that the probability of melittin to adopt a parallel orientation at the membrane surface decreases when the temperature, and/or the percentage of hydration increase<sup>14</sup>. A possible explanation for this is that the lipids in the membrane were well hydrated because of the roughness on the sensor surface, which implies that the membrane is not perfectly flat and compact but that it has some imperfections. Consequently, some water molecules could be entrapped between the MPA monolayer and the lipid layer. As showed by Yang<sup>14</sup>, the hydration increases the percentage of melittin that

assumes a perpendicular orientation at temperatures close to the  $T_m$  of DMPC, which leads to the pore-formation.

From the harmonics examined, melittin showed trans-membrane insertion (cf Fig. 25). However, melittin should translocate in the membrane adopting the disordered toroidal model, which implies that the translocation happens with peptides being mostly parallel with a small angle<sup>16,39</sup>. A possible scenario, proposed by recent simulations, is that melittin molecules could adopt both transmembrane and bent conformations<sup>64</sup>. In fact, the sequence of melittin contains a proline in position 14, which creates a hinge in the sequence<sup>12,63</sup>. Therefore, melittin insertion can be both trans-membrane and pseudo-transmembrane, which means that it inserts in only one leaflet of the bilayer assuming a U-shape<sup>12,64,66</sup>. Furthermore, this partial insertion into the bilayer has been already proposed from other investigations with QCM-D<sup>78,79</sup>: melittin in SLBs in the gel-phase state inserted partially because of the compactness of the lipid packaging, and removed membrane lipids in an irregular manner. However, these studies<sup>78,79</sup> did not propose pore formation as a transition phase to membrane disruption, although their QCM traces were very similar to those shown in the results section.

#### ***4.1.3 The lipid affinity and mode of action function of the peptide structure***

At a melittin concentration of 5  $\mu\text{M}$  showed pore formation in Fig. 25. However, the same concentration for magainin 2 was not sufficient to form pores as illustrated by Fig. 25. Clearly, the peptide concentration was not the issue since both peptides have similar molecular weight (2846.53  $\text{g mol}^{-1}$  for melittin and 2465.97  $\text{g mol}^{-1}$  for magainin 2). Thus, the peptide structure is clearly the origin for this difference in the peptide affinity and in the peptide action towards DMPC. Both peptides are amphipathic and adopt an  $\alpha$ -helical conformation in the membrane<sup>14</sup>. Consequently, magainin should adopt the same mechanism of interaction. However, in the QCM data, the frequency decrease for magainin is lower than for melittin, as shown in Fig 23-24, and also the dissipation magnitude. Thus magainin shows a lower affinity towards DMPC membranes as also reported with previous studies<sup>17,28</sup>, which also

reported an absence of pore formation for magainin. This low affinity of magainin towards DMPC membranes could be because the primary sequence is characterized by a low hydrophobicity, with a broader distribution of the charged residues along the sequence<sup>17</sup>, as displayed in Fig. 35. In contrast, the sequence of melittin can be divided in two distinct domains, as shown in Fig.35: a prevalently hydrophobic N-terminus, implied in the interaction with neutral membranes, and a charged C-terminus, which is shown to be essential for the binding with both zwitterionic and anionic membranes<sup>18,19</sup>.

However, the  $\Delta f$ - $\Delta D$  plots in Fig. 25 illustrate a minuscule increase in the dissipation for 10 and 15  $\mu\text{M}$  (cf phase iii) that appeared to be an attempt to start pore formation. After all, magainin has been shown to disrupt membranes made of neutral phosphocholines, such as POPC, but at much higher concentrations (40-100  $\mu\text{M}$ )<sup>82</sup> Thus, the inability to detect any pore formation could be attributed to a P/L not enough to overcome the threshold for that kind of membrane, as previously highlighted by Matsuzaki<sup>9</sup>.

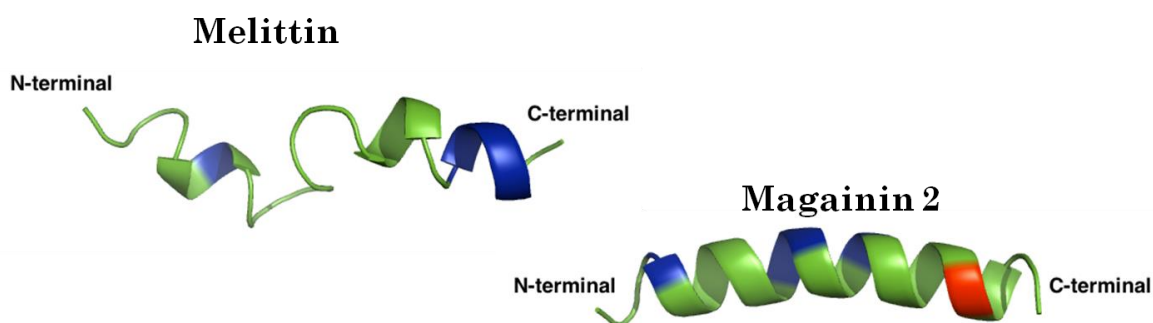


**Fig. 35:** 3-dimensional model of melittin and magainin 2 determined by Pymol (PyMOL Molecular Graphics System, Version 1.2r3pre, Schrödinger, LLC, NY, USA). Cationic residues are represented in blue while anionic residues are represented in orange. Hydrophobic residues are in green.

#### 4.1.4 The influence of DMPG in a DMPC membrane

##### 4.1.4.1 Low threshold required for melittin

Several studies have shown that melittin can act in a detergent-like manner at membranes containing only acidic phospholipids<sup>28,59</sup>. Conversely, other studies have reported an inhibition of the lysis by melittin for membranes having negatively charged phospholipids<sup>12,17,83</sup>. Wessman et al.<sup>83</sup> suggested that

this inhibition was caused by electrostatic interactions between the positive charged C-terminus of the melittin sequence and the negative charges on the membrane surface that hindered the insertion of melittin into the membrane<sup>83</sup>.

However, the results presented here, obtained with membranes composed of DMPC/DMPG (4:1 and 2:1) show a clear membrane insertion, which is immediately followed by a disruptive mechanism, for all the concentrations examined (Fig. 26). Furthermore, the  $\Delta f$ - $\Delta D$  plots for DMPC/DMPG (4:1) displayed in Fig. 28 were consistent with a pore formation followed by disruption, that is, the loss of lipids was more evident on the surface layers of the membrane. This could be deduced by their similarities in the  $\Delta f$ - $\Delta D$  plots for melittin on DMPC membrane.

The inclusion of DMPG in the membrane decreased the concentration threshold of melittin required for pore formation, which was lower than 2  $\mu\text{M}$ . Unfortunately, also the concentration threshold for membrane disruption seemed to be lower than 2  $\mu\text{M}$ , hence a clear distinction between the two stages could not be verified. Indeed, the transition from melittin adsorption to pore formation (decrease in  $\Delta D$  without changes in  $\Delta f$ ) could not be distinguished in the  $\Delta f$ - $\Delta D$  plots of Fig. 28. Consequently, it can be said that the presence of negatively charged lipids lowered the P/L required for the membrane permeabilisation due to pore formation and also for membrane lysis, probably by enhancing the clustering of melittin monomers in aggregates<sup>36</sup>.

#### 4.1.4.2 *Magainin activity influenced by the DMPG ratio*

The composition of the membrane showed greater influence on the mode of action for magainin than for melittin. Unlike melittin that did not show any major differences between the two ratios used for DMPC/DMPG, magainin showed a transition from pore only formation occurring at the 4:1 ratio, to a detergent-like mechanism with DMPC/DMPG having a ratio of 2:1. Furthermore, the  $\Delta f$ - $\Delta D$  plots regarding the interaction of magainin with DMPC/DMPG (2:1) were able to make a clear discrimination between peptide adsorption, pore formation and membrane disruption. Indeed, adsorption only

happened at the concentration of 1  $\mu\text{M}$ , while pore formation was visible at the concentration of 5  $\mu\text{M}$ . Finally, 15  $\mu\text{M}$  showed clear disruption through the membrane.

In conclusion, the increased affinity of melittin and magainin for anionic membranes<sup>17,67</sup> could be interpreted as a reduction of the local concentration threshold required for the peptide to permeabilise the membrane, as already demonstrate for magainin by Ludtke et al.<sup>43</sup>.

## **4.2 The influence of cholesterol on peptide action**

Cholesterol has been reported to inhibit pore formation in model membranes by melittin<sup>72</sup> and by magainin<sup>17</sup>. Furthermore, studies highlighted the influence of cholesterol concentration on the interaction<sup>13,70,84</sup> and consequently lysis of the membrane by melittin since membrane lysis was not detected with concentrations of cholesterol equal to or higher than 30 mol%<sup>70</sup>. This seems to agree with the melittin action reported here. Additionally, our results showed melittin having a greater affinity when cholesterol was present in membrane (see Fig. 25 & 32). Most probably, this increased adsorption could be justified as a deeper insertion into a membrane being subjected to a phase transition from gel to liquid-ordered phase due to the moderate content of cholesterol<sup>70</sup>, or by a direct binding interaction occurring between melittin and cholesterol<sup>12</sup>. Most probably, this initial adsorption consisted of melittin monomers since the  $\Delta f$ - $\Delta D$  plots for melittin showed the same initial step in DMPC membranes with or without cholesterol. These monomers could not cluster locally and thus reaching a local concentration threshold for the formation of pores, or only a very small number of pores in the membrane of DMPC/cholesterol were formed because of the decrease in available pore forming area.

In contrast, magainin did not show a significant difference for the binding at membranes of DMPC +/- cholesterol: the decrease in frequency was very similar, as shown in Fig. 24 & 33. However, this adsorption did not result in trans-membrane insertion and pore formation for the majority of magainin

peptides since the 3rd harmonic recorded a slight higher binding of magainin than the 9th harmonic and the dissipation assumed positive values in all the harmonics, as showed by the  $\Delta f$ - $\Delta D$  plots of Fig. 18. Thus, the concentrations of magainin used in this study confirm the lack of toxicity of magainin towards eukaryotic mimetic membranes containing cholesterol 30 mol%.

## 5 Conclusions

Melittin and magainin have been the object of numerous studies since their early discovery as they are the stereotypical examples of AMPs. Generally, their mode of action has been characterized and confirmed; however, there is still much debate in the explanation of their action and the variables that influence their action. In fact, the distinct transitions in the melittin and magainin actions are hardly distinguishable since the interactions happen within milliseconds<sup>12</sup>. Furthermore, the adoption of a specific mechanism is not unconditional, as already suggested by Dathe<sup>4</sup>, but there is always an interchange, a continual progression, mostly influenced by factors such by the nature of lipids, the target-dependent influence on the binding and permeabilisation steps.

Previous studies employing QCM to characterize the modes of action adopted by melittin defined melittin as a lytic peptide<sup>77-79,84,85</sup>. However, no such studies have been undertaken in the case of magainin.

In the experiments described in this chapter, the employment of various SLBs on a modified QCM sensor has permitted the confirmation of the Shai-Matsuzaki-Huang model<sup>48</sup> as the more appropriate in describing the action of melittin and magainin at the biomimetic membrane. This model consists mainly of a progressive transition from a simple adsorption to pore formation, which leads to the disruption of the membrane. However, these transitions are influenced by the structural properties of the peptides and the membrane composition as well, as revealed by comparing the action of melittin and magainin 2 using QCM. Indeed, QCM was shown to be a valid approach in

characterizing the structural interactions between melittin and magainin 2 with SLBs. This enabled a clear definition of each “transitional” step of the peptide action.

## 6 Bibliography

- 1 Shai, Y. Mechanism of the binding, insertion and destabilization of phospholipid bilayer membranes by  $\alpha$ -helical antimicrobial and cell non-selective membrane-lytic peptides. *BBA- Biomembr.* **1462**, 55-70, (1999).
- 2 Oren, Z. & Shai, Y. Mode of action of linear amphipathic  $\alpha$ -helical antimicrobial peptides. *Biopolymers* **47**, 451-463, (1998).
- 3 Tossi, A. *et al.* Amphipathic,  $\alpha$ -helical antimicrobial peptides. *Pept. Sci.* **55**, 4-30, (2000).
- 4 Dathe, M. & Wieprecht, T. Structural features of helical antimicrobial peptides: their potential to modulate activity on model membranes and biological cells. *BBA- Biomembr.* **1462**, 71-87, (1999).
- 5 Pukala, T. L. *et al.* Host-defence peptides from the glandular secretions of amphibians: Structure and activity. *Nat. Prod. Rep.* **23**, 368-393, (2006).
- 6 Apponyi, M. A. *et al.* Host-defence peptides of Australian anurans: Structure, mechanism of action and evolutionary significance. *Peptides* **25**, 1035-1054, (2004).
- 7 Zasloff, M. Magainins, a class of antimicrobial peptides from *Xenopus* skin: Isolation, characterization of two active forms, and partial cDNA sequence of a precursor. *Proc. Natl. Acad. Sci.* **84**, 5449-5453, (1987).
- 8 Matsuzaki, K. Why and how are peptide-lipid interactions utilized for self-defense? Magainins and tachyplesins as archetypes. *BBA- Biomembr.* **1462**, 1-10, (1999).
- 9 Matsuzaki, K. Control of cell selectivity of antimicrobial peptides. *BBA- Biomembr.* **1788**, 1687-1692, (2009).
- 10 Baker, M. A. *et al.* Anticancer efficacy of Magainin2 and analogue peptides. *Cancer Res.* **53**, 3052-3057, (1993).
- 11 Dempsey, C. E. The actions of melittin on membranes. *BBA- Rev. Biomembr.* **1031**, 143-161, (1990).
- 12 Raghuraman, H. & Chattopadhyay, A. Melittin: A membrane-active peptide with diverse functions. *Biosci. Rep.* **27**, 189-223, (2007).
- 13 Wessman, P. *et al.* Melittin-lipid bilayer interactions and the role of cholesterol. *Biophys. J.* **95**, 4324-4336, (2008).
- 14 Yang, L. *et al.* Barrel-stave model or toroidal model? A case study on melittin pores. *Biophys. J.* **81**, 1475-1485, (2001).
- 15 Doig, A. J. & Baldwin, R. L. N- and C-capping preferences for all 20 amino acids in  $\alpha$ -helical peptides. *Protein Sci.* **4**, 1325-1336, (1995).
- 16 Nguyen, L. T. *et al.* The expanding scope of antimicrobial peptide structures and their modes of action. *Trends Biotechnol.* **29**, 464-472, (2011).

- 17 Matsuzaki, K. *et al.* Relationship of membrane curvature to the formation of pores by magainin 2. *Biochemistry* **37**, 11856-11863, (1998).
- 18 Mozsolits, H. *et al.* Analysis of antimicrobial peptide interactions with hybrid bilayer membrane systems using surface plasmon resonance. *BBA- Biomembr.* **1512**, 64-76, (2001).
- 19 Hall, K. *et al.* The role of electrostatic interactions in the membrane binding of melittin. *J. Mol. Recognit.* **24**, 108-118, (2011).
- 20 Bechinger, B. The structure, dynamics and orientation of antimicrobial peptides in membranes by multidimensional solid-state NMR spectroscopy. *BBA- Biomembr.* **1462**, 157-183, (1999).
- 21 Yeaman, M. R. & Yount, N. Y. Mechanisms of antimicrobial peptide action and resistance. *Pharmacol. Rev.* **55**, 27-55, (2003).
- 22 Teixeira, V. *et al.* Role of lipids in the interaction of antimicrobial peptides with membranes. *Prog. Lipid Res.* **51**, 149-177, (2012).
- 23 Kinnunen, P. K. J. Amyloid formation on lipid membrane surfaces. *Open Biol.* **2**, 163-175, (2009).
- 24 Matsuzaki, K. Magainins as paradigm for the mode of action of pore forming polypeptides. *BBA- Rev. Biomembr.* **1376**, 391-400, (1998).
- 25 Ludtke, S. J. Membrane pores induced by magainin. *Biochemistry* **35**, 13723-13728, (1996).
- 26 Dempsey, C. E. *et al.* Contribution of proline-14 to the structure and actions of melittin. *FEBS Lett.* **281**, 240-244, (1991).
- 27 Hristova, K. *et al.* Structure, location, and lipid perturbations of melittin at the membrane interface. *Biophys. J.* **80**, 801-811, (2001).
- 28 Papo, N. & Shai, Y. Exploring peptide membrane interaction using surface plasmon resonance: Differentiation between pore formation versus membrane disruption by lytic peptides. *Biochemistry* **42**, 458-466, (2003).
- 29 Park, C. B. *et al.* Structure-activity analysis of buforin II, a histone H2A-derived antimicrobial peptide: The proline hinge is responsible for the cell-penetrating ability of buforin II. *Proc. Natl. Acad. Sci.* **97**, 8245-8250, (2000).
- 30 Glättli, A. *et al.* A molecular dynamics study of the bee venom melittin in aqueous solution, in methanol, and inserted in a phospholipid bilayer. *Eur. Biophys. J.* **35**, 255-267, (2006).
- 31 Terwilliger, T. C. & Eisenberg, D. The structure of melittin. I. Structure determination and partial refinement. *J. Biol. Chem.* **257**, 6010-6015, (1982).
- 32 Terwilliger, T. C. & Eisenberg, D. The structure of melittin. II. Interpretation of the structure. *J. Biol. Chem.* **257**, 6016-6022, (1982).

- 33 Lad, M. D. *et al.* Antimicrobial peptide-lipid binding interactions and binding selectivity. *Biophys. J.* **92**, 3575-3586, (2007).
- 34 Mahalka, A. K. & Kinnunen, P. K. J. Binding of amphipathic  $\alpha$ -helical antimicrobial peptides to lipid membranes: Lessons from temporins B and L. *BBA- Biomembr.* **1788**, 1600-1609, (2009).
- 35 Zhao, H. *et al.* Binding of Endostatin to Phosphatidylserine-Containing Membranes and Formation of Amyloid-like Fibers. *Biochemistry* **44**, 2857-2863, (2005).
- 36 Harris, F. *et al.* Aberrant action of amyloidogenic host defense peptides: A new paradigm to investigate neurodegenerative disorders? *FASEB J.* **26**, 1776-1781, (2012).
- 37 Zhao, H. *et al.* Interaction of the antimicrobial peptide pheromone Plantaricin A with model membranes: Implications for a novel mechanism of action. *BBA- Biomembr.* **1758**, 1461-1474, (2006).
- 38 Beschiaschvili, G. & Seelig, J. Melittin binding to mixed phosphatidylglycerol/phosphatidylcholine membranes. *Biochemistry* **29**, 52-58, (1990).
- 39 Sengupta, D. *et al.* Toroidal pores formed by antimicrobial peptides show significant disorder. *BBA- Biomembr.* **1778**, 2308-2317, (2008).
- 40 Huang, H. W. Action of antimicrobial peptides: Two-state model. *Biochemistry* **39**, 8347-8352, (2000).
- 41 Brown, L. R. *et al.* High-resolution 1H-NMR studies of self-aggregation of melittin in aqueous solution. *BBA - Protein Structure* **622**, 231-244, (1980).
- 42 Macháň, R. *et al.* Real-time monitoring of melittin-induced pore and tubule formation from supported lipid bilayers and its physiological relevance. *Chem. Phys. Lipids* **163**, 200-206, (2010).
- 43 Ludtke, S. J. *et al.* Cooperative membrane insertion of magainin correlated with its cytolytic activity. *BBA- Biomembr.* **1190**, 181-184, (1994).
- 44 Bechinger, B. Insights into the mechanisms of action of host defence peptides from biophysical and structural investigations. *J. Pept. Sci.* **17**, 306-314, (2011).
- 45 Matsuzaki, K. *et al.* An antimicrobial peptide, magainin 2, induced rapid flip-flop of phospholipids coupled with pore formation and peptide translocation. *Biochemistry* **35**, 11361-11368, (1996).
- 46 Matsuzaki, K. *et al.* Kinetics of Pore Formation by an Antimicrobial Peptide, Magainin 2, in Phospholipid Bilayers. *Biochemistry* **34**, 12553-12559, (1995).
- 47 Yang, L. *et al.* Crystallization of antimicrobial pores in membranes: Magainin and protegrin. *Biophys. J.* **79**, 2002-2009, (2000).

- 48 Zasloff, M. Antimicrobial peptides of multicellular organisms. *Nature* **415**, 389-395, (2002).
- 49 Phoenix, D. A. *et al.* in *Antimicrobial Peptides* Ch. 5, 145-180 (Wiley-VCH Verlag GmbH & Co. KGaA, 2013).
- 50 Bechinger, B. Peptide structural analysis by solid-state NMR spectroscopy. *Biopolymers* **51**, 174-190, (1999).
- 51 Huang, H. W. Molecular mechanism of antimicrobial peptides: The origin of cooperativity. *BBA- Biomembr.* **1758**, 1292-1302, (2006).
- 52 Huang, H. W. *et al.* Molecular mechanism of peptide-induced pores in membranes. *Phys. Rev. Lett.* **92**, 198304-198301, (2004).
- 53 Bechinger, B. Structure and Functions of Channel-Forming Peptides: Magainins, Cecropins, Melittin and Alamethicin. *J. Membr. Biol.* **156**, 197-211, (1997).
- 54 Lee, M. T. *et al.* Mechanism and kinetics of pore formation in membranes by water-soluble amphipathic peptides. *Proc. Natl. Acad. Sci.* **105**, 5087-5092, (2008).
- 55 Lee, M. T. *et al.* Process of inducing pores in membranes by melittin. *Proc. Natl. Acad. Sci. U. S. A.* **110**, 14243-14248, (2013).
- 56 Huang, K. & García, A. E. Free energy of translocating an arginine-rich cell-penetrating peptide across a lipid bilayer suggests pore formation. *Biophys. J.* **104**, 412-420, (2013).
- 57 Tamba, Y. *et al.* Kinetic Pathway of Antimicrobial Peptide Magainin 2-Induced Pore Formation in Lipid Membranes. *J. Phys. Chem. B* **114**, 12018-12026, (2010).
- 58 Leontiadou, H. *et al.* Antimicrobial peptides in action. *J. Am. Chem. Soc.* **128**, 12156-12161, (2006).
- 59 Ladokhin, A. S. & White, S. H. 'Detergent-like' permeabilization of anionic lipid vesicles by melittin. *BBA- Biomembr.* **1514**, 253-260, (2001).
- 60 Steinem, C. *et al.* Evidence for multilayer formation of melittin on solid-supported phospholipid membranes by shear-wave resonator measurements. *Chem. Phys. Lipids* **95**, 95-104, (1998).
- 61 Rex, S. Pore formation induced by the peptide melittin in different lipid vesicle membranes. *Biophys. Chem.* **58**, 75-85, (1996).
- 62 Sansom, M. S. The biophysics of peptide models of ion channels. *Prog. Biophys. Mol. Biol.* **55**, 139-235, (1991).
- 63 Tosteson, M. T. & Tosteson, D. C. The sting. Melittin forms channels in lipid bilayers. *Biophys. J.* **36**, 109-116, (1981).
- 64 Santo, K. P. *et al.* Melittin creates transient pores in a lipid bilayer: Results from computer simulations. *J. Phys. Chem. B* **117**, 5031-5042, (2013).

- 65 Van Den Bogaart, G. *et al.* On the mechanism of pore formation by melittin. *J. Biol. Chem.* **283**, 33854-33857, (2008).
- 66 Wiedman, G. *et al.* The electrical response of bilayers to the bee venom toxin melittin: Evidence for transient bilayer permeabilization. *BBA-Biomembr.* **1828**, 1357-1364, (2013).
- 67 Lee, T. H. *et al.* Measurement of the affinity of melittin for zwitterionic and anionic membranes using immobilized lipid biosensors. *J. Pept. Res.* **58**, 464-476, (2001).
- 68 Shai, Y. Mode of action of membrane active antimicrobial peptides. *Biopolymers - Peptide Science Section* **66**, 236-248, (2002).
- 69 Matsuzaki, K. *et al.* Translocation of a Channel-Forming Antimicrobial Peptide, Magainin 2, across Lipid Bilayers by Forming a Pore. *Biochemistry* **34**, 6521-6526, (1995).
- 70 Monette, M. *et al.* Effect of cholesterol on the polymorphism of dipalmitoylphosphatidylcholine/melittin complexes: An NMR study. *BBA- Biomembr.* **1149**, 319-328, (1993).
- 71 Monette, M. & Lafleur, M. Influence of lipid chain unsaturation on melittin-induced micellization. *Biophys. J.* **70**, 2195-2202, (1996).
- 72 Allende, D. *et al.* Melittin-induced bilayer leakage depends on lipid material properties: Evidence for toroidal pores. *Biophys. J.* **88**, 1828-1837, (2005).
- 73 Raghuraman, H. & Chattopadhyay, A. Interaction of Melittin with Membrane Cholesterol: A Fluorescence Approach. *Biophys. J.* **87**, 2419-2432, (2004).
- 74 Zhao, H. *et al.* Comparison of the membrane association of two antimicrobial peptides, magainin 2 and indolicidin. *Biophys. J.* **81**, 2979-2991, (2001).
- 75 Tytler, E. M. Molecular basis for prokaryotic specificity of magainin-induced lysis. *Biochemistry* **34**, 4393-4401, (1995).
- 76 Matsuzaki, K. *et al.* Pore formation and translocation of melittin. *Biophys. J.* **73**, 831-838, (1997).
- 77 Kannisto, K. *et al.* An impedance QCM study on the partitioning of bioactive compounds in supported phospholipid bilayers. *Colloids Surf., B* **86**, 298-304, (2011).
- 78 Lu, N. *et al.* Molecular response and cooperative behavior during the interactions of melittin with a membrane: Dissipative quartz crystal microbalance experiments and simulations. *J. Phys. Chem. B* **116**, 9432-9438, (2012).
- 79 Lu, N. Y. *et al.* Vesicle deposition and subsequent membrane-melittin interactions on different substrates: A QCM-D experiment. *BBA-Biomembr.* **1828**, 1918-1925, (2013).

- 80 Williams, T. L. & Serpell, L. C. Membrane and surface interactions of Alzheimer's A $\beta$  peptide - Insights into the mechanism of cytotoxicity. *FEBS J* **278**, 3905-3917, (2011).
- 81 Wang, K. F. *et al.* Characterization of supported lipid bilayer disruption by chrysopsin-3 using QCM-D. *J. Phys. Chem. B* **115**, 15228-15235, (2011).
- 82 Pramanik, A. *et al.* Molecular interactions of peptides with phospholipid vesicle membranes as studied by fluorescence correlation spectroscopy. *Chem. Phys. Lipids* **104**, 35-47, (2000).
- 83 Wessman, P. *et al.* Effect of  $\alpha$ -helical peptides on liposome structure: A comparative study of melittin and alamethicin. *J. Colloid Interface Sci.* **346**, 127-135, (2010).
- 84 Chen, L. Y. *et al.* Exploring the effect of cholesterol in lipid bilayer membrane on the melittin penetration mechanism. *Anal. Biochem.* **367**, 49-55, (2007).
- 85 Briand, E. *et al.* Combined QCM-D and EIS study of supported lipid bilayer formation and interaction with pore-forming peptides. *Analyst* **135**, 343-350, (2010).



# *Proline-rich AMPs*

## 1 Introduction

Many AMPs have the ability to kill bacteria by inhibiting cellular processes occurring inside the cell. These peptides are typically able to translocate the membrane and enter the cytosol without causing substantial damage to the membrane integrity. These AMPs target intracellular components, such as nucleic acids<sup>1</sup>, thus impeding their normal functionality and usually killing the cell. AMPs are therefore considered as cell penetrating peptides (CPPs), (presented in Chapter 5), and constitute a promising strategy for a more focused antibacterial therapy or for drug delivery.

Cell penetrating AMPs derived from the honey bee, are rich in proline residues. Examples include apidaecin 1a (GNNRPVYIPQPRPPHPRI), apidaecin 1b (GNNRPVYIPQPRPPHPRL)<sup>2</sup> and Api88 (GONNRPVYIPRPRPPHPRL-NH<sub>2</sub>), an optimized version of apidaecin 1b<sup>3</sup>. These peptides have been the topic of several papers presented in this chapter. In addition, oncocin (peptide 10) (VDKPPYLPRPRPPRRIYNR-NH<sub>2</sub>) and peptide 11 (VDKPPYLPRPRPPROIYNO-NH<sub>2</sub>), have been optimized from the *Oncopeltus* antibacterial peptide 4, derived from the Milkweed bug<sup>4</sup>. Since these AMPs are characterized by an amino acid sequence rich in proline residues (in bold), they form a class called proline-rich AMPs or Pr-AMPs<sup>5</sup>.

### 1.1 Proline-rich peptides

Proline-rich peptides (Pr-AMPs) share some characteristics irrespective of their origin and overall sequences: (i) a high content in proline residues (between 25 to 50%); (ii) a significant presence of arginine residues, which contribute to the net cationic charge of these peptides, (iii) and a bacteriostatic action, mainly towards Gram-negative bacteria<sup>5,6</sup>.

### 1.1.1 Examples of Pr-rich antimicrobial peptides

Pr-rich peptides are expressed widely across nature and have been isolated in insects<sup>7</sup>, mammals, amphibians, crustaceans and molluscs<sup>5</sup>.

Mammalian Pr-AMPs belong to the cathelicidin family of AMPs<sup>5,6</sup>. Some examples include Bac5 and Bac7, from bovine neutrophils<sup>8</sup> and PR-39 and prophenin from pig leukocytes<sup>5,7,9</sup> (Table 2). Despite variability in length and primary sequence, cathelicidins are characterized by a well-conserved N-terminal pre-proregion, named cathelin, and a highly variable C-terminal domain, corresponding to the active AMP after proteolytic processing<sup>5,6</sup>.

**Table 2:** Examples of pr-AMPs from vertebrate animals<sup>5</sup>.

Name	Origin	Sequence
<b>PR-39</b>	pig	RRRPRPPYLPRPRPPFFPPRLPPRIPPGFPPRFPPRFPP-NH <sub>2</sub>
<b>prophenin</b>	pig	AFPPPNFPGPRFPPNFPGPRFPPNFPGPRFPPNFPGPRF PPNFPGPPFPPPIFPGPWFPFPPPPFRPPPFPGPPRF-NH <sub>2</sub>
<b>Bac5</b>	cow	RFRPPIRRPPIR---PPFYPPFRPPIRPPIFPPIRPPFRPPLGPF-NH <sub>2</sub>
<b>Bac5</b>	sheep	RFRPPIRRPPIR---PPFNPPFRPPVRPPFRPPFRPPFRPPIGPF-NH <sub>2</sub>
<b>Bac7</b>	cow	RRIRPRPPRLPRPRPRPLPFPRPGPRPIPRPLPFPRPGPRPIPRPL PFPRPGPRPIPRPL
<b>Bac7</b>	sheep	RRLRPRRPRRLPRPRPRPRPRSLPLRPQPRRIPRPIILLPWRPPR PIPRPQPQPIPRWL

Pr-rich AMPs isolated from insects are the most identified and investigated. They are subdivided in two groups: short-chain and long-chain peptides<sup>10</sup> (as shown in Table 3). Examples of the longer peptides are the abaecins, from hymenopteran species, and lebecins, from moths. Peptides belonging to the short-chain group show some similarities in their primary amino acid sequence in terms of amino acid composition and motif pattern<sup>6</sup>. Examples of these shorter peptides are: drosocin, a 19-residue peptide from

*Drosophila melanogaster*<sup>10</sup> which contains three repeats of the PRP motif evenly distributed along the sequence; pyrrhocoricin, a peptide isolated from *Pyrrhocoris apterus*<sup>7</sup> which has some similarities to drosocin; and one of the best characterized short Pr-rich AMPs apidaecin, which has been isolated from *Apis mellifera*<sup>5,6</sup>. Pr-rich AMPs presented in other invertebrates are, for example, the penaeidins from shrimp<sup>11</sup>, astacidins from crayfish<sup>12</sup> and Cg-PRP from oysters<sup>13</sup>.

**Table 3:** Examples of insect Pr-AMPs<sup>5</sup>.

Name	Origin	Sequence
<i>short-chain</i>		
<b>Pyrrhocoricins</b>	fire bug	VDKGSYLPRPT---PPRPIYNRN
<b>Drosocin</b>	fruit fly	GKPRPYSPRPTSHPRPIRV
<b>Formaecins</b>	ant	GRPNPVNNKPTPHPRL
<i>long-chain</i>		
<b>Metchnikowin</b>	fruit fly	HRHQGPFDTRPSPFNPNQPRPGPIY
<b>Lebocins</b>	moths	DLRFLYPRGKLPVPTPPPFNPKPIYIDMGNRY
<b>Abaecins</b>	honeybee	YVPLPNIPQGRRPFPTFGQGPFNPKIRWPQGY
	bumblebee	FVPYNPPRPGQSKPFPTFGHGPFNPKIQWPYPLPNPGH

### 1.1.2 Apidaecin peptides

Apidaecin peptides were one of the first Pr-rich peptides to be identified and are of the the most investigated. Three isoform of apidaecins: HbIa, HbIb and HbII, were first isolated from the lymph fluid of honeybees that had a bacterial infection<sup>2</sup>. These isoforms contain 18 amino acid residues and are the most prominent components of the honeybee humoral defence against microbial invasion<sup>2</sup>. Further examples of apidaecins have also been isolated from other bees, wasps and hornets, all belonging to the *Apocrita* suborder of *Hymenoptera*<sup>6</sup> (Table 4).

All these apidaecins share very high homology since these different isoforms originate from a single precursor<sup>6</sup>. The peptide sequences are characterized by conservation of R/K-P or PRP motifs in the N-terminal region (the variable region) and an eight-residue PRPPHPRL motif at the C-terminus (the constant region)<sup>5,6,14</sup>. The constant region is responsible for the antibacterial activity, while the variable region is responsible for their selectivity in the antibacterial spectrum<sup>2,6,15,16</sup>.

**Table 4:** Amino acid sequences of some apidaecin-type peptides<sup>6</sup>.

Sources	Isoforms	Sequence
<b>Honey bee</b>	HbIa	GNN <b>RP</b> VYIPQ <b>PRPPHPRI</b>
	HbIb	GNN <b>RP</b> VYIPQ <b>PRPPHPRL</b>
	HbII	GNN <b>RP</b> IYIPQ <b>PRPPHPRL</b>
	HbIII	GNN <b>RP</b> IYISQ <b>PRPPHPRL</b>
<b>Bumble bee</b>	Bb +A	AN <b>RP</b> VYIPP <b>PRPPHPRL</b>
	Bb -A	- <b>NR</b> PVYIPP <b>PRPPHPRL</b>
<b>Cicada killer</b>	Ck P	<b>NR</b> PTYVPP <b>PRPPHPRL</b>
	Ck A	<b>NR</b> PTYVPA <b>PRPPHPRL</b>
<b>Bald-faced hornet</b>	Ho +	GK <b>RP</b> QQVP- <b>PRPPHPRL</b>
	Ho -	--- <b>RP</b> QQVP- <b>PRPPHPRL</b>
Conserved sequences of all the isoforms		<b>RP</b> <b>PRPPHPR</b>

## 1.2 The importance of proline

Proline plays an important role in the antimicrobial activity of many AMPs. For instance, a potent AMP, buforin II, loses the ability to translocate the cell membrane if the proline at position 11 is removed. Instead buforin II disrupts the cell membrane<sup>1</sup>. Another example is the loss of antibacterial

activity by HbIII peptides when the proline at position 9 is substituted with a serine<sup>14</sup>. Moreover, Zhang et al.<sup>17</sup> demonstrated that the substitution of proline into the sequence of a helical cationic AMP introduces bends into the peptide sequence. This affects the interaction of the AMPs with the membrane and consequently their antimicrobial activity, switching from a membrane-lytic to a non lytic action<sup>17</sup>.

Proline is the only gene-encoded amino acid that has its side-chain cyclised onto the backbone nitrogen atom<sup>18</sup> (see Fig. 36). This cyclisation affects the geometries and conformations adopted by proline itself, which are very restricted. It also restricts the conformation of the residue preceding the proline due to the bulkiness of the N-CH<sub>2</sub> group, resulting in a strong preference for a  $\beta$ -sheet structure<sup>19</sup>. When bound in an amide bond, proline is unable to act as a hydrogen-bond donor. Proline can induce  $\beta$ -turns, particularly if preceded by tyrosine or followed by phenylalanine or tryptophan residues<sup>18</sup>. The presence of proline in the overall peptide can cause both the formation of bends in transmembrane helices and changes in conformation<sup>18</sup>.

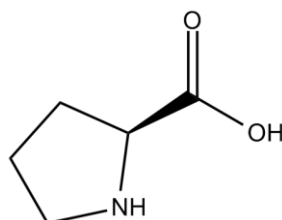


**Fig. 36:** The molecular structure of proline.

These properties of proline cause proline rich sequences to adopt the poly-L-proline type II helical conformation (PP-II helix) (see Fig.37), which is a left-handed extended helix of three residues per turn<sup>5,18,20</sup>. CD studies show that various pro-rich AMPs adopt this conformation, including Bac-5<sup>21</sup>, PR-39<sup>22</sup>, drosocin<sup>23</sup> and apidaecin<sup>6,24</sup>. All these peptides maintain an extended helix when in contact with liposomes, indicating a possible correlation between this conformation and the interaction with bacterial membranes<sup>5</sup>.

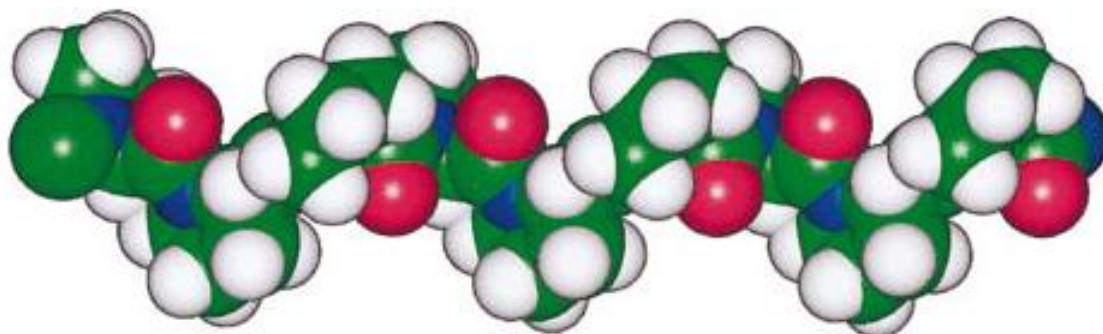


**Fig. 37:** A space-filling model of a polyproline helix. Green represents carbon atoms, red oxygen, blue nitrogen and white hydrogen<sup>18</sup>.

Indeed, the PP-II helix could be the structural basis for pro-AMPs that target and bind to specific intracellular molecular targets. Specifically, the ability of proline to establish rapid and strong interactions that are not highly specific<sup>25</sup> is due to, firstly, the restricted mobility of proline, which favours the binding. Secondly, proline binds well to other planar hydrophobic surfaces such as benzenic rings since is characterized by a flat rigid hydrophobic surface. Finally, the effect of the amide bond preceding the proline in a peptide causes proline to be a strong hydrogen bond acceptor<sup>18,25</sup>.

### 1.3 Intracellular activity

Proline-rich AMPs are mainly active towards Gram-negative bacteria<sup>5,6,8</sup>. They kill bacteria through a bacteriostatic rather than a membrano-lytic mechanism. Several studies have suggested that the main intracellular target of the insect pro-rich peptides pyrrococin, drosocin and apidaecin is the 70-kDa bacterial heat shock protein DnaK<sup>5,26,27</sup> (see Fig. 38). This interaction could happen either through an occupation of the peptide-binding pocket by the pro-rich AMP causing inhibition of the chaperone function, i.e. assisted protein folding<sup>26</sup>, or through binding to the DnaK substrate molecule. This would impede the main activity of DnaK in the refolding process of misfolded proteins and to act as an ATPase<sup>6</sup>.

Inhibition of DnaK appears to be stereo specific since studies involving both enantiomers of pyrrococin revealed the inability of the *D*-enantiomer to inhibit the activity of DnaK<sup>6</sup>. This specific binding to DnaK could be a general

mechanism as it has been identified also for the mammalian Pr-AMPs, PR-39 and Bac7(1-35)<sup>5</sup>. Interestingly, the effect of the Bac7 (1-35) peptide is a function of the peptide concentration<sup>28</sup> (Fig. 38). At concentrations close to the MIC value only the *L*-enantiomers caused cellular death via a bacteriostatic mechanism, however at concentrations well above the minimum inhibitory concentration (MIC) value, both the *D*- and *L*- enantiomers caused the cell death by lysis of the membrane<sup>28</sup>. It is important to note that DnaK might not be the only target for Pr-AMPs since DnaK-deficient *E. coli* strains were observed to be susceptible to Bac7(1-35)<sup>5</sup>.

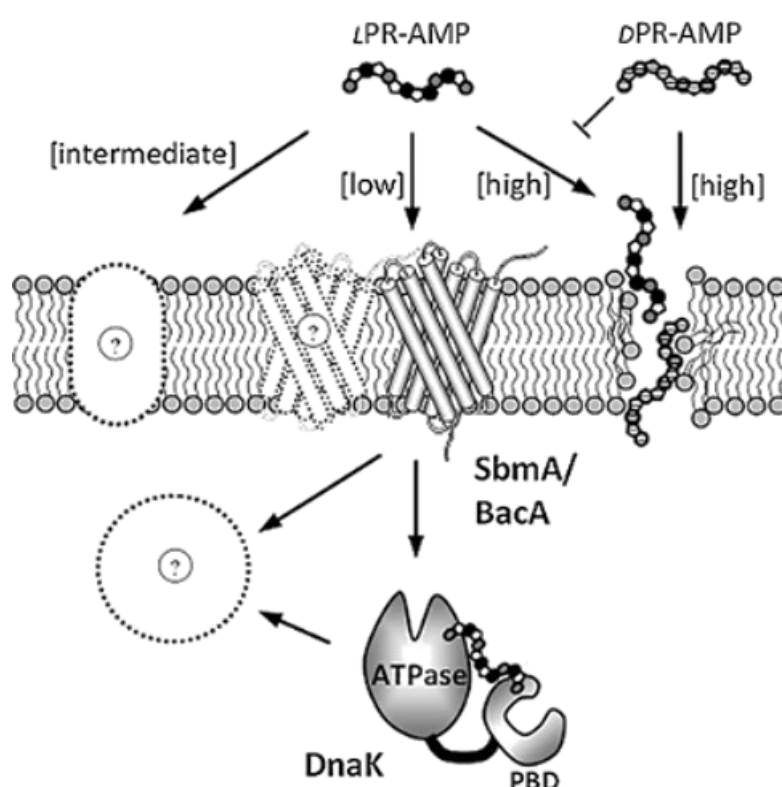


**Fig. 38:** A putative model of the mechanism of action for mammalian and insect Pr-rich AMPs. At lower concentrations, all the *L*-Pr-rich AMPs are incorporated into the bacterial cytosol by a transport system involving the membrane protein SbmA, an ABC transporter. BacA is a homologue of SbmA and it is present in some alphaproteobacteria. At very high concentrations, both *L*- and *D*-stereoisomers of Pr-rich AMPs instead are able to penetrate into the cell, killing it by disrupting the membrane. Possible other transporters might be involved in the translocation of these peptides at intermediate concentrations. Once in the cytosol, Pr-rich AMPs bind to the bacterial chaperone DnaK, but they could also target other intracellular components<sup>5</sup>.

In addition to their antimicrobial activity, some pro-rich AMPs also have immunomodulatory functions that contribute to host defence<sup>5</sup>. For instance, PR-39 also has roles in the regulation of the expression of cell surface proteoglycans, in the induction of chemotaxis of neutrophils and in promoting angiogenesis<sup>29</sup>. Immunomodulatory activity was also observed for apidaecin peptides in the presence of human immune cells. At low concentrations of apidaecins, partial antagonized LPS-stimulatory effects on both macrophages and monocytes were observed, while at higher concentrations of apidaecin, pro-inflammatory and pro-immune functions of macrophages were stimulated<sup>30</sup>.

### 1.3.1 Internalization

In order to reach cytosolic targets of Gram-negative bacteria, the proline-rich peptides must transit through a cellular envelope, which consists of an outer (OM) and inner (IM) membrane separated by the periplasmic space. It has been suggested that the initial passage through the OM is non-specific but driven by electrostatic interaction between these cationic peptides and the anionic membrane<sup>6</sup>. However, Dutta et al. suggested that apidaecin molecules form ordered oligomers to facilitate entry through the OM in a non-stereospecific manner<sup>24</sup>.

Once the proline-rich peptide has entered the periplasmic space, it is thought to pass across the cytosol bound to SbmA, an inner membrane protein that is part of an ABC transporter system<sup>31</sup>. This binding to the transporter has been suggested to be stereospecific, since *D*-enantiomers of Pro-rich AMPs show lower activity than *L*-peptides towards Gram-negative bacteria<sup>5</sup>. However, this model does not exclude other mechanisms of internalization since some peptides such as apidaecin HbIb<sup>24</sup> and Bac7 (1-35)<sup>28</sup> can act via a membrano-lytic mechanism when their concentration is equal to or above 50  $\mu$ M.

In some cases, proline-rich AMPs also exhibit the ability to be internalized by mammalian cells via an undisruptive, energy- and temperature-dependent process. This most probably involves both macropinocytosis (an endocytic process) and direct membrane translocation<sup>5</sup>, as observed with Bac7 (1-35)<sup>32</sup> and apidaecin HbIb<sup>30,33</sup>.

## 1.4 Applications for Pr-rich AMPs

Pr-rich AMPs display two interrelated potential applications, as antimicrobial peptides or as drug-delivery vectors<sup>5,8,34</sup>.

In the search for new antibiotics, some Pr-AMPs have been tested with promising results. For example: the fragment Bac7 (1-35) was able to reduce the mortality of infected animals in a mouse model of typhoid fever<sup>35</sup>; and apidaecin 14, in combination with other AMPs, proved to be a potential drug against protozoa *Trypanosoma cruzi*, which causes Chagas disease<sup>36</sup>.

As previously mentioned, Pr-rich AMPs can be considered as cell penetrating peptides (CPPs), and thus be used as drug-delivery vectors, because of their ability to cross the bacterial membrane in a selective and non-lytic manner. Furthermore, Pr-rich AMPs display low toxicity towards eukaryotic cells and can also translocate the membrane and enter the cytosol. This translocation seems to be enhanced by the presence of arginine residue in the peptide sequence, e.g. HbIb apidaecins containing additional arginine residues in the N-terminal region show higher antimicrobial activity<sup>37</sup>. Similarly, the influence of arginine on the membrane translocation process was studied for the Bac7 peptide lacking residues 1-4 (RRIR) which lost the ability to enter mammalian cells<sup>32</sup>.

Thus, Pr-AMPs represent a novel approach for the development of anti-infective drugs, but, like every natural peptide, they typically have a low serum stability and they are rapidly excreted through the liver and the kidneys<sup>5,33</sup>. This has led to a number of strategies to improve their activity in vivo. For example, by substitution with non-natural amino acids (i.e. peptoid residues, D-amino acid,  $\beta$ -amino acids), backbone modifications and glycosylation<sup>33</sup>. So far, only few examples have been successful in improving stability without affecting the antimicrobial and cell-penetrating properties. A good optimization example is the peptides derived from the pyrrhocoricin sequence, which give a high stability and low toxicity towards mice while keeping their functionality and cell-penetrating ability<sup>38</sup>. Another example is a derivative of apidaecin 1b, Api137, containing the *N,N,N',N'*-tetramethylguanidino group at the N-

terminus and L-ornithine (instead of glycine) at position 1. These modifications improved resistance to proteolysis, yet kept the antimicrobial activity intact<sup>39</sup>.

## 1.5 General outcomes for the Pr-AMPs investigated here

In general, Pr-AMPs exert their antibacterial action targeting intracellular components by translocating into the cytosol without damaging the membrane. The absence of any membrano-lytic action and the interaction with an intracellular target were confirmed for the proline-rich peptides apidaecins 1a and 1b, Api88 and peptides 10, 11. Both these studies have been published and are included in this chapter. Indeed, in all three papers the *in vitro* studies using QCM were undertaken in order to confirm the bacteriostatic action of these peptides observed *in vivo* and to give a better mechanistic understanding of the interactions using bacterial mimetic membranes.

In the first paper, the interactions between biomimetic membranes and the two isoforms of apidaecin 1a and 1b were assessed *in vitro* by using QCM and dye-filled liposome leakage studies and *in vivo* by ONPG-assay. Both *in vitro* methods confirmed the absence of lytic action by these two peptides.

In the second paper, the antimicrobial activity of an optimized apidaecin 1b peptide, Api88, was successfully tested against some Gram-negative bacteria strains, showing improved activity. In this work, the QCM experiments again confirmed the absence of any membrano-lytic activity by Api88.

Finally, the third paper investigates the antimicrobial activity of a novel Pr-rich AMP, oncocin (peptide 10) and its derivate, peptide 11. The interaction of these two peptides towards artificial bacterial membranes was investigated using QCM and compared. Once again, the QCM results confirmed that these two peptides were able to kill bacteria without damaging the artificial membrane.

## **2 Paper 3:**

### **2.1 Cell Penetrating Apidaecin Peptide Interactions with Biomimetic Phospholipid Membranes**

Monash University

**Declaration for Paper 3**

Declaration by candidate

In the case of Paper 3, the nature and extent of my contribution to the work was the following:

Nature of contribution	Extent of contribution (%)
Design and performance of QCM-D experiments, data analysis, contribution to manuscript preparation and review	40%

The following co-authors contributed to the work. If co-authors are students at Monash University, the extent of their contribution in percentage terms must be stated:

Name	Nature of contribution	Extent of contribution (%) for student co-authors only
Patricia Czihal	Dye leakage, peptide synthesis, QCM-D experiments, data analysis	
Monique Richter	Antibacterial activity, data analysis	
Ralf Hoffmann	Key ideas, manuscript preparation and review	
Adam Mechler	Key ideas, manuscript preparation and review	
Lisandra L. Martin *	Key ideas, manuscript preparation and review	

The undersigned hereby certify that the above declaration correctly reflects the nature and extent of the candidate's and co-authors' contributions to this work\*.

Candidate's Signature

Date

Main Supervisor's Signature

Date

## ***Chapter 4***

\*Note: Where the responsible author is not the candidate's main supervisor, the main supervisor should consult with the responsible author to agree on the respective contributions of the authors.

## Cell Penetrating Apidaecin Peptide Interactions with Biomimetic Phospholipid Membranes

Stefania Piantavigna · Patricia Czihal · Adam Mechler · Monique Richter · Ralf Hoffmann · Lisandra L. Martin

Accepted: 12 March 2009  
© Springer Science+Business Media, LLC 2009

**Abstract** Apidaecin peptides from *Apis mellifera* hemolymph are believed to attack intracellular bacterial targets. Our in vivo results for apidaecins 1a and 1b confirm that bacterial activity is non-lytic, however, the manner in which these peptides pass through the cell membrane to exert this activity is unknown. These data are combined with fluorescence (dye leakage) and quartz crystal microbalance studies to investigate the membrane interaction for these two wild-type peptides. It was found that the peptides penetrate the membrane in a trans-membrane manner. The amount of peptide uptake by the membrane is proportional to the concentration of the peptide, however, this appears to be a dynamic equilibrium which can be almost completely reversed by addition of buffer medium. Interestingly, a small residual mass remains within the membrane and the amount of peptide remaining in the membrane is a function of the buffer-salt concentration viz. in high salt, the residual peptide mass remaining is small whereas at low salt concentration, a larger mass of peptide remains bound. These results support a direct membrane penetration mechanism by the wild type apidaecins 1a and 1b. In both cases the peptide-membrane interaction has a negligible effect on the membrane, although, in high salt a permanent change in the membrane does occur at the highest peptide concentration which does not recover following peptide removal.

Stefania Piantavigna and Patricia Czihal contributed equally to this article.

S. Piantavigna · A. Mechler · L. L. Martin (✉)  
School of Chemistry, Monash University, Clayton,  
VIC 3800, Australia  
e-mail: [REDACTED]

P. Czihal · M. Richter · R. Hoffmann  
Institute of Bioanalytical Chemistry, Leipzig University,  
04103 Leipzig, Germany

**Keywords** Antimicrobial peptides · Insect · Peptide synthesis · Proline-rich peptides · Quartz crystal microbalance

### Abbreviations

MPA	Mercaptopropionic acid
SAM	Self-assembled monolayer
MIC	Minimal inhibitory concentration
TSB	Tryptic soy broth
QCM	Quartz crystal microbalance
TFA	Trifluoroacetic acid
ONPG	<i>o</i> -nitrophenyl- $\beta$ -galactoside
DMPC	1,2-dimyristoyl- <i>sn</i> -glycero-3-(phosphocholine)
DMPG	1,2-dimyristoyl- <i>sn</i> -glycero-3-[phospho-rac-(1-glycerol)] sodium salt
PBS	Phosphate buffered saline
DPPC	Dipalmitoylphosphatidylcholine
SUVs	Small unilamellar vesicles
Tris-HCl	Tris(hydroxymethyl)aminomethane hydrochloride
$\Delta f$	Frequency change
$\Delta D$	Dissipation change
EDTA	Ethylenediaminetetraacetic acid
RP-HPLC	Reverse phase-high performance liquid chromatography

### Introduction

The number of known drug resistant microbes is on the rise and currently multiple antibiotic-resistant pathogens constitute 50–60% of all bacterial infection-related hospitalisations (Tomasz 1994). Whereas in the 1970s resistant

Gram-negative bacteria were dominant, in the past decade multi-drug resistant Gram-positive strains appeared as well (Moellering 1998). The current, rapid emergence of resistant strains involves both Gram-positive and Gram-negative pathogens (Volles and Branan 2008). Thus, one of the most serious public health issues is the targeted development of antibacterial agents that act via a radically different mechanism compared to known antibiotics. The current scientific and commercial interest has turned towards antimicrobial peptides found in organisms, such as insects. These have highly specific activity towards microbes, thus are potential drug candidates.

Antimicrobial peptides, ranging in size from 13 to more than a 100 amino acid residues, have been isolated from microbes, plants and animals (Boman 1995). While serving the same purpose, an enormous variety of wild type peptides are known which are equally diverse in their mode of activity (Barra et al. 1998). In general terms, peptides might act via membrane disruption or by traversing the membrane to attack intracellular targets (Gallo and Huttner 1998). Most studies of antimicrobial activity focus on non-specific membrane disrupting peptides, such as melittin (Shai 1995). However, these peptides, which open holes in bacterial membranes, are often toxic to eukaryotic cells at higher concentrations, and are therefore unsuitable as systemic drugs. This is where the more specific cell penetrating peptides offer promise, with the potential to attack specific cell types such as pathogenic bacteria and fungi or even tumors. Some native cationic antibacterial peptides have already been developed into topical and systemic drugs and have reached clinical trials (Hancock 2000), however, much needs to be done before peptides can be designed to treat specific infections and/or diseases. In particular, beyond the basic models there is a general lack of understanding of the actual molecular mechanisms that implement the antimicrobial activity, especially in case of non-lytic cell penetrating peptides.

Apidaecins are 18–20 residue-long, proline-rich peptides with highly conserved PRPPHPRI/L C-termini (Casteels et al. 1989), isolated from honey bee and are lethal to bacteria (Otvos 2002). The apidaecins do not lyse erythrocytes, unlike many antimicrobial peptides, and are non-toxic to monkey kidney-originated COS-7 cells that have regular nuclei (Castle et al. 1999). A further interesting aspect to the activity of apidaecins is that their activity decreases at high ionic strength (Casteels and Tempst 1994). Thus it has long been accepted that the likely mechanism of action was via an intracellular target. It was suggested that the N- and C-terminal sequences of apidaecin function as two independent modules, one being responsible for entry into bacterial cells and the second one for binding to, and inhibiting bacterial DnaK (Czihal and Hoffmann 2009; Li et al. 2006; Kragol et al. 2001).

However, this mechanism has not been proven and also the mode of interaction for these peptides with the cell membrane is unknown.

Here we present a comprehensive study of the antibacterial action of the two wild type apidaecins 1a and 1b. We describe the membrane penetration of the peptides using quartz crystal microbalance (QCM) to measure the mass (amount) of peptide binding to a supported membrane layer together with the change in energy dissipation of this layer, which correlates to structural changes that occur within the peptide-membrane layer. These data together with other *in vitro* biophysical studies of liposome dye leakage measurements, as well as *in vivo* microbiological activity for these peptides, establish the primary mode of membrane interaction for these apidaecin peptides.

## Materials and Methods

### Buffers

Sodium chloride [Ultra,  $\geq 99.5\%$  (AT)], potassium phosphate monobasic (ACS reagent,  $\geq 99\%$ ), potassium phosphate dibasic (ACS reagent,  $\geq 99\%$ ) were all purchased from Sigma–Aldrich (Castle Hill, NSW, Australia). Ultrapure water with a resistivity of 18.2 M $\Omega$  cm was used (Sartorius).

### Peptide Synthesis

Apidaecins 1a and 1b (Table 1) were synthesized in a 25  $\mu$ mol-scale on the multiple synthesizer SYRO2000 (MultiSynTech GmbH, Witten, Germany) using the Fmoc/Bu-strategy with *in situ* activation with di-isopropyl carbodiimide in the presence of 1-hydroxy-benzotriazole (DIC/HOBt; Singer et al. 2005). All peptides were cleaved with TFA and purified by RP-HPLC using a linear acetonitrile gradient in the presence of 0.1% TFA. The purity of the peptides was judged by analytical RP-HPLC using a Jupiter C<sub>18</sub>-column (Phenomenex Inc., Torrance, USA) and their sequence was confirmed by matrix-assisted laser desorption/ionization time-of-flight mass spectrometry

**Table 1** Antimicrobial activity for apidaecins 1a and 1b were determined in a microdilution assay using either 1 or 3% TSB concentration resembling “low salt” and “high salt” concentrations

Peptide	Sequence	Antimicrobial activity, MIC values, ( $\mu$ M)	
		1% TSB	3% TSB
Apidaecin 1a	GNNRPVYIPQRPPHPRI-OH	0.2	8
Apidaecin 1b	GNNRPVYIPQRPPHPRL-OH	0.2	15

(MALDI-TOF-MS; 4700 proteomic analyzer; Applied Biosystems GmbH, Darmstadt, Germany).

#### Antibacterial Activity

The minimal inhibitory concentration (MIC) was determined in sterile 96-well microtiter plates (Greiner Bio-One GmbH, Germany) with an end volume of 100  $\mu$ l. The peptides were diluted in distilled water followed by a two-fold dilution in 1 or 3% TSB (Tryptic soy broth) starting from a concentration of 60.7  $\mu$ M. An overnight culture of *Escherichia coli* (*E. coli*) bacteria (strain BL21 AI) was diluted to  $1.5 \times 10^8$  cells/ml and 50  $\mu$ l was added to each well gaining a starting cell concentration of  $7.5 \times 10^6$  cells/well. After 18 to 22 h incubation at 37°C the amount of microorganism was determined, measuring the absorbance at 595 nm by a Sunrise microtiter plate reader (Tecan AG, Munich, Germany). The MIC was defined as the lowest peptide concentration that resulted in no visible bacterial growth. All assays were done in triplicate and repeated at least once.

#### ONPG-Assay

The membrane permeability effect *in vivo* was assayed with *E. coli* ML-35. Bacteria were grown for 20 h at 37°C in TSB, diluted 100 fold and incubated again at 37°C for approximately 3 h until a cell concentration of  $2 \times 10^8$  cells/ml ( $OD_{600} = 0.8$ ) was obtained. The cell culture was stored on ice until used for the permeabilisation assay. About 700  $\mu$ l ONPG-buffer [sodium phosphate (10 mmol/l, pH 7.4), sodium chloride (100 mmol/l), *o*-nitrophenyl- $\beta$ -D-galactoside (ONPG; 1.5 mmol/l)] and 100  $\mu$ l of the bacterial culture ( $2 \times 10^7$  bacteria) were mixed in a cuvette before 200  $\mu$ l of the peptide solutions were added providing final concentrations of 0, 1, 2, 4, 8, 15 or 30  $\mu$ M. The reaction was monitored by absorption at 405 nm for 15 min.

#### Supported Membrane Preparation

1,2-dimyristoyl-*sn*-glycero-3-phosphocholine (DMPC) and 1,2-dimyristoyl-*sn*-glycero-3-[phospho-*rac*-(1-glycerol)] sodium salt (DMPG) were purchased from Avanti Polar Lipids (Alabaster, AL, USA). Chloroform (ACS Reagent,  $\geq 99.8\%$ ) and methanol (HPLC Grade,  $\geq 99.9\%$ , Riedel-de Haen, Chromosolv) were purchased from Sigma-Aldrich (Castle Hill, NSW, Australia).

Dry lipid was dissolved in chloroform (DMPC) or a chloroform/methanol mixture  $\sim 75:25$  v/v (DMPG) to create individual stock solutions. These stock solutions were then aliquoted out into test tubes in 4:1 v/v DMPC/DMPG ratio. The solvent was then evaporated under a gentle stream of  $N_2$  and vacuum desiccated overnight.

Lipids were resuspended in either “high salt” buffer: 20 mM PBS incl. 100 mM NaCl at pH 6.9 or “low salt” buffer: 10 mM PBS incl. 30 mM NaCl at pH 6.9 with slow maceration, vortexed and briefly sonicated before use. While several sources recommend it, we did not extrude the liposomes as it was shown that the extruded liposome size depends on the applied pressure rather than the extruder pore size or the flow rate (Friskken et al. 2000). As liposomes were found to evolve towards equilibrium size, distributions created via extrusion might not remain stable.

Supported membranes were deposited by slowly flushing 1 ml of the liposome solution through the QCM cell at 50  $\mu$ l/min flow. The flow was then stopped, and the cell left to equilibrate under diffusion controlled conditions. The cell was rinsed with buffer at 30 min from the start of the experiment (that is, from the introduction of the liposome solution) with 300  $\mu$ l/min flow rate.

#### Chip Cleaning and Surface Modification

Absolute ethanol (GR for analysis ACS), acetone (Technical Grade), propan-2-ol (Extra pure) and hydrogen peroxide (30%, GR for analysis ISO) were purchased from Merck (Victoria, Australia). Ammonia solution (28%, Analytical Univar Reagent) was purchased from Ajax Finechem (NSW, Australia). 3-Mercaptopropionic acid (MPA; HPLC Grade,  $\geq 99\%$ ) was purchased from Fluka, BioChimica (Buchs, Switzerland). Before assembling into the chamber, new or electrochemically cleaned QCM chips were rinsed with ethanol and dried under a gentle stream of  $N_2$  gas, after which they were placed into a 1:1:3 mixture of ammonia (28%), hydrogen peroxide (30%) and water, at  $\sim 75^\circ\text{C}$  for 15–20 min. After this, chips were thoroughly rinsed with ultra-pure water and ethanol, then dried and immediately assembled into the QCM chamber ready to use. The gold surface of the chip was treated with MPA *ex situ* which provided a self-assembled monolayer (SAM) in approx. 20 min.

#### QCM Experiments

QCM measurements were performed with the Q-SENSE E4 system (Q-SENSE, Sweden) using the method developed by the authors (Mechler et al. 2006, 2007, 2009; Fleming et al. 2008). The sensor crystals used were 5 MHz, AT-cut, polished quartz discs (chips) with gold electrodes evaporated on both sides (Q-SENSE). The change in resonance frequency and energy dissipation were measured simultaneously at four odd harmonics (15, 25, 35, 45 MHz). In the following, the fundamental frequency of the crystal is called the 1st harmonic. The values reported throughout for  $\Delta f$  (frequency change) and  $\Delta D$  (dissipation change) are measured at the 9th harmonic (45 MHz), unless otherwise

stated. The working temperature was 19°C. The raw data was analysed using QTools (Q-SENSE) and Origin 7.5 and 8.0 (OriginLab, USA) software.

#### Dye Leakage Assay

Homogeneous small unilamellar vesicles (SUVs) were prepared as described in the literature (Rex 1996). Briefly, 500 µl DMPC solution (3.4 mg/ml CHCl<sub>3</sub>) and 240 µl DMPG solution (0.76 mg/ml in a mixture of chloroform and methanol, 3:2 by vol.) were mixed in a test tube and evaporated slowly under gentle rotation in a nitrogen stream and afterwards placed under vacuum over night. The thin lipid film was then dissolved by gentle shaking in 2 ml of either “high-salt” buffer (10 mM Tris-HCl, pH 7.4; 1 mM EDTA; 100 mM NaCl) or “low-salt” buffer (threefold dilution of “high-salt” buffer in water) both containing 25 mM 5(6)-carboxyfluorescein. The sample was vortexed for 5 min and sonicated for 7 min (157.5 W). The precipitate was removed by centrifugation and the external fluorescein was removed by gel filtration (Sephadex G-25 M, GE Healthcare, Munich, Germany). The fraction containing the 75:25 v/v DMPC/DMPG liposomes with internal fluorescein was identified by the increase of the fluorescence signal after addition of Triton X-100.

The fluorescein loaded SUVs (50 µl) were added to a 96-well polypropylene microtiter plate before the peptide solutions were added. The fluorescence signal was recorded at 535 nm (Excitation at 485 nm) after 5 min. The negative and positive controls were water and melittin, respectively. A Triton X-100 solution was added to each well at the end of the experiment to confirm the expected release of fluorescein.

### Results and Discussion

Apidaecins 1a and 1b were obtained in high yields and in good purity after solid phase peptide synthesis and RP-HPLC purification. There is only one amino acid difference between these peptides (Table 1) viz. the terminal amino acid is isoleucine (for 1a) and leucine (for 1b). Both peptides were shown to be active against bacteria with MIC values of ~0.25 µM against *E. coli* BL21 at 1% TSB (Table 1), which corresponds well to the literature (Casteels and Tempst 1994). At 3% TSB, which is commonly used to test standard antibiotics and corresponds to physiological salt conditions, the MIC values decreased about 30-fold to 60-fold (Table 1). The influence of salt is assumed to reduce ionic interaction between the positively charged peptides and the negatively charged bacterial membrane and thus prevent lytic effects (Kandasamy and Larson 2006). For proline-rich peptides, however, the

explanation might be more difficult, as they are thought to block intracellular target proteins, such as heat shock protein DnaK, and do not appear to act through lysis of the membrane. As the inhibition target itself is expected to be independent of the external salt concentration, the salt must affect either the initial ionic interaction of the peptide with the outer membrane of Gram-negative bacteria or influence how the peptide traverses through the membrane. These effects were studied on DMPC:DMPG membranes as a bacterial biomimetic membrane both by QCM and a dye leakage test.

#### In Vivo Measurements of Cell Disruption

To further confirm the non-lytic manner of membrane penetration observed for the apidaecin peptides *in vivo*, an ONPG assay was performed with *E. coli* ML-35. This assay detects the pore forming effects of antibacterial peptides by the enzymatic activity of intracellular beta-galactosidase that produces ortho-nitrophenol from ONPG, which is detected optically. Apidaecin 1a peptide over the concentration range 1–30 µM (4–100 times higher than the MIC values) did not cause further damage to the bacterial membranes than the control (buffer), assessed as ~0.5% dye formation compared to the Triton X-100 reference that was set to 100% (data not shown). Although the apidaecin 1b was not tested in this assay, together with the recently available permeation data (Dutta et al. 2008) these peptides can be considered acting in a non-lytic manner with membranes.

#### Membrane Interactions of Apidaecins by QCM

##### *Peptide Uptake as a Function of Concentration*

The interaction of apidaecins 1a and 1b on supported DMPC:DMPG 4:1 (bacterial model) membranes was measured using QCM. These data were obtained using either “high salt,” resembling physiological conditions or “low salt” buffers, corresponding to the *in vitro* conditions of the antibacterial assay, which change the interaction of the peptide with the membrane (Fig. 1).

The QCM  $\Delta f$ -t traces for both apidaecins 1a and 1b show that there is an uptake of peptide into the supported membrane, and that this uptake is concentration dependent in an approximately linear manner. The concentration of the buffer-salt solution has no qualitative effect on this concentration dependent peptide uptake, however, the amount of peptide ingress into the membrane increases at low salt, more for 1b than 1a.

It is also visible that the peptide uptake is reversible: removing peptide from the solution results in peptide diffusion out of the membrane, although a small *residual*

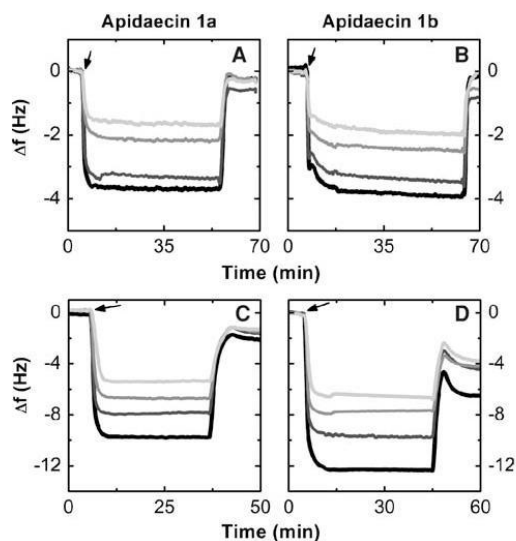


**Fig. 1** Apidaecins 1a and 1b uptake on DMPC:DMPG 4:1 membrane as a function of peptide concentration (2, 5, 10 and 20  $\mu\text{M}$  peptide concentration corresponds to lightest to darkest colour). Panel A and B, are in high salt and C and D, in low salt buffers

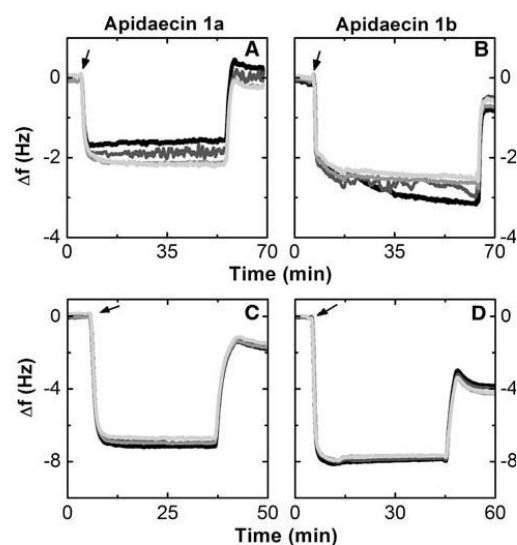


**Fig. 2** Apidaecins 1a and 1b (5  $\mu\text{M}$ ) uptake on DMPC:DMPG 4:1 membrane as observed at 3rd, 5th, 7th and 9th (lightest to darkest colour) harmonics of QCM chip resonance. Panel A and B, are in high salt and C and D, in low salt buffers. Same conditions as in Fig. 1

amount remains in all cases. The existence of this residual mass might be the result of a structural rearrangement of the peptide within the membrane as speculated by others (Dutta et al. 2008). Notably, the residual mass of peptide is greater under low salt conditions, especially in the case of 1b where it is comparable to the uptake in high salt. Thus the most significant difference between the two peptides is the higher amount of apidaecin 1b incorporated into the membrane at low salt and the higher residual mass.

#### Peptide Uptake at Different Harmonics

In order to differentiate between a membrane surface or trans-membrane interaction, the mass change on peptide incorporation was compared for a series of harmonics of the quartz crystal resonance (Mechler et al. 2007). A surface interaction would give differential response over the harmonics whereas for a trans-membrane interaction all the harmonics would respond with an equal mass change. In Fig. 2, both high and low salt cases indicate that the  $\Delta f$ -t traces for all harmonics overlap, supporting the peptide penetration as trans-membrane. That is, the apidaecins 1a and 1b predominately associate reversibly to the membrane in a trans-membrane manner. The rapid ingress into the membrane is indicated by the immediate frequency response as the peptide solution diffuses into the QCM cell. It remains within the membrane until the peptide concentration is

lowered by flushing the cell with buffer, thereby initiating peptide loss. Accordingly, peptide penetration into the membrane is an equilibrium process, suggesting that the energy for membrane penetration is low. Such a mode of action suggests that the peptides are able to transverse the membrane without first binding to the surface of the membrane.

#### $\Delta f$ - $\Delta D$ Fingerprinting and Analysis of Peptide Mechanism

Correlation of the energy dissipated into the deposit layer with the change in frequency ( $\Delta f$ - $\Delta D$ ) offers a unique opportunity to obtain a “fingerprint” for each peptide-membrane interaction and offers possible mechanistic elucidation (Mechler et al. 2009).

These  $\Delta f$ - $\Delta D$  plots for apidaecin 1a are shown in Fig. 3 for the four concentrations 2, 5, 10 and 20  $\mu\text{M}$  (top to bottom). These plots begin upon addition of the peptide at time zero in both  $\Delta f$  and  $\Delta D$  and the structural change or energy dissipation ( $\Delta D$ ) is monitored as the mass ( $\Delta f$ ) is added or removed ( $\Delta f$  decrease corresponds to added mass) (Sauerbrey 1959). Data obtained under low salt conditions (Fig. 3, right column), suggest that the energy dissipation increases only minimally upon addition of the peptide, indicating only a minor, if any, change in the membrane properties as the peptide incorporates. Removal of peptide

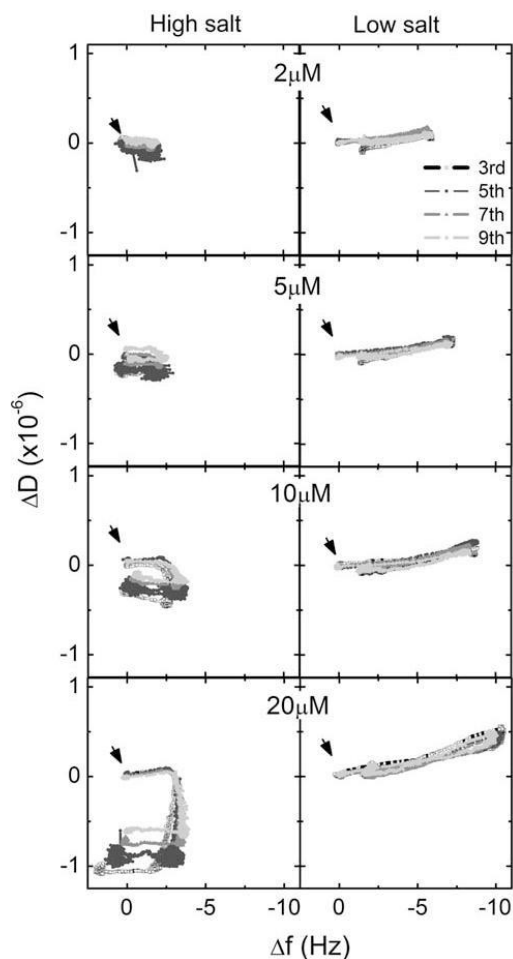


**Fig. 3** Energy dissipation ( $\Delta D$ ) vs. frequency ( $\Delta f$ ) dependence for apidaecin 1a on DMPC: DMPG 4:1 membrane. The arrow indicates the start of the experiment

by introduction of buffer indicates a full recovery of the membrane to the original dissipating value. However some residual peptide is unable to be removed ( $\sim 1.5\text{--}2$  Hz) which is both concentration and harmonic independent. Thus data collected over a range of harmonics overlap, indicating that peptide uptake is a homogeneous process over the entire cross-section of the membrane. Similar  $\Delta f$ - $\Delta D$  plots were obtained for apidaecin 1b (data not shown).

Under high salt conditions, the apidaecin 1a uptake is concentration dependent. The peptide is readily incorporated at  $2\ \mu\text{M}$ , and can be removed with no effect on the membrane ( $\Delta D \sim 0$ ). However, as the peptide concentration increases from  $5\text{--}20\ \mu\text{M}$ , the beginning of a permanent

change in the membrane can be observed i.e. penetration and removal in the  $\Delta f$ -t trace do not overlap. At  $20\ \mu\text{M}$  peptide, the permanent change is most apparent, indicated by the large change in  $\Delta D$  prior to the wash with buffer suggesting that these peptides associate in a manner which results in a permanent change in the membrane. Once again, similar data were obtained for apidaecin 1b (data not shown). Overall, the QCM results support the membrane penetration and non-lytic activity for these two peptides.

#### Dye Leakage & Fluorescent Measurements

Dye leakage experiments were performed using liposomes to explore whether any differences existed between the flat (2D) supported lipid bilayers used for QCM and the curved (3D) suspended membrane (liposomes). In a recent report of dye leakage studies with apidaecin peptides, the liposomes were prepared with zwitterionic lipids, using dipalmitoyl phosphatidyl choline (DPPC; Dutta et al. 2008), however, we used the model bacterial membrane mixture DMPC:DMPG 4:1 for dye leakage experiments in order to compare our data to the QCM studies.

Melittin was used as a positive control as it is known to act by a lytic mechanism on bacteria. Addition of melittin to the liposome released the fluorescent dye in a concentration dependent manner even at the lowest concentration of  $22\ \mu\text{M}$  (Fig. 4, squares). Under low salt conditions the relative fluorescence released was slightly larger than under high salt concentrations. Thus the effect of high salt concentration appears to be consistent with the decreased antibacterial activity of melittin in vitro i.e. with high salt. At the end of each experiment, Triton X-100 was added, which completely disrupts the remaining liposomes and thus releases the fluorescein quantitatively, giving a final increase in the signal intensity. The fact that this final increase in fluorescence was only small, indicated that most liposomes were already destroyed by melittin, consistent with the well known lytic properties.

In contrast to the melittin control, no dye leakage was observed for either apidaecin peptides up to a concentration of  $110\ \mu\text{M}$  ( $\sim 200\ \mu\text{g/ml}$ , Fig. 4, circles and triangles) confirming that no membrane disruption occurred even at 400 fold higher concentrations than the MIC-values. These data are similar to those obtained for the DPPC membranes, where only a weak lytic effect was obtained after 3 h at  $100\ \mu\text{M}$  of apidaecin (Dutta et al. 2008). Interestingly, we observed a notable decrease of the fluorescence intensity with increasing external peptide concentration, which might be attributed to: (1) shrinkage of the liposome, although the 20% size reduction seems unlikely; (2) a thickening of the liposome wall, although the QCM data do not support this; (3) change of the optical properties of the membrane by the interdigitation of the peptides with the

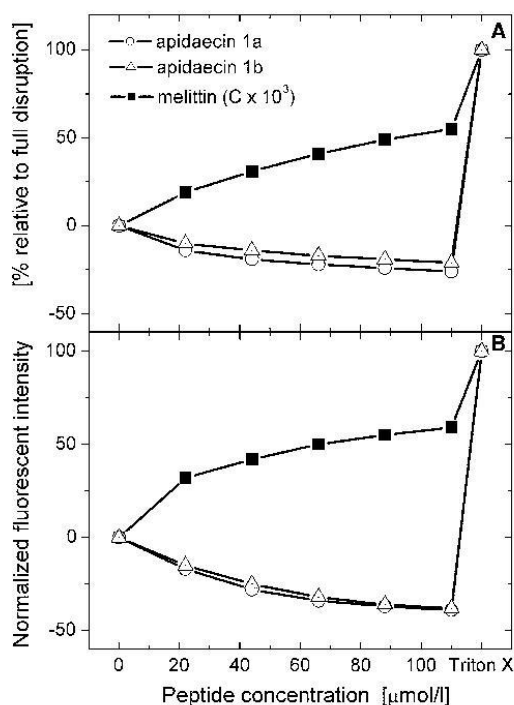


**Fig. 4** Dye leakage assay for small unilamellar vesicles (SUV) containing 5(6)-carboxyfluorescein in the presence of melittin (squares), apidaecin 1a (circles) and apidaecin 1b (triangles). Panel A shows the experiments in high salt and Panel B, in low salt conditions. Shown are the relative fluorescence intensities for different peptide concentrations with the initial fluorescence (no peptide) set to zero. Triton X-100 was used as control to confirm the total fluorescent dye concentration in the liposomes which was set to 100

membrane, however, this would cause liposome swelling, leading to an intensity increase. Thus the cause in the signal reduction is not clear, although the peptide entering the vesicles could be interacting with the dye itself causing the quenching. Clearly, the peptides could easily enter the bacterial-mimetic membranes, under both high salt and low salt conditions. The only significant difference between the salt dependent responses observed for the apidaecin peptides was the effect of dilution of the dye signal which was greater under low salt conditions. This observation is in good agreement with the QCM data and supports the observation that more peptide enters the vesicle (or membrane) under low salt conditions. Thus the lower concentration of apidaecins penetrating into the interior of the liposomes could also explain their reduced antibacterial activity *in vitro* at high salt concentrations.

#### Concluding Remarks

We have used a combination of *in vivo* and *in vitro* methods to show that apidaecin 1a and 1b penetrates the bacterial membranes in a non-lytic manner. *In vitro* dye leakage and *in vivo* ONPG assays confirmed that the peptides have no lytic activity. Uptake of the peptide by a biomimetic membrane was explored using QCM which showed they are capable of rapidly transversing bacterial type (DMPC:DMPG) phospholipid membranes without disrupting the membrane integrity. The effect was almost reversible for low concentrations i.e. 2–10  $\mu\text{M}$ . Furthermore, the salt concentration influenced the amount (mass) of peptide penetrating into the membrane with more mass observed at low buffer salt concentration. This is consistent with the observation that the peptides exhibit higher antimicrobial activity in low salt medium. There were only small differences between the two peptides observed in this study although the  $\Delta f$ - $\Delta D$  plots for apidaecin 1a revealed an irreversible change in the membrane at the highest concentration of peptide investigated (20  $\mu\text{M}$ ).

**Acknowledgments** We acknowledge the financial support from the Australian Research Council Discovery Grant DP0662816 to LLM and AM, Monash Fellowship to AM and the support of Mr Paul Barrett, ATA Scientific. This work was supported by the European Fund for Regional Structure Development (EFRE, European Union and Free State Saxony) to RH.

#### References

- Barra D, Simmaco M, Boman HG (1998) Gene encoded peptide antibiotics and innate immunity. Do 'animalcules' have defence budgets? FEBS Lett 430:130–134
- Boman HG (1995) Peptide antibiotics and their role in innate immunity. Annu Rev Immunol 13:61–92
- Casteels P, Tempst P (1994) Apidaecin-type peptide antibiotics function through a non-poreforming mechanism involving stereospecificity. Biochem Biophys Res Commun 199:339–345
- Casteels P, Ampe C, Jacobs F, Vaeck M, Tempst P (1989) Apidaecins: antibacterial peptides from honeybees. EMBO J 8:2387–2391
- Castle M, Nazarian A, Yi SS, Tempst P (1999) Lethal effects of apidaecin on *Escherichia coli* involve sequential molecular interactions with diverse targets. J Biol Chem 274:32555–32564
- Czihal P, Hoffmann R (2009) Mapping of apidaecin regions relevant for antimicrobial activity and bacterial internalization. Int J Pept Res Ther (this issue)
- Dutta RC, Naggal S, Salunke DM (2008) Functional mapping of apidaecin through secondary structure correlation. Int J Biochem Cell Biol 40:1005–1015
- Fleming BD, Praporski S, Bond AM, Martin LL (2008) Electrochemical quartz crystal microbalance study of azurin adsorption onto an alkanethiol self-assembled monolayer on gold. Langmuir 24:323–327
- Friskén BJ, Asman C, Patten PJ (2000) Studies of vesicle extrusion. Langmuir 16:928–933

- Gallo RL, Huttner KM (1998) Antimicrobial peptides: an emerging concept in cutaneous biology. *J Invest Dermatol* 111:739–743
- Hancock REW (2000) Cationic antimicrobial peptides: towards clinical applications. *Expert Opin Invest Drugs* 9:1723–1729
- Kandasamy SK, Larson RG (2006) Effect of salt on the interactions of antimicrobial peptides with zwitterionic lipid bilayers. *Biochim Biophys Acta* 1758:1274–1284
- Kragol G, Lovas S, Varadi G, Condie BA, Hoffmann R, Otvos L Jr (2001) The antibacterial peptide pyrrolicorin inhibits the ATPase actions of DnaK and prevents chaperone assisted protein folding. *Biochemistry* 40:3016–3026
- Li W-F, Ma G-X, Zhou X-X (2006) Apidaecin-type peptides: biodiversity, structure-function relationships and mode of action. *Peptides* 27:2350–2359
- Mechler A, Nawaratna G, Aguilar M-I, Martin LL (2006) A study of protein electrochemistry on a supported membrane electrode. *Int J Pept Res Therapeutics* 12(3):217–224
- Mechler A, Praporski S, Atmurt K, Boland M, Separovic F, Martin LL (2007) Specific and selective peptide-membrane interactions revealed using quartz crystal microbalance. *Biophys J* 93:3907–3916
- Mechler A, Piantavigna S, Praporski S, Heaton SM, Hall KN, Aguilar M-I, Martin LL (2009) Structure and homogeneity of pseudo-physiological phospholipid bilayers and their deposition characteristics on carboxylic acid terminated self-assembled monolayers. *Biomaterials* 30(4):682–689
- Moellering RC Jr (1998) Introduction: problems with antimicrobial resistance in gram-positive cocci. *Clin Infect Dis* 26:1177–1178
- Otvos L (2002) The short proline-rich antibacterial peptide family. *Cell Mol Life Sci* 59:1138–1150
- Rex S (1996) Pore formation induced by the peptide melittin in different lipid vesicle membranes. *Biophys Chem* 58:75–85
- Sauerbrey G (1959) Verwendung von Schwingquarzen zur Wägung dünner Schichten und zur Mikrowägung. *Zeitschrift für Physik* 155:206–222
- Shai Y (1995) Molecular recognition between membrane-spanning polypeptides. *Trends Biochem Sci* 20:460–464
- Singer D, Volke D, Hoffmann R (2005) Characterization of phosphorylation dependent antibodies to study the phosphorylation status of the Tau protein. *Int J Pept Res Ther* 11:279–289
- Tomasz A (1994) Multiple-antibiotic-resistant pathogenic bacteria. *N Engl J Med* 330:1247–1251
- Volles DF, Branan TN (2008) Antibiotics in intensive care unit: focus on agents for resistant pathogens. *Emerg Med Clin N Am* 26:813–834

### **3 Paper 4:**

#### **3.1 Api88 Is a Novel Antibacterial Designer Peptide To Treat Systemic Infections with Multidrug-Resistant Gram-Negative Pathogens.**

Monash University

**Declaration for Paper 4**

Declaration by candidate

In the case of Paper 4, the nature and extent of my contribution to the work was the following:

Nature of contribution	Extent of contribution (%)
Design and performance of QCM-D experiments, data analysis, contribution to manuscript preparation and review	10%

The following co-authors contributed to the work. If co-authors are students at Monash University, the extent of their contribution in percentage terms must be stated:

Name	Nature of contribution	Extent of contribution (%) for student co-authors only
<b>Patricia Czihal</b>	Design and performance experiments, data analysis, manuscript preparation and review	
<b>Daniel Knappe</b>	Design and performance experiments, data analysis, manuscript preparation and review	
<b>Stefanie Fritsche</b>	Experiments, manuscript preparation and review	
<b>Michael Zahn</b>	Experiments, manuscript preparation and review	
<b>Nicole Berthold</b>	Experiments, manuscript preparation and review	
<b>Uwe Müller</b>	Experiments, manuscript preparation and review	
<b>Sylvia Van Dorpe</b>	Experiments, manuscript preparation and review	
<b>Nicole Herth</b>	Experiments, manuscript preparation and review	

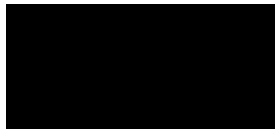
<b>Annegret Binas</b>	Experiments, manuscript preparation and review	
<b>Gabriele Köhler</b>	Experiments, manuscript preparation and review	
<b>Bart De Spiegeleer</b>	Experiments, manuscript preparation and review	
<b>Lisandra L. Martin</b>	Manuscript preparation and review	
<b>Oliver Nolte</b>	Manuscript preparation and review	
<b>Norbert Sträter</b>	Manuscript preparation and review	
<b>Gottfried Alber</b>	Manuscript preparation and review	
<b>Ralf Hoffmann*</b>	Key ideas, manuscript preparation and review	

The undersigned hereby certify that the above declaration correctly reflects the nature and extent of the candidate's and co-authors' contributions to this work\*.

Candidate's  
Signature

	Date
--	------

Main Supervisor's  
Signature

	Date
---	------

\*Note: Where the responsible author is not the candidate's main supervisor, the main supervisor should consult with the responsible author to agree on the respective contributions of the authors.

## Api88 Is a Novel Antibacterial Designer Peptide To Treat Systemic Infections with Multidrug-Resistant Gram-Negative Pathogens

Patricia Czihal,<sup>†,‡</sup> Daniel Knappe,<sup>†,‡</sup> Stefanie Fritsche,<sup>‡,§</sup> Michael Zahn,<sup>†,‡</sup> Nicole Berthold,<sup>†,‡</sup> Stefania Piantavigna,<sup>||</sup> Uwe Müller,<sup>‡,§</sup> Sylvia Van Dorpe,<sup>⊥</sup> Nicole Herth,<sup>†,‡</sup> Annegret Binas,<sup>¶</sup> Gabriele Köhler,<sup>†</sup> Bart De Spiegeleer,<sup>⊥</sup> Lisandra L. Martin,<sup>||</sup> Oliver Nolte,<sup>¶</sup> Norbert Sträter,<sup>†,‡</sup> Gottfried Alber,<sup>‡,§</sup> and Ralf Hoffmann<sup>\*,†,‡</sup>

<sup>†</sup>Institute of Bioanalytical Chemistry, Faculty of Chemistry and Mineralogy, <sup>‡</sup>Center for Biotechnology and Biomedicine, and <sup>§</sup>Institute of Immunology, College of Veterinary Medicine, Universität Leipzig, Leipzig, Germany

<sup>||</sup>School of Chemistry, Monash University, Clayton, Victoria, Australia

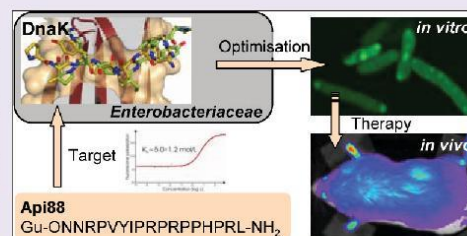
<sup>⊥</sup>Drug Quality and Registration (DruQuaR) Group, Faculty of Pharmaceutical Sciences, Ghent University, Ghent, Belgium

<sup>¶</sup>AiCuris GmbH & Co KG, Building 302, Wuppertal, Germany

<sup>\*</sup>Institute of Pathology, University Hospital Münster, Münster, Germany

### Supporting Information

**ABSTRACT:** The emergence of multiple-drug-resistant (MDR) bacterial pathogens in hospitals (nosocomial infections) presents a global threat of growing importance, especially for Gram-negative bacteria with extended spectrum  $\beta$ -lactamase (ESBL) or the novel New Delhi metallo- $\beta$ -lactamase 1 (NDM-1) resistance. Starting from the antibacterial peptide apidaecin 1b, we have optimized the sequence to treat systemic infections with the most threatening human pathogens, such as *Escherichia coli*, *Klebsiella pneumoniae*, *Pseudomonas aeruginosa*, and *Acinetobacter baumannii*. The lead compound Api88 enters bacteria without lytic effects at the membrane and inhibits chaperone DnaK at the substrate binding domain with a  $K_D$  of 5  $\mu$ mol/L. The Api88-DnaK crystal structure revealed that Api88 binds with a seven residue long sequence (PVYIPRP), in two different modes. Mice did not show any sign of toxicity when Api88 was injected four times intraperitoneally at a dose of 40 mg/kg body weight (BW) within 24 h, whereas three injections of 1.25 mg/kg BW and 5 mg/kg BW were sufficient to rescue all animals in lethal sepsis models using pathogenic *E. coli* strains ATCC 25922 and Neumann, respectively. Radioactive labeling showed that Api88 enters all organs investigated including the brain and is cleared through both the liver and kidneys at similar rates. In conclusion, Api88 is a novel, highly promising, 18-residue peptide lead compound with favorable *in vitro* and *in vivo* properties including a promising safety margin.



The discovery and subsequent use of antibiotics more than 60 years ago has revolutionized the treatment of previously deadly infections and thus dramatically reduced the rate of mortality and morbidity of infectious diseases. During the golden age of antibiotics the Surgeon General of the USA declared "It is time to close the book on infectious disease"; this was in 1967.<sup>1</sup> More recently, in 1998 the new Surgeon General stated that "infectious disease are a rising peril". Today bacterial infections are still the leading cause of death worldwide, with antibiotic resistance being one of the greatest pharmaceutical challenges. Despite recent evidence that indicates bacterial resistance is an ancient phenomenon, genetically encoded in 30,000-year-old bacterial DNA samples,<sup>2</sup> the continuous and selective antibiotic pressure has produced resistant pathogens<sup>3</sup> over recent decades. Currently, Gram-negative bacteria are causing increasing concern due to the rapid spread of multi- or even pan-resistant strains, e.g., the NDM-1 carbapenemase producing Enterobacteriaceae.<sup>4,5</sup> While

many isolates of Gram-negative bacteria respond well to antimicrobial treatments, the sudden emergence and rapid spread of an unprecedented resistance problem highlights the desperate need for novel antibiotics to combat the most threatening Enterobacteriaceae (*Escherichia coli*, *Klebsiella pneumoniae*, and *Enterobacter cloacae*) and non-fermenting species (*Acinetobacter baumannii* and *Pseudomonas aeruginosa*).

Besides the challenge to circumvent these resistance mechanisms, certain pharmacodynamic requirements make drug development even more complex. While distribution in the bloodstream is readily achieved by i.v. infusion, sufficient drug concentrations in other target organs, and in particular the cerebrospinal fluid (CSF), are much more difficult to achieve.

Received: February 11, 2012

Accepted: May 2, 2012

Published: May 17, 2012

**Table 1. Sequences of Native Apidaecin 1b and the Optimized Designer Peptides and Their MIC Values Determined in 1% TSB against Two *E. coli* and One *K. pneumoniae* strains**

code	sequence <sup>a</sup>	MIC ( $\mu\text{g/mL}$ )		
		<i>E. coli</i> BL21 AI	<i>E. coli</i> D31 <sup>b</sup>	<i>K. pneumoniae</i> K6 <sup>c</sup>
1b	GNNRPVYIPQPRPPHPRL-OH	1	32	64
Api6	GNNRPVYIPQPRPPHPRL-NH <sub>2</sub>	0.5	1	16
Api7	Ac-ONNRPVYIPQPRPPHPRL-NH <sub>2</sub>	0.5	8	64
Api39	Ac-ONNRPVYIPRPRPPHPRL-NH <sub>2</sub>	2	4	16
Api88	Gu-ONNRPVYIPRPRPPHPRL-NH <sub>2</sub>	0.5	0.5	0.5

<sup>a</sup>Gu denotes *N,N,N',N'*-tetramethylguanidine, and O denotes *L*-ornithine. <sup>b</sup>*E. coli* D31 is pathogenic with extended spectrum  $\beta$ -lactamase. <sup>c</sup>K6 is a pathogenic *K. pneumoniae* strain resistant against ampicillin, chloramphenicol, tetracyclin, etc.

Bacteria, in contrast, can traverse the blood-brain barrier (BBB) by several mechanisms and pathways or infect the central nervous system (CNS) during neurosurgical procedures. Some bacteria even produce molecules (e.g., pneumolysin) that damage the BBB and will contribute to the entry of the bacteria into the CNS. Once inside the CNS, the pathogen triggers an inflammatory reaction that contributes to degradation of the BBB. Several pathogens, such as *E. coli*, group B *Streptococcus*, *Streptococcus pneumoniae*, *Listeria monocytogenes*, and *Neisseria meningitidis*, were shown to enter the brain<sup>6,7</sup> relatively easily, causing neurological disorders. While the CNS may react to the infection, with microglia being key to the CNS immune defense cells,<sup>8</sup> this is quite often insufficient and leads to high morbidity and mortality.

Cationic gene-encoded host defense peptides (HDP) are nature's most diverse and most abundant class of antibiotics. All higher organisms produce these peptides as part of their innate immune system. A subset of the HDP, i.e., antimicrobial peptides (AMP), possesses a direct antimicrobial activity by disruption of the bacterial membrane integrity and/or by translocation through the bacterial membranes. The mechanism for translocation often results in the inhibition of intracellular targets, such as DNA/RNA synthesis, protein synthesis/folding, cell wall synthesis, and cell division.<sup>9</sup> Thus AMP provide an ideal and novel series of lead compounds. Furthermore, they can be optimized for human applications, which appears especially promising for AMP inhibition of selective bacterial targets with little or no cross reactivity toward the human analogues. Short proline-rich AMP isolated from insects represent one promising class of compounds as they can be easily synthesized on solid phase, are relatively stable against proteases due to the high proline content, are nontoxic to human cell lines, and are predominantly active against Gram-negative bacteria including *E. coli*.<sup>10</sup> Among these, the family of apidaecins consists of more than 20 highly conserved peptides isolated from different lymph fluids of bees and wasps.<sup>11</sup> Apidaecins are 18–20 residues long and contain the highly conserved C-terminal sequence PRPPHPR(L/I), believed to be responsible for the translocation through the bacterial membrane.<sup>12,13</sup> The N-terminal domain appears to modulate the activity against different Gram-negative bacteria. Apidaecin 1b, which is the best studied apidaecin representative, is highly active against *E. coli*, less active against *K. pneumoniae*, and inactive against *P. aeruginosa*.<sup>14</sup> Although some recent reports indicate potential medical applications of apidaecins, it has not been optimized for systemic therapies or tested in animal models. Recent studies with longer proline-rich AMP (~40 residues), i.e., A3-APO and Bac7, indicate a high *in vivo* efficacy in rodents, which was partially attributed to immunomodulatory effects.<sup>15–17</sup> Here, we report the rational design of a novel

18 residue peptide derivative starting from apidaecin 1b originally isolated from honey bees, which is active against the most threatening Gram-negative human pathogens, with very promising *in vitro* characteristics and high *in vivo* efficacy in two murine *E. coli* infection models.

## RESULTS AND DISCUSSION

**Improving the Activity and Expanding the Bacterial Spectrum.** Apidaecin 1b was very effective against non-pathogenic *E. coli* BL21 AI (MIC 1  $\mu\text{g/mL}$ ), but much less active against the multiresistant strains *E. coli* D31 and *K. pneumoniae* K6 (MIC 32–64  $\mu\text{g/mL}$ ) (Table 1). Amidation of the C-terminus improved the activity 32- and 4-fold, respectively (Table 1, Api6). Acetylation of the N-terminus was designed to improve the protease stability; however, this abolished the activity against both strains indicating that an N-terminal positive charge is essential. Subsequent substitution of Gly<sup>1</sup> with ornithine or lysine restored the activity against *E. coli* (Api7). As trypsin-like proteases do not cleave peptide bonds that are C-terminal to an ornithine,<sup>18</sup> this amino acid was preferred over lysine to prevent degradation of the peptide by either human proteases (e.g., serum proteases) or bacterial proteases. Another favorable substitution was replacement of the glutamine at position 10 with the basic residue arginine (Api39), which improved the activity against *K. pneumoniae* about 4-fold, although the activity against *E. coli* BL21AI was reduced by the same amount. This loss of activity against *E. coli* BL21AI appeared to be tolerable, as the dose required to treat systemic infections would be determined by the least accessible pathogen. In order to further increase the positive charge of the peptide, we replaced the N-terminal acetyl amide (CH<sub>3</sub>CO-NH-) by *N,N,N',N'*-tetramethylguanidine (((CH<sub>3</sub>)<sub>2</sub>N)<sub>2</sub>-C-NH-), which significantly reduced the MIC values to 0.5  $\mu\text{g/mL}$  for both *E. coli* and *K. pneumoniae* strains (Table 1, Api88).

Thus, having optimized the antibacterial activity for three medically relevant Gram-negative bacteria, we proceeded to test the lead compound Api88 against a panel of seven clinically important pathogens (i.e., 37 strains and clinical isolates) including nine drug-resistant strains (Table 2, also see Supplementary Table S1). Importantly, the MIC values were observed over a very narrow range (0.125–4  $\mu\text{g/mL}$ ), a promising result for the treatment of all clinically relevant Gram-negative pathogens currently causing concerns including *P. aeruginosa* and *A. baumannii*. As expected, Api88 was highly active against a single clinical isolate of *K. pneumoniae* KPC (*K. pneumoniae* carbapenemase; conferring resistance to all  $\beta$ -lactams except aztreonam) (MIC 2  $\mu\text{g/mL}$ ). A time-kill assay with *E. coli* BL21 AI performed at peptide concentrations corresponding to 10  $\times$  MIC showed that Api88 was bactericidal (i.e., reducing the colony forming units (CFU) by more than

**Table 2. Broad Spectrum Antimicrobial Activity of Lead Compound Api88 against Different Gram-Negative Pathogens<sup>a</sup>**

pathogen	no. of strains and isolates tested	range of MIC values ( $\mu\text{g/mL}$ )
<i>E. coli</i>	8	0.5–1.0
<i>K. pneumoniae</i>	6	0.25–0.5
<i>P. aeruginosa</i>	8	1.0–4.0
<i>A. baumannii</i>	5	1.0–2.0
<i>Enterobacter cloacae</i>	5	0.25
<i>Proteus vulgaris</i>	5	0.125–1.0

<sup>a</sup>For details see Supplementary Table S1.

1000-fold within 24 h) and killed these bacteria quickly by reducing the CFU within the first 30 min by 10-fold, whereas the native sequence was less effective and only bacteriostatic (see Supplementary Figure S1). Even at a 10-fold lower concentration (*i.e.*,  $1 \times \text{MIC}$ ), Api88 was still bactericidal and killed the bacteria relatively fast by reducing the bacterial load within the first 30 min by 90%.

**Cellular Toxicity.** Api88 did not influence the proliferation of SH-SY5Y-, HeLa-, HEK293-, and HepG2-cells (Figure 1).

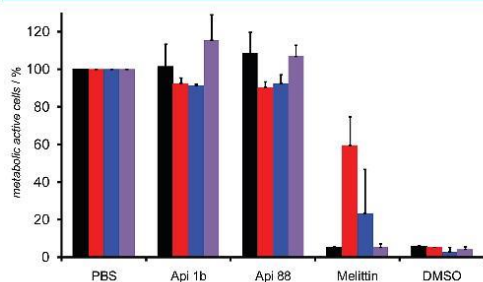


**Figure 1.** Cytotoxic effects of apidaecin 1b and its derivative Api88 against human embryonic kidney cells (HEK293; black bars), human hepatoma cells (HepG2; red bars), HeLa cells (blue bars), and differentiated SY5Y cells (purple bars). The cell lines were incubated with apidaecin 1b and Api88 at a concentration of 0.6 mg/mL for 24 h, *i.e.*, 285 and 262  $\mu\text{mol/L}$ , respectively. The cell viability was determined with the Cell Proliferation Kit I. Positive controls consisted of DMSO (12%) and melittin (100  $\mu\text{g/mL}$ , 35  $\mu\text{mol/L}$ ). The values were normalized to PBS (12%) as negative controls. The metabolic activity was determined twice in triplicates.

Moreover, it did not show any hemolytic effects on human red blood cells (see Supplementary Figure S2) within the tested concentration range up to 600  $\mu\text{g/mL}$ , which is more than 100-fold above the MIC values.

**Mode of Action.** Although the detailed mechanism has not been determined for proline-rich AMP, all the evidence suggests that all members of this peptide family penetrate freely through the membrane of Gram-negative bacteria into the periplasmic space, prior to dispersion within the cells. The latter step may involve an active transport process.<sup>19</sup> Once intracellular, it is assumed that the peptides block chaperone DnaK, as shown for pyrrolicorin *in vitro* and also *in vivo* by bimolecular fluorescence complementation (BIFC).<sup>20,21</sup> This inhibition is lethal for *E. coli* at elevated temperatures, as indicated by DnaK null mutants of *E. coli* that do not survive at temperatures above 30 °C.<sup>22</sup> Therefore, the activity of proline-

rich AMP depends on two factors, which most likely originate from different domains: the peptide uptake by the C-terminal sequence and inhibition of the intracellular target by the N-terminal sequence. As Api88 was developed stepwise from apidaecin 1b and resembled its structure closely, we assumed that the mode of action should be very similar, despite its higher net charge. Thus we compared Api88 with its native ancestor using a few key steps of the proposed mechanism. *In vitro*, a quartz crystal microbalance (QCM) was employed to compare the mass of Api88 taken up by a bacterial-mimetic membrane of composition DMPC:DMPG (4:1).<sup>13,23–25</sup> This method provided the mass of peptide binding by measurement of the frequency change of an oscillating crystal ( $\Delta m \propto \Delta f$ ).<sup>25,26</sup> The mass of Api88 taken up into the lipid bilayer was found to increase over the concentration range 2–10  $\mu\text{mol/L}$  (Figure 2, left), with membrane saturation occurring at  $\sim 10 \mu\text{M}$ . Higher concentrations resulted in no further peptide binding (data not shown). The incorporation of Api88 was rapid and reversible in a manner similar to that observed for apidaecin 1b,<sup>13</sup> although the mass of peptide binding for Api88 (*cf.* apidaecin 1b) was greater at every concentration: 2  $\mu\text{mol/L}$  ( $\sim 4.6$  and  $\sim 4.2 \mu\text{g/mL}$ ), 7.3 (2) Hz; 5  $\mu\text{mol/L}$  ( $\sim 11.5$  and 10.5  $\mu\text{g/mL}$ ), 8.3 (2.5) Hz, and 10  $\mu\text{mol/L}$  ( $\sim 23$  and  $\sim 21 \mu\text{g/mL}$ ), 10.6 (3.5) Hz. These data support the uptake of peptide into bacterial (mimetic) membranes without disruption or irreversible change to the membrane layer. The reversibility of this peptide-membrane association is consistent with cell-penetrating peptides and facile intracellular transport.

A fluorescein labeled analogue of Api88 (CF-Api88) stained *E. coli*, *K. pneumoniae*, and *P. aeruginosa* within 60 min and was not removed from the cells by washing (see Supplementary Figure S3), whereas it was not able to enter HeLa cells within 2 h (data not shown). When the same experiment was repeated without washing Api88 (CF) off the cells, but in the presence of trypan blue to quench the fluorescence in the medium and at the bacterial surface, the bacterial cross section still showed a homogeneous fluorescence stain (Figure 2, right). This clearly indicates that Api88 enters the cells and does not permeabilize the membrane for trypan blue. In a fluorescence polarization assay, the same peptide was studied for its DnaK binding. The binding constants determined with recombinant full-length DnaK were  $5.0 \pm 1.2 \mu\text{mol/L}$  ( $\sim 11.5 \pm 2.7 \mu\text{g/mL}$ ) for Api88 and  $6.3 \pm 2.3 \mu\text{mol/L}$  ( $\sim 13.2 \pm 4.8 \mu\text{g/mL}$ ) for apidaecin 1b (see Supplementary Figure S4), indicating that the sequence optimization did not alter the binding to DnaK. Interestingly, the binding constants are very similar to other native and artificial Pro-rich AMP.<sup>20,27</sup> The N-terminal sequence corresponding to residues 1–8 of apidaecin 1b had only a slightly weaker binding constant of  $17.3 \pm 3.2 \mu\text{mol/L}$ , whereas the C-terminal part (residues 9–18) bound very weakly ( $33.1 \pm 5.6 \mu\text{mol/L}$ ) (see Supplementary Figure S4). This was further confirmed by a crystal structure of the substrate binding domain of DnaK (residues 389–607) in complex with an Api88 fragment (residues 3–11) that bound to DnaK as well as apidaecin 1b ( $K_D = 5.8 \pm 1.7 \mu\text{mol/L}$ ) (Figure 3, also see Supplementary Figure S5). Interestingly, Api88 (3–11) bound within the same crystal form in a forward as well as in a reverse direction to DnaK. In both binding modes residues 5–11 bound to DnaK. The reverse binding mode was unexpected insofar as the almost identical sequence of onconin and pyrrolicorin (Y<sup>6</sup>LPRP<sup>10</sup> compared to Y<sup>1</sup>IPRP<sup>11</sup> in Api88) binds only in the forward direction to DnaK.<sup>27,28</sup> However, the ability of DnaK to bind peptides in both directions has been

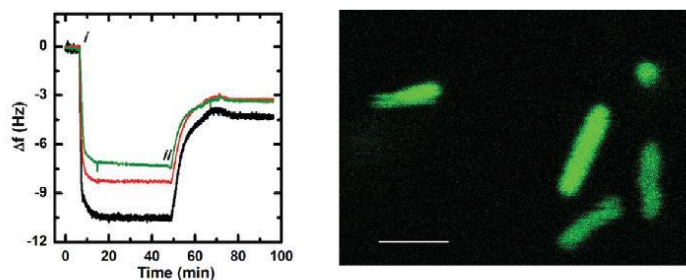


**Figure 2.** Quartz crystal microbalance (left) and confocal laser scanning microscopy image (right). The uptake of Api88 onto a preformed DMPC:DMPG (4:1) membrane layer is shown as a  $\Delta f$ - $t$  graph; *i* indicates the beginning of the peptide and membrane interaction and *ii* corresponds to the introduction of the PBS buffer rinse in the QCM chamber. The Api88 concentrations were 2  $\mu\text{mol/L}$  (green), 5  $\mu\text{mol/L}$  (red), and 10  $\mu\text{mol/L}$  (black) using the seventh harmonic. The fluorescence image was obtained by incubating an *E. coli* BL21 AI culture ( $3 \times 10^8$  cells/mL) with Api88(CF) (10  $\mu\text{mol/L}$ ) (60 min, 24  $^\circ\text{C}$ ). The bar indicates 2.5  $\mu\text{m}$ .

suggested previously following spectroscopic studies.<sup>29</sup> Both binding modes of the Api88 fragment appear to be stabilized by crystal packing interactions.

Substitution of glutamine in position 10 by arginine neither weakened nor strengthened the DnaK binding, which also agrees with the MIC values for *E. coli*. For *K. pneumoniae*, however, this substitution might strengthen the DnaK-binding and thereby the corresponding MIC values. Interestingly, apidaecin 1b and Api88 were highly active not only against *E. coli* MC4100 but also against two DnaK null mutants produced from this *E. coli* strain (see Supplementary Table S2). This clearly indicates that apidaecin 1b and the optimized Api88 do not only inhibit DnaK but can kill at least these *E. coli* strains equally efficient by inhibiting other intracellular targets, such as chaperonin GroEL and its cofactor GroES,<sup>20,30</sup> or even by a different mechanism. Such a second killing mechanism was suggested recently, based on the observation that cell division protease ftsH was overproduced in *E. coli* incubated with apidaecin 1b.<sup>31</sup> The authors speculated that the overexpressed protease will degrade cytoplasmic UDP-3-*O*-acetyl-N-acetylglucosamine deacetylase, resulting in an unbalanced synthesis of LPS and phospholipids. This multimodal killing mechanism should prevent or at least reduce the likelihood of possible resistance mechanisms caused by gene mutations or changes to the protein expression pattern.

All data suggest that Api88 kills Gram-negative bacteria by the same mechanism as apidaecin 1b, although its net charge at physiological conditions is around +7 compared to only +4 for apidaecin 1b due to substitutions in positions 2 (Om) and 19 (Arg), a guanidated N-terminus, and an amidated C-terminus. To further confirm the suggested nonlytic target-inhibiting mechanism, the antimicrobial activity of Api88 was compared to its all-D and retro-inverso analogues. Whereas Api88 was highly active against two *E. coli* and two *K. pneumoniae* strains, the all-D and retro-inverso forms were at least 64-fold less active or even inactive (Table 3). This clearly indicates that the activity of Api88 depends on its stereospecific interaction with a transporter or target protein but not on lytic effects. It will be important for the further optimization of lead compound Api88 to study the underlying mechanisms in more detail.

**Api88 Distribution in Mice.** As all the available data suggested a broad antibiotic activity against the most threatening Gram-negative pathogens, without toxic side effects, we proceeded to test Api88 in mice. *In vivo* imaging

showed that Api88 labeled at the side chain of the ornithine with DY675-Ser-Gly was systemically distributed within 30 min after intraperitoneal (i.p.) injection (see Supplementary Figure S6). These images were taken at different time points, and the fluorescence in the organs indicated that the peptide was effectively distributed throughout the body, although it is not possible to distinguish between the fluorescence of the full length peptide and any fluorescent degradation products. As the fluorescence-dye label coupled to the N-terminus of Api88 might influence the peptide distribution, we used an alternative approach that relied on Api88 labeled with <sup>125</sup>I at Tyr-7. This radioactive derivate was injected into the jugular vein of CD-1 mice, and its distribution was studied by measuring the radioactivity in six organs and in serum (Figure 4A). Interestingly, the radioactivity was detected at similar levels in liver and kidney, which confirms the unexpectedly high hepatic clearance of the polar, positively charged peptide as indicated by the *in vivo* imaging (see Supplementary Figure S6G). Importantly, fluorescence and radioactivity were detected in all organs studied and at high levels (only moderate in brain) clearly indicating that Api88 could target and kill bacteria in all parts of the body. As tissue distribution is not the most sensitive technique to characterize the permeability of the peptide toward the BBB,<sup>32</sup> this was studied by multiple time regression. The influx transfer constant ( $K_{in}$ ) was 0.37  $\mu\text{L}/(\text{g} \times \text{min})$  for Api88 with an apparent initial distribution volume ( $V_i$ ) of 26.06  $\mu\text{L}/\text{g}$ , compared to a  $K_{in}$  of 0.25  $\mu\text{L}/(\text{g} \times \text{min})$  and  $V_i$  of 14.27  $\mu\text{L}/\text{g}$  for the almost impermeable marker bovine serum albumin (BSA) (Figure 4B). This represents a small but significant influx of Api88 from the serum into the brain, with a brain distribution volume almost double that of BSA. Given the specific activity of <sup>125</sup>I-Api88 (3.95 cpm/pg), about 0.7 ng reached the brain (0.5 g) within 10 min, which corresponds to a percentage ratio brain/serum of 3%. In order to distinguish the peptide distribution between brain parenchyma and blood-brain capillaries, a capillary depletion experiment was performed, demonstrating that a significant portion of the peptide had reached the brain parenchyma ( $77.5 \pm 1.1\%$ ) rather than being trapped in the capillaries ( $22.5 \pm 1.1\%$ ). Thus the amount of peptide entering the brain is mostly transferred from the capillaries to the parenchyma. The brain to blood transport (efflux) showed only a small efflux rate ( $k_{out} = 0.061 \pm 0.075 \text{ min}^{-1}$ ), indicating that Api88 remains considerably longer in the brain tissue and is not rapidly transported back to

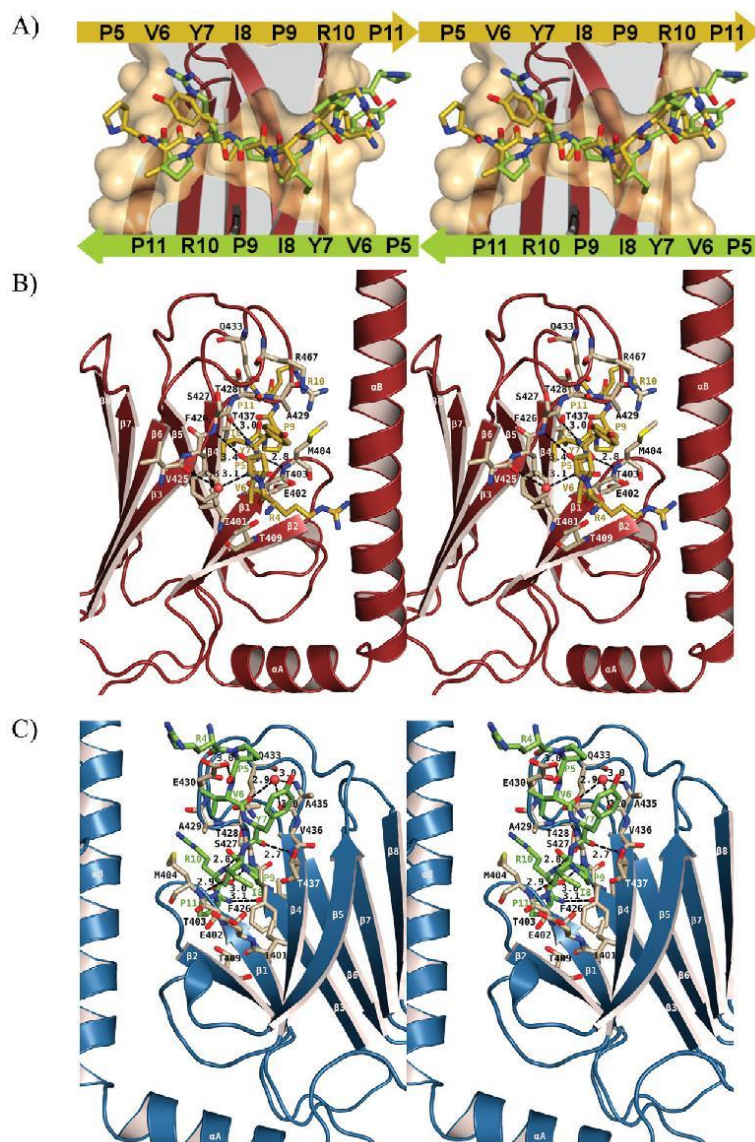


**Figure 3.** Stereoviews of the binding modes of an Api88 fragment (residues 3–11) to the substrate binding cleft of DnaK (residues 389–607). (A) This fragment binds in a forward (yellow carbon atoms) and in a reverse direction (green carbons) to the two independent DnaK molecules in the asymmetric unit of the crystal. The two binding modes are superimposed. In the forward and reverse binding modes, Ile-8 and Pro-9 occupy the central hydrophobic pockets, respectively. (B) Hydrogen bonding and van der Waals interactions between the forward binding Api88 fragment (yellow) and the substrate binding domain of DnaK (red). Residues 4–11 of the peptide are visible in the electron density. Two strong ( $\leq 3$  Å) and two weak hydrogen bonds are formed. The peptide in the forward binding mode forms less strong hydrogen bonds to DnaK compared to the DnaK-oncocin interactions.<sup>27</sup> Superposition to the oncocin structure (Supplementary Figure S5) shows a shift of the peptide that may be caused by crystal contacts. This shift most likely results in the suboptimal interaction pattern of the peptide with DnaK, which is also reflected by relatively high B-factors of the peptide and partly weak electron density for a 1.9 Å structure, especially for residues 9–11 (not shown). (C) Stereoview of the hydrogen bonding and van der Waals interactions between the reverse binding Api88 fragment (green) and the substrate binding domain of DnaK (blue). Residues 4–11 of the peptide are visible in the electron density. Six strong ( $\leq 3$  Å) and one weak hydrogen bonds are formed showing a tight

Figure 3. continued

interaction. The B-factors for the reverse binding peptide are lower as for the forward binding peptide and the electron density is well-defined (not shown).

**Table 3. Sequence MIC Values Determined in 1% TSB of Api88, All-D-Api88, and Retro-inverso Api88 against Two *E. coli* and One *K. pneumoniae* Strains**

code	sequence <sup>a</sup>	MIC ( $\mu\text{g/mL}$ )			
		<i>E. coli</i>		<i>K. pneumoniae</i>	
		ATCC 25922	DSM 10233	DSM 681	DSM 11678
Api88	Gu-ONNRPVYIPRPRPPHRL-NH <sub>2</sub>	2	1	2	8
All-D-Api88	Gu-onnrpvyyiprpphrl-NH <sub>2</sub>	128	64	256	256
Retro-inverso-Api88	lrprrpprpryivpmno-NH <sub>2</sub>	>256	128	>256	>256

<sup>a</sup>Gu denotes N,N,N',N'-tetramethylguanidine, O denotes L-ornithine, and small form letters denote D-amino acids.

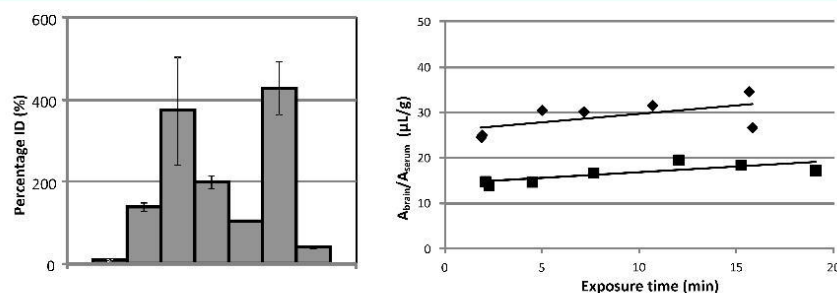


**Figure 4.** Distribution of <sup>125</sup>I-labeled Api88 in organs and serum after 15 min (left) and the brain influx of <sup>125</sup>I-labeled Api88 (right). The radiolabeled peptide (200  $\mu\text{L}$ , 30,000 cpm/ $\mu\text{L}$ ) was injected into the jugular vein of anesthetized CD-1 mice. At specified time points blood was obtained from the carotid artery, and the mouse was decapitated. Immediately after brain collection, spleen, liver, lungs, heart, and kidneys were collected and weighed. The percentage of time-corrected injected dose (ID) was then calculated from the measured gamma counts. Left: The bars represent the values calculated for brain, spleen, kidney, lungs, heart, liver, and serum (from left to right). Right: The brain influx multiple time regression of <sup>125</sup>I-Api88 ( $\blacklozenge$ ) versus <sup>125</sup>I-BSA ( $\blacksquare$ ) was calculated according to Gjedde.<sup>46</sup> The influx of <sup>125</sup>I-Api88 (cf. <sup>125</sup>I-BSA) was described by the linear regression  $y = 0.37x + 26.06$  ( $y = 0.25x + 14.27$ ).

the periphery. This global influx rate, however, is negatively influenced by the rapid and high hepatic and kidney clearance, reducing the serum concentration of Api88 passing through the brain, and hence a rapid declining exposure of Api88 to the brain tissue.

**Toxicity in NMRI Mice.** Seven healthy female NMRI outbred mice ( $\sim 7$  weeks old, 28–32 g) were treated with four doses of 20 mg/kg body weight (BW) of Api88 administered *via* i.p. bolus at 0, 3, 7, and 24 h. None of the animals showed any discomfort after the injections, and all mice showed their regular behavior and feeding pattern during the 5-day observation period. Following administration of a double dose, a few animals showed a slight discomfort after the first injection for up to 10 min, which was not observed after the three consecutive injections, but no other irregular behavior or feeding pattern. After 5 days the mice were sacrificed. The brain, kidney, pancreas, lung, urinary tract, genitals, and thymus all revealed a typical (normal) histology with no signs of inflammation, internal bleeding, or any other pathological finding (data not shown). Giemsa staining of the spleen sections did not reveal any additional basophil or eosinophil granulocyte infiltration (data not shown). The cellular architecture of the spleen was not altered in the Api88 treated mice (Figure 5C) compared with the PBS control (Figure 5D). Further histopathological investigation demonstrated no differ-

ences between the 20 and 40 mg/kg BW Api88 and the placebo groups for white pulp and red pulp of the spleen parenchyma (data not shown). Also, there were no differences in the histological appearance and the number of living cells per spleen (see Supplementary Figure S7) as well as the proportions of several splenocyte subpopulations, *i.e.*, neutrophilic granulocytes, macrophages, dendritic cells, natural killer cells, B cells, and T cells (Figure 5A). The expression of the activation marker CD86 on antigen-presenting cells was not influenced by Api88 (Figure 5B). The resulting data for peritoneal exudate cells were also similar to those of the splenocytes. There were no significant differences in the number of living peritoneal cells as well as the rate and activation levels of several peritoneal cell subpopulations (see Supplementary Figure S8). Taken together, no evidence was found for *in vivo* immunomodulatory activities of Api88, which contrasts a recent report about the *in vitro* effects of native apidaecin 1b.<sup>33</sup>

**Murine Infection Models.** The efficacy of Api88 was first evaluated in a systemic septicemia *E. coli* ATCC 25922 infection model (with 2.5% mucin) on female NMRI outbred mice (seven animals per group). Untreated mice (23–28 g) were extremely sick within 1 h and had to be euthanized based on a scoring system within  $11 \pm 3$  h post infection. Bacteria were detected after 1 h in the blood and in the liver, lung,

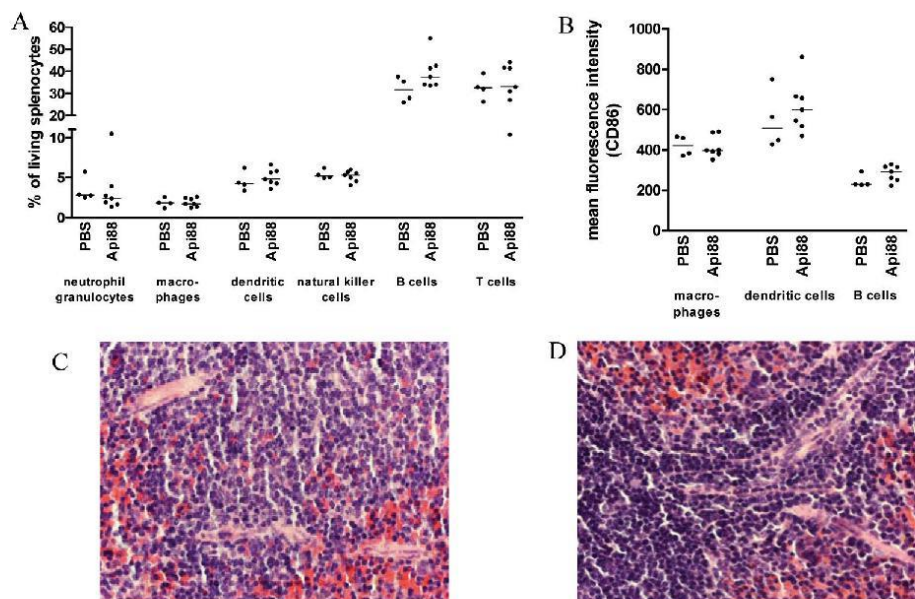


**Figure 5.** Influence of Api88 treatment on splenocyte subpopulations and their activation. Female NMRI outbred mice were treated with four doses of 20 mg/kg body weight (BW) Api88 ( $n = 7$ ) or PBS ( $n = 4$ ) as control. The rate of the splenocyte subpopulations (A) and the expression of the activation marker CD86 by professional antigen-presenting cells (B) were determined by flow cytometry analysis. The data shown are medians. Significance between the groups was determined by Mann–Whitney test. The immune cell subpopulations were identified by expression of specific markers, *i.e.*, neutrophilic granulocytes (Gr1<sup>+</sup>, exclusion of eosinophilic granulocytes by counterstaining of SiglecF), macrophages (CD11b<sup>+</sup>, F4/80<sup>+</sup>, CD11c<sup>-</sup>, B220<sup>-</sup>), dendritic cells (CD11c<sup>+</sup>), natural killer cells (NKP46<sup>+</sup>, CD3<sup>-</sup>), B cells (B220<sup>+</sup>, CD11c<sup>-</sup>, CD11b<sup>-</sup>), and T cells (CD3<sup>+</sup>, B220<sup>-</sup>). The cellular architecture of the spleen of the PBS control (D) was not altered by the Api88 treatment (C) at a magnification of 400 $\times$  (hematoxylin and eosin staining).

kidney, spleen, and brain with a further increase of the bacterial loads afterwards (see Supplementary Figure S9A). When treated with Api88 at *i.p.* bolus doses of 20, 10, 5, 2.5, or 1.25 mg/kg BW at three time points (1, 4, and 8 h post infection), the survival rates of the animals increased for all the doses to 100% (Figure 6A). The weight losses of the animals after infection increased with lower doses (see Supplementary Figure S9B). These weight changes correlated well with the scoring based on the clinical symptoms shown by the animals. The high-dose groups and the animals treated with ciprofloxacin recovered relatively fast, whereas the animals treated with the lowest dose needed  $\sim 2$  days to recover completely (see Supplementary Figure S9B). Similar to the toxicity study, the number of splenocytes or peritoneal exudate cells did not change in the infected animals that were treated with Api88 or ciprofloxacin (control) (see Supplementary Figure S10).

Finally, we tested Api88 in a second murine model (infection with *E. coli* Neumann as a clinical isolate;  $1 \times 10^7$  CFU/mL) using female CFW-1 mice (5 animals per group, BW 20–25 g, 4–5 weeks) followed by treatment with Api88 (Figure 6B). The two highest doses provided a survival rate of 100%, whereas 80% and 40% of the animals survived after the lower doses of 5 and 2.5 mg/kg BW, respectively. When the peptide was administered in Kollidon FP17, a commercially available vehicle for injections in animals, the survival rate increased to 100% for animals treated at the same time intervals with a dose

of 5 mg/kg. Interestingly, this reproducibly obtained ED<sub>100</sub> was identical to the ED<sub>100</sub> of imipenem, which was determined in the same infection model, later in the course of the experiments. However, the MIC values of imipenem and Api88 were 0.06 and 2  $\mu\text{g}/\text{mL}$ , respectively, in 25% Mueller-Hinton broth for the clinical isolate *E. coli* Neumann. Considering that no adverse effects were observed with repeated *i.p.* injections of 40 mg/kg BW during the toxicity study and there was a 100% survival rate after administration of 5 mg/kg BW in both infection models, the MOS (margin of safety) was better than eight.

Although *E. coli* ATCC 25922 is commonly used for murine infection models,<sup>34,35</sup> and despite the fact that it was passaged twice through mice to increase its virulence, it is considered to be an only moderately pathogenic strain. Still the survival rates of the NMRI mice were very impressive, especially as the lower virulence was partially compensated by the relatively late therapeutic intervention (*i.e.*, 1 h post infection) allowing the bacteria to distribute systemically. In contrast, the *E. coli* Neumann strain is adapted for infection models and is rated to be suitable for an adequate sepsis model. It was used recently to evaluate A3-APO, a lead compound developed by combining sequences from different proline-rich AMP followed by chemical optimization.<sup>16</sup> At the lowest dose administered of 2.5 mg/kg BW Api88 four out of five CFW-1 mice survived significantly longer than the control group with only two of them surviving the 5 day observation period. When Api88 was

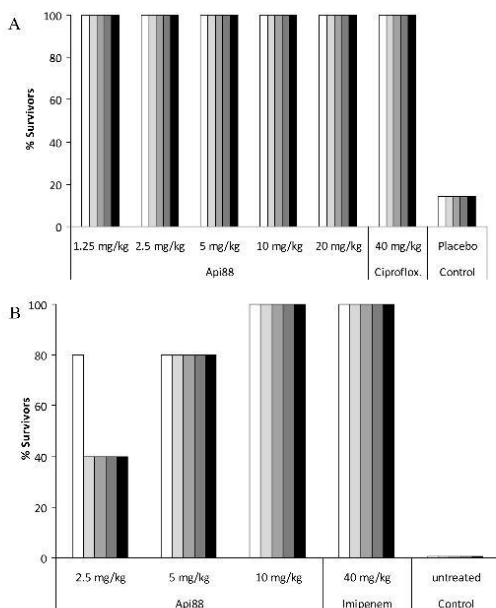


**Figure 6.** Survival rates of NMRI (A, seven per group) and CFW1 (B, five per group) mice after infecting them with *E. coli* ATCC 25922 and *E. coli* Neumann, respectively. NMRI mice were treated 1, 4, and 8 h post infection using an individual dose of 20, 10, 5, 2.5, or 1.25 mg/kg BW Api88. Ciprofloxacin was injected at a dose of 40 mg/kg BW as positive control. CFW1 mice were treated 0.5, 4, and 8 h post infection with individual doses of 10, 5, or 2.5 mg/kg BW Api88 or 40 mg/kg imipenem as control (vehicle only). Shown are the survival rates of all animal groups 12 h (white bar) and 2 (light gray), 3 (gray), 4 (dark gray), and 5 days (black) post infection.

administered i.p. in a polyvinylpyrrolidone (PVP) formulation, the ED<sub>100</sub> was 5 mg/kg BW. Thus, Api88 and imipenem were equally effective in the *E. coli* Neumann infection model, whereas imipenem was 30-fold more active *in vitro* based on the MIC values. This is in line with observations from Otvos for A3-APO.<sup>16</sup> Similar apparent contradictions were also reported for other AMP and indicated that the MIC values of peptides cannot always be simply extrapolated to murine models using the expert knowledge obtained for small molecules.

In addition, the peptide brain distribution showed a brain-serum ratio of 3% indicating that the peptide significantly entered the brain parenchyma, rather than being trapped in the blood-brain capillaries. Once in the brain, Api88 remained there for a long time, apparent from the small efflux and low metabolism rate. Considering a therapeutic dose of 10 mg/kg BW Api88 (i.e., 250 μg Api88 per mouse) and a total blood volume of 2.5 mL per mouse, the maximal Api88 concentration in blood should be around 100 μg/mL and about 3 μg/mL in CSF. This is still above the MIC value determined for *E. coli* Neumann in 25% MHB medium. As the activity of apidaecin 1b and most other cationic AMP increases with lower salt concentrations as found in the CSF, Api88 appears to be a suitable treatment option for infections of the CNS.

One explanation for the high *in vivo* activity might be additional immunomodulatory effects of AMP that are not

considered in antibacterial *in vitro* assays but may be significant toward animals. Thus AMP could act by two independent mechanisms *in vivo*. First, they could kill the pathogens directly, when injected at high doses somewhat similar to the *in vitro* testing. In parallel, the immune system might be stimulated and initiate the fight with pathogens even after the peptides were cleared from the body or degraded by proteases. Such immunomodulatory effects are well-known for mammalian HDP with *in vitro* antimicrobial activities, such as defensins or cathelicidins.<sup>36–41</sup> More surprising was a recent finding that apidaecin 1b has immunomodulatory effects on human macrophages and monocytes *in vitro* despite the evolutionary distance between honey bees and humans.<sup>33</sup> We did not find any evidence for immunomodulatory side effects here for Api88 with NMRI mice, such as modulation of the activation state of antigen-presenting cells from spleen or the peritoneal cavity or proliferative effects on splenocytes or peritoneal exudate cells. At this point it remains unclear if this effect is related to the modified sequence of Api88, differences between the murine and human immune systems or if the effect was just too weak to be identified in the mouse model at the studied time points. All of these questions need to be addressed in future studies.

In conclusion, the Api88 peptide is a highly efficient treatment for Gram-negative pathogens systemically with a therapeutic window larger than ten. Importantly, Api88 killed *E. coli* in a direct manner without apparent modulation of the immune system. This latter aspect will make it easier to develop Api88 further for clinical applications, as its mode of action can be directly linked to specific inhibition of the substrate binding domain of DnaK without any toxic effects toward human cells. Most importantly, Api88 was not able to enter HeLa cells, which provides an additional layer of safety. Future animal studies will be used as added proof that the low MIC values obtained for *K. pneumoniae*, *P. aeruginosa*, and *A. baumannii* allow also treating such systemic infections.

## METHODS

**Peptide Synthesis.** Peptides were synthesized as C-terminal amides or free acids with standard 9-fluorenylmethoxycarbonyl/*tert*-butyl (Fmoc/*t*Bu) chemistry at the 25 or 250 μmol scale using diisopropyl carbodiimide (DIC) or 2-(1*H*-benzotriazol-1-yl)-1,1,3,3-tetramethyluronium hexafluorophosphate (HBTU) activation (for details see Supporting Information).<sup>42</sup> HBTU activation was also used to manually couple acetic acid (“acetylation”) or 5,(6)-carboxyfluorescein to the unprotected N-termini after completion of the peptide synthesis. The *N,N,N,N*’-tetramethylguanidino group was obtained by incubating the N-terminally deprotected peptides with 10 equiv of HBTU and *N*-methylmorpholine.<sup>43</sup> For *in vivo* imaging, Api88 was synthesized with methyltrityl-protected ornithine, which was selectively deprotected after N-terminal guanidation. The peptide synthesis was continued at the δ-amino group of ornithine by coupling glycine and serine before the fluorescence dye DY675 (0.5 equiv, Dyomics GmbH, Jena, Germany) was coupled to the α-amino group of serine. All peptides were cleaved with trifluoroacetic acid (TFA), precipitated with cold diethyl ether and finally purified on a C<sub>18</sub>-phase using a linear aqueous acetonitrile gradient in the presence of 0.1% (v/v) TFA as ion pair reagent. The purified peptide was analyzed by analytical RP-HPLC and matrix-assisted laser desorption/ionization time-of-flight mass spectrometry. For the animal studies, the lyophilized peptides were dissolved in 0.1% (v/v) aqueous acetic acid and lyophilized twice to remove residual TFA. The tissue distribution and multiple time regression studies relied on purified Api88 and BSA (control), which were labeled with <sup>125</sup>I by the Iodogen method and purified over Ag filters (for details see Supporting Information). The

<sup>125</sup>I-Api88 purity was assessed by RP-HPLC, which confirmed also that the filtrate did not contain any free iodide.

**Antibacterial Activity.**<sup>27</sup> MIC values for *E. coli* (strains BL21 AI, D31, MC4100, ATCC 25922, DSM 10233,  $\Delta$ DnaK, and  $\Delta$ DnaK52) and *K. pneumoniae* (K6, DSM 681, and DSM 11678) were determined in triplicate by a liquid broth microdilution assay in sterile 96-well plates using a 2-fold peptide dilution series in 1% (w/v) tryptic soy broth (TSB; 33% TSB medium) (for details see Supporting Information). The inoculum ( $50 \mu\text{L}$ ,  $1.5 \times 10^7$  cells/mL) was prepared by diluting an overnight culture grown in nutrient broth (Carl Roth GmbH, Karlsruhe, Germany) with 33% TSB medium. The MIC values of all other pathogenic bacteria were tested in 1% TSB medium using an overnight culture grown on Columbia agar (Becton Dickinson, Sparks, MD, USA) at  $37^\circ\text{C}$  and diluted with 1% TSB medium first to an  $\text{OD}_{578 \text{ nm}}$  of 0.1 and then further 285-fold (inoculum:  $190 \mu\text{L}$ ,  $(1-2) \times 10^5$  CFU/mL). All plates were incubated at  $37^\circ\text{C}$  for 18 h, except the null mutants  $\Delta$ DnaK and  $\Delta$ DnaK52 (courtesy of B. Bukau, MPI, Heidelberg) that were grown at  $30^\circ\text{C}$ . The MIC was defined as the lowest peptide concentration preventing visible bacterial growth.

**DnaK Expression, Crystallization, and Structure Determination.** The substrate binding domain (SBD) of *E. coli* DnaK (residues 389–607) and the full length protein were expressed and purified as described.<sup>44</sup> The SBD was concentrated to  $16 \text{ g/L}$ , mixed with Api88 (residues 3–11) at a 1:5 molar ratio and incubated (1 h, RT).<sup>28</sup> Crystals were grown with the hanging-drop vapor diffusion method in  $2.7 \text{ mol/L}$  ammonium sulfate and  $0.1 \text{ mol/L}$  MES (pH 6.0). These crystals could be cooled to  $100 \text{ K}$  for data collection without the need to add a cryo protectant. Diffraction data were collected at the Bessy synchrotron beamline 14.1 to a resolution of  $1.9 \text{ \AA}$  and processed using XDS<sup>45</sup> and SCALA<sup>46</sup> (Supplementary Table S1). The structure was solved by molecular replacement using Molrep<sup>47</sup> and PDB ID 1DKZ.<sup>44</sup> The model was built with Coot<sup>48</sup> and refined with REFMAC.<sup>49</sup> The asymmetric unit contains two protein monomers (chain A and B) and two apidaecin peptides (chain C and D).

**Fluorescence Polarization.** The binding constants were determined with full length DnaK and 5(6)-carboxyfluorescein labeled peptides in polarization buffer ( $20 \text{ mmol/L}$  TRIS,  $0.15 \text{ mol/L}$  KCl,  $5 \text{ mmol/L}$   $\text{MgCl}_2$ ,  $1 \text{ mmol/L}$   $\text{NaN}_3$ , and  $2 \text{ mmol/L}$  dithiothreitol, pH 7.5) at  $28^\circ\text{C}$ , as described recently.<sup>27</sup> Briefly, black 384-well plates (flat bottom, Greiner Bio-One GmbH) were blocked with  $0.5\%$  (w/v) casein in washing buffer ( $10 \text{ mmol/L}$  sodium phosphate,  $0.3 \text{ mol/L}$  NaCl, pH 7.4, and  $0.05\%$  (v/v) Tween20) at RT for 1 h and washed three times with washing buffer. A 2-fold dilution series of full length DnaK ( $40 \mu\text{L/well}$ ) in polarization buffer containing a labeled peptide ( $10 \text{ nmol/L}$ ) was added and incubated ( $28 \pm 1^\circ\text{C}$ ). After 2 h the fluorescence anisotropy was measured on a Paradigm microplate reader (Beckman Coulter, Salzburg, Austria) in top read position ( $\lambda_{\text{exc}} = 485 \text{ nm}$ ,  $\lambda_{\text{em}} = 535 \text{ nm}$ ) on at least two different days in triplicates. The data were fitted to a nonlinear, dose–response logistical transition [ $y = a_0 + a_1/(1 + x/a_2)^{n_1}$ ] using the Levenberg–Marquardt algorithm with the dissociation constants ( $K_D$ ) being represented by the  $a_2$  coefficients (SlideWrite, Encinitas, CA, USA).

**Cytotoxicity.** Cell viabilities were determined with the MTT cell proliferation assay<sup>50,51</sup> for human embryonic kidney (HEK 293), human hepatoma (HepG2-), SH-SY5Y-, and HeLa-cells (for details see Supporting Information). The cell lines were cultured in DMEM/Ham's F-12 medium containing fetal bovine serum, neomycin, penicillin, and streptomycin, seeded ( $2 \times 10^4$  cells) in the same medium into 96-well plates and incubated (overnight,  $37^\circ\text{C}$ ,  $5\%$   $\text{CO}_2$ ) or differentiated with *trans*-retinoic acid (SY5Y,  $10 \mu\text{mol/L}$ , 5 days). Peptide solutions ( $0.6 \text{ g/L}$ ) were added to the cells washed with phosphate buffered saline (PBS) and incubated again at identical conditions for 24 h.

**Hemolytic Activity.**<sup>18</sup> Concentrated human erythrocytes were washed, suspended in PBS ( $2\%$ ,  $50 \mu\text{L}$ ), and added to a serial peptide dilution series from  $600$  to  $5 \mu\text{g/mL}$  in PBS ( $50 \mu\text{L}$ ) in 96-well polypropylene plates (V-bottom, Greiner Bio-One GmbH) and incubated ( $37^\circ\text{C}$ , 1 h). After centrifugation ( $1000\text{g}$ ) the absorbance

of the supernatants was determined in a 384-well plate (flat-bottom, Greiner Bio-One GmbH) at  $405 \text{ nm}$  in a Paradigm microplate reader. The positive and negative controls were  $0.1\%$  triton X-100, melittin ( $75$  to  $0.6 \mu\text{g/mL}$ ) and PBS, respectively.

**Fluorescence Microscopy.** *E. coli* ATCC 25922, *K. pneumoniae* DSM 681, and *P. aeruginosa* DSM 3227 were grown overnight in nutrient broth and diluted with  $33\%$  TSB medium. Api88 labeled N-terminally with 5(6)-carboxyfluorescein was added to the cell suspension ( $8 \times 10^7$  cells/mL) at a final concentration of  $125 \mu\text{g/mL}$ , incubated ( $90 \text{ min}$ ,  $37^\circ\text{C}$ ), and centrifuged ( $12000\text{g}$ ). The cells were washed twice with sterile NaCl solution ( $0.9\%$ ) and once with water ( $600 \mu\text{L}$  each) and resuspended in water ( $50 \mu\text{L}$ ). One-fifth of the suspension was dried on a microscope dish (darkness), embedded (mowiol mounting solution), and covered with a coverslip, and the fluorescence was measured on a confocal laser scanning microscope TCS SP5 (Leica Microsystems, Wetzlar, Germany).

Alternatively, *E. coli* BL21 AI ( $3 \times 10^8$  cells/mL) were incubated with Api88 labeled at the side chain of Orn-1 with 5(6)-carboxyfluorescein ( $10 \mu\text{mol/L}$ ,  $\sim 1.5$ -fold MIC) at RT ( $60 \text{ min}$ ). The background fluorescence was quenched with trypan blue ( $10 \mu\text{L}$ ,  $1 \text{ g/L}$ ),<sup>52</sup> and the fluorescence was measured on the confocal laser scanning microscope TCS SP5.

**Animal Studies.** All experiments started after an acclimatization period of at least 3 days in accordance with FELASA and GV-Solas guidelines. The animal studies were approved by the Animal Care and Usage Committee of the state agency (Landesdirektion Leipzig, file number: 24-9168.11/12/22).

**Api88 Distribution in Mice.** Female NMRI outbred mice ( $40-45 \text{ g}$ , 12 weeks) were anesthetized with ketamine ( $100 \text{ mg/kg}$  BW) and medetomidine ( $1 \text{ mg/kg}$  BW) in sterile NaCl solution ( $0.9\%$ ,  $200 \mu\text{L}$  i.p.). DY675-Api88 ( $40 \mu\text{g}$  in  $200 \mu\text{L}$  sterile PBS) was injected i.p., and the fluorescence was measured on a NightOWL II LB 983 (Berthold Technologies GmbH, Bad Wildbad, Germany) with the following parameters:  $\lambda_{\text{exc}} = 630 \pm 20 \text{ nm}$ ,  $\lambda_{\text{em}} = 720 \pm 20 \text{ nm}$ , sample size  $129.873$ , sample height  $55$ , camera gain low, camera readout fast, exposure time  $1.0$  or  $0.1 \text{ s}$  (Photo), and illumination  $0$  or  $10$  (Photo). The mice were euthanized with  $\text{CO}_2$ , and the organs were analyzed using the same parameters.

Male Caesarean Derived-1 mice from the Institute for Cancer Research (ICR-CD-1, Harlan Laboratories, Venray, The Netherlands;  $25-30 \text{ g}$ ) were used according to the Ethical Committee principles of laboratory animal welfare as approved by our institute (Ghent University, Faculty of Veterinary Medicine, 2009-052). CD-1 mice were anesthetized with urethane (i.p.,  $3 \text{ g/kg}$  BW), and the jugular vein and carotid artery were isolated.<sup>125</sup>I-Api88 ( $30\,000 \text{ cpm}/\mu\text{L}$ ) and <sup>125</sup>I-BSA were injected separately into the jugular vein. The radioactivity was determined after specified time periods in serum (prepared from blood collected from the carotid artery) and different organs (brain, spleen, kidney, liver, lung, heart) after decapitation (for details see Supporting Information). The theoretical background of the multiple time regression analysis is based on the Gjedde equation.<sup>53</sup> The experiments were performed in duplicate.

Capillary depletion, i.e., the extent of <sup>125</sup>I-Api88 crossing the capillary wall into the brain parenchyma instead of being trapped in the capillary cells, was determined by the method of Triguero *et al.*<sup>54</sup> as modified by Gutierrez *et al.*<sup>55</sup> (for details see Supplementary). Briefly, the peptide was injected into the jugular vein of anesthetized CD-1 mice. Blood was collected from the abdominal aorta and the brain was perfused manually, before it was collected, homogenized, weighed, and separated by centrifugation into the capillaries (pellet) and parenchyma and fat tissues (supernatant). Compartmental BBB distribution was evaluated from plotting capillaries/serum and parenchyma/serum activity ratios versus time ( $n = 2$ ).

**NMRI Mouse Model.** Acute toxicity of Api88 was studied for doses of  $20$  and  $40 \text{ mg/kg}$  BW by injecting either dose four times ( $0$ ,  $3$ ,  $7$ , and  $24 \text{ h}$ ) into NMRI mice ( $28-32 \text{ g}$ ,  $\sim 7$  weeks old). The antibacterial therapy was done with NMRI mice ( $25-28 \text{ g}$ ,  $6-8$  weeks old) infected with a lethal dose of *E. coli* strain ATCC 25922 ( $1.1 \pm 0.2 \times 10^6$  CFU in the presence of  $2.5\%$  (w/v) mucin, i.p.).<sup>56</sup> Api88 ( $20$  to  $1.25 \text{ mg/kg}$  BW) and ciprofloxacin ( $40 \text{ mg/kg}$  BW) were dissolved

in aqueous glucose solution (5% w/v) and administered three times i.p. (1, 4, and 8 h post infection). As negative control the glucose solution was added at the same time intervals. Mice were checked 3 times per day for the health status (mobility, breathing, feeding, fur appearance (plain or scrubby), etc.) for a total period of 5 days and weighed 1 day before and 1 and 5 days after infection, before the organs were removed and analyzed histopathologically. Moribund mice were euthanized in accordance with the Animal Care and Usage Committee of the Landesdirektion Leipzig.

For splenocyte analyses residual spleen not needed for the histopathological analysis was used for preparation of a single cell suspension. The portions of splenocyte subpopulations and the expression of the activation marker CD86 by professional antigen-presenting cells were determined by flow cytometry analysis. The different immune cell subpopulations were identified by their expression of the following markers: neutrophilic granulocytes (Gr1<sup>+</sup>, exclusion of eosinophilic granulocytes by counterstaining of SiglecF), macrophages (CD11b<sup>+</sup>, F4/80<sup>+</sup>, CD11c<sup>-</sup>, B220<sup>-</sup>), dendritic cells (CD11c<sup>+</sup>), B cells (B220<sup>+</sup>, CD11c<sup>-</sup>, CD11b<sup>-</sup>), and T cells (CD3<sup>+</sup>, B220<sup>-</sup>).

**CFW-1 Mouse Infection Model.** Female CFW-1 mice (body weight 20–25 g; 4–5 weeks of age) were infected i.p. with *E. coli* Neumann (an *E. coli* strain, adapted for mouse infection models) with an inoculum of  $\sim 10^7$  CFU/mL in a final volume of 200  $\mu$ L in 0.9% aqueous NaCl per animal. Peptides were dissolved in aqueous PVP (Kollidon FP17) and administered i.p. covering a dose range of 0, 2.5, 5, 10, 20 mg/kg at 0.5, 4, and 8 h post infection. Imipenem (injected as imipenem/cilastatin (500 mg/500 mg); trade name Zienam, Msd Sharp & Dohme GmbH, Haar, Germany) was administered in a dose range of 5, 10, 40 mg/kg with the same schedule. Survival of the mice was monitored every 4 h (except night time) during the first day of treatment and daily inspections afterward until day 5 post treatment.

## ■ ASSOCIATED CONTENT

### ■ Supporting Information

This material is available free of charge *via* the Internet at <http://pubs.acs.org>.

## ■ AUTHOR INFORMATION

### Corresponding Author

\*E-mail: Hoffmann@chemie.uni-leipzig.de.

### Notes

The authors declare the following competing financial interest(s): R.H. is a cofounder of AMP-Therapeutics GmbH (Leipzig, Germany) and was appointed to their scientific advisory board in 2010.

## ■ ACKNOWLEDGMENTS

G.A., R.H., and N.S. were supported by the European Fund for Regional Structure Development (EFRE, European Union and Free State Saxony) by grants 13408/2286 (G.A.), 13405/2286 and 4-0123.55-20-0631-05/4 (both to R.H.), and 13406/2286 (N.S.) and the "Bundesministerium für Bildung und Forschung" BMBF by Innoprofile (R.H.). S.V.D. and B.D.S. were supported by the Institute for the Promotion of Innovation through Science and Technology in Flanders (IWT No. 73402).

We thank Manuela Fritsch, Agneta Mewes, Sarah Leitenroth, and Monique Richter for technical assistance during the animal studies; Prof. Dr. Peter Seibel and Dr. Ingo Schäfer for recording the confocal microscope images; and the Joint Berlin MX Laboratory at the Helmholtz Zentrum Berlin (Bessy II) for beam time and assistance during synchrotron data collection, as well as for traveling support.

## ■ REFERENCES

- (1) Kotra, L. P., Golemi, D., Vakulenko, S., and Mobashery, S. (2000) Bacteria fight back. *Chem. Ind.*, 341–344.
- (2) D'Costa, V. M., King, C. E., Kalan, L., Morar, M., Sung, W. W. L., Schwarz, C., Froese, D., Zazula, G., Calmels, F., Debruyne, R., Golding, G. B., Poinar, H. N., and Wright, G. D. (2011) Antibiotic resistance is ancient. *Nature* 477, 457–461.
- (3) Michalopoulos, A., and Falagas, M. E. (2010) Treatment of Acinetobacter infections. *Expert Opin. Pharmacother.* 11, 779–788.
- (4) Kumarasamy, K. K., Toleman, M. A., Walsh, T. R., Bagaria, J., Butt, F., Balakrishnan, R., Chaudhary, U., Doumith, M., Giske, C. G., Irfan, S., Krishnan, P., Kumar, A. V., Maharjan, S., Mushtaq, S., Noorie, T., Paterson, D. L., Pearson, A., Perry, C., Pike, R., Rao, B., Ray, U., Sarma, J. B., Sharma, M., Sheridan, E., Thirunarayan, M. A., Turton, J., Upadhyay, S., Warner, M., Welfare, W., Livermore, D. M., and Woodford, N. (2010) Emergence of a new antibiotic resistance mechanism in India, Pakistan, and the UK: a molecular, biological, and epidemiological study. *Lancet Infect. Dis.* 10, 597–602.
- (5) Kumarasamy, K., and Kalyanasundaram, A. (2012) Emergence of Klebsiella pneumoniae isolate co-producing NDM-1 with KPC-2 from India. *J. Antimicrob. Chemother.* 67, 243–244.
- (6) Khan, N. A. (2008) Acanthamoeba and the blood-brain barrier: the breakthrough. *J. Med. Microbiol.* 57, 1051–1057.
- (7) Mariani, M. M., and Kielian, T. (2009) Microglia in infectious diseases of the central nervous system. *J. Neuroimmune Pharmacol.* 4, 448–461.
- (8) Rock, R. B., Gekker, G., Hu, S. X., Sheng, W. S., Cheeran, M., Lokensgard, J. R., and Peterson, P. K. (2004) Role of microglia in central nervous system infections. *Clin. Microbiol. Rev.* 17, 942–964.
- (9) Brogden, K. A. (2005) Antimicrobial peptides: Pore formers or metabolic inhibitors in bacteria? *Nat. Rev. Microbiol.* 3, 238–250.
- (10) Otvos, L. (2002) The short proline-rich antibacterial peptide family. *Cell. Mol. Life Sci.* 59, 1138–1150.
- (11) Casteels, P., Ampe, C., Jacobs, F., Vaecq, M., and Tempst, P. (1989) Apidaecins - Antibacterial peptides from honeybees. *EMBO J.* 8, 2387–2391.
- (12) Casteels, P., and Tempst, P. (1994) Apidaecin-type peptide antibiotics function through a non-poreforming mechanism involving stereospecificity. *Biochem. Biophys. Res. Commun.* 199, 339–345.
- (13) Piantavigna, S., Czihal, P., Mechler, A., Richter, M., Hoffmann, R., and Martin, L. L. (2009) Cell penetrating apidaecin peptide interactions with biomimetic phospholipid membranes. *Int. J. Pept. Res. Ther.* 15, 139–146.
- (14) Casteels, P., Romagnolo, J., Castle, M., Casteelsjesson, K., Erdjumentbromage, H., and Tempst, P. (1994) Biodiversity of apidaecin-type peptide antibiotics - prospects of manipulating the antibacterial spectrum and combating acquired-resistance. *J. Biol. Chem.* 269, 26107–26115.
- (15) Ostorhazi, E., Holub, M. C., Rozgonyi, F., Harnos, F., Cassone, M., Wade, J. D., and Otvos, L., Jr. (2011) Broad-spectrum antimicrobial efficacy of peptide A3-APO in mouse models of multidrug-resistant wound and lung infections cannot be explained by in vitro activity against the pathogens involved. *Int. J. Antimicrob. Agents* 37, 480–484.
- (16) Szabo, D., Ostorhazi, E., Binas, A., Rozgonyi, F., Kocsis, B., Cassone, M., Wade, J. D., Nolte, O., and Otvos, L. (2010) The designer proline-rich antibacterial peptide A3-APO is effective against systemic Escherichia coli infections in different mouse models. *Int. J. Antimicrob. Agents* 35, 357–361.
- (17) Benincasa, M., Pelillo, C., Zorzet, S., Garrovo, C., Biffi, S., Gennaro, R., and Scocchi, M. (2010) The proline-rich peptide Bac7(1–35) reduces mortality from Salmonella typhimurium in a mouse model of infection. *BMC Microbiol.* 10, 178.
- (18) Knappe, D., Kabankov, N., and Hoffmann, R. (2011) Bactericidal oncocin derivatives with superior serum stabilities. *Int. J. Antimicrob. Agents* 37, 166–170.
- (19) Scocchi, M., Tossi, A., and Gennaro, R. (2011) Proline-rich antimicrobial peptides: converging to a non-lytic mechanism of action. *Cell. Mol. Life Sci.* 68, 2317–2330.

- (20) Otvos, L., O. I., Rogers, M. E., Consolvo, P. J., Condie, B. A., Lovas, S., Bulet, P., and Blaszczyk-Thurin, M. (2000) Interaction between heat shock proteins and antimicrobial peptides. *Biochemistry* 39, 14150–14159.
- (21) Morell, M., Czihal, P., Hoffmann, R., Otvos, L., Aviles, F. X., and Ventura, S. (2008) Monitoring the interference of protein-protein interactions in vivo by bimolecular fluorescence complementation: the DnaK case. *Proteomics* 8, 3433–3442.
- (22) Bukau, B., and Walker, G. C. (1989) Delta-Dnak52 mutants of *Escherichia coli* have defects in chromosome segregation and plasmid maintenance at normal growth temperatures. *J. Bacteriol.* 171, 6030–6038.
- (23) Knappe, D., Piantavigna, S., Hansen, A., Mechler, A., Binns, A., Nolte, O., Martin, L. L., and Hoffmann, R. (2010) Oncocin (VDKPPYLPRPRPPRRRIYNR-NH<sub>2</sub>): A novel antibacterial peptide optimized against Gram-negative human pathogens. *J. Med. Chem.* 53, 5240–5247.
- (24) Mechler, A., Praporski, S., Atmuri, K., Boland, M., Separovic, F., and Martin, L. L. (2007) Specific and selective peptide-membrane interactions revealed using quartz crystal microbalance. *Biophys. J.* 93, 3907–3916.
- (25) McCubbin, G. A., Praporski, S., Piantavigna, S., Knappe, D., Hoffmann, R., Bowie, J. H., Separovic, F., and Martin, L. L. (2011) QCM-D fingerprinting of membrane-active peptides. *Eur. Biophys. J. Biophys. Lett.* 40, 437–446.
- (26) Sauerbrey, G. (1959) Verwendung Von Schwingquarzen Zur Wagung Dunner Schichten und Zur Mikrowagung. *Z. Phys.* 155, 206–222.
- (27) Knappe, D., Zahn, M., Sauer, U., Schiffer, G., Strater, N., and Hoffmann, R. (2011) Rational design of oncocin derivatives with superior protease stabilities and antibacterial activities based on the high-resolution structure of the oncocin-DnaK complex. *ChemBioChem* 12, 874–876.
- (28) Liebscher, M., and Roujeinikova, A. (2009) Allosteric coupling between the lid and interdomain linker in DnaK revealed by inhibitor binding studies. *J. Bacteriol.* 191, 1456–1462.
- (29) Tapley, T. L., Cupp-Vickery, J. R., and Vickery, L. E. (2005) Sequence-dependent peptide binding orientation by the molecular chaperone DnaK. *Biochemistry* 44, 12307–12315.
- (30) Zhou, Y. S., and Chen, W. N. (2011) iTRAQ-coupled 2-D LC-MS/MS analysis of cytoplasmic protein profile in *Escherichia coli* incubated with apidaecin IB. *J. Proteomics* 75, 511–516.
- (31) Zhou, Y. S., and Chen, W. N. (2011) iTRAQ-coupled 2-D LC-MS/MS analysis of membrane protein profile in *Escherichia coli* incubated with apidaecin IB. *PLoS ONE* 6, e20442.
- (32) Van Dorpe, S., Bronselaer, A., Nielandt, J., Stalmans, S., Wynendaele, E., Audenaert, K., Van De Wiele, C., Burvenich, C., Peremans, K., Hsueh, H., De Tre, G., and De Spiegeleer, B. (2011) Brainpeps: the blood-brain barrier peptide database. *Brain Struct. Funct.* DOI: 10.1007/s00429-011-0375-0.
- (33) Tavano, R., Segat, D., Gobbo, M., and Papini, E. (2011) The honeybee antimicrobial peptide apidaecin differentially immunomodulates human macrophages, monocytes and dendritic cells. *J. Invertebr. Immunol.* 3, 614–622.
- (34) van Ogtrop, M. L., Andes, D., Stamstad, T. J., Conklin, B., Weiss, W. J., Craig, W. A., and Vesga, O. (2000) In vivo pharmacodynamic activities of two glycolcyclines (GAR-936 and WAY 152,288) against various gram-positive and gram-negative bacteria. *Antimicrob. Agents Chemother.* 44, 943–949.
- (35) Andes, D., and Craig, W. A. (2006) Pharmacodynamics of a new cephalosporin, PPI-0903 (TAK-599), active against methicillin-resistant *Staphylococcus aureus* in murine thigh and lung infection models: Identification of an in vivo pharmacokinetic-pharmacodynamic target. *Antimicrob. Agents Chemother.* 50, 1376–1383.
- (36) Biragyn, A., Surenhu, M., Yang, D., Ruffini, P. A., Haines, B. A., Klyushnenkova, E., Oppenheim, J. J., and Kwak, L. W. (2001) Mediators of innate immunity that target immature, but not mature, dendritic cells induce antitumor immunity when genetically fused with nonimmunogenic tumor antigens. *J. Immunol.* 167, 6644–6653.
- (37) Biragyn, A., Ruffini, P. A., Leifer, C. A., Klyushnenkova, E., Shakhov, A., Chertov, O., Shirakawa, A. K., Farber, J. M., Segal, D. M., Oppenheim, J. J., and Kwak, L. W. (2002) Toll-like receptor 4-dependent activation of dendritic cells by beta-defensin 2. *Science* 298, 1025–1029.
- (38) Biragyn, A., Coscia, M., Nagashima, K., Sanford, M., Young, H. A., and Olkhanud, P. (2008) Murine beta-defensin 2 promotes TLR-4/MyD88-mediated and NF-kappa B-dependent atypical death of APCs via activation of TNFR2. *J. Leukocyte Biol.* 83, 998–1008.
- (39) Funderburg, N., Lederman, M. M., Feng, Z., Drage, M. G., Jaclowsky, J., Harding, C. V., Weinberg, A., and Sieg, S. F. (2007) Human beta-defensin-3 activates professional antigen-presenting cells via Toll-like receptors 1 and 2. *Proc. Natl. Acad. Sci. U.S.A.* 104, 18631–18635.
- (40) Kandler, K., Shaykhiev, R., Kleemann, P., Kleszc, F., Lohoff, M., Vogelmeier, C., and Bals, R. (2006) The anti-microbial peptide LL-37 inhibits the activation of dendritic cells by TLR ligands. *Int. Immunol.* 18, 1729–1736.
- (41) Semple, F., Webb, S., Li, H. N., Patel, H. B., Perretti, M., Jackson, I. J., Gray, M., Davidson, D. J., and Dorin, J. R. (2010) Human beta-defensin 3 has immunosuppressive activity in vitro and in vivo. *Eur. J. Immunol.* 40, 1073–1078.
- (42) Singer, D., Zauner, T., Genz, M., Hoffmann, R., and Zuchner, T. (2010) Synthesis of pathological and nonpathological human exon 1 huntingtin. *J. Pept. Sci.* 16, 358–363.
- (43) Gausepohl, H., Pieleus, U., and Frank, R. W. (1992) in *Peptides - Chemistry and Biology: Proceedings of the 12th American Peptide Symposium* (Smith, J. A., Rivier, J. E., Eds.) pp 523–524, ESCOM Science, Leiden.
- (44) Zhu, X. T., Zhao, X., Burkholder, W. F., Gragerov, A., Ogata, C. M., Gottesman, M. E., and Hendrickson, W. A. (1996) Structural analysis of substrate binding by the molecular chaperone DnaK. *Science* 272, 1606–1614.
- (45) Kabsch, W. (2010) XDS. *Acta Crystallogr., Sect. D: Biol. Crystallogr.* 66, 125–132.
- (46) Bailey, S. (1994) The Ccp4 suite - programs for protein crystallography. *Acta Crystallogr., Sect. D: Biol. Crystallogr.* 50, 760–763.
- (47) Vagin, A., and Teplyakov, A. (1997) MOLREP: an automated program for molecular replacement. *J. Appl. Crystallogr.* 30, 1022–1025.
- (48) Emsley, P., and Cowtan, K. (2004) Coot: model-building tools for molecular graphics. *Acta Crystallogr., Sect. D: Biol. Crystallogr.* 60, 2126–2132.
- (49) Murshudov, G. N., Skubak, P., Lebedev, A. A., Pannu, N. S., Steiner, R. A., Nicholls, R. A., Winn, M. D., Long, F., and Vagin, A. A. (2011) REFMACS for the refinement of macromolecular crystal structures. *Acta Crystallogr., Sect. D: Biol. Crystallogr.* 67, 355–367.
- (50) Mosmann, T. (1983) Rapid colorimetric assay for cellular growth and survival - application to proliferation and cyto-toxicity assays. *J. Immunol. Methods* 65, 55–63.
- (51) Cook, J. A., and Mitchell, J. B. (1989) Viability measurements in mammalian-cell systems. *Anal. Biochem.* 179, 1–7.
- (52) Gobbo, M., Benincasa, M., Bertoloni, G., Biondi, B., Dosselli, R., Papini, E., Reddi, E., Rocchi, R., Tavano, R., and Gennaro, R. (2009) Substitution of the arginine/leucine residues in apidaecin Ib with peptoid residues: Effect on antimicrobial activity, cellular uptake, and proteolytic degradation. *J. Med. Chem.* 52, 5197–5206.
- (53) Gjedde, A. (1981) High-affinity and low-affinity transport of D-glucose from blood to brain. *J. Neurochem.* 36, 1463–1471.
- (54) Triguero, D., Buciak, J., and Partridge, W. M. (1990) Capillary depletion method for quantification of blood-brain-barrier transport of circulating peptides and plasma-proteins. *J. Neurochem.* 54, 1882–1888.
- (55) Gutierrez, E. G., Banks, W. A., and Kastin, A. J. (1993) Murine tumor-necrosis-factor-alpha is transported from blood to brain in the mouse. *J. Neuroimmunol.* 47, 169–176.
- (56) Fridmott-Moller, N., Knudsen, J. D., and Espersen, F. (1999) *Handbook of Animal Models of Infection*, Academic Press, London.

## **4 Paper 5:**

### **4.1 Oncocin (VDKPPYLPRPRPPRRIYNR-NH<sub>2</sub>): A Novel Antibacterial Peptide Optimized against Gram-Negative Human Pathogens**

Monash University

**Declaration for Paper 5**

Declaration by candidate

In the case of Paper 5, the nature and extent of my contribution to the work was the following:

Nature of contribution	Extent of contribution (%)
Design and performance of QCM-D experiments, data analysis, contribution to manuscript preparation and review	30%

The following co-authors contributed to the work. If co-authors are students at Monash University, the extent of their contribution in percentage terms must be stated:

Name	Nature of contribution	Extent of contribution (%) for student co-authors only
<b>Daniel Knappe</b>	Design and performance experiments, data analysis, manuscript preparation and review	
<b>Anne Hansen</b>	Experiments, data analysis	
<b>Annegret Binas</b>	Experiments, data analysis	
<b>Oliver Nolte,</b>	Manuscript preparation and review	
<b>Lisandra L Martin</b>	Key ideas, manuscript preparation and review	
<b>Ralf Hoffmann*</b>	Key ideas, manuscript preparation and review	

The undersigned hereby certify that the above declaration correctly reflects the nature and extent of the candidate's and co-authors' contributions to this work\*.

Candidate's Signature		Date
Main Supervisor's Signature		Date 23/05/14

\*Note: Where the responsible author is not the candidate's main supervisor, the main supervisor should consult with the responsible author to agree on the respective contributions of the authors.

**Oncocin (VDKPPYLPRPRPPRRRIYNR-NH<sub>2</sub>): A Novel Antibacterial Peptide Optimized against Gram-Negative Human Pathogens**Daniel Knappe,<sup>†</sup> Stefania Piantavigna,<sup>‡</sup> Anne Hansen,<sup>†</sup> Adam Mechler,<sup>‡,||</sup> Annegret Binas,<sup>§</sup> Oliver Nolte,<sup>§</sup> Lisandra L. Martin,<sup>‡</sup> and Ralf Hoffmann<sup>\*†</sup><sup>†</sup>Institute of Bioanalytical Chemistry, Universität Leipzig, Deutscher Platz 5, D-04103 Leipzig, Germany, <sup>‡</sup>School of Chemistry, Monash University, Clayton, 3800, Victoria, Australia, and <sup>§</sup>AiCuris GmbH & Co. KG, Friedrich-Ebert-Strasse 475, Building 302, D-42117 Wuppertal, Germany. <sup>||</sup>Current address: School of Molecular Sciences, La Trobe University, Bundoora, Australia.

Received March 26, 2010

Small proline-rich antimicrobial peptides (AMP) have attracted considerable interest, as they target specific intracellular bacterial components and do not act by lytic mechanisms. Here, a novel peptide, termed oncocin (VDKPPYLPRPRPPRRRIYNR-NH<sub>2</sub>), is reported that was optimized for the treatment of Gram-negative pathogens. Its minimal inhibitory concentrations in tryptic soy broth medium ranged from 0.125 to 8 µg/mL for 34 different strains and clinical isolates of Enterobacteriaceae and nonfermenters, such as *Escherichia coli*, *Pseudomonas aeruginosa*, and *Acinetobacter baumannii*. Substitutions of two arginine residues by ornithine increased the half-lives in full mouse serum from about 20 min to greater than 180 min and the activity. Both optimized oncocin derivatives were neither toxic to human cell lines nor hemolytic to human erythrocytes. They could freely penetrate lipid membranes and were washed out completely without any sign of lytic activity, as assessed by quartz crystal microbalance. Fluorescence labeled peptides entered the periplasmic space within 20 min at room temperature and homogeneously stained *E. coli* within 50 min. In conclusion, the optimized oncocin represents a very promising candidate for future in vivo work and may serve as a novel lead compound for an antibacterial drug class.

**Introduction**

The incidence of serious bacterial infections is increasing, especially for pathogens resistant to traditional antibiotics. In Europe an estimated three million hospitalized patients acquire nosocomial infections every year, accounting for approximately 50 000 deaths in the EU, as reported by the ECDC (European Centre for Disease Prevention and Control).<sup>1</sup> The U.S. Center for Disease Control and Prevention estimates 2 million nosocomial infections per year in the U.S., accounting for more than 50 000 deaths and more than U.S. \$3.5 billion in additional health care costs. The Gram-positive pathogen methicillin resistant *Staphylococcus aureus*, (MRSA) attracts the most public interest. However, highly resistant Gram-negative pathogens are emerging, causing serious health care problems. Currently, three species of Enterobacteriaceae (*Escherichia coli*, *Klebsiella pneumoniae*, and *Enterobacter cloacae*) and two nonfermenting species (*Acinetobacter baumannii* and *Pseudomonas aeruginosa*) are causing much concern because of the rapid spread of multi or extremely resistant strains. This problem has developed initially from species in which single mutations were sufficient to cause clinically important resistance levels (*P. aeruginosa*) followed by bacteria with multiple mutations (*E. coli*). This has mainly been attributed to the broad prescription of fluoroquinolones.<sup>2</sup> Co-resistance to three antibiotic classes, including third-generation cephalosporins, has already become the fourth most common resistance pattern found for invasive *E. coli* in Europe.

Important mechanisms of Gram-negative bacteria resistance include extended spectrum beta lactamases (ESBL) in *E. coli* or broad range beta lactamases like *K. pneumoniae* carbapenemase (KPC) in *K. pneumoniae*.<sup>3–5</sup> Multidrug resistant *A. baumannii*, associated with invasive infections such as pneumonia, meningitis, and bacteraemia, have been found to be responsible for outbreaks in hospitals especially in intensive care units.<sup>6,7</sup> Most frightening, pan-resistant *A. baumannii* clones were reported from outbreaks in the U.S. and were uniformly susceptible against only polymyxin treatment (e.g., colistin).<sup>8</sup>

Prudent use of existing antibiotics may slow down further resistance development. However, in order to provide effective treatment for the future, innovative antimicrobials are necessary, preferably with novel modes of action and/or belonging to novel drug classes.<sup>9</sup> More recently, inducible antimicrobial peptides (AMP<sup>9</sup>) have moved into the focus of

\*To whom correspondence should be addressed. Phone: 49 (0) 341 9731330. Fax: 49 (0) 341 9731339. E-mail: Hoffmann@chemie.uni-leipzig.de.

<sup>9</sup>Abbreviations: ΔD, dissipation change; Δf, frequency change; AMP, antimicrobial peptides; ATCC, American Type Culture Collection; cfu, colony forming units; DIC, diisopropyl carbodiimide; DMPC, 1,2-dimyristoyl-*sn*-glycero-3-phosphocholine; DMPG, 1,2-dimyristoyl-*sn*-glycero-3-phosphoglycerol (sodium salt); DMSO, dimethyl sulfoxide; DSMZ, Deutsche Sammlung für Mikroorganismen und Zellkulturen; EDTA, ethylenediaminetetraacetic acid; Fmoc, 9-fluorenylmethoxycarbonyl; HOBt, 1-hydroxybenzotriazole; ICB, Identification and Classification of Bacteria database; MIC, minimal inhibitory concentration; MPA, mercaptopropionic acid; ONPG, *o*-nitrophenyl-β-galactoside; PBS, phosphate buffered saline; QCM, quartz crystal microbalance; RP-HPLC, reversed-phase high performance liquid chromatography; SAM, self-assembled monolayer; SDS, sodium dodecyl sulfate; TAM-RA, 5(6)-carboxytetramethylrhodamine; TSB, tryptic soy broth; TFA, trifluoroacetic acid; Tris-HCl, tris(hydroxymethyl)aminomethane hydrochloride; UTI, urinary tract infections.

**Table 1.** Sequences and MIC values of the *Oncopeltus* Antibacterial Peptide 4 and Its Analogues Derived by Substitutions in Positions 11, 19, and 20<sup>a</sup>

peptide	sequence	<i>t<sub>R</sub></i> <sup>b</sup> (min)	monoisotopic mass, MIC (μg/mL)			
			exptl <sup>b</sup>	calcd <sup>b</sup>	<i>E. coli</i> BL21 AI	<i>M. luteus</i> ATCC 10240
<b>1</b>	VDKPPYLPRPPPPRRRIYNNR-OH	17.18	2445.41	2445.35	128	64
<b>2</b>	VDKPPYLPRPTPPRRRIYNNR-OH	17.22	2449.38	2449.35	128	64
<b>3</b>	VDKPPYLPRPHPPRRRIYNNR-OH	17.03	2485.41	2485.36	64	32
<b>4</b>	VDKPPYLPRPKPPRRRIYNNR-OH	16.85	2476.44	2476.40	16	16
<b>5</b>	VDKPPYLPRPRPPRRRIYNNR-OH	17.01	2504.43	2504.40	8	16
<b>6</b>	VDKPPYLPRPRPPRRRIYNNR-NH <sub>2</sub>	16.93	2503.49	2503.42	8	8
<b>7</b>	VDKPPYLPRPRPPRRRIYNNR-OH	17.01	2504.44	2504.40	8	16
<b>8</b>	VDKPPYLPRPRPPRRRIYNNR-NH <sub>2</sub>	16.96	2503.41	2503.42	16	128
<b>9</b>	VDKPPYLPRPRPPRRRIYNNR-OH	17.13	2390.42	2390.36	32	64
<b>10</b>	VDKPPYLPRPRPPRRRIYNNR-NH <sub>2</sub>	17.05	2389.38	2389.38	4	8
<b>11</b>	VDKPPYLPRPRPPRRRIYNNR-NH <sub>2</sub>	16.71	2305.36	2305.33	8	8
<b>12</b>	VDKPPYLPRPRPPRRRIYNNR-OH	17.36	2234.29	2234.26	64	128
<b>13</b>	VDKPPYLPRPPRRRIYNNR-OH	16.67	1687.95	1687.97	nd	nd

<sup>a</sup>The antibacterial activities were determined against nonpathogenic *E. coli* and *M. luteus* strains using a serial dilution of the peptides in 1% TSB. nd: not determined. <sup>b</sup>*t<sub>R</sub>* denotes retention times of the purified peptides on RP-HPLC, and calcd and exptl denote the calculated and experimentally determined monoisotopic masses of the quasimolecular ion [M + H]<sup>+</sup> recorded by MALDI-MS.

antimicrobial research for a number of reasons. AMP, ranging in size from 12 to 100 amino acid residues, have been identified in plants, animals, and microbes.<sup>10</sup> A single species typically produces more than six different AMP, where each peptide often exhibits a different activity spectrum.<sup>11</sup> Most of these AMP act directly on the bacterial membrane via disruptive “lytic” or pore-forming “ionophoric” mechanisms. This is a major concern for systemic treatments due to the possible toxic effects on mammalian cellular membranes at higher concentrations, which reduce the therapeutic index and limit their clinical potential. Consequently, investigation of these peptide classes mostly considers topical applications. However, such toxic effects might be overcome where AMP specifically target bacterial proteins without cross-reactivity toward human proteins. In recent years, one class of AMP that has attracted much interest is the small, proline-rich peptide family commonly found in both mammals, including humans (cathelicidins), and insects. These are predominantly active against Gram-negative bacteria including life threatening human pathogens, such as, *E. coli*, *K. pneumoniae*, and *P. aeruginosa*. The insect-derived Pro-rich AMP, such as abaecin, apidaecin, drosocin, formaecin, lebecin, and pyrrhocoricin,<sup>12–16</sup> are typically 20–35 residues long and have a relatively high proportion of basic amino acid residues. Among these AMP, drosocin and pyrrhocoricin have attracted much interest because their favorable antibacterial activities and low toxicity toward mammalian cell lines. Most notably, analogues have been designed with improved in vivo activities and pharmaceutical properties by the Otvos laboratory.<sup>17</sup>

The 2 kDa *Oncopeltus* antibacterial peptide 4 was originally isolated from *Oncopeltus fasciatus* (milkweed bug) together with three other AMP following infection with *P. aeruginosa* and *Pseudomonas putida*.<sup>18</sup> The amino acid sequence VDKPPYLPRP(X/P)PPRRRIYNNR was determined by Edman degradation, although position 11 was uncertain and positions 19 and 20 were also questioned by the authors. This peptide showed a 70% sequence identity to pyrrhocoricin isolated from *Pyrrhocoris apterus*<sup>16</sup> as well as a 70% identity to the N-terminal 13 residues of both metalnikowin 1<sup>19</sup> and PR-39 isolated from *Palomena prasina* and *Sus scrofa*,<sup>20</sup> respectively. Because of the high proportion of proline (30%) and a large number of cationic amino acids (25%), this peptide is included in the family of Pro-rich AMP.

In this study, we investigated the antibacterial properties of the original sequence reported for *Oncopeltus* antibacterial

peptide 4, which to the best of our knowledge has not been studied previously. Initially, the synthetic peptide was completely inactive toward both *E. coli* and *Micrococcus luteus*, so substitutions of amino acids into the ambiguous positions 11, 19, and 20 in the original sequence were included. In addition, the shortened and mutated 19-mer sequence containing a C-terminal amide (termed oncocin, peptide 10 (VDKPPYLPRPPRRRIYNNR-NH<sub>2</sub>)) was found to be active toward 37 different isolates of *E. coli*, *K. pneumoniae*, *P. aeruginosa*, *A. baumannii*, *E. cloacae*, and *Proteus vulgaris*. The minimal inhibitory concentrations (MIC) for these bacterial stains and clinical isolates ranged from 0.125 to 8 μg/mL when tested in TSB medium. Oncocin (peptide 10) was also found to be relatively stable in serum, nontoxic to SH-SY5Y and HeLa cells, and nonhemolytic. Furthermore, the fluorescein-labeled oncocin peptide penetrated *E. coli* cells within 50 min. The mechanism for peptide penetration using artificial lipid layers was also investigated by quartz crystal microbalance (QCM), which indicated that oncocin can freely traverse these lipid membranes and clearly does not act by a membrane disrupting or lytic mechanism. Such peptide–membrane characteristics support activity via an intracellular target.

## Results

Surprisingly, the synthetic peptide corresponding to the reported sequence for *Oncopeltus* antibacterial peptide 4 (**1**, VDKPPYLPRPPPPRRRIYNNR) was only very slightly active against *E. coli* BL21 AI and *M. luteus* (Table 1). Because peptide **1** contained several uncertain positions, we decided to substitute some residues to improve the activity. First, several variants were constructed for position 11 and tested. Threonine was an obvious choice because of the high sequence homologies to drosocin and pyrrhocoricin in this region; however, the activity did not improve for peptide **2** (Table 1). Basic amino acid residues such as His, Lys, and Arg (peptides **3–5**) were explored because they are also found in this class of AMP, and these variants were observed to improve the MIC-values: 8 μg/mL for *E. coli* BL21 AI and 16 μg/mL for *M. luteus*. The most active of these analogues, i.e., peptide **5** containing Arg in position 11 (Table 1), was then further modified at the two C-terminal residues. The Asn-Arg variant, corresponding to residues 19 and 20 of oncopeltus 4 was constructed (peptide **9**, Table 1). As the C-termini are always difficult to identify by Edman-sequencing, Asn and Arg

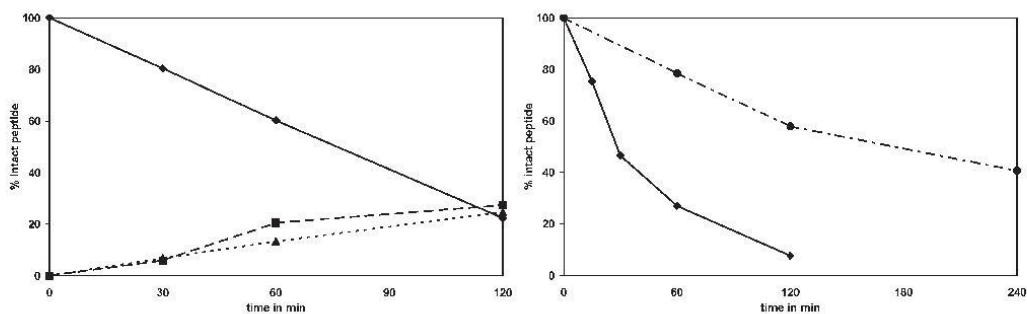


**Figure 1.** Stability of peptides **10** (solid line, both panels) and **11** (dots and dashes, right panel) in 25% aqueous (left) and undiluted mouse serum (right). The determined peptide amounts are shown relative to the peptide quantities obtained for an incubation time of 0 min (set to 100%). The two major degradation products identified by MALDI-MS corresponded to the N-terminal 18 residues (peptide **12**, dashed line, left panel) and 14 residues (peptide **13**, dotted line, left panel).

residues are typically detected as weak signals and were also questioned by Schneider's group.<sup>18</sup> Initially, these two residues were reversed (peptide **7**), as the resulting sequence would be homologous to the C-terminal last nine residues of the pyrrolic sequence. However, the MIC values did not improve (Table 1). Then amidation of the C-termini of both peptides (peptides **6** and **8**) was explored; however, these did not influence the antibacterial activity. Interestingly, shortening the sequence by deletion of Asn19 reduced the activity by about 4-fold for the C-terminal acid analogue (peptide **9**), although the C-terminal amidation improved it by approximately 2-fold (peptide **10**). Finally the MIC values for the "optimized" peptide **10** were in good agreement with other related insect derived AMP. It is noted that the optimized sequence most likely does not represent the native peptide. Therefore, we use the term oncocin for the artificial sequence **10** (VDKPPYLPRPRPPRRRIYNR-NH<sub>2</sub>) indicating its relation to peptide **1**, i.e., the reported *Oncopeltus* antibacterial peptide **4**.

The serum stability of peptide **10** (oncocin) was studied first in order to judge possible systemic pharmacological applications. Considering the unfolded, disordered peptide was only 19 residues, it was found to be relatively stable with a half-life of approximately 70 min in 25% aqueous serum at 37 °C (Figure 1, left). This compared well with peptide **9** with a free C-terminus with a half-life of less than 30 min (data not shown). Only two degradation products of peptide **10**, with cleavage sites C-terminal to Asn18 (peptide **12**) and Arg14 (peptide **13**), were detected after 30 min at the 10% level (Figure 1, left). The extent of degradation increased continuously to more than 20% of the original peptide after 2 h had elapsed. On the basis of the peak areas observed, these two metabolites and the remaining peptide **10** represented more than 60% of the original peptide content. This indicated that both metabolites were formed by two major degradation pathways and that both metabolites were more stable in serum than peptide **10** itself. The first metabolite, peptide **13**, probably results from a trypsin-like cleavage between the two Arg residues, whereas peptide **12** is more likely to be produced by the action of carboxypeptidases. The serum stabilities obtained are similar to other members of the family of short, proline-rich peptides reported recently.<sup>21,22</sup> Notably, as peptide **12** did not possess any antibacterial activity, it was deemed necessary to improve the stability of both cleavage sites. This was achieved by replacing Arg14 and Arg19 by

ornithine (peptide **11**), an amino acid that is not attacked by trypsin and trypsin-like enzymes (Figure 1, right).<sup>23</sup> The half-life for the resulting peptide **11** in full serum was approximately 180 min compared to only about 20 min for peptide **10**. More importantly, no stable metabolite was detected for peptide **11**, indicating that the peptide is not degraded at a single site but more slowly at different positions. Peptide **11** also maintained the high antibacterial activities observed for the "optimized" peptide **10** (Table 1).

The third important criterion in which to judge the pharmacological properties of AMP *in vitro* is their toxicity against mammalian cell lines. Neither the optimized peptide **10** nor its double ornithine analogue (peptide **11**) showed any toxic effects on HeLa- or neuronal-cell-like differentiated SH-SY5Y cells (Figure 2, upper panel) at a peptide concentration of 600 µg/mL, which was about 100-fold above their MIC-values against *E. coli* BL21 AI. The observed nontoxicity was also found for two other insect derived peptides of this AMP family, i.e., drosocin and apidaecin 1b (Figure 2, upper panel). Moreover, none of the tested peptides showed any hemolytic activity against human erythrocytes in the studied peptide concentration range up to 600 µg/mL (Figure 2, lower panel).

Although the nonpathogenic bacterial strains *E. coli* BL21 AI and *M. luteus* were originally used to optimize the antibacterial properties of oncocin (peptide **10**), they do not allow the pharmacological properties of this lead compound to be assessed against human pathogens. Therefore, we tested a broad panel of 37 strains and clinical isolates from seven Gram-negative bacteria (Table 2). The MIC values for the eight *E. coli* strains tested and clinical isolates were very similar ranging from 0.5 to 8 µg/mL for peptide **10** and only 0.5 to 2 µg/mL for peptide **11**. Thus, the double ornithine analogue was equally active against all *E. coli* strains with an average MIC value of 1 µg/mL. Interestingly, both peptides showed equal activities against *E. coli* strains very prone to peptide **10** but were different for strains less prone to peptide **10**, such as *E. coli* 70419002. This improved activity of peptide **11** could be related to its higher protease resistance, as indicated by the serum stability. The peptide might be stable over longer times in the medium (or bacteria) and thus kill the bacteria more effectively. This effect was also observed for *P. aeruginosa* and *K. pneumoniae* (Table 2). The MIC values of peptide **11** varied only between 1 and 4 µg/mL among the eight *P. aeruginosa* strains and clinical isolates and between 0.5 and 2 µg/mL among the six *K. pneumoniae* strains and clinical

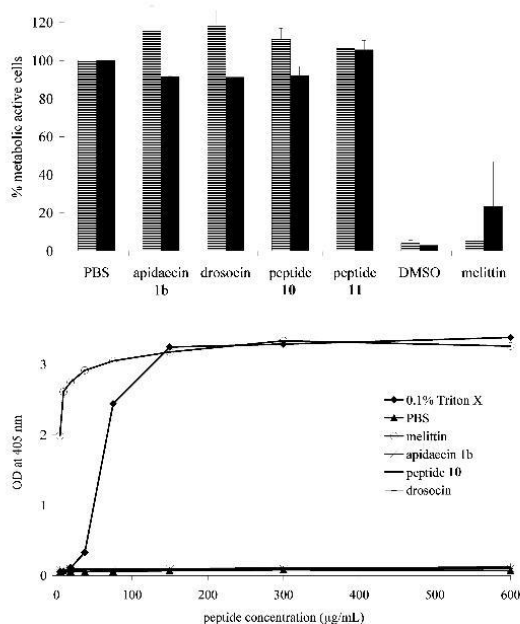


**Figure 2.** Cytotoxicity against HeLa cells (full bars) and differentiated SH-SY5Y cells (striped bars) using the MTT cell proliferation assay (upper panel) and hemolytic activity (lower panel) of different antimicrobial peptides. SH-SY5Y and HeLa cells were incubated with AMP (600  $\mu\text{g}/\text{mL}$ ), melittin (100  $\mu\text{g}/\text{mL}$ ), and DMSO (12% (v/v), positive control) for 24 h. The data were normalized to PBS (100%) as negative control. Human erythrocytes were incubated with a 2-fold serial dilution of a peptide (600 to 5  $\mu\text{g}/\text{mL}$ ), Triton X-100 (0.1%, positive control), and PBS (negative control) at 37  $^{\circ}\text{C}$  for 60 min.

isolates tested (Table 2). Thus, peptide **11** was in general more active against the tested Gram-negative human pathogens than oncocin with less variation among the bacterial strains and clinical isolates. Although *in vitro* data cannot be simply extrapolated to animal models, both peptides **10** and **11** represent new promising lead compounds with interesting antibacterial properties.

The interaction between peptides **10** and **11** with bacterial mimetic membranes was followed using a quartz crystal microbalance (QCM).<sup>24</sup> Supported lipid bilayers composed of DMPC–DMPG (4:1) were prepared on the gold coated quartz crystal, and the response of the frequency change ( $\Delta f$ ) with time for a series of harmonic resonances was monitored as described in our earlier work.<sup>24,25</sup> The concentration dependence of the peptides binding to the membrane for 1–15  $\mu\text{M}$  peptide **10** is shown in Figure 3A, and that for peptide **11** is shown in Figure 3B. The rapid incorporation of the peptides into the membrane is apparent by the initial slope of the  $\Delta f$ – $t$  traces prior to the saturation of the membrane at  $\sim 10$  min. For both peptides the 1  $\mu\text{M}$  solutions show subsaturation of the membrane, whereas 5–15  $\mu\text{M}$  appears to saturate the membranes albeit with a slightly greater mass of the modified peptide **11** binding. To elucidate the nature of the peptide–membrane interaction, these data were recorded over multiple harmonics and both peptides showed responses consistent with transmembrane binding (data not shown).

**Table 2.** Broad Spectrum Antimicrobial Activity of Peptides **10** and **11** against Different Gram-Negative Pathogens (Reference [DSM, ATCC, IBC] and Clinical Isolates) Determined in 1% TSB

pathogen	MIC ( $\mu\text{g}/\text{mL}$ )	
	peptide <b>10</b>	peptide <b>11</b>
<i>P. aeruginosa</i> DSM3227	4	4
<i>P. aeruginosa</i> Walter	8	4
<i>P. aeruginosa</i> ATCC27853	4	2
<i>P. aeruginosa</i> PAO1	2	2
<i>P. aeruginosa</i> 60811001	2	2
<i>P. aeruginosa</i> 60909001	2	1
<i>P. aeruginosa</i> 61118003	2	1
<i>P. aeruginosa</i> 70108001	4	2
<i>E. coli</i> 70329001	1	1
<i>E. coli</i> 70430001	1	0.5
<i>E. coli</i> 70419002	8	2
<i>E. coli</i> 70502001	1	1
<i>E. coli</i> Neumann	2	0.5
<i>E. coli</i> 205024	4	1
<i>E. coli</i> 455/7	0.5	0.5
<i>E. coli</i> 8474	0.5	0.5
<i>K. pneumoniae</i> DSM681	0.25	0.5
<i>K. pneumoniae</i> 57 USA	0.25	0.5
<i>K. pneumoniae</i> 63	8	2
<i>K. pneumoniae</i> 8085	0.5	0.5
<i>K. pneumoniae</i> ATCC12657	0.5	0.5
<i>K. pneumoniae</i> ATCC27799	1	1
<i>A. baumannii</i> ICB14067	1	1
<i>A. baumannii</i> ICB14072	1	1
<i>A. baumannii</i> ICB14073	2	1
<i>A. baumannii</i> ICB9250	0.5	0.5
<i>A. baumannii</i> M17	1	1
<i>E. cloacae</i> 34654	0.25	0.5
<i>E. cloacae</i> Ha088	0.125	0.25
<i>E. cloacae</i> Ha089	0.125	0.25
<i>E. cloacae</i> Ha185	0.5	0.5
<i>E. cloacae</i> Ha89	0.25	0.25
<i>P. vulgaris</i> ICB9081	4	8
<i>P. vulgaris</i> ICB9095	4	4
<i>Stenotrophomonas</i> ICB308054	32	32
<i>Stenotrophomonas</i> ICB7569	8	16
<i>Stenotrophomonas</i> ICB7789	32	32

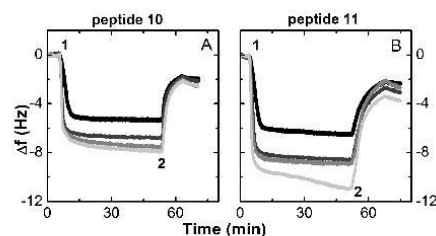


**Figure 3.** Peptides **10** (A) and **11** (B) uptake on DMPC–DMPG (4:1) membrane as a function of peptide concentration (1, 5, 10, 15  $\mu\text{M}$  peptide corresponds to darkest to lightest color). The number “1” indicates the points where the peptide solution was introduced. Only the seventh harmonic data are shown. Data have been normalized to zero for the membrane coated chip in high salt buffer. The number “2” indicates introduction of buffer wash at 100  $\mu\text{L}/\text{min}$ .

Interestingly, the peptide–membrane interactions for both peptides **10** and **11** were not permanent, as the introduction of the PBS solution (position 2 in Figure 3) resulted in removal of almost the entire mass of bound peptide. In both cases, a residual amount of peptide remained in the membrane, between  $\sim 2$  Hz for peptide **10** and  $\sim 3$  Hz for peptide **11**.

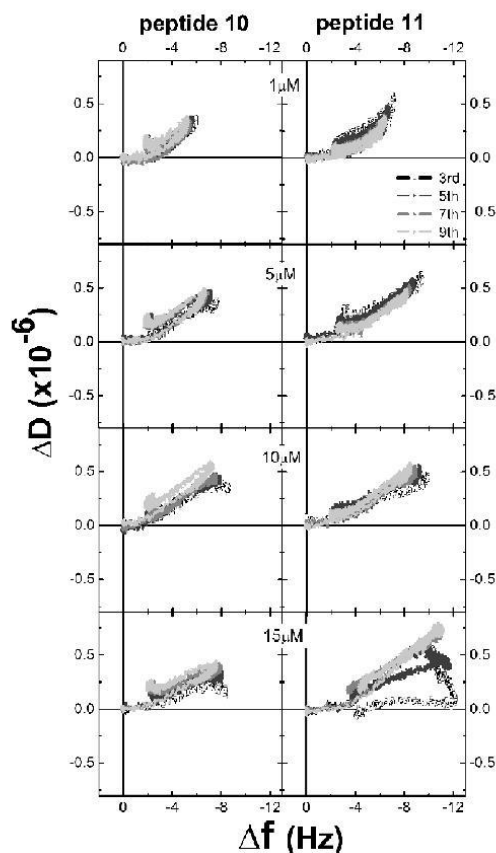


**Figure 4.** Energy dissipation ( $\Delta D$ ) vs frequency ( $\Delta f$ ) dependence for peptides **10** (left column) and **11** (right column) on DMPC–DMPG (4:1) membrane bilayer. The peptide concentrations increase from 1 to 15  $\mu\text{M}$  (top to bottom), and data from the third, fifth, seventh, and ninth harmonic are shown.

The QCM data can also contribute to our understanding of the mechanism of each peptide interacting with the membrane. The characteristic *fingerprints* for each peptide interaction is recorded as the change in energy dissipation,  $\Delta D$ <sup>25,26</sup> measured simultaneously with the temporal variation in the frequency,  $\Delta f$ . Thus, the dependence of  $\Delta D$  versus  $\Delta f$  provides an assessment of the structural influence of the peptide binding per unit mass (i.e.,  $-\Delta f$ ) on the membrane properties.<sup>25–27</sup> Figure 4 shows the  $\Delta D$ – $\Delta f$  plots for peptides **10** (left column) and **11** (right column) for 1, 5, 10, and 15  $\mu\text{M}$  (top to bottom panels). For each of these plots, the addition of the peptide solution (point 1 on Figure 3) has been set to the origin. Both peptide *fingerprints* show a similar trend, with the uptake of the peptide (more negative frequency) having a minimal effect on the membrane properties (only a small increase in dissipation). Notably, the change of the dissipation was very similar for the two peptides and over all the concentrations. This supports the same mechanism of peptide interaction with the membrane which is also independent of concentration. Furthermore, these plots confirm that the peptide uptake was reversible because the wash with PBS solution, which

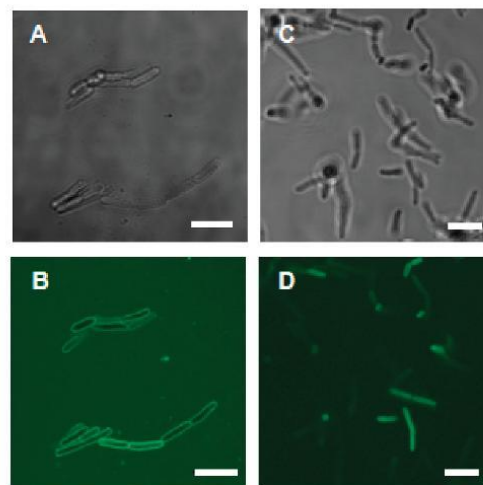


**Figure 5.** Confocal laser scanning microscopy images of *E. coli* BL21 AI cultures incubated with 5(6)-carboxyfluorescein-labeled peptide **10** (30  $\mu\text{mol/L}$ ) for 20 min (A, B) or 50 min (C, D). The fluorescence of the medium was quenched with TAMRA (180  $\mu\text{M}$ ). Shown are the phase contrast (A, C) and fluorescence images (B, D). Bars equate to 5  $\mu\text{m}$ .

corresponds to the furthest point (maximum  $-\Delta f$  and corresponding to point 2 in Figure 3), shows the dissipation returning to the origin, indicating that most of the peptide was removed from the membrane layer. Nevertheless, the buffer was unable to remove all the peptide, leaving some mass (presumably peptide molecules) associated with the membrane regardless of the concentration ( $\sim 2$  Hz for peptide **10** and  $\sim 3$  Hz for peptide **11**). The  $\Delta D$ – $\Delta f$  plots also confirmed that for both peptides all four harmonics probed in these experiments responded similarly, supporting transmembrane peptide insertion across the lipid bilayer without causing a substantial perturbation to the membrane.

On the basis of the QCM studies with artificial membranes and following the hypothesis that small, proline-rich peptides kill bacteria by entering the cells and inhibiting intracellular targets like DnaK,<sup>28</sup> peptide **10** N-terminally labeled with 5(6)-carboxyfluorescein was added to an *E. coli* BL21 AI culture. Confocal fluorescence microscopy revealed that the fluorescence is first enriched at or close to the surface of *E. coli* cells after 20 min at room temperature before it is homogeneously distributed within the living bacterial cells (Figure 5). This clearly indicates that peptide **10** penetrates the bacterial membrane relatively quickly and stays either in the membrane or in the periplasmic space before it is most likely actively transported into the cells. Similar observations were also reported for apidaecin,<sup>29,30</sup> pyrrolicoricin,<sup>28</sup> and Bac7.<sup>31</sup>

#### Discussion

Currently, most infections can be treated with available antibiotics, even if in some cases combination therapies might be mandatory. While a couple of new antimicrobials are in the pipeline or have already been launched for the treatment of MRSA and other Gram-positive pathogens, there is a lack of promising candidates active against Gram-negative pathogens. Importantly, Gram-negative bacteria are far more effective in

accumulating resistance traits; thus, new antimicrobials are needed.<sup>32</sup> In the current paper we reported the optimization of the naturally occurring *Oncopeltus* peptide 4 (peptide **1**) to the “optimized” peptide **11**, exhibiting promising antibacterial activity against the most serious Gram-negative pathogens. Starting with peptide **1**, which to the best of our knowledge has not been investigated for its antimicrobial properties, it was possible to obtain high antibacterial activity against *E. coli* by substituting position 11 against arginine and deleting asparagine at position 19. The activity of the 19-residue-long peptide **9** was further enhanced by C-terminal amidation. The limited protease resistance of peptide **10** was identified as a major weakness for therapeutic peptide applications and was overcome by substituting arginine by ornithine residues at positions 15 and 19. Despite ornithine not occurring naturally in proteins, the modified peptide **11** did not show any toxic effects against HeLa- and differentiated SH-SY5Y-cell cultures or hemolytic effects against erythrocytes. Considering the blood volume of animals and humans relative to their body weight, the tested peptide concentration of 600  $\mu\text{g}/\text{mL}$  corresponds to a peptide dose of more than 60 mg/kg administered intravenously (i.v.). Although in vitro data have to be interpreted with caution, the lack of toxicity against mammalian cells together with the high activity against Gram-negative bacteria can be explained by their mode of action. Data published for apidaecin, pyrrolicin, and drosocin<sup>28,30,31</sup> clearly indicate that this class of insect-derived short, proline-rich peptides does not act by a lytic mechanism but kills the bacteria by inhibiting intracellular targets, such as DnaK.<sup>33–35</sup> This rapid intracellular incorporation was supported by the QCM data for peptides **10** and **11**, as they showed no tendency to disrupt or remove any lipids from the bilayer within the concentration range studied. Instead both peptides entered and left the DMPC–DMPG (4:1) lipid bilayers freely and relatively quickly, although the process was not completely quantitative following the PBS wash step. This small amount of residual peptide binding, however, is most likely attributed to some nonspecific binding to the interface between the underlying negatively charged surface of the modified QCM crystal and lipid bilayer. The nonlytic mechanism was further supported by fluorescence microscopy by incubating *E. coli* with 5(6)-carboxyfluorescein-labeled oncocin. The bacterial cells were not lysed during the observation interval of 1 h. Instead the outer layer of the cells was stained indicating a fast penetration of the peptide through the bacterial membrane (Figure 5). Any peptides bound onto the outer surface of the membrane would have been quenched by TAMRA added in high concentrations to the bacterial culture. Likely, the peptides penetrated through the bacterial membrane into the periplasmic space, where they accumulated within 20 min. With the separation in the periplasmic space from TAMRA added to the surrounding medium, the fluorescence was not quenched anymore. From there the peptides entered into the cells in a second step resulting in a homogeneous fluorescence staining throughout the bacterial cell, as much as this can be judged from the limited resolution of confocal microscopy. Once inside the cell the peptides probably inhibited one or more target proteins, such as DnaK,<sup>33–35</sup> and thereby killed the cells slowly without membrane lysis. Although many steps of the peptide uptake and the inhibition of the bacterial targets remain unclear, the slowly emerging underlying mechanisms explain nicely the high specificity of oncocin toward Gram-negative bacteria together with their very low intrinsic toxicity. For all these reasons the optimized oncocin sequences

represent scientifically interesting and therapeutically promising new antibacterial candidates. Although confirmation with a larger collection of isolates is required, their antibacterial spectrum covers perfectly the currently most relevant Gram-negative human pathogens. While these continue to notoriously acquire resistance traits, our novel peptide will most likely not be affected by cross-resistance due to its novel mode of action.

Three bacteria, *E. coli*, *Klebsiella* species, and *Enterobacter* species account for 80–90% of uncomplicated urinary tract infections (UTI).<sup>36</sup> Thus, oncocin may provide complete coverage in this indication, and further research on oncocin should focus first on UTI animal models. The high serum stability obtained for peptide **11** and the ability to also kill nonfermenters (i.e., *A. baumannii* and *P. aeruginosa*) also suggest that severe systemic infections (i.e., pneumonia, bacteraemia, septicemia) could also be treated. Such in vivo and further in vitro studies have been initiated, and these will be published at a later time.

### Conclusion

Using a combination of in vitro assays to study the (i) antibacterial activity against Gram-negative human pathogens, (ii) peptide stability against serum proteases, (iii) hemolytic activity against human erythrocytes, (iv) cytotoxicity, and (v) interaction with artificial lipid bilayers, we could chemically optimize a 19-residue-long sequence called oncocin for systemic treatments. Oncocin (peptide **10**) and its even more promising analogue peptide **11** contain only natural  $\alpha$  L-amino acids and were both synthesized on solid phase in high yields and purities. Thus, oncocin and its analogues represent a promising new class of peptide candidates to treat UTI and systemic infections, based on their superior biomedical properties together with the nonlytic mode of action targeting intracellular bacterial proteins.

### Experimental Section

**Peptide Synthesis.** Peptides were synthesized on Rink amide MBHA resin or Wang resin (MultiSynTech GmbH, Witten, Germany) with standard 9-fluorenylmethoxycarbonyl/*tert*-butyl (Fmoc/Bu) chemistry using a 25  $\mu\text{mol}$  scale on the multiple synthesizer SYRO2000 (MultiSynTech). Amino acid derivatives (>99%, Orpegen Pharma, Heidelberg, Germany) were activated in situ with diisopropylcarbodiimide (DIC, >98% by GC, Fluka Chemie GmbH; Buchs, Switzerland) in the presence of 1-hydroxybenzotriazole (HOBt, >98%, Fluka Chemie).<sup>37</sup> After completion of the peptide synthesis, 5(6)-carboxyfluorescein (Fluka Chemie GmbH) was coupled to the unprotected N-terminus with DIC/HOBt using a part of the resin. The unlabeled or fluorescein-labeled peptides were cleaved with trifluoroacetic acid (TFA, >98%) containing 12.5% (v/v) of a scavenger mixture (ethanedithiols, *m*-cresole, thioanisole, and water, 2.5:5:5:5). The peptides were precipitated with cold diethyl ether and purified by RP-HPLC using a linear aqueous acetonitrile gradient in the presence of an ion pair reagent (eluent A, 0.1% aqueous TFA (>99%); eluent B, 60% aqueous acetonitrile (>99.95% by GC) containing 0.1% TFA) and a Jupiter C<sub>18</sub> column (21.2 mm internal diameter, 250 mm length, 15  $\mu\text{m}$  particle size, 30 nm pore size) (Phenomenex Inc., Torrance, CA). The purified peptides were analyzed by RP-HPLC on a Jupiter C<sub>18</sub> column (4.6 mm internal diameter, 150 mm length, 5  $\mu\text{m}$  particle size, 30 nm pore size; Phenomenex) using a linear gradient from 5% to 56% eluent B for 17 min (see Supporting Information). The purities were above 95% based on the peak areas obtained after background correction. The molecular weight of the peptide was confirmed by

matrix-assisted laser desorption/ionization time-of-flight mass spectrometry (MALDI-TOF-MS; 4700 proteomic analyzer; Applied Biosystems GmbH, Darmstadt, Germany) using  $\alpha$ -cyano-4-hydroxycinnamic acid (4 mg/mL in 60% aqueous acetonitrile containing 0.1% TFA) as matrix (see Supporting Information).

**Bacterial Strains.** Nonpathogenic strains *E. coli* BL21AI and *M. luteus* ATCC 10240 were cultured overnight at 37 °C in nutrient broth (Carl Roth GmbH, Karlsruhe, Germany). All other (pathogenic) bacteria strains were cultured on solid Columbia agar. After overnight culture, colonies were suspended in sterile 0.9% saline to an OD of 0.1. This solution was diluted 1:300 in 1% TSB broth. An amount of 90  $\mu$ L of the diluted bacteria was used for the microdilution assays per well.

**Antibacterial Activity.** The MIC values were determined in triplicate by a liquid broth microdilution assay in sterile 96-well plates (Greiner Bio-One GmbH, Frickenhausen, Germany) using a total volume of 100  $\mu$ L per well.<sup>38</sup> Aqueous peptide solutions (1 mg/mL) were serially 2-fold diluted in 1% TSB starting at 128  $\mu$ g/mL down to typically 0.5  $\mu$ g/mL in eight steps. Overnight cultures of nonpathogenic bacteria were diluted with 1% TSB to  $1.5 \times 10^7$  cells/mL (*E. coli* BL21AI) or  $4 \times 10^7$  cells/mL (*M. luteus* ATCC 10240) and an amount of 50  $\mu$ L was added to each well, gaining a starting cell concentration of  $7.5 \times 10^5$  cells/well and  $2 \times 10^6$  cells/well, respectively. An amount of 90  $\mu$ L of the diluted suspension of the other pathogenic bacteria was used per well, giving a final cfu count (colony forming units) of  $(1-2) \times 10^5$  cells/well. The plates were incubated at 37 °C, and the absorbance of each well was measured after  $20 \pm 2$  h at 595 nm. The MIC was defined as the lowest peptide concentration where the absorbance value did not exceed that of the medium only.

**Serum Stability Assays.** The serum stabilities of all peptides were determined in pure and 25% (v:v) aqueous pooled mouse serum (PAA Laboratories GmbH, Pasching, Austria).<sup>39</sup> Peptides were dissolved in serum at a final concentration of 75  $\mu$ g/mL and incubated at 37 °C. Aliquots taken in triplicate after 0, 30, 60, 120, and 240 min were precipitated by addition of trichloroacetic acid to a final concentration of 3% (v:v). After 10 min on ice, the samples were centrifuged and the supernatant was neutralized with sodium hydroxide solution (1 mol/L) and stored at -20 °C. The samples were analyzed on the analytical Jupiter C<sub>18</sub> column using a linear aqueous acetonitrile or methanol gradient containing 0.1% (v:v) TFA. The metabolites were identified by MALDI-TOF-MS.

**Quartz Crystal Microbalance (QCM).** The mechanism in which these peptides bind to artificial membranes was studied in real time using a QCM-D instrument (Q-sense, Sweden), and the experimental design and methodology are based on published procedures.<sup>24</sup> Liposomes were prepared and deposited onto the gold chip and washed with buffer using "high salt" PBS buffer (0.02 M potassium phosphate, 0.1 M NaCl, pH 6.9).<sup>25</sup> A second "low salt" (0.01 M potassium phosphate, 0.03 M NaCl, pH 6.9) wash step was included to remove unopened liposomes prior to the return to a "high salt" PBS buffer medium. The peptide solution was then introduced, and the change in frequency ( $\Delta f$ ) and dissipation ( $\Delta D$ ) was recorded for the third, fifth, seventh, and ninth harmonics over approximately 60 min for each experiment.

**Confocal Laser Scanning Fluorescence Microscopy.** An overnight culture of bacteria was diluted to  $1.5 \times 10^7$  cells/mL in 1% TSB. A 5(6)-carboxyfluorescein-labeled peptide was added to the suspension together with a 60-fold molar excess of 5(6)-carboxy-tetramethylrhodamine (TAMRA; Merck, Darmstadt, Germany) to obtain a final peptide concentration of 30  $\mu$ mol/L. Aliquots of the suspension (2  $\mu$ L) were spotted on the microscope slides and immediately analyzed on an inverted confocal laser scanning microscope TCS SP5 (argon laser line 488 nm; objective, HCX PL APO lambda blue 63.0  $\times$  1.40 Oil UV; software Leica Application Suite Advanced Fluorescence 1.7.2; Adobe Photoshop CS) (Leica Microsystems, Wetzlar, Germany).

**Hemolytic Activity.**<sup>40</sup> Peptides were serially diluted from 600 to 5  $\mu$ g/mL in phosphate buffered saline (PBS, 8.7 mmol/L Na<sub>2</sub>HPO<sub>4</sub>, 1.2 mmol/L KH<sub>2</sub>PO<sub>4</sub>, 150 mmol/L NaCl, pH 7.4) in a V-bottom 96-well polypropylene plate (Greiner Bio-One GmbH) to a final volume of 100  $\mu$ L. Concentrated human erythrocytes were washed and suspended in PBS to a final concentration of 2%. Aliquots of this suspension (100  $\mu$ L) were added to the peptide solution in each well and incubated (37 °C, 1 h). After centrifugation (1000g), the absorbance of the supernatants was determined in a fresh F-bottom 96-well plate at 405 nm in a Sunrise microplate reader. The positive and negative controls contained 0.1% Triton X-100 and PBS, respectively, added at the same volumes as the peptide solution.

**Cytotoxicity Assay.** Cells were cultured in DMEM/Ham's F-12 medium with 15% (SH-SY5Y) or 5% (HeLa) (v:v) fetal bovine serum containing 1% (w:v) nonessential amino acids and 1% (w:v) streptomycin/penicillin at 37 °C and 5% CO<sub>2</sub>. SH-SY5Y ( $2 \times 10^4$  cells per well) and HeLa cells ( $1.5 \times 10^4$  per well) were seeded in the same medium into 96-well plates (Greiner Bio-One GmbH). After 1 night (HeLa) or after 5 days of differentiation by 10  $\mu$ M *trans*-retinoic acid (SH-SY5Y), cells were washed with PBS and fresh medium was added. Subsequently, the peptide solutions (100  $\mu$ L per well, 600  $\mu$ g/mL) were added and incubated again at identical conditions for 24 h. The cell viability was determined with the cell proliferation kit I (Roche Diagnostics GmbH; Mannheim, Germany). Briefly, an amount of 10  $\mu$ L of the methylthiazolyl-diphenyl-tetrazolium bromide (MTT) reagent was added to a final concentration of 0.5 mg/mL. After incubation (4 h, 37 °C, 5% CO<sub>2</sub>) a sodium dodecyl sulfate (SDS) solution (10% (w:v) in 10 mmol/L hydrochloric acid, 100  $\mu$ L) was added and incubated again at the same conditions (16 h). The absorbance at 590 nm was measured using a Paradigm microplate reader (Beckman Coulter, Wals, Austria) relative to a reference wavelength of 650 nm. The increased absorbance was used to estimate the viability of the cells. In the positive and negative controls the peptide solution was substituted by the same volumes of dimethyl sulfoxide (DMSO) and PBS, respectively.

**Acknowledgment.** We thank Prof. Peter Seibel and Mr. Ingo Schäfer for recording the confocal microscope images. Financial supports from the European Fund for Regional Structure Development (EFRE, European Union and Free State Saxony) and the BMBF (Innoprotile) are gratefully acknowledged. L.L.M. and A.M. thank the Australian Research Council for financial support through the Discovery Grant DP0662816.

**Supporting Information Available:** Reversed phase HPLC chromatograms and MALDI mass spectra for peptides 1–12, as summarized in Table 1. This material is available free of charge via the Internet at <http://pubs.acs.org>.

## References

- Amato-Gauci, A.; Ammon, A. *The First European Communicable Disease Epidemiological Report*; European Centre for Disease Prevention and Control: Stockholm, Sweden, 2007.
- Hooper, D. C. Emerging mechanisms of fluoroquinolone resistance. *Emerging Infect. Dis.* **2001**, *7*, 337–341.
- Jones, R. N. Resistance patterns among nosocomial pathogens. Trends over the past few years. *Chest* **2001**, *119*, 397S–404S.
- Pitout, J. D. D.; Laupland, K. B. Extended-spectrum beta-lactamase-producing enterobacteriaceae: an emerging public-health concern. *Lancet Infect. Dis.* **2008**, *8*, 159–166.
- Bradford, P. A.; Bratu, S.; Urban, C.; Visalli, M.; Mariano, N.; Landman, D.; Rahal, J. J.; Brooks, S.; Cebular, S.; Quale, J. Emergence of carbapenem-resistant *Klebsiella* species possessing the class A carbapenem-hydrolyzing KPC-2 and inhibitor-resistant TEM-30 beta-lactamases in New York City. *Clin. Infect. Dis.* **2004**, *39*, 55–60.

- (6) Fournier, P. E.; Richet, H. The epidemiology and control of *Acinetobacter baumannii* in health care facilities. *Clin. Infect. Dis.* **2006**, *42*, 692–699.
- (7) Katsaragakis, S.; Markogiannakis, H.; Toutouzas, K. G.; Drimousis, P.; Larentzakis, A.; Theodoraki, E. M.; Theodorou, D. *Acinetobacter baumannii* infections in a surgical intensive care unit: predictors of multi-drug resistance. *World J. Surg.* **2008**, *32*, 1194–1202.
- (8) Lolans, K.; Rice, T. W.; Munoz-Price, L. S.; Quinn, J. P. Multicity outbreak of carbapenem-resistant *Acinetobacter baumannii* isolates producing the carbapenemase OXA-40. *Antimicrob. Agents Chemother.* **2006**, *50*, 2941–2945.
- (9) Boucher, H. W.; Talbot, G. H.; Bradley, J. S.; Edwards, J. E.; Gilbert, D.; Rice, L. B.; Scheld, M.; Spellberg, B.; Bartlett, J. Bad bugs, no drugs: no ESKAPE! An update from the Infectious Diseases Society of America. *Clin. Infect. Dis.* **2009**, *48*, 1–12.
- (10) Boman, H. G. Peptide antibiotics and their role in innate immunity. *Annu. Rev. Immunol.* **1995**, *13*, 61–92.
- (11) Barra, D.; Simmaco, M.; Boman, H. G. Gene-encoded peptide antibiotics and innate immunity. Do “animalcules” have defence budgets? *FEBS Lett.* **1998**, *430*, 130–134.
- (12) Casteels, P.; Ampe, C.; Jacobs, F.; Vaeck, M.; Tempst, P. Apidaecins. Antibacterial peptides from honeybees. *EMBO J.* **1989**, *8*, 2387–2391.
- (13) Bulet, P.; Dimarcq, J. L.; Hetru, C.; Lagueux, M.; Charlet, M.; Hegy, G.; Vanderselaer, A.; Hoffmann, J. A. A novel inducible antibacterial peptide of *Drosophila* carries an O-glycosylated substitution. *J. Biol. Chem.* **1993**, *268*, 14893–14897.
- (14) Mackintosh, J. A.; Veal, D. A.; Beattie, A. J.; Gooley, A. A. Isolation from an ant *Myrmecia gulosa* of two inducible O-glycosylated proline-rich antibacterial peptides. *J. Biol. Chem.* **1998**, *273*, 6139–6143.
- (15) Hara, S.; Yamakawa, M. A novel antibacterial peptide family isolated from the silkworm, *Bombyx mori*. *Biochem. J.* **1995**, *310*, 651–656.
- (16) Cociancich, S.; Dupont, A.; Hegy, G.; Lanot, R.; Holder, F.; Hetru, C.; Hoffmann, J. A.; Bulet, P. Novel inducible antibacterial peptides from a hemipteran insect, the sap-sucking bug *Pyrrhocoris apterus*. *Biochem. J.* **1994**, *300*, 567–575.
- (17) Otvos, L.; Wade, J. D.; Lin, F.; Condie, B. A.; Hanrieder, J.; Hoffmann, R. Designer antibacterial peptides kill fluoroquinolone-resistant clinical isolates. *J. Med. Chem.* **2005**, *48*, 5349–5359.
- (18) Schneider, M.; Dorn, A. Differential infectivity of two pseudomonas species and the immune response in the milkweed bug, *Oncopeltus fasciatus* (Insecta: Hemiptera). *J. Invertebr. Pathol.* **2001**, *78*, 135–140.
- (19) Chernysh, S.; Cociancich, S.; Briand, J. P.; Hetru, C.; Bulet, P. The inducible antibacterial peptides of the hemipteran insect *Palomena prasina*: identification of a unique family of proline-rich peptides and of a novel insect defensin. *J. Insect Physiol.* **1996**, *42*, 81–89.
- (20) Agerberth, B.; Lee, J. Y.; Bergman, T.; Carlquist, M.; Boman, H. G.; Mutt, V.; Jornvall, H. Amino-acid-sequence of Pr-39. Isolation from pig intestine of a new member of the family of proline-arginine-rich antibacterial peptides. *Eur. J. Biochem.* **1991**, *202*, 849–854.
- (21) de Visser, P. C.; van Hooft, P. A. V.; de Vries, A. M.; de Jong, A.; van der Marel, G. A.; Overkleef, H. S.; Noort, D. Biological evaluation of Tyr6 and Ser7 modified drosocin analogues. *Bioorg. Med. Chem. Lett.* **2005**, *15*, 2902–2905.
- (22) Noto, P. B.; Abbadessa, G.; Cassone, M.; Mateo, G. D.; Agelan, A.; Wade, J. D.; Szabo, D.; Kocsis, B.; Nagy, K.; Rozgonyi, F.; Otvos, L. Alternative stabilities of a proline-rich antibacterial peptide in vitro and in vivo. *Protein Sci.* **2008**, *17*, 1249–1255.
- (23) Witkowska, E.; Orłowska, A.; Sagan, B.; Smoluch, M.; Izdebski, J. Tryptic hydrolysis of hGH-RH(1–29)-NH<sub>2</sub> analogues containing Lys or Orn in positions 12 and 21. *J. Pept. Sci.* **2001**, *7*, 166–172.
- (24) Mechler, A.; Praporski, S.; Atmuri, K.; Boland, M.; Separovic, F.; Martin, L. L. Specific and selective peptide–membrane interactions revealed using quartz crystal microbalance. *Biophys. J.* **2007**, *93*, 3907–3916.
- (25) Piantavigna, S.; Czihal, P.; Mechler, A.; Richter, M.; Hoffmann, R.; Martin, L. L. Cell penetrating apidaecin peptide interactions with biomimetic phospholipid membranes. *Int. J. Pept. Res. Ther.* **2009**, *15*, 139–146.
- (26) Mechler, A.; Praporski, S.; Piantavigna, S.; Heaton, S. M.; Hall, K. N.; Aguilar, M. I.; Martin, L. L. Structure and homogeneity of pseudo-physiological phospholipid bilayers and their deposition characteristics on carboxylic acid terminated self-assembled monolayers. *Biomaterials* **2009**, *30*, 682–689.
- (27) Sherman, P. J.; Jackway, R. J.; Gehman, J. D.; Praporski, S.; McCubbin, G. A.; Mechler, A.; Martin, L. L.; Separovic, F.; Bowie, J. H. Solution structure and membrane interactions of the antimicrobial peptide fallaxidin 4.1a: an NMR and QCM study. *Biochemistry* **2009**, *48*, 11892–11901.
- (28) Kragol, G.; Hoffmann, R.; Chattergoon, M. A.; Lovas, S.; Cudic, M.; Bulet, P.; Condie, B. A.; Rosengren, K. J.; Montaner, L. J.; Otvos, L. Identification of crucial residues for the antibacterial activity of the proline-rich peptide, pyrrolicorin. *Eur. J. Biochem.* **2002**, *269*, 4226–4237.
- (29) Zhou, X. X.; Li, W. F.; Pan, Y. J. Functional and structural characterization of apidaecin and its N-terminal and C-terminal fragments. *J. Pept. Sci.* **2008**, *14*, 697–707.
- (30) Czihal, P.; Hoffmann, R. Mapping of apidaecin regions relevant for antimicrobial activity and bacterial internalization. *Int. J. Pept. Res. Ther.* **2009**, *15*, 157–164.
- (31) Mattiuzzo, M.; Bandiera, A.; Gennaro, R.; Benincasa, M.; Pacor, S.; Antcheva, N.; Scocchi, M. Role of the *Escherichia coli* SbmA in the antimicrobial activity of proline-rich peptides. *Mol. Microbiol.* **2007**, *66*, 151–163.
- (32) Livermore, D. M. Has the era of untreatable infections arrived? *J. Antimicrob. Chemother.* **2009**, *64*, 29–36.
- (33) Liebscher, M.; Roujeinikova, A. Allosteric coupling between the lid and interdomain linker in DnaK revealed by inhibitor binding studies. *J. Bacteriol.* **2009**, *191*, 1456–1462.
- (34) Morell, M.; Czihal, P.; Hoffmann, R.; Otvos, L.; Aviles, F. X.; Ventura, S. Monitoring the interference of protein–protein interactions in vivo by bimolecular fluorescence complementation: the DnaK case. *Proteomics* **2008**, *8*, 3433–3442.
- (35) Kragol, G.; Lovas, S.; Varadi, G.; Condie, B. A.; Hoffmann, R.; Otvos, L. The antibacterial peptide pyrrolicorin inhibits the ATPase actions of DnaK and prevents chaperone-assisted protein folding. *Biochemistry* **2001**, *40*, 3016–3026.
- (36) Ronald, A. The etiology of urinary tract infection: traditional and emerging pathogens. *Dis. Mon.* **2003**, *49*, 71–82.
- (37) Singer, D.; Lehmann, J.; Hanisch, K.; Hartig, W.; Hoffmann, R. Neighbored phosphorylation sites as PHF-tau specific markers in Alzheimer's disease. *Biochem. Biophys. Res. Commun.* **2006**, *346*, 819–828.
- (38) Amsterdam, D. Susceptibility Testing of Antimicrobials in Liquid Media. In *Antibiotics in Laboratory Medicine*, 4th ed.; Lorian, V., Ed.; Lippincott Williams & Wilkins: Baltimore, MD, 1996; pp 52–111.
- (39) Hoffmann, R.; Vasko, M.; Otvos, L. Serum stability of phosphopeptides. *Anal. Chim. Acta* **1997**, *352*, 319–325.
- (40) Yang, S.-T.; Lee, J. Y.; Kim, H.-J.; Eu, Y.-J.; Shin, S. Y.; Hahn, K.-S.; Kim, J. I. Contribution of a central proline in model amphipathic alpha-helical peptides to self-association, interaction with phospholipids, and antimicrobial mode of action. *FEBS J.* **2006**, *273*, 4040–4054.

## 5 Bibliography:

- 1 Park, C. B. *et al.* Structure-activity analysis of buforin II, a histone H2A-derived antimicrobial peptide: The proline hinge is responsible for the cell-penetrating ability of buforin II. *Proc. Natl. Acad. Sci.* **97**, 8245-8250, (2000).
- 2 Casteels, P. *et al.* Apidaecins: antibacterial peptides from honeybees. *EMBO J.* **8**, 2387-2391, (1989).
- 3 Czihal, P. *et al.* Api88 is a novel antibacterial designer peptide to treat systemic infections with multidrug-resistant gram-negative pathogens. *ACS Chem. Biol.* **7**, 1281-1291, (2012).
- 4 Schneider, M. & Dorn, A. Differential infectivity of two *Pseudomonas* species and the immune response in the milkweed bug, *Oncopeltus fasciatus* (Insecta: Hemiptera). *J Invertebr pathol* **78**, 135-140, (2001).
- 5 Scocchi, M. *et al.* Proline-rich antimicrobial peptides: Converging to a non-lytic mechanism of action. *Cell. Mol. Life Sci.* **68**, 2317-2330, (2011).
- 6 Li, W.-F. *et al.* Apidaecin-type peptides: Biodiversity, structure-function relationships and mode of action. *Peptides* **27**, 2350-2359, (2006).
- 7 Otvos, L. The short proline-rich antibacterial peptide family. *Cell. Mol. Life Sci.* **59**, 1138-1150, (2002).
- 8 Splith, K. & Neundorff, I. Antimicrobial peptides with cell-penetrating peptide properties and vice versa. *Eur. Biophys. J.* **40**, 387-397, (2011).
- 9 Agerberth, B. *et al.* Amino acid sequence of PR-39. Isolation from pig intestine of a new member of the family of proline-arginine-rich antibacterial peptides. *Eur. J. Biochem.* **202**, 849-854, (1991).
- 10 Bulet, P. *et al.* Antimicrobial peptides in insects; structure and function. *Dev. Comp. Immunol.* **23**, 329-344, (1999).
- 11 Destoumieux, D. *et al.* Penaeidins, a family of antimicrobial peptides from penaeid shrimp (Crunstacea, Decapoda). *Cell. Mol. Life Sci.* **57**, 1260-1271, (2000).
- 12 Jiravanichpaisal, P. *et al.* Antibacterial peptides in hemocytes and hematopoietic tissue from freshwater crayfish *Pacifastacus leniusculus*: Characterization and expression pattern. *Dev. Comp. Immunol.* **31**, 441-455, (2007).
- 13 Gueguen, Y. *et al.* Oyster hemocytes express a proline-rich peptide displaying synergistic antimicrobial activity with a defensin. *Mol. Immunol.* **46**, 516-522, (2009).
- 14 Casteels, P. *et al.* Biodiversity of Apidaecin-type Peptide Antibiotics: Prospects of Manipulating the Antibacterial Spectrum and Combating Acquired Resistance. *J. Biol. Chem.* **269**, 26107-26115, (1994).

- 15 Castle, M. *et al.* Lethal effects of apidaecin on *Escherichia coli* involve sequential molecular interactions with diverse targets. *J. Biol. Chem.* **274**, 32555-32564, (1999).
- 16 Zhou, X. X. *et al.* Functional and structural characterization of apidaecin and its N-terminal and C-terminal fragments. *J. Pept. Sci.* **14**, 697-707, (2008).
- 17 Zhang, L. *et al.* Influence of proline residues on the antibacterial and synergistic activities of  $\alpha$ -helical peptides. *Biochemistry* **38**, 8102-8111, (1999).
- 18 Kay, B. K. *et al.* The importance of being proline: The interaction of proline-rich motifs in signaling proteins with their cognate domains. *FASEB J.* **14**, 231-241, (2000).
- 19 MacArthur, M. W. & Thornton, J. M. Influence of proline residues on protein conformation. *J. Mol. Biol.* **218**, 397-412, (1991).
- 20 Pujals, S. & Giralt, E. Proline-rich, amphipathic cell-penetrating peptides. *Adv. Drug Deliv. Rev.* **60**, 473-484, (2008).
- 21 Tokunaga, Y. *et al.* Antibacterial activity of bactenecin 5 fragments and their interaction with phospholipid membranes. *J. Pept. Sci.* **7**, 297-304, (2001).
- 22 Cabiaux, V. *et al.* Secondary structure and membrane interaction of PR-39, a Pro+Arg-rich antibacterial peptide. *Eur. J. Biochem.* **224**, 1019-1027, (1994).
- 23 Bulet, P. *et al.* Enlarged scale chemical synthesis and range of activity of drosocin, an O-glycosylated antibacterial peptide of *Drosophila*. *Eur. J. Biochem.* **238**, 64-69, (1996).
- 24 Dutta, R. C. *et al.* Functional mapping of apidaecin through secondary structure correlation. *Int. J. Biochem. Cell Biol.* **40**, 1005-1015, (2008).
- 25 Williamson, M. P. The structure and function of proline-rich regions in proteins. *Biochem. J.* **297**, 249-260, (1994).
- 26 Kragol, G. *et al.* The antibacterial peptide pyrrocoricin inhibits the ATPase actions of DnaK and prevents chaperone-assisted protein folding. *Biochemistry* **40**, 3016-3026, (2001).
- 27 Otvos, L. *et al.* Interaction between heat shock proteins and antimicrobial peptides. *Biochemistry* **39**, 14150-14159, (2000).
- 28 Podda, E. *et al.* Dual mode of action of Bac7, a proline-rich antibacterial peptide. *Biochim. Biophys. Acta, Gen. Subj.* **1760**, 1732-1740, (2006).
- 29 Gennaro, R. *et al.* Pro-rich antimicrobial peptides from animals: Structure, biological functions and mechanism of action. *Curr. Pharm. Des.* **8**, 763-778, (2002).
- 30 Tavano, R. *et al.* The honeybee antimicrobial peptide apidaecin differentially immunomodulates human macrophages, monocytes and dendritic cells. *J Innate Immun* **3**, 614-622, (2011).

- 31 Mattiuzzo, M. *et al.* Role of the Escherichia coli SbmA in the antimicrobial activity of proline-rich peptides. *Mol. Microbiol.* **66**, 151-163, (2007).
- 32 Tomasinsig, L. *et al.* Mechanistic and functional studies of the interaction of a proline-rich antimicrobial peptide with mammalian cells. *J. Biol. Chem.* **281**, 383-391, (2006).
- 33 Gobbo, M. *et al.* Substitution of the arginine/leucine residues in apidaecin Ib with peptoid residues: Effect on antimicrobial activity, cellular uptake, and proteolytic degradation. *J. Med. Chem.* **52**, 5197-5206, (2009).
- 34 Henriques, S. T. *et al.* Cell-penetrating peptides and antimicrobial peptides: How different are they? *Biochem. J.* **399**, 1-7, (2006).
- 35 Benincasa, M. *et al.* The proline-rich peptide Bac7(1-35) reduces mortality from Salmonella typhimurium in a mouse model of infection. *BMC Microbiol* **10**, 178, (2010).
- 36 Fieck, A. *et al.* Trypanosoma cruzi: Synergistic cytotoxicity of multiple amphipathic anti-microbial peptides to T. cruzi and potential bacterial hosts. *Exp. Parasitol.* **125**, 342-347, (2010).
- 37 Taguchi, S. *et al.* Targeted Engineering of the Antibacterial Peptide Apidaecin, Based on an In Vivo Monitoring Assay System. *Appl. Environ. Microbiol.* **75**, 1460-1464, (2009).
- 38 Otvos Jr, L. *et al.* Designer antibacterial peptides kill fluoroquinolone-resistant clinical isolates. *J. Med. Chem.* **48**, 5349-5359, (2005).
- 39 Berthold, N. *et al.* Novel apidaecin 1b analogs with superior serum stabilities for treatment of infections by Gram-negative pathogens. *Antimicrob. Agents Chemother.* **57**, 402-409, (2013).



# ***Arginine-rich peptides: the Tat peptide, a CPP and AMP***

## **1 Introduction**

The plasma membrane constitutes an efficient and selective barrier for cells versus the extracellular environment. As a consequence, the intracellular delivery of therapeutic agents, for example peptides and proteins, is not very efficient<sup>1</sup>. Various approaches have been employed in controlled drug delivery to overcome this issue, including electroporation, microinjections, liposome delivery and viral vectors. However, these methods can have some disadvantages, such as, inefficient drug delivery efficiency, cellular damage and toxicity, and poor specificity in the drug delivery to specific targets<sup>1-3</sup>.

In recent years, AMPs have emerged as potential drug-delivery vectors to improve the intracellular delivery of therapeutic agents<sup>4,5</sup>. Indeed, some AMPs are able to associate strongly with cell membranes prior to translocation into the cytoplasm, without permeabilising the membrane permanently. This characteristic behaviour resulted in their classification as cell penetrating peptides (CPPs).

### ***1.1.1 Cell penetrating peptides (CPPs)***

CPPs were discovered more than 20 years ago and originally were called protein transduction domains (PTDs) since the first CPPs to be identified were specific regions of some intracellular proteins<sup>6</sup>. Examples are the *Drosophila* homeobox protein Antennapedia, the HIV-1 transcriptional factor TAT, and the capsid protein VP22 from HSV-1<sup>6,7</sup>. These PTDs allow the protein to traverse the mammalian cell membrane. Since then, many peptides have been shown to have cell-penetrating properties<sup>6</sup>. These CPPs, are structurally diverse and short in length, with less than 40 amino acids<sup>8</sup>. Most CPPs are cationic due to

the large number of arginine and lysine residues in their primary sequence, while some are also amphipathic<sup>4</sup>. The overarching property of all CPPs is the ability to penetrate biological membranes, and thus the capacity to transfer bioactive cargoes into cells either covalently or non-covalently attached, such as proteins, peptides, oligonucleotides, nanoparticles and liposomes, without damaging the cell membrane<sup>1,2,9,10</sup>. For this reason, CPPs have emerged as an alternative strategy in pharmacology as a delivery vector in both tissues and cells. Indeed CPPs have been used to deliver drugs to cancer cells<sup>10</sup>. Examples of these drugs are the peptide pro-drug of SN38 (DTS-108)<sup>11</sup>, plasmids<sup>12</sup>, liposomes with anticancer 2C5 monoclonal antibodies<sup>13</sup>. CPPs can also be used to target cancer cells because they can be incorporated into “smart” nanocarrier delivery platforms, sensitive to changes in pH, temperature etc. allowing specific and controlled release of the drug cargo following the stimuli. An useful review of various strategies where CPPs can target cancer cells is found in Koren et al.<sup>10</sup>.

### **1.1.2 CPP Classification**

More than 100 peptides have been classified as CPPs over the last 20 years. Taking into consideration the origin or the sequence characteristics, CPPs can be divided into groups<sup>10,14</sup>. As shown in Table 5, three groups can be distinguished, based on the origin. The first group is formed by peptides derived from specific regions of proteins that have the ability to traverse the membrane. These peptides are not specific to cells or tissue types. The two best studied PTDs are the Tat peptide, derived from Tat protein of the HIV-1 virus<sup>15</sup> and Penetratin, derived from the Antennapedia protein of *Drosophila*<sup>16</sup>. The second group includes chimeric peptides, which are partly derived from naturally occurring peptides or protein. Examples are TP10, a truncated form of Transportan<sup>17</sup> and Pep-1<sup>2,18</sup>. The third group is constituted by designed peptides: the sequence of these peptides consist of repeat motifs or poly-residues. Some examples are the poly-arginine peptides (R<sub>n</sub>)<sup>19</sup> and the model amphipathic peptide (MAP)<sup>20</sup> and most are found to form amphipathic peptides.

An alternative classification for CPPs is based on the amino acid sequence, in which peptides with low amphipathic regions have positively charged sequences at physiological pH due to the presence of arginine and lysine residues<sup>10</sup>. This group includes penetratin, Tat and polyarginine peptides<sup>19</sup>; whereas the second group includes amphipathic CPPs, such as Transportan, MAP and Pep-1<sup>18</sup> peptides. Peptides in this group have a positive net charge because of the lysine residues in their sequences. The last group, instead, comprises peptides having in their primary sequence a distinctive separation between charged and hydrophobic residues, such as the vascular endothelial-cadherin (pVEC) and MPG peptides<sup>10</sup>.

As found in Table 4, some AMPs are also CPPs, such as LL-37 and buforin 2. Furthermore, Pr-rich AMPs can represent a better option as CPPs in deliver impermeable drugs into both bacterial and eukaryotic cells since they can be internalized into the cell without damaging the cell membrane<sup>3,21</sup>.

### 1.1.2.1 *Tat peptide*

The Tat peptide is one of the most studied CPPs<sup>1,10</sup>. This peptide is the PTD of the protein Tat, a nuclear transcription-activating protein, which is necessary for the HIV-1 virus replication machinery<sup>22</sup>. Briefly, the cysteine-rich Tat protein consists of 86 amino acids that are organized into three functional domains: an acidic N-terminal region, which is important for the trans-activation; a cysteine-rich DNA-binding region; and a basic RNA-binding domain (amino acids 49-57). The basic domain, which is the Tat PTD, is rich in arginine residues, and binds to the TAR (trans-activation responsive) RNA element with a high affinity, causing a substantial increase in transcription levels<sup>23</sup>. Importantly, this basic region is responsible for the passage through the membrane of Tat-derived peptides<sup>24</sup>.

Table 5: Examples of commonly used CPPs and AMPs, their origins, structures and mechanisms<sup>1-3</sup>.

	Name	Sequence	Origin	Structure	Proposed mechanism
<i>AMPs/ protein derived</i>	Pyrrhococcin	VDKGSTLPRPTPPRIYNRN-NH <sub>2</sub>	Fire bug <i>P. apterus</i>	Random coil/reverse turns at the terminal	Receptor-mediated
	<i>Bac7</i>	<b>RRIRRRPRLRRRRPRLPFRPPGRRPIPRPL</b>	Bovine neutrophils	Hybrid of PPII helix and $\alpha$ -helix	Receptor-mediated/pore formation
	<b>(Bac7 1-24)</b>	PPRRPGRRPIPRPLPFRPPGRRPIPRP			
	LL-37	LGDFFRKSKKIKGKEFKRIVQRKIDFLR NLVPTES-NH <sub>2</sub>	Human leukocytes	$\alpha$ -helical	Pore formation
	Buforin II (BF2d)	TRSSRAGLQFPVGRVIRLLLRK TRSSRAGLQWPVGRVIRLLLRKGGC	Asian toad	Extended amphipathic, $\alpha$ -helical	Direct penetration
	Tat (48-60)	GRKKRRRQRRRPPQ-NH <sub>2</sub>	HIV-1 transcriptional activator	Random coil/PPII helix	Direct penetration/ pore formation
	Penetratin	RQIKIWFQNRRMKWKK-NH <sub>2</sub>	Antennapedia	Amphipathic; $\alpha$ -helical/	Direct penetration/ endocytosis
	pVEC	LLIILRRRIKQAHAHSK-NH <sub>2</sub>	<i>D. melanogaster</i>	$\beta$ -sheet (higher conc.)	Direct penetration/ transporter-mediated
	Pep-1	KETWWETWTEWSQPKKKRKV-NH <sub>2</sub>	Chimeric	Amphipathic; $\alpha$ -helical	Direct penetration/ pore formation
	<i>Chimeric</i>	Transportan (TP10)	GWTLNSAGYLLGKINLKALAAAKKIL-NH <sub>2</sub>	Galainin-mastoparan	Amphipathic; $\alpha$ -helical
<i>Synthetic peptides</i>		MAP	KLALKLALKALKALKLA-NH <sub>2</sub>	Designed peptide	Amphipathic; $\alpha$ -helical
<i>peptides</i>	Octa/nona arginine	RRRRRRRRR/R	Designed peptides	Random coil, $\alpha$ -helical	Direct penetration/ endocytosis

### 1.1.3 Mechanism of CPPs uptake

Although CPPs have been extensively studied and used in biotechnological applications, their mechanism of cellular uptake is still elusive. Recent reports suggest that the internalization of CPPs is influenced by the sequence and concentration of CPPs, the attached cargo and the cell lines being used<sup>5,10,14</sup>.

However, the requirement for an initial electrostatic interaction of the positively charged CPPs with the negative charges present on the membrane surface, due to the lipid head-groups, proteins (e.g. nucleolin), and proteoglycans, suggest adsorption or binding of an effective concentration before translocation<sup>1,25,26</sup>. As illustrated in Fig. 39, after the initial binding of the CPP, they can enter the cell by either: pinocytosis, a fluid-phase endocytosis<sup>27</sup> or direct translocation<sup>1,10,14</sup>.

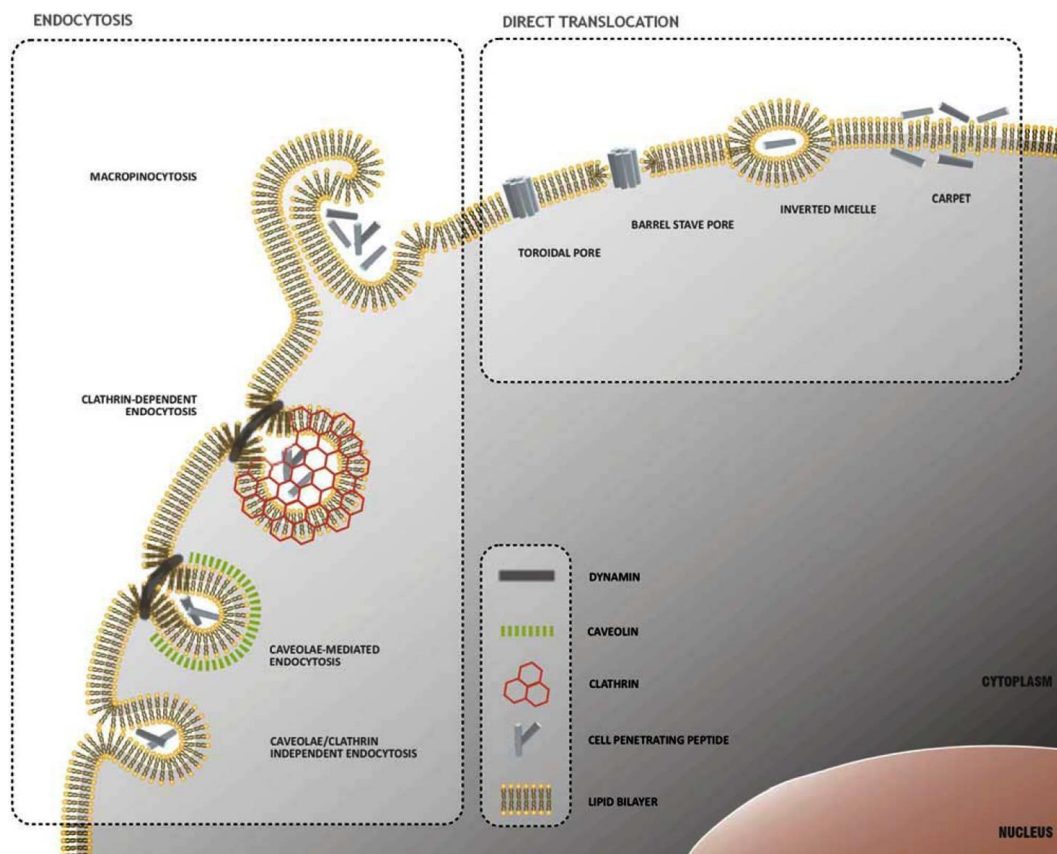


**Fig. 39:** Schematic representation of the diverse cellular uptake pathways proposed for CPPs. In general, these mechanisms can be divided into active transport, which are the various forms of endocytosis, and passive-transport where the peptide translocates directly into the cell<sup>28</sup>.

CPPs can enter the cell through an energy and temperature dependent pathway, named pinocytosis (Fig. 39)<sup>29</sup>. This process can be classified into four pathways: macropinocytosis<sup>30</sup>, clathrin-mediated endocytosis, caveolae/lipid raft-mediated endocytosis, and clathrin/caveolae-independent endocytosis<sup>27</sup>. Macropinocytosis is a fluid-phase endocytosis, which involves the generation of large irregular endocytic vesicles named macropinosomes. These vesicles are generated by actin-driven invaginations of the cell membrane, and lack in membrane receptors<sup>1,30</sup>. In the clathrin-mediated endocytosis pathway, clathrin proteins coat the invaginations of the membrane<sup>27</sup>. In the caveolae/lipid raft endocytosis instead, the peptide associates with caveolae, which are small membrane microdomains enriched in cholesterol and glycosphingolipids forming vesicles called caveosomes<sup>1,5</sup>. These endocytic pathways are the most likely used for the cellular uptake of CPPs conjugated to large cargoes whereas individual CPPs or CPPs-conjugated to small cargoes act by direct penetration of the membrane<sup>10</sup>.

Direct translocation, initiated by electrostatic and hydrogen bond interactions with lipid membranes, occurs via inverted micelles<sup>28</sup> or through transient pores in the membrane<sup>14,31</sup>, as shown in Fig. 39. Inverted micelles, which are inverted hexagonal structures, originate when the peptide associates with and unhinges the membrane. This method of “transport”, however, is only possible for small hydrophilic peptides with or without small cargo<sup>28,29</sup>. The direct transport method is via generation of a curvature of the lipid bilayer, in a toroidal-like manner. This pore is transient since the passage through the bilayer is estimated to occur in less than *circa* 1000 ns<sup>32-35</sup>. It has been suggested that the transitory formation of a pore is what distinguishes a CPP from other AMPs since the pores created by non-CPP AMPs have a longer life time<sup>31</sup>. Nevertheless, these mechanisms are variable and the same peptide might use more than one of the pathways mentioned previously, depending on the environmental conditions<sup>5,10,36</sup>. For instance, the Tat peptide has been shown to be internalized into the cell by macropinocytosis<sup>37</sup> or through direct translocation<sup>38</sup>. Even the simultaneous adoption of all three endocytic pathways has been demonstrated in the case of Antp, nona-arginine and the Tat

peptides<sup>39</sup>. In addition, a model has been proposed recently where the Tat peptide enters into the cell through an induced pore and interacts strongly with cytoplasmic actin. This interaction promotes the cellular uptake of large anchored cargoes via endocytotic pathways<sup>31</sup>.

### 1.1.3.1 *Factors that influence the cellular uptake of CPP*

Many environmental factors influence the cellular uptake of CPPs. Some of these include:

1. The peptide sequence: the presence of basic residues favours the electrostatic interaction with anionic membranes. However, translocation is influenced by the properties of the cationic residues included in the peptide sequence; arginine residues establish a more efficient interaction with the lipid head-groups than lysine residues, thus resulting in a non-lytic translocation<sup>1</sup>. Furthermore, the length and the number of arginine residues in the sequence are key factors for translocation. For example, the transduction efficiency of poly-arginine increases as the peptide length increases from 6 to 15 residues, whereas for polypeptides with more than 15 or less than five residues, the peptide uptake is not so effective<sup>1,19</sup>. Also the addition of hydrophobic residues, such as a phenylalanine, at either the N- or C-terminus of CPPs can enhance their membrane interaction<sup>40</sup>. Furthermore, the presence of tryptophan residues enhances the peptide uptake in the cell and lowers the toxicity of the poly-arginine peptides. Mechanistically, this is thought to be due to slowing of the translocation process that has been observed with model membranes<sup>31,40</sup>.
2. The peptide structure: Lättig-Tünnemann et al.<sup>41</sup> demonstrated that the transduction of Tat and other arginine-rich peptides into the cell is improved by (i) creating a distance between the arginine guanidinium groups in linear peptides or (ii) backbone cyclization of the peptides. Moreover, the structural rigidity introduced by cyclization appears to kinetically enhance the transduction efficiency of arginine-rich CPPs.
3. The peptide concentration: it has been suggested that Tat and other CPPs translocate into the cytosol by direct penetration when their concentration

is above a defined threshold level, which depends on the peptide and the cell type, but is usually in the micromolar range<sup>5,14</sup>. While for low concentrations, the peptide is delivered into the cell by pinocytosis. For instance, from studies *in vivo*, Duchardt et al.<sup>39</sup> suggested that the cellular uptake for short CPPs is driven by the peptide concentration. However, they observed that above a critical peptide concentration (10  $\mu\text{M}$ ), the peptide uptake was mainly energy independent.

4. The nature of the cargo: CPPs have been shown to enter into the cell by both active and passive transport when conjugated to low molecular cargoes, such as small peptides (less than 50 residues), drugs and fluorophores<sup>10,30,41</sup>. In the presence of high molecular weight cargoes, for example Tat conjugated to quantum dots, only endocytic pathways were employed<sup>5,10,37</sup>. Moreover, the cargo can also influence the ability of the peptide to be internalized into the cell<sup>36</sup>.
5. Membrane composition: cholesterol present in the membrane seems to be important for the peptide translocation. Indeed, the depletion of cholesterol can cause a switch from endocytosis to direct translocation, resulting in a less efficient uptake<sup>25,30</sup>. Since many of these CPPs are cationic, the presence of anionic lipids in the membrane can also facilitate their accumulation on the membrane followed by translocation<sup>42</sup>. The lipid phase also has an influence and Säälik et al.<sup>43</sup> observed that various CPPs tend to accumulate on the liquid-disordered domains when interacting with liposomes. Because of the influence of lipid composition in membranes, the peptide uptake can be limited to certain cell types and so the kinetics can be influenced as well, as shown with the different cellular localization of Tat (47-57) in three different epithelial cell culture models (MDCK, Calu-3 and TR146)<sup>22</sup>.

### ***1.1.4 Properties of the amino acid arginine***

L-Arginine is an important component of CPPs and also proteins that interact with the cell membrane<sup>44</sup>. Indeed, arginine residues are found in strategic positions along the protein and peptide sequences. For instance, arginine residues, as well as lysine and proline residues, can be found either

side of aggregation-prone stretches in some proteins. Thus, the arginine residues act as “gatekeepers” because they inhibit the aggregation of these stretches<sup>45</sup>. Another example comes from the peptide Bac7 (1-35), which is shown to aggregate if its N-terminal arginine was removed<sup>46</sup>.

Arginine is considered one of the most hydrophilic of the 20 natural amino acids. Its side chain consists of a hydrophobic propyl moiety and a large, polar, cationic guanidinium group (Fig. 40). Arginine is protonated and positively charged in almost all biological fluids (the pKa of the side chain is over 12) and inserts into the membrane. This ability is due to the guanidinium group, which interacts electrostatically with the lipid head-groups and forms bidentate hydrogen bonds with them. In addition, this guanidinium group also creates hydrogen bond also with water molecules<sup>47</sup>.

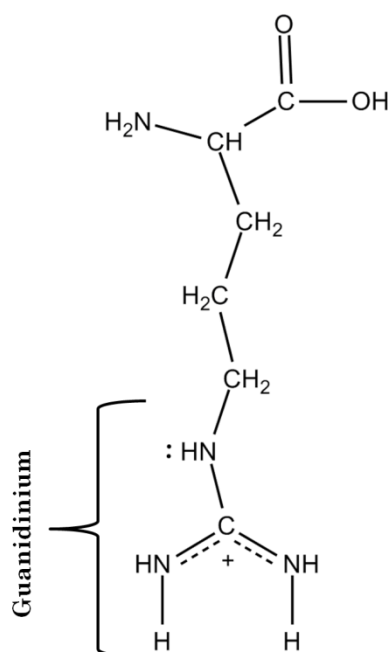


**Fig. 40:** The amino acid arginine. The guanidinium group has five dipolar N-H protons capable of acting as hydrogen bond donors and one pair of electrons capable of being a hydrogen bond acceptor.

This ability of the arginine side chain to establish extensive hydrogen bond networks with donors e.g. phosphates, is relevant for many biological interactions, e.g. in recognizing specific RNA structures<sup>48</sup>, in stabilizing the voltage-sensor domain of the channel proteins KvAP<sup>49</sup>, and in inserting arginine-containing hydrophobic sequences deep in the membrane<sup>47</sup>. Indeed,

the partitioning of the arginine amino acid into the membrane layer is energetically favourable due to the hydrogen bonds established between the phosphate head-groups and water molecules<sup>47</sup>. This interaction between the guanidinium and phosphate moieties of multiple lipid headgroups generates a negative “Gaussian” curvature in the membrane, also called saddle-splay<sup>31,50</sup>. This curvature seems to be a necessary requisite for blebbing, which is observed in macropinocytosis, for the dimples in the caveoli-based endocytosis and as well as for pore formation in membranes<sup>1,31</sup>.

### ***1.1.5 Applications: examples of CPPs as AMPs:***

CPPs have been used for a number of applications, for example fluorescently labelling native tumours<sup>51</sup> and delivery of anticancer drugs<sup>14</sup>. However, CPPs can also act as anti-infective agents, since some CPPs exhibited antimicrobial activity<sup>52</sup>. For example, the peptide Tat showed antifungal properties and potent antibacterial activity (MIC 2-8  $\mu\text{M}$ ) against a broad spectrum of pathogens both Gram-positive and Gram-negative bacteria<sup>53,54</sup>. A further example is represented by the CPP penetratin, which showed high antimicrobial activity towards some Gram-positive and Gram-negative bacteria, with a MIC value of 0.5-4  $\mu\text{M}$ <sup>4,52</sup>. Other examples of CPPs with antimicrobial properties are transportan and MAP peptides<sup>4</sup>.

### ***1.1.6 Papers included in this chapter***

Tat peptide is the most studied CPPs and it is employed in many studies for delivery of cargos. However, the mechanism of how this peptide crosses the membrane without causing any damage is still the object of discussion. This peptide has been shown to adopt both energy dependent and passive transports across the membrane. In the case of passive transport, i.e., direct translocation, the mechanism that Tat peptide (and other CPPs) adopts, is still unclear. The use of QCM (**paper 6**) and QCM in combination with SECM and AFM techniques (**paper 7**) gave a more detailed understanding of the mechanism adopted by Tat during its translocation. These studies demonstrated the

presence of pores, and furthermore suggested differences in this translocation between prokaryotic and eukaryotic-mimetic membranes. Two Tat peptides were studied: Tat peptide (44-57) and Tat (49-57), and their action was compared. Tat (49-57) was chosen because its sequence included the basic domain (amino acids 49-57) of the Tat protein of HIV virus. This domain is responsible for the translocation of the protein across the membrane<sup>55</sup>. Tat (44-57) peptide was also investigated to probe the influence of presence of hydrophobic/polar residues that could change the peptide action towards membranes.

Both peptides were shown to vary little in action for artificial membranes. Tat acted as a CPP towards mammalian-mimetic membranes, whereas disruption of bacterial-mimetic membranes occurred for both Tat peptides. This duality in membrane activity was further examined (**Paper 7**) in which it was shown that these peptides could 'passively' translocate across mammalian-mimetic membranes through 'worm-hole' pores.

## 2 Bibliography

- 1 Schmidt, N. *et al.* Arginine-rich cell-penetrating peptides. *FEBS Lett.* **584**, 1806-1813, (2010).
- 2 Henriques, S. T. *et al.* Cell-penetrating peptides and antimicrobial peptides: How different are they? *Biochem. J.* **399**, 1-7, (2006).
- 3 Pujals, S. & Giralt, E. Proline-rich, amphipathic cell-penetrating peptides. *Adv. Drug Deliv. Rev.* **60**, 473-484, (2008).
- 4 Splith, K. & Neundorff, I. Antimicrobial peptides with cell-penetrating peptide properties and vice versa. *Eur. Biophys. J.* **40**, 387-397, (2011).
- 5 Milletti, F. Cell-penetrating peptides: Classes, origin, and current landscape. *Drug Discovery Today* **17**, 850-860, (2012).
- 6 Järver, P. & Langel, Ü. Cell-penetrating peptides—A brief introduction. *BBA- Biomembr.* **1758**, 260-263, (2006).
- 7 Heitz, F. *et al.* Twenty years of cell-penetrating peptides: from molecular mechanisms to therapeutics. *Br. J. Pharmacol.* **157**, 195-206, (2009).
- 8 Madani, F. *et al.* Mechanisms of Cellular Uptake of Cell-Penetrating Peptides. *J. of Biophysics* **2011**, 10, (2011).
- 9 Eiríksdóttir, E. *et al.* Secondary structure of cell-penetrating peptides controls membrane interaction and insertion. *BBA- Biomembr.* **1798**, 1119-1128, (2010).
- 10 Koren, E. & Torchilin, V. P. Cell-penetrating peptides: breaking through to the other side. *Trends Mol. Med.* **18**, 385-393, (2012).
- 11 Meyer-Losic, F. *et al.* DTS-108, A Novel Peptidic Prodrug of SN38: In vivo Efficacy and Toxicokinetic Studies. *Clin. Cancer Res.* **14**, 2145-2153, (2008).
- 12 Torchilin, V. P. *et al.* Cell transfection in vitro and in vivo with nontoxic TAT peptide-liposome–DNA complexes. *Proc. Natl. Acad. Sci.* **100**, 1972-1977, (2003).
- 13 Koren, E. *et al.* Multifunctional PEGylated 2C5-immunoliposomes containing pH-sensitive bonds and TAT peptide for enhanced tumor cell internalization and cytotoxicity. *J. Controlled Release* **160**, 264-273, (2012).
- 14 Lindgren, M. & Langel, U. Classes and prediction of cell-penetrating peptides. *Methods Mol. Biol.* **683**, 3-19, (2011).
- 15 Frankel, A. D. & Pabo, C. O. Cellular uptake of the tat protein from human immunodeficiency virus. *Cell* **55**, 1189-1193, (1988).
- 16 Derossi, D. *et al.* Cell internalization of the third helix of the antennapedia homeodomain is receptor-independent. *J. Biol. Chem.* **271**, 18188-18193, (1996).

- 17 Pooga, M. *et al.* Cell penetration by transportan. *FASEB J.* **12**, 67-77, (1998).
- 18 Morris, M. C. *et al.* A new peptide vector for efficient delivery of oligonucleotides into mammalian cells. *Nucleic Acids Res.* **25**, 2730-2736, (1997).
- 19 Futaki, S. *et al.* Arginine-rich peptides. An abundant source of membrane-permeable peptides having potential as carriers for intracellular protein delivery. *J. Biol. Chem.* **276**, 5836-5840, (2001).
- 20 Oehlke, J. *et al.* Cellular uptake of an  $\alpha$ -helical amphipathic model peptide with the potential to deliver polar compounds into the cell interior non-endocytically. *BBA- Biomembr.* **1414**, 127-139, (1998).
- 21 Scocchi, M. *et al.* Proline-rich antimicrobial peptides: Converging to a non-lytic mechanism of action. *Cell. Mol. Life Sci.* **68**, 2317-2330, (2011).
- 22 Trehin, R. & Merkle, H. P. Chances and pitfalls of cell penetrating peptides for cellular drug delivery. *Eur. J. Pharm. Biopharm.* **58**, 209-223, (2004).
- 23 Liu, Y. *et al.* Visualizing a specific contact in the HIV-1 Tat protein fragment and trans-activation responsive region RNA complex by photocross-linking. *J. Biol. Chem.* **271**, 10391-10396, (1996).
- 24 Vives, E. *et al.* A truncated HIV-1 Tat protein basic domain rapidly translocates through the plasma membrane and accumulates in the cell nucleus. *J. Biol. Chem.* **272**, 16010-16017, (1997).
- 25 Futaki, S. *et al.* Arginine-rich peptides and their internalization mechanisms. *Biochem. Soc. Trans.* **35**, 784-787, (2007).
- 26 Ziegler, A. Thermodynamic studies and binding mechanisms of cell-penetrating peptides with lipids and glycosaminoglycans. *Adv. Drug Deliv. Rev.* **60**, 580-597, (2008).
- 27 Conner, S. D. Regulated portals of entry into the cell. *Nature* **422**, 37-44, (2003).
- 28 Trabulo, S. *et al.* Cell-Penetrating Peptides—Mechanisms of Cellular Uptake and Generation of Delivery Systems. *Pharmaceuticals* **3**, 961-993, (2010).
- 29 Green, I. *et al.* Protein transduction domains: Are they delivering? *Trends Pharmacol. Sci.* **24**, 213-215, (2003).
- 30 Kaplan, I. M. *et al.* Cationic TAT peptide transduction domain enters cells by macropinocytosis. *J. Controlled Release* **102**, 247-253, (2005).
- 31 Mishra, A. *et al.* Translocation of HIV TAT peptide and analogues induced by multiplexed membrane and cytoskeletal interactions. *Proc. Natl. Acad. Sci.* **108**, 16883-16888, (2011).
- 32 Huang, K. & García, A. E. Free energy of translocating an arginine-rich cell-penetrating peptide across a lipid bilayer suggests pore formation. *Biophys. J.* **104**, 412-420, (2013).

- 33 Herce, H. D. & Garcia, A. E. Molecular dynamics simulations suggest a mechanism for translocation of the HIV-1 TAT peptide across lipid membranes. *Proc. Natl. Acad. Sci.* **104**, 20805-20810, (2007).
- 34 Herce, H. D. *et al.* Arginine-rich peptides destabilize the plasma membrane, consistent with a pore formation translocation mechanism of cell-penetrating peptides. *Biophys. J.* **97**, 1917-1925, (2009).
- 35 Choi, D. *et al.* Insertion mechanism of cell-penetrating peptides into supported phospholipid membranes revealed by X-ray and neutron reflection. *Soft Matter* **8**, 8294-8297, (2012).
- 36 Ruzza, P. *et al.* Cell-penetrating peptides: A comparative study on lipid affinity and cargo delivery properties. *Pharmaceuticals* **3**, 1045-1062, (2010).
- 37 Ruan, G. *et al.* Imaging and tracking of Tat peptide-conjugated quantum dots in living cells: New insights into nanoparticle uptake, intracellular transport, and vesicle shedding. *J. Am. Chem. Soc.* **129**, 14759-14766, (2007).
- 38 Ter-Avetisyan, G. *et al.* Cell entry of arginine-rich peptides is independent of endocytosis. *J. Biol. Chem.* **284**, 3370-3378, (2009).
- 39 Duchardt, F. *et al.* A comprehensive model for the cellular uptake of cationic cell-penetrating peptides. *Traffic* **8**, 848-866, (2007).
- 40 Jones, A. T. & Sayers, E. J. Cell entry of cell penetrating peptides: tales of tails wagging dogs. *J. Controlled Release* **161**, 582-591, (2012).
- 41 Lättig-Tünnemann, G. *et al.* Backbone rigidity and static presentation of guanidinium groups increases cellular uptake of arginine-rich cell-penetrating peptides. *Nat Commun* **2**, 453, (2011).
- 42 Ciobanasu, C. *et al.* Cell-Penetrating HIV1 TAT Peptides Can Generate Pores in Model Membranes. *Biophys. J.* **99**, 153-162, (2010).
- 43 Säälik, P. *et al.* Penetration without cells: Membrane translocation of cell-penetrating peptides in the model giant plasma membrane vesicles. *J. Controlled Release* **153**, 117-125, (2011).
- 44 Herrera, F. E. *et al.* Molecular Dynamics Study of the Interaction of Arginine with Phosphatidylcholine and Phosphatidylethanolamine Bilayers. *J. Phys. Chem. B* **116**, 4476-4483, (2012).
- 45 Greenwald, J. & Riek, R. Biology of Amyloid: Structure, Function, and Regulation. *Structure (London, England : 1993)* **18**, 1244-1260, (2010).
- 46 Tomasinsig, L. *et al.* Mechanistic and functional studies of the interaction of a proline-rich antimicrobial peptide with mammalian cells. *J. Biol. Chem.* **281**, 383-391, (2006).
- 47 Hristova, K. & Wimley, W. A Look at Arginine in Membranes. *J. Membr. Biol.* **239**, 49-56, (2011).
- 48 Calnan, B. J. *et al.* Arginine-mediated RNA recognition: The arginine fork. *Science* **252**, 1167-1171, (1991).

- 49 Schmidt, D. *et al.* Phospholipids and the origin of cationic gating charges in voltage sensors. *Nature* **444**, 775-779, (2006).
- 50 Mishra, A. *et al.* HIV TAT forms pores in membranes by inducing saddle-splay curvature: Potential role of bidentate hydrogen bonding. *Angew. Chem. Int. Ed.* **47**, 2986-2989, (2008).
- 51 Metildi, C. A. *et al.* Fluorescence-Guided Surgery and Fluorescence Laparoscopy for Gastrointestinal Cancers in Clinically-Relevant Mouse Models. *Gastroenterol. Res. Pract.* **2013**, 8, (2013).
- 52 Palm, C. *et al.* Quantitatively determined uptake of cell-penetrating peptides in non-mammalian cells with an evaluation of degradation and antimicrobial effects. *Peptides* **27**, 1710-1716, (2006).
- 53 Jung, H. J. *et al.* Biological activity of Tat (47-58) peptide on human pathogenic fungi. *Biochem. Biophys. Res. Commun.* **345**, 222-228, (2006).
- 54 Jung, H. J. *et al.* Effective antibacterial action of Tat (47-58) by increased uptake into bacterial cells in the presence of trypsin. *J. Microbiol. Biotechnol.* **18**, 990-996, (2008).
- 55 Vives, E. *et al.* Structure-activity relationship study of the plasma membrane translocating potential of a short peptide from HIV-1 Tat protein. *Lett. Pept. Sci.* **4**, 429-436, (1997).

### **3 Paper 6:**

#### **3.1 A mechanistic investigation of cell-penetrating Tat peptides with supported lipid membranes**

Monash University

**Declaration for Paper 6****Declaration by candidate**

In the case of Paper 6, the nature and extent of my contribution to the work was the following:

<b>Nature of contribution</b>	<b>Extent of contribution (%)</b>
Design and performance of QCM-D, data analysis, contribution to manuscript preparation and review	40%

The following co-authors contributed to the work. If co-authors are students at Monash University, the extent of their contribution in percentage terms must be stated:

<b>Name</b>	<b>Nature of contribution</b>	<b>Extent of contribution (%) for student co-authors only</b>
<b>George A. McCubbin</b>	Data analysis, manuscript preparation and review	30%
<b>Solveig Boehnke</b>	Peptide synthesis	20%
<b>Bim Graham</b>	Manuscript preparation and review	
<b>Leone Spiccia</b>	Key ideas, manuscript review	
<b>Lisandra L. Martin *</b>	Key ideas, manuscript preparation and review	

The undersigned hereby certify that the above declaration correctly reflects the nature and extent of the candidate's and co-authors' contributions to this work\*.

**Candidate's  
Signature**

	<b>Date</b> 23/05/14
--	-------------------------

**Main  
Supervisor's  
Signature**

	<b>Date</b> 23/05/14
---	-------------------------

\*Note: Where the responsible author is not the candidate's main supervisor, the main supervisor should consult with the responsible author to agree on the respective contributions of the authors.



## A mechanistic investigation of cell-penetrating Tat peptides with supported lipid membranes

Stefania Piantavigna<sup>a</sup>, George A. McCubbin<sup>a</sup>, Solveig Boehnke<sup>a</sup>, Bim Graham<sup>b</sup>, Leone Spiccia<sup>a</sup>, Lisandra L. Martin<sup>a,\*</sup>

<sup>a</sup> School of Chemistry, Monash University, Clayton, Victoria 3800, Australia

<sup>b</sup> Medicinal Chemistry and Drug Action, Monash Institute of Pharmaceutical Sciences, Monash University, Parkville, Victoria 3052, Australia

### ARTICLE INFO

#### Article history:

Received 20 December 2010

Received in revised form 8 March 2011

Accepted 9 March 2011

Available online 15 March 2011

#### Keywords:

Tat peptide

Quartz crystal microbalance

Disruption

Antimicrobial peptide

Peptide antibiotic

### ABSTRACT

The multifarious Tat peptide derived from the HIV-1 virus exhibits antimicrobial activity. In this article, we use Quartz Crystal Microbalance with Dissipation monitoring (QCM-D) to investigate the mechanisms of action of Tat (44–57) and Tat (49–57) on bacterial-mimetic 1,2-dimyristoyl-*sn*-glycero-3-phosphocholine (DMPC)/1,2-dimyristoyl-*sn*-glycero-3-phospho-*rac*-(1-glycerol) (sodium salt) (DMPG) membranes. The results reveal that both peptides disrupt DMPC/DMPG membranes via a surface-active (carpet-like) mechanism. The magnitude of this disruption is dependent on both membrane and peptide properties. Firstly, less disruption was observed on the more negatively charged membranes. Secondly, less disruption was observed for the longer and slightly more hydrophobic Tat (44–57) peptide. As a comparison, the behaviour of the two Tat peptides on mammalian-mimetic DMPC/cholesterol membranes was investigated. Consistent with the literature no membrane disruption was observed. These results suggest that both electrostatic and hydrophobic interactions, as well as peptide geometry, determine the antimicrobial activity of Tat. This should guide the development of more potent Tat antibiotics.

© 2011 Elsevier B.V. All rights reserved.

### 1. Introduction

The increasing number of antibiotic-resistant bacteria and the decreasing number of new antibiotics in development are leading to a public health crisis [1,2]. Antimicrobial peptides (AMPs) are a promising solution because they are generally selective for bacterial membranes; they have broad-spectrum antibacterial activity and some show antifungal, antiviral and anticancer activity; and the development of bacterial resistance to AMPs is difficult [3–8]. AMPs are also a realistic solution with, for example, MSI-78 (Pexiganan) reaching phase III clinical trials for topical treatment of diabetic foot ulcers (although FDA approval was later denied) [9]. Recently, it was demonstrated by Jung and co-workers that the HIV-1 virus nuclear transcription activating protein Tat (residues 47–58) exhibits antifungal and antibacterial activity [10,11]. Importantly, Tat (47–58) exerted toxic activity towards all multi-drug resistant *Staphylococcus aureus* and *Pseudomonas aeruginosa* strains tested (with minimum inhibitory concentrations (MICs) of 0.625–20 μM), had no hemolytic activity over that range, and the D-enantiomer was resistant to proteolytic degradation, making it a potential therapeutic agent [11].

In contrast to the hotly debated mechanism of action of Tat on eukaryotic cells [12–14], there are relatively few studies concerning

how Tat exerts its antibacterial activity. The current view is that, firstly, on addition of Tat to bacterial-mimetic liposomes consisting of phosphocholine (PC) and phosphoglycerol (PG) lipids, Tat binds with high affinity and remains unstructured on the membrane surface [15,16]. The binding of the positively charged Tat to the negatively charged PC/PG membrane results in charge neutralisation, which facilitates liposome aggregation [17]. Fusion was then observed for the unsaturated dioleoyl (DO) liposomes, which suggests that binding causes membrane destabilisation [17]. However, any Tat-induced membrane destabilisation is small, as fluorescent dye leakage experiments showed that only <10% of the entrapped dye was released from the PC/PG liposomes [15,17]. Furthermore, Tat caused negligible membrane depolarisation of *Staphylococcus aureus* cells [18]. These results suggest that Tat does not act via a pore or carpet mechanism [19]. Instead, it is thought that Tat translocates through bacterial membranes and acts on an intracellular target [18], as observed for its antifungal activity [10] and for other AMPs [20,21]. While Tat is non-disruptive, dimerisation of the peptide at the C-terminus confers a membrane-disruptive mode of action [18].

Quartz Crystal Microbalance with Dissipation monitoring (QCM-D) has been employed by us and others to investigate the mode of action of AMPs [20–26]. A biomimetic lipid membrane can be deposited onto the QCM-D sensor ‘chips’ in situ [27]. Upon addition of an AMP solution, the mass and structural changes to the lipid membrane can be monitored in real time by the QCM-D instrument. QCM-D can therefore provide direct information about the effect of the AMP on

\* Corresponding author. Tel.: +61 3 99054514; fax: +61 3 99054597.  
E-mail address: [ll.martin@monash.edu](mailto:ll.martin@monash.edu) (L.L. Martin).

the lipid membrane, without the need for dyes or other chemicals. In this study, QCM-D is used to investigate the behaviour of Tat (44–57) (Ac-GISYGRKKRRQRRR-NH<sub>2</sub>, basic residues are underlined) and Tat (49–57) (Ac-RKKRRQRRR-NH<sub>2</sub>) on bacterial-mimetic membranes and, as a comparison, mammalian-mimetic membranes. Consistent with the reported non-lytic activity of Tat on eukaryotic cells, we show that both Tat peptides add to the membrane with no loss of mass. However, in contrast to the current literature, Tat is shown to disrupt bacterial membranes via a surface-active mechanism. Reasons for this discrepancy are considered.

## 2. Materials and methods

### 2.1. Peptide synthesis

Tat (44–57) and Tat (49–57) with N-terminal acetylation and C-terminal amidation were synthesised with L-amino acids by automated solid phase peptide synthesis on a Rink amide resin.

### 2.2. Buffer preparation

Sodium chloride ( $\geq 99.5\%$ ), potassium phosphate monobasic (anhydrous,  $\geq 99.0\%$ ) and potassium phosphate dibasic (anhydrous,  $\geq 98\%$ ) were purchased from Sigma-Aldrich (Castle Hill, Australia). Ultrapure water was used with an initial resistivity of 18.2 M $\Omega$ ·cm (Sartorius AG, Göttingen, Germany). Phosphate buffered saline (PBS, pH 6.9  $\pm$  0.1) was prepared having 20 mM phosphate and either 100 mM ("high-salt") or 30 mM ("low-salt") sodium chloride in water.

### 2.3. Liposome preparation

1,2-Dimyristoyl-*sn*-glycero-3-phosphocholine (DMPC) and 1,2-dimyristoyl-*sn*-glycero-3-phospho-*rac*-(1-glycerol) (sodium salt) (DMPG) were purchased from Avanti Polar Lipids (Alabaster, USA). Cholesterol, chloroform ( $\geq 99.8\%$ ) and methanol ( $\geq 99.9\%$ ) were purchased from Sigma-Aldrich (Castle Hill, Australia). DMPC and cholesterol were dissolved in chloroform and DMPG was dissolved in chloroform/methanol (ca. 3:1) to create individual 5 mM stock solutions. These solutions were then aliquoted into test tubes to obtain the desired lipid composition (DMPC/cholesterol 7:3 v/v, and DMPC/DMPG 4:1 and 2:1 v/v). The solvent was evaporated under N<sub>2</sub> and the test tubes were then dried under vacuum. To prepare the liposomes, the lipids were resuspended in high-salt PBS (100 mM NaCl) to a lipid concentration of 0.5 mM and then incubated at 37 °C, vortexed and briefly sonicated (<5 min) in a bath sonicator before use. The resultant liposomes are unilamellar and have a bimodal size distribution, with the radii of the two populations on average ca. 50 and 300 nm [28].

### 2.4. Modification of QCM-D sensor chips

Absolute ethanol ( $\geq 99.7\%$ ), propan-2-ol ( $\geq 99.0\%$ ) and hydrogen peroxide (30%) were purchased from Merck (Kilsyth, Australia). Ammonium hydroxide solution (28%) was obtained from Ajax Finechem (Seven Hills, Australia). 3-Mercaptopropionic acid (MPA,  $\geq 99.0\%$ ) was purchased from Fluka, BioChimica (Buchs, Switzerland). The QCM-D sensor crystals used were polished, gold-coated, AT-cut quartz chips with a fundamental frequency of ca. 5 MHz (Q-Sense, Västra Frölunda, Sweden). Immediately before measurements the chips were cleaned in a solution of ammonium hydroxide; hydrogen peroxide; water (1:1:3 v/v) for 20–25 min at ca. 70 °C. The chips were then rinsed thoroughly with water. Surface modification with MPA was conducted by immersing a freshly cleaned chip into a 1 mM solution of MPA in propan-2-ol for at least 1 h. This creates a self-assembled monolayer of negative charge on the chip surface. Excess

MPA was removed by rinsing with propan-2-ol. The chips were then dried under N<sub>2</sub> and assembled into the QCM-D chambers ready for use.

### 2.5. QCM-D experiments

QCM-D experiments were performed using the E4 system with flow cells (Q-Sense, Västra Frölunda, Sweden). The QCM-D instrument measures the relative changes to the resonance frequency ( $f$ ) and energy dissipation ( $D$ ) of the chip over the course of the experiment.  $\Delta f$  and  $\Delta D$  were measured simultaneously at the fundamental frequency and the 3rd, 5th, 7th and 9th harmonics. All plots presented in this study will use the 7th harmonic unless otherwise stated. Data for the fundamental frequency is not presented as it is inherently noisy and unreliable. The original data was processed in QTools (Q-Sense) before being exported for further analysis in OriginPro 8 (OriginLab Corp., Northampton, USA). All experiments were conducted at a temperature of 19.10  $\pm$  0.05 °C and repeated at least three times.

In a typical experiment, firstly, a lipid membrane was formed on the chip surface by the introduction of a liposome solution into the QCM-D chamber at a flow rate of 50–100  $\mu$ L/min. The liposomes adsorb onto the MPA-monolayer, deform, rupture and fuse together to form a lipid bilayer [28]. Weakly attached liposomes were removed by washing with high-salt PBS (100 mM NaCl) at 300  $\mu$ L/min and any embedded liposomes were ruptured by washing with low-salt PBS (30 mM NaCl) at 300  $\mu$ L/min. This second washing step was introduced to ensure the formation of a homogeneous membrane and works by creating an osmotic pressure difference between the interior of the embedded liposomes (having a high salt concentration) and the low-salt exterior environment, which causes the liposomes to swell and then burst. Secondly, after a stable baseline was observed, 1 mL of peptide solution (1, 2, 5, 10 and 15  $\mu$ M in PBS) was introduced at 50  $\mu$ L/min. After the flow was stopped, the peptide was left to incubate with the lipid membrane for 30 min and then the chamber was rinsed with high-salt PBS.

The change in mass of the chip ( $\Delta m$ ) can be calculated using the Sauerbrey equation [29]:

$$\Delta m = -C \left( \frac{\Delta f n}{n} \right) \quad (1)$$

where  $C$  is the mass sensitivity constant (17.7 ng/cm<sup>2</sup>·Hz for a chip with a fundamental frequency of 5 MHz) and  $n$  is the harmonic number. All mass values reported use the 7th harmonic ( $n = 7$ ) unless otherwise stated. Cho and co-workers have demonstrated that the Sauerbrey equation effectively models lipid bilayers in aqueous buffer [30].

## 3. Results and discussion

### 3.1. QCM-D results for Tat interaction with mammalian membranes

The behaviour of Tat (44–57) and Tat (49–57) on mammalian-mimetic membranes is presented here as a comparison since, despite being the subject of intense debate, it is accepted that Tat does not disrupt mammalian cells (Tat penetration is thought to proceed via one or all of endocytosis, pore formation, inverted micelle formation and/or direct translocation [12,31,32]). A lipid combination of DMPC/cholesterol was used, as phosphocholine and cholesterol are the major constituents of mammalian membranes [33]. The model systems were kept as simple as possible to focus on the peptide-phospholipid interaction.

In a QCM-D instrument, an alternating-current (AC) voltage is applied across a quartz chip to cause the chip to oscillate in shear mode at its fundamental frequency ( $f_0$ ) and harmonics of the fundamental frequency ( $f_n$ , where  $n$  is the harmonic number). The driving AC

voltage is periodically removed to measure the energy loss of the chip into the surrounding environment, giving the dissipation factor ( $D$ ) [34]. The results from a typical QCM-D experiment are shown in Fig. 1. The  $\Delta f$ -time plot in panel A shows changes in mass over the course of the experiment; a decrease in  $\Delta f$  corresponds to an increase in mass density (see Equation (1) and ref. [29]). The  $\Delta D$ -time plot in panel B shows changes in structure; an increase in  $\Delta D$  means the chip dissipates its energy more quickly when the driving AC voltage is removed and suggests the film on the chip is thicker, softer or more loose [34,35]. The experiment in Fig. 1 commenced with the chip oscillating in high-salt PBS and at point (i) the liposome solution was introduced into the QCM-D chamber. This causes an increase in mass of the chip, as liposomes adsorb, deform, rupture and fuse to form a lipid membrane. Flow was stopped after a change in  $\Delta f$  of ca.  $-15$  Hz, which corresponds to one complete bilayer (as explained in ref. [28]). A high-salt PBS rinse was performed at point (ii) to remove unadsorbed liposomes from the chamber. The decrease in mass resulting from the removal of weakly bound liposomes is offset by an increase in mass caused by residual liposomes from the tubing entering the QCM-D chamber and adsorbing and rupturing on the chip surface. At point (iii) the chamber was rinsed with low-salt PBS, which causes a rapid increase in  $\Delta f$  and decrease in  $\Delta D$ . This is because of, firstly, the sensitivity of the resonance frequency and energy dissipation of the chip to the density and viscosity of the surrounding solution [36] and, secondly, the rupturing of embedded liposomes due to osmotic pressure difference. This rupturing expels water trapped inside the liposomes, causing the decrease in mass observed, and increases the rigidity of the membrane, resulting in the lower energy dissipation. The chamber was flushed with high-salt PBS at point (iv) until a baseline was established, whereupon the peptide solution was introduced at point (v). After allowing the peptide and membrane to incubate for 30 min, the chamber was washed with high-salt PBS at point (vi), concluding the experiment.

### 3.1.1. Tat (44–57) on DMPC/cholesterol

First we investigated the interaction of Tat with DMPC/cholesterol membranes over a concentration range of 1–15  $\mu\text{M}$ , which corresponds to the MIC range for Tat on bacterial cells [11,18]. The results are presented in Fig. 2. On introduction of Tat (44–57) into the QCM-D chamber there was a small decrease in  $\Delta f$ , which corresponds to an

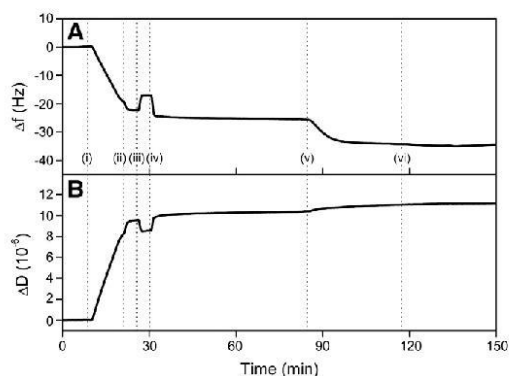


**Fig. 1.** Results for a typical QCM-D experiment.  $\Delta f$ - $t$  (A) and  $\Delta D$ - $t$  (B) plots are presented. At time point (i) a liposome solution was introduced into the chamber; at points (ii), (iv) and (vi) the chamber was flushed with high-salt PBS; at point (iii) the chamber was flushed with low-salt PBS; and at point (v) the peptide solution was introduced into the chamber. See text for further explanation.

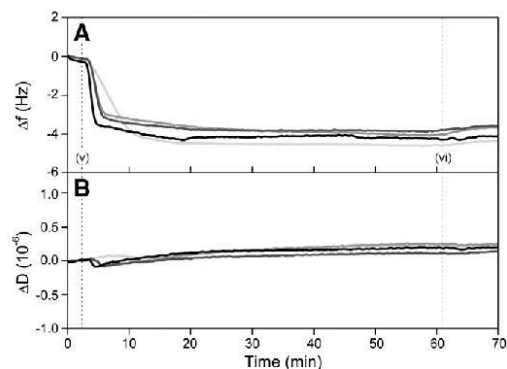


**Fig. 2.**  $\Delta f$ - $t$  (A) and  $\Delta D$ - $t$  (B) plots obtained for the interaction of Tat (44–57) with a DMPC/cholesterol membrane. The response of four peptide concentrations is shown (1, 5, 10 and 15  $\mu\text{M}$ ; lightest to darkest lines). Time points (v) and (vi) correspond to peptide addition and buffer rinse, respectively.

increase in mass of the chip. This mass addition caused negligible change in  $\Delta D$  ( $<0.5 \times 10^{-6}$ ), suggesting that there is no change in the membrane structure. Similar results were observed for Tat (49–57) (data not shown).

Several conclusions can be drawn from Fig. 2. Firstly, as expected and consistent with the literature, Tat does not disrupt mammalian membranes; a one-step mass addition process was observed at all concentrations. Secondly, Tat addition only proceeds until membrane saturation is reached. That is, while the rate of Tat addition was dependent on the concentration of peptide in solution, the overall amount of peptide added was independent; a change in  $\Delta f$  of  $-4.0 \pm 0.3$  Hz ( $\Delta m = 57 \pm 4$  ng) was observed for all concentrations. Thirdly, the buffer wash performed after incubation (point (vi) in Fig. 2) removes a negligible amount of material from the surface ( $<5\%$ ), which suggests that binding is irreversible. We have previously studied known membrane-penetrating AMPs e.g. apidaecin 1a and 1b and oncocin (peptide 10). They show a similar QCM-D response to Tat, i.e. peptide addition with no change in energy dissipation, however, on washing with buffer  $>50\%$  of the bound peptide is removed [20,21,24]. Thus the strong affinity between Tat and the membrane is unique compared with some other cell-penetrating peptides that we have studied using QCM-D.

These conclusions are consistent with three possible mechanisms. The first mechanism involves strong Tat binding to the phosphate residues of the membrane. Shaw and co-workers observed using atomic force microscopy that bilayer association of Tat was phase-dependent, causing an apparent height increase of liquid-phase domains (either due to peptide aggregation on or membrane restructuring of these domains) [37]. At the cholesterol concentration of 30 mol% used in our experiments only the liquid-ordered phase would be present [38,39]. Thus the small increase in  $\Delta D$  upon peptide addition could be explained by the height increase observed by Shaw et al. However, according to Shaw et al. there should be a difference between Tat interaction with gel-phase DMPC and liquid-ordered phase DMPC/cholesterol membranes. We observed negligible difference between the two membranes (data not shown), suggesting either that Tat association is not always phase-dependent or our experimental conditions are promoting a different mechanism of action. Furthermore, Dennison and co-workers demonstrated that Tat (48–60) binds weakly to DMPC monolayers, due to its low hydrophobicity [40]. This first mechanism would therefore be unlikely according to their study, as we observed an irreversible and strong association to the membrane.

Secondly, and alternatively, the QCM-D data is consistent with pore formation, which has been observed experimentally and demonstrated *in silico* [41–45]. We have previously postulated that if the change in resonance frequency is similar for all harmonics in an experiment, this is an indication that the peptide has inserted into the membrane in a transmembrane manner [22]. This is because the depth probed by a harmonic is inversely proportional to its frequency [46]; higher harmonics probe close to the surface of the chip and lower harmonics probe further away from the surface. If all harmonics measure the same change in frequency, this means that mass density is the same across the whole thickness of the membrane (i.e. pore formation). This is observed for Tat addition to DMPC/cholesterol (data not shown).

The third mechanism is direct translocation through the membrane. Tat penetration has been observed in the absence of endocytosis or pore formation, hinting to the existence of a currently unspecified direct translocation mechanism [31,47]. In our experiments the membrane is supported by a negatively charged carboxylic acid-terminated monolayer. It is possible that the highly positively charged Tat penetrates through the membrane and binds to this MPA-monolayer. This would weaken the interaction between the sensor chip and the membrane, resulting in the increase in energy dissipation observed.

Therefore, the QCM-D results are consistent with three alternative mechanisms that cannot be distinguished using this data alone. We are currently employing complementary techniques to further clarify the mechanism of action. However, the interaction of Tat with DMPC/cholesterol provides an experiment from which we can compare the behaviour of Tat on bacterial-mimetic membranes.

### 3.2. QCM results for Tat interaction with bacterial membranes

#### 3.2.1. Tat (49–57) on DMPC/DMPG 4:1

A DMPC/DMPG (4:1) membrane is used as the model system for prokaryotic membranes, as the inclusion of DMPG mimics the negatively charged components found on the surface of bacteria [48]. The behaviour of Tat (49–57) on this membrane is shown in Fig. 3. It is important to point out that Fig. 3 presents one peptide concentration and the response of four different harmonics (cf. Fig. 2). The results show that interaction between Tat (49–57) and DMPC/DMPG (4:1) occurs via a biphasic mechanism: peptide addition followed by membrane disruption. On introduction of the peptide into

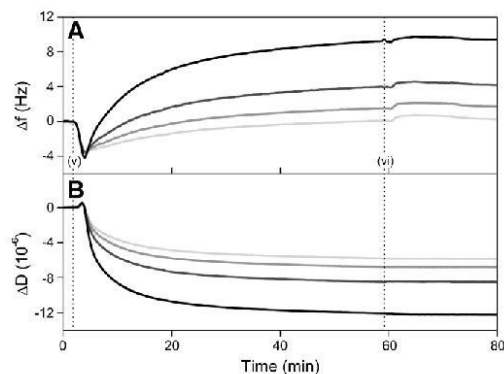


**Fig. 3.**  $\Delta f$ - $t$  (A) and  $\Delta D$ - $t$  (B) plots obtained for the interaction of a 10  $\mu\text{M}$  solution of Tat (49–57) with a DMPC/DMPG 4:1 membrane. The response of four harmonics is shown (3rd, 5th, 7th and 9th harmonics; darkest to lightest lines). Time points (v) and (vi) correspond to peptide addition and buffer rinse, respectively.

the QCM-D chamber, there was a decrease in frequency of ca. 4 Hz at all harmonics. This value was consistent across all experiments ( $\Delta f_{av} = -3.8 \pm 0.7$  Hz). After membrane saturation was reached, mass was removed from the chip surface in a harmonic-dependent manner. That is, the greatest mass loss was observed at the 3rd and 5th harmonics, which probe further from the chip surface, while less mass loss was observed at the chip surface-sensing 7th and 9th harmonics (Fig. 3A). Therefore, disruption occurs on the surface of the membrane; consistent with a “carpet mechanism” [19,22,24]. The loss of mass was accompanied by a decrease in  $\Delta D$  (Fig. 3B). This is because energy dissipation is proportional to thickness, according to the Kelvin–Voigt model of viscoelasticity. Furthermore, highly dissipating bilayer patches sitting on top of the complete bilayer may have been removed, contributing to the decrease in  $\Delta D$ . The buffer rinse performed at the end of the experiment (point (vi) in Fig. 3) resulted in a negligible change in mass.

Disruption of PC/PG membranes has not been previously observed. Thorén and co-workers reported that TatP59W (Ac-GRKKRRQRRRPWQ-NH<sub>2</sub>) caused the leakage of only 1.9% of entrapped carboxyfluorescein from DOPC/DOPG (3:2) vesicles [17]. Zhu and Shin reported that Tat (48–60; GRKKRRQRRRPQ) induced the release of ca. 10% of entrapped calcein from egg yolk phosphoethanolamine/PG (7:3) vesicles [18]. Under the same conditions, TatP59W caused the leakage of ca. 20% of the fluorescent dye [18], in contrast to the 1.9% determined by Thorén et al. Ruzza and co-workers observed that Tat (48–61; GRKKRRQRRRPQ) caused the leakage of ca. 10% of calcein from DMPC/DMPG (3:1) vesicles [15]. Finally, Yang and co-workers reported that Tat (48–61; GRKKRRQRRRPQ) caused <5% leakage of ANTS/DPX dye from DOPC/DOPG (1:1) vesicles [49]. Therefore, experimental differences could explain the discrepancy between the results of this study and earlier work. Firstly, higher peptide concentrations were used in our study (1–15  $\mu\text{M}$ ) and significant loss of mass from the membrane was only observed at concentrations above 5  $\mu\text{M}$ . This concentration range is lower than the MIC values of Tat of 0.6–20  $\mu\text{M}$  as determined by Jung et al. [11]. Secondly, Tat (44–57) and Tat (49–57) peptides were studied here and differences in sequence will change membrane activity (see below). Thirdly, the aforementioned studies were conducted on bilayers in the liquid-phase, whereas in our study the bilayers were in the gel-phase. Membrane defects tend to exist in bilayers formed below their phase-transition temperature and it is possible that these defects make the membrane more susceptible to disruption [50]. Finally, the dye-leakage studies summarised above used small ( $\leq 100$  nm) vesicles, which exhibit high shear moduli, lower deformation, and hence are less likely to undergo disruption compared with planar bilayers [28,51]. The results of this study are, therefore, not inconsistent with the existing literature but instead outline a set of prerequisite factors for observable bacterial membrane disruption by the Tat peptide.

#### 3.2.2. Effect of hydrophobicity of Tat and negative charge of membrane

The effect of peptide hydrophobicity on bacterial membrane disruption was investigated by using the longer-sequence peptide Tat (44–57). Both Tat (49–57) and Tat (44–57) have a net charge of +9 at pH 7.4. However, the free energy of transfer from water to lipid interface for Tat (44–57) is 3.77 kcal/mol and for Tat (49–57) it is 4.87 kcal/mol, according to the Wimley and White (WW) scale [52,53]. That is, Tat (44–57) is more hydrophobic than Tat (49–57). The effect of membrane charge was investigated by increasing the percentage of DMPG in the membrane from 20% to 33%. The results are presented as plots of  $\Delta f$  versus  $\Delta D$  in Fig. 4 (called “ $\Delta f$ - $\Delta D$  plots”). A comprehensive explanation of the interpretation of  $\Delta f$ - $\Delta D$  plots can be found in ref. [24]. In summary, these plots illustrate how the structure of the lipid membrane changes per unit mass addition [35]. Each discrete point in the plot represents the value of  $\Delta f$  and  $\Delta D$  at a certain time. In Fig. 4, the point (0,0) corresponds to the time when the peptide solution was introduced into the QCM-D chamber. The last point in each trace corresponds to the end of the incubation

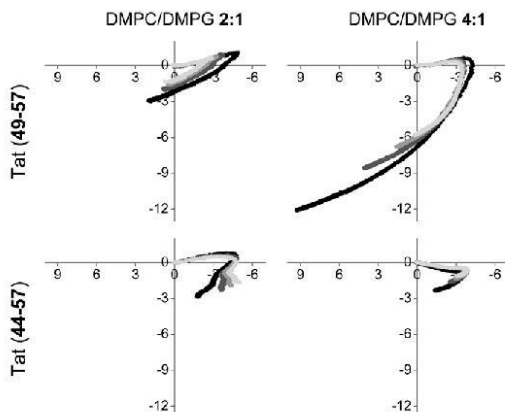


**Fig. 4.** Representative  $\Delta f$ - $\Delta D$  plots for the interaction of a 10  $\mu\text{M}$  solution of either Tat (49–57) or Tat (44–57) on a DMPC/DMPG 2:1 or 4:1 membrane. The x-axis is  $\Delta f$  and the y-axis is  $\Delta D$ . The coordinate (0,0) corresponds to the time when the peptide solution was introduced into the QCM-D chamber. Time increases along the trace and the last point in the trace corresponds to the end of the incubation period (i.e. the time window from points (v) to (vi) is shown; see Fig. 1). The response of the 3rd, 5th, 7th and 9th harmonics is presented (darkest to lightest dots).

period. That is, the time window from points (v) to (vi) is presented (see Fig. 1).

For example, for Tat (49–57) on DMPC/DMPG 4:1 in Fig. 4 (top-right panel) the  $\Delta f$ - $\Delta D$  plot has one turning point at  $\Delta f \approx -3$  Hz and  $\Delta D \approx 0$ . Therefore, it interacts with the membrane via a two-phase mechanism [24]. The first phase can be described by an arrow beginning at (0,0) and ending at the turning point at  $(-3,0)$ . Using Fig. 5 as a guide, it can be seen that this due east arrow corresponds to mass addition with no change in membrane structure. The second phase can be described by an arrow beginning at the turning point at  $(-3,0)$  and ending at the last point in the trace (e.g. point  $(0,-6)$  for the 9th harmonic). This is a south-west arrow, which corresponds to mass loss and increase in rigidity of the membrane. This south-west arrow extends into  $+\Delta f$  values, which indicates a net loss of mass from the surface and not merely a desorption of peptide. Therefore, either using the  $\Delta f$ - $t$  and  $\Delta D$ - $t$  plots or one  $\Delta f$ - $\Delta D$  plot, the same conclusion that Tat interacts with bacterial membranes according to a biphasic mechanism is reached.  $\Delta f$ - $\Delta D$  plots are used in this section of the article because they enable easy comparison between different QCM-D experiments (see Fig. 4).

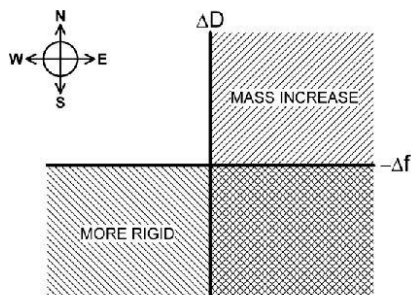


**Fig. 5.** Interpretative guide for  $\Delta f$ - $\Delta D$  plots. This guide was first introduced by us in ref. [24] to assist in the interpretation of  $\Delta f$ - $\Delta D$  plots.

For both Tat peptides, less membrane disruption was observed on the more negatively charged DMPC/DMPG (2:1) membranes (Fig. 4). This seems counter-intuitive; prima facie, more peptide would be expected to bind to the more negatively charged membrane in order to achieve charge neutralisation, inducing greater stress in the membrane and causing larger disruption. Indeed, more peptide was observed to bind to the DMPC/DMPG (2:1) membranes (e.g. for Tat (49–57),  $\Delta f_{av} = -5.8 \pm 1.3$  for 2:1 membrane versus  $\Delta f_{av} = -3.7 \pm 1.3$  for 4:1 membrane, at the 3rd harmonic). Thus increasing the negative charge on the membrane increases the amount of Tat that adsorbs. However, this increased adsorption does not lead to increased disruption. The reason for reduced disruption on DMPC/DMPG (2:1) must be due to how the Tat peptides interact with the surface. It was demonstrated by Ruzza and co-workers that Tat (48–61) shows a lower affinity towards neat DMPG liposomes than DMPC/DMPG (3:1) liposomes [15]. Similarly, various oligoarginines (e.g.  $R_6$ ,  $R_8$  and  $R_{10}$ ) all exhibited lower affinity towards the more negatively charged DMPG liposomes [15]. This suggests that both electrostatic and hydrophobic interactions dictate binding strength [15,54]. Increasing the negative charge of the membrane may increase electrostatic attraction, but binding strength is lowered overall because of weakened hydrophobic interactions. Lower affinity means less stress is placed on the membrane and, therefore, less disruption is observed on DMPC/DMPG (2:1) membranes compared with DMPC/DMPG (4:1) membranes.

On both membranes, less disruption was observed for the more hydrophobic Tat (44–57) peptide (Fig. 4). This result seems inconsistent with the analysis above. Indeed, Zhu and Shin reported that the more hydrophobic TatP59W had smaller MIC values and induced more dye leakage in bacterial-mimetic liposomes than the native Tat peptide [18]. Furthermore, Thorén and co-workers hypothesised that this tryptophan substitution would reorientate the amidated C-terminus of the peptide deeper into the membrane, creating defects in lipid packing that should enhance membrane destabilisation [17]. However, in Tat (44–57) the hydrophobic residues Ile45 and Tyr47 are separated by hydrophilic Ser46 and are located near the hydrophilic acetylated N-terminus. Therefore, it is unlikely that the N-terminus would protrude into the membrane interior as Thorén et al. suggested for their peptides. Similarly, Zhu and Shin were comparing Tat (48–60), with a WW free energy of 8.64 kcal/mol, with amidated TatP59W, which has a WW free energy of 4.44 kcal/mol. Therefore, the difference in liposome dye leakage between the two peptides is explained by the drastic difference in hydrophobicity (95% variation in free energy values). In our study, this difference is much less (30%). Because the difference in hydrophobicity between Tat (44–47) and Tat (49–57) is relatively small it is possible that other differences between the two peptides dominate. For example, length may be a determining factor. The shorter Tat (49–57) peptide may enable closer packing, resulting in a greater membrane strain over a smaller area, which would enhance membrane disruption. Several groups have reported that increasing peptide length increases antimicrobial activity [55,56]. However, these studies investigated the effect of length by varying the number of repeat units e.g.  $(RW)_n\text{-NH}_2$  (where  $n = 1-5$ ) [56]. This means the interaction between peptide and membrane will be consistent over the length of the peptide. In our study, the longer Tat (44–57) is not necessary more active, because the  $^{44}\text{GISYG}_{48}$  unit may have no activity. Therefore, the slight increase in hydrophobicity, the inability of the N-terminus to protrude into the membrane and the longer length of Tat (44–57) may explain why it exhibits less disruptive activity compared with Tat (49–57).

#### 4. Conclusion

In this study, we determined that two truncated Tat sequences, Tat (44–57) and Tat (49–57), exert their antimicrobial activity via the

carpet-like mechanism on planar, gel-phase DMPC/DMPG lipid membranes. This surface-active mechanism occurs in two stages, both observable in the QCM-D data. Firstly, the Tat peptides bind to the membrane surface. The adsorption amount is proportional to the negative charge of the membrane; the higher the negative charge, the greater the amount of peptide that adsorbs to achieve charge neutralisation. Secondly, after a threshold surface coverage is reached, the peptides disintegrate the membrane by disrupting the membrane structure [3]. Both electrostatic and hydrophobic interactions determine the peptide-lipid binding strength and, thus, the magnitude of membrane disruption. For example, even though more peptide adsorbed onto the more negatively charged DMPC/DMPG (2:1) membranes, less disruption was observed due to weakened hydrophobic interactions. Furthermore, the length of the peptide may be important. It was observed that Tat (44–57) was less active than the shorter Tat (49–57). The shorter peptide may induce a greater membrane strain per unit area, increasing disruption. Finally, as a comparison it was determined that neither Tat sequence disrupted the mammalian-mimetic DMPC/cholesterol membranes, consistent with the reports that Tat exerts no hemolytic activity [10,11,18]. Our results suggest that Tat does not simply act through an intracellular mechanism but also acts on the bacterial membrane, making it a promising antibiotic for further development [7].

### Acknowledgements

Financial support from grants from the Australian Research Council (ARC) and National Health and Medical Research Council (NH&MRC) to L.L.M. is acknowledged.

### References

- [1] IDSA, bad bugs, no drugs: as antibiotic discovery stagnates, a public health crisis brews (2004). <http://www.idsociety.org/>. Accessed 28 Sept 2010.
- [2] M.L. Katz, L.V. Mueller, M. Polyakov, S.F. Weinstock, Where have all the antibiotic patents gone? *Nat. Biotechnol.* 24 (2006) 1529–1531.
- [3] Y. Shai, Mode of action of membrane active antimicrobial peptides, *Biopolymers* 66 (2002) 236–248.
- [4] D.W. Hoskin, A. Ramamoorthy, Studies on anticancer activities of antimicrobial peptides, *Biochim. Biophys. Acta* 1778 (2008) 357–375.
- [5] G. Wang, X. Li, Z. Wang, APD2: the updated antimicrobial peptide database and its application in peptide design, *Nucleic Acids Res.* 37 (2009) D933–D937.
- [6] M. Zasloff, Antimicrobial peptides of multicellular organisms, *Nature* 415 (2002) 389–395.
- [7] A. Peschel, H.-G. Sahl, The co-evolution of host cationic antimicrobial peptides and microbial resistance, *Nat. Microbiol.* 4 (2006) 529–536.
- [8] R. Pálffy, R. Gardlik, M. Behuliak, L. Kadasi, J. Turna, P. Celec, On the physiology and pathophysiology of antimicrobial peptides, *Mol. Med.* 15 (2009) 51–59.
- [9] L.M. Gottler, A. Ramamoorthy, Structure, membrane orientation, mechanism, and function of pexiganan—a highly potent antimicrobial peptide designed from magainin, *Biochim. Biophys. Acta* 1788 (2009) 1680–1686.
- [10] H.J. Jung, Y. Park, K.-S. Hamm, D.G. Lee, Biological activity of Tat (47–58) peptide on human pathogenic fungi, *Biochem. Biophys. Res. Commun.* 345 (2006) 222–228.
- [11] H.J. Jung, K.-S. Jeong, D.G. Lee, Effective antibacterial action of Tat (47–58) by increased uptake into bacterial cells in the presence of trypsin, *J. Microbiol. Biotechnol.* 18 (2008) 990–996.
- [12] I. Green, R. Christison, C.J. Voyce, K.R. Bundell, M.A. Lindsay, Protein transduction domains: are they delivering? *Trends Pharmacol. Sci.* 24 (2003) 213–215.
- [13] R. Tréhin, H.P. Merkle, Chances and pitfalls of cell penetrating peptides for cellular drug delivery, *Eur. J. Pharm. Biopharm.* 58 (2004) 209–223.
- [14] H. Brooks, B. Lebleu, E. Vivès, Tat peptide-mediated cellular delivery: back to basics, *Adv. Drug Deliv. Rev.* 57 (2005) 559–577.
- [15] P. Ruzza, B. Biondi, A. Marchiani, N. Antolini, A. Calderan, Cell-penetrating peptides: a comparative study on lipid affinity and cargo delivery properties, *Pharmaceuticals* 3 (2010) 1045–1062.
- [16] E. Eiriksdóttir, K. Konate, Ü. Langel, G. Divita, S. Deshayes, Secondary structure of cell-penetrating peptides controls membrane interaction and insertion, *Biochim. Biophys. Acta* 1798 (2010) 1119–1128.
- [17] P.E.G. Thorén, D. Persson, P. Lincoln, B. Nordén, Membrane destabilizing properties of cell-penetrating peptides, *Biophys. Chem.* 114 (2005) 169–179.
- [18] W.L. Zhu, S.Y. Shin, Effects of dimerization of the cell-penetrating peptide Tat analog on antimicrobial activity and mechanism of bactericidal action, *J. Pept. Sci.* 15 (2009) 345–352.
- [19] Y. Shai, Mechanism of the binding, insertion and destabilization of phospholipid bilayer membranes by  $\alpha$ -helical antimicrobial and cell non-selective membrane-lytic peptides, *Biochim. Biophys. Acta* 1462 (1999) 55–70.
- [20] S. Piantavigna, P. Cizhal, A. Mechler, M. Richter, R. Hoffmann, L.L. Martin, Cell penetrating apidaecin peptide interactions with biomimetic phospholipid membranes, *Int. J. Pept. Res. Ther.* 15 (2009) 139–146.
- [21] D. Knappe, S. Piantavigna, A. Hansen, A. Mechler, A. Binas, O. Nolte, L.L. Martin, R. Hoffmann, Oncocin (VDKPPYLPKPPRRRIYNR-NH<sub>2</sub>): a novel antibacterial peptide optimized against Gram-negative human pathogens, *J. Med. Chem.* 53 (2010) 5240–5247.
- [22] A. Mechler, S. Praporski, K. Atmuri, M. Boland, F. Separovic, L.L. Martin, Specific and selective peptide-membrane interactions revealed using quartz crystal microbalance, *Biophys. J.* 93 (2007) 3907–3916.
- [23] P.J. Sherman, R.J. Jackway, J.D. Gehman, S. Praporski, G.A. McCubbin, A. Mechler, L.L. Martin, F. Separovic, J.H. Bowie, Solution structure and membrane interactions of the antimicrobial peptide fallaxidin 4.1a: an NMR and QCM study, *Biochemistry* 48 (2009) 11892–11901.
- [24] G.A. McCubbin, S. Praporski, S. Piantavigna, D. Knappe, R. Hoffmann, J.H. Bowie, F. Separovic, L.L. Martin, QCM-D fingerprinting of membrane-active peptides, *Eur. Biophys. J.* 40 (2011) 437–446.
- [25] K. Christ, I. Wiedemann, U. Bakowsky, H.-G. Sahl, G. Bendas, The role of lipid II in membrane binding of and pore formation by nisin analyzed by two combined biosensor techniques, *Biochim. Biophys. Acta* 1768 (2007) 694–704.
- [26] S.B. Nielsen, D.E. Otzen, Impact of the antimicrobial peptide Novicidin on membrane structure and integrity, *J. Colloid Interface Sci.* 345 (2010) 248–256.
- [27] C.A. Keller, B. Kasemo, Surface specific kinetics of lipid vesicle adsorption measured with a quartz crystal microbalance, *Biophys. J.* 75 (1998) 1397–1402.
- [28] A. Mechler, S. Praporski, S. Piantavigna, S.M. Heaton, K.N. Hall, M.-I. Aguilari, L.L. Martin, Structure and homogeneity of pseudo-physiological phospholipid bilayers and their deposition characteristics on carboxylic acid terminated self-assembled monolayers, *Biomaterials* 30 (2009) 682–689.
- [29] G. Sauerbrey, The use of quartz oscillators for weighing thin layers and for microweighing, *Z. Phys.* 155 (1959) 206–222.
- [30] N.-J. Cho, K.K. Kanazawa, J.S. Glenn, C.W. Frank, Employing two different quartz crystal microbalance models to study changes in viscoelastic behavior upon transformation of lipid vesicles to a bilayer on a gold surface, *Anal. Chem.* 79 (2007) 7027–7035.
- [31] S.T. Henriques, M.N. Melo, M.A.R.B. Gastanho, Cell-penetrating peptides and antimicrobial peptides: how different are they? *Biochem. J.* 399 (2006) 1–7.
- [32] N. Schmidt, A. Mishra, G.H. Lai, G.C.L. Wong, Arginine-rich cell-penetrating peptides, *FEBS Lett.* 584 (2010) 1806–1813.
- [33] G. van Meer, D.R. Voelker, G.W. Feigenson, Membrane lipids: where they are and how they behave, *Nat. Rev. Mol. Cell Biol.* 9 (2008) 112–124.
- [34] M. Rodahl, F. Höök, A. Krozer, P. Brzezinski, B. Kasemo, Quartz crystal microbalance setup for frequency and Q-factor measurements in gaseous and liquid environments, *Rev. Sci. Instrum.* 66 (1995) 3924–3930.
- [35] M. Rodahl, F. Höök, C. Fredriksson, C.A. Keller, A. Krozer, P. Brzezinski, M. Voinova, B. Kasemo, Simultaneous frequency and dissipation factor QCM measurements of biomolecular adsorption and cell adhesion, *Faraday Discuss.* 107 (1997) 229–246.
- [36] K.K. Kanazawa, J.G. Gordon, Frequency of a quartz microbalance in contact with liquid, *Anal. Chem.* 57 (1985) 1770–1771.
- [37] J.E. Shaw, R.F. Epanand, J.C.Y. Hsu, G.C.H. Mo, R.M. Epanand, C.M. Yip, Cationic peptide-induced remodeling of model membranes: direct visualization by in situ atomic force microscopy, *J. Struct. Biol.* 162 (2008) 121–138.
- [38] H.J. Hinz, J.M. Sturtevant, Calorimetric investigation of the influence of cholesterol on the transition properties of bilayers formed from synthetic L- $\alpha$ -lecithins in aqueous suspension, *J. Biol. Chem.* 247 (1972) 3697–3700.
- [39] S.L. Veatch, S.L. Keller, Seeing spots: complex phase behavior in simple membranes, *Biochim. Biophys. Acta* 1746 (2005) 172–185.
- [40] S.R. Dennison, R.D. Baker, I.D. Nicholl, D.A. Phoenix, Interactions of cell penetrating peptide Tat with model membranes: a biophysical study, *Biochem. Biophys. Res. Commun.* 363 (2007) 178–182.
- [41] A. Mishra, V.D. Gordon, L. Yang, R. Coridan, G.C.L. Wong, HIV Tat forms pores in membranes by inducing saddle-splay curvature: potential role of bidentate hydrogen bonding, *Angew. Chem. Int. Ed.* 47 (2008) 2986–2989.
- [42] C. Ciobanasu, J.P. Siebrasse, U. Kubitschek, Cell-penetrating HIV1 Tat peptides can generate pores in model membranes, *Biophys. J.* 99 (2010) 153–162.
- [43] H.D. Hecce, A.E. Garcia, Molecular dynamics simulations suggest a mechanism for translocation of the HIV-1 Tat peptide across lipid membranes, *PNAS* 104 (2007) 20805–20810.
- [44] S. Yesylevskyy, S.-J. Marrink, A.E. Mark, Alternative mechanisms for the interaction of the cell-penetrating peptides penetratin and the Tat peptide with lipid bilayers, *Biophys. J.* 97 (2009) 40–49.
- [45] H.D. Hecce, A.E. Garcia, J. Litt, R.S. Kane, P. Martin, N. Enrique, A. Rebollo, V. Milesi, Arginine-rich peptides destabilize the plasma membrane, consistent with a pore formation translocation mechanism of cell-penetrating peptides, *Biophys. J.* 97 (2009) 1917–1925.
- [46] M. Rodahl, B. Kasemo, On the measurement of thin liquid overlayers with the quartz-crystal microbalance, *Sens. Actuators A* 54 (1996) 448–456.
- [47] G. Ter-Avetisyan, G. Tünnemann, D. Nowak, M. Nitschke, A. Herrmann, M. Drab, M.C. Cardoso, Cell entry of arginine-rich peptides is independent of endocytosis, *J. Biol. Chem.* 284 (2009) 3370–3378.

- [48] C.S.B. Chia, J. Torres, M.A. Cooper, I.T. Arkin, J.H. Bowie, The orientation of the antibiotic peptide maculatin 1.1 in DMPG and DMPC lipid bilayers. Support for a pore-forming mechanism, *FEBS Lett.* 512 (2002) 47–51.
- [49] S.-T. Yang, E. Zaitseva, L.V. Chernomordik, K. Melikov, Cell-penetrating peptide induces leaky fusion of liposomes containing late endosome-specific anionic lipid, *Biophys. J.* 99 (2010) 2525–2533.
- [50] L. Bakás, H. Ostolaza, W.L.C. Vaz, F.M. Goñi, Reversible adsorption and nonreversible insertion of *Escherichia coli*  $\alpha$ -hemolysin into lipid bilayers, *Biophys. J.* 71 (1996) 1869–1876.
- [51] P.E.G. Thorén, D. Persson, E.K. Esbjörner, M. Goksör, P. Lincoln, B. Nordén, Membrane binding and translocation of cell-penetrating peptides, *Biochemistry* 43 (2004) 3471–3489.
- [52] W.C. Wimley, S.H. White, Experimentally determined hydrophobicity scale for proteins at membrane interfaces, *Nat. Struct. Biol.* 3 (1996) 842–848.
- [53] C. Snider, S. Jayasinghe, K. Hristova, S.H. White, MPEX: a tool for exploring membrane proteins, *Protein Sci.* 18 (2009) 2624–2628.
- [54] L.-P. Liu, C.M. Deber, Anionic phospholipids modulate peptide insertion into membranes, *Biochemistry* 36 (1997) 5476–5482.
- [55] L. Ringstad, A. Schmidtchen, M. Malmsten, Effect of peptide length on the interaction between consensus peptides and DOPC/DOPA bilayers, *Langmuir* 22 (2006) 5042–5050.
- [56] Z. Liu, A. Brady, A. Young, B. Rasimick, K. Chen, C. Zhou, N.R. Kallenbach, Length effects in antimicrobial peptides of the (RW)<sub>n</sub> series, *Antimicrob. Agents Chemother.* 51 (2007) 597–603.

## **4 Paper 7:**

### **4.1 Membrane perforation and passive translocation of Tat peptides**

Monash University

**Declaration for Paper 7****Declaration by candidate**

In the case of Paper 7, the nature and extent of my contribution to the work was the following:

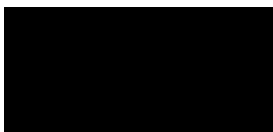
<b>Nature of contribution</b>	<b>Extent of contribution (%)</b>
Design and performance of QCM-D and SECM experiments, data analysis, contribution to manuscript preparation and review	35%

The following co-authors contributed to the work. If co-authors are students at Monash University, the extent of their contribution in percentage terms must be stated:

<b>Name</b>	<b>Nature of contribution</b>	<b>Extent of contribution (%) for student co-authors only</b>
<b>Muhammad E. Abdelhamid</b>	Design and performance of QCM-D and SECM experiments, data analysis, manuscript preparation and review	
<b>Chuan Zhao</b>	Design and performance of SECM experiments, manuscript preparation	
<b>Xiaohu Qu</b>	AFM experiments, data analysis	
<b>George A. McCubbin</b>	Manuscript preparation and review	10%
<b>Bim Graham</b>	Review manuscript in preparation	
<b>Leone Spiccia</b>	Review manuscript in preparation	

<b>Anthony P. O'Mullane</b>	Key ideas, manuscript preparation and review	
<b>Lisandra L. Martin *</b>	Key ideas, manuscript preparation and review	

The undersigned hereby certify that the above declaration correctly reflects the nature and extent of the candidate's and co-authors' contributions to this work\*.

<b>Candidate's Signature</b>		<b>Date</b> 23/05/14
<b>Main Supervisor's Signature</b>		<b>Date</b> 23/05/14

\*Note: Where the responsible author is not the candidate's main supervisor, the main supervisor should consult with the responsible author to agree on the respective contributions of the authors.

## Membrane perforation and passive translocation of Tat peptides

Stefania Piantavigna,<sup>1</sup> Muhammad E. Abdelhamid,<sup>2</sup> Chuan Zhao<sup>3</sup> Xiaohu Qu,<sup>1,4</sup> George A. McCubbin,<sup>1</sup> Bim Graham,<sup>5</sup> Leone Spiccia,<sup>1</sup> Anthony P. O'Mullane<sup>2\*</sup> and Lisandra L. Martin<sup>1\*</sup>

<sup>1</sup> School of Chemistry, Monash University, Clayton, VIC 3800, Australia

<sup>2</sup> School of Applied Sciences, GPO Box 2476V, RMIT University, Melbourne VIC 3001, Australia

<sup>3</sup> School of Chemistry, The University of New South Wales, Sydney, NSW 2052, Australia

<sup>4</sup> Current address: Ionode Pty Ltd, 8/148 Tennyson Memorial Avenue, Tennyson, Queensland, 4105, Australia

<sup>5</sup> Monash Institute of Pharmaceutical Sciences, Monash University, Parkville, VIC 3052 Australia

*Tat peptide, worm-hole pore, quartz crystal microbalance, scanning electrochemical microscopy, cell penetrating peptide*

---

**ABSTRACT:** The Tat peptide was the first, and is regarded as the 'gold standard' for cell-penetrating peptides; capable of traversing a mammalian membrane passively into the cytosolic space. This feature has been exploited for applications, such as drug delivery. However, the mechanism by which Tat achieves this extraordinary function remains ambiguous and unresolved. Mechanistic details of peptide uptake are revealed here using three complementary methods; quartz crystal microbalance with dissipation, scanning electrochemical microscopy and atomic force microscopy. Accordingly, we combined three scales of measurement, providing information on the uptake of Tat via trans-membrane insertion, 'worm-hole' pore formation leading to ion permeability of the membrane layer and nanometer-scale visualisation of Tat punctuation into a biomimetic mammalian membrane bilayer. This comprehensive investigation illustrates the energy-independent uptake of the cationic Tat peptide and provides empirical data that clarifies the precise mechanism by which Tat is membrane active, which has long challenged the field. Detailed knowledge of the mechanism and specificity for Tat peptide translocation is essential for improvements in the cellular delivery of Tat-conjugated cargoes including therapeutic agents required to target specific intracellular locations.

---

### Introduction

The cell membrane constitutes an efficient barrier that is impermeable to hydrophilic molecules. As a consequence, the internalisation of therapeutic agents can be difficult to achieve. The human immunodeficiency virus type 1 (HIV-1) uses a nuclear transcription-activating protein, Tat, that has the ability to translocate across the mammalian cell membrane<sup>1,2</sup> and carry conjugated molecules to intracellular locations.<sup>3,5</sup> There is enormous interest in revealing the molecular basis of the translocation

of Tat, as an extensive range of biomolecules can be conjugated to the Tat peptide and this cargo delivered to an intracellular location. Application to the intracellular delivery of drugs and therapeutics through modification with such membrane translocation sequences, especially using Tat peptides, was immediately recognized (see review by Fisher, 2005) and the exploration of cell-penetrating peptides (CPPs) is now a well established field.<sup>6,7</sup> This knowledge will enable the next generation of pharmaceuticals to reach site-

specific targets and more effective drug delivery to be achieved.

Cellular localisation studies using fluorescent conjugates with the Tat (37-60) peptide have revealed two distinct membrane active motifs.<sup>8,9</sup> The Tat (38-49) region, which adopts an  $\alpha$ -helical, amphipathic secondary structure and a highly cationic, basic domain, Tat (49-58). Remarkably, the basic region, GRKKRRQRRRQ (Tat (49-58)), is responsible for membrane translocation through the plasma membrane.<sup>8,9</sup> Cell-penetrating and tumor-targeting peptides that specifically target and kill cancerous cells by exploiting the microenvironment of specific tumors are the future alternatives to small molecule-based chemotherapeutics.<sup>10</sup>

A large number of peptides are now recognised as being capable of crossing cellular membranes using a variety of mechanisms. Members of the CPP family include Tat and penetratin peptides, which are arginine-rich<sup>11</sup> and proline-rich apidaecin and oncocin peptides<sup>12-15</sup> as well as many others.<sup>16,17</sup> Over the past decade there has been intense debate as to the mechanism of action of CPPs. Several models are used to describe how membrane-active peptides interact with biomembranes (biomimetic and plasma membranes). The most common interactions are classically described as either pore formation (either barrel-stave or toroidal pores) or carpet-like membrane disruption.<sup>10,16,18</sup> However, the results of specific investigations of the membrane translocation process for the Tat peptide are confusing and often ambiguous and considerable uncertainty remains regarding the precise mechanism for cellular internalization of Tat. Both non-endocytotic and endocytotic (clathrin-dependent, caveolae-dependent, clathrin- and caveolae independent and/or macropinocytosis) pathways have been suggested with proponents of the former differing in their views as to whether the Tat translocation occurs via pore, carpet or inverted micelle formation.<sup>11,19-22</sup> The current view predominantly favours endocytosis for Tat uptake by cells, although substantial evidence exists for direct translocation (via pore formation)<sup>23-26</sup> occurring in an energy-independent, non-receptor mediated manner.

Biophysical studies using supported lipid bilayers (SLB) eliminate endocytosis mechanisms, however they still do not provide unequivocal clarification of the membrane activity of the Tat peptide. Previously, we demonstrated that Tat's activity is dependent on membrane composition, with the presence of 20% negatively charged lipid in the

membrane leading to rapid disruption via a surface-active 'carpet' mechanism.<sup>15</sup> However, a neutral 'mammalian' biomimetic membrane containing phosphocholine and cholesterol showed no disruption, suggesting roles for both electrostatic and hydrophobic interactions of the Tat peptide with membranes<sup>15</sup>. Using neutron and X-ray reflectivity measurements, Choi<sup>27</sup> concluded that the Tat peptide formed membrane defects rather than pores in phosphocholine-containing membranes. Using giant unilamellar liposomes (GUVs) and single-molecule fluorescence, Ciobanasu et al.<sup>28</sup> showed that diffusion mobility of the Tat peptide was independent of membrane phase (liquid-ordered or liquid-disordered) and that the peptides 'float' on the lipid layers rather than incorporate into membranes containing neutral lipids. Interestingly, they subsequently reported evidence for pore formation.<sup>29</sup> *In silico* mechanistic studies employing molecular dynamics also support translocation via a pore.<sup>30</sup> Recently, Lattig-Tunnemann et al.<sup>31</sup> used molecular dynamics, analytical ultracentrifugation and cellular microscopy to demonstrate improved membrane translocation for a cyclic Tat peptide, suggesting that positional fixation of the guanidinium groups of the arginine residues leads to more efficient occupation of the membrane surface. They concluded that the spatial orientation of the arginines and structural rigidity were the driving factors for membrane translocation and importantly, that no 'needle-like' structures were required for uptake.<sup>31</sup> Taken together, each of these studies provide important 'pieces of the puzzle', however the detailed mechanism of direct membrane translocation of Tat and other hydrophilic peptides through a hydrophobic lipid bilayer remains controversial and unresolved.

This study explored the membrane activity of two Tat peptides, Tat (44-57) (amino acid sequence Ac-GI<sup>45</sup>SYGRK<sup>50</sup>KRRQR<sup>55</sup>RR-NH<sub>2</sub>) and Tat (49-57), towards neutral phosphocholine + cholesterol (PCc) mammalian and phosphocholine + phosphoglycerol (PC:PG, 2:1) bacterial membrane mimetics. These Tat peptides act via both electrostatic and hydrophobic interactions towards biomimetic membranes.<sup>15</sup> Specifically, here interrogation of the two Tat peptides employed *three scales* of measurement: (i) monitoring of binding and structural changes using a quartz crystal microbalance (QCM), (ii) measurement of the permeability of the Tat-treated membranes towards ionic conductance using scanning electrochemical microscopy (SECM) and (iii) high resolution

structural investigation of membrane morphology following addition of Tat using atomic force microscopy (AFM). (The experimental approach for the QCM and SECM measurements is illustrated in Figure 1a.) This complementary combination of biophysical techniques enabled the Tat peptide biomimetic lipid bilayer interaction to be comprehensively scrutinised at millimetre, micrometre and nanometre scales with concentration-dependent and spatially and

temporally resolved measurements made in solution under pseudo-physiological conditions.

As detailed below, the QCM, SECM and AFM data were all found to be in accord with the Tat (44-57) peptide spontaneously forming 'worm-hole' pores within the biomimetic lipid bilayers. Furthermore, we showed that the shorter Tat (49-57) peptide (Ac-R<sup>39</sup>KKRRQR<sup>55</sup>RR-NH<sub>2</sub>) behaved similarly towards these biomimetic membranes (see Supporting Information).

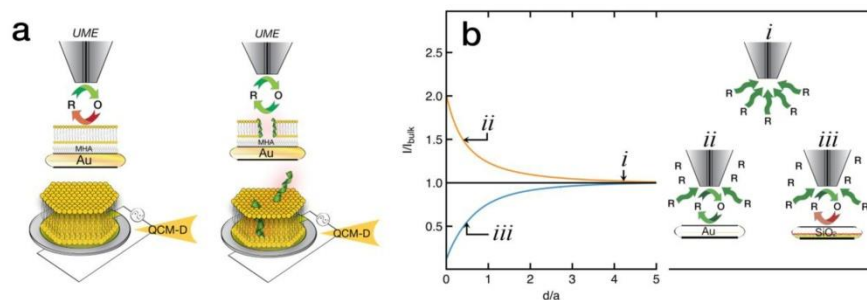


Figure 1. The experimental design for the SECM and QCM experiments. Panel a) LHS: before addition of Tat, the QCM shows the intact lipid bilayer and the SECM shows an insulating membrane layer, in which a redox mediator, converted to the oxidized form (O) by an ultramicroelectrode (UME), is unable to be reduced back to the reduced form by the underlying gold electrode (negative feedback mode); see also b(iii). RHS: after addition of Tat, the QCM responds with a decrease in frequency as the Tat binds to the membrane and a concomitant change in dissipation due to the effect of Tat on the membrane viscoelasticity. SECM will now respond if a pore-like structure is formed in which the redox mediator can be regenerated (positive feedback mode); see also b(ii). Panel b) approach curves for a conducting (ii) and insulating (iii) material are indicated. If an insulating material (membrane) is compromised to allow access of a solution-based mediator to the underlying conductor (gold), an approach curve that is intermediate between the presented extremes will be expected to be recorded.

## Results and Discussion

### QCM study of Tat binding to membranes.

QCM measures changes in the harmonic frequency ( $f$ ) of an oscillating sensor as mass is added.<sup>32</sup> The QCM-D<sup>33</sup> instrument simultaneously measures the energy loss to the surrounding environment, or dissipation factor ( $D$ ), thus providing an assessment of the viscoelasticity of the resulting peptide-membrane layer.<sup>34</sup> Additional information about mass and structure are obtained using the different harmonics of the QCM sensor, providing a *depth-profile* orthogonal to the sensor surface.<sup>35</sup> The penetration depth of each harmonic wave adjacent to the sensor is inversely proportional

to the frequency.<sup>36</sup> Thus, a surface-active peptide will influence the third more than the ninth harmonic, whereas a peptide that traverses the membrane bilayer will affect all of the harmonics similarly.

Biomimetic membranes, formed by liposome deposition<sup>37,38</sup> and composed of either 7:3 DMPC:cholesterol ('PC' eukaryotic/mammalian mimetic) or 2:1 DMPC:DMPG ('PC:PG' bacterial/prokaryotic mimetic) bilayers, were used to examine the effect of the Tat peptides. The change in frequency ( $\Delta f$ ) and energy dissipation ( $\Delta D$ ) over time (Fig. S1) comprise the raw data acquired following the introduction of the Tat

peptides into the QCM-D chamber. These data were analysed and presented as  $\Delta f$ - $\Delta D$  plots that represent the structural change(s) that occur as the Tat interacts with the membrane (per unit frequency or mass), as described previously.<sup>34</sup> Introduction of Tat (44-57) to the membrane layers yielded the  $\Delta f$ - $\Delta D$  plots in Figure 2a for 1 and 10  $\mu\text{M}$  Tat (44-57); similar  $\Delta f$ - $\Delta D$  plots for Tat (49-57) are shown in Figure S2. For the PC:PG membrane layer, the interaction of the Tat occurs via a two-stage mechanism (Figure 2a), consistent with our previous reports.<sup>15</sup> The initial binding of the peptide (from the origin in a negative direction) is followed by a loss of mass ( $f$  shifts in a positive direction). At higher concentrations (10  $\mu\text{M}$ ), the binding phase is less prominent but is followed by the same loss of mass (i.e.  $\Delta f$  positive).

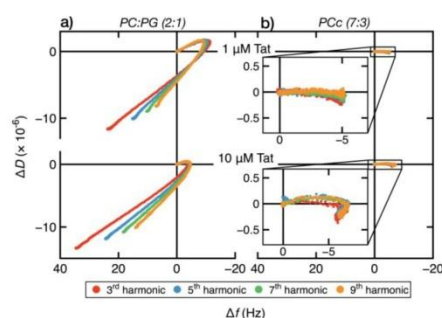


Figure 2. QCM data analysed using  $\Delta D$  vs.  $\Delta f$  profiles examining the effects of the Tat (44-57) peptide interaction on the sensors with bacterial (PC:PG) and mammalian (PCc) mimetic membranes.  $\Delta D$  vs.  $\Delta f$  profiles examining the effect on the sensor harmonics as the Tat peptide (at two different peptide concentrations) interacts with the lipid bilayers previously deposited. In each case, the peptide inserts in a trans-membrane manner, discerned by all the harmonics overlapping. No difference is observed between the two concentrations studied. However, for the PC:PG membrane a dramatic effect is observed upon introduction of the Tat (44-57) peptide, with a huge mass loss ( $\Delta f$  increases) and simultaneous dramatic decrease in viscoelasticity ( $\Delta D$  decreases) occurring. This is consistent with membrane disruption.

The QCM-D results for mammalian-mimetic (PCc) membrane (Fig. 2b) show no change in dissipation ( $\Delta D \sim 0$ ) as the Tat peptide binds ( $\Delta f \sim 5$  Hz). Unlike the PC:PG membrane, no removal of mass is observed, ruling out the occurrence of

carpet disruption, inverted micelle formation or endocytosis under our experimental conditions. Similar data were observed for Tat (49-57) and at higher concentrations (10  $\mu\text{M}$ ) (Fig. S2). We previously reported this QCM-D behavior as consistent with either pore formation or direct translocation, as all would result in the observed mass increase.<sup>15</sup> Pore formation is considered more likely, as the overlap of the response of the harmonic frequencies in the  $\Delta f$ - $\Delta D$  plot suggests that the peptides insert into the membrane in a trans-membrane manner (Figure 2a).<sup>35</sup> However, QCM-D data alone is insufficient to conclusively distinguish between the three mechanisms.

### SECM study of membrane permeability to redox mediators.

SECM is an ideal tool to characterize the permeability of self-assembled monolayers, lipid membranes and biological systems at the micrometer scale and has found increasing biological applications in recent years.<sup>39-41</sup> After the QCM-D experiments, the sensor crystals were carefully removed from the chambers and the permeability of the peptide-membrane layers was measured using the 'approach curve' method (see Figure 1b). In this manner, the SECM results could be directly correlated with the QCM-D data. Figure 3 presents normalized approach curves obtained for the sensor crystal and various adlayers: 6-mercaptophexanoic acid (MHA) self-assembled monolayer; MHA + bilayer; MHA + bilayer + 1  $\mu\text{M}$  Tat (44-57); and MHA + bilayer + 10  $\mu\text{M}$  Tat (44-57). For comparison, theoretical approach curves for a pure insulator and a pure conductor are also presented.<sup>39</sup> Using this SECM method, the ultramicroelectrode (UME) is made to approach the surface at a constant rate while oxidizing ferrocyanide ( $[\text{Fe}(\text{CN})_6]^{4-}$ ) at a diffusion-limited rate. The current ( $i_{\text{tip}}$ ) is measured during this approach and the data then normalized by plotting  $i_{\text{tip}}/i_{\text{bulk}}$  versus  $d/a$  where  $i_{\text{bulk}}$  is the diffusion-limited current measured at the tip when it is far away from the surface,  $a$  is the tip radius and  $d$  is the tip-sample distance. Therefore, any increase in the value of  $i_{\text{tip}}/i_{\text{bulk}}$  over that of the insulator approach curve indicates that the oxidized form, ferricyanide ( $[\text{Fe}(\text{CN})_6]^{3-}$ ) is converted back to ferrocyanide at the gold electrode surface, thereby resulting in a positive feedback effect. For this to occur, the redox mediator needs to access the underlying gold electrode, as neither the MHA layer nor the bilayers investigated in this study can facilitate reduction of the oxidized mediator.

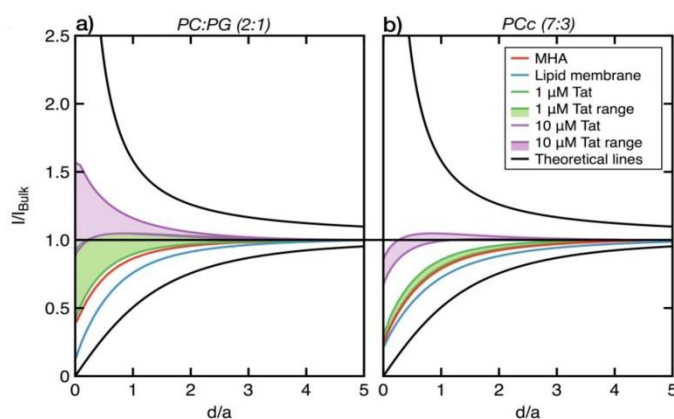


Figure 3. SECM data for the Tat (44-57) peptide interaction with bacterial (PC:PG) and mammalian (PCc) mimetic membranes. SECM approach curves for the study of the interaction of Tat peptide on different regions of the SLBs deposited *ex-situ*. A comparison of the current feedback measured upon exposure of the PC:PG and PCc membranes to the same peptide concentration, reveals the much more dramatic and selective effect of Tat on PC:PG membrane is evident. These data are plotted as a normalised range of data (values measured for the feedback current). The experiments were carried out on unbiased substrates and the potential of the Pt UME (25  $\mu\text{m}$  diameter) was held at 0.4 V (a Pt wire counter and Ag/AgCl reference electrode were used to complete the electrochemical cell). An approach speed of 1  $\mu\text{m/s}$  was used in an electrolyte consisting of 1 mM  $\text{K}_4[\text{Fe}(\text{CN})_6]$  in PBS buffer.

As expected, the MHA significantly decreases the accessibility of the gold surface to the hydrophilic redox mediator  $[\text{Fe}(\text{CN})_6]^{4-}$  (Figure 2b), in accord with previous studies for SAMs on gold electrodes.<sup>42,43</sup> The formation of both types of lipid bilayer on the MHA layer (PC:PG (2:1) and PCc (7:3)) further decreased the normalized current to values closer to that of a pure insulating surface, indicating that the permeability of the biomimetic membrane to the ferricyanide mediator is very low. This is consistent with the earlier results of Tsionsky and co-workers.<sup>44</sup>

Significantly, the addition of Tat (44-57) increased the permeability of the membrane, as evidenced by the increase in feedback current (Figure 3b) and indicates that this particular peptide is capable of creating pathways via which the redox mediator can access the underlying gold substrate and be regenerated. It should be noted that the data is represented by a range of different approach curves measured at different regions on the same QCM chip, as indicated by the shaded areas in Figure 3. This indicates that the interaction of Tat with the membrane is not homogeneous on the micron scale. Therefore, the three possible mechanisms espoused to explain the QCM-D data could be narrowed

down to one using the SECM results: pore formation. Neither surface association nor direct translocation would increase membrane permeability. A concentration dependence is observed in both cases, whereby increasing the Tat concentration to 10  $\mu\text{M}$  results in further permeation of the membrane by the redox species. Perhaps most significantly, however, the composition of the lipid bilayer plays a crucial role and significantly influences the magnitude of the feedback current. In the case of PC:PG (2:1), the QCM-D data indicates disruption of the membrane. This disruption corresponds to a broad range of data with higher feedback current in the SECM measurements (green band (1  $\mu\text{M}$ ) and mauve band (10  $\mu\text{M}$ ) in Figure 3a) with the high variance indicating loss of membrane integrity. The SECM response observed upon exposure of PCc to Tat (44-57) is dramatically different, with tight bands of increased feedback current data observed (i.e. small error bars) that are consistent with a much less disruptive mechanism of membrane interaction, namely worm-hole pore formation.

#### Worm-hole formation observed by AFM.

Having determined that Tat (44-57) acts on PCc bilayers via a pore mechanism, AFM was then used

to investigate the nanoscale structure of the peptide-membrane layer. The AFM measurements used single crystalline facets of gold on a gold bead electrode. The high mobility of peptides in model membranes, combined with the transience of peptide pores, makes it difficult to image these structures in solution.<sup>30,35,45</sup> Thus, in an attempt to trap the pore assemblies, the samples were carefully dried under a stream of  $N_2$  immediately prior to imaging. This involved some trial-and-error to ensure that the lipid head groups were not completely dehydrated (which can cause membrane defects) while removing the bulk solution. The membrane surface in Figure 4 shows no drying-induced defects on the PCc layer. Additional AFM images are displayed in Figure S4.

The thickness of the membranes was determined to be  $\sim 5$  nm by punching holes in the membranes

with the AFM tip, with a depth close to that expected for a PCc bilayer.<sup>46</sup> Furthermore, the lipid domains (possibly cholesterol-rich) did not move or change over time, suggesting that drying had reduced lipid mobility. Upon the addition of a  $10 \mu\text{M}$  solution of Tat (44-57), a small number of discrete pores were observed on the bilayer surface (Figure 4). These pores were less than 1 nm in depth (generally  $\sim 0.5$  nm, although some were smaller), as shown in two cross-sectional regions (Figure 4 (i and ii)) and hence not trans-membrane in nature. It is possible, however, that the removal of water partially collapsed the pores. The pores were found to cover *ca.* 0.58% of the membrane surface. This low coverage is consistent with the SECM results, which showed that after saturation with Tat (44-57), the membrane permeability increased only slightly, as evidenced by the feedback current (Figure 2b).

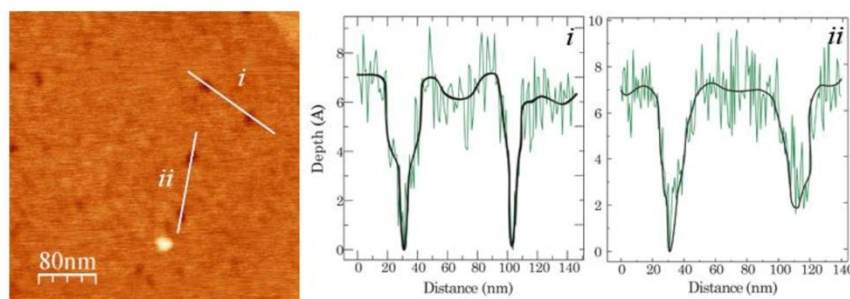


Figure 4. AFM height image and cross-sectional analysis of worm-hole pores. Morphology of a MHA-modified gold bead covered with a membrane (PCc) bilayer, 20 mins after addition of  $10 \mu\text{M}$  Tat (44-57); vertical scale is 0-1.5 nm. The membrane surface is punctuated with small pores. Cross sectional analyses across the two regions (i and ii) are highlighted, revealing that these pores are  $\sim 0.5$  nm deep. The AFM images of the bilayer taken before the addition of the peptide and additional AFM images are found in Figure S4.

Computational analysis was used to estimate the Tat (44-57) peptide dimensions based on  $\alpha$ -helical secondary structure is shown in Supporting Information (Fig. S5). The energy minimised  $\alpha$ -helical representation gave the estimated length of 2.1 nm compared with the extended peptide that gave a length of 4.8 nm.

To, summarise, through the novel application of three 'spatially-resolved' techniques with very different, but complementary, analytical powers, we have accumulated strong evidence for worm-hole pore formation upon exposure of a mammalian membrane mimetic to tat peptides (Figure 5). The QCM data for the PPC membrane reveal saturation of the membrane ( $\sim 5 \pm 2$  Hz), with increased

concentration of the Tat causing a stiffening of the membrane, whilst more pronounced disruption (loss of membrane and peptide) occurs for the PC:PG bilayer. Although the QCM sensor provides an 'average' large-scale measurement ( $\sim 0.8 \text{ cm}^2$  resolution), the similar response observed in all the harmonics upon exposure of the PCc membrane to the peptides is indicative of trans-membrane insertion. The AFM images support this model, revealing worm-hole pores across the membrane at various depths. The approach curves from the SECM analyses provide extremely valuable information about the permeability of these worm-hole pore structures, through measurement of the ability of a redox mediator to traverse the cross-sectional axis of the membrane bilayer (albeit prior

to membrane disruption for the PC:PG bilayer). Our experimental design provided the ability to probe the same surface with the QCM and SECM measurements (although the QCM was undertaken

at least 30 minutes before the SECM in all cases), thus it is difficult to reconcile the observed effects as micron scale-detection in the case of SECM measurements.

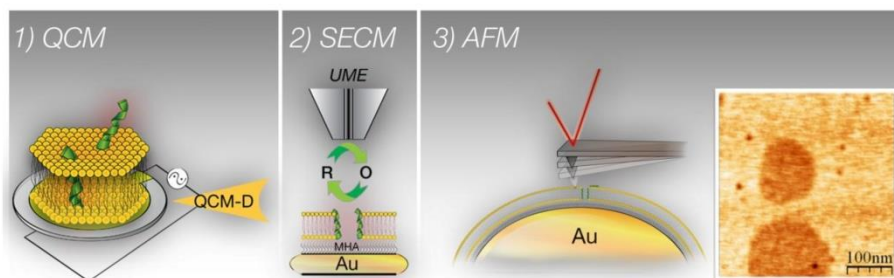


Figure 5. Illustration of the combination of techniques that, in concert, provide evidence for the formation of a worm-hole pore by Tat in a PC membrane layer. The three *scales* of measurement used in this study combine to support a worm-hole mechanism: 1) QCM shows Tat binding in a transmembrane manner (mm resolution), 2) the UME probes membrane permeability with the redox mediator  $[\text{Fe}(\text{CN})_6]^{4/3-}$  (R/O) revealing a greater feedback current due to the pore formation at the  $25\ \mu\text{m}$  (electrode diameter) resolution and 3) AFM reveals *punctures* within the PC membrane due to the addition of Tat peptide, penetrating approximately  $0.5\ \text{nm}$  into the lipid bilayer (nm level resolution).

### Conclusions

The combination of three techniques (QCM, SECM, AFM) providing scales of measurement from millimetre to nanometre reveal a consistent mechanism for the uptake of Tat peptides by mammalian membranes, through the formation of 'worm-hole' pores. Pore formation can occur spontaneously, with membrane saturation occurring at low concentrations ( $\leq\ \mu\text{M}$ ) and only a small number of worm-hole pores existing at any instant, explaining the low hemolytic activity of Tat. Additional data using SECM supported the lytic mechanism towards the bacterial mimetic (PC:PG) membrane, supporting our previous work.<sup>15</sup> Although questions remain unanswered as to the nature of peptide aggregation (stoichiometry) prior to and during translocation these results place us a step closer to fully comprehending the elusive unified mechanism of translocation of the Tat peptide and possibly related arginine-rich peptides. These findings together with structural flexibility<sup>31</sup> considerations determined using cyclic Tat peptides reinforce the development of cell-penetrating peptide-based technologies for future applications. The 'worm-hole' pores formed by the Tat peptide translocation are transmembrane and explain the

ability of the Tat-conjugated cargoes to specifically traverse cellular mammalian membranes. Future applications of the Tat peptide or related cell-penetrating peptides for the intracellular delivery of therapeutics can now be designed with 'tunable' specificity towards membranes with specific composition or characteristics.

### Methods

#### Peptide synthesis

Tat (44–57) and Tat (49–57) with N-terminal acetylation and C-terminal amidation were synthesised with L-amino acids by automated solid phase peptide synthesis on a Rink amide resin.

#### Buffer preparation

Sodium chloride ( $\geq 99.5\%$ ), potassium phosphate monobasic (anhydrous,  $\geq 99.0\%$ ) and potassium phosphate dibasic (anhydrous,  $\geq 98\%$ ) were purchased from Sigma-Aldrich (Castle Hill, Australia). Ultrapure water was used with an initial resistivity of  $18.2\ \text{M}\Omega\text{-cm}$  (Sartorius AG, Göttingen, Germany). Phosphate buffered saline (PBS, pH  $6.9\pm 0.1$ ) was prepared having  $20\ \text{mM}$  phosphate and either  $100\ \text{mM}$  or  $30\ \text{mM}$  sodium chloride (NaCl) in water.

### Liposome preparation

1,2-Dimyristoyl-sn-glycero-3-phosphocholine (DM-PC) and 1,2-dimyristoyl-sn-glycero-3-phospho-rac-(1-glycerol) (sodium salt) (DMPG) were purchased from Avanti Polar Lipids (Alabaster, USA). Cholesterol, chloroform ( $\geq 99.8\%$ ) and methanol ( $\geq 99.9\%$ ) were purchased from Sigma-Aldrich (Castle Hill, Australia). DMPC and cholesterol were dissolved in chloroform whereas DMPG was dissolved in chloroform/methanol (ca. 3:1) to create individual 5 mM stock solutions. These solutions were then aliquoted into test tubes to obtain the desired lipid composition (DMPC:cholesterol 7:3 v/v, and DMPC:DMPG 2:1 v/v). Afterward, the solvent was evaporated under a gentle stream of nitrogen gas and the test tubes were then dried under vacuum. To prepare the liposomes, the lipids were re-suspended in PBS (NaCl 100 mM) to a lipid concentration of 0.5 mM and then incubated at 37 °C, vortexed and sonicated for less than 10 minutes in a bath sonicator before use. Mechler et al. have demonstrated that the liposomes, obtained with this protocol, are unilamellar and have a bimodal size distribution, with the radii of the two populations on average ca. 50 and 300 nm.

### Modification of QCM-D sensor chips

Absolute ethanol ( $\geq 99.7\%$ ), propan-2-ol ( $\geq 99.0\%$ ) and hydrogen peroxide (30%) were purchased from Merck (Kilsyth, Australia). Ammonium hydroxide solution (28%) was obtained from Ajax Finechem (Seven Hills, Australia). 6-Mercaptohexanoic acid (MHA, 90%) was purchased from Sigma-Aldrich (Castle Hill, Australia). The QCM-D sensor crystals used were polished, gold-coated, AT-cut quartz chips with a fundamental frequency of ca. 5 MHz (Q-Sense, Västra Frölunda, Sweden). At least 24 hours before an experiment, the chips were cleaned in a solution of ammonium hydroxide: hydrogen peroxide: ultrapure water (1:1:3 v/v) for 20–25 min at ca. 70 °C. The chips were then rinsed thoroughly with ultrapure water. Surface modification with MHA was conducted by immersing a freshly cleaned chip into a 1 mM solution of MHA in propan-2-ol for at least 24 h. This creates a self-assembled monolayer of uniform negative charge on the chip surface. Excess MHA was removed by rinsing with propan-2-ol. The chips were then dried under a gentle stream of nitrogen gas and assembled into the QCM-D chambers ready for use.

### QCM-D experiments

QCM-D measurements were performed using a Q-SENSE E4 system with flow cells (Q-SENSE,

Västra Frölunda, Sweden). The QCM-D instrument measures the relative changes to the resonance frequency ( $f$ ) and energy dissipation ( $D$ ) of a sensor chip. The natural frequency of this gold-coated chip is a function of the overall mass in the oscillating system, which consists of the mass of the sensor chip as well as the mass of the material deposited on the surface. During the experiment, the difference in resonance frequency ( $\Delta f$ ) and energy dissipation ( $\Delta D$ ) were measured simultaneously at four odd overtones of the natural frequency (3<sup>rd</sup> overtone at 15 MHz, 5<sup>th</sup> overtone at 25 MHz, 7<sup>th</sup> overtone at 35 MHz, and 9<sup>th</sup> overtone at 45 MHz). The fundamental resonance frequency has not been considered because of its high sensitivity to the bulk solution changes. All experiments were conducted at a temperature of  $19.10 \pm 0.05$  °C and repeated at least three times.

In a typical experiment, firstly, supported membranes were created on a chip surface modified with a MHA monolayer through a slow flush of liposome solution in the QCM chambers at a 50  $\mu\text{L}/\text{min}$  flow rate. The liposomes adsorb onto the MHA-monolayer, deform, rupture and fuse together to form a lipid bilayer.<sup>38</sup> The flow was then stopped, and then PBS solution (100 mM NaCl) was flushed in the cell at a 300  $\mu\text{L}/\text{min}$  to eliminate any weakly attached liposomes. In addition, a flow with PBS buffer (30 mM NaCl), at the same speed, was adopted to help any burst of embedded liposomes. This second washing step was introduced to ensure the formation of a homogeneous membrane and works by creating an osmotic pressure difference between the interior of the embedded liposomes (having a high salt concentration) and the low-salt exterior environment, which causes the liposomes to swell and then rupture. Once a stable lipid membrane was obtained, the next step was flushing 1 mL of peptide solution (1 and 10  $\mu\text{M}$  in PBS) in the cell at a 50  $\mu\text{L}/\text{min}$  flow rate. After the flow was stopped, the system was left for a minimum of 30 minutes to equilibrate, before rinsing with PBS buffer at 200  $\mu\text{L}/\text{min}$ . After the flow was stopped, the peptide was left to incubate with the lipid membrane for 30 min and then the chamber was rinsed with high-salt PBS. Data were recorded as frequency change corresponding to a change in mass of the sensor chips. The value of this mass was calculated by using the Sauerbrey equation:<sup>47</sup>

$$\Delta m = -(Afn)C$$

where  $C$  ( $17.7 \text{ ng}\cdot\text{cm}^{-2}\cdot\text{Hz}^{-1}$  at 5 MHz) is the mass sensitivity constant, and  $n$  (1, 2, 3...) is the overtone number. Cho and co-workers have demonstrated

that the Sauerbrey equation efficiently models lipid bilayers in aqueous buffer.<sup>48</sup> Furthermore, the structural changes of the deposited layers were revealed by measuring the ratio of energy loss to energy stored (dissipation, *D*) into the surface bound material.<sup>49-51</sup>

The raw data resulting from every experiment has been processed using QTools (Q-SENSE), and then exported for advanced analysis in OriginPro 8 (OriginLab Corp., Northampton, MA, USA) software.

#### SECM experiments

The current feedback experiments were carried out at unbiased substrate in 1 mM  $K_4[Fe(CN)_6]$  in PBS, as a mediator, using a 25  $\mu\text{m}$  Pt ultramicroelectrode (UME), Ag/AgCl and a Pt wire as working, reference and counter electrodes, respectively. Prior to measurements, the QCM sensor was pre-modified through treatment with 6-mercaptopentanoic acid (MHA) solution overnight, then washed with iso-propanol to eliminate loosely-bound and excess MHA from the surface, and dried under a gentle stream of nitrogen. MHA was chosen as its chain length is sufficient to form an insulating self assembled monolayer (SAM) on the sensor's gold surface. In order to ensure the formation of the MHA layer on the gold, the sensor was then placed in the mediator solution, followed by probing the conductivity of three different spots on the sensor by biasing the UME at 0.4 V and approaching the surface at 1  $\mu\text{m/s}$ . The QCM sensor was taken out of the mediator solution after measurements and rinsed with PBS buffer several times. This was followed by adding the lipid suspension onto the MHA-modified sensor and leaving to incubate for 30 minutes in order to form a supported lipid bilayer (SLB) on the MHA. The QCM sensor was then placed back into the mediator solution and the conductivity was probed as previously explained. Subsequently, 1 and 10  $\mu\text{M}$  Tat-treated membrane samples were probed in similar manner, although with an incubation time of 10 minutes.

#### AFM

The substrate for AFM measurements was a gold bead prepared by melting the end of a gold wire (diameter 1.2 mm, purity 99.99%, Goodfellow, UK) in a hydrogen-oxygen flame.<sup>52-53</sup> Several small Au(111) facets (approximately 0.5-1.0  $\mu\text{m}$  long) would appear on the well-prepared gold bead surface and could be observed with the unaided eye. These small facets were of atomic flatness and served as the AFM substrate.

The gold bead that contained crystalline facets was freshly prepared and this bead was immediately plunged into an ethanolic solution of MHA to form a self-assembled monolayer. The membrane coating was achieved by immersion in a suspension of DMPC:cholesterol hydrated with buffer (prepared as described for the QCM-D measurements). Following rinsing with buffer and water, the bead was dried under a stream of nitrogen gas, to remove the macroscopic water, but not to complete dryness. The resulting membrane patches were identified on the crystalline 'triangular' features on the Au(111) facets of the bead. Cholesterol-rich regions were evident within the membrane structure. No particular specificity was observed for the Tat peptide towards cholesterol-rich or -poor domains.

#### ASSOCIATED CONTENT

##### Supporting Information

QCM-D data for 10  $\mu\text{M}$  Tat (44-57), data analysis for shorter Tat (49-57) peptide, scanning electrochemical microscopy graphs for Tat (44-57), additional AFM measurements as well as Computational analysis for Tat (44-57). This material is available free of charge via the Internet at <http://pubs.acs.org>.

#### AUTHOR INFORMATION

##### Corresponding Authors

\*Lisa.Martin@monash.edu and

\*Anthony.OMullane@rmit.edu.au.

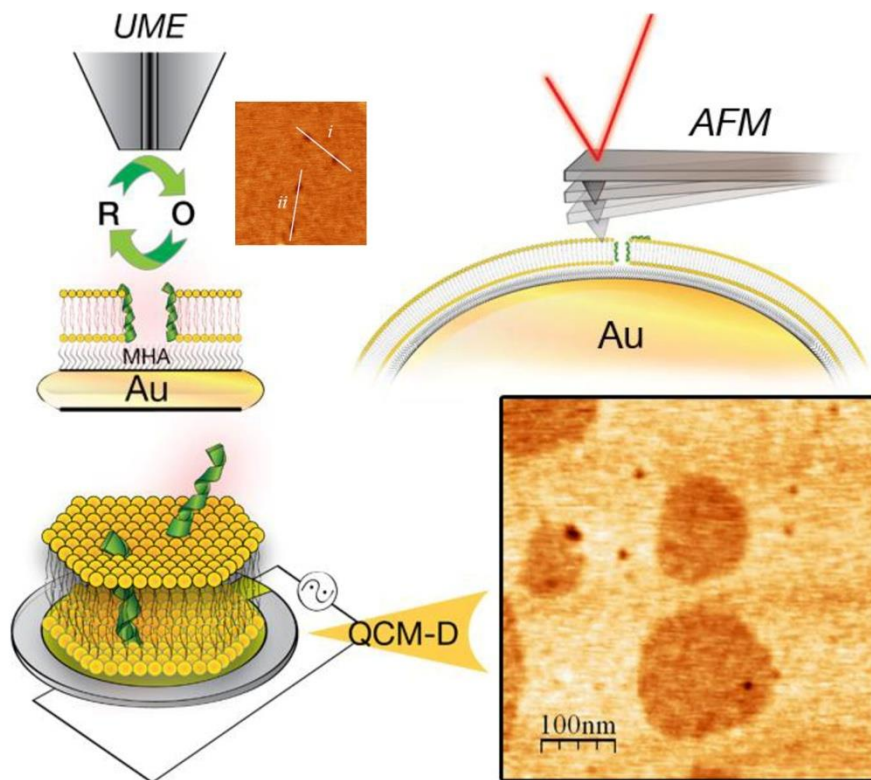
#### REFERENCES

- (1) Frankel, A. D.; Pabo, C. O. *Cell* **1988**, *55*, 1189.
- (2) Green, M.; Loewenstein, P. *Cell* **1988**, *55*, 1179.
- (3) Fawell, S.; Seery, J.; Daikh, Y.; Moore, C.; Chen, L.; Pepinsky, B.; Barsoum, J. *Proc. Natl. Acad. Sci. USA* **1994**, *91*, 664.
- (4) Foged, C.; Nielsen, H. M. *Expert Opin. Drug Deliv.* **2008**, *5*, 105.
- (5) Schwarze, S. R.; Ho, A.; Vocero-Akbani, A.; Dowdy, S. F. *Science* **1999**, *285*, 1569.
- (6) Jones, A. T.; Sayers, E. J. *Journal of Controlled Release* **2012**, *161*, 582.
- (7) Fischer, R.; Fotin-Mleczek, M.; Hufnagel, H.; Brock, R. *ChemBioChem* **2005**, *6*, 2126.
- (8) Vivès, E.; Brodin, P.; Lebleu, B. *Journal of Biological Chemistry* **1997**, *272*, 16010.
- (9) Vivès, E.; Granier, C.; Prevot, P.; Lebleu, B. *Letters in Peptide Science* **1997**, *4*, 429.
- (10) Boohaker, R. J.; Lee, M. W.; Vishnubhotla, P.; Perez, J. M.; Khaled, A. R. *Curr Med Chem* **2012**, *19*, 3794.
- (11) Tanaka, G.; Nakase, I.; Fukuda, Y.; Masuda, R.; Oishi, S.; Shimura, K.; Kawaguchi, Y.; Takatani-Nakase, T.; Langel, Ü.; Gräslund, A.; Okawa, K.; Matsuoka, M.; Fujii,

- N.; Hatanaka, Y.; Futaki, S. *Chemistry & biology* **2012**, *19*, 1437.
- (12) Czihal, P.; Knappe, D.; Fritsche, S.; Zahn, M.; Berthold, N.; Piantavigna, S.; MÄVÄller, U.; Van Dorpe, S.; Herth, N.; Binas, A.; KÄHler, G.; De Spiegeleer, B.; Martin, L. L.; Nolte, O.; StrÄtter, N.; Alber, G.; Hoffmann, R. *ACS Chemical Biology* **2012**, *7*, 1281.
- (13) Knappe, D.; Piantavigna, S.; Hansen, A.; Mechler, A.; Binas, A.; Nolte, O.; Martin, L. L.; Hoffmann, R. *Journal of Medicinal Chemistry* **2010**, *53*, 5240.
- (14) Piantavigna, S.; Czihal, P.; Mechler, A.; Richter, M.; Hoffmann, R.; Martin, L. L. *International Journal of Peptide Research and Therapeutics* **2009**, *15*, 139.
- (15) Piantavigna, S.; McCubbin, G. A.; Boehnke, S.; Graham, B.; Spiccia, L.; Martin, L. L. *Biochim. Biophys. Acta* **2011**.
- (16) Shai, Y. *Biopolymers* **2002**, *66*, 236.
- (17) SÄalik, P.; Niinep, A.; Pae, J.; Hansen, M.; Lubenets, D.; Langel, Ä.; Pooga, M. *Journal of Controlled Release* **2012**, *153*, 117.
- (18) Shai, Y. *Biopolymers* **2002**, *66*, 236.
- (19) Green, I.; Christison, R.; Voyce, C. J.; Bundell, K. R.; Lindsay, M. A. *TRENDS in Pharmacological Sciences* **2003**, *24*, 213.
- (20) Patel, L. N.; Zaro, J. L.; Shen, W.-C. *Pharmaceutical Research* **2007**, *24*, 1977.
- (21) Richard, J. P.; Melikov, K.; Vives, E.; Ramos, C.; Verbeure, B.; Gait, M. J.; Chernomordik, L. V.; Lebleu, B. *Journal of Biological Chemistry* **2003**, *278*, 585.
- (22) Trabulo, S.; Cardoso, A. L.; Mano, M.; de Lima, M. C. P. *Pharmaceuticals* **2010**, *3*, 961.
- (23) Schmidt, N.; Mishra, A.; Lai, G. H.; Wong, G. C. L. *FEBS Letters* **2010**, *584*, 1806.
- (24) Ter-Avetisyan, G.; Tünnemann, G.; Nowak, D.; Nitschke, M.; Herrmann, A.; Drab, M.; Cardoso, M. C. *Journal of Biological Chemistry* **2009**, *284*, 3370.
- (25) Thorén, P. E. G.; Persson, D.; Isakson, P.; Goksör, M.; Önfelt, A.; Nordén, B. *Biochemical and Biophysical Research Communications* **2003**, *307*, 100.
- (26) Tünnemann, G.; Martin, R. M.; Haupt, S.; Patsch, C.; Edenhofer, F.; Cardoso, M. C. *FASEB Journal* **2006**, *20*, 1775.
- (27) Choi, D.; Moon, J. H.; Kim, H.; Sung, B. J.; Kim, M. W.; Tae, G. Y.; Satija, S. K.; Akgun, B.; Yu, C. J.; Lee, H. W.; Lee, D. R.; Henderson, J. M.; Kwong, J. W.; Lam, K. L.; Lee, K. Y. C.; Shin, K. *Soft Matter* **2012**, *8*, 8294.
- (28) Ciobanasu, C.; Harms, E.; Tünnemann, G.; Cardoso, M. C.; Kubitscheck, U. *Biochemistry* **2009**, *48*, 4728.
- (29) Ciobanasu, C.; Siebrasse, J. P.; Kubitscheck, U. *Biophysical Journal* **2010**, *99*, 153.
- (30) Herce, H. D.; Garcia, A. E. *PNAS* **2007**, *104*, 20805.
- (31) Lättig-Tünnemann, G.; Prinz, M.; Hoffmann, D.; Behlke, J.; Palm-apergi, C.; Morano, I.; Herce, H. D.; Cardoso, M. C. *Nature Communications* **2011**, *2*, 453.
- (32) Sauerbrey, G. *Zeitschrift für Physik* **1959**, *155*, 206.
- (33) Rodahl, M.; Höök, F.; Krozer, A.; Brzezinski, P.; Kasemo, B. *Review of Scientific Instruments* **1995**, *66*, 3924.
- (34) McCubbin, G. A.; Praporski, S.; Piantavigna, S.; Knappe, D.; Hoffmann, R.; Bowie, J. H.; Separovic, F.; Martin, L. L. *European Biophysics Journal* **2010**.
- (35) Mechler, A.; Praporski, S.; Atmuri, K.; Boland, M.; Separovic, F.; Martin, L. L. *Biophysical Journal* **2007**, *93*, 3907.
- (36) Rodahl, M.; Kasemo, B. *Sensors and Actuators A: Physical* **1996**, *54*, 448.
- (37) Keller, C. A.; Kasemo, B. *Biophysical Journal* **1998**, *75*, 1397.
- (38) Mechler, A.; Praporski, S.; Piantavigna, S.; Heaton, S. M.; Hall, K. N.; Aguilar, M.-I.; Martin, L. L. *Biomaterials* **2009**, *30*, 682.
- (39) Bard, A. J.; Mirkin, M. V. *Scanning Electrochemical Microscopy*; Marcel Dekker: New York, **2001**.
- (40) Sun, P.; Laforge, F. O.; Mirkin, M. V. *Phys. Chem. Chem. Phys.* **2007**, *9*, 802.
- (41) Koley, D.; Bard, A. J. *Proceedings of the National Academy of Sciences* **2010**, *107*, 16783.
- (42) Boldt, F.-M.; Baltes, N.; Borgwarth, K.; Heinze, J. *Surface Science* **2005**, *597*, 51.
- (43) Kiani, A.; Alpuche-Aviles, M. A.; Eggers, P. K.; Jones, M.; Gooding, J. J.; Paddon-Row, M. N.; Bard, A. J. *Langmuir* **2008**, *24*, 2841.
- (44) Tsionsky, M.; Zhou, J.; Amemiya, S.; Fan, F.-R. F.; Bard, A. J. *Anal. Chem.* **1999**, *71*, 4300.
- (45) Shaw, J. E.; Epand, R. F.; Hsu, J. C. Y.; Mo, G. C. H.; Epand, R. M.; Yip, C. M. *Journal of Structural Biology* **2008**, *162*, 121.
- (46) Pearson, R. H.; Pascher, I. *Nature* **1979**, *281*, 499.
- (47) Sauerbrey, G. *Zeitschrift für Physik* **1959**, *155*, 206.
- (48) Cho, N. J.; Kanazawa, K. K.; Glenn, J. S.; Frank, C. W. *Analytical Chemistry* **2007**, *79*, 7027.
- (49) Hook, F.; Rodahl, M.; Brzezinski, P.; Kasemo, B. *Langmuir* **1998**, *14*, 729.
- (50) Hook, F.; Rodahl, M.; Kasemo, B.; Brzezinski, P. *Proceedings of the National Academy of Sciences of the United States of America* **1998**, *95*, 12271.
- (51) McCubbin, G. A.; Praporski, S.; Piantavigna, S.; Knappe, D.; Hoffmann, R.; Bowie, J. H.; Separovic, F.; Martin, L. L. *European Biophysics Journal* **2011**, *40*, 437.
- (52) Clavilier, J.; Armand, D.; Wu, B. L. *Journal of Electroanalytical Chemistry and Interfacial Electrochemistry* **1982**, *135*, 159.
- (53) Qu, X.; Bond, A. M.; Martin, L. L. *Electroanalysis* **2009**, *21*, 681.

---

Insert Table of Contents artwork here



## Membrane perforation and passive translocation of Tat peptides

Stefania Piantavigna,<sup>1</sup> Muhammad E. Abdelhamid,<sup>2</sup> Chuan Zhao,<sup>1,3</sup> Xiaohu Qu,<sup>1,4</sup> George A. McCubbin,<sup>1</sup> Bim Graham,<sup>5</sup> Leone Spiccia,<sup>1</sup> Anthony P. O'Mullane<sup>2\*</sup> and Lisandra L. Martin<sup>1\*</sup>

<sup>1</sup> School of Chemistry, Monash University, Clayton, VIC 3800, Australia

<sup>2</sup> School of Applied Sciences, GPO Box 2476V, RMIT University, Melbourne VIC 3001, Australia

<sup>3</sup> Current address: School of Chemistry, The University of New South Wales, Sydney, NSW 2052, Australia

<sup>4</sup> Current address: Ionode Pty Ltd, 8/148 Tennyson Memorial Avenue, Tennyson, Queensland, 4105, Australia

<sup>5</sup> Monash Institute of Pharmaceutical Sciences, Monash University, Parkville, VIC 3052 Australia

### SUPPORTING INFORMATION

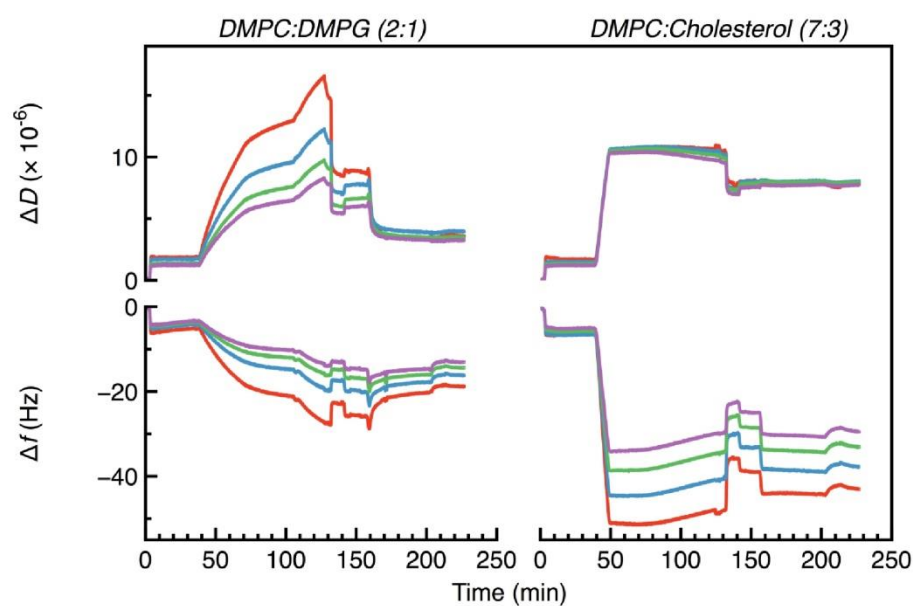


Fig. S1. QCM-D data for 10  $\mu\text{M}$  Tat (44-57) on DMPC:DMPG (2:1) and DMPC:cholesterol (7:3). Upper panels show the change in dissipation ( $\Delta D$ ) and lower panels the change in frequency ( $\Delta f$ ) over time. For DMPC:DMPG (2:1), at time = 155 mins, the Tat rapidly inserts into the membrane (decrease in  $\Delta f$ ) followed by removal of the membrane (and peptide) material. Following a wash with PBS buffer (at ~205 mins) remnants of the membrane layer remains. However at the DMPC:cholesterol membrane the Tat binds and resides in the lipid layer.

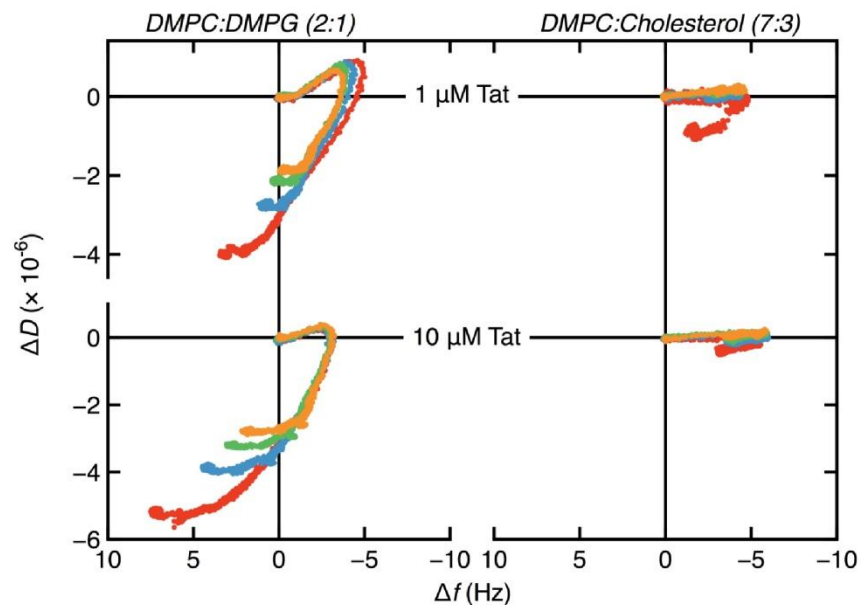


Fig. S2. Analysis of the QCM-D data for 1.0 and 10  $\mu\text{M}$  Tat (49-57) on DMPC:DMPG (2:1) and DMPC:cholesterol (7:3).  $\alpha$  QCM sensor harmonics shown are the 3<sup>rd</sup> (red), 5<sup>th</sup> (blue), 7<sup>th</sup> (green) and 9<sup>th</sup> (orange).

The  $\Delta D$  vs.  $\Delta f$  profiles examining the effects on the sensor harmonics<sup>a</sup> as the Tat (44-49) peptide interacts with either bacterial (DMPC:DMPG) or eukaryotic (DMPC:cholesterol) mimetic membranes. In each case, the peptide inserts trans-membrane discerned by all the harmonics overlapping; each harmonic probes the membrane depth,  $\propto 1/\text{frequency}$ . No significant difference is observed between the two concentrations studied. However, on DMPC:DMPG (2:1) membrane a dramatic effect of Tat peptide was observed, with a large mass loss ( $\Delta f$  increases) and simultaneously, a dramatic decrease in the viscoelasticity ( $\Delta D$  decreases). This is consistent with membrane disruption.

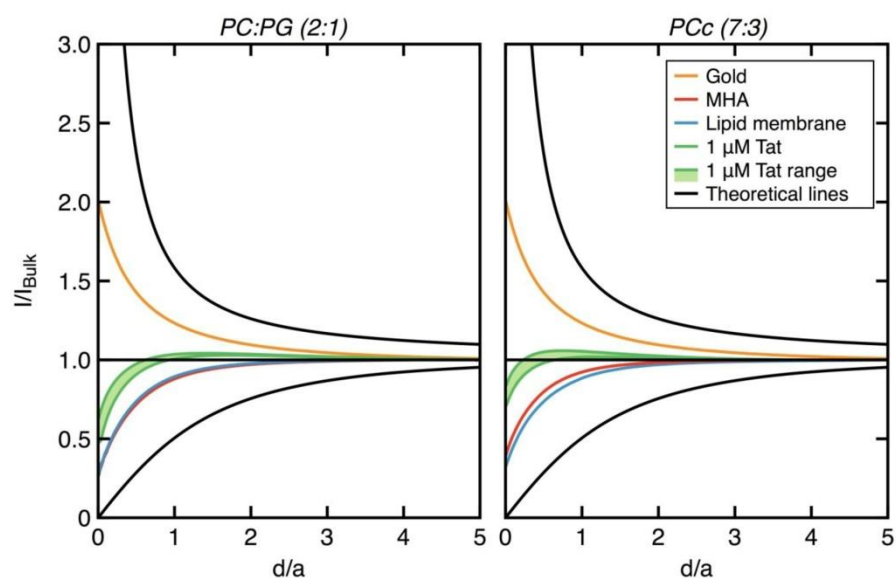


Fig. S3. SECM for the shorter Tat (49-57) reveals similar data to the longer Tat (44-57) peptide at 1  $\mu\text{M}$ .

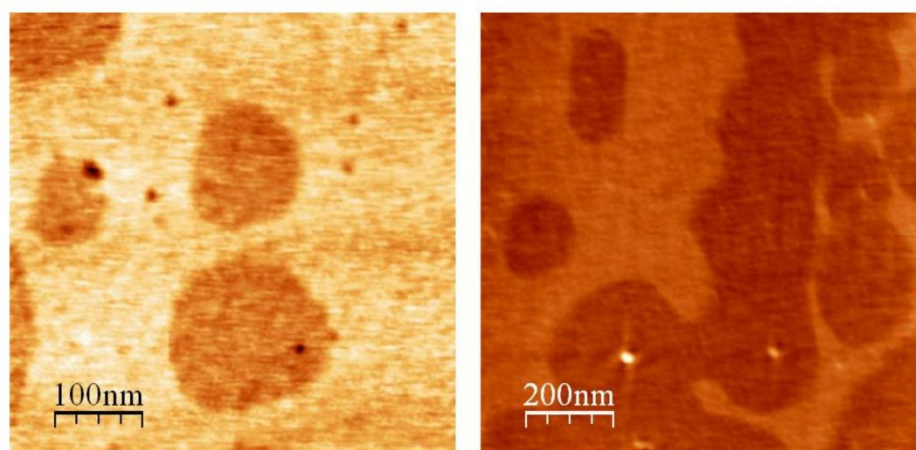


Fig. S4. AFM height images of the MHA-modified gold bead with a DMPC:cholesterol bilayer: a) 20 min after addition of 10  $\mu\text{M}$  Tat (44-57); and b) before addition. Note: a) and b) correspond to different areas on the bead surface. Images were acquired in air and at room temperature. Vertical scales are as follows: a) 0-1.49 nm and b) 0-4.55 nm. In both images the hole (larger pore-like feature) was made by punching the AFM tip through the membrane to check that a lipid bilayer was present (A at  $\sim$  10 o'clock and B at  $\sim$  6 o'clock using a clock analogy). Images were processed using WSxM.

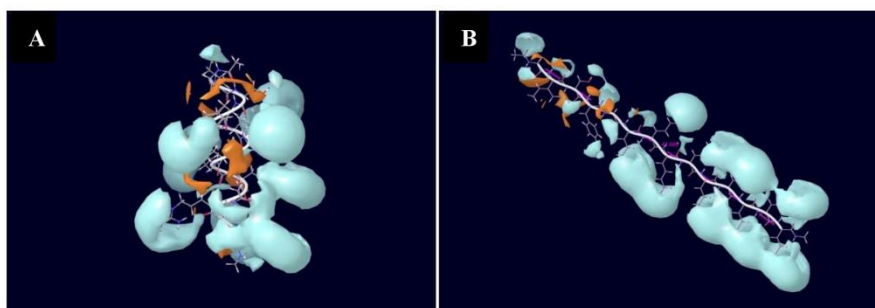


Fig. S5. Computational analysis for Tat (44-57) in terms of estimation of peptide dimension based on  $\alpha$ -helical secondary structure obtained using Maestro 9.3. (A) represents an energy minimised  $\alpha$ -helical representation with estimated length of 2.1 nm and (B) shows the extended peptide structure generating an estimated length of 4.8 nm. The hydrophilic surface is shown in light blue and the hydrophobic regions in brown.



# *Ruthenocenoyl moiety incorporated in short tryptophan and arginine rich peptides*

## 1 Introduction

Synthetic antimicrobial peptides (synAMPs) are *de novo* peptides that are promising weapons for possible therapeutic treatments<sup>1</sup>. SynAMPs comprise short antimicrobial peptides enriched in arginine (Arg) and tryptophan (Trp) residues. These synAMPs are amongst the smallest peptides that still have significant antibacterial activity<sup>2</sup>. In particular, the short peptides (RW)<sub>3</sub> (see Fig. 41A) and the metallocene RcCO-W(RW)<sub>2</sub> (Fig. 41B), where RcCO is for ruthenocenoyl, are two synAMPs reported by the Metzler-Nolte laboratory and tested for antimicrobial activity<sup>2,3</sup>. When tested against some Gram-positive and Gram-negative bacteria strains, these peptides showed MIC values of 1-11  $\mu\text{M}$  for (RW)<sub>3</sub> and 2-6  $\mu\text{M}$  for RcCO-W(RW)<sub>2</sub> but no haemolytic activity<sup>2</sup>. The Metzler-Nolte laboratory reported bacterial killing experiments, which determine if the compound in question has bacteriostatic or bactericidal activity, and growth kinetics experiments, which were undertaken to determine the bacteriolytic activity of these two peptides towards the bacterial membrane. Consequently, in this work the mechanistic details regarding the interaction of these two peptides with SLBs have been investigated using QCM. The outcomes will be presented and discussed in the following section.

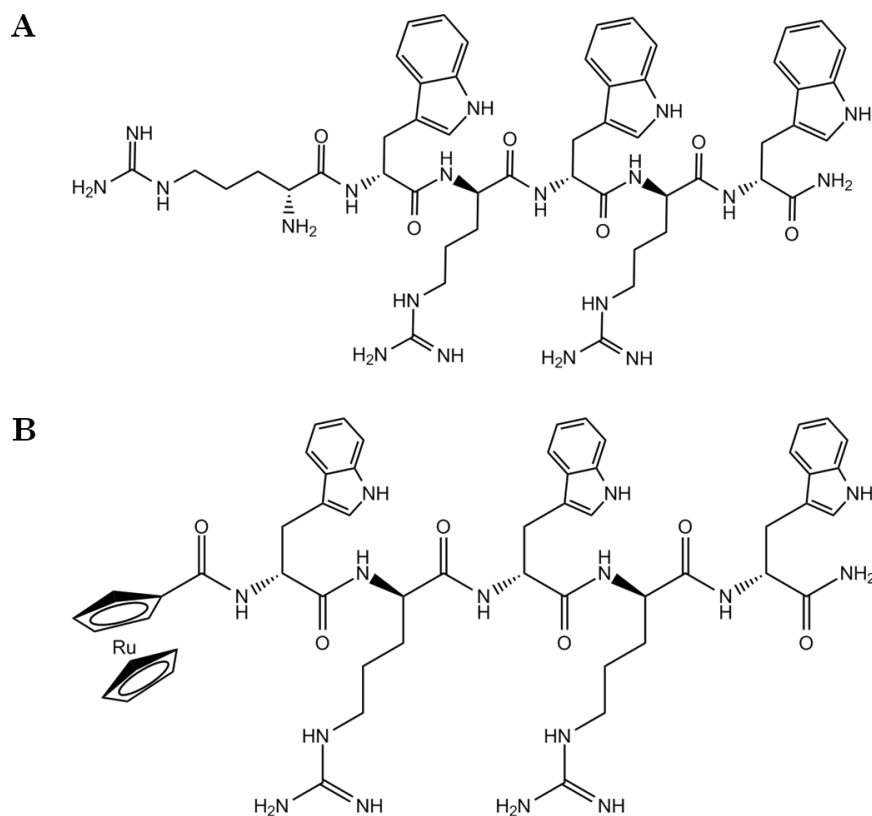


**Fig. 41:** The linear structures of the two short synAMPs: (A)  $(RW)_3$  and (B)  $RcCO-W(RW)_2$ .

## 1.1 The benefits and disadvantages of synAMPs

SynAMPs represent an interesting new class of AMPs. Firstly, because they are designed to have a cost-effective synthesis, to be unaffected by fast enzymatic degradation and to be effective with the lowest toxicity possible<sup>1,2</sup>. Furthermore, interesting and innovative molecular species can be introduced in the synthesis of *de novo* peptides such conjugates of metallocenes<sup>3,4</sup> or organometallic derivatives of platensimycin (a metabolite of *Streptomyces platensis*, which has antimicrobial activity)<sup>2,4,5</sup>. Moreover, synAMPs with short sequences and with relatively simple amino acid composition are easy to make and modify according their activity profile. Thus, these peptides are suitable for a range of therapeutic applications, although to date the mode of action has not been defined or compared with more “traditional” AMPs, such as, magainin, melittin and temporin<sup>6</sup>.

## 1.2 The influence of Tryptophan

Incorporation of Trp residues into peptide sequences has been employed as a probe in fluorescence spectroscopy for the determination of peptide-binding affinities or the penetration depth of peptides such melittin<sup>7</sup> in model membranes<sup>8</sup>.

Trp has been shown to have an important influence on the peptide activity. For instance, the single Trp residue in melittin is crucial for its haemolytic activity<sup>7,9</sup>. Trp is present in quite high proportions in natural AMPs and CPPs, as are Arg residues<sup>10</sup>. Furthermore, the location of Trp in many CPPs is interesting, with one or more Trp residues often found at one end of a helix<sup>11</sup>.

Synthetic oligoarginine peptides, containing repeating units of six to nine Arg residues, are well known<sup>11-13</sup>. These highly positively charged peptides are considered CPPs since they have been shown to be internalized by various cells without damaging the plasma membrane<sup>14-17</sup>. The translocation of these peptides was shown to be influenced by addition of a Trp residue<sup>11</sup>. For example, the inclusion of Trp at the C-terminal end of a hepta-arginine peptide (R<sub>7</sub>W) gives a peptide with a higher cellular uptake and a lower toxicity than R<sub>7</sub> alone<sup>14</sup>. Another example of the influence of a single Trp residue is the hexa-arginine peptide R<sub>6</sub>, interacting with GUVs. The addition of tryptophan slows down the translocation of this peptide, leaving the vesicles intact<sup>18</sup>.

### 1.2.1 Location in the membrane

Trp is a hydrophobic amino acid having an indole ring sidechain. This aromatic region is responsible for the positioning of Trp close to the head-groups of lipid molecules in the membrane. This preference for being located at the interfacial region of the bilayer makes Trp an anchor motif that affects the partitioning of peptides and trans-membrane proteins into the bilayer<sup>10,19</sup>.

Investigations by NMR and neutron diffraction show that Trp does not penetrate into the hydrocarbon core of the lipid bilayer, but it is located at the membrane-water interface<sup>19</sup>. Thus Trp experiences hydrophobic forces, which tend to expel the Trp residue from the aqueous phase, complex electrostatic interactions, which favour the location of Trp among the polar headgroups of

the bilayer, and cohesive repulsions due to the hydrocarbon core<sup>19</sup>. The latter interactions (cohesive repulsion) arise from deeper insertion of the bulky “paddle-like” indole sidechain in the bilayer, which disrupts the highly favourable and cohesive hydrophobic interactions between the lipid acyl chains<sup>10</sup>. In addition to these interactions, computer simulations of pentapeptides WLRL and WLKLL, show that the Trp residues, when inserted into the membrane, associate with the positively charged choline head-groups, thus forming hydrogen bonds with both the ester carbonyl of the lipid molecules and with water molecules<sup>20</sup>. To conclude, Trp offers a complex range of interactions with lipid bilayers, whether neutral (DMPC), cholesterol-rich (DMPC/chol) or negatively charged (DMPC/DMPG). It has also been suggested that Trp might form a stable complex with the rigid ring system of the cholesterol molecule<sup>7</sup>.

#### 1.2.1.1 *The cation- $\pi$ interactions*

Trp is considered to be a hydrophobic amino acid because the indole ring does not carry a charge. However, a quadrupole moment can arise across the  $\pi$ -electron system of the aromatic indole ring. This quadrupole moment can be envisioned as two dipole moments extending perpendicularly out of either surface of the ring plane (see Fig. 42A). Specifically the positively charged tails of each dipole reside close to the plane of the ring, while the negative charges constitute the ends of the dumbbell type shape that is formed. Thus, the  $\pi$ -electron system of Trp results in negatively charged clouds that can establish electrostatic interactions with various cationic species, such as ions and the sidechains of positively charged amino acids<sup>10</sup>. These interactions are named cation- $\pi$  interactions<sup>21</sup> and, in some proteins, are involved in biological processes such as catalysis, substrate binding and ion channel activity<sup>22</sup>.

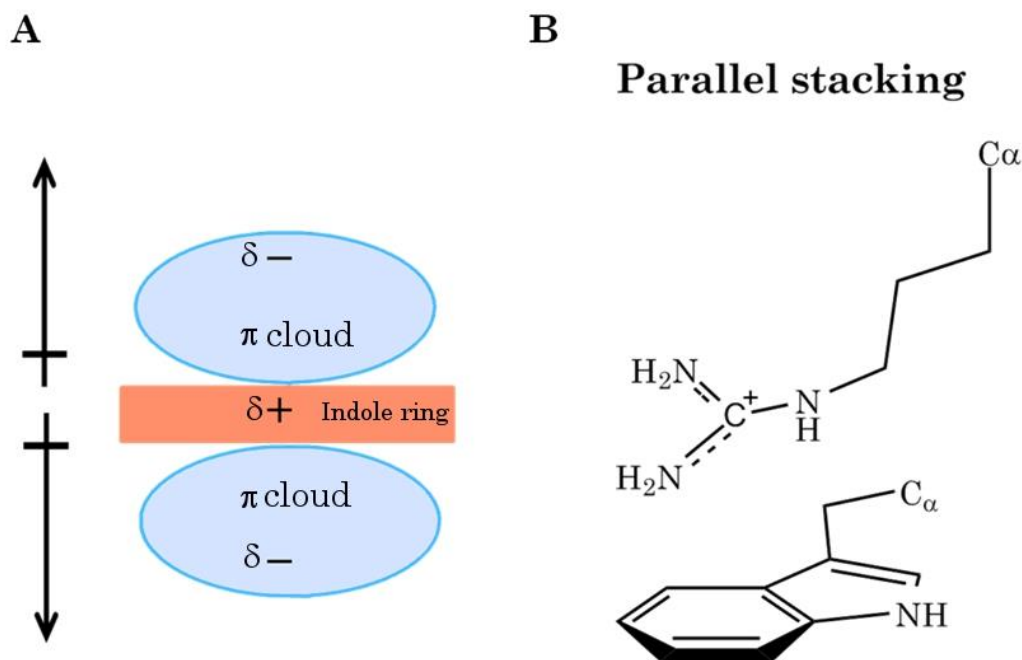


**Fig. 42:** (A) A representation of the  $\pi$ -electron clouds above and below the aromatic indole sidechain. The arrows on the left indicate dipole moments. (B) The parallel cation- $\pi$  interaction between an Arg and a Trp sidechain. Both figures have been modified from Chan et al.<sup>10</sup>

Cation- $\pi$  interactions have been demonstrated to occur and to be quite strong when involving cationic amino acid side chains (Arg, Lys, or protonated His)<sup>22</sup>. The peptides presented in this chapter consist of Trp intercalated with Arg residues. The proximity of the side chains of these two amino acids allows for cation- $\pi$  interactions that can take place in either a parallel (i.e. stacked) or orthogonal, T-shaped orientation<sup>22</sup>. The parallel arrangement between Arg and Trp residues is preferred (see Fig. 42), since it is energetically favourable in aqueous solution, allowing Arg to form almost as many hydrogen bonds with water molecules as when it is not involved in interactions with Trp sidechains. Furthermore, these cation- $\pi$  interactions shelter the Arg residue from the hydrophobic core of the bilayer, thus making the entry of Arg into the bilayer more energetically favourable<sup>10,21</sup>.

### 1.2.2 Examples of Trp-Arg containing AMPs

As previously mentioned, Trp and Arg residues are present in high proportion in the sequences of many AMPs and CPPs<sup>10</sup>. This mutual presence allows for a more effective antimicrobial action, since the cationic charges and

hydrogen bonds from Arg enhance the interaction with negatively charged species on the bacterial membrane surface (eg. LPS, teichoic acid and negatively charged phospholipids), while the nature of Trp enables the peptide to maintain a prolonged association with the membrane<sup>10</sup>.

#### *1.2.2.1 Indolicidin*

The first and most representative Trp-rich AMP to be identified was Indolicidin (Table 6)<sup>10</sup>. This peptide was found in the cytoplasmic granules of bovine neutrophils and it is a member of the cathelicidin family of AMPs<sup>10,23</sup>. Indolicidin is 13 residues long, with a C-terminal amide. It contains the highest proportion of Trp residues ever found (39%). This peptide has a broad activity towards both Gram-positive and Gram-negative bacteria, as well as fungi and protozoa, and has also been shown to be haemolytic<sup>10,23</sup>.

NMR studies show that indolicidin adopts an extended structure when bound to zwitterionic dodecylphosphocholine (DPC) and anionic sodium dodecyl sulfate (SDS) micelles<sup>24</sup>. This structure has a “wedge-type” shape since the tryptophan and proline residues forming a hydrophobic core, flanked by the positively charged arginine and lysine residues localized at the ends of the structure (see Fig. 43)<sup>10</sup>. It has been suggested that indolicidin, when inserted into the DPC membrane, interacts with the interfacial layer of the bilayer through the hydrophobic core and with the lipid head-groups through the positively charged regions. Traditionally, indolicidin is considered a pore forming peptide<sup>23,24</sup>. However, how this AMP permeabilises the membrane is still not clear. Recent investigations suggest it acts as organic anion carrier in the presence of zwitterionic membrane<sup>23</sup> and translocate into the cytosol and subsequently binds to DNA<sup>10</sup>.

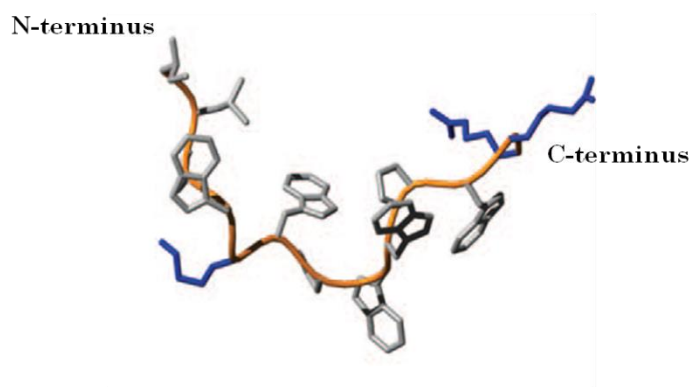


**Fig. 43:** NMR structure determined in solution of indolicidin (PDB ID: 1G89) when bound to dodecylphosphocholine (DPC) micelles<sup>24</sup>. Positively charged side chains are coloured in blue and remaining side chains in grey. Figure modified from Nguyen et al.<sup>25</sup>

#### 1.2.2.2 *Tritrpticin*

Tritrpticin (see Table 6) is a 13 amino acid peptide. It is also a member of the cathelicidin family and it is characterized by having four Arg residues and three consecutive Trp residues, which forms a tryptophan motif in the centre of the peptide. In the presence of SDS micelles, this peptide adopts an amphipathic conformation resembling a “wedge-type” shape, as observed for indolicidin, with the Trp residues clustered together and inserted in the hydrophobic core of the micelle<sup>26</sup>.

Tritrpticin induces membrane leakage to various degrees in different types of model membranes<sup>26</sup>. It has a higher lytic effect towards membranes containing negatively charged lipids. It has been suggested that this membrane lysis is caused by the formation of toroidal pores at sufficiently high concentrations of tritrpticin, in accordance with the Shai-Matsuzaki-Huang model (cf Chapter 3). These toroidal pores result from a large hydrophobic cluster formed by the three Trp residues during the membrane insertion by tritrpticin<sup>26</sup>.

#### 1.2.2.3 *Synthetic Combi-1 and Combi-2*

Combi-1 and combi-2 (see Table 6) are *de novo* hexapeptides derived from the screening of synthetic combinatorial libraries<sup>10</sup>. They are unstructured in solution, but adopt ordered structures when in contact with zwitterionic DPC or anionic SDS micelles. Interestingly, combi-1 only adopts an amphipathic

structure when in contact with SDS micelles, unlike combi-2, which adopts a coiled and amphipathic structure in both micelle types<sup>10,27</sup>.

Several studies have shown that both combi peptides have a high preference for anionic membrane surfaces<sup>10,28</sup>. Moreover, the Trp residues have been shown to be buried deeper in anionic lipids<sup>10</sup>. Confocal microscopy studies of fluorescein-labelled combi peptides show that these peptides rapidly penetrate bacterial cells without lysis<sup>27,29</sup>. Consequently, it has been suggested that both combi peptides utilize their amphipathic structure to first interact with the membrane and then to aggregate. Finally, they translocate via pores with a very short life time to reach their intracellular target<sup>10</sup>.

**Table 5:** Amino acid sequences of some Trp-rich AMPs<sup>10</sup>.

Name	Sequence	Origin
<i>Indolicidin</i>	<i>ILPWKWPWWPWR-NH<sub>2</sub></i>	<i>Bovine neutrophils</i>
<i>CP-10A</i>	<i>ILAWKAWWAWRR-NH<sub>2</sub></i>	<i>Synthetic derivative of indolicidin</i>
<i>CP-11</i>	<i>ILKKWPWWPWRK-NH<sub>2</sub></i>	<i>Synthetic derivative of indolicidin</i>
<i>Tritrpticin</i>	<i>VRRFPWWPFLRR</i>	<i>Porcine leukocytes</i>
<i>Combi-1</i>	<i>Ac-RRWRF-NH<sub>2</sub></i>	<i>Synthetic</i>
<i>Combi-2</i>	<i>Ac-FRWWHR-NH<sub>2</sub></i>	<i>Synthetic</i>

### 1.2.3 Organometallic compounds as antibacterial agents

A new strategy in fighting bacterial infection comes from the organometallic derivatives of biomolecules<sup>3</sup>. Organometallic compounds (that is, metal complexes including at least one direct, covalent metal-carbon bond) have already been used as anticancer drug candidates<sup>30,31</sup> and as antibacterial agents<sup>4</sup>.

Recent antibacterial testing highlights the potential efficacy of synAMPs containing a metal ion within their amino acid sequences<sup>2,3</sup>. The metallo-

peptides of interest here are classified as metallocene-peptides. Metallocenes are compounds involving two  $\pi$ -bonded cyclopentadienyl (Cp) ligands coordinated to a metal atom<sup>30</sup>. They are part of a class of organometallic compounds, which are defined as metal complexes containing at least one direct, covalent, metal-carbon bond<sup>30</sup>. Other types of organometallic compounds include metal-arenes (half-sandwich), metal-carbenes and metal-carbonyls. All these compounds have characteristics of lipophilicity, kinetically stable, often uncharged and typically have the metal in a low oxidation state<sup>30</sup>. Some examples of organometallic compounds used in anticancer drugs are: ferrocene (Cp<sub>2</sub>Fe), found in the drug Ferrocifen, which is effective against some kinds of breast cancer cells; half-sandwich complexes based on ruthenium and osmium that are selective inhibitors of protein kinases; and ruthenium- and osmium-arene compounds<sup>31</sup>. In addition, there have been reports of organometallic derivatives of quinolone antibiotics containing ruthenium which show good antimicrobial activity<sup>3,4</sup>.

#### **1.2.4 Ruthenocene**

The metallocene ruthenocene (Rc: dicyclopentadienyl ruthenium, Cp<sub>2</sub>Ru) is part of the more generic group of “sandwich compounds”, since it consists of a ruthenium ion bound symmetrically (sandwiched) between the planes of two cyclopentadienyl rings. The role of ruthenium in anticancer drugs has been already demonstrated<sup>30,31</sup>. More recently, the ruthenium-organometallic compounds contained in synAMPs have been investigated as antibacterial drugs<sup>2</sup>. In terms of antibacterial agents, another metallocene, ferrocene (Fc, Cp<sub>2</sub>Fe), has been employed in the *de novo* synthesis of AMPs and shows encouraging results against the Gram-positive *S. aureus*<sup>3</sup>.

The increase in antibacterial activity showed by these synAMPs containing Rc or Fc two compounds is most probably due to the higher cellular uptake due to the presence of the metallocenes, which should increase the peptides' hydrophobicity. However, the hydrophobicity of these two organometallic moieties was not believed to be the predominant factor for antibacterial activity of the synAMPs since the substitution of Rc with Fc

resulted in an increase of the MIC values towards Gram-positive bacteria<sup>2</sup>. Differences on the MIC values could be due to the size of the two metallocene: Rc is slightly larger than Fc ( $\sim 0.17 \text{ \AA}$ ), which might result in a more disruptive interaction towards bacterial membranes. Furthermore, the physicochemical properties of the metallocenes could also contribute to the enhanced antibacterial activity. For example, the more extended *d*-orbitals of Rc form stronger hydrogen bonds with OH or NH groups on the peptide backbone or with other entities, e.g. lipid head-groups, than Fc<sup>32</sup>.

### **1.3 Aims**

The peptides (RW)<sub>3</sub> and RcCO-W(RW)<sub>2</sub> are two short Arg- and Trp-containing synAMPs. They have shown rapid bactericidal and bacteriolytic properties against Gram-negative and Gram-positive bacteria. These results suggest the bacterial membrane is a target for both synAMPs<sup>2</sup>. Furthermore, these two peptides show different bacterial killing kinetics, with the metallocene-peptide being faster than (RW)<sub>3</sub>, although their MICs values are similar. Therefore, an investigation using QCM was valuable to characterize the mechanism of activity of (RW)<sub>3</sub> and RcCO-W(RW)<sub>2</sub> peptides and explore the role of the metallocene moiety.

## 2 Material and methods

### 2.1 Peptides

Peptide stock solutions of 500  $\mu\text{M}$  were made by dissolving a certain amount of peptide in ultrapure water and then stored at  $-20\text{ }^{\circ}\text{C}$ . For the experiments, aliquots from stock solution were diluted in phosphate-buffered saline (PBS) at the desired concentration. However, the peptide RcCO-W(RW)2, was dissolved in a stock solution of DMSO 1% because of its low solubility in water.

### 2.2 Buffer preparation

Sodium chloride ( $\geq 99.5\%$ ), potassium phosphate monobasic (anhydrous,  $\geq 99.0\%$ ) and potassium phosphate dibasic (anhydrous,  $\geq 98\%$ ) were purchased from Sigma-Aldrich (Castle Hill, Australia). Ultrapure water was used with an initial resistivity of  $18.2\text{ M}\Omega\cdot\text{cm}$  (Sartorius AG, Göttingen, Germany). Phosphate buffered saline (PBS, pH  $6.9 \pm 0.1$ ) was prepared having 20 mM phosphate and either 100 mM (“high-salt”) or 30 mM (“low-salt”) sodium chloride in water.

### 2.3 Liposome preparation

1,2-Dimyristoyl-sn-glycero-3-phosphocholine (DMPC) and 1,2-dimyristoyl-sn-glycero-3-phospho-rac-(1-glycerol) (sodium salt) (DMPG) were purchased from Avanti Polar Lipids (Alabaster, USA). Cholesterol, chloroform ( $\geq 99.8\%$ ) and methanol ( $\geq 99.9\%$ ) were purchased from Sigma-Aldrich (Castle Hill, Australia). DMPC and cholesterol were dissolved in chloroform and DMPG was dissolved in chloroform/methanol (ca. 3:1) to create individual 5 mM stock solutions. These solutions were then aliquoted into test tubes to obtain the desired lipid composition (DMPC/cholesterol 7:3 v/v, and DMPC/DMPG 4:1 v/v). The solvent was evaporated under a stream of nitrogen and the test tubes were then dried under vacuum. To prepare the liposomes, the lipids were resuspended in high-salt PBS (100 mM NaCl) to a lipid concentration of 0.5 mM

and then incubated at 37 °C, vortexed and briefly sonicated (between 5 and 10 min) in a bath sonicator prior to use.

## 2.4 Modification of QCM-D sensor chips

Absolute ethanol ( $\geq 99.7\%$ ), propan-2-ol ( $\geq 99.0\%$ ) and hydrogen peroxide (30%) were purchased from Merck (Kilsyth, Australia). Ammonium hydroxide solution (28%) was obtained from Ajax Finechem (Seven Hills, Australia). 3-Mercaptopropionic acid (MPA,  $\geq 99.0\%$ ) was purchased from Fluka, BioChimica (Buchs, Switzerland). The QCM-D sensor crystals used were polished, gold-coated, AT-cut quartz chips with a fundamental frequency of ca. 5 MHz (Q-Sense, Västra Frölunda, Sweden). Immediately before measurements the chips were cleaned in a solution of ammonium hydroxide: hydrogen peroxide: water (1:1:3 v/v) for 20–25 min at ca. 70 °C. The chips were then rinsed thoroughly with water. Surface modification with MPA was conducted by immersing a freshly cleaned chip into a 1 mM solution of MPA in propan-2-ol for at least 1 h. This creates a self-assembled monolayer of negative charge on the chip surface. Excess MPA was removed by rinsing with propan-2-ol. The chips were then dried under a stream of nitrogen and assembled into the QCM-D chambers ready for use.

## 2.5 QCM-D experiments

QCM-D experiments were performed using the E4 system with flow cells (Q-Sense, Västra Frölunda, Sweden). The QCM-D instrument measures the relative changes to the resonance frequency ( $f$ ) and energy dissipation ( $D$ ) of the chip over the course of the experiment.  $\Delta f$  and  $\Delta D$  were measured simultaneously at the fundamental frequency and the 3rd, 5th, 7th and 9th harmonics. Data for the fundamental frequency is not presented as it is inherently noisy and unreliable. The original data was processed in QTools (Q-Sense) before being exported for further analysis in OriginPro 8 (OriginLab Corp., Northampton, USA). All experiments were conducted at a temperature of  $19.10 \pm 0.05$  °C and repeated at least three times. In a typical experiment, firstly, a lipid membrane was formed on the chip surface by the introduction of

a liposome solution into the QCM-D chamber at a flow rate of 50  $\mu\text{L}/\text{min}$ . The liposomes adsorb onto the MPA-monolayer, deform, rupture and fuse together to form a lipid bilayer. Weakly attached liposomes were removed by washing with high-salt PBS (100 mM NaCl) at 300  $\mu\text{L}/\text{min}$  and any embedded liposomes were ruptured by washing with low-salt PBS (30 mM NaCl) at 300  $\mu\text{L}/\text{min}$ . This second washing step was introduced to ensure the formation of a homogeneous membrane and works by creating an osmotic pressure difference between the interior of the embedded liposomes (having a high salt concentration) and the low-salt exterior environment, which causes the liposomes to swell and then burst. Secondly, after a stable baseline was observed, 1 mL of peptide solution was introduced at 50  $\mu\text{L}/\text{min}$ . After the flow was stopped, the peptide was left to incubate with the lipid membrane for 30 min and then the chamber was rinsed with high-salt PBS.

## 3 Results

### 3.1 In DMPC membranes

The actions of  $(RW)_3$  and  $RcCO-W(RW)_2$  peptides were firstly examined with SLBs of pure DMPC. The actions of these two short peptides are displayed in Figs. 44 and 45 as plots of  $\Delta f$  vs  $t$  and  $\Delta D$  vs  $t$ . Both these peptides showed disruption of the membrane layer, since an increase in the frequency and a corresponding decrease in the dissipation occurred simultaneously.

#### 3.1.1 $(RW)_3$

As illustrated in Fig. 44, introduction of the  $(RW)_3$  peptide resulted in disruption of the DMPC membrane. This disruption could be identified by the rapid increase in the frequency for all four concentrations investigated (1, 5, 10 and 20  $\mu\text{M}$ ), as shown by the  $\Delta f-t$  data in Fig. 44. However, close inspection of the  $\Delta f-t$  data shows that an initial small decrease ( $\leq 1$  Hz) was detected after approx. three minutes which was more obvious as the concentration increased. This initial binding feature was rapid and it was followed by an equally rapid mass loss, which could be quantified as 4, 6 and 7 Hz for 1, 5, 20 and 10  $\mu\text{M}$ , respectively. Then, still during the introduction of peptide solution (*i* phase), a “secondary” binding could be detected for the concentrations 5, 10, 20  $\mu\text{M}$ . This “secondary binding” ( $\leq 1$  Hz) is most probably due to peptide molecules from the peptide solution still running into the chamber, which they bind to the surface instead of removing more membrane from the sensor surface.

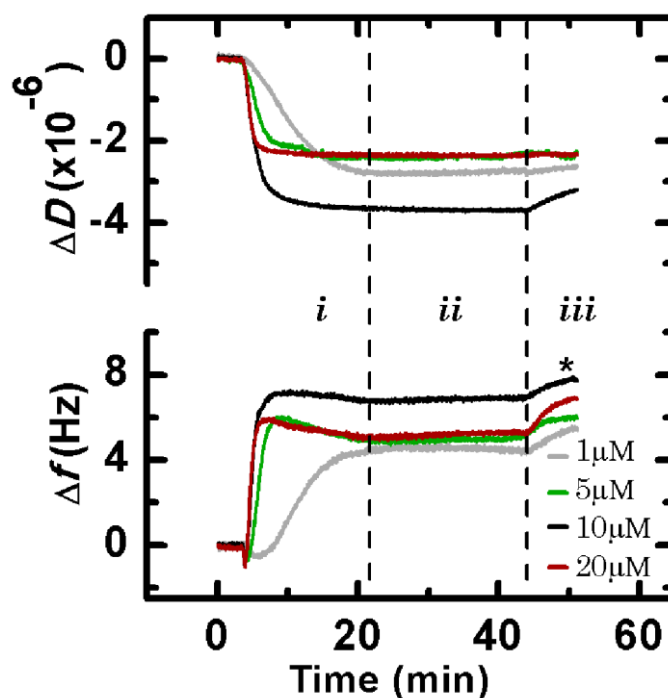


**Fig. 44:** Typical  $\Delta f$  and  $\Delta D$  versus time plots of  $(RW)_3$  peptide interacting with supported membranes of DMPC. The dashed lines mark the end of each phase. Phase *i* corresponds to the flow of peptide solution, whereas *ii* denotes the peptide incubation phase. The rinse with PBS solution corresponds to phase *iii*. The \* symbol indicates the end of the PBS wash. The 7<sup>th</sup> harmonic is illustrated.

Simultaneously, the dissipation decreased between  $2.4 \times 10^{-6}$  and  $3.6 \times 10^{-6}$  in all four traces. This is consistent with rapid removal of the viscoelastic lipid, leaving a more rigid sensor surface.

During the incubation (phase *ii*), no further changes in the frequency or dissipation were detected. Only with the introduction of PBS buffer (phase *iii*), a very small mass change ( $\Delta f \sim 1$  Hz) was observed for all concentrations, although the dissipation remained unchanged except for  $10 \mu\text{M}$ .

### 3.1.2 *RcCO-W(RW)<sub>2</sub>*

The  $\Delta f-t$  plots for the  $RcCO-W(RW)_2$  peptide are shown in Fig. 45. These show that the main action of this peptide is membrano-lytic. An immediate increase in  $\Delta f$  of 11.35 Hz for the concentrations 5, 10 and  $20 \mu\text{M}$  could be observed during the first phase (*i*). Although a peptide concentration of  $1 \mu\text{M}$  was just enough to initiate the solubilisation of the DMPC membrane, concentrations of 10 and  $20 \mu\text{M}$  clearly overcame the threshold required for

membrane lysis. Interestingly for the higher concentrations, a second addition of materials was observed, as indicated by the blue arrow. This mass addition corresponds to a decrease in frequency of 9 and 11 Hz for 10 and 20  $\mu\text{M}$ , respectively. This “secondary” binding indicates a threshold concentration between 5  $\mu\text{M}$  and 10  $\mu\text{M}$ . It is likely that all the peptide in the 5  $\mu\text{M}$  stock was involved in the disruption of the membrane, which continued at the end of phase *i*. It is relevant to note that the initial interaction with the membrane at 1 and 5  $\mu\text{M}$  presented “a threshold”, with insertion into the membrane preceding the disruption process ( $\Delta f \sim 1.3$  Hz). In contrast, concentrations of 10 and 20  $\mu\text{M}$  disrupted the membrane immediately.

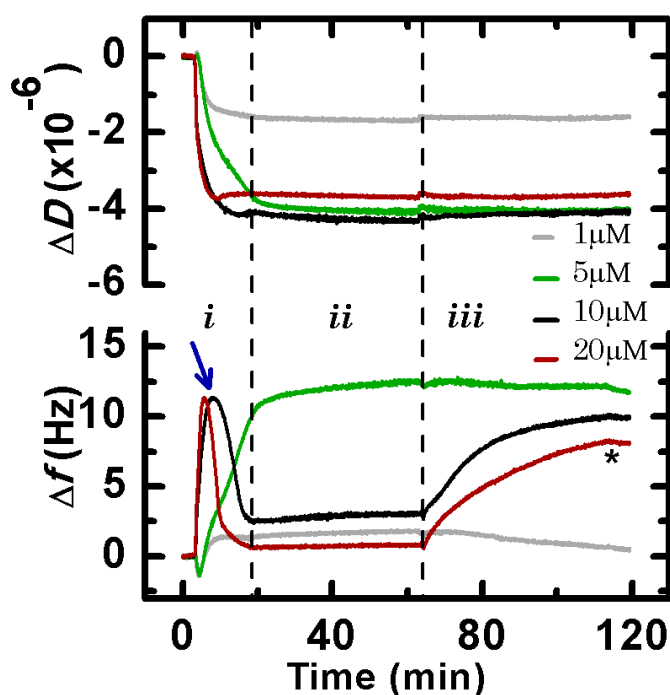


**Fig. 45:** Typical  $\Delta f$  and  $\Delta D$  versus time plots for the RcCO-W(RW)<sub>2</sub> peptide interacting with supported membranes of DMPC. See Fig. 44 for the description of each phase. The 7<sup>th</sup> harmonic is illustrated.

During phase *i*, as the disruption and re-accretion occurred (i.e. during the flow phase), the dissipation decreased for all the concentrations. This dissipation was between  $1.6 \times 10^{-6}$  for 1  $\mu\text{M}$  and  $4.3 \times 10^{-6}$  for 20  $\mu\text{M}$ , as shown in Fig. 45, upper panel. No further change in dissipation was observed for the “secondary” addition process observed in the  $\Delta f$ -*t* data.

During the incubation phase (*ii*), the dissipation and the frequency remained unchanged. The exception was a small removal of mass ( $\Delta f \sim 2$  Hz) for 5  $\mu\text{M}$  peptide.

Phase *iii* involved ending the process by rinsing the sensor surface thoroughly with PBS until no more mass was removed (approx 51 minutes). The result was that almost all the mass re-bound during the “secondary” addition was removed (7 and 7.3 Hz for 10 and 20  $\mu\text{M}$  respectively).

### ***3.1.3 Evaluation of $\Delta f$ - $\Delta D$ plots for DMPC***

As described for other peptides in previous chapters, the  $\Delta D$  of these two short peptides have been plotted versus  $\Delta f$  in order to examine the structural changes within the DMPC membrane due to these peptides. These data are displayed in Fig. 46, with the main action for both peptides being substantial membrane disruption. However, the action of these two peptides was differentiated in terms of the second mass binding process, since it was more accentuated for the metallocene peptide RcCO-W(RW)<sub>2</sub>.

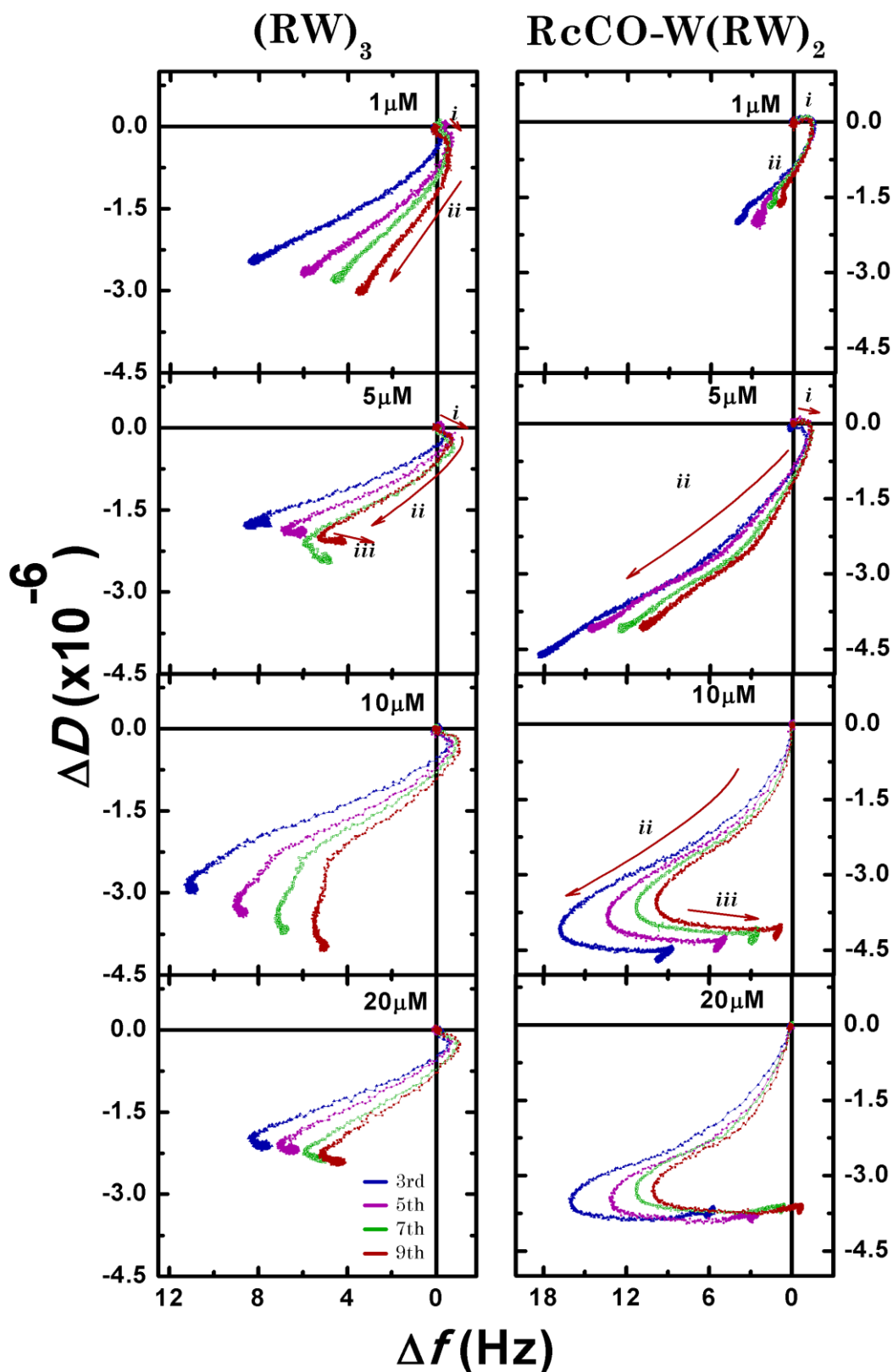


**Fig. 46:** Typical  $\Delta f$ - $\Delta D$  plots for the interaction of various concentrations of  $(RW)_3$  (left column) and  $RcCO-W(RW)_2$  (right column) on a DMPC SLB. The response of the 3<sup>rd</sup>, 5<sup>th</sup>, 7<sup>th</sup>, and 9<sup>th</sup> harmonics is presented. The wash with PBS is not included.

3.1.3.1  $(RW)_3$ 

The  $(RW)_3$  hexapeptide data, presented in the left column in Fig. 46, show initial insertion firstly into the membrane (arrow *i*). However, this initial insertion is small and precedes membrane disruption at all the concentrations used. In all cases, a positive frequency shifts is seen for all four harmonics, and the dissipation decreases continuously (arrow *ii*). This indicates a disruptive action across the membrane bilayer. For most concentrations, the increase in frequency, and corresponding decrease in mass, reaches a max. value of 8 Hz, for the 3<sup>rd</sup> harmonic. The exception is the 10  $\mu\text{M}$  data where the max. value is  $\sim 11$  Hz. Interestingly, the dissipation decrease was slightly larger for the 9<sup>th</sup> harmonic than for the 3<sup>rd</sup>. This could mean that a more significant restructure of the membrane occurred closer to the sensor surface.

However, the last step of the process, indicated by the arrow *iii*, coincided with a small decrease in the frequency occurring for the 5, 10 and 20  $\mu\text{M}$  solutions. This secondary binding did not cause any change in the viscoelastic properties of the system, since the dissipation remained constant. Thus, the  $\Delta f$ - $\Delta D$  plots confirmed the trend already observed in Fig. 44.

3.1.3.2  $RuCO-W(RW)_2$ 

As previously mentioned, the metallocene-peptide had a similar action as  $(RW)_3$ . Indeed, the right column in Fig. 46 shows that, after an initial adsorption (step *i*), the peptide starts to disrupt the membrane. However, no initial insertion could be observed for 10  $\mu\text{M}$  and 20  $\mu\text{M}$  of peptide, presumably due to the rapid nature of the association.

The 1  $\mu\text{M}$  solution showed the biggest adsorption ( $\Delta f \sim 1.4$  Hz) without any change in the dissipation. This was immediately followed by an increase in the frequency while the dissipation decreased (step *ii*). This trend was observed in all the harmonics, meaning that the whole cross-section of the membrane was removed.

Finally, a third phase (*iii*) was observed. This consisted of a turning of the frequency towards more negative values while the dissipation remained almost

unchanged. This secondary binding could be observed only for 10  $\mu\text{M}$  and 20  $\mu\text{M}$ . Hence, a concentration threshold could be located between 5 and 10  $\mu\text{M}$ . Contrary to the disruption action, all the harmonics showed a similar decrease of  $\sim 9$  Hz for 10  $\mu\text{M}$  and  $\sim 10$  Hz for 20  $\mu\text{M}$ . This suggested that a uniform layer of “fresh” peptides molecules was introduced during phase *i* in Fig. 45. In order to verify the nature of this addition, a further experiment was done, involving washing the DMPC/DMPG (4:1) membrane exhaustively after the binding and then adding the same concentration of the peptide. However, the membrane used in this case was DMPC/DMPG (4:1) and so the results will be discussed in the following section.

## 3.2 The second addition of material at DMPC/DMPG (4:1)

The deposition of the DMPC/DMPG (4:1) was found to be variable. Therefore, after a careful analysis, a few experiments performed with this membrane could not be included in the analysis due to poor lipid deposition. As consequence, the concentration study was not as reliable as might have been hoped.

Both peptides showed the same action with DMPC/DMPG (4:1) as seen with DMPC, that is, an initial disruption of the membrane followed by small mass binding to the surface. Even so, some differences could be identified between these two peptides. In addition, a second step was included in the experiment, introducing more peptides at the same concentration as in step one. This was done to prove that the “second” binding step involved peptide attachment and not the re-deposition of the peptide-membrane previously detached. Hence, it was confirmed that the final addition step could be attributed to peptide molecules binding to exposed MPA on the sensor surface.

### 3.2.1 $(RW)_3$

Fig. 47 illustrates the  $\Delta f-t$  and  $\Delta D-t$  plots for the interaction of 20  $\mu\text{M}$   $(RW)_3$  with a DMPC/DMPG (4:1) SLB. Phases *i* and *iv* indicate the injection of two distinct batches of peptides into the QCM chamber. Two opposite actions could be identified: in the first phase, the peptide action was predominantly lytic (7

Hz (3<sup>rd</sup> harmonic) and 3 Hz (9<sup>th</sup> harmonic)), in the second addition of peptide (phase *iv*) only binding occurred (~3Hz for all the harmonics). Furthermore, during the first phase a small late binding could be detected only for the 7<sup>th</sup> and the 9<sup>th</sup> harmonics (0.6 and 1.2 Hz, respectively) while traces of the 3<sup>rd</sup> and 5<sup>th</sup> harmonics showed a continuous disruption. During the incubation (phase *ii*), disruption was still recorded for the latter overtones, with the 7<sup>th</sup> overtone showing a slight effect. The first wash with PBS (phase *iii*) was able to remove a little material, between 1.6 to 2 Hz, which could be a mixture of lipid and peptide, or possibly lipid only. Interestingly, the second and last wash with PBS was not able to remove any of the material bound during the second peptide addition. In fact, further decrease of the frequency was recorded, although it was very minor (less than 1 Hz).

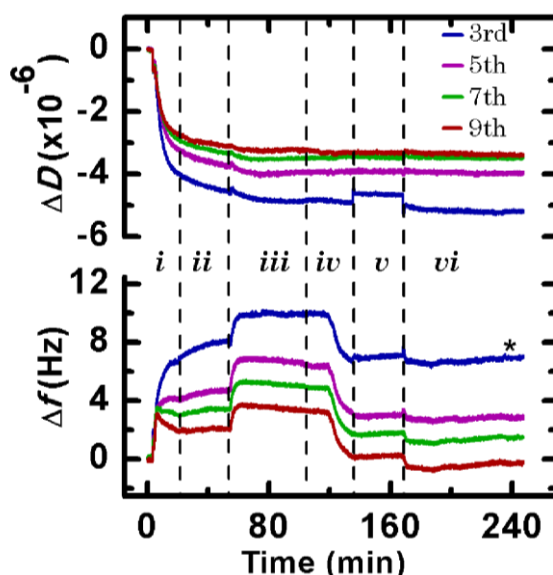


**Fig. 47:** Typical  $\Delta f$  and  $\Delta D$  versus time plots of  $(RW)_3$  peptide interacting with supported membranes of DMPC/DMPG (4:1) at the concentration of 20  $\mu\text{M}$ . The dashed lines mark the end of each phase. Phases *i* and *iv* correspond to the introduction of peptide solution, whereas *ii* and *v* denote the peptide incubation phase. The rinse steps with PBS solution corresponds to phases *iii* and *vi*. The \* symbol indicates the end of the PBS wash.

In the meantime, the dissipation (upper panel) decreased from the first phase until the beginning of the 3<sup>rd</sup> phase (*iii*), and after that, it remained constant. Only the 3<sup>rd</sup> harmonic showed a subtle increase during the second incubation time (phase *v*), but this could be an artefact due to the pump motor starting.

### 3.2.2 RcCO-W(RW)<sub>2</sub>

The interaction of RcCO-W(RW)<sub>2</sub> (20 μM) with DMPC/DMPG (4:1) is displayed as  $\Delta f$ - $t$  and  $\Delta D$ - $t$  plots in Fig. 48. As seen for (RW)<sub>3</sub>, the initial interaction of the peptide resulted in an increase in the frequency of 4.1, 2.4 and 2.1 Hz for the 3<sup>rd</sup>, 5<sup>th</sup>, 7<sup>th</sup> and 9<sup>th</sup> harmonics, respectively. Then, still during phase *i*, rapid adsorption of material began, resulting in a frequency decrease of 6.7, 8.7, 10.1, 10.9 Hz for the 3<sup>rd</sup>, 5<sup>th</sup>, 7<sup>th</sup> and 9<sup>th</sup> harmonics, respectively. During the incubation phase *ii*, no changes in frequency occurred. During the first rinse with PBS (phase *iii*), the increase in frequency was very similar for all the overtones ( $\Delta f \sim 11$  Hz). However, while for the 9<sup>th</sup> harmonic, the increase in  $\Delta f$  was very similar to the decrease of  $\Delta f$  during the phase *i*, for the 3<sup>rd</sup> harmonic, the loss of mass in phase *iii*, was higher than the mass adsorbed in phase *i*.

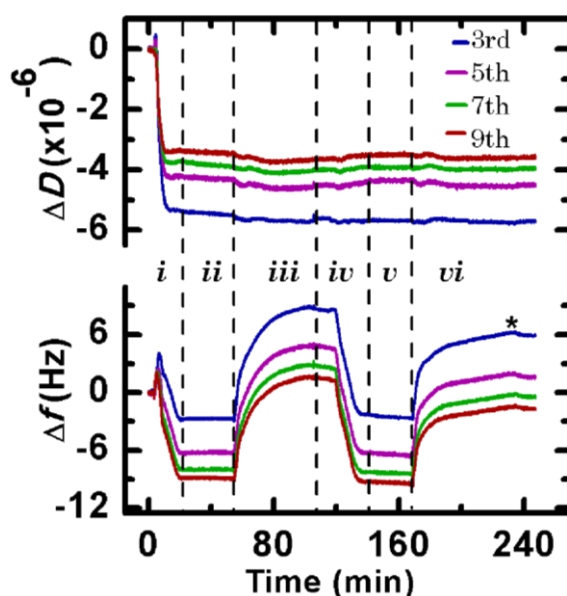


**Fig. 48:**  $\Delta f$  and  $\Delta D$  versus time plots of RcCO-W (RW)<sub>2</sub> peptide, at the concentration of 20 μM, interacting with supported membranes of DMPC/DMPG (4:1). See Fig. 47 for the identification of each phase. The 7<sup>th</sup> harmonic is illustrated.

Subsequently, the second addition of fresh peptide solution (phase *iv*) showed a decrease in the  $\Delta f$  ( $\sim 11$  Hz) for all the overtones. This decrease was much larger and more homogeneous in comparison with that of phase *i*. The final exhaustive wash with PBS (phase *vi*) was able to remove almost all the adsorbed material ( $\sim 8.5$  Hz in all the overtones).

Meanwhile, the dissipation decreased rapidly during the first phase, in agreement with a disruptive mechanism. This decrease came to a halt between  $5.3 \times 10^{-6}$  for the 3<sup>rd</sup> harmonic and  $3.3 \times 10^{-6}$  for the 9<sup>th</sup> harmonic, and no further changes in  $\Delta D$  were detected in each phase (*ii* → *vi*). One feature in the dissipation was a minuscule increase in  $\Delta D$  observed for the 3<sup>rd</sup> and 5<sup>th</sup> harmonic at the very beginning of the peptide interaction. However, this effect could be due to the rupture of small unopened vesicles at the membrane surface.

### 3.3 The peptide interaction with DMPC/cholesterol

The interactions of both peptides, (RW)<sub>3</sub> and RcCO-W(RW)<sub>2</sub>, with membranes of DMPC/chol were also examined. Interestingly, the addition of 30 mol % cholesterol in a DMPC membrane caused a shift in the action of both peptides from a lytic mechanism to adsorption and insertion into the membrane layer.

#### 3.3.1 (RW)<sub>3</sub>

As shown in the  $\Delta f$ - $t$  plots of Fig. 49, the (RW)<sub>3</sub> peptide showed a great affinity at the DMPC/chol membrane (a decrease in  $\Delta f$  of 16, 17 and 19 Hz for 1, 5, 10 and 20  $\mu$ M, respectively). Interestingly, the peptide adsorption on the membrane was not a function of concentration. A very similar level of binding could be observed for all the concentrations at the termination of the peptide flow (*i*), although the rate of binding did increase with concentration.

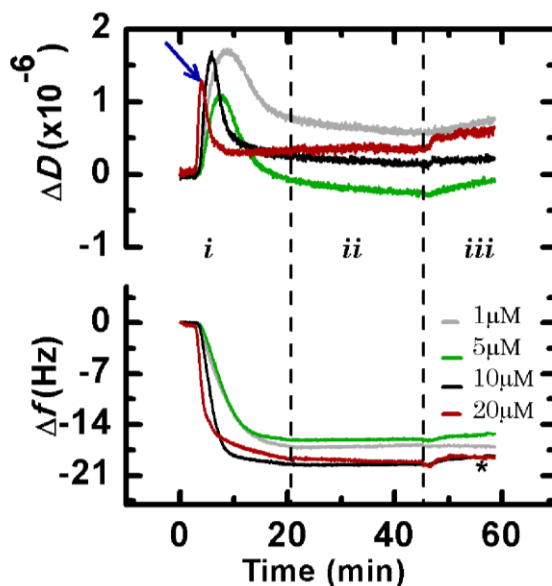


**Fig. 49:** Typical  $\Delta f$  and  $\Delta D$  versus time plots of  $(RW)_3$  peptide interacting with supported membranes of DMPC/chol 30 mol %. The dashed lines mark the end of each phase. Phase *i* corresponds to the flow of peptide solution, whereas *ii* denotes the peptide incubation phase. The rinse with PBS solution corresponds to phase *iii*. The \* symbol indicates the end of the PBS wash. The 7<sup>th</sup> harmonic is illustrated.

More precisely, the  $(RW)_3$  peptide adsorption was revealed by inspection of the dissipation traces are displayed in the upper panel of Fig. 49 to be a trans-membrane insertion. As the frequency decreased, the dissipation showed an increase (less than  $2 \times 10^{-6}$ ) before decreasing to an average of  $1 \times 10^{-6}$ , consistent with a stable pore. Interestingly, the largest increase in  $\Delta D$  was observed for  $1 \mu\text{M}$ . All the four concentrations followed the same trend, although the lower concentrations responded more slowly. The dissipation also showed a small, slow decrease during the incubation time (phase *ii*), while the frequency remained quite stable.

The insertion of  $(RW)_3$  into the DMPC/chol membrane also appeared to be a strong interaction. If it had simply involved weak electrostatic surface interactions, a loss of mass would have been observed during the PBS wash in the last phase (*iii*) of the experiment. This is not seen in Fig 49. Further evidence of this strong peptide association comes also from the dissipation, which did not change during the PBS wash.

### 3.3.2 RcCO-W(RW)<sub>2</sub>

The  $\Delta f$ - $t$  plot of RcCO-W(RW)<sub>2</sub> with a DMPC/chol membrane is illustrated in the lower panel of Fig. 50. RcCO-W(RW)<sub>2</sub> interacted with the DMPC/chol membrane in a similar way to (RW)<sub>3</sub>, i.e. only peptide adsorption was observed. The binding was concentration dependent, with the trace corresponding to 1  $\mu$ M having the smallest  $\Delta f$  (-10 Hz), whereas 5, 10 and 20  $\mu$ M showed a binding of 16, 18 and 21 Hz, respectively. Importantly, the 1  $\mu$ M showed a smaller adsorption than the 10.4 Hz seen in other experiments carried out.

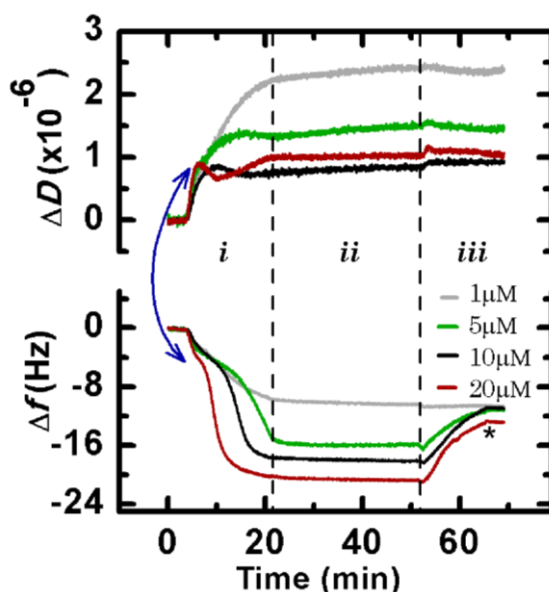


**Fig 50:** Typical  $\Delta f$  and  $\Delta D$  versus time plots of RcCO-W(RW)<sub>2</sub> peptide interacting with supported membranes of DMPC/chol 30 mol %. See Fig. 49 for the phase description. The 7<sup>th</sup> harmonic is illustrated.

Further details of the binding are seen in Fig. 50. The blue arrows point to an undulation profile of  $\Delta f$  and  $\Delta D$  at the start of the experiment, after  $\sim 7$  minutes from the introduction of the peptide solution. This effect was more pronounced for the 20 and 10  $\mu$ M traces and could be interpreted as an attempt of peptide molecules to relocate more deeply into the membrane. This could be an indication of pore formation, as described in Chapter 3. However, a deeper understanding could be obtained by looking at the  $\Delta f$ - $\Delta D$  plots which will be discussed in the next section.

As can be seen from the last stage of the experiment (*iii*), some material was lost from the membrane (with the exception of 1  $\mu$ M), which resulted in a

peptide leftover of  $\sim 13$  Hz in the case of  $20 \mu\text{M}$  and  $\sim 11$  Hz for the higher peptide concentrations.

### 3.3.3 $\Delta f$ - $\Delta D$ in DMPC/cholesterol

The  $\Delta f$ - $\Delta D$  plots in Fig. 51 show some substantial differences between the two peptides in their interactions with the DMPC/chol membrane.

The (RW)<sub>3</sub> peptide shows a classical trans-membrane insertion which is uniform in terms of  $\Delta f$  for each concentration. All the harmonics decreased in  $\Delta f$ :  $\sim 17$  Hz for  $1 \mu\text{M}$ ,  $\sim 16$  Hz for  $5 \mu\text{M}$ ,  $\sim 19.5$  Hz for  $10 \mu\text{M}$  and  $\sim 18.5$  Hz for  $20 \mu\text{M}$ . Looking at the dissipation, the entire process of insertion could be divided in two steps: firstly, the dissipation increased until approximately half of the peptide adsorbed at the membrane (step *i*), then it started to decrease (step *ii*) until no more peptide was available to penetrate the membrane (as shown also in Fig. 49). The  $20 \mu\text{M}$  concentration was the only one in which the dissipation stabilized while the frequency was still decreasing.

The RcCO-W(RW)<sub>2</sub> peptide action was initially similar in effect: i.e. a trans-membrane insertion occurred for most of the concentrations, resulting in a decrease for  $\Delta f$  of  $16.5 \pm 1.5$  Hz for  $5 \mu\text{M}$ ,  $18.5 \pm 1$  Hz for  $10 \mu\text{M}$  and  $21 \pm 1$  Hz for  $20 \mu\text{M}$ . However, the biggest difference from the non-metalated (RW)<sub>3</sub> peptide was in the dissipation.  $\Delta D$  for the RcCO-W(RW)<sub>2</sub> showed an increase similar to that observed for the (RW)<sub>3</sub> peptide at the beginning of its action (step *i*), however,  $\Delta D$  stopped changing at around 4-5 Hz, an effect which was more pronounced for the 9<sup>th</sup> harmonic (step *ii*). The dissipation for RcCO-W(RW)<sub>2</sub> remained almost invariable or had only a small increase until the frequency varied no more (step *ii*). The last step (*iii*) showed a small increase in dissipation. In this last phase, the frequency was constant for  $5$  and  $10 \mu\text{M}$ , while it showed a small decrease for  $20 \mu\text{M}$ .

A threshold concentration could be identified between  $1 \mu\text{M}$  and  $5 \mu\text{M}$ , in terms of the interaction with DMPC/chol, where only the first step was observed at  $1 \mu\text{M}$  at the membrane.

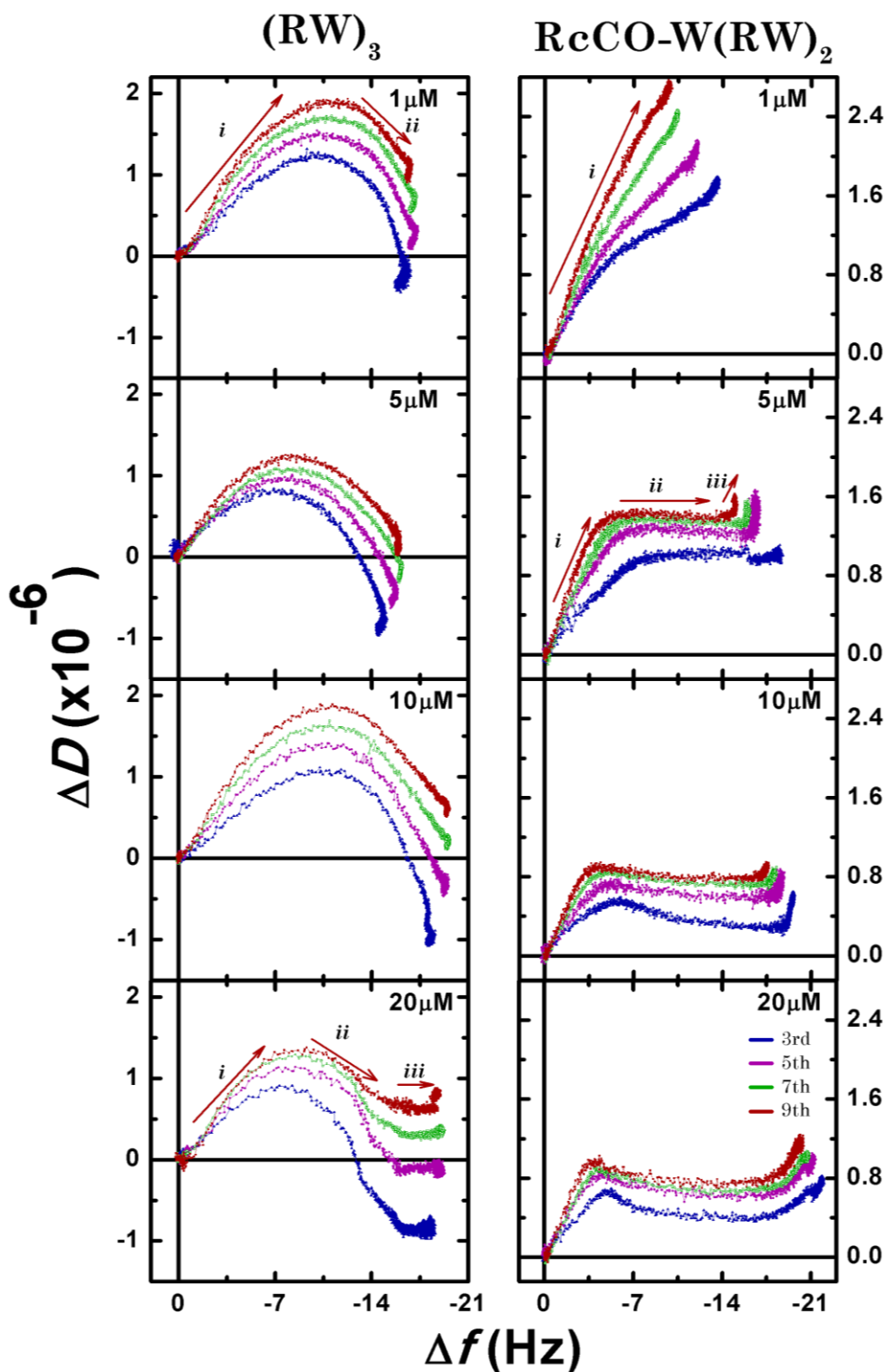


**Fig. 51:** Typical  $\Delta f$ - $\Delta D$  plots for the interaction of various concentrations of  $(RW)_3$  (left column) and  $RcCO-W(RW)_2$  (right column) on a DMPC/chol 30 mol % SLB. The response of the 3<sup>rd</sup>, 5<sup>th</sup>, 7<sup>th</sup>, and 9<sup>th</sup> harmonics is presented. The final wash is not included.

In both  $\Delta f$ - $\Delta D$  plots, it is interesting to notice that the increase in dissipation observed in the *i* step was more dramatic for the 9<sup>th</sup> than for the for

the 3<sup>rd</sup> harmonic. This could suggest that interactions eventually established between the cholesterol and peptide molecules might form a hydrophobic region within the inner membrane, creating a looser, more viscoelastic surface. Moreover, it seems that the Trp residues could be responsible for this process rather than the ruthenocenoil group, since this increase was observed in both peptides.

## 4 Discussion

Many synthetic AMPs and CPPs contain Arg and Trp residues which are believed to be crucial for their actions. Furthermore, the addition of conjugates such as metallocenes to peptides has produced interesting antibacterial activity towards some Gram-positive and Gram-negative bacteria<sup>3</sup>. This suggests that the integration of organometallics into peptides enriched in Arg and Trp residue could be a new and effective way to prepare novel antibacterials. In particular, preliminary results regarding the antibacterial activity for both (RW)<sub>3</sub> and RcCO-W(RW)<sub>2</sub> peptides showed their potential for future application as drugs<sup>2</sup>. The QCM results presented in this chapter are in agreement with the definition of these peptides as bacteriolytic<sup>2</sup>.

### 4.1 The influence of Trp on the interaction with DMPC membranes

Both of the Arg-Trp-rich short peptides acted via a lytic mechanism, since their interaction caused the loss of mass from a DMPC membrane. The presence of bulky lipophilic Trp residues (three for (RW)<sub>3</sub> and four in RcCO-W(RW)<sub>2</sub>) balanced the positive charges due to the Arg groups (four for (RW)<sub>3</sub> and two for RcCO-W(RW)<sub>2</sub>). This amino acid composition and the alternation of Arg and Trp residues in the peptide primary sequence could be responsible for the lysis of the membrane. Previous work done by Mishra, et al.<sup>18</sup> showed the complete lysis of GUVs by a hexapeptide of exclusively Arg residues (Arg<sub>6</sub>) during peptide translocation into vesicles. The inclusion of some hydrophobicity, by adding only one Trp residue to this peptide, caused the formation of more stable pores. This in turn allowed slower leakage from the GUVs without bursting them. However, the vesicles formed by Mishra were of a mixed lipid composition, with some negatively charged components (PS/PE/PC). In addition, Mishra highlighted that the absence of a support underneath the bilayer (like the cytoskeleton, which stabilize and enclose the membrane) could be responsible in part for the lytic action<sup>18</sup>. Here, despite the use of SLBs, which do act as a mimic for a bilayer interacting with the cytoskeleton, membrane disruption happened anyway.

In view of this, the lytic action could come from the high number of Trp groups relative to the total number of residues. This enhances structural rearrangement of the membrane, since Trp is a lipophilic amino acid with a bulky indole ring and prefers to be situated at the polar-apolar interface of the bilayer<sup>19,20,33</sup>. Indeed, MD simulations have shown that the Trp side chain establishes cation- $\pi$  interactions with the choline groups of phosphocholines, with either a methyl group or the choline head-group quite close to the indole ring<sup>20</sup>. Other interactions set up by the indole ring are hydrogen bonds with interfacial water molecules and with the acyl carbonyl group of the lipids<sup>20</sup>. It is relevant to note that these simulations showed that, when the Trp side chain is buried deeply in the hydrocarbon core, it still able to make hydrogen bonds (one or two) with the interfacial water<sup>20</sup>. Moreover, the stacked conformation between Arg and Trp side chains allows a deeper and energetically more favourable penetration of Arg into the hydrophobic core of the lipid bilayer<sup>10</sup>. In conclusion, the composition and position of the residues in the sequence could be the reason that these peptides are able to insert deeper into the membrane, “carrying” with them water molecules. This results in the membrane being disrupted by a “detergent like” action. The formation of pores cannot be validated with this membrane composition because the entire action was too fast. However, it also cannot be ruled out, since an attempt of pore formation could be detected when cholesterol was present (see results). Furthermore, peptide aggregation at the membrane, which could lead to pore formation, could occur since a low amount of DMSO was required to prevent aggregation in solution.

Peptide aggregation could also be seen in the case of the small “secondary addition” observed in Fig. 44 & 45. It is also highlighted as a third step in the  $\Delta f$ - $\Delta D$  plots. This could be an indication of two possible scenarios. Firstly, the resulting “peptide-membrane” complex could, after the initial disruption, attract peptide monomers which start to aggregate at the membrane. The other possibility might be that interactions between peptide monomers and the underlying MPA become exposed, the result of a localized disruption of the membrane. This “secondary addition” has also been recently observed by Lu et

al.<sup>34</sup>. Indeed, during the interaction of the melittin peptide with zwitterionic artificial membranes, investigated through QCM, a “secondary mass adsorption” was observed after the solubilisation of membrane due to the insertion of melittin. This “secondary adsorption” was interpreted as the continuous adsorption of additional melittin peptides to those already inserted in the remaining membrane during the flow-through of peptide solution<sup>34</sup>.

## **4.2 Secondary adsorption highlights the equilibrium, between two processes**

The interactions of the (RW)<sub>3</sub> peptide with SLBs of DMPC/DMPG (4:1) did not provide any new perspectives on the lytic mechanism that had already been seen with SLBs of DMPC. As in previous studies, the primary disruption event was followed by an initial small adsorption. However, the experiments on DMPC/DMPG membranes also revealed that the overtones probing the outer membrane layers (3<sup>rd</sup> and 5<sup>th</sup> harmonic) did not show any “secondary” binding during the first peptide interaction, unlike the 7<sup>th</sup> and 9<sup>th</sup> overtone. Disruption continued at the surface of the membrane while mass addition was happening at the deeper membrane layers sensed by the higher harmonics. This non homogeneous response of  $\Delta f$  across overtones could be interpreted as the result of peptide (RW)<sub>3</sub> inserting in the membrane. This caused an initial deep disruption across the membrane, since all four overtones reveal the same trend. This means that the membrane disruption was delimited only at the layer of the membrane close to the surface.

As already mentioned, the ruthenocene peptide acted on the DMPC/DMPG membrane in the same way as already seen for the DMPC membrane. Moreover, its action on the membrane was very similar to the action of the (RW)<sub>3</sub> peptide. However, the mass removed at the initial disruption was less than what was recorded for the (RW)<sub>3</sub> peptide. Perhaps the presence of a metallocene enhanced the peptide aggregation on the surface, causing it to become the prevailing event. This would have resulted in a higher amount of peptide uptake than with (RW)<sub>3</sub>.

### 4.3 The presence of a metallocene: the secondary addition in zwitterionic and negatively charged SLBs

DMPC/DMPG (4:1) experiments in which a second addition of fresh peptide was made after initial disruption gave a better idea about the nature of the interactions between the peptides and the underlying layer on the sensor surface. Most probably the “fresh” peptide adsorbed on the MPA layer, which was exposed after the membrane disruption. This possibility is justified by the absence of any variation in the dissipation values. Moreover, the decrease in  $\Delta f$  during the second peptide addition is very similar to the increase in  $\Delta f$  caused by the first PBS rinse. This similarity in  $\Delta f$  suggests a “secondary binding” of peptides happened in areas of membrane being removed, thus leaving exposed MPA.

However, the presence of ruthenocenoil in  $\text{RcCO-W(RW)}_2$  peptide was shown to influence the interaction with MPA, since the introduction of the second PBS rinse removed a mass nearly equivalent to that of the entire second peptide addition.

### 4.4 Attempts to form pores in SLBs containing cholesterol

Cholesterol is well known for its condensing and ordering effect on the membrane<sup>35-37</sup>. As already observed with peptides discussed in this thesis, the presence of cholesterol in the membrane has a significant effect on the action of these short peptides, often switching from a more AMP-lytic action to a CP one.

First, considering the length of these two  $\text{RW}_x$  peptides, the decrease in  $\Delta f$ , displayed in Figs. 49 & 50 was greater for both peptides than that seen with Tat (44-57) and Tat (49-57) ( $\Delta f \sim 4$  Hz), the short Arg-rich peptides discussed in Chapter 5. This higher affinity could be the consequence of the presence of the Trp residues in the peptide, which favour the penetration in the lipids by shielding the Arg residues<sup>10,21</sup>. Further evidence comes from the analysis of the  $\Delta D$  vs  $\Delta f$  plots displayed in Fig.51. These indicate a rearrangement of the

membrane as a result of the deeper insertion of the peptide (RW)<sub>3</sub> to the lower leaflet. Thus, deeper insertion could be the start of a pore-like structure, as suggested by the increase and decrease of the dissipation. These structures are “pore-like” because a single peptide monomer is too short to span the membrane width, which generally requires peptides with 20 or more amino acid residues<sup>38,39</sup>. Even the possibility of dimerization for the formation of the classical toroidal pores is not available here because it has only been suggested for peptides longer than 13 residues<sup>40</sup>. One possible explanation could be the genesis of a “disordered pore-like” structure, resulting from the association and aggregation of peptide monomers onto the membrane. In addition, the insertion of bulky residues could be the reason for the increased dissipation for the 9<sup>th</sup> overtone in comparison with the 3<sup>rd</sup>. This indicates a more viscoelastic surface on the inner side of the membrane due to the bulkiness of the Trp residues. Either way, the inserted peptide creates strong interactions with the membrane since the final wash with PBS does not remove any of the peptide inserted, as shown in Fig. 49.

The presence of the ruthenocenoyl group on the peptide appears instead to have an influence on the peptide interaction. As the peptide molecules start to insert and to expand the membrane layer, the dissipation remains unchanged after its initial increase. Afterwards a small increase in dissipation without any change in frequency occurs during the incubation time (step *iii*, Fig. 51), suggesting unstable surface binding due to the presence of the metallocene group preventing the RcCO-W(RW)<sub>2</sub> peptide inserting like the (RW)<sub>3</sub> peptide. Indeed, some of the RcCO-W(RW)<sub>2</sub> peptide adsorbed in step *i+ii* is washed away by the PBS buffer rinse step. Another hint of a possible unstable insertion is seen in the small decrease of the dissipation during step *ii*, which appears somewhat like an attempt to insert like a “pore-like” manner.

## 5 Conclusions

Peptides (RW)<sub>3</sub> and RcCO-W(RW)<sub>2</sub> have been previously analysed for their antibacterial activity<sup>2</sup>. The results obtained suggested that these peptides target the bacterial membrane. Moreover, the high concentrations required for hemolysis and for toxicity against human cancer cell lines make these two peptides possible candidates for therapeutic use. Consequently, it is important to understand how these two peptides interact with artificial membranes that reflect the compositions of prokaryotic and eukaryotic membranes. It is also important to support the outcomes of antimicrobial testing through *in vitro* studies.

The QCM data for these two peptides showed their activity to be non-selective and lytic towards both neutral and negatively charged membranes. Furthermore, the screening of the action of these two peptides by QCM was undertaken to detect any effects that could be ascribed uniquely to the presence of the ruthenocene moiety. In summary, the ruthenocene moiety did not show any specific contribution to the disruption mechanism of the peptide RcCO-W(RW)<sub>2</sub>; however, it seemed instead to reduce the affinity of this peptide towards eukaryotic-mimetic membranes, which resulted in a weaker interaction.

## 6 Bibliography

- 1 Fjell, C. D. *et al.* Designing antimicrobial peptides: form follows function. *Nat. Rev. Drug Discov.* **11**, 37-51, (2012).
- 2 Bauke Albada, H. *et al.* Modulating the activity of short arginine-tryptophan containing antibacterial peptides with N-terminal metallocenoyl groups. *Beilstein J. Org. Chem.* **8**, 1753-1764, (2012).
- 3 Chantson, J. T. *et al.* Solid-Phase Synthesis, Characterization, and Antibacterial Activities of Metallocene–Peptide Bioconjugates. *ChemMedChem* **1**, 1268-1274, (2006).
- 4 Patra, M. *et al.* Small organometallic compounds as antibacterial agents. *Dalton Trans.* **41**, 6350-6358, (2012).
- 5 Wang, J. *et al.* Platensimycin is a selective FabF inhibitor with potent antibiotic properties. *Nature* **441**, 358-361, (2006).
- 6 Albada, H. B. *et al.* Tuning the activity of a short arg-trp antimicrobial peptide by lipidation of a C- or N-terminal lysine side-chain. *ACS Medicinal Chemistry Letters* **3**, 980-984, (2012).
- 7 Raghuraman, H. & Chattopadhyay, A. Melittin: A membrane-active peptide with diverse functions. *Biosci. Rep.* **27**, 189-223, (2007).
- 8 Long Zhu, W. L. & Shin, S. Y. Effects of dimerization of the cell-penetrating peptide Tat analog on antimicrobial activity and mechanism of bactericidal action. *J. Pept. Sci.* **15**, 345-352, (2009).
- 9 Blondelle, S. E. *et al.* Influence of tryptophan residues on melittin's hemolytic activity. *Biochim. Biophys. Acta, Protein Struct. Mol. Enzymol.* **1202**, 331-336, (1993).
- 10 Chan, D. I. *et al.* Tryptophan- and arginine-rich antimicrobial peptides: Structures and mechanisms of action. *BBA- Biomembr.* **1758**, 1184-1202, (2006).
- 11 Jones, A. T. & Sayers, E. J. Cell entry of cell penetrating peptides: tales of tails wagging dogs. *J. Controlled Release* **161**, 582-591, (2012).
- 12 Madani, F. *et al.* Mechanisms of Cellular Uptake of Cell-Penetrating Peptides. *J. of Biophysics* **2011**, 10, (2011).
- 13 Järver, P. & Langel, Ü. Cell-penetrating peptides—A brief introduction. *BBA- Biomembr.* **1758**, 260-263, (2006).
- 14 Maiolo, J. R. *et al.* Effects of cargo molecules on the cellular uptake of arginine-rich cell-penetrating peptides. *BBA- Biomembr.* **1712**, 161-172, (2005).
- 15 Bahnsen, J. S. *et al.* Antimicrobial and cell-penetrating properties of penetratin analogs: Effect of sequence and secondary structure. *BBA- Biomembr.* **1828**, 223-232, (2013).

- 16 Fuchs, S. M. & Raines, R. T. Pathway for Polyarginine Entry into Mammalian Cells. *Biochemistry* **43**, 2438-2444, (2004).
- 17 Futaki, S. *et al.* Arginine-rich peptides and their internalization mechanisms. *Biochem. Soc. Trans.* **35**, 784-787, (2007).
- 18 Mishra, A. *et al.* Translocation of HIV TAT peptide and analogues induced by multiplexed membrane and cytoskeletal interactions. *Proc. Natl. Acad. Sci.* **108**, 16883-16888, (2011).
- 19 Yau, W. M. *et al.* The preference of tryptophan for membrane interfaces. *Biochemistry* **37**, 14713-14718, (1998).
- 20 Aliste, M. P. *et al.* Molecular dynamics simulations of pentapeptides at interfaces: Salt bridge and cation- $\pi$  interactions. *Biochemistry* **42**, 8976-8987, (2003).
- 21 Dougherty, D. A. Cation- $\pi$  interactions in chemistry and biology: A new view of benzene, Phe, Tyr, and Trp. *Science* **271**, 163-168, (1996).
- 22 Ma, J. C. & Dougherty, D. A. The cation- $\pi$  interaction. *Chem. Rev.* **97**, 1303-1324, (1997).
- 23 Rokitskaya, T. I. *et al.* Indolicidin action on membrane permeability: Carrier mechanism versus pore formation. *BBA- Biomembr.* **1808**, 91-97, (2011).
- 24 Rozek, A. *et al.* Structure of the bovine antimicrobial peptide indolicidin bound to dodecylphosphocholine and sodium dodecyl sulfate micelles. *Biochemistry* **39**, 15765-15774, (2000).
- 25 Nguyen, L. T. *et al.* The expanding scope of antimicrobial peptide structures and their modes of action. *Trends Biotechnol.* **29**, 464-472, (2011).
- 26 Schibli, D. J. *et al.* Tryptophan-rich antimicrobial peptides: Comparative properties and membrane interactions. *Biochem. Cell Biol.* **80**, 667-677, (2002).
- 27 Rezansoff, A. J. *et al.* Interactions of the antimicrobial peptide Ac-FRWWHR-NH<sub>2</sub> with model membrane systems and bacterial cells. *J. Pept. Res.* **65**, 491-501, (2005).
- 28 Arouri, A. *et al.* Peptide induced demixing in PG/PE lipid mixtures: A mechanism for the specificity of antimicrobial peptides towards bacterial membranes? *BBA- Biomembr.* **1788**, 650-659, (2009).
- 29 Park, C. B. *et al.* Structure-activity analysis of buforin II, a histone H2A-derived antimicrobial peptide: The proline hinge is responsible for the cell-penetrating ability of buforin II. *Proc. Natl. Acad. Sci.* **97**, 8245-8250, (2000).
- 30 Gasser, G. *et al.* Organometallic anticancer compounds. *J. Med. Chem.* **54**, 3-25, (2011).

- 31 Hartinger, C. G. *et al.* Challenges and opportunities in the development of organometallic anticancer drugs. *Organometallics* **31**, 5677-5685, (2012).
- 32 Shubina, E. S. *et al.* Intermolecular hydrogen bonds with d-electrons of transition metal atoms. H-complexes with metallocenes of the iron subgroup. *J. Mol. Struct.* **301**, 1-5, (1993).
- 33 De Planque, M. R. R. *et al.* Interfacial anchor properties of tryptophan residues in transmembrane peptides can dominate over hydrophobic matching effects in peptide-lipid interactions. *Biochemistry* **42**, 5341-5348, (2003).
- 34 Lu, N. *et al.* Molecular response and cooperative behavior during the interactions of melittin with a membrane: Dissipative quartz crystal microbalance experiments and simulations. *J. Phys. Chem. B* **116**, 9432-9438, (2012).
- 35 Simons, K. & Vaz, W. L. C. MODEL SYSTEMS, LIPID RAFTS, AND CELL MEMBRANES1. *Annu. Rev. Bioph. Biom.* **33**, 269-295, (2004).
- 36 Yeagle, P. L. Cholesterol and the cell membrane. *BBA- Rev. Biomembr.* **822**, 267-287, (1985).
- 37 Hung, W. C. *et al.* The condensing effect of cholesterol in lipid bilayers. *Biophys. J.* **92**, 3960-3967, (2007).
- 38 Mahalka, A. K. & Kinnunen, P. K. J. Binding of amphipathic  $\alpha$ -helical antimicrobial peptides to lipid membranes: Lessons from temporins B and L. *BBA- Biomembr.* **1788**, 1600-1609, (2009).
- 39 Kinnunen, P. K. J. Amyloid formation on lipid membrane surfaces. *Open Biol.* **2**, 163-175, (2009).
- 40 Harris, F. *et al.* Aberrant action of amyloidogenic host defense peptides: A new paradigm to investigate neurodegenerative disorders? *FASEB J.* **26**, 1776-1781, (2012).



# *Dual behaviour of the self-aggregating AMP, Uperin 3.5, on SLBs*

## 1 Introduction

### 1.1 Uperin 3.5

Many amphibians release host defence compounds into the surrounding environment in response to attack by microorganisms and/or predators<sup>1</sup>. These compounds are released primarily from glands situated in the skin that can store a wide variety of peptides, including neuropeptides, toxins, membrane-active peptides, hormones and opioids<sup>1</sup>. These skin gland secretions are found in species of Australian frogs and toads, from the genera *Litoria*, *Uperoleia*, *Limnodynastes*, *Cyclorana* and *Crinia* and have been examined during the past decade with the aim to identify new bioactive peptides<sup>2</sup>. The primary structure of various host-defence peptides (HDPs) isolated from these secretions was determined by positive and negative ion electrospray mass spectrometry and automated Edman sequencing<sup>2,3</sup>. Among the peptides identified, a large group are antibacterial and anticancer active peptides. This group comprises both short (<20 residues) and longer peptides. The longer peptides are mostly caerins, which are a class subdivided into four groups. The caerins from group 1 are the most active AMPs in solution. They consist of two alpha helices, separated by a more flexible hinge region initiated by Pro15<sup>2</sup>. The shorter peptides include aureins 1–3, the citropins 1, dahlein 1.2, maculatin 2.1 and uperin 3.5 and 3.6<sup>2</sup>.

The uperin peptides have mostly been isolated from *Uperoleia inundata* and *Uperoleia mjobergii* species and they are divided into two groups: the uperin 2.x (eg. uperin 2.1) and the uperin 3.x (e.g. uperin 3.1). All these uperins show antimicrobial activity with the uperins 3.x showing good activity against a wide

range of Gram-positive bacteria. Interestingly, uperin 1.1 is a neuroactive peptide<sup>1</sup>.

Among the uperin 3.x, uperin 3.5 (GVGDLIRKAVSVIKNIV-NH<sub>2</sub>), from the toadlet *Uperoleia mjobergii*<sup>1</sup>, is of particular interest since it is able to self-aggregate to form amyloid fibrils (see Fig. 52), whereas the other uperins do not aggregate (e.g. uperin 3.6), or aggregate with a much lower efficiency (e.g. uperin 3.4)<sup>3</sup>. Uperin 3.5 (U3.5) self-aggregates into fibrils rapidly, following dissolving in a phosphate buffer at pH 7.4 (Fig. 52)<sup>3</sup>.

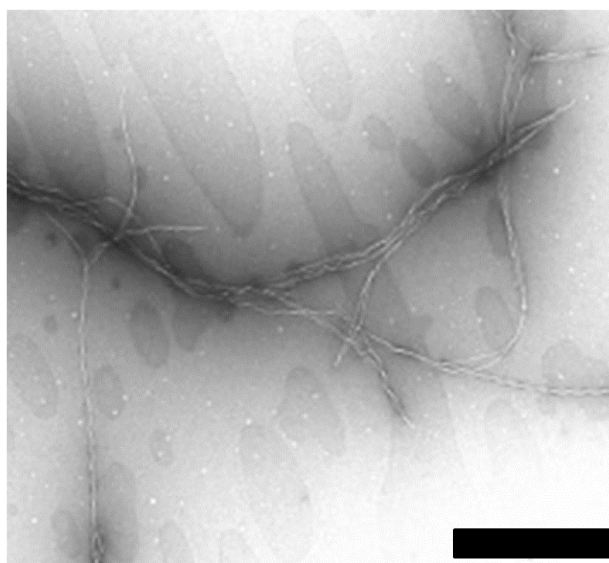


**Fig. 52:** TEM image of the fibrils produced by U3.5. The peptide concentration was 0.5 M in 50 mM phosphate buffer with 5% ethanol. Self-aggregation is complete in 70 min at 25 °C. Scale bar = 1  $\mu\text{m}$ <sup>3</sup>. Figure modified from Bowie et al.<sup>3</sup>

## 1.2 HDPs as amyloidogenic peptides

Some host defence peptides (HDPs) are known to aggregate in solution and/or with either liposomes or supported lipid bilayers (SLBs)<sup>4,5</sup>. They are known to adopt a unique protein quaternary structure named amyloid, as a result of this aggregation<sup>4,6</sup>. Typical examples are the amphibians peptides temporins B and L, magainin-2 and dermaseptins, which form amyloid fibrils in the presence of acidic phospholipids (i.e. DPPG, POPG)<sup>5,7,8</sup>. Presumably there are other antimicrobial peptides capable of forming fibrils, yet those listed in Table 7 are the only ones investigated to date<sup>5,6</sup>. Only a few of these

antimicrobial peptides, protegrin-1<sup>9</sup>, dermaseptin PD-3-7<sup>10</sup> and uperin 3.5<sup>3</sup> can form amyloid fibrils in solution.

**Table 6:** Examples of host defense peptides that form amyloid fibrils<sup>5,6</sup>.

Source	Peptide
<i>Humans</i>	LL-37
	A $\beta$ 40 and A $\beta$ 42
	Eosinophil cationic protein
	Lactoferrin
<i>Amphibians</i>	Magainin 2
	Dermaseptin PD 3-7 and S9
	Temporin B and L
<i>Insects</i>	Melittin
<i>Cow</i>	Indolicin
<i>Pigs</i>	Protegrin-1
<i>Bacteria</i>	Plantaracin
<i>Synthetic</i>	VP1

All these amyloidogenic HDPs share structural cross-beta ( $\beta$ ) sheet architecture that is characteristic of the amyloid fibril<sup>11</sup>. A number of amyloid proteins and peptides are thought to be the causative agents in neurodegenerative diseases, such as Alzheimer's disease (A $\beta$ : Amyloid- $\beta$  peptide)<sup>12-14</sup>, Parkinson's disease ( $\alpha$ -Synuclein protein)<sup>15,16</sup>, systemic disorders, such as type II diabetes mellitus (IAPP: islet amyloid polypeptide)<sup>16,17</sup> and haemodialysis-related amyloidosis (Beta<sub>2</sub>-microglobulin: A $\beta$ 2M)<sup>17,18</sup>.

Recently, a suggestion has been made that neurodegenerative diseases could be linked to the mal-functioning of antibodies in the host defense system<sup>6</sup>.

Hence, an investigation of the properties of U3.5 would be a valuable addition to the understanding of the structure and function of amyloidogenic peptides.

### 1.3 Amyloid structure

The biophysical definition of amyloid is a long filament with a diameter between 6 and 12 nm<sup>19</sup>. Each filament is composed of a repeating substructure, which consists of stacked hydrogen-bonded  $\beta$ -strands separated from each other by a distance of 4.7 Å (see Fig. 53). The  $\beta$ -strands run perpendicular to the fibril long axis, thus forming a cross- $\beta$  sheet of indefinite length, which extends laterally along the fibrils<sup>20</sup>. These associate via side-chain packing, with a distance from each other of  $\sim$ 6-11 Å. These stacked  $\beta$  sheets form a final protofilament by twisting around the central axis of the fibril<sup>11</sup>. Therefore, the protofilament represents the core structure of the amyloid fibrils although originating from different proteins and peptides<sup>12,21</sup>.

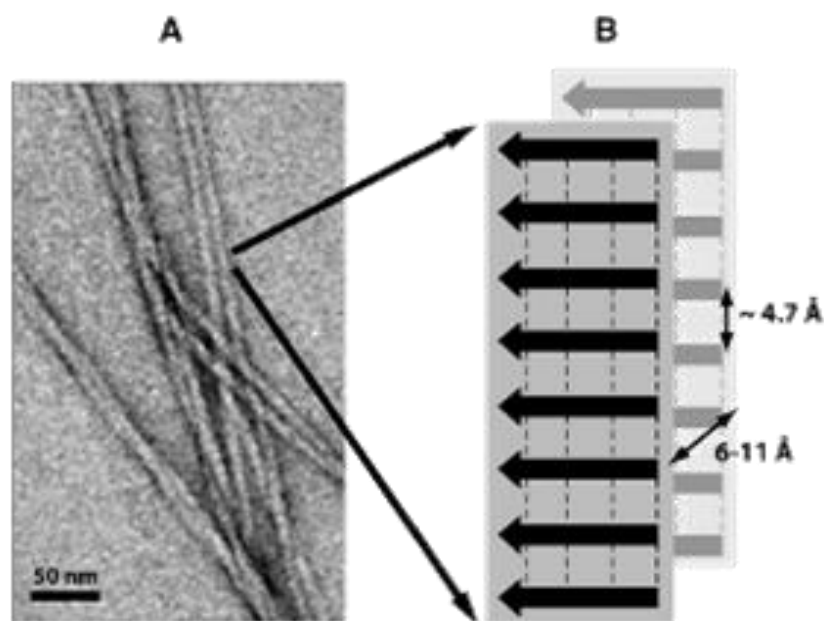


**Fig. 53:** (A) Visualisation of amyloid fibrils in negatively stained TEMs. (B) The schematic diagram of the cross- $\beta$  sheets in a fibril, with the backbone hydrogen bonds represented by dashed lines, indicating the repetitive spacing<sup>20</sup>.

#### 1.3.1 The process of amyloid formation

Typically, the generation of amyloid fibrils is via a nucleation-dependent process<sup>22</sup> and is adopted by various peptides such as the HDP temporins and

the A $\beta$  peptide<sup>4,6</sup>. Fig. 54 illustrates that this process can occur both in aqueous solutions (Fig. 54A) and within a membrane (Fig. 54B). In general, the formation of fibrils is described by an initial rate-limiting step, during which monomers of soluble peptides are converted into small oligomers (dimers, trimers) of  $\beta$ -sheet secondary structure (Fig. 54A and B). These oligomers then organize as nuclei, which assemble into higher-ordered protofibrils (Fig. 54). After this organizational lag phase, the elongation of these protofibrils occurs rapidly through the addition of monomers, with the resulting generation of mature fibrils. These fibrils then become insoluble and their deposition gives formation to amyloid plaques<sup>16</sup>.

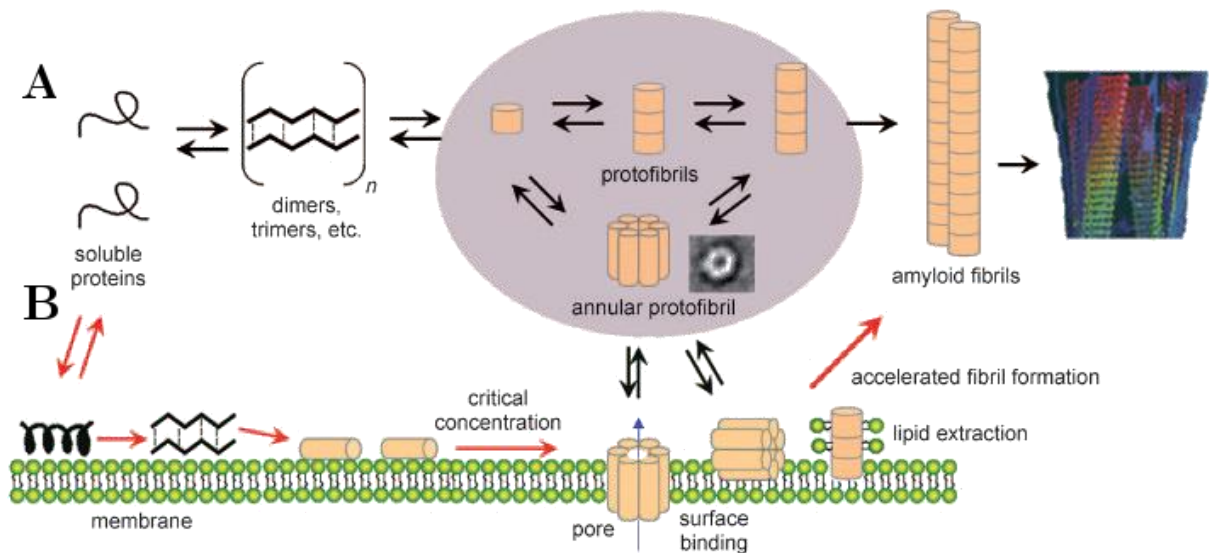


**Fig. 54:** Model for the interconnectivity between amyloid formation and membrane disruption. The process of amyloid-fibril formation is illustrated at the top **(A)** in which misfolded proteins are converted to  $\beta$ -sheet oligomers. These oligomers aggregate in protofibrils then into mature fibrils. The role of membranes in amyloid formation and toxicity is represented on the bottom **(B)** in which peptides are assumed to be in  $\alpha$ -helix conformation at the membrane interface. The accumulation of more peptides generates oligomers that can assume a  $\beta$ -sheet conformation. Once a threshold is reached, insertion into the membrane then occurs via a transmembrane pore, which creates leakages within the membrane layer. Preformed annular protofibrils can also form which can cause membrane thinning via a detergent-like mechanism, or causing the extraction and incorporation of lipids into the developing fibrils<sup>16</sup>.

## 1.4 The role of the membrane in fibrillogenesis

The presence of the membrane is believed to enhance the fibrillogenesis process of protein/peptides<sup>23</sup>. For this scenario, a model has been proposed (Fig. 55), which has been extrapolated from the four-step thermodynamic model of White & Wimley about the partitioning, folding, insertion and association of a  $\alpha$ -helix<sup>24</sup>.

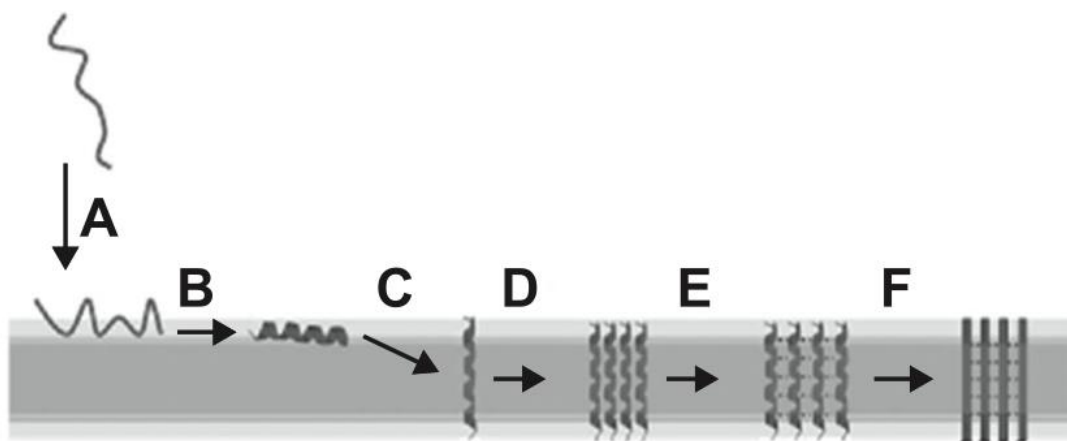


**Fig. 55:** The process of peptide association and insertion in a lipid bilayer<sup>4,6</sup>. Details are discussed in the text.

In this model, the membrane is involved into every step of amyloid formation<sup>4</sup>:

- A.** The membrane attracts and concentrates unfolded peptides by establishing electrostatic interactions between the basic residues of the polypeptides and the anionic lipid head-groups<sup>25</sup>.
- B.** The anisotropic environment of the lipid surface orients the binding peptide in a way that the hydrophobic domains are in contact with the lipid acyl chains, while the hydrophilic domains stay on the membrane surface in contact with the aqueous phase.

At the same time that the peptide enters the membrane interfacial environment, a change in the peptide conformation occurs, from random coil to  $\alpha$ -helix. This change is very rapid, beginning in approximately  $10^{-5}$  sec and is mainly promoted by the establishment of intramolecular hydrogen bonds<sup>4</sup>. Examples are

the peptides IAPP and temporins, which adopt an amphipathic  $\alpha$ -helical conformation upon associating with phosphatidylcholine membranes<sup>7,15</sup>.

- C.** Once a peptide concentration threshold is reached, peptide monomers and/or oligomers insert perpendicular to the membrane. This step is influenced by the physicochemical characteristics of the bilayer, for instance the lipid packing density; in particular, the presence of anionic lipids promotes the membrane intercalation of amphipathic peptides.
- D.** The presence of anionic lipids that are associated with peptide molecules neutralize the charges of the basic residues. This favours the peptide molecules to be aligned.
- E.** The alignment of these peptide molecules facilitates the oligomerisation of multiple  $\alpha$ -helices. The oligomerisation of the  $\alpha$ -helical peptide IAPP is an example of this kind<sup>15</sup>.
- F.** These oligomers change their conformation into a more energetically favourable  $\beta$ -sheet<sup>22</sup>. These  $\beta$ -sheet oligomers, which might form channel-like structures, aggregate further into inert and mature amyloid fibrils. During the generation of mature fibrils some lipid membrane could be extracted and incorporated into the developing fibrils resembling thus a disruptive process<sup>4,16</sup>.

An interesting point is that the peptide-to-lipid ratio (P/L) has an important role in the transition to  $\beta$ -sheet conformation. At high lipid ratios, the  $\alpha$ -helical conformation of the peptide adsorbed in the membrane predominates, because the interactions between  $\alpha$ -helices are hindered. Instead, once a threshold of peptide concentration is reached, the number of peptide-peptide interactions increase thus promoting the conversion to  $\beta$ -sheet<sup>16</sup>.

### ***1.4.1 Permeabilisation of the membrane by the protofibrils***

There is a general consensus that the mature amyloid fibrils are an inert species, whereas the prefibrillar intermediates (oligomers and protofibrils) cause damage to the cell membrane<sup>6,15,16,26</sup>. Regardless of the origin, these “toxic” protofibrils share some properties that are necessary to permeabilise the plasma membrane. Firstly, the amino acid composition of the monomers is not very important, however, the length of these peptide monomers should be between 3.3 to 4.5 nm, which corresponds to ~20 or more residues in order to span the width of the lipid bilayer (shorter peptides might dimerize)<sup>6</sup>. Furthermore, the sequence of the amyloid peptides should be amphiphilic, in order to both bind and concentrate with the polar head-groups at the membrane interface and interaction with the hydrophobic bilayer core<sup>4</sup>.

The permeabilisation of the membrane could happen at several stages: either at the initial interaction of the monomers with the membrane, i.e. after their binding but within the lag phase of fibril formation, or during the development of the fibril at the membrane surface<sup>15,16,27</sup>. Once a high peptide: lipid ratio is reached, leakage in the membrane can occur through the formation of stable pores or ion channels<sup>9,16</sup>. Otherwise, disruption of the lipid bilayer is also possible via a carpet<sup>27,28</sup>, or detergent-like mechanism<sup>15</sup>. Precisely, it has been suggested that a possible cause of membrane permeabilisation could be due to the physical state of the peptide molecules binding to the membrane: when oligomeric species are preformed in solution, a perturbative activity through pore formation occurs, while the binding of monomers or small oligomers could be responsible for carpet/ detergent action on the membrane<sup>12,15</sup>.

### ***1.4.2 Factors that influence membrane activity***

The formation of protofibrils and their action on the membrane is influenced by many environmental factors, such as pH, temperature and the composition of the solution they are dissolved in<sup>4,12</sup>. However, a significant contribution to amyloidosis comes from the lipid bilayer, both the biophysical

properties as well as its highly dynamic organization of the membrane<sup>4</sup>. The presence of anionic lipids has been shown to trigger the fibrillogenesis process, promoting the binding and the insertion of oligomers into the membrane and their conversion into  $\beta$ -sheet, which then results in cytotoxic activity<sup>4,16,27</sup>. The presence of cholesterol in the membrane also demonstrates an influence on the adsorption, the activity of peptides and on the fibrillisation process as well<sup>29,30</sup>. An example is the insertion and amyloid formation of the A $\beta$  peptide influenced by the molar concentration of cholesterol present in the membrane<sup>31,32</sup>.

## **1.5 Aims**

Early studies highlighted the antibacterial and anticancer activity of the self-aggregating uperin 3.5 (U3.5) peptide<sup>1,2</sup>. However, the membrane activity of this peptide has not been determined. U3.5 could adopt a carpet mechanism as observed for the related uperin 3.6, since they are both toxic to Gram-positive bacteria. Both these peptides have 17 amino acid residues in their sequence, which should be too little to span the lipid bilayer and hence formation of pores<sup>2,6</sup>. However, the formation of pores seems to be characteristic to amyloidogenic peptides, i.e. oligomeric species aggregate in anular protofibrils creating pores in the membrane<sup>15,16</sup>. Hence, the unusual combination of the properties of U3.5, which has been shown to aggregate in an amyloid manner<sup>3</sup>, and also has antimicrobial activity, provides an exciting opportunity to explore the role of fibrillar aggregates in antimicrobial action.

Thus, the properties of U3.5 were investigated with SLBs by QCM-D. This label-free technique has been previously successful in investigating interactions between artificial lipid membranes and amyloid peptides<sup>33-35</sup>.

In this study, QCM-D has been used to investigate the properties of U3.5 towards SLBs formed by DMPC, or by a mixture of DMPC and DMPG (4:1) v/v. The membrane composition was chosen to determine how this influenced the peptide association and if the peptide aggregation was affected, and/or behaved differently from non-aggregate state. Furthermore, the membrane consisted of

a mixture of DMPC and cholesterol, which was used to determine the effect of cholesterol on peptide properties.

Both the U3.5 monomers and prefibrillar forms showed a lytic activity, regardless of the presence of anionic lipid. However, a switch in the uperin behaviour, from a lytic to a “cell-penetrating” peptide, happened when cholesterol was introduced into zwitterionic membranes. The information extracted from this investigation could be helpful in understanding the association between amyloid formation and toxicity peculiar of some amyloid disease associating peptides.

## 2 Materials and methods

U3.5 was synthesised commercially by GenicBio (Shanghai, China), using L-amino acids and standard solid-phase methods, and were typically greater than 85 % pure (by High Performance Liquid Chromatography and MS)<sup>36</sup>. Peptide stock solutions of 400-800  $\mu\text{M}$  were made by dissolving a certain amount of peptide in ultrapure water and then stored at  $-80\text{ }^{\circ}\text{C}$ . For the experiments, aliquots from stock solution were diluted in phosphate-buffered saline (PBS) at the desired concentration.

Samples of U3.5 were incubated at  $37\text{ }^{\circ}\text{C}$  for a minimum of 15 hours before being used. In order to investigate the action of “fibrils” on the membrane, samples of U3.5, previously incubated, were spinned at 10.000 rpm for 15 min at  $4\text{ }^{\circ}\text{C}$ . The resulting supernatant was transferred in another eppendorf while the pellet was resuspended in PBS.

### 2.1 Buffer preparation

Sodium chloride ( $\geq 99.5\%$ ), potassium phosphate monobasic (anhydrous,  $\geq 99.0\%$ ) and potassium phosphate dibasic (anhydrous,  $\geq 98\%$ ) were purchased from Sigma-Aldrich (Castle Hill, Australia). Ultrapure water was used with an initial resistivity of  $18.2\text{ M}\Omega\cdot\text{cm}$  (Sartorius AG, Göttingen, Germany). Phosphate buffered saline (PBS,  $\text{pH } 7.4 \pm 0.1$ ) was prepared having 20 mM phosphate and either 100 mM (“high-salt”) or 30 mM (“low-salt”) sodium chloride in water.

### 2.2 Liposome preparation

1,2-Dimyristoyl-sn-glycero-3-phosphocholine (DMPC) and 1,2-dimyristoyl-sn-glycero-3-phospho-rac-(1-glycerol) (sodium salt) (DMPG) were purchased from Avanti Polar Lipids (Alabaster, USA). Cholesterol, chloroform ( $\geq 99.8\%$ ) and methanol ( $\geq 99.9\%$ ) were purchased from Sigma-Aldrich (Castle Hill, Australia). DMPC and cholesterol were dissolved in chloroform and DMPG was dissolved in chloroform/methanol (ca. 3:1) to create individual 5 mM stock

solutions. These solutions were then aliquoted into test tubes to obtain the desired lipid composition (DMPC/cholesterol 7:3 v/v, and DMPC/DMPG 4:1 v/v). The solvent was evaporated under a stream of nitrogen and the test tubes were then dried under vacuum. To prepare the liposomes, the lipids were resuspended in high-salt PBS (100 mM NaCl) to a lipid concentration of 0.5 mM and then incubated at 37 °C, vortexed and briefly sonicated (between 5 and 10 min) in a bath sonicator prior to use.

### **2.3 Modification of QCM-D sensor chips**

Absolute ethanol ( $\geq 99.7\%$ ), propan-2-ol ( $\geq 99.0\%$ ) and hydrogen peroxide (30%) were purchased from Merck (Kilsyth, Australia). Ammonium hydroxide solution (28%) was obtained from Ajax Finechem (Seven Hills, Australia). 3-Mercaptopropionic acid (MPA,  $\geq 99.0\%$ ) was purchased from Fluka, BioChimica (Buchs, Switzerland). The QCM-D sensor crystals used were polished, gold-coated, AT-cut quartz chips with a fundamental frequency of ca. 5 MHz (Q-Sense, Västra Frölunda, Sweden). Immediately before measurements the chips were cleaned in a solution of ammonium hydroxide: hydrogen peroxide: water (1:1:3 v/v) for 20–25 min at ca. 70 °C. The chips were then rinsed thoroughly with water. Surface modification with MPA was conducted by immersing a freshly cleaned chip into a 1 mM solution of MPA in propan-2-ol for at least 1 h. This creates a self-assembled monolayer of negative charge on the chip surface. Excess MPA was removed by rinsing with propan-2-ol. The chips were then dried under a stream of nitrogen and assembled into the QCM-D chambers ready for use.

### **2.4 QCM-D experiments**

QCM-D experiments were performed using the E4 system with flow cells (Q-Sense, Västra Frölunda, Sweden). The QCM-D instrument measures the relative changes to the resonance frequency ( $f$ ) and energy dissipation ( $D$ ) of the chip over the course of the experiment.  $\Delta f$  and  $\Delta D$  were measured simultaneously at the fundamental frequency and the 3rd, 5th, 7th and 9th harmonics. Data for the fundamental frequency is not presented as it is

inherently noisy and unreliable. The original data was processed in QTools (Q-Sense) before being exported for further analysis in OriginPro 8 (OriginLab Corp., Northampton, USA). All experiments were conducted at a temperature of  $22\pm 0.05$  °C and repeated at least three times. In a typical experiment, firstly, a lipid membrane was formed on the chip surface by the introduction of a liposome solution into the QCM-D chamber at a flow rate of 50  $\mu\text{L}/\text{min}$ . The liposomes adsorb onto the MPA-monolayer, deform, rupture and fuse together to form a lipid bilayer. Weakly attached liposomes were removed by washing with high-salt PBS (100 mM NaCl) at 300  $\mu\text{L}/\text{min}$  and any embedded liposomes were ruptured by washing with low-salt PBS (30 mM NaCl) at 300  $\mu\text{L}/\text{min}$ . This second washing step was introduced to ensure the formation of a homogeneous membrane and works by creating an osmotic pressure difference between the interior of the embedded liposomes (having a high salt concentration) and the low-salt exterior environment, which causes the liposomes to swell and then burst. Secondly, after a stable baseline was observed, 1.5 mL of peptide solution was introduced at 50  $\mu\text{L}/\text{min}$ . After the flow was stopped, the peptide was left to incubate with the lipid membrane for 30 min and then the chamber was rinsed with high-salt PBS.

## 3 Results

### 3.1 Control of aggregation

The action of fresh and mature uperin 3.5 (U3.5) interacting with a supported artificial membrane was investigated using a QCM-D. Samples of uperin were prepared by dissolving U3.5 into a PBS buffer solution having 100 mM NaCl and a pH of 7.4, at room temperature. The resulting solution was clear without any sign of aggregation. The U3.5 concentration used for all the experiments reported here was 25  $\mu$ M. This concentration was chosen because it showed a clear and consistent aggregation visible to the naked eye, which was not possible to detect at lower concentration.

Samples of “freshly” prepared U3.5 were then incubated at 37 °C for a minimum of 15 hours, in order to examine mature U3.5 aggregates. After 15 hours, a cloudy formation suspended in these solutions was visible to the naked eye. This characteristic formation was interpreted as peptide aggregation, in concordance with the finding of Calabrese’s work, which demonstrated the ability of U3.5 wild type to aggregate in phosphate buffer<sup>36</sup>. However, it was assumed that this solution was a heterogeneous mixture as not all the oligomers aggregated and some remained in solution. In some samples of the incubated peptide, centrifugation was used to separate the aggregated pellet from the supernatant. In this way the components of the aggregates could be investigated separately, these being the fibrillar species and the supernatant. Thus, detection of variations in the mechanism exerted by the aggregated species could be compared with soluble oligomers on the membrane. It is important to mention that in the heterogeneous sample that was fractionated, the concentrations of the two phases (fibrillar and supernatant) resuspended in buffer could not be determined.

#### 3.1.1 DMPC versus DMPC/ DMPG (4:1) SLBs

Firstly, the four U3.5 samples, “fresh”, incubated, supernatant and pellet U3.5 were added both to DMPC and DMPC/DMPG (4:1) membranes. As shown in Fig. 56 increase in the frequency versus time, consistent with the removal of

mass attached to the sensor area, was observed. Thus, the QCM-D data is illustrating a lytic action on both membranes.

The DMPC and DMPC/DMPG (4:1) data will be described in more detail in the next section.

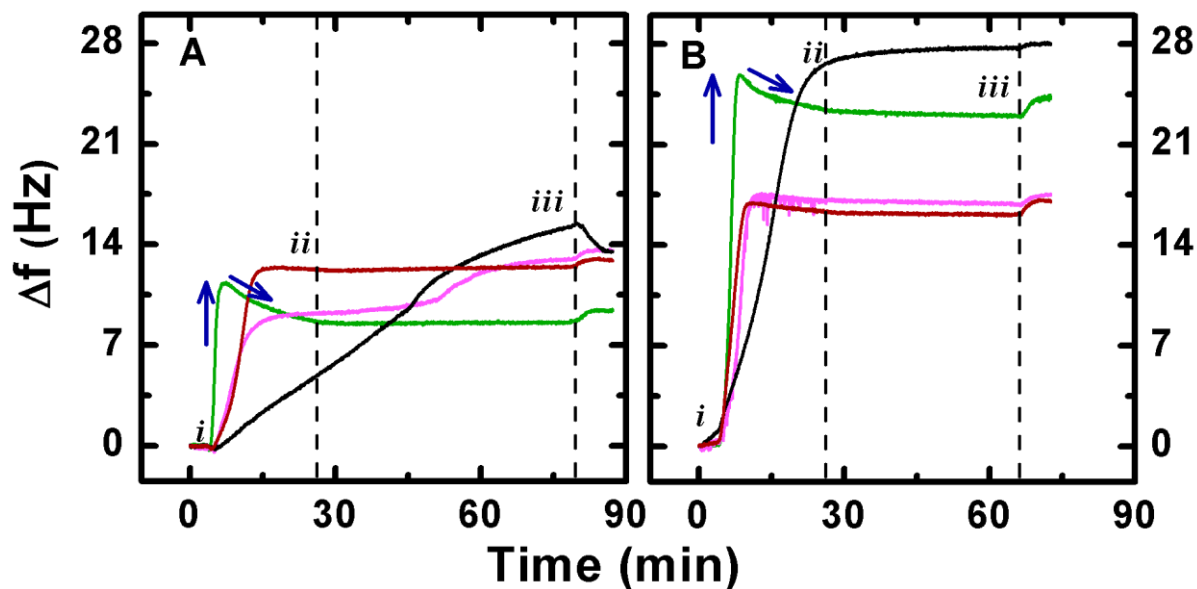


**Fig. 56:** Typical  $\Delta f$  versus time plots of U3.5 wild type interacting with supported membranes of DMPC (A) and DMPC/DMPG (4:1) (B). Time point *i* indicates the beginning of peptide action, whereas *ii* denotes termination of the peptide flow (highlighted also by a vertical line). The rinse with PBS solution is also highlighted by a vertical line corresponding to point *iii*. Traces correspond to fresh (green), incubated (purple), supernatant (red) and pellet (black) as described in the text. The initial peptide concentration was 25  $\mu\text{M}$ . The 7<sup>th</sup> harmonic is represented.

### 3.1.1.1 Uperin action on DMPC

The action of U3.5 towards the DMPC membrane is disruptive regardless of the sample which is introduced. However, some small variations were observed among these preparations as illustrated in Fig. 56A.

The “fresh” (unaggregated) uperin showed the most rapid loss of membrane and two distinct stages were clearly observed (green trace). The first stage reached a maximum frequency at about 11 Hz (illustrated by a vertical arrow, in Fig. 56A). After  $\sim 5$  min, a small ( $\sim 2.5$  Hz;  $44.5 \text{ ng/cm}^2$ ) addition of mass (second arrow) occurred until the flow was ceased at  $\sim 25$  mins. No further

change in frequency (mass) was observed during the equilibration phase, (25–80 mins) and there was only a miniscule change during the final wash step.

The uperin peptide, when incubated (purple line), initially showed a disruptive action similar to that observed for the fresh sample on DMPC membrane, Fig. 56A. However, in this case there was only one disruptive stage observed before the flow ended (point *ii.*). A plateau in the frequency was maintained from the initial flow to the equilibrium phase and before a second disruptive stage occurred at ~50 mins. This later process showed a monotonic increase that exhibited similarities to the pellet (from the centrifuged sample, discussed below). This second stage in the process is most likely due to the physical properties of the fibrillar materials present in the aged sample.

The data for the remaining two samples shown in Fig. 56A, are the pellet (black) and the supernatant (red) derived from an incubated uperin sample that has been fractionated by centrifugation. As expected, the supernatant (red trace) showed the disruption characteristics similar to the incubated and the “fresh” uperin, although the second stage, which was observed for the “fresh” uperin, is not evident.

The pellet (Fig 56A, black trace) also showed disruption at the DMPC membrane although, unlike the other samples, the disruption was monotonic with a rise in frequency steadily progressing over time, irrespective of whether the solution was flowing into the chamber or equilibrating. As noticed earlier for the incubated uperin sample, this steady disruption appears to be a feature of samples that are rich in fibrillar material.

### 3.1.1.2 *Uperin action on DMPC/DMPG (4:1) membranes*

DMPC/DMPG (4:1) introduces 20% anionic lipid into the membrane composition, representing a bacterial mimetic surface. As observed on DMPC, the uperin samples acted similarly with a net disruptive activity on DMPC/DMPG (see Fig. 56B). However, the removal of mass from the DMPC/DMPG membrane was significantly greater for this sample. In fact, almost twice the amount of lipid mass was removed by the uperin sample whether in the “fresh” or the pellet formulation.

As observed for the action of “fresh” U3.5 on DMPC, on DMPC/DMPG the two distinct phases are observed in the curve of “fresh” U3.5. However, on DMPC/DMPG, the initial loss of mass ( $\sim 25$  Hz) is much greater and preceded the second acquisition phase (observed during the flow). As a consequence, the net  $\Delta f$  of 23 Hz is maintained during the equilibration phase of the experiment. The incubated (purple) and supernatant (red) U3.5 samples behaved in a similar manner with rapid disruption to the membrane occurring before the flow had ceased (i.e. the sample was still entering the chamber).

The most significant difference observed by QCM upon introduction of the pellet was observed towards the anionic DMPG membrane. The pellet caused disruption on DMPC/DMPG that was more rapid than on DMPC, and ceased when the flow stopped. This resulted in  $\sim 28$  Hz increase in frequency during the equilibration phase of the experiment.

This dramatic increase in rate and amount of material removed by the U3.5 pellet in the presence of DMPG lipid points towards an electrostatic component to the membrane activity of fibrils, which will be discussed later.

### 3.1.1.3 *Rate of the frequency versus time*

The first derivatives of the  $\Delta f$  versus time traces are able to provide some information on the rates of the peptide-membrane interaction, especially when these experiments are done with identical flow and equilibrium conditions. Thus, the first derivatives ( $\delta f/\delta t$ ) for the experiments are presented in Fig. 57. This analysis has been done to highlight the number and nature of each interaction as well as the rate. Generally, the traces in Fig. 56 show either one rapid (9-12 Hz/min) or two slower steps ( $< 5$  Hz/min), during the first 15-20 minutes of the U3.5 interaction with the membrane as well as the rate. Moreover, in the presence of anionic (DMPC/DMPG) lipids the rates are faster for all the samples examined. However, some variations were apparent and are compared (DMPC vs DMPC/DMPG) below.

The “fresh” U3.5 sample acted rapidly towards both DMPC and DMPC/DMPG membranes in what appeared, despite the two apparent stages, observed in the  $\Delta f$  vs  $t$  data. The incubated U3.5 peptide, however, showed two

clear events; (i) a slower 3.5-4 Hz/min and a faster  $\sim 6$ -11 Hz/min, however, the pellet was the slowest, with a very low rate, close to zero. Indeed, the pellet disrupted the DMPC membranes with a constant speed, since its rate was nearly zero ( $\sim 0.2$ ), as illustrated by the black trace in Fig. 57A. The supernatant sample was similar to the aged U3.5 on DMPC but behaved more like the “fresh” sample on DMPC/DMPG, albeit more slowly.

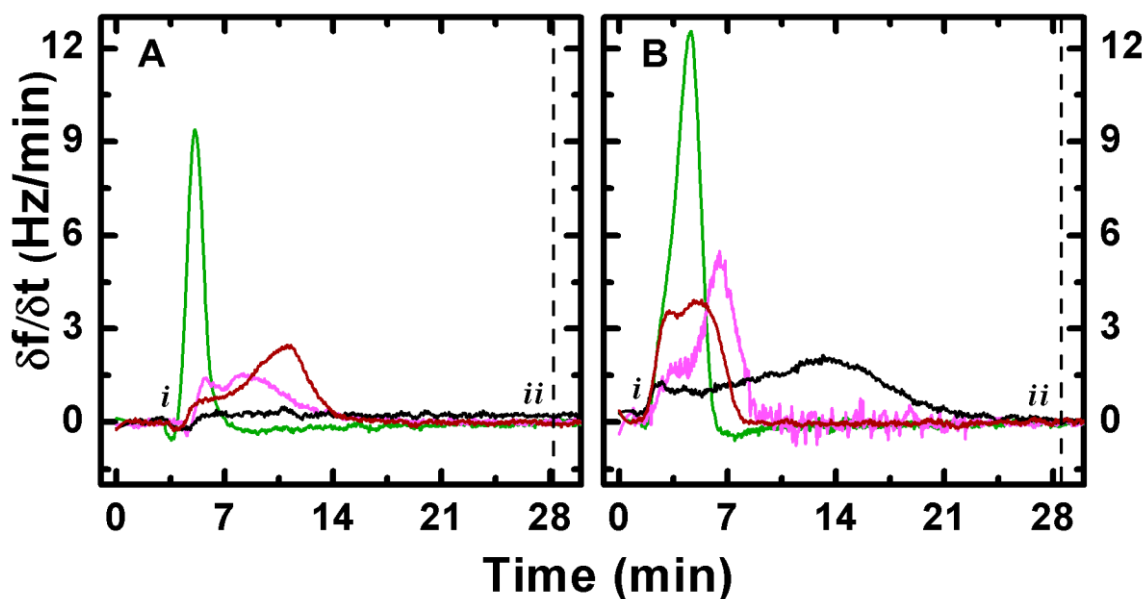


**Fig. 57:** Typical first derivative of  $\Delta f$  versus time plots of U3.5 interacting with supported membranes of DMPC (A) and DMPC/DMPG (4:1) (B). Time point *i* indicates the beginning of the introduction of the peptide solution, whereas *ii* denotes termination of the peptide flow (highlighted also by a vertical line). Traces correspond to fresh (green), incubated (purple), supernatant (red) and pellet (black) as described in the text. The initial peptide concentration was 25  $\mu$ M. The 7<sup>th</sup> harmonic is represented.

#### 3.1.1.4 *Trans-membrane interaction*

Thus far, only the  $\Delta f$ -t data has been described for the U3.5 samples. However, inclusion of the dissipation data, obtained concomitantly with the frequency is displayed as plots of  $\Delta f$  versus  $\Delta D$  in Fig. 58 (“ $\Delta f$ - $\Delta D$  plots”) for the “fresh” U3.5 wild type interacting with DMPC and DMPC/DMPG (4:1) membranes. In Fig. 58, the coordinates (0,0) indicate the point where the peptide solution was introduced into the QCM chamber, cf Fig. 56. The last point in each trace corresponds to the end of the incubation stage (*iii*, in Fig. 56) just before the PBS buffer wash. The “fresh” U3.5 demonstrated a similar

interaction for both DMPC and DMPC/DMPG membranes. Furthermore, all four harmonics (3<sup>rd</sup>, 5<sup>th</sup>, 7<sup>th</sup> and 9<sup>th</sup>) had very similar traces, but the 3<sup>rd</sup> harmonic showed the greatest disruption, consistent with a disruption process prevalent on the membrane surface. A more dramatic disruption occurred at the surface when DMPG was included in the membrane since the  $\Delta f$  values between the 3<sup>rd</sup> and the 9<sup>th</sup> overtone is 11 Hz, whereas this  $\Delta f$  is 2.5 Hz with DMPC membranes. Interestingly, the insert in Fig. 58A reveals an insertion, decrease in  $\Delta D$  with only a small change in  $\Delta f$ , before the disruption on DMPC. Whereas, for the DMPC/DMPG surface, the disruption was immediate and effective in loss of the membrane.

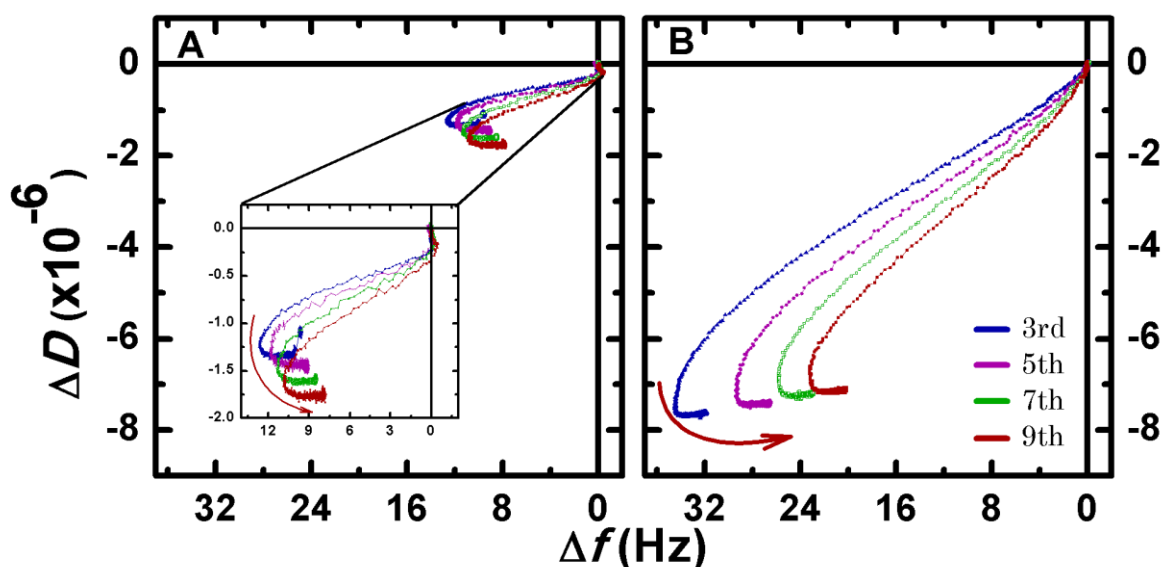


**Fig. 58:** Typical  $\Delta f$ - $\Delta D$  plots for the interaction of 25  $\mu\text{M}$  freshly prepared U3.5 in PBS on a DMPC (A) or DMPC/DMPG (4:1) (B) artificial membrane. The response of the 3<sup>rd</sup>, 5<sup>th</sup>, 7<sup>th</sup>, and 9<sup>th</sup> harmonics is presented. The wash with PBS is not included.

### 3.1.2 The role of cholesterol in DMPC membrane

The U3.5 samples were studied with SLBs composed of DMPC and cholesterol at 30% mol. The addition of cholesterol 30 mol % to the DMPC creates a more mammalian mimetic membrane. The  $\Delta f$  vs time plots relating to U3.5 interacting with a DMPC/cholesterol bilayer are illustrated in Fig. 59. The presence of cholesterol showed a dramatic change in the membrane properties. In each sample, “fresh”, incubated, supernatant and pellet, the uperin bound to

the bilayer instead of disrupting the membrane. However, this interaction was slightly different for all the conditions tested.

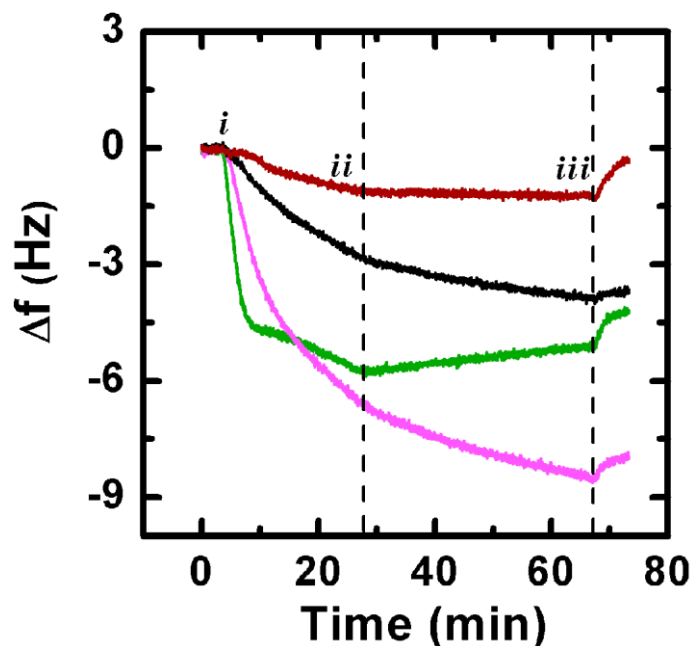


**Fig. 59:** Typical  $\Delta f$  versus time plots of U3.5 interacting with supported membranes of DMPC/cholesterol 30 mol %. Time point *i* indicates the beginning of peptide action, whereas *ii* denotes termination of the peptide flow (highlighted also by a vertical line). Traces correspond to fresh (green), incubated (purple), supernatant (red) and pellet (black) as described in the text. The initial peptide concentration was 25  $\mu\text{M}$ . The 7<sup>th</sup> harmonic is represented.

As shown in Fig. 59, the largest binding was observed for the “fresh” and the incubated U3.5 (-6.5 and -5.8 Hz, respectively). The minor binding corresponded to the supernatant and the pellet samples (< 3 Hz). An obvious reason is that the fractioned samples interacted less than the “fresh” or incubated U3.5 as these samples were lower in concentration than 25  $\mu\text{M}$ . Moreover, from the same figure, the incubated and the pellet samples appeared to continue to bind the membrane even after the flow was stopped. At the same time instead, the “fresh” U3.5 appeared to slowly disrupt the membrane.

The final step in these experiments was the rinse with PBS buffer, which showed some variation between samples. The buffer wash removed 1-1.5 Hz for the “fresh” and supernatant samples; less than 1 Hz for incubated and effectively no mass loss for the pellet sample on DMPC/cholesterol. Thus, the presence of fibrils in the uperin 3.5 samples seem to favour a strong interaction

with the membrane, although the small changes in frequency (mass) means that there is considerable error in these data.

### 3.1.2.1 DMPC/cholesterol rate analysis

The analysis of the rate of binding for all the uperin samples at the DMPC/cholesterol membrane is shown in Fig. 60. Overall, the rate of interaction was much slower compared with the DMPC membranes (cf Fig. 57A). However, similar trends were found with the “fresh” uperin showing the highest rate at 1.5 Hz/min among all the conditions undertaken. The incubated U3.5 showed two processes, similar to those found on DMPC (cf Fig. 57A). Finally, the rate observed for the supernatant and the pellet was approximately zero and was difficult to determine with precision the process.

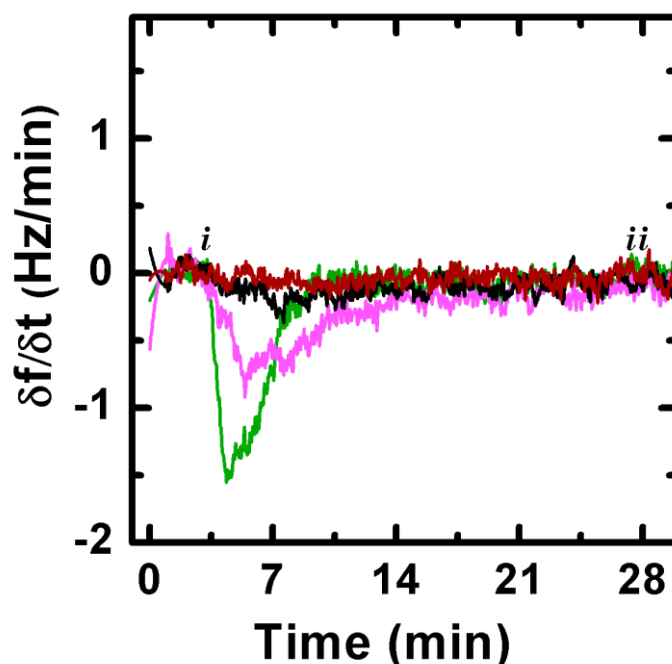


**Fig. 60:** Typical first derivative of  $\Delta f$  versus time plots of U3.5 wild type interacting with supported membranes of DMPC/cholesterol. Time point *i* indicates the beginning of peptide action, whereas *ii* denotes the termination of the peptide flow (highlighted also by a vertical line). Traces correspond to fresh (green), incubated (purple), supernatant (red) and pellet (black) as described in the text. The initial peptide concentration was 25  $\mu\text{M}$ . The 7<sup>th</sup> harmonic is represented.

3.1.2.2 DMPC/cholesterol  $\Delta f$  vs  $\Delta D$  plots

The harmonic data were once again used to assess if the interaction by U3.5 was trans-membrane at the DMPC/chol bilayers. The “fresh” peptide showed complete overlap of the harmonics (Fig. 61A) supporting a trans-membrane insertion spanning through the membrane layer. In conjunction with the dissipation values, a two steps process is observed. The initial decrease in frequency (-4.5 Hz) and a small increase in dissipation ( $0.6 \times 10^{-6}$ ) is followed by a decrease in the dissipation, which reaches a value very close to zero before beginning to stabilize. Then, at the point where the flow is halted, a very slow disruption process initiates, resulting in the dissipation reaching approximately zero and the frequency increasing by 1 Hz. The incubated uperin (Fig. 61B) shows an approximately linear increase in dissipation as the mass is binding. Interestingly, the harmonics overlap until  $\sim -6$  Hz is reached, then a small spread occurs, albeit much less than observed for the DMPC or DMPC/DMPG membranes. It seems that the prevalent presence of fibrils in the sample (see the traces for the pellet) promoted a higher binding and affected the viscoelastic properties of the system assessed by the steady increase in dissipation.

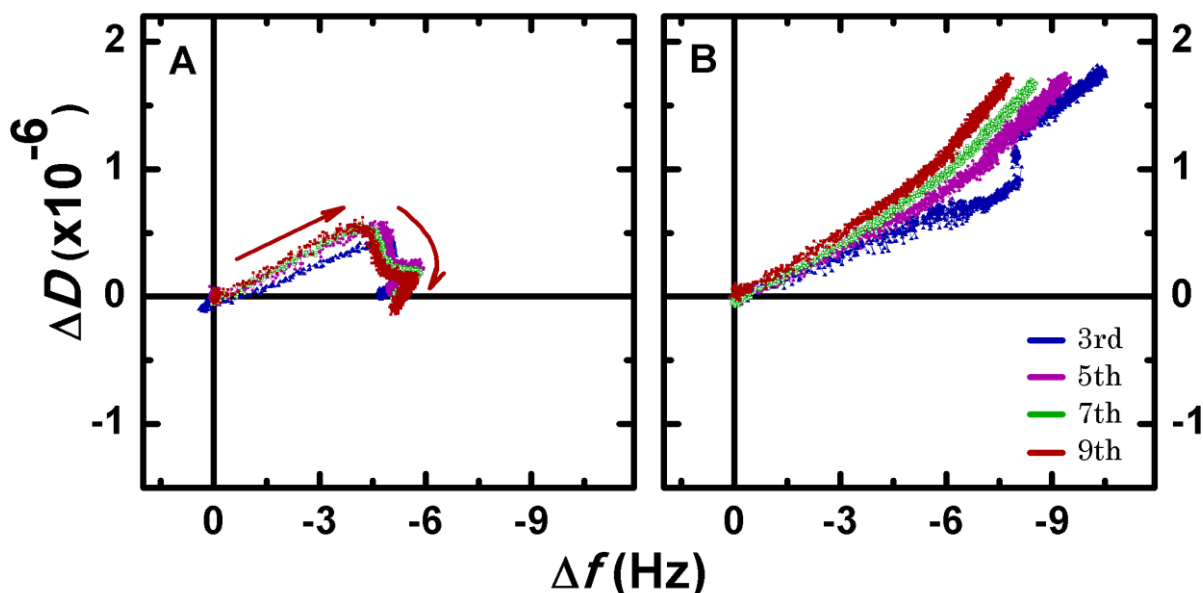


**Fig. 61:** Typical  $\Delta f$ – $\Delta D$  plots for the interaction of a 25  $\mu\text{M}$  of either “fresh” (A) or incubated U3.5 (B) in PBS DMPC/cholesterol SLBs. The response of the 3<sup>rd</sup>, 5<sup>th</sup>, 7<sup>th</sup>, and 9<sup>th</sup> harmonics is presented.

## 4 Discussion

### 4.1 DMPC membranes

U3.5 is an amphibian antimicrobial peptide that has the unusual ability to aggregate in amyloid-like fibres<sup>3</sup>. Moreover, it has the peculiarity to aggregate in saline buffer solutions, whereas other AMPs (i.e. magainin 2, LL-37 and melittin) aggregate only in the presence of acid phospholipid bilayers<sup>5</sup>. However, the ability of U3.5 to aggregate does not appear necessary for the membrane activity. The QCM data clearly show that the presence of monomers and small oligomers in the “fresh” U3.5 samples, incubated and centrifuged samples are sufficient for disrupting the membrane, as shown in Fig. 56. Thus, uperin behaves as many other amyloidogenic peptides (i.e. A $\beta$  peptide and the  $\alpha$ -synuclein peptide) that show membrane toxicity even at early stage of the aggregation process<sup>12,37</sup>.

QCM experiments show that U3.5 does not require the presence of anionic lipids in the membrane for disruption to occur, unlike some literature suggestions<sup>6,7</sup>. Far-UV CD spectra showed U3.5 assuming a helical structure in the presence of 2,2,2-Trifluoroethanol(TFE) 50% v/v<sup>36</sup>. The adoption of this  $\alpha$ -helical structure is presumed to be the driving force for the interaction and disruption of the membrane<sup>4,6</sup>. The peptide concentration used in this study (25  $\mu$ M) was more than enough to have disruption by uperin.

#### 4.1.1 *The disruption mechanism*

The membrane disruption that was observed for DMPC surfaces could happen through a detergent-like manner adopted by monomers and/or small protofibrils that are presumably always present in fresh and aged samples. This interaction causes the thinning, and splitting of the bilayer, i.e. resulting in disruption<sup>15</sup>. Moreover, all the conditions examined present the same trend. This justifies an overall detergent action by increasing the local concentration of the peptide on the membrane; originally by the monomers or small oligomers coating the membrane surface and afterward by membrane-bound amyloid<sup>38</sup>.

Thus, the resulting bilayer could be thinner following the removal of lipids from the outer leaflet. Alternatively, pore holes could initiate a trans-membrane interaction followed by removal of membrane material<sup>15</sup>. The latter scenario seems likely for U3.5 samples that disrupted the whole membrane layer corresponding to a change in frequency between -5 Hz and -23 Hz. The “incomplete” disruption of the membrane was not because of the shortage in the availability of U3.5 since the disruption was completed before the peptide solution ceased. Thus, a hypothesis is that uperin acted in localized areas of the membrane. As a consequence, a hypothetical scenario is that the resulting membrane has a riddled appearance with breaches that are the result of the disruptive action of U3.5.

From Fig. 56A, it is notable that during the introduction of “fresh” U3.5 on the QCM sensor, the lysis of the membrane was immediately followed by a “re-deposition” of material, which was between 2 and 3 Hz. Most probably, this “re-deposition” consisted of U3.5 only since the peptide-lipids micelles, originating during the membrane disruption, were flushed away from the sensor during the flow. Furthermore, this “re-deposition” consisted probably of monomers present in the “fresh” U3.5 sample since this behaviour was not observed with the incubated and pellet samples. Besides, the supernatant sample did not show this feature, most probably because the concentration, which was not determined, was enough for the membrane disruption only.

This “re-deposition” could be driven by electrostatic interactions between U3.5, which contains three positive amino acid residues, and negatively charged surfaces such as membranes or SAMs, i.e. MPA. In this case, MPA, which was exposed after the disruption of membrane areas, could enhance the adsorption of U3.5 at localized surface areas by electrostatic interactions. This localized binding might initiate the aggregation/fibrillation of U3.5, as already showed in the case of other amyloid peptides such the A $\beta$  peptide that adsorbed on the surface of vesicles containing positively charged phospholipids, which lead to a higher fibril nucleation rate<sup>39</sup>.

### 4.1.2 The “leaky slit model”

The entire process of membrane disruption followed by a “re-deposition” of “fresh” U3.5 could be explained by the “leaky slit model”<sup>7,28</sup>. This model has been already proposed for AMPs forming fibrils such Plantaricin A<sup>28</sup> and Temporins<sup>7</sup>, where these peptides insert into the membrane with their hydrophobic side binding the bilayer. The hydrophilic side of these peptides, instead forces the opposing contacting bilayer to assume a highly positive curvature. The membrane thus presents permanent leakages (called the “leaky slit”) (see Fig. 62). The peptides in the membrane form oligomers, which are disposed linearly in an alpha-sheet structure, like a ribbon<sup>40</sup>. As the  $\Delta f$  vs  $\Delta D$  plots show for U3.5 on DMPC (Fig. 58A), a stiffening of the membrane results in the second “aggregation” phase.

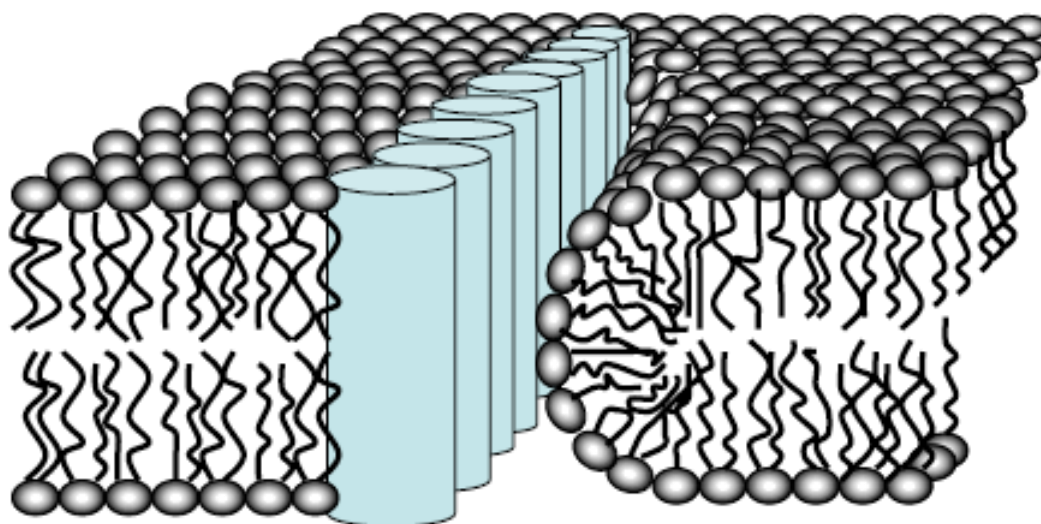


**Fig. 62:** The proposed “Leaky slit “model for the membrane disruption by an amphipathic AMP oligomer: a fibrillar ribbon, consisting of a peptide oligomer, is formed within the membrane<sup>28</sup>.

The aggregation stage observed is very rapid (Fig. 57) and could be initiated by the presence of the membrane<sup>7,15,23,39</sup> or more likely to the exposure of a negative charge MPA<sup>41</sup> that enhances this process. Further support for this interpretation was provided by data from the supernatant addition to DMPC and DMPC/DMPG membranes, although the concentration is unknown in these cases and may not be sufficient to overcome the peptide threshold required<sup>16</sup>. The “re-deposition” stage does not occur in the case of the incubated U3.5. That is, the heterogeneity of this sample seems to discourage further membrane

binding. Presumably the incubation of U3.5 results in fibrils formed in solution thus reducing the number of monomers or small oligomers required to establish local high concentrations on the membrane<sup>15</sup>. Indeed, the lytic activity of the incubated sample on the DMPC bilayer is much slower (Fig. 57A) and follows at a much later time if compared with the “fresh” U3.5 sample. Therefore, it could be that the membrane disruption is initiated by the presence of monomers plus small oligomers, as the initial  $\Delta f-t$  data for the supernatant and the incubated traces suggest in Fig. 57A, but is followed by the action of protofibrils. The slower removal of mass from the membrane for the incubated U3.5 could be due to the action of protofibrils, which fragment upon exposure to the lipid layer since these protofibrils are less stable compared to mature fibres<sup>15,42</sup>. Alternatively, the reverse process of fibrillogenesis could be active, i.e. oligomers could be slowly dissociating from the amyloid fibrils and permeabilising the bilayer, a phenomenon that has been already reported by Martins and co-workers with the disassembling of A $\beta$ 42 amyloid fibrils by DOPC liposomes<sup>43</sup>. This scenario is also valid for both the aged sample and the pellet. Finally, another possible reason for the disruption of the DMPC membrane being slow could be that the size of some amyloid aggregates present in the flow affects their speed, slowing the arrival time at the membrane surface.

## 4.2 DMPC/DMPG (4:1) artificial membranes

U3.5 interacts in a similar way with DMPC/DMPG (4:1) membranes, the only difference being that the removal of membrane is more rapid and extensive. Moreover, the membrane disruption was greater on the membrane surface since the highest mass loss was observed by the 3<sup>rd</sup> overtone. The influence of an increase in negatively charged lipids has been reported previously in the literature: i.e. that the lipid composition of the membrane has a big influence on the peptide interaction and aggregation. Of particular note is the presence of negatively charged lipids that promote the peptide association and aggregation on the membrane, thus reducing time in the formation of protofibrils<sup>15,16</sup>.

Interestingly, the presence of the anionic lipids also triggered a different membrane action for the pellet, in which membrane disruption ended before the peptide flow was stopped. This could be explained by an increase in the breakage of protofibrils by the anionic lipids as the rate data (first derivative of the  $\Delta f-t$ ) supports an initial step followed by a slower process. Otherwise, the presence of more homogeneous sample did not affect the velocity of the incoming flow into the QCM chambers.

### 4.3 DMPC/Cholesterol

The nature of the interaction between U3.5 with the membrane is influenced by many factors including the composition and biophysical properties of the membrane, the temperature, and the pH of the buffer solution<sup>4,12</sup>. However, it was a remarkable switch in membrane activity that was observed upon addition of cholesterol to a membrane. U3.5 no longer showed any lytic activity towards the supported bilayer of DMPC/cholesterol (30 mol %). All the U3.5 samples were able to insert into the membrane, as shown by the  $\Delta f-t$  data in Fig. 59. Similar action has been shown by Ji et al.<sup>32</sup> with the A $\beta$  peptide. Here they reported A $\beta$  peptide insertion into the membrane layer and a reduction in aggregation into protofibrils or fibrils when the cholesterol:phospholipids ratio is greater or equal to 30 mol %<sup>32</sup>.

The rate at which uperin adsorbs on the membrane is also much slower than the disruption observed on pure DMPC layers (Fig. 57A). Presumably, this can be explained by the permeability of the membrane decreasing due to the presence of cholesterol, which influences the membrane fluidity, the permeability to molecular species and the dielectric properties of the membrane<sup>12,44</sup>. Cholesterol also prevents the crystallization of the hydrocarbons and increases the lateral packing of the lipids thereby establishing tight interactions, especially for saturated hydrocarbon chains, therefore making it more difficult for peptides to insert into the membrane<sup>7,45</sup>. Hence, it is possible that the insertion process into the membrane by monomers or prefibrillar species is reduced considerably and is slower. In the case of “fresh” U3.5, the membrane action can be broken down into two steps, as illustrated in Fig. 61A.

The first step consists of an initial weak binding, which is followed by a decrease in the viscoelasticity of the bilayer with any further binding. This initial binding is interrupted when the flow is terminated and membrane reorganization, with the release of some molecules, creates a stiffer membrane layer overall.

The incubated U3.5 sample showed the greatest membrane binding overall, which could be due to the presence of more lipid molecules on the surface (approximately 4 Hz more), or it could be that the increased fluidity of the membrane, by cholesterol, increased the affinity towards fibrillar peptide aggregates<sup>46</sup>. In addition, the continuation of binding, which occurs for incubated U3.5 once the peptide flow finished, could be due to an enhanced fibrillation to mature aggregates that would require removal of uperin molecules from the available solution<sup>47</sup>.

## 5 Conclusions

The ability of U3.5 wild type to aggregate can be confirmed by a simple examination to the naked eye. However, QCM experiments reported here confirmed that the presence of fibrillar material is not necessary for the disruption of a DMPC or DMPC/DMPG membrane. These studies provide an important insight into the peptide aggregation phenomena as the aggregation, which occurs in buffer solution containing salt, and the lytic activity of the U3.5 peptide are features that the most characterized amyloid peptides, such as A $\beta$ , IAPP and  $\alpha$ -synuclein are shown to have as well<sup>15,16</sup>. As consequence, the antimicrobial activity exhibited by some typical amyloid peptides<sup>48</sup> can be justified as an application of the classical lytic mechanisms adopted by the “standard” AMP. Conversely study of amyloid peptide action on the membrane highlight the fundamental role of aggregation, which can be seen as an intermediate state also for many AMPs<sup>5,6,28</sup>.

The presence of cholesterol in DMPC showed an important switch in the mode of action of the uperin sample. The uperin samples all interacted the same way towards DMPC/cholesterol, now acting in a “cell-penetrating” action

instead of “lytic” action observed on DMPC. However, further investigation using various ratios of cholesterol/lipid could give more information about the role of the cholesterol in this process. Further studies will be conducted in examining the peptide concentration threshold necessary to detect the concentration where the association with the membrane is followed by a lytic action.

## 6 Appendix:

### 6.1 The action of U3.5 retro on DMPC artificial membranes

A reverse sequence of U3.5 was synthesised (VINKIVSVAKRILDGVG-NH<sub>2</sub>) with the aim to explore the role of primary structure on the aggregation. No fibril formation was detected to the visible eye for either incubated or freshly prepared U3.5 (retro).

These samples were studied by QCM on DMPC membranes. The retro U3.5 acted on the membrane with the same mechanism adopted by the U3.5 wild type. The mass removed by the retro U3.5 was greater on the membrane surface, as showed in the Fig. A1-B. The larger increase in frequency was observed for the 3<sup>rd</sup> harmonic, which was approximately 4 Hz, whereas for the 9<sup>th</sup> harmonic, the removal corresponded to only 0.9 Hz. Interestingly, also for the retro U3.5, “fresh” samples, the presence of an adsorption process following the disruption was apparent and was more accentuated for the 9<sup>th</sup> harmonic.

Interestingly, introduction of the PBS wash on the residual material on the membrane (Fig. A1-A, step *iii*) caused a decrease in frequency, indicating peptide insertion into the membrane. This usually is an increase in the frequency due both to loosened material having been observed as washed away or to sensitivity to the bulk solution<sup>49</sup>. However, in this case the reason is most probably the result of residual monomers of uperin that were still in the tubing when all of peptide solution was introduced. Thus, this binding affected the structural properties of the membrane since the dissipation increased slightly (data not shown).

Interestingly, the disruption of the membrane was minor for the retro U3.5 (3Hz for the “fresh” sample) than for the U3.5 wild type (11 Hz for the “fresh” sample). This origin of this weaker activity is not known, however it could be because the retro and the wild type U3.5 could have a different conformation upon contact with the membrane, resulting in the retro U3.5

showing a lower affinity for the lipids than the U3.5 wild type. Overall, these results and the absence of aggregation for the retro U3.5 were not able to support the notion that the oligomeric species may be contributing to membrane disruption.

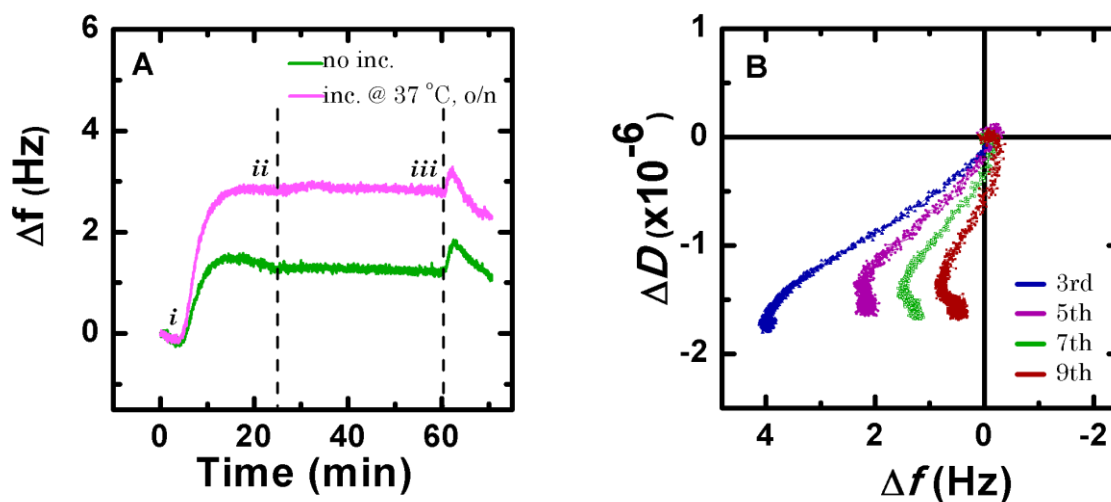


**Fig.A1:** Typical interaction between 25  $\mu\text{M}$  retro U3.5 and SLBs of DMPC. Panel A illustrates the  $\Delta f$  versus time plots, for the 7<sup>th</sup> harmonic, of preincubated (pink trace) and no incubated uperin (green trace). The time points *i* indicate the beginning of peptide action, whereas *ii* denotes the moment when the peptide flow was terminated (highlighted also by a vertical line). The time points *iii* indicate the flush of PBS in the chamber. Panel B represents the corresponding  $\Delta f$ - $\Delta D$  plots of “fresh” U3.5 retro. The coordinate (0,0) corresponds to the time when the peptide solution was introduced into the QCM-D chambers. Time increases along the trace and the last point in the trace corresponds to the end of the incubation period (i.e. the time window from points (*i*) to (*iii*) is shown). The response of all the three overtones considered is presented.

## 7 Bibliography

- 1 Bradford, A. M. *et al.* New antibiotic upeirin peptides from the dorsal glands of the Australian Toadlet *Uperoleia mjobergii*. *Aust. J. Chem.* **49**, 1325-1331, (1996).
- 2 Apponyi, M. A. *et al.* Host-defence peptides of Australian anurans: Structure, mechanism of action and evolutionary significance. *Peptides* **25**, 1035-1054, (2004).
- 3 Bowie, J. H. *et al.* Host-defense peptides of Australian anurans. Part 2. Structure, activity, mechanism of action, and evolutionary significance. *Peptides* **37**, 174-188, (2012).
- 4 Kinnunen, P. K. J. Amyloid formation on lipid membrane surfaces. *Open Biol.* **2**, 163-175, (2009).
- 5 Zhao, H. *et al.* Binding of Endostatin to Phosphatidylserine-Containing Membranes and Formation of Amyloid-like Fibers. *Biochemistry* **44**, 2857-2863, (2005).
- 6 Harris, F. *et al.* Aberrant action of amyloidogenic host defense peptides: A new paradigm to investigate neurodegenerative disorders? *FASEB J.* **26**, 1776-1781, (2012).
- 7 Mahalka, A. K. & Kinnunen, P. K. J. Binding of amphipathic  $\alpha$ -helical antimicrobial peptides to lipid membranes: Lessons from temporins B and L. *BBA- Biomembr.* **1788**, 1600-1609, (2009).
- 8 Hirsh, D. J. *et al.* Secondary structure and location of a magainin analogue in synthetic phospholipid bilayers. *Biochemistry* **35**, 12733-12741, (1996).
- 9 Jang, H. Antimicrobial protegrin-1 forms amyloid-like fibrils with rapid kinetics suggesting a functional link. *Biophys. J.* **100**, 1775-1783, (2011).
- 10 Gößler-Schöfberger, R. *et al.* An orphan dermaseptin from frog skin reversibly assembles to amyloid-like aggregates in a pH-dependent fashion. *FEBS J* **276**, 5849-5859, (2009).
- 11 Jahn, T. R. *et al.* The Common Architecture of Cross- $\beta$  Amyloid. *J. Mol. Biol.* **395**, 717-727, (2010).
- 12 Williams, T. L. & Serpell, L. C. Membrane and surface interactions of Alzheimer's A $\beta$  peptide - Insights into the mechanism of cytotoxicity. *FEBS J* **278**, 3905-3917, (2011).
- 13 DaSilva, K. A. *et al.* Amyloid- $\beta$  fibrillogenesis: Structural insight and therapeutic intervention. *Exp. Neurol.* **223**, 311-321, (2010).
- 14 Lansbury, P. T. & Lashuel, H. A. A century-old debate on protein aggregation and neurodegeneration enters the clinic. *Nature* **443**, 774-779, (2006).

- 15 Hebda, J. A. & Miranker, A. D. The Interplay of Catalysis and Toxicity by Amyloid Intermediates on Lipid Bilayers: Insights from Type II Diabetes. *Annu. Rev. Biophys.* **38**, 125-152, (2009).
- 16 Butterfield, S. M. & Lashuel, H. A. Amyloidogenic protein-membrane interactions: Mechanistic insight from model systems. *Angew. Chem. Int. Ed.* **49**, 5628-5654, (2010).
- 17 Merlini, G. & Bellotti, V. Molecular mechanisms of amyloidosis. *N. Engl. J. Med.* **349**, 583-596, (2003).
- 18 Eichner, T. & Radford, S. E. Understanding the complex mechanisms of  $\beta$  2-microglobulin amyloid assembly. *FEBS J* **278**, 3868-3883, (2011).
- 19 Serpell, L. C. *et al.* The protofilament substructure of amyloid fibrils. *J. Mol. Biol.* **300**, 1033-1039, (2000).
- 20 Greenwald, J. & Riek, R. Biology of Amyloid: Structure, Function, and Regulation. *Structure (London, England : 1993)* **18**, 1244-1260, (2010).
- 21 Sunde, M. *et al.* Common core structure of amyloid fibrils by synchrotron X-ray diffraction. *J. Mol. Biol.* **273**, 729-739, (1997).
- 22 Jahn, T. R. & Radford, S. E. Folding versus aggregation: Polypeptide conformations on competing pathways. *Arch. Biochem. Biophys.* **469**, 100-117, (2008).
- 23 Relini, A. *et al.* The two-fold aspect of the interplay of amyloidogenic proteins with lipid membranes. *Chem. Phys. Lipids* **158**, 1-9, (2009).
- 24 White, S. H. & Wimley, W. C. Membrane protein folding and stability: Physical principles. *Annu. Rev. Biophys.* **28**, 319-365, (1999).
- 25 Aisenbrey, C. *et al.* How is protein aggregation in amyloidogenic diseases modulated by biological membranes? *Eur. Biophys. J.* **37**, 247-255, (2008).
- 26 Williams, T. L. *et al.* The effect of Alzheimer's A $\beta$  aggregation state on the permeation of biomimetic lipid vesicles. *Langmuir* **26**, 17260-17268, (2010).
- 27 Engel, M. F. M. *et al.* Membrane damage by human islet amyloid polypeptide through fibril growth at the membrane. *Proc. Natl. Acad. Sci.* **105**, 6033-6038, (2008).
- 28 Zhao, H. *et al.* Interaction of the antimicrobial peptide pheromone Plantaricin A with model membranes: Implications for a novel mechanism of action. *BBA- Biomembr.* **1758**, 1461-1474, (2006).
- 29 Sood, R. & Kinnunen, P. K. J. Cholesterol, lanosterol, and ergosterol attenuate the membrane association of LL-37(W27F) and temporin L. *Biochimica et Biophysica Acta , Biomembranes* **1778**, 1460-1466, (2008).
- 30 Papo, N. & Shai, Y. Can we predict biological activity of antimicrobial peptides from their interactions with model phospholipid membranes? *Peptides* **24**, 1693-1703, (2003).

- 31 Qiu, L. *et al.* Cholesterol modulates the interaction of  $\beta$ -amyloid peptide with lipid bilayers. *Biophys. J.* **96**, 4299-4307, (2009).
- 32 Ji, S.-R. *et al.* Cholesterol Is an Important Factor Affecting the Membrane Insertion of  $\beta$ -Amyloid Peptide (A $\beta$ 1–40), Which May Potentially Inhibit the Fibril Formation. *J. Biol. Chem.* **277**, 6273-6279, (2002).
- 33 Kotarek, J. A. *et al.* Quartz crystal microbalance analysis of growth kinetics for aggregation intermediates of the amyloid-[beta] protein. *Anal. Biochem.* **378**, 15-24, (2008).
- 34 Kotarek, J. A. & Moss, M. A. Impact of phospholipid bilayer saturation on amyloid- $\beta$  protein aggregation intermediate growth: A quartz crystal microbalance analysis. *Anal. Biochem.* **399**, 30-38, (2010).
- 35 Sasahara, K. *et al.* Binding of islet amyloid polypeptide to supported lipid bilayers and amyloid aggregation at the membranes. *Biochemistry* **51**, 6908-6919, (2012).
- 36 Calabrese, A. N. *Characterisation of Protein Structure and Interactions: Novel Applications to the Study of Bioactive Peptides* Doctor of Philosophy thesis, The University of Adelaide, (2013).
- 37 Dobson, C. M. Protein folding and misfolding. *Nature* **426**, 884-890, (2003).
- 38 Shai, Y. Mechanism of the binding, insertion and destabilization of phospholipid bilayer membranes by  $\alpha$ -helical antimicrobial and cell non-selective membrane-lytic peptides. *BBA- Biomembr.* **1462**, 55-70, (1999).
- 39 Chi, E. Y. *et al.* Lipid membrane templates the ordering and induces the fibrillogenesis of Alzheimer's disease amyloid- $\beta$  peptide. *Proteins: Struct., Funct., Genet.* **72**, 1-24, (2008).
- 40 Daggett, V.  $\alpha$ -sheet: The toxic conformer in amyloid diseases? *Acc. Chem. Res.* **39**, 594-602, (2006).
- 41 White, D. A. *et al.* Protein aggregation in crowded environments. *J. Am. Chem. Soc.* **132**, 5170-5175, (2010).
- 42 Widenbrant, M. J. O. *et al.* Lipid-induced  $\beta$ -amyloid peptide assemblage fragmentation. *Biophys. J.* **91**, 4071-4080, (2006).
- 43 Martins, I. C. *et al.* Lipids revert inert A $\beta$  amyloid fibrils to neurotoxic protofibrils that affect learning in mice. *EMBO J.* **27**, 224-233, (2008).
- 44 Róg, T. *et al.* Ordering effects of cholesterol and its analogues. *BBA- Biomembr.* **1788**, 97-121, (2009).
- 45 Needham, D. *et al.* Thermomechanical and transition properties of dimyristoylphosphatidylcholine/cholesterol bilayers. *Biochemistry* **27**, 4668-4673, (1988).
- 46 Subasinghe, S. *et al.* Cholesterol is necessary both for the toxic effect of A $\beta$  peptides on vascular smooth muscle cells and for A $\beta$  binding to vascular smooth muscle cell membranes. *J. Neurochem.* **84**, 471-479, (2003).

- 47 Zhou, X. & Xu, J. Free Cholesterol Induces Higher  $\beta$ -Sheet Content in A $\beta$  Peptide Oligomers by Aromatic Interaction with Phe19. *PLoS One* **7**, e46245, (2012).
- 48 Soscia, S. J. *et al.* The Alzheimer's disease-associated amyloid  $\beta$ -protein is an antimicrobial peptide. *PLoS One* **5**, (2010).
- 49 Fleming, B. D. *et al.* Electrochemical quartz crystal microbalance study of azurin adsorption onto an alkanethiol self-assembled monolayer on gold. *Langmuir* **24**, 323-327, (2008).



## *Conclusions*

Antimicrobial peptides are emerging as an attractive alternative to “traditional” antibiotics. These new therapeutics are “ancient weapons” from the innate immune system from various organisms. Understanding the ‘mode of action’ of these peptides is therefore essential in order to develop these new antibiotics or enable improvements the activities of existing antibiotics.

However, despite numerous studies on the activity of AMPs, employing various techniques, a clear picture, of antimicrobial activity is still far from conclusive. This thesis has presented QCM to be an invaluable approach providing a good mechanistic understanding of the interaction between AMPs and SLBs, the later reproducing an artificial membrane. The structural changes caused by the AMPs at the membrane have provided an important contribution, defining and characterizing the peptide action with confidence. These changes were discerned using both the change in frequency and the dissipation factor, the latter demonstrated here to be a valuable parameter for the detection, in real time, changes in the viscoelastic properties of the membrane due to the interaction with AMPs

The utilisation of SLBs as a simple, tuneable model of the plasma (or bacterial) membrane allowed the focus of the role that some variables to have a determining role in the action of AMPs. Indeed, the membrane composition was shown to have a significant influence on which of the mechanisms was adopted by the AMPs. The peptide concentration was found to influence the peptide activity showing a transition from insertion into the membrane through to disruption. Another important factor is the amino acid composition of the peptide sequence, since the peptides rich in one particular amino acid residue distinguish the peptide in terms of “bacteriostatic” or lytic activity. This was well demonstrated for the apidaecin and oncocin peptides and also the (RW)<sub>3</sub> peptides, respectively.

The biophysical techniques, QCM, and SECM were employed to study the Tat peptide activity, and used in combination, these techniques demonstrated a consistent and reliable mechanistic story, highlighting the role of lipid composition on the Tat activity. In particular, QCM was able to distinguish every transition during the Tat peptide interaction with SLBs and provided “fingerprints” for interactions with the membranes. These QCM “fingerprints” have provided a clear and unique mechanism for each peptide investigated here to be gleaned, specifically where the peptide action towards the membrane is a complex transition of various mechanisms, e.g. from pore to “detergent-like” mechanism.

In summary, this study has highlighted the different mechanisms of action of various AMPs towards bio-mimetic membranes. In particular this project has pioneered the QCM technique that is capable of distinguishing detailed mechanistic activities of these AMPs: QCM can be used together with other biophysical approaches, such as, AFM and SECM with synergistic outcomes achieved. Therefore, this study proves an important contribution on properties of AMPs and provides the basis for the development of new approaches or class of antimicrobial therapeutics.

# *Appendices*



**Vesicular Destabilizing Organometallic Bioconjugates of Polyarginine  
Inducing Apoptosis: Synthesis, Characterization and Biological Activity**

Annika Gross <sup>a</sup>, Hamed Alborzina <sup>b</sup>, Stefania Piantavigna <sup>c</sup>, Lisandra L. Martin <sup>c</sup>, Stefan Wölfl <sup>b</sup> and Nils Metzler-Nolte <sup>a</sup>

<sup>a</sup>: Department of Chemistry and Biochemistry  
University of Bochum, Universitätsstrasse 150, D-44801 Bochum (Germany)



<sup>b</sup>: Institute of Pharmacy and Molecular Biotechnology, Ruprecht-Karls-Universität  
Heidelberg, Im Neuenheimer Feld 364, D-69120 Heidelberg, Germany

<sup>c</sup>: School of Chemistry, Monash University, Clayton, Victoria, Australia

**Keywords:** Bioconjugates, Medicinal Organometallic Chemistry, Metallocenes, Peptides,  
Lysosomal Membrane Permeabilization (LMP), Polyarginine

**Abstract**

Compounds, able to destabilize the lysosomal membrane, have been proposed as interesting candidates for targeted anticancer drugs due to the strong lysosomal changes in cancer cells. For this purpose, novel metallocene derivatives of the cell penetrating peptide, namely, polyarginine were designed and their biological activities were investigated. In this study, we describe the synthesis of a ferrocene- and ruthenocene polyarginine bioconjugates, using Fmoc solid-phase peptide synthesis (SPPS) protocols on a microwave assisted synthesizer.

To demonstrate their antiproliferative utilities as cytotoxic compound for a targeted anticancer drug, cell viability, apoptosis, reactive oxygen species (ROS) induction, and changes in cancer cell metabolism e.g. respiration and glycolysis were studied.

Our results reveal a weak toxicity for the metal free polyarginine peptide, which could be rendered by coupling ferrocene and ruthenocene to the N-terminus. The investigation of the cellular uptake and localization revealed an enhanced vesicular disruption by the metallocene

bioconjugate compared to the metal free derivative which could be triggered by light and chemicals. Further studies of apoptosis, respiration, glycolysis and ROS reveal the superior characteristics of the metallocene compounds for the purpose of a targeted anticancer drug.

## **INTRODUCTION**

Recently, targeting lysosomes was discovered as interesting target for cancer therapy, whereas in the past LMP (lysosomal membrane permeabilization) was only known to release hydrolases resulting in uncontrolled necrosis. However, this is valid in the case of massive lysosomal leakage, whereas minor leakage reveals to be an important part of the apoptotic pathway.<sup>1</sup> LMP is able of either start early events by releasing cathepsins and to amplify later events in the apoptotic pathway by various apoptotic stimuli, including death receptor activation.<sup>2</sup> Furthermore, ROS play an important role, which leads to destabilization via peroxidation of membrane lipids. Alternatively, modification in the intracellular redox balance may start a redox-dependent signaling cascade resulting in LMP.<sup>2</sup> Iron complexes or iron-containing proteins increasing lysosomal vulnerability,<sup>3-7</sup> furthermore, changes in the membrane structure may lead to a revised fluidity, which can result in lysosomal destabilization.<sup>8-12</sup> Lysosomotropic detergents, basic compounds that accumulate in acidic lysosomes and disrupt them from within, were considered as putative anticancer drugs.<sup>1</sup> Cancer cells and interestingly, also multidrug-resistant cancer cells are able to be targeted by this method,<sup>1</sup> due to their strong lysosomal changes which promotes in cancer cells invasive growth and angiogenesis.<sup>13, 14</sup> However, these changes should sensitize cells to the lysosomal cell death pathway even when apoptosis is inhibited.<sup>15</sup>

For our studies we are interested in the basic peptide polyarginine, a cell-penetrating peptide (CPP).<sup>16-18</sup> CPPs are artificially designed peptides or variegated sequences based on natural peptides or proteins to guide a wide variety of substance classes into living cells.<sup>19-21</sup> Polyarginine can enter cells in a receptor independent way, making the excess into nearly all types of cells and tissues possible revealing them as optimal tools to deliver molecules into cells. The mechanism is not known in details,<sup>22, 23</sup> but one possible mode of action is the interaction of the cationic peptide with the cell surface glycosaminoglycans, followed by an energy dependent cellular uptake mechanism, probably via endocytosis. In live cell experiments endocytotic vesicles are visible. To escape the vesicles, heparan sulfate has to be degraded by heparanases to free the peptide.<sup>24</sup> The basic nature of polyarginine makes it a

promising candidate for LMP with the purpose of utilizing this peptide and its derivatives as an anticancer drug in the future.

Since iron compounds were able to enhance vesicular disruption, we were interested in the effect of metallocenes especially ferrocene linked to the basic peptide polyarginine for the purpose of lysosomal disruption for anticancer therapy. Recently, organometallic compounds have attracted great attentions and have been recently reviewed.<sup>25-27</sup> Ferrocene is the by far most important and investigated metallocene and often used in medicinal chemistry.<sup>28-30</sup> It is very stable towards air and water, which makes it ideal to work within a biological context. Furthermore it has interesting characteristics due to its redox properties like its ability to undergo fenton chemistry, which makes intracellular ROS production possible. Ruthenocene is very similar to ferrocene regarding its structure, lipophilicity and size, but it is more stable and non toxic due to its lack of undergoing fenton chemistry. There is a wide variety of ferrocene conjugates known, but much less attention has been drawn to the investigation of ruthenocene bioconjugates. Our group recently presented the synthesis of a ruthenocene PNA oligomer and peptide conjugates.<sup>31-35</sup>

For the investigation of metallocene-polyarginine bioconjugates as candidates for LMP, we functionalize the peptide with metallocenes, ferrocene (**2**, **5**) and ruthenocene (**3**, **6**) and furthermore, labeled the compounds with the fluorophore FITC (**5**, **6**) to investigate their intracellular biological properties in terms of cytotoxicity and lysosomal membrane permeabilization. We have chosen a polyarginine sequence based on an optimized sequence by Inversen et al. which contains besides nine arginines, two phenylalanines for an improved interaction with the cell membrane resulting in an enhanced uptake<sup>36, 37</sup> and for an facile HPLC purification.<sup>38</sup>

### EXPERIMENTAL SECTION

**General Experimental Conditions.** All reagents and HPLC-grade solvents were purchased from Acros (Geel, Belgium), Aldrich/Sigma/Fluka (Deisenhofen, Germany), E. Merck (Darmstadt, Germany), Novabiochem (Laufelfingen, Switzerland) and IRIS Biotech (Marktredwitz, Germany) and were used without further purification. The Rink Amid (IRIS

Biotech) and only L-amino acids were used throughout the synthesis. FITC was ordered from Fluka Chemicals, DMF from Roth. All materials for cell culture were purchased from Invitrogen Corporation (Karlsruhe, Germany) unless otherwise specified. HPLC fractions of all products were frozen in liquid nitrogen and lyophilized using a Christ Alpha 1-4 LD plus freeze dryer. All aqueous solutions were prepared from Millipore® water and filtered with a 0.22 µm syringe filter before use.

**Instrumentation and Analytical Measurements.** A Liberty Microwave Peptide Synthesizer from CEM was used for peptide synthesis. MALDI-TOF mass spectra were recorded on a 'Daltonics® Autoflex' instrument (Bruker, Karlsruhe, Germany) in linear mode with positive polarity using sinapic acid as the matrix. ESI mass spectra were recorded on an Esquire 6000 instrument (Bruker, Karlsruhe, Germany). Nuclear magnetic resonance spectra were recorded on a Bruker DRX 600 MHz spectrometer. <sup>1</sup>H and <sup>13</sup>C chemical shifts are given in ppm and were referenced with the residual solvent resonances relative to tetramethylsilane (TMS). Absorption was measured with a Tecan Microplate Platereader Sapphire<sup>2</sup> (Tecan, Crailsheim, Germany). Uptake studies were implemented on the Olympus IX51 fluorescence microscope equipped with an Olympus XC10 camera and localization studies were performed on a Leica DMIRE2 confocal microscope containing a Leica TCS SP2 and Leica CTRMIC.

**HPLC Analysis and Purification.** HPLC analysis and purifications were carried out using C18 analytical (Varian Dynamax, 4.6 mm x 250 mm) and C18 semipreparative (Varian Dynamax, 21.4 mm x 250 mm) columns on a customised Varian Prostar instrument. Linear gradient, 5-95% MeCN in 18 min., eluents: H<sub>2</sub>O and MeCN both containing 0.1% (v/v) TFA. Analytical (flow rate: 1.0 mL min<sup>-1</sup>) and preparative (flow rate: 4.0 mL min<sup>-1</sup>) runs were performed with a linear gradient of A (95 % millipore® water, 5 % MeCN, 0.1 % TFA (v/v/v)) and B (5 % millipore® water, 95 % MeCN, 0.1 % TFA (v/v/v)). Analytical runs: t = 0 min: 0 % B; t = 18 min: 100 % B; t = 26 min: 0 % B; t = 30 min: 0 % B. Preparative runs: t = 0 min: 0 % B; t = 45 min: 50 % B; t = 55 min: 100 % B; t = 65 min: 0 % B. All samples were filtrated before injection using a 0.22 µm syringe filter. Spectra were recorded at 254 nm and ambient temperature, retention times (t<sub>R</sub>[min]) were noted in each case.

**Solid Phase Peptide Synthesis.** The resin bound Fmoc-polyarginine was synthesized on an automated peptide synthesizer using standard protocols. Afterwards, aliquots of 100 mg peptide containing resin was transferred into a filter-containing syringe for further

derivatization. For the synthesis of all compounds, the N-terminal Fmoc group was deprotected and either acetylated (**1**, **4**) or coupled with ferrocenecarboxylic acid (**2**, **5**) or ruthenocenecarboxylic acid (**3**, **6**). After each step the resin was washed 5 times using 2 mL DMF.

Deprotection of Fmoc. The deprotection was performed twice by treating the Fmoc protected peptide with 2 mL of 20% piperidine in DMF (1 and 5 min).

Acetylation. The N-terminus was acetylated after Fmoc deprotection using 5% acetic anhydride and 6% N,N-diisopropylethylamine (DIPEA) in DMF for 5 min. This step was repeated five times.

Metallocene coupling. After Fmoc-deprotection, metallocenes were coupled to the free N-terminus using metallocene carboxylic acid, 1-hydroxybenzotriazole (HOBt), 2-(1H-benzotriazole-1-yl)-1,1,3,3-tetramethyluronium-tetrafluoroborate (TBTU), DIPEA, (4:4:4:6 equiv.) in DMF for 1 h for ferrocene- or 3 h for the coupling of ruthenocenecarboxylic acid.

FITC coupling. To label the bioconjugates with the fluorophore FITC the Mtt-protecting group of the additional lysine was cleaved orthogonally (1% (v/v) TFA, 5% (v/v) TIS in DCM after N-terminus functionalization; The resin was treated with this cleavage mixture (2 mL) for 5 min, this step was repeated five times. Afterwards, FITC was coupled to the side chain (4 eq. FITC, 10 eq. DIPEA in DMF, incubation time 10 h) to result in **4**, **5** and **6**. After each step the resin was washed 5 times with 2 mL DMF.

Cleavage. The resin was washed with DMF and DCM, shrunk with MeOH and dried under vacuum for 30 min. Finally, cleavage of the bioconjugate from the resin was performed using TFA/water/triisopropylsilane (TIS) (2 mL, 95:2.5:2.5) or TFA/phenol/TIS (2 mL, 85:10:5) for 90 minutes at room temperature. The resin was filtered and washed with 0.5 mL TFA. Addition of cold diethyl ether yielded a white precipitate, which was washed repeatedly with diethyl ether. The crude product was dissolved in acetonitrile/water, filtered, lyophilized and afterwards purified and analyzed with RP-HPLC and finally characterized with MALDI-TOF mass spectrometry.

**1**: White solid, C<sub>80</sub>H<sub>143</sub>N<sub>41</sub>O<sub>13</sub> (1887.26 g/mol): MS (MALDI-TOF): m/z 1888.0 [M+H]<sup>+</sup>, 1910.0 [M+Na]<sup>+</sup>, HPLC: t<sub>R</sub> = 10.5 min. <sup>1</sup>H NMR (90% H<sub>2</sub>O: 10% D<sub>2</sub>O, 600.13 MHz): δ = 8.49–8.42 (m, 6H, H<sub>NH, Arg</sub>), 8.37–8.33 (m, 4H, H<sub>NH, Arg</sub>), 8.33 (m, 1H, H<sub>NH, Phe1</sub>), 8.23 (m, 1H, H<sub>NH, Lys</sub>), 8.21 (m, 1H, H<sub>NH, Phe2</sub>), 7.57 (br, 3H, H<sub>γ, Lys</sub>), 7.39 (m, 2H, H<sub>phenyl, PheA</sub>), 7.38 (m, 2H, H<sub>phenyl, PheB</sub>), 7.35 (m, 2H, 1H<sub>phenyl, PheA</sub>, 1H<sub>phenyl, PheB</sub>), 7.28 (m, 2H, H<sub>phenyl, PheA</sub>), 7.27 (m, 2H, H<sub>phenyl, PheB</sub>), 6.71 (br, 36H, H<sub>η, Arg</sub>), 4.65 (m, 1H, H<sub>α, Phe1</sub>), 4.63 (m, 1H, H<sub>α, Phe2</sub>), 4.39–

4.28 (m, 9H, H<sub>α</sub>, Arg), 4.20 (m, 1H, H<sub>α</sub>, Lys), 3.29–3.14 (m, 18H, H<sub>δ</sub>, Arg), 3.11 (m, 1H, H<sub>β2</sub>, Phe1), 3.10 (m, 1H, H<sub>β2</sub>, Phe2), 3.06 (m, 1H, H<sub>ε2</sub>, Lys), 3.04 (m, 1H, H<sub>ε3</sub>, Lys), 3.03 (m, 1H, H<sub>β3</sub>, Phe1), 3.01 (m, 1H, H<sub>β3</sub>, Phe2), 2.10 (s, 3H, H<sub>Acetyl</sub>), 1.90–1.84 (m, 9H, H<sub>β2</sub>, Arg), 1.89–1.45 (m, 18H, H<sub>γ</sub>, Arg), 1.83–1.75 (m, 9H, H<sub>β3</sub>, Arg), 1.82 (m, 1H, H<sub>β2</sub>, Lys), 1.74 (m, 1H, H<sub>γ2</sub>, Lys), 1.72 (m, 1H, H<sub>β3</sub>, Lys), 1.71 (m, 1H, H<sub>γ3</sub>, Lys), 1.43 (m, 1H, H<sub>γ2</sub>, Lys), 1.40 (m, 1H, H<sub>γ3</sub>, Lys). <sup>13</sup>C NMR (90% H<sub>2</sub>O:10% D<sub>2</sub>O, 150.92 MHz): δ = 182.6, 175.9 (CON), 174.6 (CON), 174.3 (CON), 173.6 (CON), 173.5 (CON), 173.4 (CON), 173.3 (CON), 173.1 (CON), 172.7 (CON), 172.2 (CON), 172.1 (CON), 136.2, 136.1 (C<sub>γ</sub>Phe1, Phe2), 129.3, 129.2, 128.8, 128.7 (C<sub>δ</sub>, Phe1, C<sub>δ</sub>, Phe2, C<sub>ε</sub>, Phe1, C<sub>ε</sub>, Phe2), 127.2, 127.1 (C<sub>ζ</sub>, Phe1, C<sub>ζ</sub>, Phe2), 54.8 (C<sub>α</sub>, Phe1, C<sub>α</sub>, Phe2), 54.6–53.1 (C<sub>α</sub>, Arg), 53.5 (C<sub>α</sub>, Lys), 40.9–40.7 (C<sub>δ</sub>, Arg), 39.5 (C<sub>ε</sub>, Lys), 37.5 (C<sub>β</sub>, PheA, C<sub>β</sub>, PheB), 30.5 (C<sub>β</sub>, Lys), 28.5–27.6 (C<sub>β</sub>, Arg), 26.6 (C<sub>δ</sub>, Lys), 24.9–24.1 (C<sub>γ</sub>, Arg), 22.1 (C<sub>γ</sub>, Lys).

**2:** Orange solid, C<sub>89</sub>H<sub>149</sub>FeN<sub>41</sub>O<sub>13</sub> (2056.16 g/mol): MS (ESI, pos.): m/z 1029.4 [M+2H]<sup>2+</sup>, 686.8 [M+3H]<sup>3+</sup>, 515.6 [M+4H]<sup>4+</sup>, 412.9 [M+5H]<sup>5+</sup>, 344.4 [M+6H]<sup>6+</sup>, HPLC: t<sub>R</sub> = 11.4 min. <sup>1</sup>H NMR (DMSO-d<sub>6</sub>, 600.13 MHz): δ = 8.32 (d, J = 7.1 Hz, 1H, H<sub>NH</sub>, Phe1), 8.07 (m, 7H, 1H<sub>NH</sub>, Lys, 6H<sub>NH</sub>, Arg), 8.02 (m, 2H, 1H<sub>NH</sub>, Arg, 1H<sub>NH</sub>, Phe2), 7.97 (d, J = 7.5 Hz, 1H, H<sub>NH</sub>, Arg), 7.92 (d, J = 7.7 Hz, 1H, H<sub>NH</sub>, Arg), 7.80–7.60 (m, 12H, 9H<sub>ε</sub>, Arg, 3H<sub>ζ</sub>, Lys), 7.60–6.80 (m, 46H, 36H<sub>η</sub>, Arg, 10H<sub>phenyl</sub>, Phe1, Phe2), 4.89 (m, 1H, H<sub>Cp2</sub>), 4.87 (m, 1H, H<sub>Cp5</sub>), 4.57 (m, 2H, 1H<sub>α</sub>, Phe1, 1H<sub>α</sub>, Phe2), 4.42 (m, 2H, H<sub>Cp3,4</sub>), 4.41–4.17 (m, 9H, H<sub>α</sub>, Arg), 4.23 (s, 5H, H<sub>Cp'</sub>), 4.20 (m, 1H, H<sub>α</sub>, Lys), 3.22–3.00 (m, 18H, H<sub>δ</sub>, Arg), 3.08 (m, 1H, H<sub>β2</sub>, Phe1), 3.03 (m, 1H, H<sub>β2</sub>, Phe2), 2.88 (m, 1H, H<sub>β3</sub>, Phe1), 2.79 (m, 2H, H<sub>ε</sub>, Lys), 2.77 (m, 1H, H<sub>β3</sub>, Phe2), 1.84–1.62 (m, 9H, H<sub>β2</sub>, Arg), 1.71 (m, 1H, H<sub>β2</sub>, Lys), 1.62–1.40 (m, 9H, H<sub>β3</sub>, Arg), 1.57 (m, 2H, H<sub>δ</sub>, Lys), 1.56 (m, 1H, H<sub>β3</sub>, Lys), 1.33 (m, 2H, H<sub>γ</sub>, Lys). <sup>13</sup>C NMR (DMSO-d<sub>6</sub>, 150.92 MHz): δ = 174.1 (CON), 173.0 (CON), 172.3 (CON), 172.0 (CON), 171.8 (CON), 171.6 (CON), 171.0 (CON), 170.7 (CON), 130.1, 130.0, 129.0, 128.8 (C<sub>δ</sub>, Phe1, C<sub>δ</sub>, Phe2, C<sub>ζ</sub>, Phe1, C<sub>ζ</sub>, Phe2), 127.2, 121.4 (C<sub>ε</sub>, Phe1, C<sub>ε</sub>, Phe2), 70.8 (C<sub>Cp3,4</sub>), 69.9 (C<sub>Cp'</sub>), 69.9 (C<sub>Cp2,5</sub>), 54.4 (C<sub>α</sub>, Phe1, Phe2), 53.6–52.7 (C<sub>α</sub>, Arg), 52.9 (C<sub>α</sub>, Lys), 41.1 (C<sub>δ</sub>, Arg), 39.3 (C<sub>ε</sub>, Lys), 38.3 (C<sub>β</sub>, Phe2), 38.1 (C<sub>β</sub>, Phe1), 32.2 (C<sub>β</sub>, Lys), 29.8 (C<sub>β</sub>, Arg), 27.4 (C<sub>δ</sub>, Lys), 25.6 (C<sub>γ</sub>, Arg), 22.8 (C<sub>γ</sub>, Lys).

**3:** White solid, C<sub>89</sub>H<sub>149</sub>N<sub>41</sub>O<sub>13</sub>Ru (2102.0 g/mol): MS (MALDI-TOF, Sinap.): m/z 2103.1 [M+H]<sup>+</sup>, HPLC: t<sub>R</sub> = 12.8 min. <sup>1</sup>H NMR (DMSO-d<sub>6</sub>, 400.13 MHz): δ = 8.27 (d, J = 7.5 Hz, 1H, H<sub>NH</sub>, Phe1), 8.16–8.11 (m, 2H, H<sub>NH</sub>, Arg), 8.06 (d, J = 7.8 Hz, 1H, H<sub>NH</sub>, Lys), 8.00–7.90 (m, 3H, H<sub>NH</sub>, Arg), 7.98 (d, J = 7.1 Hz, 1H, H<sub>NH</sub>, Phe2), 7.88–7.72 (m, 4H, H<sub>NH</sub>, Arg), 7.85–7.72 (m, 12H, 9H<sub>ε</sub>, Arg, 3H<sub>ζ</sub>, Lys), 7.55–7.02 (m, 46H, 36H<sub>η</sub>, Arg, 4H<sub>δ</sub>, Phe, 4H<sub>ε</sub>, Phe, 2H<sub>ζ</sub>, Phe), 5.23 (m, 1H,

$H_{Cp2}$ ), 5.20 (m, 1H,  $H_{Cp5}$ ), 4.70 (m, 2H,  $H_{Cp3,4}$ ), 4.58 (s, 5H,  $H_{Cp'}$ ), 4.52 (m, 1H,  $H_{\alpha, Phe1}$ ), 4.50 (m, 1H,  $H_{\alpha, Phe2}$ ), 4.33–4.14 (m, 9H,  $H_{\alpha, Arg}$ ), 4.16 (m, 1H,  $H_{\alpha, Lys}$ ), 3.15–2.69 (m, 18H,  $H_{\delta, Arg}$ ), 3.04 (m, 1H,  $H_{\beta2, Phe1}$ ), 2.98 (m, 1H,  $H_{\beta2, Phe2}$ ), 2.84 (m, 1H,  $H_{\beta3, Phe1}$ ), 2.75 (m, 2H,  $H_{\epsilon, Lys}$ ), 2.72 (m, 1H,  $H_{\beta3, Phe2}$ ), 1.69–1.58 (m, 18H,  $H_{\beta, Arg}$ ), 1.67 (m, 2H,  $H_{\beta, Lys}$ ), 1.57–1.33 (m, 18H,  $H_{\gamma, Arg}$ ), 1.52 (m, 2H,  $H_{\delta, Lys}$ ), 1.29 (m, 2H,  $H_{\gamma, Lys}$ ).  $^{13}C$  NMR (DMSO- $d_6$ , 100.61 MHz):  $\delta$  = 173.3 (CON), 171.8 (CON), 171.7 (CON), 171.5 (CON), 171.4 (CON), 171.3 (CON), 171.1 (CON), 170.9 (CON), 170.7 (CON), 168.5 (CON), 137.6, 137.5 ( $C_{\gamma, Phe1}$ ,  $C_{\gamma, Phe2}$ ), 129.3, 128.8, 128.1, 128.0, 123.1, 120.6 ( $C_{\delta, Phe1}$ ,  $C_{\delta, Phe2}$ ,  $C_{\epsilon, Phe1}$ ,  $C_{\epsilon, Phe2}$ ,  $C_{\zeta, Phe1}$ ,  $C_{\zeta, Phe2}$ ), 72.1 ( $C_{Cp3,4}$ ), 71.6 ( $C_{Cp'}$ ), 70.5 ( $C_{Cp5}$ ), 70.3 ( $C_{Cp2}$ ), 54.1, 53.6 ( $C_{\alpha, Phe1}$ ,  $C_{\alpha, Phe2}$ ), 52.6–51.9 ( $C_{\alpha, Arg}$ ), 52.1 ( $C_{\alpha, Lys}$ ), 41.738.7 ( $C_{\delta, Arg}$ ), 38.4 ( $C_{\epsilon, Lys}$ ), 37.6 ( $C_{\beta, Phe2}$ ), 37.5 ( $C_{\beta, Phe1}$ ), 31.4 ( $C_{\beta, Lys}$ ), 31.3 ( $C_{\delta, Lys}$ ), 29.4–28.3 ( $C_{\beta, Arg}$ ), 25.3, 25.0–24.8 ( $C_{\gamma, Arg}$ ), 22.0 ( $C_{\gamma, Lys}$ ).

**4:** Yellow solid,  $C_{101}H_{154}N_{42}O_{18}S$  (2275.21 g/mol): MS (MALDI-TOF, Sinap.):  $m/z$  2282.7  $[M]^+$ ; MS (ESI, pos.):  $m/z$  1138.8  $[M+2H]^{2+}$ , 944.4  $[M-FITC+3H]^{2+}$ , 759.6  $[M+3H]^{3+}$ , 629.9  $[MFITC+4H]^{3+}$ , HPLC:  $t_R$  = 13.1 min.

**5:** Yellow solid,  $C_{110}H_{160}FeN_{42}O_{18}S$  (2445.20 g/mol): MS (MALDI-TOF, Sinap.):  $m/z$  2447.1  $[M+H]^+$ ; MS (ESI, pos.):  $m/z$  1223.8  $[M+2H]^{2+}$ , 1029.4  $[M-FITC+2H]^{2+}$ , 816.8  $[M+3H]^{3+}$ , 686.6  $[MFITC+3H]^{3+}$ , HPLC:  $t_R$  = 14.8 min.

**6:** Yellow solid,  $C_{110}H_{160}N_{42}O_{18}RuS$  (2491.17 g/mol): MS (ESI, pos.):  $m/z$  831.5  $[M+3H]^{3+}$ , 701.7  $[MFITC+4H]^{3+}$ , 390.0  $[FITC+H]^+$ . HPLC:  $t_R$  = 14.9 min.

**Cell Culture.** General Procedure. The human HepG2 cell line was obtained from “Deutsche Sammlung von Mikroorganismen und Zellkultur ACC 180”. The cell lines HeLa, IMIM-PC2 and PT45 were a gift of Prof. Heumann (Biochemistry, Ruhr-University Bochum) and Prof. Hahn (Molecular Oncology, Ruhr-University Bochum, Bochum, Germany). Cells were grown in RPMI 1640 with 1% sodium pyruvate, 1% L-glutamine, 100 units/mL Pen Strep, 10% fetal bovine serum. The cells were maintained at 37 °C in a humidified incubator under an atmosphere containing 5%  $CO_2$ . Wells used for HeLa cells were coated with 0.2% gelatine solution before use. Cytotoxicity experiments. To determine the activity of **2** and **3** in comparison to **1**, two antiproliferative assays, resazurin and crystal violet were performed (see Supporting information for details). 6000 cells/well of HeLa, PT45 and HepG2 cells were incubated in 96-well plates at 37 °C and 5%  $CO_2$  for 24 h. To determine the initial cell

viability and biomass, a  $t_0$ -plate with HeLa, HepG2 and PT45 was additionally plated and after 24 h incubation the resazurin assay was performed. Subsequently the cells were fixed with 0.2% glutardialdehyde solution, followed by the crystal violet assay. In the remaining plates the medium was replaced with medium containing **1**, **2** or **3** with 0.5% DMSO added to improve the solubility of the compound. Concentrations between 1–1000  $\mu\text{M}$  were used and later adapted regarding their antiproliferative activity. Each concentration was tested six times in parallel, as positive control, cisplatin was used and as negative control, medium containing 0.5% DMSO. To determine the effect of metallocenes, ferrocene- and ruthenocenecarboxylic acid were tested. The incubation time of the compounds was 48 h. Then, the compound-containing medium was removed, the cells were washed with PBS and the resazurin assay and afterwards the crystal violet assay (see Supporting information) was performed. The mean absorption of the initial cell plate ( $t_0$ -plate) for each cell line was subtracted from the absorption of each experiment and control. For both assays the negative control (non-treated) was set to 100%.

**Cellular uptake.** The uptake was investigated by fluorescence microscopy using conjugates labeled with the fluorophore FITC (compounds **4**, **5** and **6**).  $8 \times 10^4$  cells were seeded in flat bottom 24 well plates and incubated for 24 h at 37 °C and 5 (HepG2) or 10%  $\text{CO}_2$  (IMIM-PC2, PT45). Due to an enhanced solubility of the compounds, 0.5% DMSO (maximal concentration in the cell medium) was added. The compounds were dissolved in a DMSO/PBS solution, added to the cell medium and incubated with the cells for 14 h using five different concentrations (1, 5, 10, 25, 50  $\mu\text{M}$ ). After completion of the incubation, the cell medium was removed and the cells were washed five times with PBS. The PBS was replaced with cell culture medium and the fluorescence of the cells was measured on a fluorescence microscope Olympus IX51 (magnification 100, 200 or 400 times). To assess the effect of the cellular uptake qualitatively the amount of fluorescent cells and the intensity of the fluorescence were compared.

**Colocalization.** Colocalization studies were performed using confocal microscopy. For colocalization, commercially available dyes were used according to the specifications of the manufacturer for live cell experiments. To visualize lysosomes LysoTracker Red<sup>®</sup> was used, for endosomes the FM 4-64<sup>®</sup> dye was employed.  $2.5 \times 10^4$  cells were seeded in manually poly-L-lysine coated ibidi  $\mu$ -slides (8 wells) for 14 h. The cells were incubated with 10  $\mu\text{M}$  of **5** for 2 h. 30 Min before the end of the incubation

time LysoTracker Red<sup>®</sup> (75 nM) or FM 4-64<sup>®</sup> (10  $\mu$ M) were added. After completion of the incubation, the culture medium was removed and the cells were washed 5 times using PBS and replaced with RPMI 1640 medium without phenol red and supplements. The colocalization was measured on a Leica confocal microscope. Measurement parameters used for colocalization studies of **5** are as followed: Excitation wavelength of 488 nm and emission range between 500–525 nm, for LysoTracker Red<sup>®</sup> excitation wavelength of 543 nm and emission range of 590–620 nm, for FM 4-64<sup>®</sup> excitation wavelength of 514 nm and emission range of 700–800 nm. Pictures were recorded using the sequential imaging mode. To obtain one image, an average of at least three recorded images and an average of two recorded lines were used.

**ROS measurements.** After the treatment of HeLa cells with indicated concentrations of the compound, the cells were collected, washed and re-suspended ( $2.5 \times 10^5$  cells/0.5 ml) in FACS buffer [D–PBS (Gibco) with 1% BSA (PAA)]. 1.25  $\mu$ l of 5 mM dihydroethidium (D1168, Molecular Probes, Invitrogen) solution was added to each sample followed by 15 minutes incubation at RT in the dark. Signal intensity in which represent the intracellular ROS level was analyzed using a FACS<sup>®</sup>Calibur (Becton Dickinson) and CellQuest Pro (BD) analysis software. Excitation and emission settings were 488 nm and 564–606 nm (FL2 channel).

**Apoptosis.** Annexin V/propidium iodide (AnnV/PI) staining. HeLa cells were treated with indicated concentrations of the substances for 48 h, collected and stained with Annexin V-FITC conjugate (eBioscience) according to manufacturer's recommendation. Briefly, approximately  $5 \times 10^5$  cells were resuspended in 50  $\mu$ l of Annexin V binding buffer, 2.5  $\mu$ l of Annexin V conjugate was added to each probe and 1.25  $\mu$ l of PI solution (1 mg/ml) and incubated in the dark at room temperature for 15 minutes. Signal intensity was analyzed using a FACS<sup>®</sup>Calibur (Becton Dickinson) and CellQuest Pro (BD) analysis software. Excitation and emission settings were 488 nm, 515–545 nm (FL1 channel) for Annexin V-FITC and 564–606 nm (FL2 channel) for PI.

**Cell cycle.** After 24 h treatment of  $5 \times 10^5$  HeLa cells with indicated concentrations of substances, cells were harvested and fixed with 70% ethanol. Fixed cells were kept at -20 °C for at least one day and then washed with PBS and stained with propidium iodine for 30 min at dark. Samples were then analyzed by FACS<sup>®</sup>Calibur to determine the DNA content and cell cycle analysis.

**BIONAS real-time cell metabolism assay.** Approximately  $2 \times 10^5$  HeLa cells were seeded in 450  $\mu$ L medium in each biosensor chips (SC1000) 24 h prior insertion of the chips into the Bionas 2500 analyzer (Bionas, Rostock, Germany). The cell number used results in approximately 80% cell confluence on the chip surface after 24 h. During the analysis of cell metabolism, cells were fed with DMEM running medium (PAN Cat. Nr. P03-0010) without sodium bicarbonate, and only buffered with 1 mM Hepes, supplemented 0.1% FCS.

Bionas 2500 analyzing system was used to continuously record two important physiological cellular parameters over time: oxygen consumption, change in medium pH.<sup>39</sup> The metabolic sensor chips (SC1000) include ion-sensitive field effect transistors (ISFETs) to record pH changes in which linked with glycolytic activity of the cells, and Clark-type electrodes to monitor oxygen consumption representing mitochondrial activity. To measure the activity of the compounds we included the three following steps: i) 6 h equilibration with running medium (RM). ii) drug incubation with substances freshly dissolved in medium at the indicated concentrations for treatment periods of up to 24 h, and iii) a drug-free step in which cells are again fed with running medium only. At the end of each experiment, the cells were killed by addition of 0.2% Triton X-100 to get a basic signal without living cells on the sensor surface as a negative control.

**Membrane studies.** A Quartz crystal microbalance (QCM) was used to assess the interaction between polyarginine peptides and a supported biomimetic membrane (SBM). This approach has been extensively explained in previous works.<sup>40, 41</sup> Briefly, QCM-D experiments were performed using the E4 system with flow cells (Q-Sense, Västra Frölunda, Sweden). The QCM instrument measures the relative changes to the resonance frequency ( $f$ ) of the sensor over the course of the experiment. The variation in the resonance frequency is proportional to the change of the mass ( $\Delta m$ ) coupled to the sensor surface by the Sauerbrey equation:<sup>41</sup>

$$\Delta m = -C (\Delta f/n)$$

where  $C$  is the mass sensitivity constant ( $17.7 \text{ ng/cm}^2 \cdot \text{Hz}$  for a chip with a fundamental frequency of 5 MHz) and  $n$  is the harmonic number. Each experiment was implemented, firstly by the creation of a SBM, by introducing liposomes consisting of DMPC, DMPC/Chol (7:3 v/v) or DMPC/DMPG (4:1 v/v), suspended in a 20 mM PBS buffer with 100 mM of NaCl, into the QCM chamber. The deposition occurred thus in-situ, onto a gold sensor, which has been previously modified with a layer of 3-mercaptopropionic acid (MPA) or with 6-

mercaptohexanoic acid (MHA). Once a stable bilayer (membrane) was formed, various concentrations of peptide, dissolved in PBS, were introduced. The interaction of the peptide and subsequent effects were recorded in real time at the various harmonics (3<sup>rd</sup>, 5<sup>th</sup>, 7<sup>th</sup> and 9<sup>th</sup>), simultaneously. However, only the 7<sup>th</sup> is represented in this study, since all the harmonics did not show any substantial difference. The last step of the experiment, after the incubation time for the peptide-membrane system, was to a PBS flush with the purpose of remove any peptide molecule weakly bound to the membrane. All experiments were conducted at a temperature of  $19.10 \pm 0.05$  °C.

## RESULTS AND DISCUSSION

**Synthesis.** For our purpose, we adapted the polyarginine sequence designed by Inversen et al. with minor changes.<sup>38</sup> Instead of including a cysteine as part of the original sequence, we integrated a lysine to accommodate the fluorophore FITC (Fig.1).

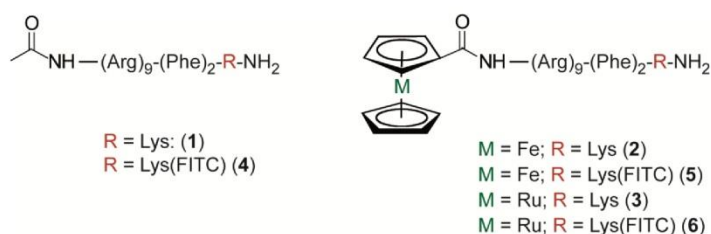
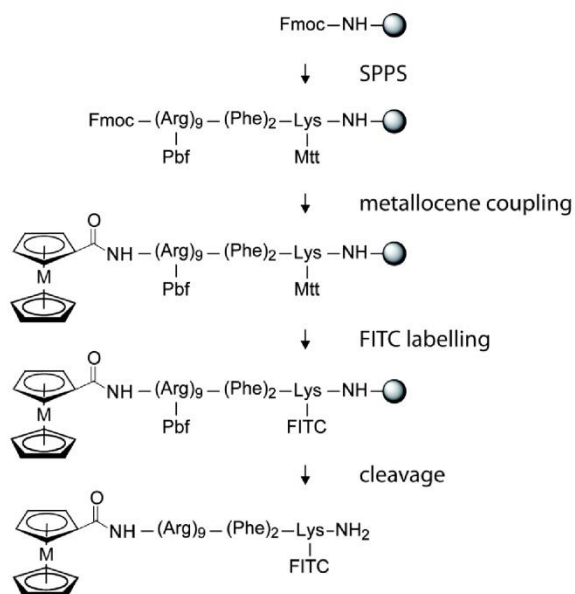


**Figure 1.** Conjugates 1–6.

The synthesis route of the bioconjugates reported in this article is shown in Scheme 1. The polyarginine peptide was prepared by solid-phase peptide synthesis (SPPS) using Fmoc technique. The complete peptide sequence ((Arg)<sub>9</sub>-(Phe)<sub>2</sub>-Lys) was assembled on an automated, micro-wave assisted synthesizer. All subsequent steps were performed manually. After deprotection of the terminal Fmoc group the peptide was either acetylated (**1**, **4**), or ferrocenecarboxylic acid (**2**, **5**) or ruthenocenecarboxylic acid (**3**, **6**) were coupled to the N-terminus of the sequence. In compounds **1**, **2** and **3** the fluorophore is absent (see Fig. 1), with the sequence containing an unmodified Lysin. The synthesis of compounds **4**, **5** and **6** required an orthogonally cleavable protecting group to bind FITC. Therefore, we have chosen the rather acid labile Mtt group. The fluorophore labeling was achieved by removal of the Mtt group by 1% TFA, followed by FITC coupling to the side chain of the unprotected lysine.



**Scheme 1.** Schematic preparation of FITC labeled metallocene polyarginine conjugates; M = Fe (**5**), Ru (**6**).

The conjugates were successfully cleaved from the resin after 6 hours by 85–95% TFA, which leaves the metallocene units untouched.

The conjugates were purified by reverse-phase HPLC on a C18 column and found to be >98% pure by subsequent analytical HPLC of all metallocene-containing fractions. The identity of the purified products was verified by mass spectrometry (ESI and MALDI-TOF). Furthermore, compounds **1**, **2** and **3** were additionally characterized by 2D NMR spectroscopy.

The compounds were obtained successfully in a good yield and purity. The crude product of **1** and **3** were obtained with a purity of >95%.

HPLC chromatograms of the purified compounds reveal a short retention time of the bioconjugate due to the hydrophilicity of the peptide moiety. Coupling of ferrocene or ruthenocene to polyarginine results in a higher lipophilicity which was further increased by the FITC label (**5**, **6**). Ferrocene and ruthenocene conjugation show a longer but comparable retention time, due to these metallocenes very similar lipophilicity (see Experimental Section and Supporting Information Fig. S1).

**Biological Studies.** The biological properties were examined to evaluate the potential of metallocene polyarginine bioconjugates towards lysosomal destabilizing anticancer drugs. Therefore, we studied their cytotoxicity, cellular uptake, localization and lysosomal destabilization. To get further insights of the mode of action and properties of their antiproliferative activity, apoptosis/necrosis induction, ROS formation, influence towards an eukaryotic-mimic membrane were studied. Furthermore, the impact on cell cycle, cellular respiration and glycolysis were also investigated.

**Cellular Uptake.** Cellular uptake of polyarginine and its conjugates was reported to happen in a receptor independent way and therefore, independent of the cell line. The proposed mechanism includes the uptake via binding of the positively charged arginine side chains to the cell membrane, in an electrostatic manner.<sup>23, 24</sup>

Fluorophore labeled bioconjugates **4**, **5** and **6** were tested on three cell lines, HepG2, IMIM-PC2 and PT45, revealing a good uptake in all three cell lines.

Incubation of cells with a high concentration of 50  $\mu$ M reveals a good cellular uptake into the tested cell lines (Fig. 2A). Interestingly, here the breakage of the vesicular structure was observed while exposed to the excitation light of the microscope (Fig. 2B).

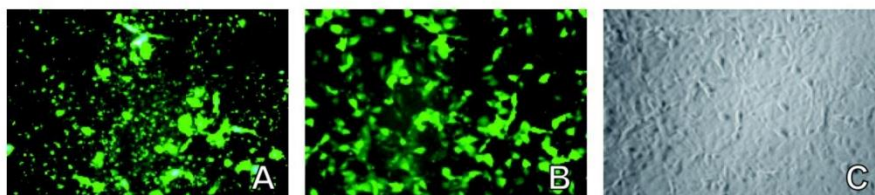


**Figure 2.** Cellular uptake of **5** (50  $\mu$ M) in PT45 cells after 12 h incubation. A: fluorescence image,  $t=0$ ; B: fluorescence image,  $t=3$  min; C: phase contrast. FITC-filter, 200x magnification.

Figure S2 (see Supporting Information) presents the results of the cellular uptake studies of PT45, bearing in mind, that the uptake into the other two cell lines HepG2 and IMIM-PC2 is comparable. Cellular uptake studies of the polyarginine bioconjugates **4**, **5** and **6** revealed a good uptake in PT45 cells (Fig. S2) appearing in a vesicular perinuclear localization. Incubation of 10  $\mu$ M of **4** results in a cellular uptake in around 50 % of the cells by visual appearance. The amount of fluorescent cells can increase by using a higher peptide concentration. Photo induced breakage of the vesicular structure was observed for **4** by the microscope's excitation light after approximately 5 min (Fig. S2, B), which could be impelled

by a higher compound concentration, revealing a concentration depending light induced vesicular breakage for the fluorophore labeled polyarginine peptide.

Uptake studies of the metallocene peptides **5** and **6** show in comparison to **4** a stronger destabilization of the vesicles and an enhanced breakage (see Fig 2 and Fig. S2, D-I), which is in agreement with the observed higher uptake for both compounds. Furthermore, with a higher peptide concentration the exposure time could be dramatically reduced. Therefore, as seen in Figure 2A the breakage of the vesicular structure starts immediately.

Incubation of the cells with a 10  $\mu$ M concentration of the metallocene bioconjugates **5** and **6** exhibit a good uptake with an intense fluorescence and photo induced breakage of vesicles in nearly all plated PT45 cells (Fig. S2, D-F, G-I). They show a comparable vesicular, perinuclear localisation to **4**, but additionally exhibit a low cytosolic localization, indicating a light independent leakage of compound out of the vesicles into the cytosol. However, metallocene peptides **5** and **6** reveal an enhanced uptake compared to **4**, this is presented by an increased content of fluorescent cells exhibiting a higher intensity of the fluorescence and a quicker and more extensive light induced breakage of the vesicular structure, with a homogeneous distribution in the cytosol and a higher intensity in the nucleus. Efficiency of the cellular uptake was observed in the order acetyl-polyarginine (**4**) < ruthenocenoyl-polyarginine (**6**) < ferrocenoyl-polyarginine (**5**).

**Localization.** The intracellular localization of **5** was studied in living cells by confocal microscopy. The previously presented uptake studies revealed a comparable vesicular distribution in the tested cells for all FITC-labelled compounds. In order to identify the cellular targets of these compounds, colocalization studies were performed in the human liver cancer cell line HepG2. By visual inspection, all metal-peptide conjugates exhibit the same intracellular distribution, and therefore, **5** was used as a model compound. The cells were co-incubated with vesicular compartment dyes LysoTracker Red<sup>®</sup> for visualizing lysosomes and FM 4-64<sup>®</sup> for endosomes.

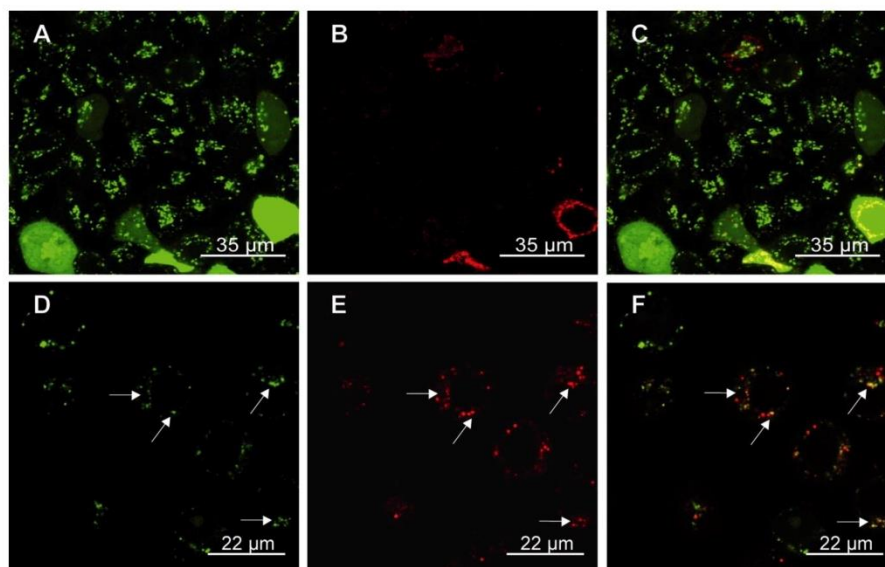


**Figure 3.** Colocalization study in HepG2 cells; A: **5** (10  $\mu\text{M}$ ), B: FM 4-64<sup>®</sup> (10  $\mu\text{M}$ ), C: overlay of A and B. D: **5** (10  $\mu\text{M}$ ), E: LysoTracker Red<sup>®</sup> (75 nM), F: overlay of D and E.

Colocalization of **5** results in a detained uptake of FM 4-64<sup>®</sup>. Cells containing FM 4-64<sup>®</sup> after the incubation reveal the release of **5** into the cell body indicating the chemically induced disruption of the vesicles. Breakage of vesicles due to incubation with FM4-46<sup>®</sup> was not seen by us with previous tested bioconjugates and shows the sensitivity of the cells towards the ferrocene containing polyarginine (**2**, **5**), not be seen with other ferrocene conjugates.<sup>35</sup> Partly colocalization was observed with LysoTracker Red<sup>®</sup> (Fig. 3, D-F). No light induced disruption was visible by confocal microscopy. We observed leakage of vesicles in the fluorescence microscopy after 14 h incubation, however, not by using confocal microscopy after 2 h incubation. This might be originated in the different incubation times and light intensity/energy. In conclusion we can observe enhanced leakage for metallocene conjugates, as well as enhanced photoinduced breakage of vesicles by coupling of ferrocene and ruthenocene and enhanced chemical induced breakage for ferrocene polyarginine.

**Cytotoxicity.** The cytotoxicity was determined by two different assays, the resazurin and crystal violet assay.<sup>42-44</sup> Bioconjugates **1**, **2** and **3** were tested in the range of 1  $\mu\text{M}$  to 1 mM. To distinguish the metal-based cytotoxicity, the metal-free peptide (**1**) was studied as well as the metallocene carboxylic acids (CpFeC<sub>5</sub>H<sub>4</sub>COOH and CpRuC<sub>5</sub>H<sub>4</sub>COOH). Metallocene carboxylic acids revealed no antiproliferative effect on all three cell lines up to the tested

concentration of 500  $\mu\text{M}$ . In literature, the antiproliferative activity of polyarginine peptides has been discussed controversially.<sup>45-47</sup> However, in our studies, the peptide shows a very low activity on all three tested cell lines, revealing  $\text{IC}_{50}$  values between 200–300  $\mu\text{M}$  in both assays (Table 1 and see Supporting Information, Table S1).

**Table 1.**  $\text{IC}_{50}$  values, crystal violet assay.

Compound	HeLa	PT45	HepG2
	[ $\mu\text{M}$ ]	[ $\mu\text{M}$ ]	[ $\mu\text{M}$ ]
<b>1</b>	178.6 $\pm$ 35.7	245.7 $\pm$ 39.0	290.6 $\pm$ 38.3
<b>2</b>	48.0 $\pm$ 9.1	91.8 $\pm$ 13.6	69.3 $\pm$ 7.0
<b>3</b>	70.0 $\pm$ 8.9	123.6 $\pm$ 22.4	101.9 $\pm$ 11.6
FcC(O)OH, RcC(O)OH	> 500	> 500	> 500
cisplatin	1.3 $\pm$ 0.2	0.9 $\pm$ 0.2	2.4 $\pm$ 0.4

This antiproliferative effect was increased by functionalization of the peptide with the metallocenes ruthenocene or ferrocene (**2**, **3**) by 2–4-fold.

Interestingly, the enhanced toxicity is dependent on the metallocene couple to the peptide. Both metallocenes do enhance the bioconjugates lipophilicity and therefore expected unspecific uptake in a comparable way, as shown by HPLC's retention times as well as previous logP experiments on metallocene peptide bioconjugates.<sup>35</sup> Nevertheless, they show distinct difference (around 1.5-fold) in their toxicity. This result either indicates a higher cellular uptake of ferrocene over ruthenocene or an additional cytotoxic effect of ferrocene moiety like enhanced ROS production due to its ability to undergo fenton chemistry.

**Induction of Apoptosis.** In the past, compounds inducing LMP have been reported to result in necrosis and therefore, have not been recognized as interesting candidates for anticancer therapy. More recent research reveals apoptosis induction by these compounds with necrosis present only when massive leakage of the lysosomes occurs. Consequently, the measurement of apoptosis is an important factor for the evaluation of these compounds towards an anticancer drug.

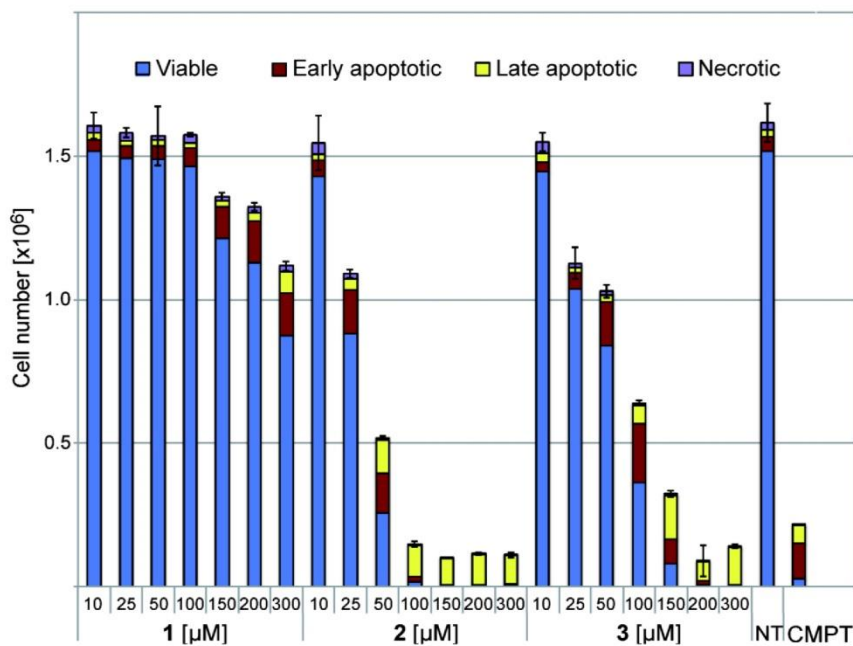


**Figure 4.** Apoptosis induction of **1**, **2** and **3** in HeLa cells at the indicated concentrations.

HeLa cells were treated for 48 h with indicated concentrations of compounds **1**, **2** and **3** and flow cytometry analysis upon Annexin V/propidium iodide (AnnV/PI) staining was performed. AnnV staining indicates apoptotic cells, whereas propidium iodide stains only dead cells/necrotic cells. Single staining of AnnV reveals early apoptosis, combined AnnV-PI coloring shows late apoptosis whereas PI staining alone reveals necrosis due to the complete cell membrane destruction. As shown in Figure 4, none of the tested compounds induce necrosis. Depending on their antiproliferative activity the compounds promote early and late apoptosis. Samples of the metal free bioconjugate **1** reveal, most cells are still viable even at a high concentration of 300 μM, whereas treatment with 200 μM of ruthenocene derivative **3**, most cells are in the stage of late apoptosis. The ferrocene containing compound, the most active compound of this series shows mainly late apoptosis already at a concentration of 100 μM without inducing necrosis.

ROS Formation. An important parameter for LMP is the ROS formation since it results in a destabilization of the membrane lipids which results to an increased vesicular vulnerability. Furthermore, increased intracellular ROS level leads to apoptosis due to DNA damage and also destabilization of the intracellular redox balance, which might start a redox-dependent signaling cascade and finally resulting in LMP.<sup>3-7</sup> All these facts reveal ROS as an important factor for apoptosis and lysosomal membrane permeabilization. Especially iron complexes have shown to increase the lysosomal vulnerability due to their influence upon intracellular redox balance.

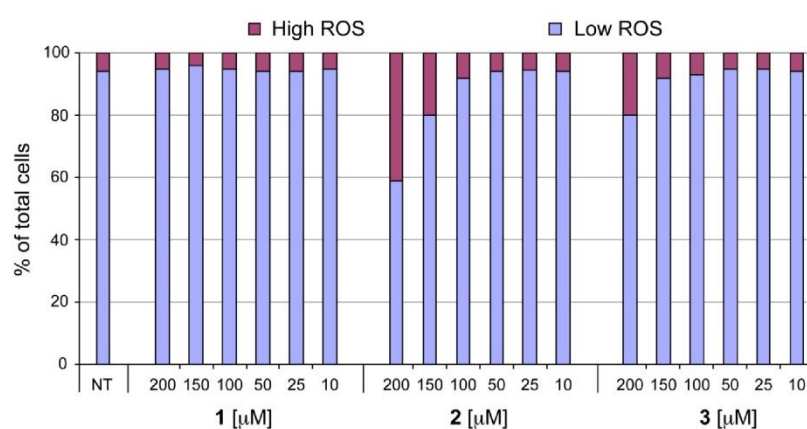


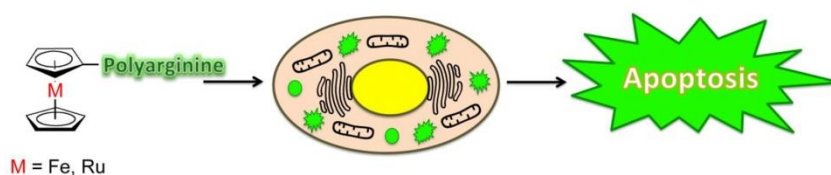
**Figure 5.** Intracellular ROS level of HeLa cells treated with **1**, **2** and **3** at indicated concentrations for 48 h.

The intracellular ROS level of **1**, **2** and **3** were quantified upon treatment of HeLa cells. Cells were treated with indicated concentrations of the compound and the intracellular ROS levels were measured after 48 h using flow cytometry upon dihydroethidium staining.

The metal free reference compound **1** shows no significant ROS formation compared to the non treated cells (NT). However, the metallocene-poyarginine bioconjugates (**2**, **3**) clearly reveal an enhanced intracellular ROS induction. As expected the iron containing bioconjugate **2** shows the highest ROS formation of the three tested compounds, whereas if this is the consequence of the higher toxicity and therefore secondary effect of a higher apoptosis induction or due to the redox chemistry of the iron of the ferrocene head group is not clear and needs further investigation. For compound **3**, no redox activity is expected of the Ru(II) under the intracellular condition present. Therefore, here the increase in ROS seems to be the

- (44) Yang, Y.-I., Jung, D.-W., Bai, D.-G., Yoo, G.-S., and Choi, J.-K. (2001) Counterion-dye staining method for DNA in agarose gels using crystal violet and methyl orange, *Electrophoresis* 22, 855-859.
- (45) Jones, S. W., Christison, R., Bundell, K., Voyce, C. J., Brockbank, S. M. V., Newham, P., and Lindsay, M. A. (2005) Characterization of cell-penetrating peptide-mediated peptide delivery, *Br. J. Pharmacol.* 145, 1093-1102.
- (46) Ko, K. H., Lee, C. J., Shin, C. Y., Jo, M., and Kim, K. C. (1999) Inhibition of mucin release from airway goblet cells by polycationic peptides, *Am. J. Physiol. Lung Cell. Mol. Physiol.* 277, 811-815.
- (47) Miklan, Z., Szabo, R., Zsoldos-Mady, V., Remenyi, J., Banoczi, Z., and Hudecz, F. (2007) New ferrocene containing peptide conjugates: Synthesis and effect on human leukemia (hl-60) cells, *Biopolymers* 88, 108-114.
- (48) Ji, S.-R., Wu, Y., and Sui, S.-F. (2002) Cholesterol is an important factor affecting the membrane insertion of  $\beta$ -amyloid peptide ( $\alpha\beta$ 1-40), which may potentially inhibit the fibril formation, *J. Biol. Chem.* 277, 6273-6279.
- (49) Czihal, P., Knappe, D., Fritsche, S., Zahn, M., Berthold, N., Piantavigna, S., Mueller, U., Van Dorpe, S., Herth, N., Binas, A., Koehler, G., De Spiegeleer, B., Martin, L. L., Nolte, O., Straeter, N., Alber, G., and Hoffmann, R. (2012) Api88 is a novel antibacterial designer peptide to treat systemic infections with multidrug-resistant gram-negative pathogens, *ACS Chemical Biology* 7, 1281-1291.

TOC Graphic



result of the induced apoptosis. Compound **2** exhibits a two times higher ROS induction than **3** which is in agreement to the antiproliferative activity of the compounds and therefore, seems to be a secondary effect of the apoptosis. This assumption is consistent to the rather high concentration needed to induce ROS formation in comparison to the IC<sub>50</sub> values.

Cell Cycle. In comparison to non-treated HeLa cells our data seems to indicate that slightly more cells are in the S- and G2/M phase whereas consequently a lower percentage of cells are present in the G1 phase (see Figure S3, Supporting Information). The G2/M arrest might be correlated with DNA damage as the consequence of ROS generation.

BIONAS Assay. The standard acidification and respiration rate were measured in real-time for 24 h (Fig. 6).

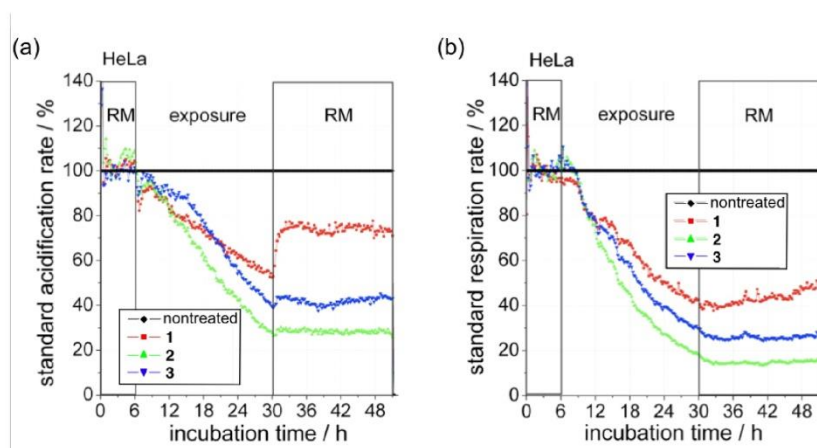


**Figure 6.** (a) Standard acidification and (b) standard respiration rate of **1**, **2** and **3** (100  $\mu$ M) in HeLa cells.

The result reveals a negative influence of 100  $\mu$ M of **1**, **2** and **3** towards the respiration and acidification resulting from an almost immediate inhibition of the glycolysis and respiration. However, the way the respiration as well as glycolysis have been effected shows a general toxicity rather a direct block of the energy production. Moreover the ruthenocene (**3**) and stronger the ferrocene compound (**2**) reveal an enhanced distortion of the energy production compared to the metal free compound **1**. Interestingly, after removal of the metal free

compound **1**, the cells show a recovery especially in the acidification rate and more slowly but constant recovery of the respiration rate. However, compound **3** reveals only a weak recovery of the acidification whereas **2** seems to show no recovery of the cells after compound removal.

#### Peptide uptake with artificial membranes

To test the influence of the compounds towards a membrane, we investigated the effect of **1**, **2** and **3** on an artificial eukaryotic membrane model. Figure 7 illustrates the interaction between **1** (Figure 7A) or **3** (Figure 7B) peptide and a DMPC/Cholesterol membrane (3:1 v/v) (eukaryotic mimic).<sup>40,48</sup>

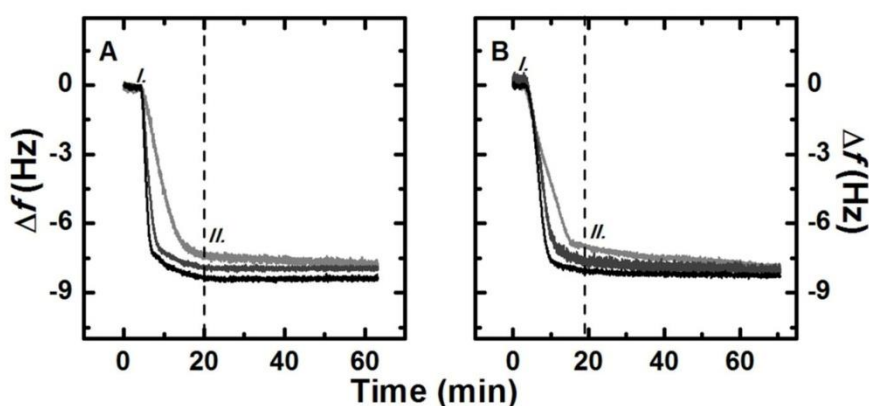


**Figure 7:**  $\Delta f$ -t plots obtained for peptides **1** (A) and **3** (B) interacting with a DMPC/Cholesterol membrane. The concentrations used are 1, 5 and 10  $\mu\text{M}$  (from the lightest to the darkest trace). The 7<sup>th</sup> harmonic only is shown. The vertical dash line indicates the time when the peptide flow stopped (II.), while I. corresponds to the beginning of the peptide injection into the QCM chamber.

The QCM traces reveal, firstly, that peptides bind very strongly only, and in a trans-membrane manner with no indication of membrane removal (see Supporting Information Figure S4). Furthermore, the change in frequency is the same for both the peptides ( $\Delta f = -8$  Hz for 5  $\mu\text{M}$ ). To notice also that this frequency change occurs for all the three concentrations tested, with a difference of  $\pm 0.3$  Hz. Indeed, the peptides at these three concentrations nearly saturate the membrane, since the traces start to flatten when the peptide flow terminates (II.). Similar behaviour was observed also for the peptide **2**, which showed a similar uptake (see Figure S5). However, these peptides acted as membrano-lytic peptides towards when negatively

charged membranes (DMPC/DMPG, 4:1 v/v), that mimic a bacterial cell membrane.<sup>40, 49</sup> Indeed, these peptides inserted into the membrane although this binding is immediately followed by removal of material (mass), presumably lipid-rich molecules, which correspond to an increase in frequency (see Supporting Information Figure S6).

An important matter of discussion is the origin of the antiproliferative activity. In comparison of the literature the toxicity of polyarginine itself is controversial discussed.<sup>45-47</sup> Previously, Miklan et al. reported a ferrocenoyl-polyarginine compound with a slightly modified polyarginine sequence than the here presented ferrocenoyl-polyarginine **2**.<sup>47</sup> This already published ferrocene conjugate has shown a comparable toxicity to **2**, but the origin of its activity was reported to be due to the ferrocene functionalization. In their study the unmodified peptide revealed no cytotoxic effect up to a concentration of 10 mM. However, in our study polyarginine sequence reveals a weak but distinct activity.

For our system, we propose, the bioconjugate's toxicity is not based on the ferrocene or ruthenocene moieties, which is in agreement with the lack of an antiproliferative effect of our previously studied ruthenocenoyl and monsubstituted ferrocenoyl peptides and PNA bioconjugates.<sup>32, 33, 35</sup>

Most likely, the cytotoxicity is the result of a higher uptake of the weak active peptide polyarginine when coupled to a metallocene. Both metallocenes are not charged to contribute to the electrostatic binding mode of polyarginine, but both metallocenes do enhance the bioconjugates lipophilicity in a comparable way, as shown by HPLC retention times. Nevertheless, they show distinct difference (around 1.5-fold) in their toxicity. Which either indicates a superior uptake of ferrocene over ruthenocene or an additional cytotoxic effect of ferrocene like enhanced ROS production due to its ability to undergo fenton chemistry. In our studies we were able to observe an increased uptake for both metallocene conjugates (ruthenocene<ferrocene) in comparison to the acetylated peptide evaluated by fluorescence microscopy (Figure S2, Supporting Information). This result is supported by previous uptake studies, where we could recently showed that ferrocene bound to PNA reveals an enhanced uptake by 3.8 times over its ruthenocene analogue in HT-29 cells, quantified by an AAS study.<sup>33</sup> Therefore, the higher cytotoxic activity is probably a marker for a metallocene enhanced uptake rather than a metal based toxicity.

When we assume, the toxicity of the peptide is dependent only on the intracellular compound concentration with no additional cytotoxic effect, we can postulate from the IC<sub>50</sub> values a semi-quantitative value of 2- to 3-fold enhanced uptake of **3** by the ruthenocene headgroup

compared to **1**. For ferrocene, we can expect an iron based enhancement of the toxicity due to its redox properties and therefore, a likely enhanced ROS production and consequently enhanced lysosomal leakage. Here the comparison of uptake and cytotoxicity might be more intricate.

### CONCLUSIONS

In this study, a series of novel metallocene polyarginine bioconjugates were synthesized by Fmoc-SPPS. This approach includes the synthesis of the first ruthenocene cell penetrating peptide derivative. Metallocene bioconjugates as well as their fluorophore labelled derivatives were successfully synthesized and characterized containing the ferrocene or ruthenocene headgroup. We could show only a low toxicity for our acetylated polyarginine (**1**), which could be enhanced by coupling of a metallocene to the peptide sequence. Thereby, ferrocene increases the antiproliferative activity of around 3–4-fold and ruthenocene by 2–3-fold, depending on the cell line, compared to the metal free compound **1**. We proposed this improved antiproliferative effect of the metallocene bioconjugates is the result of a higher uptake. Differences in the internalization of the compounds were also observed by fluorescent microscopy and these results are in agreement with the found difference in cell viability.

Furthermore, by fluorescent microscopy we could observe enhanced leakage of the intracellular vesicles due to the metallocene headgroup, as well as enhanced photo-induced and chemical-induced leakage by the metallocene coupled peptides. In a eukaryotic-mimic membrane model, the incorporation of the bioconjugates **1**, **2** and **3** was found to be independent of the metallocene. Furthermore, we could not observe any sign of membranolytic activity towards an artificial membrane model, which supports a lysosomal disruption based on the basic guanidine of the polyarginine peptide due to protonation inside lysosomes. However, in our assay no increased necrosis was observed and especially **2** and **3** show strong apoptosis induction. The favorable properties of metallocene polyarginine conjugates are also reflected in other experiments as the investigation of ROS induction, respiration- and acidification rate. Here, the metal free compound (**1**) shows no or only reversible activity after compound removal, whereas **2** and **3** reveal higher activity without showing reversibility.

All taken together, the metallocene polyarginine bioconjugates **2** and **3** clearly excite the properties of the metal free compound **1** regarding their antiproliferative and lysosomal destabilizing properties and therefore, we propose these compounds as interesting candidates for the development of lysosomal targeting anticancer drugs.

## ASSOCIATED CONTENT

### Supporting Information

HPLC chromatograms of chosen compounds (**1**, **2**, **3** and **5**) Fig. S1, cellular uptake data of **4**, **5** and **6** in PT45 cells Fig. S2, resazurin assay of **1**, **2** and **3** Table S1 and abbreviations. This material is available free of charge via the internet at <http://pubs.scs.org>.

## AUTHOR INFORMATION

### Corresponding Author

\*Fax: +49 (0)234 - 32 14378; Tel.: [REDACTED]

E-mail: [REDACTED]

### Notes

The authors declare no competing financial interest.

## ACKNOWLEDGEMENTS

This research was supported by the German Research Foundation (DFG) through the Research Unit “Biological Function of Organometallic compounds” (FOR 630, [www.rub.de/for630](http://www.rub.de/for630)). A. G. thanks Joachim Lügger for synthesizing ruthenocenecarboxylic acid and the RUB Research School for further financial support and Prof. Hahn for the gift of cell lines and usage of the facilities.

## REFERENCES

- (1) Groth-Pedersen, L., and Jaattela, M. (2013) Combating apoptosis and multidrug resistant cancers by targeting lysosomes, *Cancer Lett.* 332, 265-274.
- (2) Johansson, A.-C., Appelqvist, H., Nilsson, C., Kagedal, K., Roberg, K., and Oellinger, K. (2010) Regulation of apoptosis-associated lysosomal membrane permeabilization, *Apoptosis* 15, 527-540.
- (3) Garner, B., Li, W., Roberg, K., and Brunk, U. T. (1997) On the cytoprotective role of ferritin in macrophages and its ability to enhance lysosomal stability, *Free Radical Res.* 27, 487-500.
- (4) Persson, H. L., Nilsson, K. J., and Brunk, U. T. (2001) Novel cellular defenses against iron and oxidation: Ferritin and autophagocytosis preserve lysosomal stability in airway epithelium, *Redox Report* 6, 57-63.
- (5) Persson, H. L., Kurz, T., Eaton, J. W., and Brunk, U. T. (2005) Radiation-induced cell death: Importance of lysosomal destabilization, *Biochem. J* 389, 877-884.
- (6) Persson, H. L., Yu, Z., Tirosh, O., Eaton, J. W., and Brunk, U. T. (2003) Prevention of oxidant-induced cell death by lysosomotropic iron chelators, *Free Radical Biol. Med.* 34, 1295-1305.

- (7) Yu, Z., Persson, H. L., Eaton, J. W., and Brunk, U. T. (2003) Intralysosomal iron: A major determinant of oxidant-induced cell death, *Free Radical Biol. Med.* 34, 1243-1252.
- (8) Kagedal, K., Zhao, M., Svensson, I., and Brunk, U. T. (2001) Sphingosine-induced apoptosis is dependent on lysosomal proteases, *Biochem. J* 359, 335-343.
- (9) Zhao, H.-F., Wang, X., and Zhang, G.-J. (2005) Lysosome destabilization by cytosolic extracts, putative involvement of  $Ca^{2+}$ /phospholipase c, *FEBS Lett.* 579, 1551-1556.
- (10) Zhang, G., Yi, Y.-P., and Zhang, G.-J. (2006) Effects of arachidonic acid on the lysosomal ion permeability and osmotic stability, *J. Bioenerg. Biomembr.* 38, 75-82.
- (11) Hu, J.-S., Li, Y.-B., Wang, J.-W., Sun, L., and Zhang, G.-J. (2007) Mechanism of lysophosphatidylcholine-induced lysosome destabilization, *J. Membr. Biol.* 215, 27-35.
- (12) Yi, Y. P., Wang, X., Zhang, G., Fu, T. S., and Zhang, G. J. (2006) Phosphatidic acid osmotically destabilizes lysosomes through increased permeability to  $K^+$  and  $H^+$ , *Gen. Physiol. Biophys.* 25, 149-160.
- (13) Joyce, J. A., Baruch, A., Chehade, K., Meyer-Morse, N., Giraudo, E., Tsai, F.-Y., Greenbaum, D. C., Hager, J. H., Bogoy, M., and Hanahan, D. (2004) Cathepsin cysteine proteases are effectors of invasive growth and angiogenesis during multistage tumorigenesis, *Cancer Cell* 5, 443-453.
- (14) Kirkegaard, T., and Jaeeattelae, M. (2009) Lysosomal involvement in cell death and cancer, *Biochim. Biophys. Acta, Mol. Cell Res.* 1793, 746-754.
- (15) Fehrenbacher, N., Bastholm, L., Kirkegaard-Sorensen, T., Rafn, B., Bottzauw, T., Nielsen, C., Weber, E., Shirasawa, S., Kallunki, T., and Jaeeattelae, M. (2008) Sensitization to the lysosomal cell death pathway by oncogene-induced down-regulation of lysosome-associated membrane proteins 1 and 2, *Cancer Res.* 68, 6623-6633.
- (16) Vives, E., Brodin, P., and Lebleu, B. (1997) A truncated hiv-1 tat protein basic domain rapidly translocates through the plasma membrane and accumulates in the cell nucleus, *J. Biol. Chem.* 272, 16010-16017.
- (17) Fischer, P. M., Krausz, E., and Lane, D. P. (2001) Cellular delivery of impermeable effector molecules in the form of conjugates with peptides capable of mediating membrane translocation, *Bioconjugate Chem.* 12, 825-841.
- (18) Futaki, S., Suzuki, T., Ohashi, W., Yagami, T., Tanaka, S., Ueda, K., and Sugiura, Y. (2001) Arginine-rich peptides: An abundant source of membrane-permeable peptides having potential as carriers for intracellular protein delivery, *J. Biol. Chem.* 276, 5836-5840.
- (19) Berchanski, A., and Lapidot, A. (2008) Bacterial rna p rna is a drug target for aminoglycoside-arginine conjugates, *Bioconjugate Chem.* 19, 1896-1906.
- (20) Schwarze, S. R., Ho, A., Vocero-Akbani, A., and Dowdy, S. F. (1999) In vivo protein transduction: Delivery of a biologically active protein into the mouse, *Science* 285, 1569-1572.
- (21) Rothbard, J. B., Kreider, E., Pattabiraman, K., Pelkey, E. T., VanDeusen, C. L., Wright, L., Wylie, B. L., and Wender, P. A. (2002) Arginine-rich molecular transporters for drugs: The role of backbone and side chain variations on cellular uptake, *Cell-Penetrating Pept.*, 141-160.
- (22) Richard, J. P., Melikov, K., Vives, E., Ramos, C., Verbeure, B., Gait, M. J., Chernomordik, L. V., and Lebleu, B. (2003) Cell-penetrating peptides, *J. Biol. Chem.* 278, 585-590.
- (23) Fuchs, S. M., and Raines, R. T. (2005) Polyarginine as a multifunctional fusion tag, *Protein Sci.* 14, 1538-1544.
- (24) Fuchs, S. M., and Raines, R. T. (2004) Pathway for polyarginine entry into mammalian cells, *Biochemistry* 43, 2438-2444.
- (25) Gasser, G., Ott, I., and Metzler-Nolte, N. (2011) Organometallic anticancer compounds, *J. Med. Chem.* 54, 3-25.

- (26) Gasser, G., and Metzler-Nolte, N. (2012) The potential of organometallic complexes in medicinal chemistry, *Curr. Opin. Chem. Biol.* 16, 84-91.
- (27) Hartinger, C. G., Metzler-Nolte, N., and Dyson, P. J. (2012) Challenges and opportunities in the development of organometallic anticancer drugs, *Organometallics* 31, 5677-5685.
- (28) Noor, F., Wuestholz, A., Kinscherf, R., and Metzler-Nolte, N. (2005) A cobaltocenium-peptide bioconjugate shows enhanced cellular uptake and directed nuclear delivery, *Angew. Chem. Int. Ed.* 44, 2429-2432.
- (29) Hillard, E., Vessieres, A., Thouin, L., Jaouen, G., and Amatore, C. (2006) Ferrocene-mediated proton-coupled electron transfer in a series of ferrocifen-type breast-cancer drug candidates, *Angew. Chem. Int. Ed.* 45, 285-290.
- (30) Biot, C., Nosten, F., Fraisse, L., Ter-Minassian, D., Khalife, J., and Dive, D. (2011) The antimalarial ferroquine: From bench to clinic, *Parasite* 18, 207-214.
- (31) Gross, A., and Metzler-Nolte, N. (2009) Synthesis and characterization of a ruthenocenoyl bioconjugate with the cyclic octapeptide octreotate, *J. Organomet. Chem.* 694, 1185-1188.
- (32) Gross, A., Huesken, N., Schur, J., Raszeja, L., Ott, I., and Metzler-Nolte, N. (2012) A ruthenocene-pna bioconjugate - synthesis, characterization, cytotoxicity, and aas-detected cellular uptake, *Bioconjugate Chem.* 23, 1764-1774.
- (33) Gross, A., Neukamm, M., and Metzler-Nolte, N. (2011) Synthesis and cytotoxicity of a bimetallic ruthenocene dicobalt-hexacarbonyl alkyne peptide bioconjugate, *Dalton Trans.* 40, 1382-1386.
- (34) Patra, M., and Metzler-Nolte, N. (2011) Azidomethyl-ruthenocene: Facile synthesis of a useful metallocene derivative and its application in the 'click' labelling of biomolecules *Chem. Commun.* 47, 11444-11446.
- (35) Gross, A., Habig, D., and Metzler-Nolte, N. Synthesis and structure-activity relationship study of organometallic bioconjugates of the cyclic octapeptide octreotate, *ChemBioChem*, Ahead of Print.
- (36) Futaki, S., Ohashi, W., Suzuki, T., Niwa, M., Tanaka, S., Ueda, K., Harashima, H., and Sugiura, Y. (2001) Stearylated arginine-rich peptides: A new class of transfection systems, *Bioconjugate Chem.* 12, 1005-1011.
- (37) Chen, L., Wright, L. R., Chen, C.-H., Oliver, S. F., Wender, P. A., and Mochly-Rosen, D. (2001) Molecular transporters for peptides: Delivery of a cardioprotective epkc agonist peptide into cells and intact ischemic heart using a transport system, *r7, Chem. Biol.* 8, 1123-1129.
- (38) Moulton, H. M., Nelson, M. H., Hatlevig, S. A., Reddy, M. T., and Iversen, P. L. (2004) Cellular uptake of antisense morpholino oligomers conjugated to arginine-rich peptides, *Bioconjugate Chem.* 15, 290-299.
- (39) Alborzinia, H., Can, S., Holenya, P., Scholl, C., Lederer, E., Kitanovic, I., and Woelfl, S. (2011) Real-time monitoring of cisplatin-induced cell death, *PLoS One* 6, e19714.
- (40) Piantavigna, S., McCubbin, G. A., Boehnke, S., Graham, B., Spiccia, L., and Martin, L. L. (2011) A mechanistic investigation of cell-penetrating tat peptides with supported lipid membranes, *Biochimica et Biophysica Acta, Biomembranes* 1808, 1811-1817.
- (41) McCubbin, G. A., Praporski, S., Piantavigna, S., Knappe, D., Hoffmann, R., Bowie, J. H., Separovic, F., and Martin, L. L. (2011) Qcm-d fingerprinting of membrane-active peptides, *Eur. Biophys. J.* 40, 437-446.
- (42) O'Brien, J., Wilson, I., Orton, T., and Pognan, F. (2000) Investigation of the alamar blue (resazurin) fluorescent dye for the assessment of mammalian cell cytotoxicity, *Eur. J. Biochem.* 267, 5421-5426.
- (43) Gillies, R. J., Didier, N., and Denton, M. (1986) Determination of cell number in monolayer cultures, *Anal. Biochem.* 159, 109-113.

**Supporting Information**

Vesicular Destabilizing Organometallic Bioconjugates of Polyarginine Inducing  
Apoptosis: Synthesis, Characterization and Biological Activity

Annika Gross <sup>a</sup>, Hamed Alborzina <sup>b</sup>, Stefania Piantavigna <sup>c</sup>, Lisandra L. Martin <sup>c</sup>,  
Stefan Wölfl <sup>b</sup> and Nils Metzler-Nolte <sup>a</sup>

<sup>a</sup>: *Department of Chemistry and Biochemistry*

*University of Bochum, Universitätsstrasse 150, D-44801 Bochum (Germany)*

*Fax: +49 (0)234 - 32 14378*

*E-Mail:* 

<sup>b</sup>: *Institute of Pharmacy and Molecular Biotechnology, Ruprecht-Karls-Universität  
Heidelberg, Im Neuenheimer Feld 364, D-69120 Heidelberg, Germany*

<sup>c</sup>: *School of Chemistry, Monash University, Clayton, Victoria, Australia*

**Cytotoxicity assays:**

*Resazurin Assay.* 1 mL of resazurin solution per plate was diluted with 9 mL medium without phenol red. 100  $\mu$ L of this solution was added per well and their absorbance was measured using a Tecan plate reader at 600 nm, using a reference wavelength of 690 nm. The plates were incubated for 2 h at 37 °C and 5% CO<sub>2</sub> and were measured again.

*Crystal Violet Assay.* To perform the crystal violet assay, the resazurin solution was removed and the cells were fixed using 0.2% glutardialdehyde for 25 min. The glutardialdehyde solution was removed and exchanged for 100  $\mu$ L of 0.1% triton solution. After a short incubation, all liquids were removed and the fixed cells were stained with a 0.02 M crystal violet solution for 30 min. Afterwards the wells were washed intensely with H<sub>2</sub>O and were filled with 100  $\mu$ L of 96% ethanol, followed by shaking on a softly rocking rotary shaker for 3 h. The absorption of the ethanolic solution was measured using a microplate reader at 570 nm.

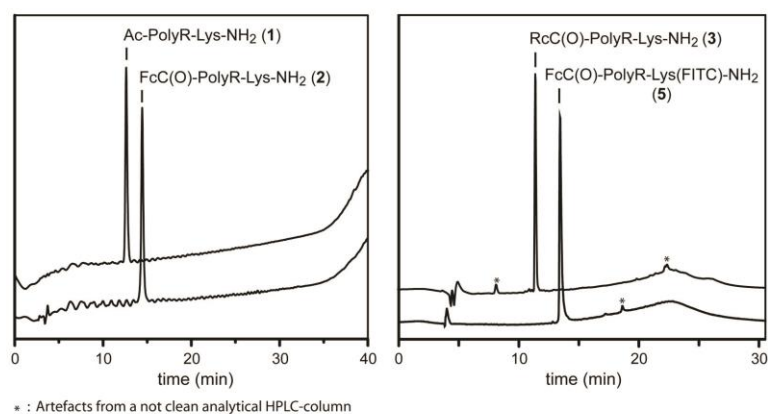


**Figure S1.** HPLC-chromatogram of the purified compounds **1** and **2** detected at 220 nm, method B (left); HPLC-chromatogram of the purified compounds **3** and **5** detected at 254 nm, method A (right).

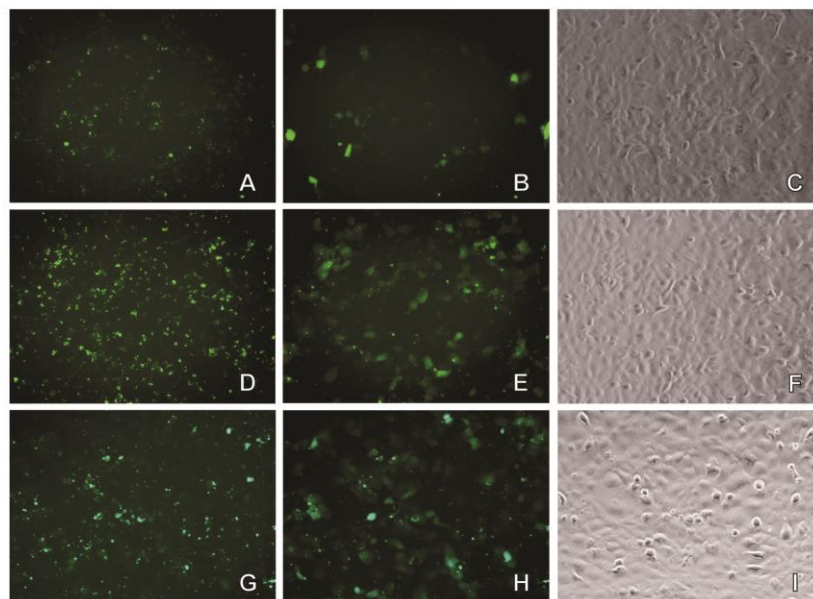


**Figure S2.** Cellular uptake of **4** (10  $\mu$ M) in PT45 cells after 14 h incubation. A: fluorescence image,  $t=0$ ; B: fluorescence image,  $t=5$  min; C: phase contrast. FITC-filter, 200x magnification. Cellular uptake of **5** (10  $\mu$ M) in PT45 cells after 14 h incubation. D: fluorescence image,  $t=0$ ; E: fluorescence image,  $t=5$  min; F: phase contrast. FITC-Filter, 200x magnification. Cellular uptake of **6** (10  $\mu$ M) in PT45 cells after 14 h incubation. G: fluorescence image,  $t=0$ ; H: fluorescence image,  $t=5$  min; I: phase contrast. FITC-Filter, 200x magnification.

**Table S1.**  $IC_{50}$  values, resazurin assay.

Compound	HeLa	PT45	HepG2
	[ $\mu$ M]	[ $\mu$ M]	[ $\mu$ M]
<b>1</b>	250.5 $\pm$ 19.0	289.9 $\pm$ 9.8	307.2 $\pm$ 38.0
<b>2</b>	62.2 $\pm$ 2.7	133.4 $\pm$ 17.6	86.1 $\pm$ 12.8
<b>3</b>	133.7 $\pm$ 15.0	215.1 $\pm$ 8.7	195.0 $\pm$ 16.6
FcC(O)OH, RcC(O)OH	> 500	> 500	> 500
cisplatin	1.8 $\pm$ 0.1	2.3 $\pm$ 0.1	2.1 $\pm$ 0.1

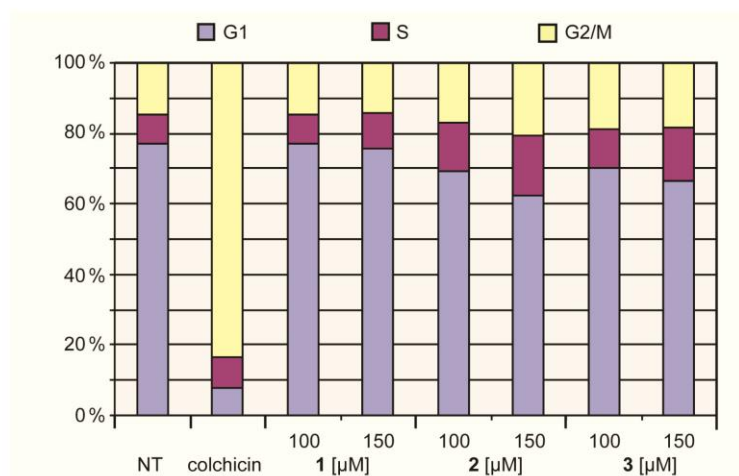


Figure S3. Cell cycle studies of 1, 2 and 3 in HeLa cells at indicated concentrations.

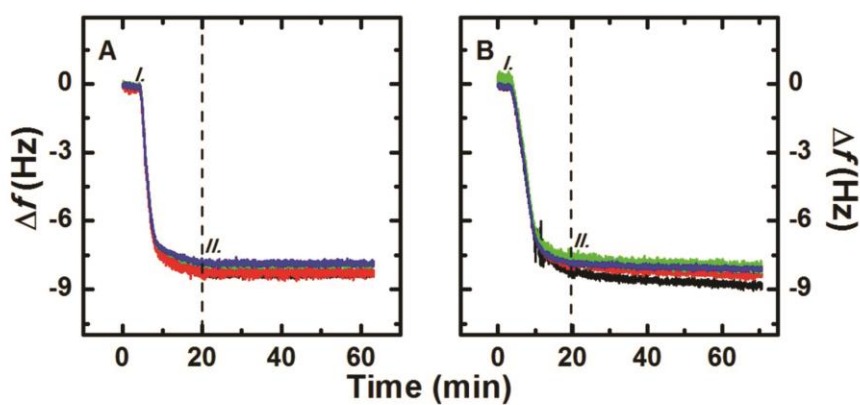
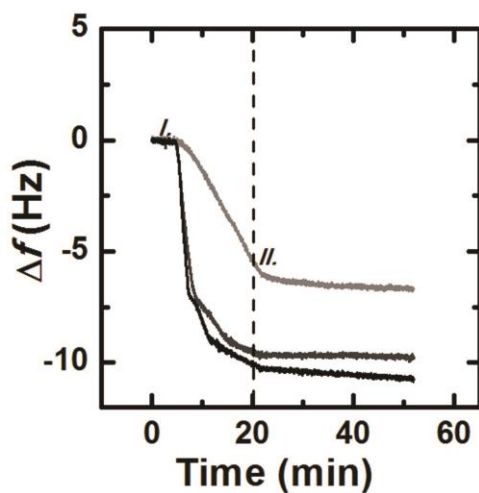
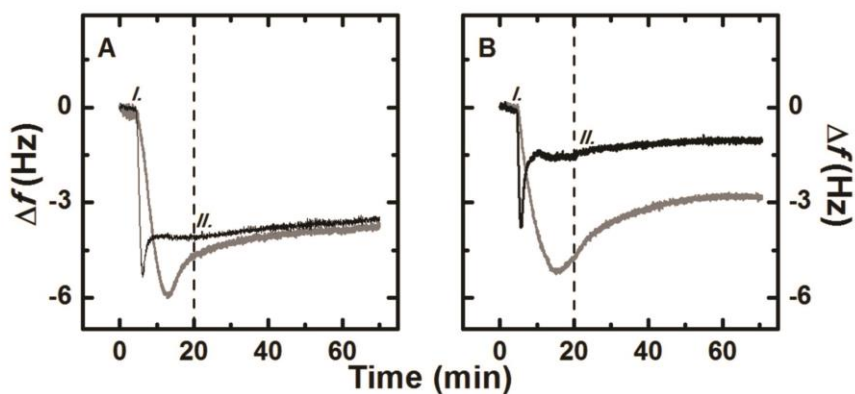


Figure S4:  $\Delta f$ -t plots obtained for peptide 1 (A) and peptide 3 (B) interacting with a DMPC/Cholesterol membrane. The plots are for 5  $\mu$ M. The harmonics represented are: 3<sup>rd</sup> (black line), 5<sup>th</sup> (red line), 7<sup>th</sup> (green line) and 9<sup>th</sup> (blue line). The vertical dash line indicates the time when the peptide flow stopped (II), while I corresponds to the beginning of the peptide injection into the QCM chamber.



**Figure S5:**  $\Delta f$ - $t$  plots obtained for peptide 2 interacting with a DMPC/Cholesterol membrane. The concentrations used are 1, 5 and 10  $\mu\text{M}$  (from the lightest to the darkest trace). The harmonic examined was the 7<sup>th</sup>. The vertical dash line indicates the time when the peptide flow stopped (*II.*), while *I.* corresponds to the beginning of the peptide injection into the QCM chamber.



**Figure S6:**  $\Delta f$ - $t$  plots obtained for peptide 1 (A) and peptide 3 (B) interacting with a DMPC/DMPG membrane. The concentrations used are 1  $\mu\text{M}$  (light grey) and 10  $\mu\text{M}$  (black trace). The harmonic examined was the 7<sup>th</sup>. The vertical dash line indicates the time when the peptide flow stopped (*II.*), while *I.* corresponds to the beginning of the peptide injection into the QCM chamber.

### ABBREVIATIONS

AAS, atomic absorption spectrometry; AnnV, Annexin V; ATP, adenosine triphosphate; BSA, bovine serum albumin; MeCN, acetonitrile; Cp, cyclopentadiene; CPP, cell-penetrating peptide; DCM, dichloromethane; DIPEA, N,N-diisopropylethylamine; DMF, dimethylformamide; DMPC, 1,2-dimyristoyl-*sn*-glycero-3-phosphocholine; DMPG, 1,2-dimyristoyl-*sn*-glycero-3-phosphoglycerol; DMSO, dimethyl sulfoxide; ESI, electrospray ionization; FITC, fluorescein isothiocyanate; Fmoc, 9-fluorenylmethyloxycarbonyl; HeLa, immortal cell line (cervical cancer cells); HepG2, immortal cell line (hepatocellular carcinoma); HOBt, N-hydroxybenzo-triazole-H<sub>2</sub>O; HT-29, immortal cell line (colon carcinoma); IMIM-PC2, immortal cell line (ductal pancreas carcinoma); LMP, lysosomal membrane permeabilization; MALDI-TOF, matrix-assisted laser desorption/ionization-time-of-flight; MeCN, acetonitrile; MeOH, methanol; Mtt, 4-methyltrityl; NT, non treated cells; Pbf, 2,2,4,6,7-pentamethyldihydrobenzofurane-5-sulfonyl; PBS, phosphate buffered saline; Pen Strep, penicillin streptomycin solution; PI, propidium iodide; PNA, peptide nucleic acids; PT45, immortal cell line (pancreatic carcinoma cells); ROS, reactive oxygen species; SPPS, solid-phase peptide synthesis; RT, room temperature; TBTU, 2-(1H-benzotriazole-1-yl)-1,1,3,3-tetramethyluronium tetrafluoroborate; TFA, trifluoroacetic acid; TIS, triisopropylsilane.

*SLO pore formation characterised by QCM-D*

Assembly of Streptolysin O Pores Assessed by Quartz Crystal Microbalance and Atomic Force Microscopy Provides Evidence for the Formation of Anchored but Incomplete Oligomers\*

Sarah E. Stewart<sup>1</sup>, Michael E. D'Angelo<sup>1</sup>, Stefania Piantavigna<sup>2</sup>, Rico F. Tabor<sup>2</sup>, Lisandra L. Martin<sup>2</sup>, Phillip I. Bird<sup>1</sup>

<sup>1</sup>Department of Biochemistry and Molecular Biology, Monash University, Clayton, Australia

<sup>2</sup>School of Chemistry, Monash University, Clayton, Australia

\*Running Title: *SLO pore formation characterised by QCM-D*

To whom correspondence should be addressed: Phillip I. Bird, Department of Biochemistry and Molecular Biology, Monash University, Clayton, Victoria 3800, Australia, Tel: [REDACTED], fax: [REDACTED]

**Keywords:** Streptolysin O, pore, quartz crystal microbalance, bacterial toxins, atomic force microscopy, biophysics, cholesterol, membrane

**Background:** Quartz crystal microbalance with dissipation (QCM-D) was used to monitor Streptolysin O (SLO) interaction with membranes.

**Results:** QCM-D distinguished between binding and insertion, atomic force micrographs suggest incomplete pores are common.

**Conclusions:** QCM-D is a sensitive technique for assessing pore formation.

**Significance:** The first application of QCM-D to a large pore forming protein, yielding valuable insights into SLO biology.

**ABSTRACT**

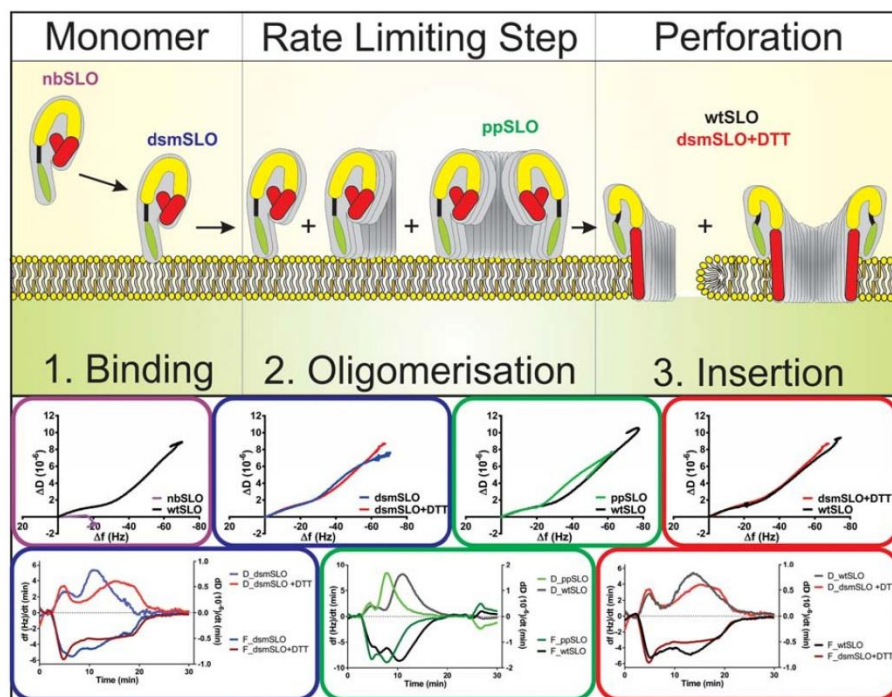
Streptolysin O (SLO) is a bacterial pore forming protein that is part of the cholesterol dependent cytolysin (CDC) family. We have used quartz crystal microbalance with dissipation monitoring (QCM-D) to examine SLO membrane binding and pore formation. In this system, SLO binds tightly to cholesterol-containing membranes, and assembles into partial and complete pores confirmed by atomic force microscopy. SLO binds to the lipid bilayer at a single rate consistent with the Langmuir isotherm model

of adsorption. Changes in dissipation illustrate that SLO alters the viscoelastic properties of the bilayer during pore formation, but there is no loss of material from the bilayer as reported for small membrane-penetrating peptides. SLO mutants were used to further dissect the assembly and insertion processes by QCM-D. This shows the signature of SLO in QCM-D changes when pore formation is inhibited, and that bound and inserted SLO forms can be distinguished. Furthermore a pre-pore locked SLO mutant binds reversibly to lipid, suggesting that the partially complete wt SLO forms observed by AFM are anchored to the membrane.

Pore forming toxins are produced by a variety of organisms. These include the cholesterol dependent cytolysin (CDC) family of virulence factors from Gram-positive bacteria. CDCs are released as monomers which interact with the host cell membrane and oligomerise to form large aqueous pores, reviewed in detail (1). The current model for pore formation suggests soluble CDC monomers bind to the membrane via cholesterol (2,3), initiating a change in conformation that allows membrane bound monomer-monomer

SLO pore formation characterised by QCM-D

FIGURE 6



*SLO pore formation characterised by QCM-D*

binding (4-6). The monomers oligomerise until a ring structure is completed, which is termed the pre-pore complex. The pre-pore complex subsequently undergoes conformational change involving concerted vertical collapse as each monomer unravels two  $\alpha$ -helical bundles to form two  $\beta$ -hairpins that penetrate the membrane. This creates a large  $\beta$ -barrel pore (7-9).

Streptolysin O (SLO) is a CDC expressed by *Streptococcus pyogenes*. SLO is required to translocate nicotinamide adenine dinucleotide (NAD<sup>+</sup>)-glycohydrolase across the host cell membrane during infection; but interestingly this does not appear to be dependent on pore formation (10). The average diameter of the SLO pore is 25-30 nm and is made up of 36-40 monomers (11-14). Molecules of up to 150 kDa are able to diffuse through the pore *in vitro* (15,16).

SLO pores have been studied using electrochemistry in combination with surface plasmon resonance (17,18) and electron microscopy (EM) (11,12,14,19-21). Kinetic data using radioactively labelled SLO on red blood cells suggests that binding is a first order process (with respect to surface site availability) and oligomerisation is a second order process limited by initial monomer-monomer dimerization (22). Furthermore these data suggest that the SLO dimer inserts into the membrane and the pore then forms rapidly (20,22). This is in contrast to the model described above which requires the formation of a complete uninserted pre-pore intermediate, which is thought to be more energetically favourable and represents the rate limiting step necessary for pore formation (7-9).

The mechanism of pore formation remains controversial because the pre-pore model cannot explain the incomplete pores (arcs) that are consistently observed by EM of membrane-bound SLO (11,12,14,19-21). Instead these are dismissed as artefacts caused by the EM process (1). Nevertheless SLO arcs are abundant and are thought to be functional (20). If so, it is unclear whether pores simultaneously grow and insert, or incomplete pre-pores form and then insert into the membrane.

Here we characterise SLO binding and pore formation by quartz crystal microbalance with dissipation monitoring (QCM-D). QCM-D exploits the ability of AT-cut quartz to oscillate at a specific frequency when alternating current is

applied. When a molecule adsorbs on the surface of the quartz-based sensor the frequency of oscillation decreases in proportion to the mass added. Simultaneously, the energy dissipated from the crystal can be measured, providing information about the viscoelasticity of the material on the surface. By covering the sensor with a lipid bilayer the rate of protein binding to mimetic mammalian membranes, and changes in membrane properties due to oligomerisation and pore formation, can be monitored in real time. We find that the binding/adsorption of SLO is concentration and cholesterol dependent. The initial binding proceeds at a single rate and fits the Langmuir isotherm model, indicating there is no cooperation between monomers during this process. Through the use of various mutants we study the succeeding steps of pore formation, demonstrating that QCM-D can distinguish between binding and insertion. Using QCM-D with atomic force microscopy (AFM) we suggest that oligomerisation need not be complete for membrane insertion to occur.

**EXPERIMENTAL PROCEDURES***Reagents*

1,2-dimyristoyl-sn-glycero-3-phosphocholine (DMPC) (cat. 850345P, Avanti polar lipids), Cholesterol (Chol) (cat. C8667, Sigma-Aldrich), L- $\alpha$ -Phosphatidylcholine from egg yolk (eggPC) (cat. P3556, Sigma-Aldrich), 3-mercaptopropionic acid (MPA) (cat. M5801, Sigma-Aldrich), 30% hydrogen peroxide solution (cat. 108597, Merck Millipore), 28% ammonium hydroxide solution (cat. CAS 1336-21-6, Ajax Finechem), Sodium dodecyl sulfate (cat. 0227, Amresco), Hepes (cat. 7365-45-9, Amresco), NaCl (cat. 7647-14-5, Amresco).

*Buffers*

Hepes buffered saline (HBS) contains 20 mM Hepes, pH 7.5, 150 mM NaCl; Low salt buffer (LS) contains 20 mM Hepes, pH 7.4, 30 mM NaCl. All buffers were made up in double distilled water (MilliQ water) and then filtered through a 0.22  $\mu$ m filter and degassed.

*Proteins*

The plasmid for MBP-SLO was a generous gift from Prof Bhakdi. Recombinant SLO was made as described and used with MBP still fused to SLO (21). Mutants were produced by Genscript and cloned in frame with MBP in

*SLO pore formation characterised by QCM-D*

pMALc2. Mutants were also produced as described (21).

*sRBC lysis assays*

Sheep erythrocytes were washed in 0.9% saline solution to remove any contaminating haemoglobin in the buffer. The erythrocytes were then counted and resuspended at  $2 \times 10^8$  cells/ml. SLO was serially diluted in HBS and  $2 \times 10^7$  cells were added to each dilution in a final volume of 200  $\mu$ l. This was then incubated at 37°C or 22°C for 20 min and supernatant collected and its absorbance measured at 405 nm to detect the release of haemoglobin.

*Liposome preparation*

Liposomes were prepared as described (23). Briefly, DMPC, eggPC and cholesterol powder was dissolved in ethanol-free chloroform to make a 5 mM stock solution. Lipid mixtures were made up in a ratio of 40:60 (v/v) DMPC:Chol 50:50 (v/v) eggPC:Chol. Chloroform was evaporated under a gentle stream of nitrogen gas leaving a film of lipid on the wall of the test tube. Any remaining solvent was removed by placing the test tubes in a vacuum desiccator for 2 h and lipids stored at -20°C. Lipids were rehydrated in HBS to a final concentration of 0.5 mM at 37°C for 1 hour, vortexed for 2-5 min and sonicated for 7 min 1-3 times at ~50°C. Liposome suspensions were stored at 4°C for up to 7 days.

*Surface cleaning and modification*

Gold coated sensors were cleaned by immersion in ammonium hydroxide:hydrogenperoxide:water (1:1:3 v/v) at 70°C for 15-20 min as described (23). The gold surface was modified by immersion in 1 mM MPA made in propan-2-ol for at least 1 h at room temperature. Silicon dioxide sensors were cleaned by immersion in 2% (w/v) SDS solution for 1 h at room temperature. The sensors were then rinsed with water and dried under a stream of nitrogen. Any remaining organic material was removed with UV-ozone treatment (3 x 10 min).

*Quartz Crystal Microscopy with Dissipation monitoring*

QCM-D measurements were performed with the E4 system with flow cells (Q-Sense, Sweden) as described (23). Briefly, changes to the resonance frequency ( $\Delta f$ ) and energy dissipation ( $\Delta D$ ) were measured simultaneously. All plots presented represent the 7<sup>th</sup> harmonic unless stated. All experiments were conducted at 22°C.

Lipid was deposited until a change in frequency equal to 25-30 Hz was achieved as this corresponds to a fully covered sensor with a lipid bilayer (24). When forming a bilayer on SiO<sub>2</sub> lipids are injected until a steady baseline was achieved. Washing with a low salt buffer (LS-HBS) generates osmotic stress to burst any intact liposomes. Once base line is established in buffer the protein is added to the system by flowing it over the sensor at a rate of 50  $\mu$ l/min. Once all the protein is used the flow is stopped and binding allowed to continue for at least 10 min before washing any unbound material off the surface with HBS at 300-500  $\mu$ l/min.

*Atomic Force Microscopy*

SiO<sub>2</sub> sensors modified with lipid and treated with SLO were taken directly from the QCM-D cells and immersed in HBS-LS. Sensors were then washed extensively by pipette with HBS-LS and placed in a glass petri-dish containing HBS-LS. Imaging was performed in contact mode using a JPK NanoWizard 3 Bioscience AFM, at a line scan rate of 4 Hz and a force set-point <1 nN. This instrument is equipped with capacitive sensors to ensure accurate reporting of height, z, and x-y lateral distances. Cantilevers used were HYDRA6V-200W Series from AppNano, with a nominal force constant and resonance frequency of 0.081 N/m and 17 kHz respectively.

*Theoretical model*

The change in mass ( $\Delta m$ ) on the surface of the sensor can be calculated according to the Sauerbrey equation (25):

$$\Delta m = -C(\Delta f/n)$$

Where C is the mass sensitivity constant (in this case 17.7 ng/cm<sup>2</sup> for a sensor with a fundamental frequency of 5 MHz) and n is the harmonic number (here we use the seventh (i.e. n=7)).

The kinetic form of the Langmuir adsorption model provides the simplest descriptor for the dynamics of adsorption at a solid-solution interface (26):

$$\Gamma^{max} = k^{ads}(1-\theta) [M \cdot C_b + k^{des} \theta / k^{ads}(1-\theta) + M] - k^{des} \theta$$

where  $\Gamma^{max}$  is the maximum adsorbed amount in mol/m<sup>2</sup> (solved using the Sauerbrey equation

## SLO pore formation characterised by QCM-D

for a saturating concentration),  $M$  is a mass transport factor that represents how quickly molecules can get to the surface in  $\text{ms}^{-1}$ ,  $k^{\text{ads}}$  is the rate of adsorption in  $\text{ms}^{-1}$ ,  $k^{\text{des}}$  is the rate of desorption in  $\text{mol/m}^2/\text{s}^{-1}$  and  $Cb$  is the bulk concentration  $\text{mol/m}^3$ . The fractional surface coverage,  $\theta$  is calculated by dividing the adsorbed amount at a given time,  $\Gamma(t)$  by the maximum adsorbed amount ( $\Gamma^{\text{max}}$ ). At low surface coverage, the adsorption process is assumed to be broadly controlled by diffusion of molecules to the surface, and so the initial slope of  $\theta$  vs  $t$ , i.e.  $d\theta/dt$  is used to calibrate  $M$  (27).

**Results**

*SLO monomer binding to lipids is non-cooperative* - We prepared recombinant SLO with maltose binding protein (MBP) fused to the N-terminus as previously described (21). The N-terminal MBP was not removed as it has been shown previously to have no impact on pore formation (21), and we confirmed the biological activity of this SLO fusion protein via erythrocyte lysis at both 37°C and 22°C (Fig. 1A(i)). The recombinant protein is approximately 100 kDa and pure (Fig. 1A(ii)). We used QCM-D to study SLO binding and activity on DMPC:Chol membranes at 22°C, using gold sensors modified with MPA (Au-MPA) to support the lipid bilayer. Changes in frequency and dissipation were monitored in real time as various concentrations of SLO flowed over the lipid-covered sensors. After the flow was stopped the sensor was monitored for any further changes for approximately 10-20 min, then washed with buffer to remove any unbound material (Fig. 1B). A decrease in frequency indicates protein binding to the lipid, and according to the Sauerbrey equation (25), mass accumulation is proportional to the change in frequency ( $\Delta f$ ). Changes in dissipation ( $\Delta D$ ) indicate alterations to the viscoelastic properties of the lipid-protein layer, where an increase in dissipation means the layer is becoming more fluid (more energy-dissipating) and a decrease in dissipation means the layer is becoming more rigid (less energy-dissipating). These data can also be plotted as  $\Delta f$  vs.  $\Delta D$  (28), which provides a 'signature trace' for SLO interactions on the sensor (Fig. 1C).

We observed concentration-dependent binding of SLO to the lipid layer, indicated by the

decrease in frequency, with  $\Delta f$  following the same trend in increasing SLO concentrations and reaching saturation with 100 and 200 nM SLO (Fig. 1B). No change in frequency was observed during the final wash, indicating that SLO does not dissociate from the membrane (Fig. 1B). As molecules of SLO bind and interact with the lipid layer  $\Delta D$  increases, suggesting the lipid layer becomes more fluid upon addition of SLO (Fig. 1B). From the  $\Delta f$  vs.  $\Delta D$  plot it is evident that as SLO binds to the membrane the frequency decreases and dissipation increases, and the shape of these traces remains very similar over various SLO concentrations (Fig. 1C).

We also analysed the first derivative of the frequency and dissipation functions for the concentrations of SLO plotted in Fig. 1B. This highlights subtle changes in the gradient of the frequency and dissipation functions, which may reflect binding to the membrane, conformational changes to the protein on the membrane, or other effects such as membrane changes including densification or solvation. The first derivatives of the frequency data ( $\Delta f'$ ) indicate that two events (seen as minima) occur as SLO interacts with membrane. The first of these appears to be essentially concentration-independent, whereas the second appears to be strongly concentration-dependent (Fig. 1D). Similarly the first derivative of  $\Delta D$  ( $\Delta D'$ ) also shows two events (maxima) which appear to mirror  $\Delta f'$  and indicate the viscoelasticity of the composite layer is changing due to SLO (Fig. 1D).

An interpretation of these two events consistent with available literature is that the first event corresponds to initial protein binding, and the second to lateral diffusion and oligomerisation. The latter process would free surface sites for further binding, thus explaining the large shifts in both frequency and dissipation.

To assess the overall rate of SLO binding we used the  $\Delta f$  data from the 200 nM SLO experiment and plotted this against the Langmuir isotherm adsorption model. 200 nM SLO was used for this analysis because all available binding sites are saturated (Fig. 1B). The data overlay with the Langmuir adsorption isotherm curve, reflecting a single rate of binding, with no evidence for cooperative binding as the concentration of monomers on the surface increases (Fig. 1E). This is consistent with

*SLO pore formation characterised by QCM-D*

previous data where monomers first bind to the membrane and then laterally diffuse to oligomerise and form pores (5,6,17,22,29). It is also consistent with the first derivative analysis (Fig. 1D) as this highlights subtle deviations in the protein-membrane interaction that can be attributed to changes in the protein conformation once it is already bound to the lipid bilayer.

The QCM-D system also allows changes on the sensor to be monitored over various harmonics. The closer to the sensors surface, the higher the harmonic number. Variation in  $\Delta f$  and  $\Delta D$  in the different harmonics has been observed with small, lipid-penetrating peptides (30). We monitored the 3<sup>rd</sup>, 5<sup>th</sup>, 7<sup>th</sup> and 9<sup>th</sup> harmonics in this study. As illustrated by traces obtained for 100 nM SLO, overall there was little difference between the harmonics in either dissipation or frequency (Fig. 1F). There was however a small but reproducible spread in these harmonics for the frequency which may reflect more mass on the surface of the lipid (3<sup>rd</sup> harmonic), compared to very close to the sensors surface (9<sup>th</sup> harmonic). The signature  $\Delta f$  vs.  $\Delta D$  trace of SLO showed the same trend over the 4 harmonics (Fig. 1G). We conclude that the limited variation in the harmonic read-out, compared to other studies using peptides, is probably due to the much larger size of SLO. Therefore we only display the 7<sup>th</sup> harmonic for subsequent experiments, as it is less prone to interfacial effects at the lipid-solution interface.

To rule out effects of non-specific binding of SLO or trace proteins to the DMPC:Chol lipid layer or any exposed MPA we compared SLO binding to eGFP binding (the latter chosen because it is not membrane active). When eGFP was introduced into the QCM-D cell a small and transient decrease in  $\Delta f$  (-15 Hz) was observed, which quickly returned to zero (Fig. 1H). There was no change in the dissipation, and no further changes during the incubation or washing periods. This trace represents a negative control showing protein does not non-specifically adsorb to the lipid layer, and demonstrating that the binding ( $\Delta f$ ) and rearrangement ( $\Delta D$ ) seen with SLO reflects its authentic biological function and not non-specific protein-lipid or protein-MPA interactions.

*Cholesterol is required for maximal SLO binding* - A defining characteristic of the CDCs is

cholesterol binding. To determine if this is recapitulated in the QCM-D system, we prepared lipids with or without cholesterol and analysed SLO binding. A concentration of 60%mol cholesterol was chosen because it has been reported that the CDCs do not bind membranes containing less than 45%mol cholesterol and show maximal binding at 55%mol (31,32). To assess the cholesterol dependence of SLO we used 100 nM SLO on PC alone or on 20%mol, 40%mol or 60%mol cholesterol. On DMPC alone there was limited binding ( $\Delta f$  = -35 Hz) (Fig. 2A). Of the cholesterol concentrations tested, a major increase in mass accumulation ( $\Delta f$  = -75 Hz) was observed only at 60%mol cholesterol, in agreement with previous data (31,32).

We also made a 'no binding' mutant SLO (nbSLO) based on mutations made in PFO to render it incapable of binding cholesterol (2). We mutated both T564 and L565 to glycine and as expected the purified mutant displayed no haemolytic activity (Fig. 2B). When assessed by QCM-D on Au-MPA with DMPC:Chol we detected a small amount of binding similar to wtSLO on PC alone (Fig. 2C). There was no change in the dissipation, unlike wtSLO on PC alone where an increase in dissipation is seen. The differences between wtSLO and nbSLO are highlighted in the  $\Delta f$  vs.  $\Delta D$  trace (Fig. 2D).

In the first derivative analysis of the frequency data the limited binding seen in Fig. 2C corresponds to the first event seen for wtSLO. However, it does not reach the same magnitude, and the second event is completely absent. No clear events occurred in the dissipation with this mutant (Fig. 2E). This indicates that the first event is monomer binding (whether through cholesterol or another lipid element) and the second reflects a subsequent step in wtSLO pore assembly.

*QCM-D traces reflect SLO rearrangement into pores* - We next examined whether rearrangement and assembly of SLO into pores was occurring on the sensor and contributing to the changes in frequency and dissipation observed in QCM-D. Formation of pores should alter the conductance of the sensor as measured by cyclic voltammetry (33), and pores should be evident via atomic force microscopy (AFM) (7). However, we found the Au-MPA sensors unsuitable for conductance measurements, and

*SLO pore formation characterised by QCM-D*

they are also too rough for AFM. To circumvent these problems we conducted QCM-D experiments on SiO<sub>2</sub> sensors, which are atomically flat and suitable for AFM. We used L- $\alpha$ -PC from chicken egg yolk (eggPC) as the source of PC because DMPC deposited onto SiO<sub>2</sub> sensors do not bind SLO, indicating cholesterol is either not incorporated into the lipid bilayer or it is inaccessible (data not shown). To ensure that the interaction of SLO with eggPC head groups was no different to its interaction with DMPC head groups we tested SLO with eggPC:Chol on Au-MPA sensors. The QCM-D traces for 100 nM SLO on eggPC:Chol (Fig. 3A) and DMPC:Chol (Fig. 1B) on Au-MPA sensors were comparable. The QCM-D trace for SLO on eggPC:Chol coated SiO<sub>2</sub> sensors showed slightly different dissipation traces compared to eggPC:Chol coated Au-MPA sensors, illustrated by the small spread in the different harmonics for the dissipation on SiO<sub>2</sub> (Fig. 3B). We speculate that this is due to the higher sensitivity of the SiO<sub>2</sub> sensors. Despite these small differences the kinetics of SLO binding to the eggPC:Chol membrane were essentially the same as on Au-MPA with DMPC:Chol, and also fit the Langmuir adsorption isotherm (Fig. 3C). Hence we continued with eggPC:Chol on SiO<sub>2</sub> sensors for the AFM studies.

AFM images of SiO<sub>2</sub> sensors taken from the QCM-D instrument after SLO binding revealed canonical pore structures, similar to those reported for PFO (7). Importantly, we observed a mixture of full ring structures and partial ring structures (also termed arcs (11,20)) that often interlocked (Fig. 3 D and E). The full ring structures were approximately 30 nm in diameter, consistent with previous reports of the size of the SLO pore (11-14), however we were unable to measure the height of these structures because they covered the lipid completely, preventing establishment of an accurate baseline. Nevertheless, these images clearly demonstrate that the changes in frequency and dissipation measured by QCM-D as SLO interacts with lipid capture the entire process of binding, oligomerisation and pore formation.

*Monomer-locked SLO changes the QCM-D signature* - To probe the self-assembly process from monomers to pores we made a 'disulfide-locked monomer' mutant SLO (dsmSLO)

containing T393C and V408C substitutions, based on mutations made previously to PFO (29). Although not completely pure, recombinant dsmSLO was validated with sRBC lysis assays, and these showed that it was not lytic unless treated with DTT to reduce the disulfide bond (Fig. 4A). Once reduced, dsmSLO was as lytic as wtSLO on red blood cells (Fig. 4A). To assess the binding and activity of dsmSLO by QCM-D we compared untreated and DTT pre-treated wtSLO and dsmSLO. DTT did not affect wtSLO (Fig. 4B), and as expected reduced dsmSLO was indistinguishable from wtSLO in both  $\Delta f$  and  $\Delta D$  (Fig. 4C). The non-reduced dsmSLO also looked very similar to wtSLO in  $\Delta f$ , however there was a small but reproducible difference in  $\Delta D$  in the form of a shift to the left and a smaller total  $\Delta D$  (Fig. 4C). This is also evident when the data is plotted as  $\Delta f$  vs.  $\Delta D$ : the signatures of wtSLO (+/- DTT) and reduced dsmSLO overlay, whereas non-reduced dsmSLO does not overlay the wtSLO trace (Fig. 4D).

Furthermore when the first derivative of  $\Delta f$  is plotted it is clear that these proteins differ. The first event for the dsmSLO overlays with the wtSLO data but the second event is not apparent (Fig. 4E). The second event however is evident in the reduced dsmSLO (Fig. 4E). The final minimum of the reduced dsmSLO is not the same as wtSLO; we suggest this may be due to incomplete reduction of the mutant disulfide bond. Interestingly there are still two clear events in the first derivative of  $\Delta D$  for dsmSLO, however in contrast to wtSLO and reduced dsmSLO the second event appears to occur earlier in the adsorption cycle (Fig. 4E).

The differences between non-reduced and reduced dsmSLO were more pronounced on SiO<sub>2</sub> eggPC:Chol. Less of the non-reduced dsmSLO bound to the lipid initially, and it dissociated from the lipid during the wash step. By contrast, reduced dsmSLO remained bound to the surface (Fig. 4F). These data also show a shifted signature trace when plotted as  $\Delta f$  vs.  $\Delta D$  (Fig. 4G). Together these results indicate that for stable binding to the bilayer, SLO must actively rearrange.

*Pre-pore locked SLO displays a similar profile to monomer-locked SLO* - To distinguish oligomerisation from pore formation we made the pre-pore locked mutant SLO (ppSLO) described

*SLO pore formation characterised by QCM-D*

previously (10). This mutant is reported to oligomerise into a ring structure that cannot puncture the membrane. When assessed by sRBC lysis assays the lytic ability of the mutant was reduced but not completely abolished. Nevertheless, there was a 17-fold increase in the concentration of ppSLO required to lyse 50% of red blood cells compared to wtSLO (Fig. 5A). When compared to wtSLO by QCM-D ppSLO binds faster than wtSLO and reaches a plateau earlier (Fig. 5B), there was a difference in the dissipation between wt and ppSLO, similar to that seen for dsmSLO (Fig. 5B), and the signature of the  $\Delta f$  vs.  $\Delta D$  plot changed in a similar way to dsmSLO (Fig. 5C). When the first derivatives of these functions were assessed, it was evident that the ppSLO displays two events for both the  $\Delta f'$  and  $\Delta D'$ , similar to wtSLO. The second minimum however, occurred earlier in both the  $\Delta f'$  and  $\Delta D'$  (Fig. 5D). This change in dissipation is again very similar to that of the dsmSLO mutant where the second event (maximum) occurs earlier than that for wtSLO. Monomer binding remains a single-order process as determined by fitting into the Langmuir isotherm equation (Fig. 5E).

When using eggPC:Chol on SiO<sub>2</sub> there was also more efficient ppSLO binding to the lipid as well as differences in the dissipation, again shifted towards the left (Fig. 5F). However the most interesting feature of this trace was that ppSLO dissociated from the lipid easily and completely, similar to dsmSLO (Fig. 5F). This again suggests that in order to stably bind to the lipid surface, SLO must be conformationally competent to self-assemble into membrane-penetrating structures. When these data were plotted as  $\Delta f$  vs.  $\Delta D$  it was again apparent that the ppSLO signature differs from wtSLO, in a similar vein to the difference seen with dsmSLO (Fig. 5G).

**DISCUSSION**

Here we have probed the mechanism of SLO pore formation on lipid bilayers using QCM-D, and find that SLO adsorption and binding behavior is concentration and cholesterol dependent and the kinetics are consistent with the Langmuir isotherm model. Through changes to the QCM-D signature exhibited by SLO mutants we can distinguish between binding/rearrangement and insertion, which

makes QCM-D an excellent tool to study the dynamics of pore formation.

*SLO binding* - Analysis of  $\Delta f$  confirms that SLO binding to lipids proceeds in a concentration-dependent manner that is enhanced by cholesterol. Using these data we can investigate the kinetics of binding to the lipid layer because  $\Delta f$  is proportional to the accumulation of mass according to the Sauerbrey equation (25). We find that when the decay of available binding sites (probably cholesterol) is accounted for, there is only one rate of binding, consistent with the Langmuir isotherm adsorption model. Wilkop and colleagues have previously hypothesized that SLO binding would fit this model (17), and here, using QCM-D, we have demonstrated that this is indeed realized. Other kinetic analyses by Palmer and colleagues also demonstrate that binding to red blood cells is a single order process and is non-cooperative (22). Thus we add to the body of evidence that demonstrates that SLO monomers first bind to the membrane and then undergo a structural change that allows oligomerisation and perforation to proceed (5,6,17,22,34).

In addition to analyzing the overall rate of binding we also analyzed the first derivative of the frequency and dissipation. We find that there are changes to the gradients of these functions that are not large enough to change the overall binding profile significantly. But rather these reflect more subtle changes due to coupling between events such as binding, loss of coupled water from the protein and conformational changes of the protein on the membrane surface in real time. For wtSLO, two events occurred during binding, the first of which was significantly less concentration dependent than the second. We hypothesize that the first minimum/maximum corresponds to the initial binding of monomers to the membrane, whereas the second minimum/maximum relates to the oligomerisation and insertion process. The reasons that lead to this hypothesis are discussed below.

The first derivative of the dsmSLO mutant trace fails to make a clear transition into the second minimum for  $\Delta f'$ , which can be corrected by reducing dsmSLO, whereas the ppSLO mutant clearly shows this second minimum (event).  $\Delta D'$  does not exactly mirror  $\Delta f'$  as the dsmSLO

*SLO pore formation characterised by QCM-D*

mutant still displays two clear events however, analogous to the ppSLO mutant, the second maximum occurs much earlier than the wtSLO. This shift in  $\Delta D'$  is reversed when using reduced dsmSLO: here the second event occurs later and the timing is similar to wtSLO. Therefore we suggest that the second event reports the diffusion of monomers on the surface of the membrane; in the wtSLO and reduced dsmSLO they oligomerise and insert which changes the rate of diffusion or at least the number of monomers moving around on the surface of the membrane, which is reflected in the timing of this second maximum. The ppSLO mutant displays this second event earlier than wtSLO which may be due to its inability to insert into the membrane.

The first derivative is very useful for identifying small changes in the frequency and dissipation, which have allowed us to highlight differences between the mutants. The data fit with previous kinetic data for SLO self-assembly, where binding is one clear event with a single rate and oligomerisation/insertion is a second event with a separate rate which is limited by the formation of an intermediate (22).

*Dissecting the rearrangement process* - The current model for CDC pore formation invokes three main steps (Fig. 6): 1. Cholesterol-dependent binding of monomers to the membrane. 2. Monomer rearrangement/lateral diffusion on the membrane to bind other monomers or oligomers and form a pre-pore structure. Implicit in this step is that the tightness of the association of the growing (non-inserted pre-pore) with the membrane increases with the addition of each subunit. 3. Conformational change involving vertical collapse to form a transmembrane pore or arc.

Mutants that arrest at various points were used to provide further information about pore formation. The first step in this process is binding to the membrane via cholesterol, therefore we studied a mutant (nbSLO) unable to bind cholesterol (2). As expected we observed very little binding to the membrane and the pore formation process was inhibited at the first step (Fig. 6 step 1). Interestingly, SLO on DMPC alone and nbSLO on DMPC:Chol behave slightly differently: both bind poorly as expected but the nbSLO mutant does not show an increase in the dissipation whereas SLO exhibits a small but

reproducible increase in dissipation. This may indicate that the orientation of the protein on the surface or the interaction with the lipid layer is different when cholesterol-binding residues are mutated. Perhaps these sites also interact with PC in some circumstances. This interaction with PC is SLO specific as eGFP does not bind any membrane on Au-MPA and is washed off easily, arguing against non-specific protein-MPA interactions.

The next step in the process is association and rearrangement of bound monomers via lateral diffusion (Fig. 6 step 2), which we studied by inhibiting monomer-monomer interactions using a disulfide-locked monomer SLO mutant (29). We showed that the initial binding ( $\Delta f$ ) is generally unaffected but the  $\Delta f'$  trace indicated that there is a lack of a clear second minimum, which is therefore likely to represent oligomerisation. Furthermore the effects on lipid viscoelasticity,  $\Delta D$ , differ from wtSLO in that the change is faster and of lower total magnitude (this was more obvious in  $\Delta D'$  and signature trace ( $\Delta f'$  vs.  $\Delta D$ )). These differences were reversed when the disulfide bridge ('lock') was reduced, allowing the process of pore formation to proceed from step 1 through to completion (Fig. 6). To separate the effects of oligomerisation (step 2) and insertion (step 3) we used a pre-pore locked mutant which is able to oligomerise but is unable to insert into the membrane (10). This produced traces similar to the disulfide-locked monomer mutant: thus the changes in the QCM-D signatures of both dsmSLO and ppSLO report lack of membrane insertion, rather than rearrangement and pre-pore formation. Subtle differences between monomer locked SLO and pre-pore locked SLO were highlighted when the first derivative was analyzed. This showed that ppSLO like wtSLO, displays two minima in  $\Delta f'$  however the second event occurred earlier. By contrast, dsmSLO lacked this second event. However the signature trace,  $\Delta D'$  for ppSLO is similar to the dsmSLO trace, indicating that the lack of insertion results in the shift to the left for the second maximum.

In addition, on SiO<sub>2</sub> with eggPC:Chol these mutant SLOs bind but, unlike SLO or reduced dsmSLO, are easily washed off the lipid layer, suggesting that only inserted molecules are stably associated with the membrane. Therefore, using

*SLO pore formation characterised by QCM-D*

this experimental system we can apparently distinguish between binding/oligomerisation (steps 1 and 2) and insertion (step 3), however the molecular changes occurring between steps 1 and 2 do not produce detectable differences in either mass ( $\Delta f$ ) or viscoelasticity ( $\Delta D$ ) (Fig. 6).

**Pore formation** - It is currently thought that before CDCs can penetrate membrane a complete ring structure (pre-pore) must be formed, which then triggers insertion (4). Yet EM studies have consistently shown evidence of arcs (11,12,14,19-21,35). Arcs are also apparent in a study by Czajkowsky and co-workers who used AFM to view another CDC, PFO (7). They appear more frequently in images of wtPFO than in images of a disulfide trapped pre-pore locked mutant unable to unfurl transmembrane hairpin 1; this mutant shows predominantly full ring structures (7). A simple explanation for the latter observation is that if insertion is prevented, partially completed pre-pores (containing fewer subunits) are more easily washed off the surface than completed pre-pores.

We also observed a high percentage of arcs on QCM-D sensors imaged by AFM. Many these were intertwined and cannot easily be explained by breakage of completed rings, nor are they likely to be artifacts of the imaging process as it is much gentler compared to EM. In the conditions used for our AFM ( $\text{SiO}_2$  with eggPC:Chol), mutants unable to insert into the lipid layer bind efficiently but wash off easily and essentially completely (Fig. 4E and 5E). Thus we suggest that the incomplete rings of wtSLO we see under AFM after washing are stably associated with the membrane via insertion, and hence completed pre-pore formation is not essential for insertion into the membrane. We do not suggest that oligomerisation and insertion is a coupled process, rather we suggest that insertion is possible after a threshold of subunit addition is reached but before ring formation is complete. Whether arcs are biologically active and occur *in vivo*, or represent failed and functionally irrelevant artifacts, are questions for future investigation, however earlier evidence suggests they are in fact functional (20).

**Monitoring SLO pore formation by QCM-D** - The traces obtained for  $\Delta f$  and  $\Delta D$  are a similar shape over various concentrations, indicating that

there is not a critical monomer concentration required for pore formation and insertion. Unlike the peptide malcalatin (30) there is no evidence for decrease of mass from the surface of the sensor following initial binding, suggesting that lipids are not lost from the surface when SLO inserts and it is likely the lipid rearranges to accommodate the SLO pore. The shape of the curve for binding of SLO is identical over the various harmonics but the magnitude of the change in  $\Delta f$  is greatest in the harmonic that is furthest from the sensor surface (3<sup>rd</sup>), suggesting that there is more weight on the lipid compared to very close to the sensors surface. This is consistent with the mode of SLO function, as the bulk of the protein remains above the membrane during and after pore formation. However we see very little difference in the spread of harmonics between SLO, dsmSLO and ppSLO, meaning that insertion of the  $\beta$  strands into the bilayer does not produce changes that can be measured via different harmonics. We were unable to investigate DMPC:Chol on  $\text{SiO}_2$  due to the absence or inaccessibility of cholesterol in the final lipid layer (this was unexpected and limited our ability to directly compare Au-MPA and  $\text{SiO}_2$ ). Whether this reflects differences in membrane structure remains unclear. Furthermore, differences between sensors were also evident when using the SLO mutants. On Au-MPA dsmSLO and ppSLO bind to the DMPC:Chol surface and do not easily wash off. On  $\text{SiO}_2$  these mutants readily washed off the surface whereas the SLO and reduced dsmSLO did not. This indicates potential differences in the structure of lipid layers formed on Au-MPA vs  $\text{SiO}_2$ .

**CONCLUSION**

In summary we have analyzed membrane binding by SLO and monitored the changes in the lipid layer in real time using QCM-D. We have demonstrated that oligomerisation and pore formation occur on the sensors, thus providing new insight into pore formation by SLO. Binding mutants unable to form pores demonstrate that QCM-D can distinguish between binding and insertion through changes in dissipation. Contrary to the current model, our work suggests that partially completed, membrane-inserted pores can be formed by SLO.

*SLO pore formation characterised by QCM-D*

## SLO pore formation characterised by QCM-D

## References:

1. Hotze, E. M., and Tweten, R. K. (2012) Membrane assembly of the cholesterol-dependent cytolysin pore complex. *Biochimica et biophysica acta* **1818**, 1028-1038
2. Farrand, A. J., LaChapelle, S., Hotze, E. M., Johnson, A. E., and Tweten, R. K. (2010) Only two amino acids are essential for cytolytic toxin recognition of cholesterol at the membrane surface. *Proceedings of the National Academy of Sciences* **107**, 4341-4346
3. Ohno-Iwashita, Y., Iwamoto, M., Mitsui, K., Ando, S., and Iwashita, S. (1991) A cytolysin, theta-toxin, preferentially binds to membrane cholesterol surrounded by phospholipids with 18-carbon hydrocarbon chains in cholesterol-rich region. *Journal of biochemistry* **110**, 369-375
4. Hotze, E. M., Wilson-Kubalek, E., Farrand, A. J., Bentsen, L., Parker, M. W., Johnson, A. E., and Tweten, R. K. (2012) Monomer-monomer interactions propagate structural transitions necessary for pore formation by the cholesterol-dependent cytolysins. *J Biol Chem* **287**, 24534-24543
5. Palmer, M., Vulicevic, I., Saweljew, P., Valeva, A., Kehoe, M., and Bhakdi, S. (1998) Streptolysin O: A Proposed Model of Allosteric Interaction between a Pore-Forming Protein and Its Target Lipid Bilayer†. *Biochemistry* **37**, 2378-2383
6. Abdel Ghani, E. M., Weis, S., Walev, I., Kehoe, M., Bhakdi, S., and Palmer, M. (1999) Streptolysin O: Inhibition of the Conformational Change during Membrane Binding of the Monomer Prevents Oligomerization and Pore Formation†. *Biochemistry* **38**, 15204-15211
7. Czajkowsky, D. M., Hotze, E. M., Shao, Z., and Tweten, R. K. (2004) Vertical collapse of a cytolysin prepore moves its transmembrane beta-hairpins to the membrane. *The EMBO journal* **23**, 3206-3215
8. Shepard, L. A., Shatursky, O., Johnson, A. E., and Tweten, R. K. (2000) The mechanism of pore assembly for a cholesterol-dependent cytolysin: formation of a large prepore complex precedes the insertion of the transmembrane beta-hairpins. *Biochemistry* **39**, 10284-10293
9. Hotze, E. M., Wilson-Kubalek, E. M., Rossjohn, J., Parker, M. W., Johnson, A. E., and Tweten, R. K. (2001) Arresting pore formation of a cholesterol-dependent cytolysin by disulfide trapping synchronizes the insertion of the transmembrane beta-sheet from a prepore intermediate. *J Biol Chem* **276**, 8261-8268
10. Magassa, N., Chandrasekaran, S., and Caparon, M. G. (2010) Streptococcus pyogenes cytolysin-mediated translocation does not require pore formation by streptolysin O. *EMBO Rep* **11**, 400-405
11. Bhakdi, S., Trantum-Jensen, J., and Sziegoleit, A. (1985) Mechanism of membrane damage by streptolysin-O. *Infection and immunity* **47**, 52-60
12. Sekiya, K., Danbara, H., and Futaesaku, Y. (1993) [Mechanism of pore formation on erythrocyte membrane by streptolysin-O]. *Kansenshogaku zasshi. The Journal of the Japanese Association for Infectious Diseases* **67**, 736-740
13. Walch, M., Ziegler, U., and Groscurth, P. (2000) Effect of streptolysin O on the microelasticity of human platelets analyzed by atomic force microscopy. *Ultramicroscopy* **82**, 259-267
14. Niedermeyer, W. (1985) Interaction of streptolysin-O with biomembranes: kinetic and morphological studies on erythrocyte membranes. *Toxicon : official journal of the International Society on Toxinology* **23**, 425-439
15. Walev, I., Bhakdi, S. C., Hofmann, F., Djonder, N., Valeva, A., Aktories, K., and Bhakdi, S. (2001) Delivery of proteins into living cells by reversible membrane permeabilization with streptolysin-O. *Proc Natl Acad Sci U S A* **98**, 3185-3190
16. Bhakdi, S., Weller, U., Walev, I., Martin, E., Jonas, D., and Palmer, M. (1993) A guide to the use of pore-forming toxins for controlled permeabilization of cell membranes. *Medical microbiology and immunology* **182**, 167-175

## SLO pore formation characterised by QCM-D

17. Wilkop, T., Xu, D., and Cheng, Q. (2007) Characterization of pore formation by streptolysin O on supported lipid membranes by impedance spectroscopy and surface plasmon resonance spectroscopy. *Langmuir* **23**, 1403-1409
18. Helmholtz, H. (2010) Selective toxin-lipid membrane interactions of natural, haemolytic Scyphozoan toxins analyzed by surface plasmon resonance. *Biochimica et biophysica acta* **1798**, 1944-1952
19. Harris, J. R., Adrian, M., Bhakdi, S., and Palmer, M. (1998) Cholesterol-Streptolysin O Interaction: An EM Study of Wild-Type and Mutant Streptolysin O. *Journal of structural biology* **121**, 343-355
20. Palmer, M., Harris, R., Freytag, C., Kehoe, M., Tranum-Jensen, J., and Bhakdi, S. (1998) Assembly mechanism of the oligomeric streptolysin O pore: the early membrane lesion is lined by a free edge of the lipid membrane and is extended gradually during oligomerization. *The EMBO journal* **17**, 1598-1605
21. Weller, U., Muller, L., Messner, M., Palmer, M., Valeva, A., Tranum-Jensen, J., Agrawal, P., Biermann, C., Dobereiner, A., Kehoe, M. A., and Bhakdi, S. (1996) Expression of active streptolysin O in Escherichia coli as a maltose-binding-protein-streptolysin-O fusion protein. The N-terminal 70 amino acids are not required for hemolytic activity. *European journal of biochemistry / FEBS* **236**, 34-39
22. Palmer, M., Valeva, A., Kehoe, M., and Bhakdi, S. (1995) Kinetics of streptolysin O self-assembly. *European journal of biochemistry / FEBS* **231**, 388-395
23. Piantavigna, S., McCubbin, G. A., Boehnke, S., Graham, B., Spiccia, L., and Martin, L. L. (2011) A mechanistic investigation of cell-penetrating Tat peptides with supported lipid membranes. *Biochimica et biophysica acta* **1808**, 1811-1817
24. Mechler, A., Praporski, S., Piantavigna, S., Heaton, S. M., Hall, K. N., Aguilar, M. I., and Martin, L. L. (2009) Structure and homogeneity of pseudo-physiological phospholipid bilayers and their deposition characteristics on carboxylic acid terminated self-assembled monolayers. *Biomaterials* **30**, 682-689
25. Sauerbrey, G. (1959) Verwendung von Schwingquarzen zur Wägung dünner Schichten und zur Mikrowägung. *Z. Physik* **155**, 206-222
26. Tabor, R. F., Eastoe, J., and Dowding, P. J. (2010) A two-step model for surfactant adsorption at solid surfaces. *Journal of colloid and interface science* **346**, 424-428
27. Torn, L. H., Koopal, L. K., de Keizer, A., and Lyklema, J. (2005) Adsorption of nonionic surfactants on cellulose surfaces: adsorbed amounts and kinetics. *Langmuir* **21**, 7768-7775
28. McCubbin, G. A., Praporski, S., Piantavigna, S., Knappe, D., Hoffmann, R., Bowie, J. H., Separovic, F., and Martin, L. L. (2011) QCM-D fingerprinting of membrane-active peptides. *Eur Biophys J* **40**, 437-446
29. Ramachandran, R., Tweten, R. K., and Johnson, A. E. (2004) Membrane-dependent conformational changes initiate cholesterol-dependent cytolysin oligomerization and intersubunit beta-strand alignment. *Nat Struct Mol Biol* **11**, 697-705
30. Mechler, A., Praporski, S., Atmuri, K., Boland, M., Separovic, F., and Martin, L. L. (2007) Specific and selective peptide-membrane interactions revealed using quartz crystal microbalance. *Biophysical journal* **93**, 3907-3916
31. Heuck, A. P., Hotze, E. M., Tweten, R. K., and Johnson, A. E. (2000) Mechanism of membrane insertion of a multimeric beta-barrel protein: perfringolysin O creates a pore using ordered and coupled conformational changes. *Mol Cell* **6**, 1233-1242
32. Flanagan, J. J., Tweten, R. K., Johnson, A. E., and Heuck, A. P. (2009) Cholesterol exposure at the membrane surface is necessary and sufficient to trigger perfringolysin O binding. *Biochemistry* **48**, 3977-3987

## SLO pore formation characterised by QCM-D

33. Wilkop, T., Xu, D., and Cheng, Q. (2008) Electrochemical characterization of pore formation by bacterial protein toxins on hybrid supported membranes. *Langmuir* **24**, 5615-5621
34. Hugo, F., Reichwein, J., Arvand, M., Kramer, S., and Bhakdi, S. (1986) Use of a monoclonal antibody to determine the mode of transmembrane pore formation by streptolysin O. *Infection and immunity* **54**, 641-645
35. Gilbert, R. J. (2005) Inactivation and activity of cholesterol-dependent cytolysins: what structural studies tell us. *Structure* **13**, 1097-1106

*Acknowledgements* - We thank Prof. Bhakdi for providing the pMAL-SLO plasmid. This work was supported by grants to PIB from the National Health and Medical Research Council (Australia) and LLM and RFT from the Australian Research Council.

**FIGURE LEGENDS**

**FIGURE 1.** Binding and activity of wtSLO on DMPC:Chol membranes assessed by QCM-D. A)(i) Increasing concentrations of recombinant wtSLO was tested on sRBC for lytic activity at 22°C (squares) and 37°C (circles). (ii) Recombinant wtSLO (2 µg) resolved by SDS-PAGE. B) Au-MPA sensors with a DMPC:Chol (40:60) bilayer with increasing concentrations of wtSLO (25-200 nM) were introduced at 50 µl/min over a total volume of 2 ml. Flow was stopped for 10 min (STOP) to allow the protein to incubate, the cell was then washed with HBS at 300 µl/min (Wash). The change in frequency in Hertz ( $\Delta f$ ) is plotted on the left axis as solid lines and the change in dissipation ( $\Delta D$ ) is plotted on the right axis as broken lines, concentrations are indicated. C) WtSLO  $\Delta f$ - $\Delta D$  signature traces. Data from panel (B) is replotted as  $\Delta f$  on the x-axis versus  $\Delta D$  on the y-axis. D) The first derivative of the frequency and dissipation as plotted in (B). The first derivative of the frequency ( $df(\text{Hz})/dt(\text{min})$ ) is plotted on the left hand side with the functions in darker colours and the first derivative of the dissipation ( $dD(10^{-6})/dt(\text{min})$ ) is plotted in the right in lighter colours. E) The wtSLO binding rate overlays the Langmuir Isotherm model of absorption. Data from panel (B) for 200 nM wtSLO is plotted as theta ( $\theta$ ) against the Langmuir Isotherm absorption model over time. F) The effect of 100 nM wtSLO on the 3<sup>rd</sup>, 5<sup>th</sup>, 7<sup>th</sup> and 9<sup>th</sup> harmonics,  $\Delta f$  is plotted on the left axis and  $\Delta D$  is plotted on the right. The harmonic furthest from the surface of the sensor (3<sup>rd</sup>) is plotted as the lightest grey line, increasing in darkness to the (9<sup>th</sup>) harmonic which is closest to the sensor surface. G)  $\Delta f$ - $\Delta D$  signature trace for 100 nM wtSLO over the various harmonics, the 3<sup>rd</sup> is plotted as light grey increasing in darkness to the 9<sup>th</sup>. H) QCM-D characterisation of 100 nM eGFP on DMPC:Chol. Data plotted as per panel (B).

**FIGURE 2.** wtSLO binding and activity on lipid membranes is dependent on cholesterol. A) QCM-D trace of 100 nM wtSLO on increasing concentrations of cholesterol (percentages indicated) in DMPC membranes, on Au-MPA.  $\Delta f$  is plotted as solid lines and  $\Delta D$  is plotted a dotted lines. B)(i) sRBC lysis assay comparing wtSLO and no binding mutant SLO. Increasing concentrations of wtSLO (black) and nbSLO (purple) are plotted as % lysis where 100% is the lysis seen in detergent treated sRBCs. (ii) Recombinant nbSLO (2 µg) resolved by SDS-PAGE. C) QCM-D trace of 100 nM wtSLO (black) and nbSLO (purple) on Au-MPA sensors with a DMCP:Chol bilayer. Data plotted as per panel (A). D)  $\Delta f$ - $\Delta D$  trace for 100 nM wtSLO (black) and nbSLO (purple). Data from panel C. E) The first derivative of nbSLO (purple) and wtSLO (black) for the frequency and dissipation functions plotted in C.  $df(\text{Hz})/dt(\text{min})$  is plotted on the left hand side with the function in darker colours and  $dD(10^{-6})/dt(\text{min})$  plotted on the right in lighter colours.

**FIGURE 3.** wtSLO pore formation in QCM-D. A) Trace for 100 nM wtSLO on Au-MPA with an eggPC:Chol (50:50) bilayer,  $\Delta f$  is plotted as solid lines and  $\Delta D$  as dotted lines. Harmonics are graded darkest for closest to the sensors surface to lightest for furthest from the sensors surface. B) 100 nM wtSLO on SiO<sub>2</sub> with an eggPC:Chol (50:50) bilayer,  $\Delta f$  is plotted as solid line and  $\Delta D$  plotted as dotted

## SLO pore formation characterised by QCM-D

lines. Different harmonics are represented as per panel (A). C) WtSLO binding to eggPC:Chol overlays the Langmuir Isotherm model of absorption. Experimental data for 300 nM wtSLO is plotted as theta ( $\theta$ ) against the Langmuir Isotherm absorption model over time. D) AFM image of 100 nM wtSLO on SiO<sub>2</sub> eggPC:Chol (50:50) taken from the QCM-D flow cell. E) AFM image, conditions as in (D), smaller scan from a different experiment. Interlocking incomplete pores are indicated by the white arrow head, full pores are located either side of the asterisk.

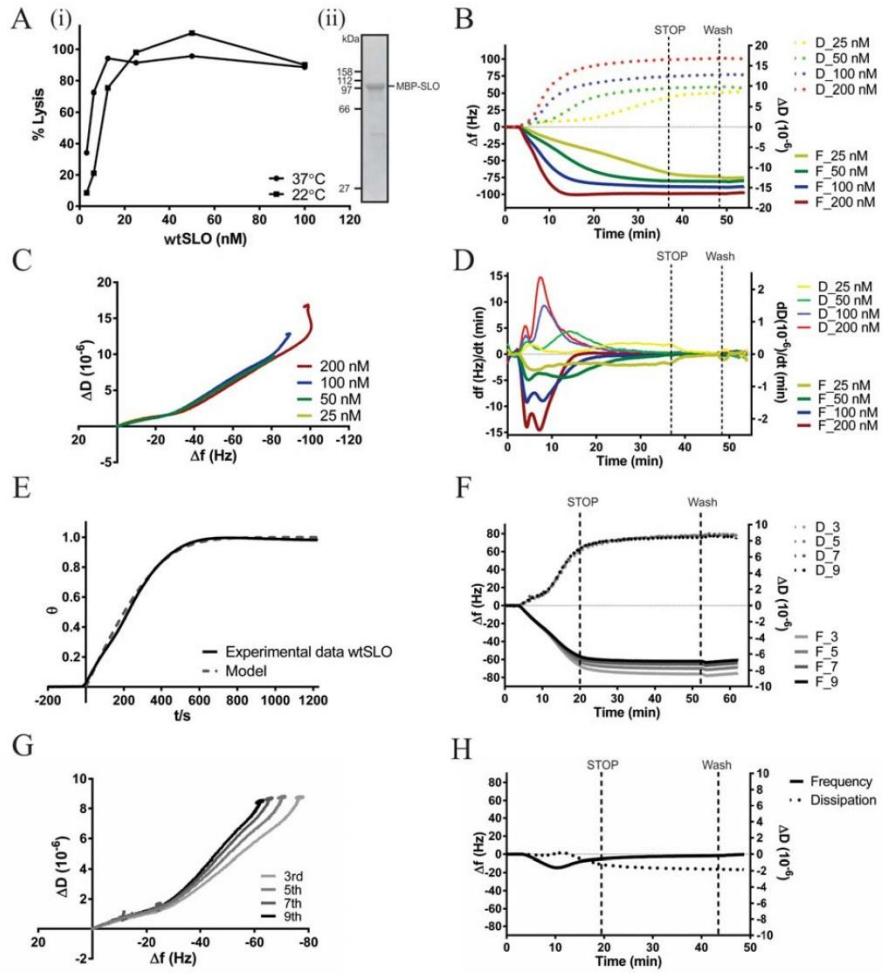
**FIGURE 4.** Effect of monomer locked SLO binding assessed by QCM-D. A)(i) sRBC lysis assay of increasing concentrations of reduced (red) and non-reduced (blue) disulfide locked monomer mutant SLO (dsmSLO). (ii) Purified dsmSLO (2  $\mu$ g) resolved by SDS-PAGE. B) QCM-D trace on Au-MPA with a DMPC:Chol bilayer of 100 nM wtSLO pre-treated with DTT (dark red) and 100 nM untreated wtSLO (black).  $\Delta f$  (solid lines) is plotted on the left axis and  $\Delta D$  (broken lines) is plotted on the right. C) QCM-D trace on Au-MPA with a DMPC:Chol bilayer of 100 nM dsmSLO pre-treated with DTT (red) and 100 nM untreated dsmSLO (blue), plotted as per panel (B). D)  $\Delta f$ - $\Delta D$  signature trace of wtSLO (black), reduced wtSLO (dark red), dsmSLO (blue) and reduced dsmSLO (red). Data from panels (B) and (C) are replotted as  $\Delta f$  on the x-axis versus  $\Delta D$  on the y-axis. E) The first derivative of the dsmSLO (blue), reduced dsmSLO (red) and wtSLO (black) functions for frequency and dissipation plotted in (B and C).  $df(\text{Hz})/dt$  (min) is plotted on the left hand side with the function in darker colours and  $dD(10^{-6})/dt$  (min) plotted on the right in lighter colours. F) QCM-D trace of 100 nM dsmSLO reduced (red) and non-reduced (blue) on SiO<sub>2</sub> sensors with an eggPC:Chol bilayer.  $\Delta f$  and  $\Delta D$  plotted as per panel (B). G)  $\Delta f$ - $\Delta D$  signature trace for 100 nM reduced (red) and non-reduced (blue) dsmSLO on SiO<sub>2</sub> with an eggPC:Chol bilayer, plotted as per panel (F).

**FIGURE 5.** Pre-pore locking SLO changes the QCM-D signature similarly to monomer locked SLO. A)(i) sRBC lysis assay with increasing concentrations of wtSLO (black) and ppSLO (green). (ii) ppSLO (2  $\mu$ g) resolved by SDS-PAGE. B) QCM-D trace on Au-MPA with a DMPC:Chol bilayer of 100 nM each of ppSLO (green) and wtSLO (black).  $\Delta f$  (solid lines) is plotted on the left axis and  $\Delta D$  (broken lines) is plotted on the right. C)  $\Delta f$ - $\Delta D$  signature trace of wtSLO (black) and ppSLO (green). Data from panel (B) replotted as  $\Delta f$  on the x-axis versus  $\Delta D$  on the y-axis. D) The first derivative of the ppSLO (green) and wtSLO (black) functions for frequency and dissipation plotted in (B and C).  $df(\text{Hz})/dt$  (min) is plotted on the left hand side with the function in darker colours and  $dD(10^{-6})/dt$  (min) plotted on the right in lighter colours. E) The ppSLO binding rate overlays the Langmuir Isotherm model of absorption. Data from panel (B) for 100 nM ppSLO is plotted as theta ( $\theta$ ) against the Langmuir Isotherm absorption model over time. F) QCM-D trace of 100 nM wtSLO (black) and ppSLO (green) on SiO<sub>2</sub> sensors with an eggPC:Chol bilayer.  $\Delta f$  and  $\Delta D$  plotted as per panel (B). G)  $\Delta f$ - $\Delta D$  signature trace plotted as per panel (C) for wtSLO (black) and ppSLO (green) on SiO<sub>2</sub> with an eggPC:Chol bilayer, data from panel (F).

**FIGURE 6.** Model for streptolysin O pore formation. Soluble monomers bind to the membrane through cholesterol specific residues in domain 4 (green) (1. Binding). Once bound the monomer diffuses laterally to bind other membrane bound monomers to form a growing circular complex (2. Oligomerisation). At some point during oligomerisation after a subunit threshold is reached (rate limiting step), whether it be dimer, half a ring or when ring formation is complete, two bundles of helices (red) from each monomer unravel to form beta hairpins that puncture the membrane and form the walls of the pore. This is accompanied by a vertical collapse due to changes in the MACPF domain (yellow). The existence of arcs suggests that oligomerisation cannot continue once membrane insertion has occurred (3. Insertion). Under each step depicted in this pathway a corresponding QCMD  $\Delta f$ - $\Delta D$  trace is shown as well as the first derivative (both frequency and dissipation) of dsmSLO, ppSLO and wtSLO to illustrate how these steps can be distinguished through the use of mutants which halt the process at various points.

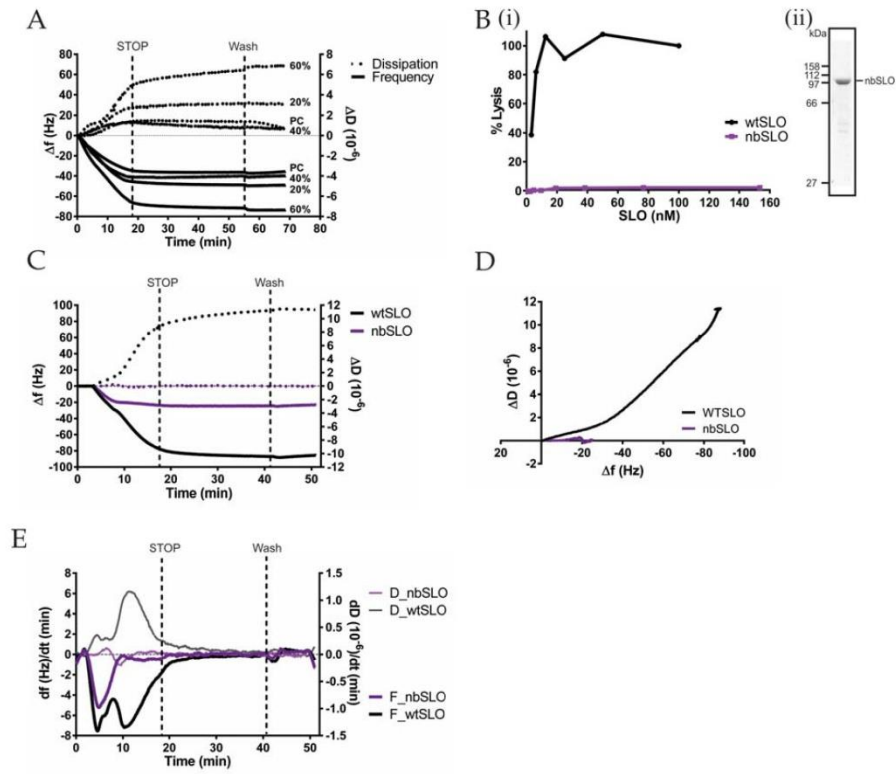
SLO pore formation characterised by QCM-D

FIGURE 1



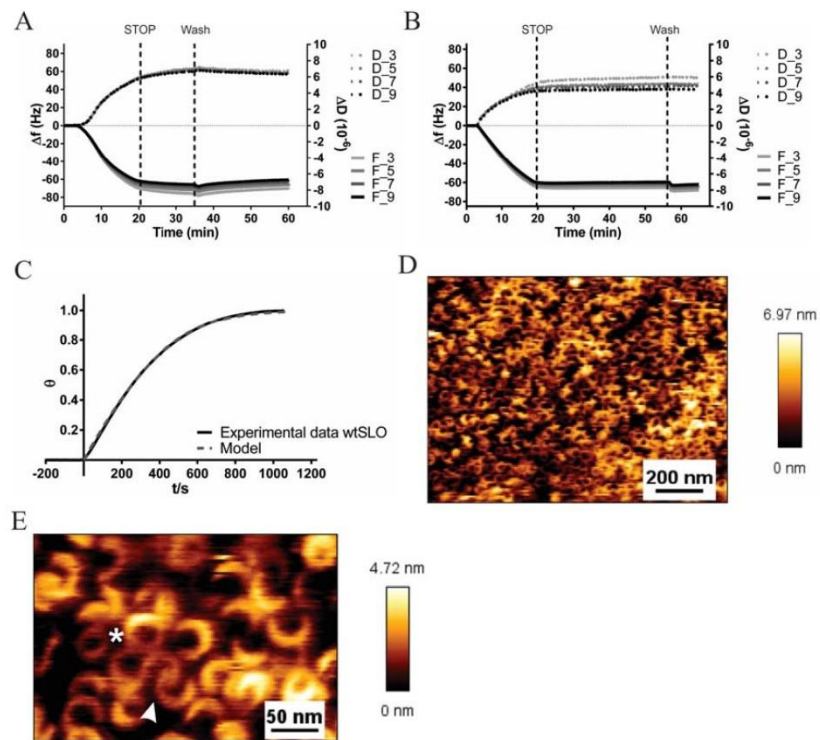
SLO pore formation characterised by QCM-D

FIGURE 2



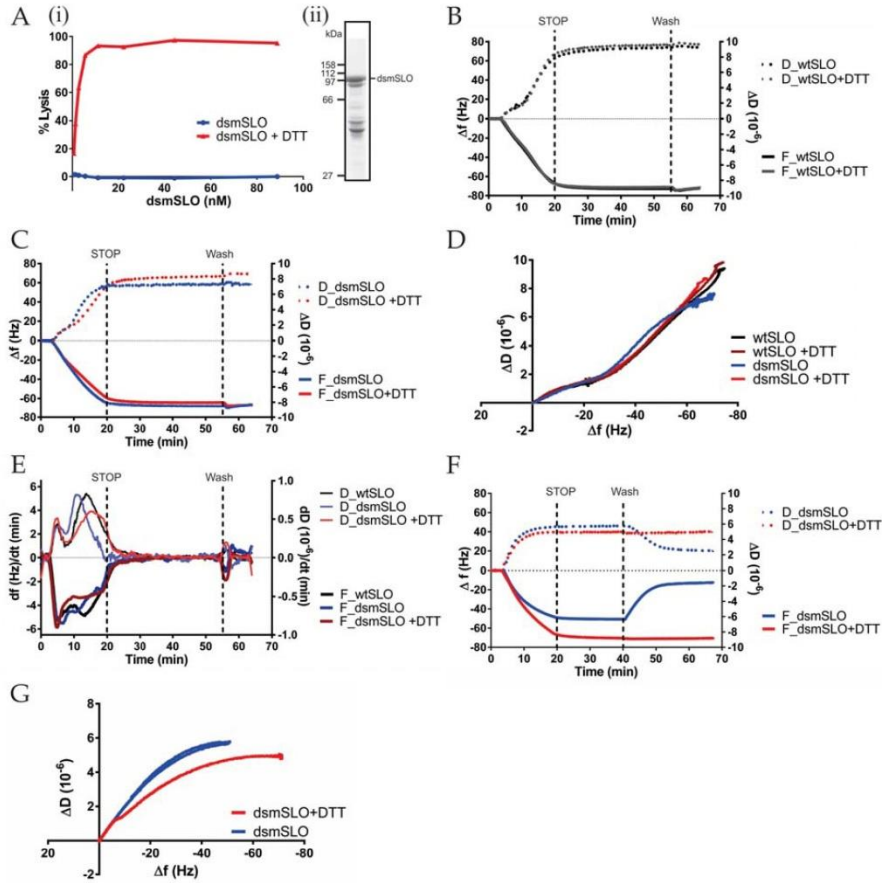
SLO pore formation characterised by QCM-D

FIGURE 3



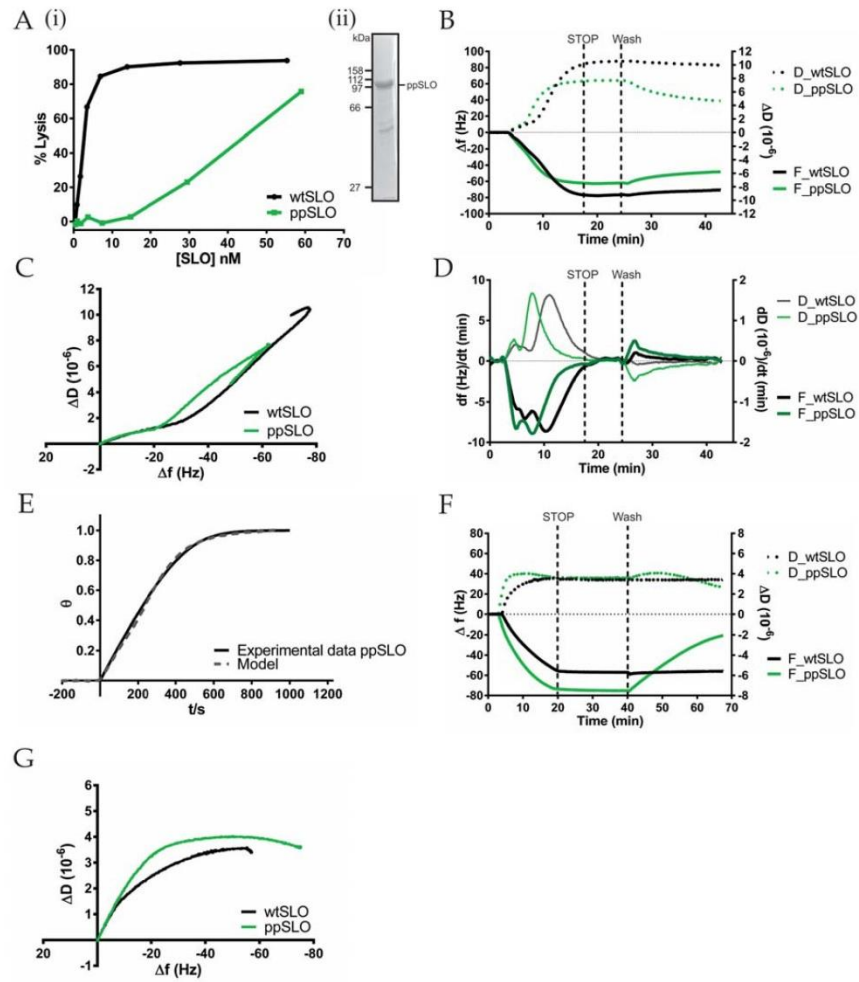
SLO pore formation characterised by QCM-D

FIGURE 4



SLO pore formation characterised by QCM-D

FIGURE 5



*Proceedings of the 32<sup>nd</sup> European Peptide Symposium*  
 George Kokotos, Violetta Constantinou-Kokotou, John Matsoukas (Editors)  
 European Peptide Society, 2012

## Binary switch activity of the Tat peptide: From membrane penetration to lytic action

Stefania Piantavigna,<sup>1</sup> Muhammad E. Abdelhamid,<sup>1</sup> Anthony P. O'Mullane,<sup>2</sup> Chuan Zhao,<sup>3</sup> Xiaohu Qu,<sup>1</sup> Bim Graham,<sup>4</sup> Leone Spiccia,<sup>1</sup> Lisandra L Martin<sup>1</sup>

<sup>1</sup>*School of Chemistry, Monash University, Clayton, Victoria 3800, Australia;* <sup>2</sup>*School of Applied Sciences, RMIT University, Melbourne, Victoria 3000, Australia;* <sup>3</sup>*School of Chemistry, The University of New South Wales, Sydney, NSW 2052, Australia;* <sup>4</sup>*Monash Institute of Pharmaceutical Sciences, Monash University, Parkville, Victoria 3052, Australia*

*E-mail: Lisa.Martin@monash.edu*

### Introduction

Cell penetrating peptides (CPP) possess the ability to cross the plasma membrane of eukaryotic cells. Among these peptides, the Tat peptide has been subject to intensive studies [1]. The amino acid sequence of Tat includes the basic RNA-binding domain of the HIV-1 Tat protein (YGRKKRRQRRR) that is responsible for its translocation across the cell membrane [2]. However, the mechanism by which these CPP enter the cell still remains unclear.

Quartz Crystal Microbalance with Dissipation monitoring (QCM-D) has been employed to elucidate the mechanism in which the Tat (44-57 and 49-57) peptides (Ac-GISYGRKKRRQRRR-NH<sub>2</sub> and Ac-RKKRRQRRR-NH<sub>2</sub>) interact with supported lipid bilayers (SLBs) [3]. The artificial membrane can be composed to mimic either eukaryotic or prokaryotic plasma membranes. In addition, Scanning Electrochemical Microscopy (SECM) was employed to measure changes in the permeability of the membrane to a redox active mediator hence, report on the interaction of these Tat peptides.

### Results and Discussion

Typically, the QCM technique monitors the temporal variation in frequency ( $\Delta f$ ) and in Dissipation ( $\Delta D$ ), in real time. These parameters correlate with the changes in mass and viscoelasticity due to binding events [4]. In this case, the Tat peptides bind to a membrane coated layer, which consists of 6-mercaptohexanoic acid (MHA) modified gold sensor. In the presence of DMPC/Cholesterol (7:3 v/v) bilayer, an eukaryotic mimetic membrane, Tat (49-57) (10  $\mu$ M) bound to the membrane (Fig.1a, black line). This appears to be a trans-membrane insertion as the mass uptake is similar for a series of harmonics  $n = 3, 5, 7$  and  $9$ , where every harmonic probes various depths within the membrane layer (data not shown). In contrast, using the DMPC/DMPG (2:1 v/v), a prokaryotic mimetic membrane, a two stage process occurs; the Tat peptides insert into the membrane followed by a rapid removal of lipid (Fig. 1a, grey line). The same behavior was observed also for Tat (44-57).

Fig. 1b and c show the SECM approach curves revealing the change in the permeability of the various membrane layers measured with a Pt microelectrode of 10  $\mu$ m diameter. The

effect of the interaction with the Tat peptides is shown as an increase in permeability of the  $[\text{Fe}(\text{CN})_6]^{3-/4-}$  redox-active mediator. In Fig. 1b and c approach curves correspond to: *i.* the theoretical conducting response, *ii.* the theoretical insulating response, *iii.* MHA on gold surface, *iv.* lipid layer on MHA, *v.* after the addition of Tat (44-57) 10  $\mu\text{M}$  on the lipid layer. Similar SECM data were observed for Tat (49-57).

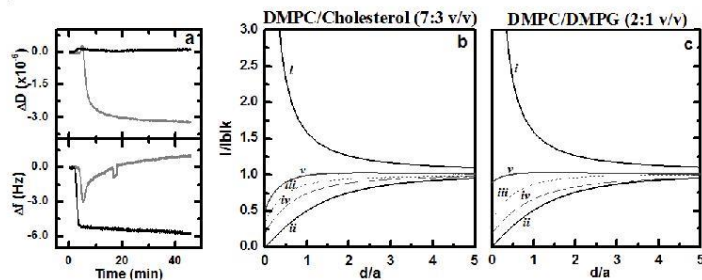


**Figure 4:** (a) QCM traces of Tat (49-57) and (b and c) SECM approach curves of Tat (44-57) interacting with biomimetic membrane.

In summary, the combination of QCM and SECM data reveals that the Tat peptides translocate across the membrane in a facile and passive way. This finding is contrary to some literature in which it is reported that the translocation of Tat peptides through the cell membrane requires active transport [5]. Of particular note in our study, it has been showed that these peptides act specifically and differently towards prokaryotic or eukaryotic biomimetic membranes.

#### Acknowledgments

The authors thank George McCubbin for discussions in the early stages of this work.

#### References

- [1] Trehin, R.; Merkle, H. P. *Eur. J. Pharm. Biopharm.* **2004**, *58* (2), 209.
- [2] Hecce, H. D.; Garcia, A. E. *Proc. Natl. Acad. Sci. USA* **2007**, *104* (52), 20805.
- [3] Piantavigna, S.; McCubbin, G.A.; Boehnke, S.; Graham, B.; Spiccia, L.; Martin, L.L. *Biochem. Acta – Biomembranes*, **2011**, *1808*(7), 1811.
- [4] Mechler, A.; Praporski, S.; Piantavigna, S.; Heaton, S. M.; Hall, K. N.; Aguilar, M.-I.; Martin, L. L. *Biomaterials* **2009**, *30* (4), 682.
- [5] Green, I.; Christison, R.; Voyce, C. J.; Bundell, K. R.; Lindsay, M. A., *Trends Pharmacol. Sci.* **2003**, *24* (5), 213.